Environmentally Assisted Cracking:

Predictive Methods for Risk Assessment and Evaluation of Materials, Equipment, and Structures

Russell D. Kane, editor

STP 1401



STP 1401

Environmentally Assisted Cracking: Predictive Methods for Risk Assessment and Evaluation of Materials, Equipment, and Structures

Russell D. Kane, editor

ASTM Stock Number: STP1401



ASTM
100 Barr Harbor Drive
PO Box C700
West Conshohocken, PA 19428-2959

Printed in the U. S. A.

Library of Congress Cataloging-in-Publication Data

Environmentally assisted cracking : predictive methods for risk assessment and evaluation of materials, equipment, and structures / Russell D. Kane, editor.
p. cm. — (STP; 1401)
"ASTM stock number: STP1401"
Proceedings of a symposium held Nov. 13–15, 2000, Orlando, Fla.
Includes bibliographical references.
ISBN 0-8031-2874-6
1. Metals—Stress corrosion—Testing—Congresses. 2. Metals—Hydrogen embrittlement—Congresses. 3. Risk assessment—Congresses. I. Kane, R. D., 1949– II. ASTM special technical publication; 1401.

TA462 .E66 2000
620.1'623—dc21

00-061817

Copyright © 2000 AMERICAN SOCIETY FOR TESTING AND MATERIALS, West Conshohocken, PA. All rights reserved. This material may not be reproduced or copied, in whole or in part, in any printed, mechanical, electronic, film, or other distribution and storage media, without the written consent of the publisher.

Photocopy Rights

Authorization to photocopy items for internal, personal, or educational classroom use, or the internal, personal, or educational classroom use of specific clients, is granted by the American Society for Testing and Materials (ASTM) provided that the appropriate fee is paid to the Copyright Clearance Center, 222 Rosewood Drive, Danvers, MA 01923; Tel: 978-750-8400; online: http://www.copyright.com/.

Peer Review Policy

Each paper published in this volume was evaluated by two peer reviewers and the editor. The authors addressed all of the reviewers' comments to the satisfaction of both the technical editor(s) and the ASTM Committee on Publications.

To make technical information available as quickly as possible, the peer-reviewed papers in this publication were prepared "camera-ready" as submitted by the authors.

The quality of the papers in this publication reflects not only the obvious efforts of the authors and the technical editor(s), but also the work of the peer reviewers. In keeping with long-standing publication practices, ASTM maintains the anonymity of the peer reviewers. The ASTM Committee on Publications acknowledges with appreciation their dedication and contribution to time and effort on behalf of ASTM.

Printed in Philadelphia, PA
October 2000

Foreword

This publication, *Environmentally Assisted Cracking: Predictive Methods for Risk Assessment and Evaluation of Materials, Equipment, and Structures,* contains papers presented at the symposium of the same name held in Orlando, Florida, on 13–15 November 2000. ASTM Committee G01 on Corrosion of Metals and the G01.06 subcommittee on Environmentally Assisted Cracking in cooperation with NACE International, The Materials Properties Council (MPC), Inc., The Materials Technology Institute of the Chemical Process Industries (CPI), European Structural Integrity Society (ESIS), and The Electric Power Research Institute (EPRI) sponsored the symposium. The symposium chairman was Russell D. Kane, *InterCorr* International, Inc.

Contents

Overview vii

KEYNOTE PRESENTATION

Material Aging and Reliability of Engineered Systems—R. P. WEI 003

PLENARY PROGRAM—I

Issues in Modeling of Environment Assisted Cracking—A. TURNBULL 023

Environment-Assisted Intergranular Cracking: Factors that Promote Crack Path Connectivity—J. R. SCULLY 040

Micromechanical Modeling of Hydrogen Transport—A Review—P. SOFRONIS AND A. TAHA 070

Strain Rate Dependent Environment Assisted Cracking of α/β-Ti Alloys in Chloride Solution—E. RICHEY III AND R. P. GANGLOFF 104

PLENARY PROGRAM—II

Framework for Predicting Stress Corrosion Cracking—R. W. STAEHLE 131

Deterministic Prediction of Localized Corrosion Damage in Power Plant Coolant Circuits—D. D. MACDONALD AND G. R. ENGELHARDT 166

EPRI SPONSORED SESSION—PREDICTION OF IASCC PERFORMANCE IN REACTOR COOLING WATER SYSTEMS

Status of JAERI Material Performance Database (JMPD) and Its Use for Analyses of Aqueous Environmentally Assisted Cracking Data—Y. KAJI, T. TSUKADA, Y. MIWA, H. TSUJI, AND H. NAKAJIMA 191

An Analysis of Baffle/Former Bolt Cracking in French PWRs—P. M. SCOTT, M.-C. MEUNIER, D. DEYDIER, S. SILVESTRE, AND A. TRENTY 210

Improvement of IASCC Resistance for Austenitic Stainless Steels in PWR Environment—T. YONEZAWA, K. FUJIMOTO, T. IWAMURA, AND S. NISHIDA 224

NACE SPONSORED SESSION—UNDERSTANDING AND PREDICTING EAC PERFORMANCE IN INDUSTRIAL APPLICATIONS

Prediction of Conditions Leading to Stress Corrosion Cracking of Gas Transmission Lines—N. SRIDHAR, D. S. DUNN, AND A. ANDERKO 241

Considerations in Using Laboratory Test Data as an Indicator of Field Performance: Stress Corrosion Cracking—R. H. JONES 259

Effects of Environmental Factors and Potential on Stress Corrosion Cracking of Fe-Ni-Cr-Mo Alloys in Chloride Solutions—Y.-M. PAN, D. S. DUNN, AND G. A. CRAGNOLINO 273

Environmentally Assisted Cracking in the Chemical Process Industry. Stress Corrosion Cracking of Iron, Nickel, and Cobalt Based Alloys in Chloride and Wet HF Services—R. B. REBAK 289

ESIS SPONSORED SESSION—EAC TESTING AND IN-SERVICE EXPERIENCES

Hydrogen Embrittlement - Loading Rate Effects in Fracture Mechanics Testing—R. W. J. KOERS, A. H. M. KROM, AND A. BAKKER 303

Standardization of Rising Load/Rising Displacement SCC Testing—W. DIETZEL 317

RESEARCH SESSION—MECHANISTIC STUDIES FOR UNDERSTANDING AND CONTROL OF EAC

Role of Cyclic Pre-Loading in Hydrogen Assisted Cracking—J. TORIBIO AND V. KHARIN 329

Improvement of Stress-Corrosion Cracking (SCC) Resistance by Cyclic Pre-Straining in FCC Materials—I. DE CURIERE, B. BAYLE, AND T. MAGNIN 343

Influence of Surface Films and Adsoption of Chloride Ions on SCC of Austenitic Stainless Steels in 0.75M HCI at Room Temperature—P. H. CHOU, R. ETIEN, AND T. M. DEVINE 352

Toward a More Rational Taxonomy For Environmentally Induced Cracking—P. F. ELLIS II, R. E. MUNSON, AND J. CAMERON 363

Environmentally Influenced Near-Threshold Fatigue Crack Growth in 7075-T651 Aluminum Alloy—E. U. LEE, H. C. SANDERS, K. GEORGE, AND V. V. AGARWALA 382

The Use of Atomic Force Microscopy to Detect Nucleation Sites of Stress Corrosion Cracking in Type 304 Stainless Steel—M. P. H. BRONGERS, G. H. KOCH, AND A. K. AGRAWAL 394

An Electrochemical Film-Rupture Model for SCC of Mild Steel in Phosphate Environment—R. RAICHEFF AND L. MALDONADO 411

INDUSTRIAL SESSION—ENGINEERING APPLICATIONS FOR NEW EXPERIMENTAL AND ANALYTICAL METHODS

Cyclic Strain Cracking of Stainless Steels in Hot Steam-Hydrocarbon Reformer Condensates: Test Method Development—S. W. DEAN, J. G. MALDONADO, AND R. D. KANE 429

Environmentally Assisted Cracking of Cold Drawn Eutectoid Steel for Civil Engineering Structures—J. TORIBIO AND E. OVEJERO 444

Premature Failures of Copper Alloy Valves and Fittings in the New York City Water Supply System—G. A. ANDERSEN 458

Stress Corrosion Cracking of Linepipe Steels in Near-Neutral pH Environment: A Review of the Effects of Stress—W. ZHENG, R. SUTHERBY, R. W. REVIE, W. R. TYSON, AND G. SHEN 473

Indexes 485

Overview

For over 40 years ASTM Committee G01 on Corrosion of Metals has been a leading resource on the influence of corrosion on metals and engineering alloys. In keeping with this tradition, its subcommittee G01.06 on Environmentally Assisted Cracking-(EAC) sponsored a major international symposium entitled **"Environmentally Assisted Cracking: Predictive Methods for Risk Assessment and Evaluation of Materials, Equipment, and Structures"** held November 13–15, 2000 in Orlando, Florida. This symposium was a major technical event with participation from major industrial corporations and research, government and academic organizations from around the world. Organizations co-sponsoring the symposium included:

- NACE International
- The Materials Properties Council, Inc.
- The Materials Technology Institute of the Chemical Process Industries
- European Structural Integrity Society
- The Electric Power Research Institute

Several of these co-sponsor organizations assisted by organizing featured sessions, which focused on specific topics of interest.

Background

In recent years, there has been an increased interest in prevention of stress corrosion cracking failures based on assessment of materials compatibility and prediction of operational risk. This has resulted in:

- Improved mechanistic understandings of EAC (i.e. stress corrosion cracking, hydrogen embrittlement cracking, liquid metal embrittlement, corrosion fatigue).
- Development of better predictive models for crack initiation and growth and analytical methods for assessment of the impact of corrosion induced damage on structural integrity.
- Generation of material data bases under simulated service conditions to identify and assess critical parameters
- Development of new methods for electrochemical monitoring and interpretation of data.
- Enhanced non-destructive inspection capabilities with increased reliability for detection of AEC-induced damage

The goal of this international symposium was to address two important areas of EAC investigation:

1. recent developments in the generation of relevant materials properties data based on laboratory tests, and
2. methodologies for evaluation and assessment of environmental assisted cracking in equipment and structures exposed to corrosive environments.

The symposium also was developed with the aim of highlighting a broad range of industrial and civil applications including marine, aerospace, chemical, petroleum, electric power, consumer prod-

ucts, and public infrastructure. Additionally, it provided a global forum through which a sharing of state-of-the-art ideas and concepts could be transformed into cost-effective solutions. The papers in the symposium included topics related to:

- Uses of electrochemical, surface analysis, slow strain rate, and fracture mechanics techniques.
- Correlation between laboratory and in-service cracking resistance
- State-of the art developments in fitness-for-service and risk assessment methodologies
- Monitoring of equipment and structure for environmentally assisted cracking

The theme for the symposium was developed to be of high interest to those involved in materials engineering, corrosion science, as well as many specialists involved in maintaining and monitoring the ongoing reliability of plant equipment, structures, and end-user products. One of the greatest features of the technical program was the combined focus on both theoretical and applied topics in the same forum. A specific effort was made to make sure that the keynote and plenary program included the foremost scientists in corrosion and material science. Their mission was to present the forefront of modern day thinking as it relates to mechanistic and predictive models for understanding EAC and materials performance. These presentations were followed by those from academics, researchers, and industrial practitioners illustrating new and more quantitative methodologies for the assessment of materials, equipment, and structures. This publication will serve as a fine reference for specialists and general practitioners alike that want to utilize the most current methodologies for prediction and assessment of materials performance and system reliability with respect to damage caused by EAC.

Keynote and Plenary Session

The symposium was started with an extensive keynote and plenary program entitled **"EAC Models—Theory to Practice"** that ran most of the first day of the symposium. The theme of the symposium was illustrated in the first presentation by Prof. Robert Wei entitled, "Material Aging and Reliability of Engineered Systems." His paper focused on a supreme challenge faced by both researchers and engineers when addressing "real" systems. These challenges include the addressing of the changing properties of materials as the materials age in service, and the even more demanding aspects of assessing system integrity in the face of these changing properties and changing usage. Following the keynote presentation, A. Turnbull, J. Scully, P. Sofronis and R. Gangloff reviewed the state-of-the-art methodologies for dealing with hydrogen transport, strain rate and crack morphology in current day EAC models. The plenary program was completed with presentations by R. Staehle and D. Macdonald. These presentations address a major industrial challenge: Implementation of these models on a broad scale for management of practical industrial problems that have very large economic consequences. Examples are given for electric power systems, which can also be extended to many other plant and field scenarios, as well.

Featured Co-Sponsor Session Papers

Three featured sessions were organized by symposium co-sponsors. These included sessions by the Electric Power Research Institute (EPRI), NACE International and European Structural Integrity Society (ESIS). These papers primarily address practical industry problems associated with EAC and the use of fitness-for-purpose and risk-based inspection (RBI) methodologies to better manage plant assets for long term service.

- **EPRI Session—Prediction of IASCC Performance in Reactor Cooling Water Systems.** Three papers were included in this session. Kaji et al. discussed a 14 year data analysis effort including information on irradiation assisted stress corrosion cracking (IASCC). This study assessed the role of alloy composition, dissolved oxygen in the cooling water, and neutron flux as major variable in IASCC performance of stainless steels. Scott et al. also focused on IASCC but through a statistical analysis of plant observations of baffle/former bolts in French reactors. The data served as the basis for decision making concerning inspection frequency, possible replacement of cracked bolts and selection of alternative alloys. Yonezawa et al. emphasized the understanding of alloying and segregation in the prediction of IASCC performance. Alternative materials were investigated with controlled alloying and metallurgical processing to enhance IASCC resistance.
- **NACE Session—Understanding and Predicting EAC Performance in Industrial Applications.** Four papers were included in this session. Sridhar et al. focused on predicting stress corrosion cracking (SCC) performance of gas transmission lines and included information on SCC occurring in both alkaline and near-neutral conditions. The use of thermodynamic models to relate SCC tendencies and water composition in crevices was examined. Jones addressed the basis of laboratory testing to assess field SCC performance and identifies some of the present day limitations in merely conducting routine SCC tests, and the need for lab-field correlations to assist in predicting service performance. Pan et al. examined the role of chlorides in hot aqueous solutions and the relationship between SCC and the pitting potential in AISI 316L stainless steels. Rebak presented a summary of SCC performance in chemical process environments containing chloride and HF based on laboratory testing and failure analysis.
- **ESIS Session—EAC Testing and In-Service Experiences.** Two papers were presented in this session. Koers et al. related experiences in petroleum applications using fitness-for-purpose methodologies and the requirements for fracture data involving the influence of hydrogen and loading rate on pressure vessel steels. Dietzel describes an intensive effort to standardize rising load/rising displacement fracture tests using precracked specimens. This technique has great potential for accelerated testing.

Research Session: Mechanistic Studies for Understanding and Control of EAC

Following the featured co-sponsor sessions, a session containing the results of somewhat more fundamental studies was held. These investigations utilized new analysis techniques and approaches to reveal various aspects of EAC in engineering alloys. Seven papers were presented. Toribio and Kharin examined the role of cyclic preloading on hydrogen assisted cracking of carbon steel. de Curiere et al. also relates the effects of cyclic pre-straining through corrosion/ plasticity interactions at the crack tip, but this time involving SCC of stainless steel. Numerical modeling of localized stresses and hydrogen diffusion was used show that residual stress distributions as affected by preloading cycles influenced hydrogen accumulation at fractures sites. Brongers et al. described a method for in-situ atomic force microscopy study for use in locating initiation sites for EAC. Chou et al. used Raman spectroscopy to investigate surface films on stainless steels in acidic and chloride-containing media, and their relationship to EAC susceptibility. Ellis et al. proposed a more systematic nomenclature (taxonomy) to reduce confusion when referring to the various forms of EAC. Lee et al. described a study of near threshold fatigue crack growth in an aluminum alloy in air, vacuum and a NaCl solution. Raicheff and Maldonado used SEM, X-ray and Mossbauer analysis techniques to examine the surface films and their relationship to SCC of steel in phosphate solution. Modeling was used to establish crack propagation rates and conditions favorable for SCC.

Industrial Session: Engineering Applications for New Experimental and Analytical Methods

A total of four papers were presented which look at a wide range of practical plant and field problems and approaches used to assess the extent of the problem and prescribe solutions. Dean et al. utilized a cyclic slow strain rate technique for laboratory simulation of an EAC situation in a hot steam hydrocarbon reformer. Data was developed that assisted in the evaluation of conditions particularly conductive to in-service cracking, and for evaluation of alternative materials of construction. Toribio and Ovejero examined the EAC of cold drawing steel used in prestressed concrete structures. Resistance to cracking in $Ca(OH)_2$ solution increased with the amount of cold drawing based on time to failure alone; however, based on fracture load, an optimum (intermediate) amount of drawing was observed. Andersen described premature EAC failures in copper alloy valves in a major city water supply system, and efforts to simulate the failures in the laboratory. Alternative materials were identified through laboratory testing which yielded greater resistance to EAC and increased system reliability. Zheng et al. focused on external SCC in pipeline steels in near neutral pH solutions. Laboratory tests were used to examine the role of mean stress and cyclic stress on susceptibility to cracking. Full-scale pipe tests also showed the beneficial effect of hydrostatic pressure and resultant compressive residual stress on resistance to cracking.

Acknowledgements

As symposium chairman, I hope that this STP benefits both researchers and engineers, alike. The authors of the papers contained herein have worked diligently, and in some cases, dedicated their careers to advancing corrosion science, solving important and challenging problems, increasing the reliability of operating equipment, and minimizing economy losses and loss of life resulting from EAC failures. I would like to thank them for their contributions to this volume and personally acknowledge their personal and professional efforts in this regard. Additionally, I wish to greatfully thank the ASTM staff that has worked so hard to make this publication a reality.

Dr. Russell D. Kane
InterCorr International, Inc.
14503 Bammell N. Houston Road
Suite 300
Houston, Texas 77014
Email:rdk@intercorr.com
Symposium Chairman and Editor

Keynote Presentation

Robert P. Wei[1]

Material Aging and Reliability of Engineered Systems

Reference: Wei, R. P., **"Material Aging and Reliability of Engineered Systems,"** *Environmentally Assisted Cracking: Predictive Methods for Risk Assessment and Evaluation of Materials, Equipment, and Structures, ASTM STP 1401*, R. D. Kane, Ed., American Society for Testing and Materials, West Conshohocken, PA, 2000.

Abstract: Material aging is a principal cause for the aging of engineered systems that can lead to reductions in their reliability and continued safety, and increases in the costs of operation and sustainment. To meet the challenges of designing systems for a competitive global market and of ensuring their reliability and continued safety, a new paradigm for design is needed to quantitatively integrate materials aging into the processes of design, reliability assessment and life-cycle management planning. In this paper, a multidisciplinary, mechanistically based probability approach is reviewed as a framework for this new design paradigm. The efficacy and value of this approach is demonstrated through an example on the aging of aluminum alloys used in aircraft construction that showed the feasibility of using a simplified model to predict the distribution in damage in transport aircraft that had been in long-term commercial service. The need and directions for further research are discussed.

Keywords: material aging, life prediction, life-cycle management, mechanisms, probability, modeling, mechanistically based probability model, corrosion, pitting, fracture mechanics, fatigue crack growth.

Introduction

Material aging is a principal cause for the aging of engineered systems and the associated reduction in their reliability and margin of safety. This process impacts not only the reliability and continued safety but also the costs of operation and sustainment of these systems. It is of particular concern for those that affect the efficient functioning of a modern technologically oriented society. Currently, experientially and statistically based design methodologies and accelerated life testing are largely used to assess the impact of aging, and the findings are reflected in the so-called *design service objectives (DSO)* and planned sustainment programs. Operational experiences suggest, however, that more mechanistically based probability methodologies are needed to meet the challenges of designing for the increasingly competitive global market, both technologically and financially. In essence, a new design paradigm needs to be developed to balance the initial capital investments against the cost of operations; *i.e.*, to estimate and optimize the life-cycle cost or cost of ownership at the design stage. Such methodologies are needed

[1] Paul B. Reinhold Professor, Department of Mechanical Engineering and Mechanics, Lehigh University, 327 Sinclair Laboratory, 7 Asa Drive, Bethlehem, PA, 18015

Copyright© 2000 by ASTM International www.astm.org

as well to ensure the reliability and continued safety of aging systems that remain in service well beyond their original DSO.

In this paper, a multidisciplinary, mechanistically based probability approach for life estimation is reviewed and is proposed as a framework for life-cycle design and sustainment planning, and for the supporting research. The efficacy and value of this approach is demonstrated through an example on aging of aluminum alloys that connects scientific research and mechanistically based probability modeling with tear-down inspection data from transport aircraft that had been in long-term commercial service. The need and directions for future research to broaden and incorporate this approach into a new paradigm for design of engineered systems are discussed.

A Contextual Framework

To provide a contextual framework for the mechanistically based probability approach for life estimation, a simplified flow diagram is given in Figure 1 to depict the requisite new paradigm for design. The principal elements are grouped into four categories: Design, Manufacturing, Operations, and Disposal or Recycle, with life estimation imbedded as a key component in Operations. For simplicity, the initial capital investment is assigned to Design and Manufacturing. The costs of operation and sustainment (*e.g.*, maintenance and repairs), as well as loss of use, are included in Operations. The costs associated with retirement of the system are embedded in Disposal or Recycling. The overall goal is to optimize the life cycle cost, or the cost of ownership, of the engineered system, vis-à-vis separately optimizing each of the elements in Figure 1, with due consideration for the reliability and safety of the system and societal concerns. The process of optimization requires quantitative models that functionally represent each of the elements in Figure 1, both in terms of the engineering and scientific issues and that of cost, as well as a complete integration of these elements.

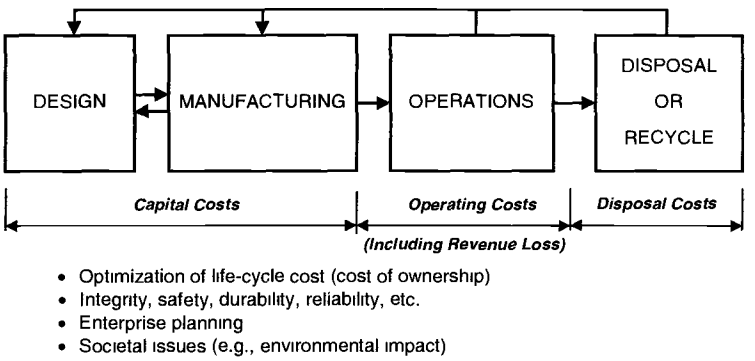


Figure 1 – *A new design paradigm: contextual framework and simplified flow diagram.*

Consideration here will be focused on the operations perspective, in particular, assessments of the impact of materials aging on the reliability and continued safety, and

the availability and sustainment planning (and enterprise planning, in a broader context) of engineered systems. For these assessments, a structured framework is needed and is depicted by the schematic flow diagram in Figure 2. The materials aging process (*i.e.*, system wear and tear) is reflected in the evolution of some form of *damage* that compromises *safety* or *function*. The key issues relate, therefore, to assessments of the reliability and safety of an engineered system under given sets of operating conditions, given by the forcing functions and environmental conditions, in relation to its '***current state***' or its '***initial state***' (either new or after major maintenance) and its '***future state***'. Such assessments are typically made through the use of a comprehensive set of diagnostic or nondestructive evaluation (NDE) tools and supporting (*e.g.*, structural) analysis tools. The NDE tools are used to ascertain the current damage-state of the system. Based on this information, the set of supporting analysis tools are then used to judge its reliability and safety in the current state.

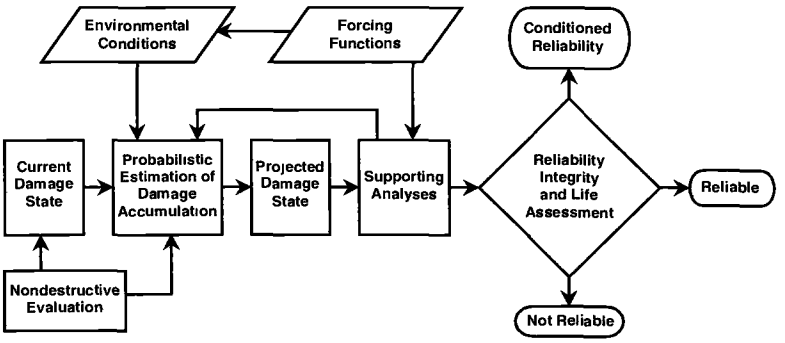


Figure 2 – *Schematic flow diagram for reliability and safety assessments and sustainment planning.*

Assurance of reliability and continued safety requires more importantly, however, an assessment of the system in its '***projected future state***'. As such, a quantitative method is needed for estimating the accumulation of damage over its projected period of operation, and for assuring the reliability and safety of the system over this projected period. The outcome of this assessment then serves as the basis for certification and approval of *continued operation* as reflected in Figure 2 by the labels *Reliable, Conditioned Reliability and Not Reliable.* A system that is judged to be reliable would be approved for unrestricted operation until the next maintenance cycle, and those with conditioned reliability would be constrained by restrictions on operations. A system that is deemed to be unreliable would be sent for maintenance and repair, or be retired. The frequency and duration of maintenance determine system reliability and availability, and contribute to the overall cost of operations; they reflect choices made in design and manufacturing, and must be reconciled through a structured optimization process in the new design paradigm. The process labeled as *Probabilistic Estimation of Damage Accumulation* in Figure 2 is a key element of this process, and requires the development of methods that are *predictive* and that can provide accurate estimates of the evolution and probabilistic distribution in damage over time (*i.e.*, methods for service life prediction).

A Mechanistically Based Probability Approach

A mechanistically based probability approach for damage evolution and life prediction is proposed and has been described in detail elsewhere [*1,2*]. The essence of the approach is to develop a time-dependent damage function $D(x_i,y_i,t)$ that incorporates all of the key *internal* (x_i; *e.g.*, materials) and *external* (y_i; *e.g.*, loading) variables, and their variability. The approach is illustrated in Figure 3 for corrosion fatigue crack growth, where the damage is the crack length a, and the rate of damage evolution is given by the crack growth rate $(da/dN)_e$. The internal and external variables are those that are inside or outside of the *proverbial black box* (*i.e.*, the material-environment system), respectively.

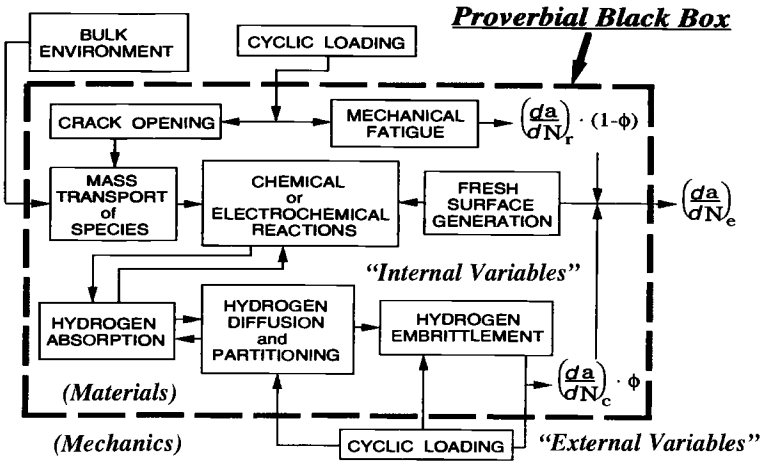


Figure 3 – *A schematic diagram of the chemical, mechanical, and microstructural processes and their interactions in corrosion fatigue crack growth.*

The development of this damage function is based on an understanding of the mechanisms of damage nucleation and growth, and requires the coordination and integration of the disciplines of fracture and solid mechanics, electrochemistry and surface chemistry, materials science, and probability and statistics. The damage function forms the basis of probability models that can provide an accurate estimate of the probabilistic distribution of damage as a function of time in service, or the distribution in service lives. The models are then incorporated into appropriate methodologies for materials and systems that can accurately *predict* performance and assess risk beyond the range of conditions covered by the supporting design data. Information derived from these methodologies is then used for reliability analysis and life-cycle management.

The traditional, experientially based statistical approaches differ from this approach in two principal aspects. Firstly, these approaches make use of parametric representations of statistical fits to the experiential data. Secondly, the *internal* variables are seldom, if ever, considered in these approaches. The resulting methodologies, therefore are

interpolative (or postdictive) rather than predictive, and cannot explicitly account for their contributions to the variability in the rates of damage evolution or service lives.

The essential elements of the modeling process and their interrelationships, using the mechanistically based probability approach, are as follows [*1*].

1. Identification of damage mechanisms.
2. Identification and characterization of key (random) variables.
   Variables – *internal* and *external*.
   Probability density function (PDF) for each of the variables.
   Independence or dependence of the variables.
3. Mechanistic (deterministic) model of damage accumulation process.
   Functional dependence on the key (random) variables.
   Validation and range of applicability.
4. Joint probability density function (JPDF).
5. Mechanistically based probability model for damage evolution and life prediction.
   Integration of JPDF with the mechanistic (deterministic) model.
   Validation (beyond the range and conditions of the supporting data).
   Revise and refine on the basis of new data or service experience.

The strength of this approach is that it is iterative, in that the model can be refined to include additional information as longer-term data and better insight become available. The approach has been applied to corrosion fatigue crack growth [*3*], corrosion and corrosion fatigue of aluminum alloys [*2,4,5*], and creep controlled crack growth [*6*]. To illustrate the efficacy of this approach, the results from studies of corrosion and corrosion fatigue of aluminum alloys are summarized here to demonstrate the feasibility of correlating *predictions*, based upon scientific understanding and short-term laboratory data, with inspection data obtained from aircraft that had been in long-term service.

Corrosion and Corrosion Fatigue of Aluminum Alloys – An Illustrative Example

Corrosion and corrosion fatigue of aluminum alloys is considered here in the context of aging of aircraft components and structures. This example provides an overall perspective for the multidisciplinary approach. It serves as a road map for the process of integrating information on damage accumulation in estimating the service life and damage distribution that are needed for structural integrity and reliability analyses, and life-cycle management. The example draws upon recent studies by the author and his colleagues at Lehigh University.

The impact of pitting corrosion on fatigue cracking has been recognized since the early 1900s [*7*]. More recent studies [*8-12*] have shown that pitting corrosion in aluminum alloys is induced by galvanic coupling of the matrix with constituent particles in the alloys to promote localized matrix dissolution. The pits, thus formed, serve as nuclei for subsequent fatigue cracking and significantly reduce the serviceable life of a component or structure. The processes of one form of aging, or damage accumulation, in airframe aluminum alloys is considered to be dominated by localized (or pitting) corrosion in the early stage, and by corrosion fatigue crack growth in the later stage (see Figure 4). Corrosion fatigue cracking would nucleate at severe corrosion pits formed at

clusters of constituent particles in the alloys. Cracking from the nucleating corrosion pits would undergo a regime of chemically short and then long crack growth. In the following subsections, brief summaries of the experimental findings on pitting and crack nucleation and growth in 2024-T3 and 7075-T6 aluminum alloys are given. A simplified probabilistic model for damage accumulation that integrates the individual processes is described, and the model predictions are compared against measured damage distributions from two aircraft that had been in long-term commercial service.

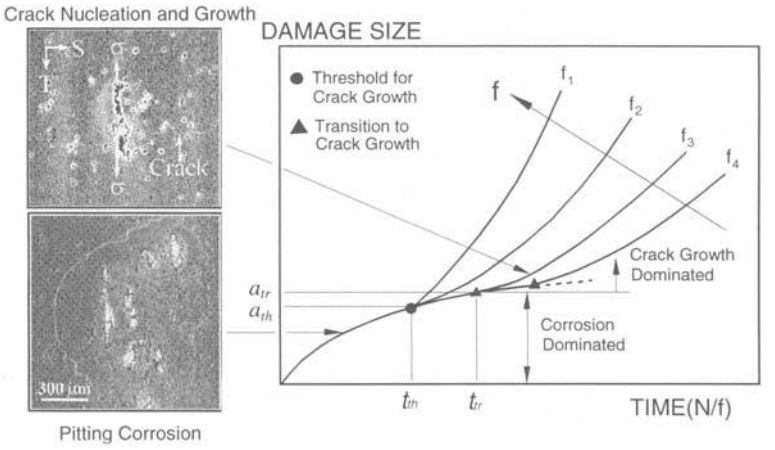


Figure 4 – *Schematic diagram of the development of corrosion and corrosion fatigue crack growth.*

Processes of Damage Evolution

Particle Induced Pitting Corrosion – Localized (pitting) corrosion in the 2024-T3 and 7075-T651 (bare) alloys in 0.5M NaCl solutions resulted from galvanic dissolution of the matrix through its coupling with constituent particles in the alloys [*8-12*]. Two modes of pitting corrosion were identified: namely, (i) *general* pitting at the surface and (ii) *severe* localized pitting at selected sites. General pitting occurred almost immediately upon exposure to the solution, and led to the formation of small, shallow pits over the entire surface [*10*]. Each pit is identified with a constituent particle on the surface (Figure 5), and the process is confirmed by transmission electron microscopy (Figure 6) [*12*]. Severe localized pitting resulted from interactions of the matrix with *a cluster or clusters* of constituent particles. The clusters form local galvanic cells to sustain continued matrix dissolution and produce larger and deeper pits. The three-dimensional nature and complex form of the severe pits are illustrated by scanning electron (SEM) micrographs of the replica of a typical *severe* pit in Figure 7 [*10,11*]. The main body of the pit is approximately 250 μm long, 150 μm wide and 150 μm deep; the actual pit opening at the surface is much smaller. The individual rounded features are consistent with galvanic corrosion of the matrix by the constituent particles in the alloy (*cf.*, Figures 5 and 7). Pitting depended strongly on temperature and solution pH. The pitting rate increased with

increasing temperature (corresponding to an activation energy of about 40 kJ/mol.), and was higher at more basic pH levels. Pitting sensitivity depended upon orientation, and was more severe in the thickness orientations because of local segregation of constituent particles.

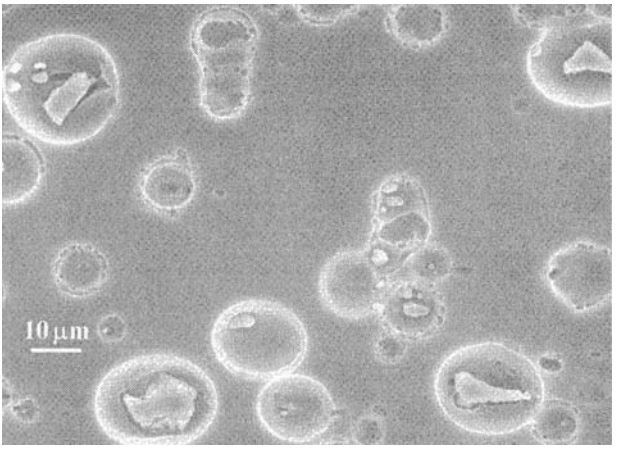


Figure 5 – *Scanning electron micrograph showing pitting induced by constituent particles in a 2024-T3 aluminum alloy.*

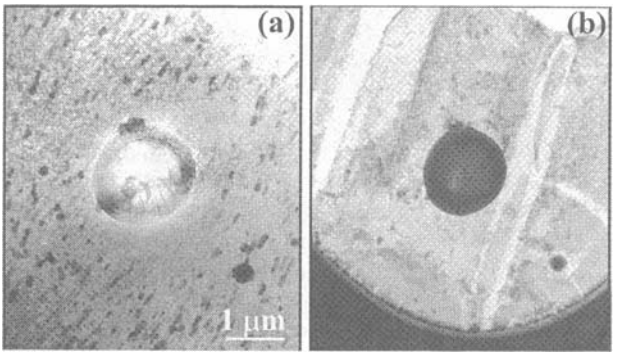


Figure 6 – *Transmission electron micrographs showing an Al_2Cu particle and its environs in a 2024-T3 aluminum alloy (a) before and (b) after (with Cu deposition on the particle) 180 min. (cumulative) immersion in 0.5m NaCl solution at room temperature.*

Fatigue Crack Nucleation (Transition from Pitting to Crack Growth) – Corrosion fatigue crack nucleation reflects the competition between pitting and fatigue crack growth, and is characterized by the transition to fatigue crack growth from a growing corrosion pit. Two criteria for this transition have been proposed and validated [*13*].

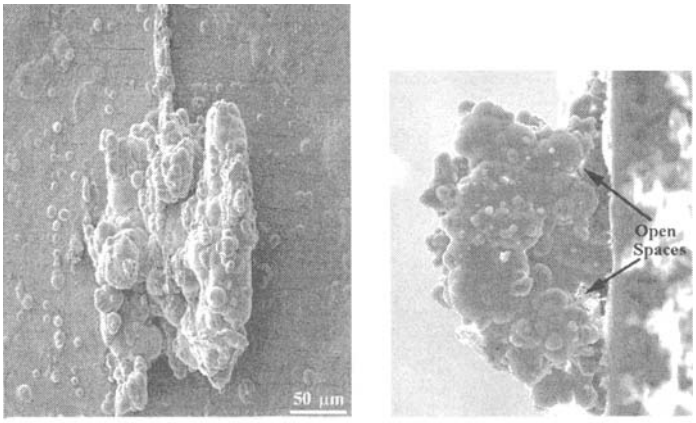


Figure 7 – *Scanning electron micrographs of the epoxy replica of a severe corrosion pit in a 2024-T3 aluminum alloy: (a) plan (bottom) and (b) elevation (side) view relative to the original pit.*

They are: (i) the cyclic stress intensity range (ΔK) for an equivalent crack must exceed the fatigue crack growth threshold ΔK_{th}, and (ii) the time-based fatigue crack growth rate must exceed the pit growth rate; *i.e.*

$$\Delta K \geq \Delta K_{th} \quad \text{and} \quad \left(\frac{da}{dt}\right)_{crack} \geq \left(\frac{da}{dt}\right)_{pit} \tag{1}$$

where a is the depth of the equivalent crack or the corresponding pit depth. (If the half-length of the equivalent crack at the surface, c, or the corresponding pit dimension is less than a, then the half-length should be used in calculating the stress intensity factor and growth rates in Eq 1. The criteria can be represented graphically in a corrosion/fatigue map to delineate the ΔK at transition (ΔK_{tr}) in relation to frequency f (see [*13*]).

Fatigue Crack Growth (Chemically Short Cracks) – Studies of the transition from pitting to corrosion fatigue crack growth (or crack nucleation) in the aluminum alloys suggested that the pit size at transition is in the range of 40 to 200 μm [*13*]. The extent of fatigue crack growth of interest, on the other hand, is on the order of a few millimeters (for example, in aircraft fuselage lap joints where the rivets are typically spaced 25.4 mm apart). As such, characterization and modeling of the early stage (or chemically short regime) of corrosion fatigue crack growth is important to the accurate and reliable assessment of the integrity of aircraft structures.

Experimental data on 2024-T3 and 7075-T651 aluminum alloy sheets in 0.5M NaCl solutions, at room temperature and 10 Hz, showed chemically short-crack growth behavior [*14,15*]. The behavior is quite complex and depended on ΔK and dissolved

oxygen concentration, as well as frequency. The effect is reflected in increased crack growth rates relative to those of a long crack, by as much as a factor of three at a crack length of 0.5 mm, at the lower ΔK levels. It decreased subsequently to the long-crack rates at crack lengths of 4 to 8 mm, depending on ΔK, and gradually disappeared at higher ΔK levels; the particular level depended on oxygen concentration. Loss of the short-crack effect is attributed to the decrease in dissolved oxygen at the crack tip with crack prolongation and the larger amount of new surfaces created by crack growth each cycle with increasing ΔK [*14,15*].

A Simplified Mechanistically Based Probability Model

To illustrate the integration of the damage processes into a mechanistically based probability framework, a simplified probability model for pitting and corrosion fatigue was formulated and is summarized here [*2,4,5*]. This model assumed pitting corrosion to predominate initially and to be at a constant volumetric rate, and the subsequent fatigue crack growth to follow a simple power-law model (see Figure 4). Clusters of particles in the alloys determine the rate and extent of pit growth, and naturally, the larger clusters lead to more severe damage. Severe pits that occur in high stress regions of components or structures are sites from which corrosion fatigue cracks nucleate and grow. The pits are assumed to be hemispherical in shape, and the cracks are assumed to begin as semi-circular surface cracks that eventually transition into through-the-thickness cracks. Most of the principal features of the damage process are included in this model. Randomness associated with material properties and their sensitivity to the environment are represented explicitly. The random variable (*rv*) of interest is the size of the damage as a function of time. For this illustration, localized damage is described by a single variable; *i.e.*, the pit depth, a, during pitting and the crack depth, or length, a, during fatigue cracking. The model may be used to assess the impact of corrosion on service life, the probability of occurrence (PoO) of damage at a given site, and the distribution of damage for use in multiple site damage analyses.

Pitting corrosion model – Pits are assumed to be hemispherical throughout and grow at a constant volumetric rate that is determined by Faraday's law, with the temperature dependence expressed through an Arrhenius relation. The pit depth a, up to the transition size a_{tr} at which a crack nucleates, is given by Eq 2

$$a = \left[\left(\frac{3MI_{Po}}{2\pi nF\rho}\right)\exp\left(-\frac{\Delta H}{RT}\right)t + a_o^3\right]^{1/3} \quad ; \quad a \le a_{tr} \tag{2}$$

In Eq 2, $M = 27$ is the molecular weight; $n = 3$ is the valence; $\rho = 2{,}700$ kg/m^3 is the density; $\Delta H = 40$ kJ/mol is the activation enthalpy; $F = 96{,}514$ C/mol is Faraday's constant; $R = 8.314$ J/mol-K is the universal gas constant; $T = 293$ K is an average of typical values for the absolute temperature when the aircraft is on the ground; I_{Po} is the pre-exponential term in the Arrhenius relationship for the pitting current; a_o is the initial pit radius; and t is the time required for a pit to develop to a depth of a. The values for M, n, ρ and ΔH are for aluminum. For this model, a_o and I_{Po} are considered to be *rvs*.

Corrosion fatigue model – The standard power law form for corrosion fatigue crack growth rate, $(da/dN)_c = C_c \Delta K^{n_c}$ is assumed to be the mechanistically based model. The crack growth exponent, n_c, which represents the functional dependence of the crack growth rate on ΔK, is taken to be deterministic. The coefficient C_c is assumed to be an *rv* that characterizes the variability in the material properties, including microstructural and environmental parameters. Also, it is assumed that the number of cycles can be expressed in terms of time by $N = ft$, where the frequency $f = 4$ cyc/day is taken for an aircraft used for intermediate flight lengths.

The driving force ΔK is different for a surface crack and a through-the-thickness crack. For a surface crack emanating from a circular hole, ΔK is given by Eq 3

$$\Delta K_{sc} = \frac{2.2}{\pi} K_t \Delta\sigma \sqrt{\pi a} \tag{3}$$

In Eq 3, $\Delta\sigma$ is the far field stress range, $2.2/\pi$ is for a semi-circular surface crack in an infinitely large plate, and $K_t = 2.8$ is the stress concentration factor for a circular hole. For a through-the-thickness crack, emanating from a hole of radius $r_o = 3$ mm, ΔK is assumed to be equal to the following

$$\Delta K_{tc} = F_{tc}(a/r_o)\Delta\sigma\sqrt{\pi a} \tag{4}$$

Numerical values for $F_{tc}(a/r_o)$ can be fit empirically, to within graphical resolution, by the following function

$$F_{tc}(a/r_o) = \frac{0.865}{(a/r_o)+0.324} + 0.681 \tag{5}$$

Taking t_{tr} and t_{tc} to be the time at which a pit transitions into a surface crack and the surface crack transitions into a through-thickness crack, respectively, the surface-crack depth with time, for $t_{tr} \le t < t_{tc}$, is obtained by direct integration of the growth rate relationship, using ΔK_{sc}, and is given by Eq 6

$$a = \left[a_{tr}^b + b f C_c \left(\frac{2.2 K_t \Delta\sigma}{\sqrt{\pi}} \right)^{n_c} (t - t_{tr}) \right]^{1/b}; \quad b = \frac{2 - n_c}{2}; \quad n_c \neq 2 \tag{6}$$

For growth as a through-thickness crack, at $t \ge t_{tc}$, the relationship is obtained implicitly from Eq 7 by using ΔK_{tc}, where a_{tc} is the size of the damage (taken here to be one-half the plate the plate thickness) at t_{tc}

$$t = t_{tc} + \frac{1}{f C_c (\Delta\sigma\sqrt{\pi})^{n_c}} \int_{a_{tc}}^{a} \frac{da}{[F_{tc}(a/r_o)\sqrt{a}]^{n_c}} \tag{7}$$

The integral in Eq 7 typically must be evaluated numerically.

Transition Criteria – Since pitting controls early damage growth, the transition criteria for pitting to corrosion fatigue crack growth (crack nucleation) given by Eq 1 are used. They are repeated below to emphasize their reference to a surface crack.

Selection of random variables –Statistical variability is modeled through I_{Po}, a_o, C_c, and ΔK_{th}, which are chosen to be mechanistically and statistically independent of time. Scatter in material properties, environmental sensitivity, and resistance to fatigue crack growth is reflected in C_c. Material and manufacturing quality is depicted by a_o and ΔK_{th}. The scatter associated with the electrochemical reaction for pit growth is reflected through I_{Po}. The three-parameter Weibull cumulative distribution function (cdf) was found to characterize each *rv* adequately and was used [*2,4,5*].

Model Predictions, Comparisons with Service Data, and MSD

Based on the foregoing model, the evolution and probability of occurrence (PoO) of damage were calculated for simplified aircraft fuselage pressurization-depressurization cycling. The viability of the model for estimating the PoO of damage in service is assessed in terms of the results from tear-down inspections of the lower wing panels from two transport aircraft that had been in commercial service for 24 and 30 years. The use of the methodology in estimating the probabilistic distributions of MSD is illustrated.

Impact of Corrosion – To portray the impact of pitting corrosion on the life of a structure, a graph of the average damage size versus time (using mean values of the *rvs* obtained at the author's laboratory) is given in Figure 8 [*16*]. Predictions based on two models, with an identical initial damage size (a_o = 5 μm), are shown. The first model (represented by the solid curve) included pitting corrosion, which is dominant up to t_{tr},

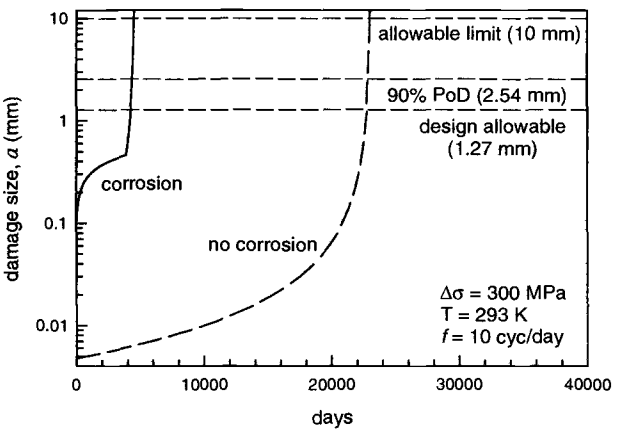


Figure 8 – *Average damage size modeled by pitting corrosion with corrosion fatigue crack growth and corrosion fatigue crack growth only.*

and the second one (dashed curve) did not. The three dashed horizontal lines represent the United States Air Force (USAF) allowable size for a single crack (1.27 mm), the PoD of 90% (2.54 mm) [*17*], and a reasonable allowable limit for a fuselage panel (10.0 mm). A comparison of the two models clearly shows that the fatigue-life potential is significantly compromised by pitting corrosion, with pitting corrosion truncating the early stage of fatigue crack growth. At a damage size of 1.27 mm, the predicted life with corrosion is only 19% of that without corrosion (Figure 8). Clearly pitting corrosion would contribute to the onset of early fatigue damage (or MSD) and its early detection (*i.e.*, at sizes much smaller than 1.27 mm) and mitigation would improve service life.

PoO of Damage in Wing Panels – The efficacy of this simplified model was assessed in relation to the PoO of damage in service. Predicted PoOs are compared with the results from tear-down inspections of the lower wing panels from two transport aircraft that had been in commercial service for 24 and 30 years [*18*]. The inspections were a part of the USAF Joint Surveillance, Target and Attack Radar System (J-STARS) program to convert retired Boeing 707 aircraft for this service. The aircraft were designated as CZ-180 and CZ-184. CZ-180 is a Boeing 707-123 aircraft that had been in commercial service for about 30 years, and had accumulated 78,416 flight hours and 36,359 flight cycles. CZ-184 is a Boeing 707-321B with about 24 years of commercial service, and 57,383 flight hours and 22,533 flight cycles; the CZ-184 aircraft was reported to have evidence of greater corrosion damage.

The lower wing panels and associated stiffeners and frames were examined visually for evidence of cracking. Here, only damage on the walls of fastener holes in the wing panels is considered. The fasteners were removed and the damage (cracks) were measured optically, with the aid of dye penetrants, using a magnifying lens at 20X. Multiple crack indications, designated as multiple hole-wall cracks (MHWC), were observed at the highly stressed regions of the fastener holes. In each case, however, only the longest estimated crack from the group was reported. Metallographic examinations of this damage in the CZ-184 aircraft were made recently [*5,18*]. Typical findings are illustrated in Figure 9, and show the conjoint actions of corrosion and cracking, with post-cracking corrosion of the crack flanks seen in the sectional view in Figure 9.

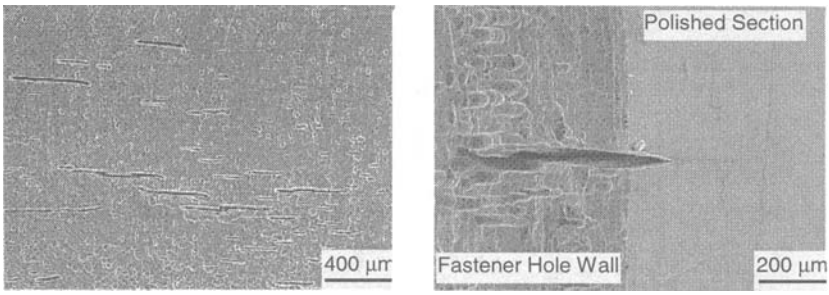


Figure 9 – *Scanning electron micrographs of typical MHWC (left) and a section through a typical elongated damage (right) at a fastener hole in the lower wing panel of the CZ-184 aircraft showing corrosion attack of the hole surface and the fatigue crack.*

For the sections that had been inspected [*18*], 350 cracks were reported for the CZ-180 aircraft, and 494 cracks for the CZ-184 aircraft. (The difference in number reflected, in part, the larger area that was inspected for the CZ-184 aircraft.) The reported damage sizes (visual measurements of surface lengths) for each aircraft were pooled, and the distribution of damage for each of the aircraft is shown on Weibull cumulative probability plots by the filled symbols in Figures 10 and 11, respectively. Because many of the estimated damage had the same size, the number of data points in the each of the figures appears limited.

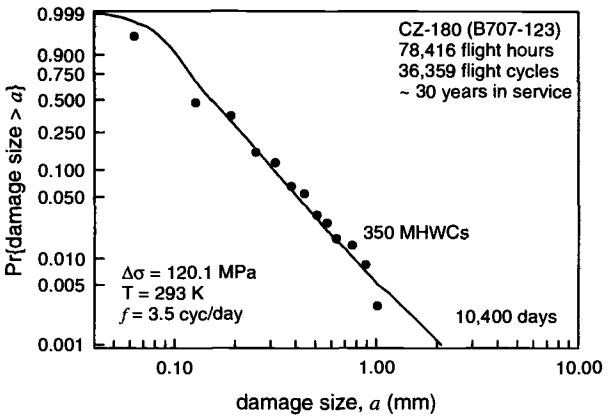


Figure 10 – *A comparison between the predicted and observed PoO for hole-wall damage in the lower wing skins (2024-T3 aluminum alloy) of the CZ-180 aircraft.*

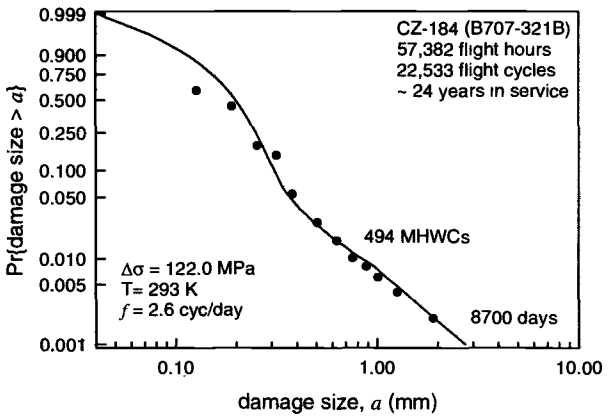


Figure 11 – *A comparison between the predicted and observed PoO for hole-wall damage in the lower wing skins (2024-T3 aluminum alloy) of the CZ-184 aircraft.*

Based on reasonable values of localized corrosion and corrosion fatigue crack growth rates and by considering the primary loading from ground-air-ground (adjusted for average gust loading) cycles, the PoO of damage is estimated for each aircraft [*5,18*], and is shown as a solid line in each of the figures. The agreement is very encouraging, and suggests that it is feasible to estimate service performance on the basis of laboratory data. Metallographic data for these aircraft suggest that the postulated mechanistic models are reasonable [*5,18*].

Estimation of MSD – The availability of a validated predictive model for PoO provides a rational method for estimating the distribution of damage for use in multiple site damage (MSD) analyses. Such analyses represent a change in scale from local damage (principally discrete damage at the materials level) to that of a component or a structure involving interactions of damage at neighboring locations that can compromise its integrity and safety. The approach and methodology is illustrated by using the predicted PoO distribution for the CZ-184 aircraft (Figure 11). Using Monte Carlo simulation for the largest crack length in each fastener hole, the damage distribution for a collection of fastener holes may be estimated. Damage from hole to hole, as well as at the two highly stressed sides of each hole, is considered to be statistically independent. A simulated distribution for 1000 fastener holes is shown in Figure 12 [*18*]. Each simulation may represent different locations in a single aircraft, or the same location for different aircraft under comparable service conditions. It is seen that different levels of damage are possible, and critical locations may be identified through the size and clustering of damage at a given stage in service. A number of critical areas can be identified readily. This illustration demonstrates the value of this approach in airworthiness assurance and management of civil and military aircraft, and for safety and reliability, and life-cycle management in general.

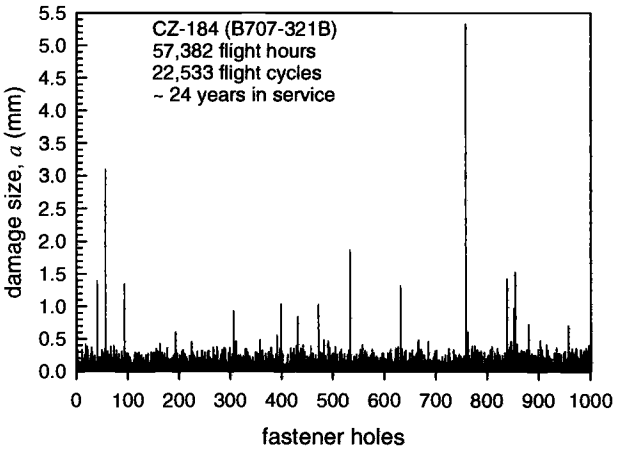


Figure 12 – *Simulated damage distribution for 1000 fastener holes based on the PoO for the skin of the CZ-184 aircraft.*

The Challenge

The essential challenges for the *environmentally assisted cracking* community, therefore, are in the following two areas. The first is for the community to take a leadership role in the development of quantitative methodologies that can be used in the assurance of reliability and continued safety of engineered systems and in life-cycle management and design. The second is to form a working relationship with the design and manufacturing community. To meet these challenges, it is necessary to adopt a mechanistically based probability approach and to undertake the critical task of understanding and formulating mechanistic models for the processes of material aging, *vis-à-vis,* parametric characterizations of these processes. Integration of the resulting models into the design paradigm is essential. The mechanistically based probability approach outlined and illustrated in this paper provides a reasonable starting framework for meeting these challenges in the new millennium.

Summary

To meet the challenges of designing engineered systems for a competitive global market and ensuring their reliability and continued safety, a new paradigm for design is needed to integrate quantitatively materials aging into the processes of design, reliability and safety assessments, and life-cycle management planning. A mechanistically based probability approach has been outlined, and is offered as a starting framework for developing the necessary understanding and design methodology. The efficacy and value of this approach was demonstrated through an example on corrosion and corrosion fatigue of aluminum alloys used in airframe construction. The feasibility of predicting long-term service performance was demonstrated for aircraft that had been in commercial service for 24 to 30 years by using simplified mechanistic models developed from mechanistic understanding and short-term laboratory data. The extension of this understanding at the materials level to the analyses of reliability and safety (*e.g.*, MSD) at the component and system level was illustrated. It is hoped that the community would rise to the challenge and take the leadership in nurturing the development of the new design paradigm.

Acknowledgment

The underlying research is supported by the Air Force Office of Scientific Research, under Grant F49620-98-1-0198 and by the Federal Aviation Administration under Grant 92-G-0006. The author is indebted to his students and co-workers for their careful and skillful work over the years and, in particular, to his colleague, Prof. D. Gary Harlow, for his insightful contributions to the formulation and development of the mechanistically based probability approach over the past decade.

References

[1] Wei, R. P., "Life Prediction: A Case for Multi-Disciplinary Research," *Fatigue and Fracture Mechanics, 27th Volume, ASTM STP 1296*, R. S. Piascik, J. C. Newman

and N. E. Dowling, Eds., American Society for Testing and Materials, West Conshohocken, PA, 1997, pp. 3-24.

[2] Harlow, D. G. and Wei, R. P., "Probability Approach for Corrosion and Corrosion Fatigue Life," *Journal of the American Institute of Aeronautics and Astronautics*, Vol. 32, No. 10, 1994, pp. 2073-79.

[3] Harlow, D. G. and Wei, R. P., "A Mechanistically Based Approach to Probability Modeling for Corrosion Fatigue Crack Growth," *Engineering Fracture Mechanics*, Vol. 45, No. 1, 1993, pp. 79-88.

[4] Wei, R. P., Li, C., Harlow, D. G. and Flournoy, T. H., "Probability Modeling of Corrosion Fatigue Crack Growth and Pitting Corrosion," *ICAF97: Fatigue in New and Aging Aircraft*, Vol. 1, R. Cook and P. Poole, Eds., Engineering Material Advisory Services Ltd., London, 1997, pp. 197-214.

[5] Wei, R. P. and Harlow, D. G., "Probabilities of Occurrence and Detection, and Airworthiness Assessment," *Proceedings of ICAF'99 Symposium on Structural Integrity for the Next Millennium*, Bellevue, WA, 12-16 July 1999.

[6] Wei, R. P., Masser, D., Liu, H. W. and Harlow, D. G., "Probabilistic Considerations of Creep Crack Growth," *Materials Science and Engineering*, Vol. A189, 1994, pp. 69-76.

[7] Gough, H. J., "Corrosion-Fatigue of Metals," *Journal of Institute of Metals*, Vol. 49, 1932, pp. 17-92.

[8] Chen, G. S., Gao, M. and Wei, R. P., "Microconstituent-Induced Pitting Corrosion in a 2024-T3 Aluminum Alloy," *Corrosion*, Vol. 52, No. 1, 1996, pp. 8-15.

[9] Wei, R. P., Liao, C. M. and Gao, M., "A TEM Study of Micro-Constituent Induced Corrosion in 2024-T3 and 7075-T6 Aluminum Alloys," *Metallurgical and Materials Transactions*, Vol. 29A, April 1998, pp. 1153-1160.

[10] Liao, C. M., "Particle Induced Pitting Corrosion of Aluminum Alloys," *Ph.D. Dissertation*, Lehigh University, 1997.

[11] Liao, C. M., Chen, G. S. and Wei, R. P., "A Technique for Studying the 3-Dimensional Shape of Corrosion Pits," *Scripta Materialia,* Vol. 35, No. 11, 1996, pp. 1341-1346.

[12] Chen, G. S., Wan, K.-C., Gao, M., Wei, R. P. and Flournoy, T. H., "Transition From Pitting to Fatigue Crack Growth – Modeling of Corrosion Fatigue Crack Nucleation in a 2024-T3 Aluminum Alloy," *Materials Science and Engineering*, Vol. A219, 1996, pp. 126-132.

[13] Wan, K.,-C., Chen, G. S., Gao, M. and Wei, R. P., "Interactions between Mechanical and Environmental Variables for Short Fatigue Cracks in a 2024-T3 Aluminum

Alloy in 0.5M NaCl Solutions," *Metallurgical and Materials Transactions (to appear).*

[14] Dolley, E. J., Jr., "Chemically Short-Crack Behavior of the 7075-T6 Aluminum Alloy," *Ph.D. Dissertation*, Lehigh University, 1999.

[15] Harlow, D. G. and Wei, R. P., "Aging of Airframe Materials: Probability of Occurrence Versus Probability of Detection," *2nd Joint NASA/FAA/DoD Conference on Aging Aircraft*, Williamsburg, VA, 1998, NASA/CP-1999-208982/PART 1, C. E. Harris, Ed., Jan. 1999, pp. 275-283.

[16] Berens, A. P., Hovey, P. W. and Skinn, D. A., "Risk Analysis for Aging Aircraft Fleets: Volume 1-Analysis," USAFWL-TR-91-3066, 1991.

[17] Hug, A. J., et al., "Laboratory Inspection of Wing Lower Surface Structure From 707 Aircraft for the J-STARS Program," Boeing FSCM No. 81205, Document No. D500-12947-1, 4 April 1996.

[18] Harlow, D. G., Domanowski, L. D., Dolley, E. J., Jr. and Wei, R. P., "Probability Modeling and Analysis of J-STARS Tear-Down Data from Two B707 Aircraft," *Proceedings of Third Joint FAA/DoD/NASA Conference on Aging Aircraft*, Albuquerque, NM, September 20-23, 1999.

Plenary Program—I

Alan Turnbull[1]

Issues in Modelling of Environment Assisted Cracking

Reference: Turnbull, A., **"Issues in Modelling of Environment Assisted Cracking,"** *Environmentally Assisted Cracking: Predictive Methods for Risk Assessment and Evaluation of Materials, Equipment, and Structures, ASTM STP 1401,* R. D. Kane, Ed., American Society for Testing and Materials, West Conshohocken, PA, 2000.

Abstract: Risk-based inspection is becoming the cornerstone of modern practice in ensuring the integrity of engineering structures and components in a cost effective manner. The approach relies heavily on experience, insight and awareness of the likelihood of crack initiation and on models to predict the evolution of crack size. Environment assisted cracking poses a particular problem because of the sensitivity to transients and excursions in service behaviour and because models of crack growth kinetics, both empirical and deterministic, have significant limitations. A number of the existing issues in prediction are highlighted with recommendations for future development.

Keywords: Risk based inspection, environment assisted cracking, modelling, pitting, hydrogen embrittlement

Limitations in service prediction of environment assisted cracking (EAC) exist because of the complex dependence of initiation and crack growth on interacting operational variables and uncertainty in the mechanism of cracking. Although engineering design will be optimised to minimise the probability of occurrence of cracking, or to provide an acceptable life using appropriate design codes, there are several reasons why cracking may still be of concern:

- the operating conditions may be altered to improve the process;
- welding may not be ideal and may introduce defects and change the material characteristics;
- transient variations in stress, temperature or environment chemistry may occur, either from scheduled excursions (e.g. shutdown) or from unintentional fluctuation in system control (e.g. contamination);

[1] Head, Aqueous Corrosion Group, National Physical Laboratory, Teddington, Middlesex, TW11 OLW, UK.

Copyright© 2000 by ASTM International www.astm.org

- the character of the metal surface may change with time of operation (e.g. precipitation of a scale or deposit) or the material may "age" (e.g. irradiation effects);
- localised corrosion processes, such as pitting and crevice corrosion, may be initiated and become precursors for EAC;
- the ideal engineering choice of material for the specified process conditions may not be economically viable; and
- laboratory testing and modelling assumptions may not be realistic.

The risk that cracks will initiate and grow to the critical size for unstable fracture has to be identified and linked to a risk-based inspection (RBI) protocol. For most practical situations this is an empirical process, being based on a probabilistic assessment of crack size evolution using service or laboratory data. The reliability of that process depends on the quality and relevance of experimental data. Quantitative mechanistic models of cracking are used to-date in only limited industrial applications, primarily in the nuclear industry or in long-term waste containment. The challenge for the research and testing community is to develop an extensive and reliable EAC database and to provide an accessible framework for application of data and models to engineering prediction. A number of relevant issues are now discussed.

Risk Based Inspection

The traditional risk equation (Risk = Probability x Consequence) contains two components: the probability that a failure event will occur and the consequences if that failure event does occur. Historically, inspection was carried out at regular set time intervals with often limited evaluation of the probability of a failure event and of the significance of the inspection sites. Modern methods are based on a more structured analysis involving assessment of criticality *[1,2]*. The principles are exemplified by Table 1 *[2]*, which describes how a risk severity index may be apportioned to different sections of a plant. The severity index is calculated by multiplying the Failure Potential, F, by the sum of two consequence values relating to safety and economic risk, S and E, and has a maximum of 24 in this scheme.

The scheme in Table 1 is relatively simple, for illustrative purposes, but can be expanded using a more detailed classification *[1]*. High and low risk situations are often readily identified and appropriate action taken. The problem for materials engineers is in the medium risk region where judgement has to be exercised. Here, more support to industry in terms of improved predictive tools is required.

Table 1 - *Failure potential and consequence evaluation.*

Failure potential: F (assigned by inspector)	Failure consequences (assigned by operations)		Severity Index
	Safety/ Environment: S	Economics : E	
4: Item could fail in an unpredictable manner. 3: Failure could occur within one year but not in an unpredictable manner. 2: Item could fail in 1-5 years. 1: Item could fail within 5-10 years	3: High concern that failure will result in injury or unacceptable release to the environment. 2: Moderate concern 1: Low concern 0: No concern	3: High impact on operations if the failure occurs. 2: Moderate impact. 1: Minimum impact. 0: No impact.	F x (S+E)

Probabilistic Failure Analysis

For mass-produced items, which have proportionally a greater number of failures, failure frequency analysis can be used to establish the probability of a particular failure mode. The major difficulty for engineering structures in terms of establishing such probability relationships is that failures are relatively rare and information from service behaviour may be limited. Indeed, the failure may be a one-off, induced by upset conditions.

However, there are exceptions. The common design and incidence of failures by cracking for sensitised stainless steels in boiling water reactors *[3]* and of Alloy 600 in pressurised water reactors *[4]* enables statistical treatment. In such cases, the analysis of service failures is often based on fitting to statistical distributions, *e.g.* exponential, log-normal, extreme value, and Weibull *[5]*. The Weibull cumulative probability of failure is commonly used and is given by

$$F(t) = 1 - exp\{-[(t-t_0)/\eta]^{\beta}\} \qquad (2.1)$$

where F(t) is the fraction of components failed after time, t, t_0 is the origin of the distribution (when $t=t_0$ the fraction of failures goes to zero), η is the characteristic life or scale parameter (understood as the time when $F(t) = 0.632$), and β is the shape parameter of the linear transform. The shape parameter determines whether the risk of failure decreases or increases with time and the extent of variability in times to failure. For example, it can reflect the change in crack velocity with time. The dependence of η and β on the physical variables that influence cracking (stress, temperature, pH,

etc.) can be identified using quantitative relationships for the dependence of time to failure on those variables *[4,6]* (assuming such relationships exist). The use of a distribution for the physical variables can then be linked to Monte Carlo simulation (to impose randomness), enabling a computed distribution of failure times. Subsequent presentation in a Weibull plot can then be used to establish the link between β and η and material parameters.

In the absence of sufficient failure data from service the probability of failure is usually deduced from laboratory measurements and modelling of crack growth kinetics.

Predicting Crack Size as a Function of Exposure Time

The primary requirement for guiding inspection intervals is to establish the probability of obtaining a crack of a certain effective size (which may include incorporating the depth of a precursor pit) after a service exposure time. The basic principle is illustrated schematically in Figure 1, for a crack developing from a pit, in which the effective exposure time, t_{eff}, is used rather than the total elapsed time. This is an important consideration in order to allow for transient situations in a plant for which the conditions are conducive to pitting/cracking only intermittently (measured using a corrosion monitor, for example). It may also relate to the number of significant operating or loading cycles.

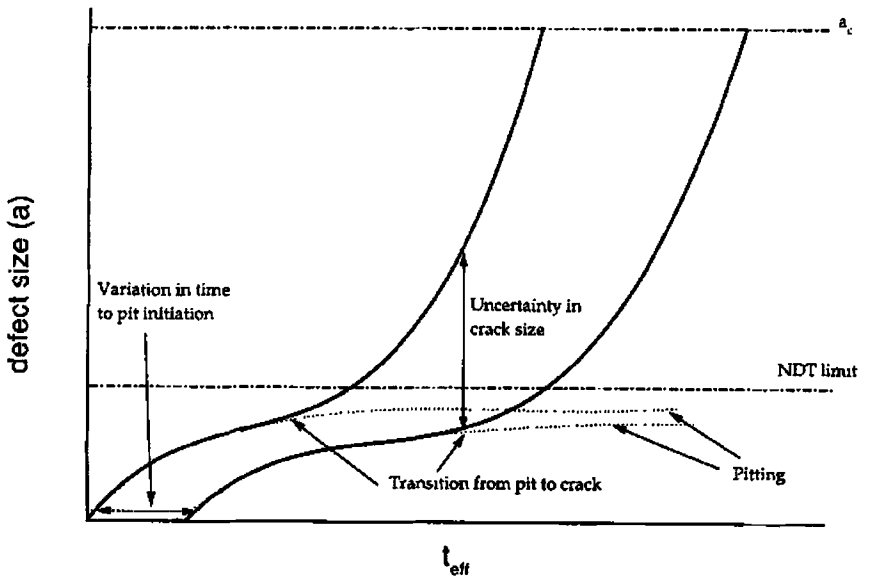


Figure 1 - *Schematic illustration of the time-evolution of crack size with the crack initiated from a corrosion pit.*

There will not be a discrete relationship between the effective crack size and time because of the statistical variability associated with the various stages of crack development. The requirement is to bound the crack depth-time relationship sensibly using a probabilistic approach. Following the initial inspection, the actual crack sizes obtained for a component should be compared with the reference crack size distributions based on the probabilistic analysis in order to benchmark the predictions. Revised predictions of likely crack size distribution can then be generated and used to evaluate the probability of failure and subsequently lead to an update of the inspection program. The information would be linked to a structural integrity assessment, an example of which is the R6 method *[7]*.

For most service applications the evolution of crack size is predicted on an empirical basis using crack growth measurements perhaps coupled with statistical analysis. Whilst there are inherent limitations in the *deductive* nature of empirical modelling, it is prevalently used and the requirement from a research and testing perspective is to establish readily accessible databases, to ensure the reliability and relevance of the data, and to provide an intelligent basis for estimating inspection intervals and remnant life. In the nuclear industry, for example, a conservative upper bound growth rate is used often as the basis of the inspection protocol *[8]*.

Measurement and Reliability of Threshold and Crack Growth Data

Long crack growth measurement is now soundly based insofar as there are a number of standards developed. There is still a lack of guidelines in dealing with time dependent processes, transients in service conditions, short crack issues and in extrapolating short term data. Furthermore, Poole noted in his lecture at the ECF-12 meeting *[9]* that a modest exercise of fitting da/dN vs. ΔK data by three different software organisations led to significant variations in the prediction of cycles to failure. Hence, even with relatively long cracks, uncertainty in prediction can arise.

An important advance in determining the threshold for stress corrosion cracking and hydrogen embrittlement is the refocusing on dynamic loading/straining. Several major failures have occurred that can be attributed to unexpected excursions in loading and straining and would not be predicted by most conventional constant load tests. A recent round-robin study *[10]* has shown that the value of K_{ISCC} determined under slow rising displacement conditions can be lower than that derived from long-term static load tests (Figure 2). Turnbull *[11]* has recently illustrated the potential advantages of the interrupt slow strain rate test for evaluation of the threshold strain for EAC of duplex stainless steels, highlighting the importance of strain rate and the need to rethink the approach to testing for materials selection.

The time-dependence of environment assisted cracking is an important issue in testing, especially in relation to hydrogen transport and hydrogen embrittlement. The key factor is the distance of the site of cracking from the primary source of hydrogen atoms, which can be external to the crack or at the crack tip itself. When the susceptible region of the microstructure is internal or the primary source of supply is on the external surface rather than the crack tip, there has to be sufficient time in

testing to allow the hydrogen atom concentration to attain the steady value at the site of cracking. In some systems, this can take hundreds of days *[12]*.

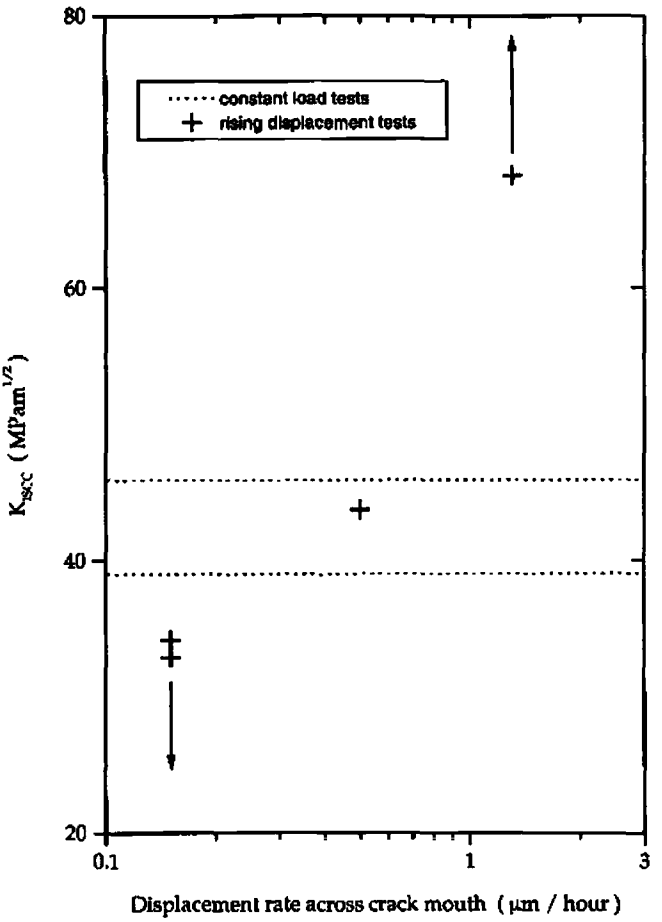


Figure 2 - *K_{ISCC} vs load-line displacement rate for AISI 4340 steel in ASTM seawater at 20 °C; NPL data in Reference [10].*

The other major issue in hydrogen embrittlement which has not been tackled well to-date is the problem of temperature transients, e.g. in the oil production and refining industries. Systems which do not fail because the hydrogen is too mobile at the more elevated temperature can suffer embrittlement when the temperature is decreased. Arguably, this could be a possible source of cracking in the nuclear industry where significant hydrogen atoms are generated and absorbed under operating conditions but may only become a potential problem at the lower temperature associated with an outage.

For stress corrosion cracking, pitting or crevice corrosion is a necessary precursor to cracking in many systems. For example, transient excursions in chemistry in chemical plant may give rise to initiation of localised attack but the behaviour following restoration of normal chemistry is less well understood: will pits continue to grow; will cracks initiate and continue to propagate; what is the impact of repetitive excursions. Such issues are important to resolve in order to guide inspection and decisions based on it. Pitting corrosion as a precursor to cracking has been studied very actively over the last few years and a short summary of the key issues is pertinent.

Pits as Precursors to Cracks

The mechanism of EAC emanating from pits can be divided into four consecutive stages: pit initiation, pit growth, crack initiation, and crack growth, with an associated statistical distribution which must be accounted for. Each stage can be modelled separately and the individual models combined in series to produce a probability of a crack of a given size existing after a given time *[13,14]*. The statistical approach to pit initiation and growth is well developed. The challenge is to establish the criteria for the onset of cracking from pits, as these will determine the extent of pit growth to be accounted for in the prediction.

Kondo *[15]* derived an expression for the critical pit depth (a_{cr}) in corrosion fatigue based on the assumption that the transition occurred when the crack growth rate exceeded the pit growth rate, as shown schematically in Figure 3. The growth rate of the pit ($\propto t^{1/3}$) was expressed in terms of the pit size and (assuming the pit acted like a crack) thence ΔK to give

$$a_{cr} = Q/\pi[\Delta K_p/2.24\sigma_a]^2 \qquad (3.1)$$

where Q is a shape factor and σ_a is the stress amplitude. The value of ΔK_p is derived experimentally by comparing the growth rate of the pit with that of the crack (see Figure 3). No short crack correction factor was used in defining the critical pit size. This approach has subsequently been adopted by Chen et al. *[16]* with the only distinction being a slightly more elaborate relationship for the stress intensity factor.

Tsujikawa *[17]* has reported the pit base to comprise micro-etch pits, which initiate microcracks providing the micro-etch pits grow slower than the microcracks can propagate. Tsujikawa held similar views to Kondo with the refinement that the development of macrocracks from pits in stainless steels only occurred when the crack growth rate was higher than the *faceting* dissolution rate. A minimum pit size was also established.

The phenomenological approach of defining the transition as when the crack growth rate exceeds the pit growth rate is reasonable insofar as it is a *necessary* condition. Crack growth has to be feasible (the threshold must be exceeded) and must be greater than the pit growth rate. This explains an upper limit in the electrode potential for chloride SCC of stainless steels. If the potential is too high the corrosion rate in the pit is faster than the crack for the prevailing conditions. The decrease in pit

growth rate with pit size in open circuit conditions would imply that, at some depth, cracking may always ensue provided the pit continues to grow.

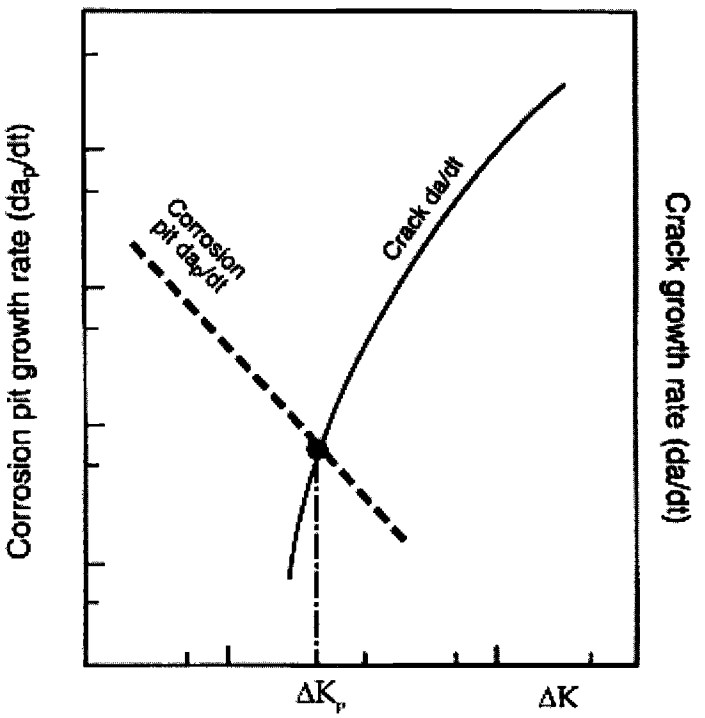


Figure 3 - *Schematic illustration of the conditions for the transition from a pit to a corrosion fatigue crack [15].*

A limitation of existing analyses has been the use of long crack growth measurement. The growth rate of short cracks is not necessarily the same as for a long crack of the same stress intensity factor because of interactions with the microstructure, plastic wake effects in long cracks, or differences in chemistry and electrochemistry *[18]*. Crack growth may occur below the threshold value determined from long crack growth studies. Also, it may be necessary to assign an effective crack size to the pit. The importance of the latter was demonstrated by Zhou and Turnbull *[19]*. There is also an issue of whether the pit can be treated using simple analytical expressions for the stress intensity factor. This may depend on the precise geometry of the pit base. The systematic evaluation of the effect of environmental and loading variables on short crack growth rate is non-trivial. Correspondingly, the extent of usable data is limited.

The main requirements in relation to cracks developing from pits are measurements of the crack growth (and crack shape) as the crack emerges at a pit site and characterisation of the local mechanical driving force. The difficulty is that pit

growth in service may proceed under intermittent exposure conditions and it may be years before a crack initiates. Hence, controlled acceleration of the pitting process may be required. This usually involves a pre-pitting procedure with acceleration induced by an increase in the severity of the environment, increasing the electrode potential or raising the temperature. From the viewpoint of controlled crack monitoring, it is desirable to have a dominant pit, whose depth is controlled, and adjacent to which crack monitoring probes can be attached. Effective methods of pre-pitting with control of pit numbers and size have been developed by Zhou and Turnbull *[19,20]*. The combined use of scanning vibrating electrode probe, which can measure the current flowing from individual pits, and analysis of electrochemical noise may provide complementary information.

Short Cracks and Crack Coalescence

The outstanding issues in predicting crack size evolution are in the area of short crack development, multiple cracks with interacting plastic fields, complex stress states and complex loading histories. These pose formidable challenges, although there are approaches being developed which claim eventually to deal with such situations *[21]*.

Where multiple cracking is observed, with possible interactions between neighbouring cracks and crack coalescence, a predictive approach is more difficult. Cracks may initiate and then slow down due to changes in mechanical or electrochemical driving force, the latter incorporating changes in material chemistry due to limited connectivity of MnS inclusions or of Cr-depleted zones at grain boundaries for example. Crack coalescence may occur, cracks may nucleate at different times, dormant cracks may re-start, and all of these steps prior to establishment of a crack size described by the conventional stress intensity factor approach. Some progress in dealing with these problems has been made by Parkins on natural gas pipeline steels *[22]*. For that system most of the lifetime is spent in the process of crack coalescence. Parkins makes use of Weibull distribution functions in analysing crack size data from field and laboratory data and is able to generate predictions (aided by Monte Carlo methods) of crack size vs. time curves. However, he concludes that critical information regarding the rate of nucleation and coalescence of cracks is seldom available to improve the predictive capability. This area remains a major challenge.

Simulation of service conditions in the laboratory is of primary concern, not only in relation to the exposure conditions and exposure history but because laboratory specimens are often carefully prepared and the surface finish and surface composition in some alloys can differ significantly from service. In many cases, surface grinding of laboratory specimens introduces residual stresses which are not always measured or accounted for in testing.

Mechanistically-based Modelling of Cracking

In the case of the slip-dissolution model there has been some degree of success in service crack size prediction *[23]*, despite some limitations of the crack chemistry

modelling, but widespread application of mechanistically-based models is very limited. The primary value in deterministic or mechanistically-based modelling is to provide a better understanding of the controlling variables, ensuring that testing is relevant and that there is some basis for answering the "what if?" question for circumstances not encompassed by laboratory testing. The details of such models were reviewed by Turnbull elsewhere *[24]*. However, the fundamental issue as to which mechanism of crack advance applies in a particular industrial application continues to be a matter of debate. The test from an engineering perspective should be the ability to quantitatively predict the threshold for cracking and crack size evolution as a function of service operational variables.

In this context, there remain important requirements if there is to be confidence that the proposed failure mechanism can be translated into quantitative prediction. These include reliable crack chemistry characterisation (which provides the basis for predicting the nature of crack-tip films and measurement and prediction of crack-tip reaction kinetics), quantification of crack tip hydrogen concentrations in the case of hydrogen embrittlement, and prediction of the impact of excursions. Finally, there has to be a sensible basis for validation of mechanistically-based models.

Crack Chemistry Prediction - Predicting the kinetics of crack tip reactions and the nature of crack tip films is a necessary requirement for most predictive models. Whilst specific measurements can be made, modelling is required to predict the impact of a range of test and operational variables and to ascertain the controlling factors. Unfortunately, untenable assumptions have been made in too much of recent published work. A common feature, which applies not only to crack chemistry but to crevice chemistry, is the neglect of internal cathodic reactions and of precipitation processes in the crack. The significance of these factors has been highlighted in a recent paper *[25]* and is exemplified in modelling of the chemistry and electrochemistry in cracks in 304 stainless steel in high temperature water with NaCl as an impurity *[26]*. The impact of the internal cathodic reactions on the electrode potential at the tip of a crack (E_{tip}) is clearly illustrated in Figure 4, for which the term "standard" refers to experimentally derived current densities; k_c is the rate constant for the reduction of hydrogen ions and for water, i_p is the passive current density, and K is the stress intensity factor. In the absence of internal cathodic reactions, the potential would be that for the isolated value, about -0.49 V SHE.

In high temperature water, the solubility of metal cations is very low. In contrast, the solubility of metal cations at ambient temperatures is high and anions from the bulk, e.g. Cl^-, can be drawn into the crack with the result that the crack solution can be saturated in metal chlorides even for a bulk environment of very low conductivity. The formation of saturated salt solutions poses particular problems in modelling crack chemistry and in predicting the rates of electrochemical kinetics. No rigorous model exists. Nevertheless, Jones and Simonen *[27]* have incorporated salt precipitation into a prediction of Stage I stress corrosion crack growth, which was assumed to be determined by transport controlled dissolution of the salt film. However, it is less clear that a system exhibiting mass transport controlled dissolution kinetics should exhibit *intergranular* stress corrosion cracking (assuming a dissolution mechanism of crack

advance). It might be expected that, under mass transport control, the rate of dissolution at the crack tip would be independent of the local material composition and that matrix and grain boundary dissolution rates might be comparable. Crack size would also be important.

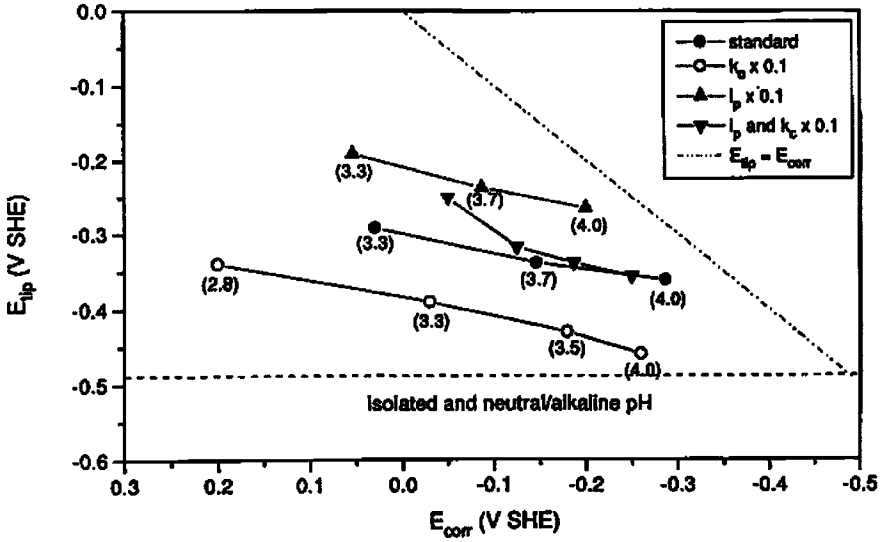


Figure 4 - *Crack tip potential (pH_{tip} in parenthesis) as a function of corrosion potential for 304 stainless steel in NaCl; K =10 MPam$^{1/2}$; σ_{293}=0.3 μScm^{-1}; i_p=1.5x10^{-6} Acm^{-2}; T=561K; pH_{bulk}=5.7.*

In summary, with the exception of concentrated salt solutions, modelling of crack chemistry is at the stage where the primary uncertainty in prediction should be associated only with the paucity of data for the input parameters. In many applications, the lack of such data is a major constraint.

Crack-tip Hydrogen - Prediction of crack growth kinetics due to hydrogen embrittlement depends critically on predicting the crack tip hydrogen distribution. As described in the review article *[24]*, the modelling of Sofronis and McMeeking *[28]* represented a significant advance in characterising the distribution of hydrogen atoms at a crack tip insofar as it included elastic-plastic analysis combined with diffusion and trapping. Krom et al *[29]* developed this further pointing out an error in the construction of the model of Sofronis and McMeeking. A particular conclusion was that increasing the strain rate should lead to a reduction in lattice hydrogen concentration (the atoms going into the new dislocation trap sites), thus explaining the effect of strain rate on cracking. However, the assumption that cracking is associated only with lattice hydrogen and that depletion of this explains the role of strain rate needs to be validated and should not be generalised since there is much evidence for a direct role of trapping and of dislocation transport in redistributing hydrogen *[30]*.

A more important limitation of these models is that the concentration of hydrogen is assumed to have a constant and fixed value at the crack tip and on adjacent crack walls (or the flux of hydrogen at the crack surfaces is assumed zero which is a very special case). Indeed for all models of crack-tip hydrogen, this has been the primary assumption but is not realistic since crack-tip mechanical straining will induce different rates of hydrogen ion and water reduction due to disruption of surface films, even if only adsorbed films.

This problem was addressed by Turnbull et al *[31]*, albeit with a simplified elastic-plastic model. For ferritic steels, for which the lattice diffusivities are relatively rapid, the crack-tip concentrations were significantly lower than predicted if constant concentration boundary conditions applied, which would be applicable if diffusion was the slow step in overall transport. The implication was that transport of hydrogen atoms was surface reaction controlled. (For alloys of low lattice diffusivity, *e.g.* nickel-base alloys, transport would be diffusion controlled). The observation of surface reaction controlled hydrogen supply for ferritic steels shows some support for the views of Wei et al. *[32]* although not with the details in the model set out by Thomas and Wei *[33]*.

These models of crack-tip hydrogen are important in providing better understanding of the distribution of hydrogen at the crack tip. However, there remains the need to develop a model which is robust from an elastic-plastic perspective, has the appropriate crack electrochemistry component with respect to the boundary conditions, and can account for local crack tip straining with respect to the redistribution of hydrogen atoms to cracking sites. Such a mechanistic model has to be linked to a failure mechanism which takes into account local microstructural sensitivity on a quantitative basis. It appears still some years off in terms of realistic service life prediction. In addition, defining the hydrogen distribution at the tip when bulk charging is important poses real problems. Although Turnbull et al *[31]* made some initial progress in the latter case, it is difficult to envisage a reliable quantitative crack growth model emerging for such a complex situation.

Validation of Models - Given the complexity of the factors that are important in deterministic modelling, validation becomes critical and this must reflect the capability of the model of predicting the effect of a range of variables on the threshold and crack growth kinetics, ideally without partial fitting. Aspects which need some discussion are the temperature dependence of crack growth kinetics, the significance of the activation energy, the reliability and relevance of input data in model calculations and, linked to the latter, statistical variability in the parameters.

The temperature dependence of cracking is often considered to reflect the activation energy of the rate determining step (RDS) in the overall process. This, of course, is an erroneous assumption since all temperature sensitive processes prior to the RDS will have an influence on the measured activation energy. For example, if cracking is considered limited by transport of oxygen (along grain boundaries) *[34]* or hydrogen atom diffusion ahead of the crack tip *[35]*, the activation energy for crack growth will not be related simply to the activation energy for diffusion, although that must be a contributing factor. The activation energy for overall supply of the diffusing species to the site of cracking will depend also on the sub-surface

concentration of these species at the crack tip which brings in the temperature dependence of the relative rates of absorption and desorption and any other reaction process (e.g. electrochemical). Crack chemistry changes and refilming kinetics will also be temperature dependent. It would seem unlikely that the temperature dependence of these would be so weak compared with that for diffusion that no impact on crack growth would be observed. Despite this limitation, such comparisons have been used by Scott *[34]* and by Vogt and Speidel *[35]* (and historically by many others) in support of particular mechanisms. It poses the interesting question that if such good agreement is claimed between the activation energy for cracking and that solely for the diffusion coefficient, may that invalidate the proposed rate controlling mechanism?

A problem with validation of many models is the uncertainty in the input data used which allows some flexibility so that the mechanistic model becomes fitted to some extent. Vogt and Speidel *[35]* carried out an interesting exercise to evaluate the predictive capabilities of various models in explaining the temperature dependence of cracking in two aluminium alloys exposed to 3.5%NaCl or water. The model of Gerberich *[37]* for the crack growth rate due to hydrogen embrittlement was shown to predict well the temperature dependence of crack growth rate. The major concern is that the model was designed for cracking due to *internal* hydrogen in a precharged sample. There is no interface with the chemistry or electrochemistry in the crack which would both be temperature sensitive and would be expected to influence crack growth. The irony of course is that a good fit was obtained. To understand this, it is important to recognise that there is some selectivity in the parameters; for example, a value for the binding energy is chosen which best fits the data.

Quite clearly, with such flexibility in selection of parameters, there is so much scope for fitting that the observation of a fit cannot be used to assess the relevance of the model, especially one which would not be considered relevant even by the originating author. In the original work by Gerberich *[36]*, applied to a pre-charged 4340 steel coated with cadmium to retain the hydrogen, a reasonable prediction of the temperature dependence of cracking was obtained. However, since crack tip straining would break the cadmium film and cause the hydrogen to flow out through the crack tip, thus disturbing the boundary conditions assumed in the model, there remains unease about the predictive claims. In addition, the choice of diffusion coefficient is open to question since the effective diffusion coefficient for hydrogen atoms can be a sensitive function of the hydrogen atom concentration and data are not directly transferable from one condition to the other *[37]*.

Vogt and Speidel also showed a reasonable fit of a slip-dissolution model of Shoji et al *[38]* to stress corrosion crack growth of 2014 which was wet twice a day with 3.5%NaCl. The concern is that a single set of input parameters appeared to be used with no apparent account of the transient conditions at the crack tip induced by intermittent exposure. In another application, Galvele's surface mobility model *[39]* was shown to be a poor fit to the temperature dependence of stress corrosion crack growth of one alloy but a good fit to another. However, a partial fitting was involved.

It is evident that much more consideration must be given to the concept of model validation. The lack of relevant input data is often a major limitation in the

application of many models, however well-developed. In addition, there can be a degree of selectivity on the choice of input parameters, which may not have been determined under applicable conditions, and some degree of fitting. The process does not inspire confidence when critical judgements in service have to be made.

Aside from the need to ensure relevant input data are used, there is recognition that in many systems the input parameters may have to be described in terms of statistical distribution functions. A useful example of such an approach is that of Wei and Harlow *[40]*, although it is important to distinguish distributed functions reflecting potential variability in parameters from the adoption of inappropriate and irrelevant data.

Conclusions

In most service applications, the prediction of crack size evolution is empirically based. Accordingly, readily accessible databases for threshold and crack growth kinetics for a range of industrially relevant conditions are required to guide inspection intervals and to enable rapid estimates of residual life if cracks are detected during scheduled outages.

The reliability and relevance of data can be improved by more attention to the importance of dynamic loading, time-dependent effects and the impact of transients/excursions in temperature and environment.

Characterisation of short crack growth rates and multiple crack development and coalescence is still a major challenge.

Pitting is a precursor to cracking in a number of systems but the detailed evaluation of the evolution of a crack from a pit needs further study with the focus on short crack fracture mechanics and the use of short crack growth kinetics.

The application of mechanistically-based models to engineering applications is still comparatively rare. There is still debate about the applicability of different mechanisms. In addition, the critical components of modelling, viz. crack-tip chemistry, crack-tip hydrogen, and relevant input data for both are not as well developed as they should be. In view of these factors, attempts at validation can be fraught with uncertainty and misplaced deductions.

References

[1] Browne, R.J., Breare,J.M. Cane, B.J.and Williamson, J., **"Risk-Based Inspection Approach (RBI) to Plant Life Management,"** *Proceedings of the 3rd International Conference on Life Assessment and Life Extension of Engineering Plant, Structures and Components*, J. H. Edwards, P. E. J. Flewitt, B. C. Gasper, K. A. McLarty, P. Stanley, and B. Tomkins, Eds., Chameleon Press Ltd. (London), Cambridge, UK, 1996, pp. 59-74.

[2] Harnly, J.A., **"Risk-based prioritization of maintenance repair work,"** *Safety Progress Report*, Vol 17, No.1, 1998, pp. 32-38.

[3] Scott, P.M., **"A review of environment sensitive fracture of water reactor materials,"** *Corrosion Science*, Vol 25, 1985, pp.583-606.

[4] Scott, P.M., Meyzaud, Y. and Benhamou, C., **"Prediction of stress corrosion cracking of Alloy 600 components exposed to primary water reactor,"** *Proceedings of International Symposium on Plant Ageing and Life Prediction of Corrodible Structures*, T. Shoji and T. Shibata, Eds., NACE, Houston, Sapporo, Japan, May 1995, pp. 285-293.

[5] Hahn, G.J. and Shapiro, S.S., *Statistical Models in Engineering*, John Wiley, 1967.

[6] Gorman, J.A., Staehle, R.W., Stavropoulos, K.D. and Welty, C., **"Prediction of the performance of tubes in steam generators in pressurised water reactors,"** *Proceedings of Conference on 'Life Prediction of Corrodible Structures,'* R.N. Parkins, ed., Cambridge, UK, September 1991, NACE, Houston, Tx,1991, Paper 18.

[7] Milne, I., Ainsworth, R.A., Dowling A.R. and Stewart, A.T., **"Assessment of the integrity of structures containing defects,"** *International Journal of Pressure Vessels and Piping*, Vol.32, No.3, 1988, pp. 3-104.

[8] Koch, G.H. and Jaske, C.E., **"Prediction of remaining life of equipment operating in corrosive environments,"** *Life Prediction of Corrodible Structures*, R.N. Parkins, ed., Cambridge, UK, September 1991, NACE, Houston, 1991, Paper 25.

[9] Poole, P. and Cook, R. **"Current airframe fatigue problems,"** *Fracture from Defects, ECF-12*, M.W. Brown, E.R. de los Rios, and K.J. Miller, eds, Sept., Sheffield, 1998, EMAS, UK,1998, pp. 23-29.

[10] Dietzel, W., **"Characterisation of susceptibility of metallic materials to environmentally assisted cracking - Final Report,"** Programme Measurement and Testing of the European Commission, Contract No. MAT1 CT 930038, 1999.

[11] Reid, T.A. and Turnbull, A., **"Hydrogen embrittlement of duplex stainless steels evaluated by the interrupted slow stain rate test,"** *Proceedings of Eurocorr 99*, Dechema (Frankfurt am Main), 1999, Paper 10 (Oil and Gas Section).

[12] Griffiths, A J and Turnbull, A, **"Impact of long term exposure on corrosion fatigue crack growth of low alloy steels,"** *Proceedings of Corrosion '96*, National Association of Corrosion Engineers (Houston) 1996.

[13] Wei, R.P., **"Life prediction: A case for a multidisciplinary research,"** *Fatigue and Fracture Mechanics*, Vol. 27, ASTM STP 1296, eds. R. S. Piascik, J. C. Newman, and N. E. Dowling, eds., American Society for Testing and Materials, PA, 1997, pp. 3-24.

[14] Macdonald, D.D., **"The electrochemistry of turbine cracking,"** *Proc. Specialist Workshop on Corrosion of Steam Turbine LP Blades and Disks*, EPRI report TR-111340, eds. C. Wells, D. Rosario, and B. Dooley, Palo Alto , California, February 1998, EPRI.

[15] Kondo, Y., **"Prediction of fatigue crack initiation life based on pit growth,"** *Corrosion*, Vol 45, No. 1, 1989, pp. 7-11.

[16] Chen, G.C., Liao, C-M., Wan, K-C, Gao, M. and Wei, R.P., **"Pitting corrosion and fatigue crack nucleation,"** *Effects of the Environment on the Initiation of*

Crack Growth, ASTM STP 1298, , W.A. Van der Sluys, R.S. Piascik, and R. Zawierucha, Eds, American Society for Testing of Materials, PA, 1997, pp.18-33.

[17] Tsujikawa, S., **"Role of localised corrosion on initiation of stress corrosion cracks for austenitic stainless steels in chloride environment,"** *Proceedings of Conference on 'Stainless Steels '91*, ISIJ, Chiba, 1991, pp 48-55.

[18] Gangloff, R.P. and R.O. Ritchie, R.O., **"Environmental effects novel to the propagation of short fatigue cracks"**, *Fundamentals of Deformation and Fracture*, K.J. Miller, ed., Cambridge University Press, Cambridge, 1984

[19] Zhou, S and Turnbull, A, **"Impact of pitting on fatigue life of turbine blade material,"** *Fatigue of Engineering Materials*, in press, 1999.

[20] Zhou, S and Turnbull, A., **"Development of a pre-pitting procedure for turbine disc steel,"** NPL Report CMMT(B)282, submitted to *British Corrosion Journal*, 1999.

[21] Richard, H.A., May, B., Schollman, M., **"A finite element program for the prediction of crack growth and lifetime,"** *Lifetime Management and Evaluation of Plant, Structures and Components*, J.H. Edwards, P.E. Flewitt, B.C. Gasper, K.A. McLarty, P.Stanley and B. Tomkins, eds, Sept. 1998, EMAS, 1998, pp.267-274.

[22] Parkins, R.N. **"Realistic stress corrosion crack velocities for life prediction estimates,"** *Proceedings of Conference on 'Life Prediction of Corrodible Structures,'* R.N. Parkins, ed., Cambridge, UK, September 1991, NACE, Houston, Tx,1991, Paper 52.

[23] Ford, P.F. and Andresen, P.L., **"Development and use of a predictive model of crack propagation in 304/316L, A533B/A508 and Inconel 600/182 alloys in 288 °C water,"** *Environmental Degradation of Materials in Nuclear Power Systems*, G.J. Theus and Weeks, J.R.,Eds., The Metallurgical Society, 1988, p.789.

[24] Turnbull, A., **"Modelling of environment assisted cracking,"** *Corrosion Science*, Vol 34, (6), 1993, pp. 921-960.

[25] Turnbull, A, **"Importance of internal cathodic reactions for crevice and crack chemistry,"** *Proceedings of Environmental Degradation of Engineering Materials '99*, A. Zielinsli, D. Desjardins, J. Labanowski, J. Cwiek, Eds., Technical University of Gdansk1999 pp.73-82.

[26] Turnbull, A, **"Modelling of crack chemistry in boiling water reactor environments,"** *Corrosion Science*, Vol 39 (4) 1997, pp. 789-805.

[27] Jones, R.H. and Simonen, E.P., **"Crack tip chemistry of Stage I stress corrosion cracking,"** *Parkins Symposium on Fundamental Aspects of Stress Corrosion Cracking*, S.M. Brummer, E.I. Meletis, R.H. Jones, W.W. Gerberich, F.P. Ford and R.W. Staehle, Eds., The Minerals, Metals and Materials Society, 1992, pp.69-83.

[28] Sofronis, P. and McMeeking, R.M., **"Numerical analysis of hydrogen transport near a blunting crack tip,"** *J. Mechanics and Physics of Solids*, Vol 37, 1989, p.317-350.

[29] Krom, A.H.M., Koers. R.W.J. and Bakker, A., **"Hydrogen transport near a blunting crack tip,"** *J. Mechanics and Physics of Solids*, Vol 47, 1999, p.971.

[30] Lecoester, F., Chene, J. and Noel, D., *Materials Science and Engineering*, Vol A262, 1999, p.173-183.

[31] Turnbull, A. and Ferriss, D.H., **"Modelling of the hydrogen distribution at a crack tip,"** *Materials Science and Engineering*, Vol A206, 1996, p.1-13.

[32] Wei, R.P., Shim, G. and Tanaka, K., **"Corrosion fatigue and modelling,"** *Embrittlement by the Localised Crack Environment,* R.P. Gangloff, ed., AIME (Warrendale, Pa) 1984, pp.243-264.

[33] Thomas, J.P. and Wei, R.P., **"Corrosion fatigue crack growth of steels in aqueous solutions II: Modelling the effects of ΔK,"** *Materials Science and Engineering*, Vol. A159, 1992, pp.223- 228.

[34] Scott, P.M. and M. Le Calvar, **"On the role of oxygen in stress corrosion cracking as a function of temperature,"** *Corrosion-Deformation Interactions '96*, Ed. T. Magnin, The Institute of Materials (London), 1997, pp.384-393.

[35] Vogt, H. and Speidel, M.O., **"Stress corrosion cracking of two aluminium alloys: A comparison between experimental observations and data based on modelling,"** *Corrosion Science*, Vol. 40, N0. 2/3, 1998, pp 251- 270.

[36] Gerberich, W.W., Livne, T., Chen, X.-F., Kaczorowski, M., **"Crack growth form internal hydrogen - Temperature and microstructural effects in 4340 steel,"** *Metallurgical Transactions*, Vol 19A, 1988, pp 1319-1334.

[37] Griffiths, A.J. and Turnbull, A., **"On effective diffusivity of hydrogen in low alloy steel,"** *Corrosion Science*, Vol 37, No. 11, 1995, pp.1879-1881.

[38] Shoji, T., Suzuki, S. and Ballinger, R.G., *"Proceedings of International Symposium on Plant Ageing and Life Prediction of Corrodible Structures*, T. Shoji and T. Shibata, Eds., Sapporo, Japan, May 1995, NACE, Houston, 1995, p.881.

[39] Galvele, J.R., **"A stress corrosion cracking mechanism based on surface mobility,"** *Corrosion Science*, Vol 27, 1987, p.1.

[40] Wei, R.P. and Harlow, D.G., **"A mechanistically-based probability approach for predicting corrosion and corrosion fatigue life,"** *17th Symposium on Aeronautical fatigue. Durability and Structural Integrity of Airframes. Vol 1. Engineering materials* Advisory Services Ltd., Warley, UK, 1993, pp.347-366.

John R. Scully[1]

Environment-Assisted Intergranular Cracking: Factors that Promote Crack Path Connectivity

Reference: Scully, J. R., **"Environment-Assisted Intergranular Cracking: Factors that Promote Crack Path Connectivity,"** *Environmentally Assisted Cracking: Predictive Methods for Risk Assessment and Evaluation of Materials, Equipment, and Structures, ASTM STP 1401,* R. D. Kane, Ed., American Society for Testing and Materials, West Conshohocken, PA, 2000.

Abstract: Environment-assisted intergranular cracking occurs in many polycrystalline materials as a result segregation of impurities to grain boundaries, precipitation of second phases and solute depletion at grain boundaries, or precipitate free zone (PFZ) formation. The presence of a specific environment and sustained tensile stress can render a material susceptible if the required grain boundary metallurgical conditions exist. Models have been developed to describe conditions for intergranular cracking. Such models are usually based on either dissolution-controlled intergranular cracking or hydrogen embrittlement along grain boundary paths. Currently, these models rely on average descriptions of grain boundary segregation level, solute depletion, and PFZ character. However, solute depletion, segregation, and PFZ character can vary from grain boundary to boundary depending on boundary energy, crystallographic mis-orientation, and other factors. The propagation of an continuous intergranular crack through a component requires a high population of such highly susceptible grains, favorable geometrical grain facet orientation relative to direction of uniaxial tensile stress, or high hydrostatic tensile stress to overcome unfavorable geometric grain facet orientation. Statistical theories of fracture and bond percolation provide methods to quantify whether a critical population of susceptible grains is necessary to provoke extensive intergranular cracking. These theories provide insight into whether or not a well-connected intergranular crack can propagate through a structure. Two examples explore the existence of a bond percolation threshold in two substantially different systems that exhibit intergranular cracking by either anodic dissolution or hydrogen embrittlement.

Keywords: Bond percolation, crystallographic grain misorientation, geometric-grain misorientation, environment-assisted intergranular cracking, hydrogen trapping, solute segregation, solute depletion

[1] Professor, Center for Electrochemical Science and Engineering, Department of Materials Science and Engineering, University of Virginia, 116 Engineer's Way, Charlottesville, VA 22904-4745.

Copyright© 2000 by ASTM International www.astm.org

Introduction

Intergranular separation by cracking in polycrystalline materials involves severance of metallic bonds along grain boundaries in response to applied, residual, or corrosion product-induced stresses. The surfaces created in this manner expose the grain facets on either side of the original boundary as seen in Fig. 1. This mode of fracture often occurs at a much lower fracture stress and energy than cracking by ductile transgranular processes through the interior of grains. The exposure of specific materials to certain environments and stress can promote this low energy intergranular mode of separation even when fracture of the same material in vacuum would occur along a ductile transgranular path. Three types of environment-assisted intergranular cracking can occur in a wide variety of alloy/environment systems. These are known as intergranular stress corrosion cracking (IGSCC), intergranular hydrogen embrittlement, and intergranular solid as well as liquid metal embrittlement. An example of IGSCC is shown in Fig. 1.

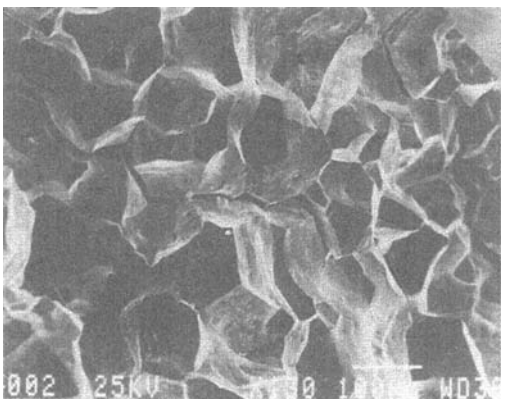


Figure 1 - *Intergranular stress corrosion cracking of sensitized AISI 304 (100 h at 600 °C) stainless steel during slow rising tensile testing in 0.5 M H_2SO_4 + 0.01 M KSCN solution under conditions where greater than 23% of grain boundaries were activated by Cr depletion.*

IGSCC is a pervasive problem in many technological applications that leads to extensive repairs, loss of service function, and safety-reliability concerns. IGSCC occurs in the weld heat affected zones of stainless steels pipes in high purity primary coolant waters in nuclear power plants, and in nickel-base alloys utilized as heat exchanger tubing when exposed to both the high purity primary as well as secondary coolant waters in power plants. It is also seen in Al-based precipitation age hardened alloys used in structural components in military and commercial aircraft exposed to humid atmospheric conditions. Ferrous alloys used in the oil and gas industry are also susceptible. For instance, intergranular stress corrosion cracking of mild steels used in buried gas transmission pipelines is a widespread international problem that has led to explosions caused by the ignition of leaking natural gas.

Common requirements include the need for a specific aqueous or non-aqueous environmental composition containing a corrosive, depassivating species (e.g., acids, halides, sulfur compounds, etc.) along with depletion of a protective alloying element along grain boundaries. Alternatively, segregation of foreign or impurity atoms that weaken grain boundary strength (e.g., atomic hydrogen, sulfur, phosphorus, or liquid mercury, etc.) may induce intergranular cracking. Another requirement is sustained tensile stress. The precise role of stress varies considerably depending upon whether or not intergranular separation is controlled by locally favorable electrochemical dissolution along a chemically weakened interface, or by locally favorable fracture along a mechanically weakened interface. In case of dissolution controlled IGSCC, stress can alter the thermodynamics of the corrosion reaction through the influence of lattice strain energy on the free energy of the atom being corroded. However, strain energy only alters the free energy and, hence, equilibrium oxidation potential of a stressed metal by a negligible amount compared to an unstressed metal. More likely, stress acts to separate and lift away corroded boundaries, fracture remaining uncorroded ligaments that hold boundaries together, and rupture any protective surface oxide films that protect boundaries from corrosive attack. In the case of a foreign atom that segregates to a grain boundary, a local applied stress or strain equal to the critical fracture stress (or strain) of the weakened interface causes grain boundary fracture.

Grain boundaries are often susceptible crack paths because they have lower surface energies than surfaces, as well as different nano-structure, and nano-chemistry compared to grain interiors. These differences can establish a preferred intergranular crack path along homophase (grain boundaries in a single phase alloy) as well as heterophase interfaces. Differences in structure and energy result from creation of a solid state interface even in high purity metals. Homophase interface energy was first described by nearest-neighbor broken bond models[*1*], later by dislocations[*2*], and recently by atomic simulation[*3*]. Given the five macroscopic and three microscopic degrees of freedom of homophase boundaries, their the energy and structure can vary greatly[*1*]. Their chemical character often differs as a result of segregation of detrimental impurities to boundaries or depletion of beneficial elements during precipitation and growth of a second phase. Such segregation often further lowers the energy of the interface.[*1*] Detrimental foreign atom impurities (e.g., S, P in Fe, Pb, Sn in Fe, Bi in Cu, S in Ni, etc.) are often dissolved in dilute solid solution within many engineering alloys[*4*], or are absorbed within polycrystalline materials during exposure to an environment (e.g., atomic hydrogen produced from electrochemical reduction of water or exposure to H_2 gas). The foreign atom may become enriched at grain boundaries (i.e., segregated and/or "trapped") with enrichment factors > 10,000,[*4*] subject to the equilibrium or non-equilibrium thermodynamic process governing the concentration of solute at such an interface[*5*]. Segregation tendencies also depend in a complex manner on boundary structure and energy[*1*].

The impact of interfacial segregation on materials properties are numerous; it influences grain boundary diffusion, grain growth, creep by interface cavitation, precipitate ripening kinetics as well as intergranular corrosion and cracking. In the case of electrochemically controlled intergranular dissolution, the segregant may depassivate the grain boundary region by disrupting the formation of protective oxide films. Two critical aspects of the IGSCC phenomena are (a) the monolayer coverage of the segregant at the

planar boundary in question, and (b) the degree to which a given segregant monolayer coverage alters interface strength and/or disrupts resistance to corrosion (i.e., its potency). For instance, sulfur locally depassivates nickel (i.e., disrupts the protective oxide film) and raises the *active* dissolution rate in acids depending on its coverage[*6*]. Intergranular dissolution occurs in acid solutions when sulfur is segregated to nickel boundaries. Sulfur segregation is also observed to embrittle nickel grain boundaries upon the application of stress[*7-12*]. In nickel, grain boundary impurities have been expressed in terms of a sulfur equivalent, C_S^{eq}[*8*]

$$C_S^{eq} = C_S + \kappa_P C_p + \kappa_{Sb} C_{Sb} + \kappa_X C_X \tag{1}$$

where C_X is the grain boundary concentration of the impurity element expressed in boundary monolayers and κ describes the potency of an element, x, compared to sulfur.

An unresolved issue concerns whether or not co-segregation of atomic hydrogen is required[*10*], and whether co-segregation of hydrogen and sulfur act in an additive manner[*8,9*] or synergistically[*7,10,11*] to embrittle boundaries. The atomistic process by which interface strength is reduced by a foreign atom is also under debate with two schools of thought. The decohesion model proposes that a sufficient enrichment of hydrogen or sulfur at boundaries causes a discernible weakening of bonds between adjacent atoms[*13*]. If hydrogen, sulfur or phosphorus, etc., accumulate at a planar defect then the decohesive strength is lowered[*14*] selectively along that interface. This can lead to preferential breakage of bonds given sufficient applied stress[*15*]. Embedded atom calculations show that a $\Sigma 9$ (221) tilt boundary in nickel experiences a decrease in cohesive strength from 18 to 8 GPa when the segregated monolayer coverage increases from 1×10^{-17} to 6×10^{-16} H atoms/cm^2[*15*]. Various expressions have been used to describe how transgranular cleavage or grain boundary fracture stresses are each reduced by such impurity segregation. The general form of these expressions, as first described by Briant[*16*], is

$$\sigma_{frac} = \sigma_{frac}^{Vacuum} - \alpha C_H^{\,x} - \beta C_X^{\,y} \tag{2}$$

where x and y are typically fractions (e.g., ½), σ_{frac}^{vacuum} describes fracture stress of a clean grain boundary in vacuum, and α as well as β describe the potency of each impurity. The concept is that σ_{frac} must fall below the applied stress on a significant fraction of grain boundaries to decrease the fracture toughness. In the case of grain boundary fracture, the concentrations of interest are the local boundary concentrations. The general view is that the local applied stress can be raised to σ_{frac} at a crack tip, corrosion pit, or machined notch as a function of the geometric stress concentration (e.g., notch or crack tip radius), plastic flow characteristics of the material, as well as global and local plastic constraint. Equation (3) does not predicts a critical impurity or hydrogen concentration threshold, yet one may still be observed. This is because it is reasonable to assume that some grain boundary concentration will decrease σ_{frac} below some other critical stress or strain associated with the criteria for ductile transgranular fracture. Therefore, the local fracture stress must be lowered and the applied stress must be raised, otherwise a transition from ductile to intergranular cracking is not seen. Another issue is

whether the mean or the extreme value of C_X determined from the distribution of measured values should be used. The distribution is expected due to various crystallographic grain boundary misorientations that alter segregation tendencies on certain grain boundaries.

In the second proposed mechanism, boundary segregants are observed to enhance local dislocation activity by shielding dislocation-dislocation and dislocation-particle interactions[*17*]. Dislocation generation and motion occur at a much lower stresses than required for decohesion. It has been shown that the activation enthalpy for dislocation slip in pure nickel decreases with increasing hydrogen[*18*]. Since hydrogen is segregated near nickel boundaries[*11*], it follows that slip is locally enhanced at the boundary.

Many examples of depletion of beneficial elements from grain boundaries also exist. Often depletion of a beneficial alloying element in polycrystalline materials occurs as a result of the "collector-plate" mechanism describing heterogeneous precipitation of a second phase at grain boundaries[*19*]. Numerous other phenomena also result from elemental depletion including precipitate free zone development and intergranular corrosion as well as IGSCC. An example of elemental depletion that promotes intergranular corrosion and stress corrosion is grain boundary Cu depletion in Al-Cu[*20,21*], Al-Cu-Mg[*22*], and Al-Cu-Li alloys[*23*]. Beneficial Cu is depleted from the Al-rich matrix near the grain boundaries and collected at θ-Al_2Cu, S-Al_2CuMg, and T_1-Al_2CuLi precipitate phases, respectively. Another example involves grain boundary Cr depletion (commonly referred to as sensitization) in Fe-Ni-Cr alloys containing interstitially dissolved carbon[*24,25*]. Here, Cr depletion occurs upon formation of $Cr_{23}C_6$ and other carbides[*26*]. Carbide formation occurs profusely on boundaries due to C segregation, heterogeneous carbide nucleation and fast transport of carbon along boundaries to support carbide growth. Equilibrium grain boundary Cr concentrations as low as 6.6, 8.4, and 10.8 wt. % are seen in AISI 316LN stainless steel (containing 18 wt. % Cr) after sensitization at 600, 650, and 700°C, respectively[*27*]. A minimum of about 13 wt. % Cr in solid solution is required to form protective passive films on Fe-Ni-Cr alloys in corrosive solutions. Hence, depletion of Cr at grain boundaries creates zones along grain boundaries that are iron-rich and highly susceptible to corrosion in specific environments in comparison to a "stainless steel." IGSCC of sensitized AISI 304 stainless steel can be very extensive (Fig. 1). Such boundary depletions usually occur during processing (e.g., slow quenching of thick sections, isothermal age hardening) or subsequent fabrication practices (e.g., weld heat affected zones). Note that properties such as toughness and ductility in vacuum or laboratory air are usually unaltered by sensitization.

The Influence of Grain Boundary Character on Environment-Assisted Intergranular Cracking

The variation of grain boundary misorientation, interface energy and structure have long been known to be significant factors affecting grain boundary segregation[*28*], fracture[*29*], boundary creep-cavitation[*30*] and sliding[*31*], liquid metal embrittlement[*32*], intergranular corrosion[*33-35*] and stress corrosion[*36*]. Several

studies indicate that coincident site lattice (CSL) boundaries are extremely resistant to these phenomena[*35,36*] and that a material could be rendered more resistant to them by creating a network of these special resistant boundaries[*37-39*]. Bicrystals studies as a function of tilt and twist angle of cross-boundary misorientation consistently indicate a strong relationship between IGSCC susceptibility and misorientation angle with deep minima in susceptibility at certain "special" angles including very low tilt angles below 15-20 degrees[*33,35,36*]. Some studies find a correlation between grain boundary energy and intergranular corrosion and IGSCC properties[*34,36*]. However, such relationships are not always observed and, consequently, variation in grain boundary energy with misorientation angle can not be used, alone, to forecast all the grain boundary properties necessary to predict IGSCC. Unfortunately, there is currently no quantitative model that can predict precisely how segregation or IGSCC varies with boundary structure. Still, the impact of grain-to-grain differences in IGSCC susceptibilities are profound.

In the slip/film rupture/dissolution model of IGSCC applied to Fe-Cr-Ni alloys[*40*], a decrease in the Cr concentration at grain boundaries increases the corrosion rate and decreases the boundary repassivation rate when bare surfaces are created by oxide film rupture[*41*]. Therefore, the extent of Cr depletion at individual grain boundaries governs IGSCC susceptibility. Sensitization is a strong function of misorientation angle and coincident site lattice relationship[*42*]. However, the factors governing Cr depletion at boundaries are complex. The Cr concentration in equilibrium with the carbide precipitate is fixed thermodynamically by the sensitization temperature, Cr and C activities and the equilibrium constant for carbide formation in the alloy. However, most grain boundaries contain only a few carbide particles and some variable Cr concentration exists near or along grain boundaries due to Cr concentration profiles that develop between separated boundary carbide precipitates[*43*]. The exact profile on each boundary depends upon misorientation, carbide spacing, time, temperature, and exact alloy composition[*27,43*]. The distribution of Cr concentration profiles from boundary-to-boundary causes a variation of crack growth rates on a grain-by-grain basis, explaining crack-front tortuosity[*43*], crack branching and scatter in macroscopic measures of cracking velocities as well as times-to-failure. Such distributions govern whether or not continuous IGSCC can initiate, propagate, and continue from one grain boundary to the next. The challenge exists to characterize the relevant homophase boundary properties that govern IGSCC for a large population and variety of boundaries.

Hydrogen embrittlement at grain boundaries would also be expected to be a function of grain boundary misorientation through the influence of each boundary's structure and energy on grain boundary hydrogen trapping as well as decohesion strength. Hydrogen segregation (e.g., trapping) at grain boundaries in the absence of stress is often described by a model where the trapped hydrogen, expressed as a fractional coverage of grain boundary sites θ_T, depends on the global or mean interstitial hydrogen coverage, θ_L, trap binding energy for the particular boundary, E_B, and temperature, T

$$\frac{\theta_T}{1-\theta_T} = \left(\frac{\theta_L}{1-\theta_L}\right)\exp\left(\frac{E_B}{RT}\right) \tag{3}$$

This simple expression considers all sites on a particular grain boundary to be equal. In reality, differences in trap binding energy will exist between sites on a single boundary. In Equation (3), the trap coverage is defined as the fraction of grain boundary sites that are occupied. The interstitial hydrogen coverage θ_L, expressed as the fraction of interstitial sites occupied by hydrogen atoms, depends on the specific material, temperature, and hydrogen overpotential during electrochemical charging or gas pressure during gaseous charging. Additionally, the hydrogen coverage on interstitial sites can be modified by a hydrostatic elastic tensile stress field. In the simplest case assuming negligible effect of hydrogen on the elastic modulus, interstitial coverage is enhanced by hydrostatic tensile stress. Fig. 2 illustrates the effect of increasing interstitial lattice coverage and trap binding energy on the coverage of trapped hydrogen at a grain

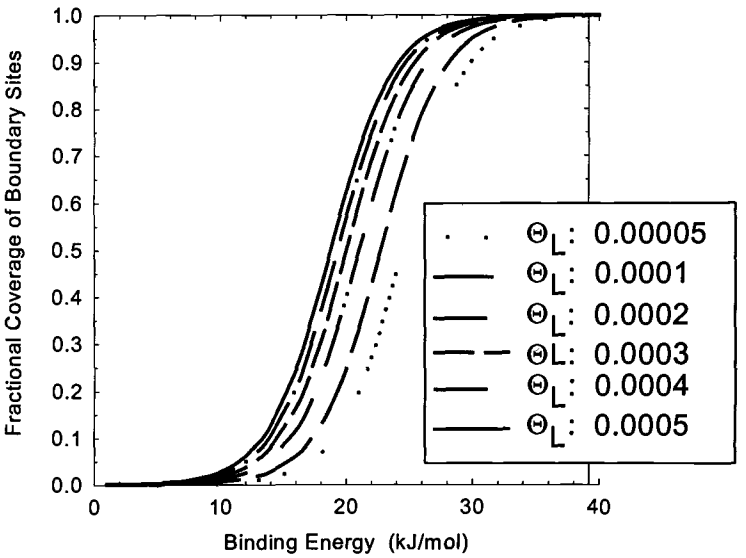


Figure 2 – *Grain boundary hydrogen monolayer coverage versus interstitial lattice hydrogen coverage for fixed grain boundary hydrogen trap binding Energies using a trapping law as defined in Equation 3.*

boundary in an unstressed lattice. It can be seen that variations in trap binding energy from grain to grain, if caused by differences in boundary nanostructure and nanochemistry, would produce grain-to-grain differences in trap coverage at a given interstitial hydrogen coverage. Unfortunately, trap binding energies as a function of crystallographic misorientation have not been reported. However, Kirchheim accurately accounted for the effect of variable grain boundary trapping on global hydrogen diffusion in a nanocrystalline Pd-Si alloy by assuming a Gaussian distribution of grain boundary trap binding energies[*45,46*]. Angelo, Moody and Baskes performed embedded atom

calculations of hydrogen trapping at $\sum 11$ (113), $\sum 9$ (221) and $\sum 3$ (112) tilt boundaries[(2)] in nickel[*47*]. Although specific boundary sites on one type of boundary possessed different binding energies, the maximum trap binding energy varied from 0.24-0.28 eV/atom (23.2-27 KJ/mol) depending on coincident site lattice (CSL) type. Experimental measurements of individual grain boundary trap binding energies may be lacking, but such simulations support the notion that boundary impurity segregation, hydrogen trapping, and decohesion strength differ depending on grain boundary structure and chemistry.

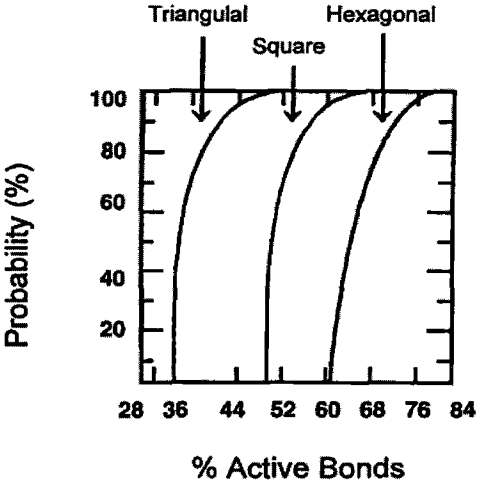
Bond Percolation Concepts Applied to Environment-Assisted Intergranular Cracking

A critical question is whether a continuous intergranular crack path made up of a connected cluster of highly susceptible boundaries can grow in a polycrystalline material and whether there exists a critical threshold percentage of *active* boundaries (i.e., *active* bonds) that enables intergranular cracking. Theories on fracture in disordered media have long considered the idea of a critical connected cluster of defects and statistical distributions of clustered defects[*48*]. In bond percolation theory, the probability of forming an infinite cluster of connected bonds rapidly approaches one at a critical percentage of active bonds. This critical percentage is called the percolation threshold[*49,50*]. In two dimensions, uniformly sized grains can be modeled by arrays of hexagons where each of the six sides forming boundaries is a bond. The bond percolation threshold for a hexagonal array of bonds is 0.65, i.e., 65% of the bonds are defective[*50*] as seen in Fig. 3a. A three-dimensional array of grain boundaries can be represented as a collection of two-dimensional planar interfaces, each representing a grain boundary facet (called bonds) that represents the interface between two grains[*51*]. An array of such grain boundaries has been represented by a Kelvin tetrakaidecahedron consisting of eight hexagonal facets and six square facets[*52*]. In a binary approach where bonds are described as either active of inactive, each of the grain boundaries (bonds) can be *active* (e.g., sensitized, in the case of IGSCC of stainless steel, or high enough trap coverage to trigger intergranular cracking in the case of hydrogen embrittlement) or in*active* (e.g., not sensitized or unable to fail by hydrogen embrittlement due to low coverage). Monte Carlo computer simulations have revealed the fraction of active bonds required for percolation in this three-dimensional structure[*52*]. The simulations were performed on arrays of 54 000 tetrakaidecahedral shaped grains, and 10 simulations were performed at each percentage of *active* bonds to produce statistically valid results[*52*]. The critical percentage of *active* grain boundary facets required to form a large cluster of connected grain boundary facets, each touching one another along a common edge of the Kelvin's tetrakaidecahedron, was found to be 23% as shown in Fig. 3b[*52*]. The meaning of such

(2) Sigma is defined as the number of lattice sites that are in coincidence across a homophase boundary or the reciprocal of this site density. For a sigma 3 boundary, one out of ever three atom sites is shared across a boundary. These sites are coincident to both grains. See M.L. Kronberg, F.H. Wilson, Trans. AIME, 185, p. 501 (1949).

a percolation threshold, once exceeded, is that a high probability exists of obtaining infinite cluster of connected, *active* grain facets (Fig. 3b). Another percolation threshold at 89% *active* bonds was found for a two-dimensional array of connected *active* grain facets that form a "rumpled" sheet within the three-dimensional array of grains[*52*].

(a)



(b)

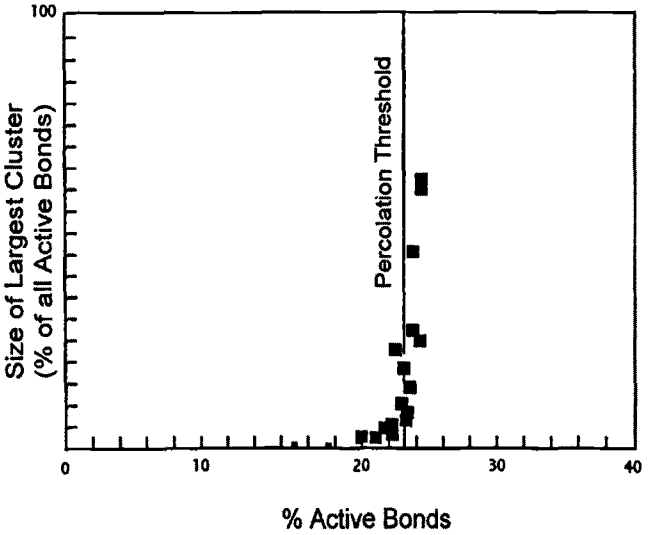


Figure 3 - *(a) Bond percolation thresholds predicted for two dimensional arrays of space filling boundaries consisting of various geometries [reg. 50]. (b) size of largest connected grain boundary cluster expressed as a percentage of all boundaries versus % active grain boundaries for an array of space filling, tetrakaidecahedral-shaped grains. The connected cluster size increases abruptly at he 23% percolation threshold. [ref. 52, reprinted with permission of the National Association of Engineers].*

In the context of environment-assisted intergranular cracking, the resulting premise is that a material possessing greater that 23, 65 or 89% of easily embrittled or easily corroded "*active*" grain boundaries will undergo cracking with a significant degree of intergranular separation and a drastic change in tensile properties from relatively ductile to extremely brittle. Moreover, any material with a percentage of *active* grain boundaries less than 23% will not separate in a brittle fashion with significant intergranular fracture since a large continuous connected path of *active* grain boundaries can not exist. Additional fracture across *inactive* grains must occur in a ductile manner with a corresponding higher fracture energy requiring a larger mechanical driving force. It is useful to ascertian whether a strong threshold percentage of *active* grain boundaries defines an abrupt change from ductile to brittle behavior in a polycrystalline material in order to better understand environment assisted intergranular cracking. However, a critical need exists to define the relevant grain boundary properties that define *active* behavior and control IGSCC for a large population of grains.

Characterizing the Structure, Energy, and Chemistry of Grain Boundaries

Structure and Interface Energy

In order to extend bond percolation theory to anodic dissolution controlled IGSCC or hydrogen controlled intergranular cracking, information on the structure, energy, and chemistry of grain boundaries is required. It is well known that surface and grain boundary energy depend on structure[*1*]. For a homophase interface such as a grain boundary, the interfacial energy depends on misorientation angle in both earlier[*2*] and more recent models[*3*]. Recent advances in orientation imaging microscopy (OIM) enable determination of misorientation angle and coincident site lattice categorization of special boundaries for a large population of grain boundaries[*39,53*]. OIM analysis was performed on 99.98 wt.% Ni to determine the misorientation angles of the grains. Fig. 4 shows the high angle boundaries where the misorientation angle is greater than 15% and CSL boundaries. A histogram of the population of high angle boundaries possessing certain misorientation angles has a skewed Gaussian shape with a median misorientation angle of 45 to 50°. Unfortunately grain boundary structure and interface energy are not by themselves sufficient information to forecast IGSCC. Therefore, the critical need also exists to characterize the factors that directly govern fracture (i.e., the local boundary chemistry and trapped hydrogen concentration for a large population of grains).

Sulfur and Hydrogen Segregation on Nickel Grain Boundaries

In order to extend bond percolation theory to anodic dissolution controlled IGSCC or hydrogen controlled intergranular cracking, the challenge also exists to determine the foreign atom grain boundary segregation (e.g., hydrogen trapping, sulfur segregation) characteristics and beneficial alloying element depletion levels of individual grains for a large population of grains. In past studies, analytical electron microscopy methods, secondary ion mass spectroscopy, auger electron spectroscopy, and tritium autoradiography have characterized such local chemical characteristics of single grain boundaries. However, these methods can only be reasonably applied to a limited number

of boundaries. Other methods must be devised to characterize the large population of grains necessary to test statistical theories of fracture.

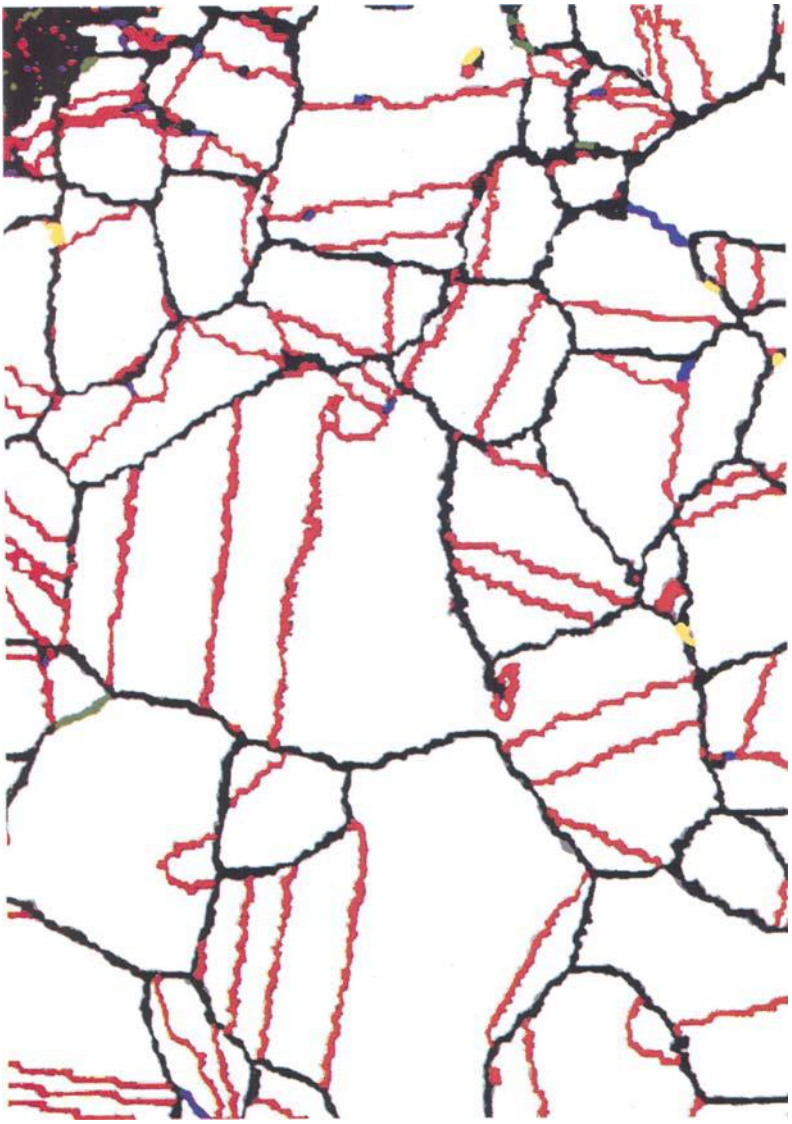


Figure 4 - *Results of orientation imaging microscopy on 99.98% nickel after recrystallization anneal for 30 minutes at 1100°C. High angle boundaries with greater than 15% misorientation are represented by thick black lines. Thin black lines represent low angle grain boundaries (<15%). Coincidence site boundaries are defined by colors; $\Sigma 3$ boundaries are orange, $\Sigma 5$ are green, $\Sigma 7$ are yellow, and $\Sigma 9$ are blue.*

Polycrystalline nickel is susceptible to environment-assisted intergranular cracking[*7-10,12*]. It is desirable to determine the fraction of boundaries containing embrittling levels of sulfur and hydrogen. High levels of sulfur and other elements at the grain boundaries of nickel will have a significant effect on grain boundary dissolution since sulfur poisons surface sites and prevents oxygen adsorption, limiting passivity[*6*]. The extent of dissolution is related to the S coverage; a longer segregating heat treatment will produce more grain boundaries that corrode. This phenomena can be exploited to find the percentage of grains in nickel with high levels of sulfur segregation. Electrochemical experiments were conducted under appropriate conditions to accelerate etching of only those grain boundaries containing segregated sulfur. The fraction of grain boundaries etched increased with increasing sulfur segregation promoted by heat treatment between 400-800°C. Optical image analysis was used to ascertain the fraction of grains experiencing preferential grain boundary etching.

Other methods can characterize *active* grain boundaries in terms of their propensity for hydrogen segregation. Two methods with spatial resolution include silver decoration of hydrogen-rich trap sites detected by backscattered scanning electron microscopy[*54,55*] and secondary ion mass spectroscopy[*11*]. Thermal desorption methods enable quantification of the trap binding energy associated with hydrogen attachment to defects (e.g., trapping) but lack spatial resolution. Subsequent to determination of trap binding energy, the hydrogen monolayer coverage at specific trapping states such as grain boundaries dislocations, or second phase particles can be calculated from a trapping law such as given by Equation 3[*56-59*]. The thermal desorption method enables determination of an "effective" binding energy associated with a spectrum of defects each possessing a slightly different specific trap binding energy. A population of distinctly different trap states with considerably different binding energies can yield a desorption spectrum containing desorption peaks that can be analyzed for the distinct binding energies associated with each trapping state.

An effective grain boundary hydrogen trap binding energy ranging from 19-28 kJ/mole has been obtained for high purity polycrystalline nickel[*47,60,61*]. A critical interstitial hydrogen concentration, $C_{H\text{-}crit}$, (where $C_{H\text{-}crit} = N_L \times \theta_{L\text{-}crit}$) can be suitably defined as the concentration of interstitial hydrogen located at interstitial lattice sites needed to produce experimentally greater than 50% intergranular fracture surface area. $C_{H\text{-}crit}$ has been defined from constant extension rate tests on cathodically polarized polycrystalline 99.98% Ni (aged 1h at 550°C) under cathodic polarization in 0.1 M H_2SO_4 [*61*]. In turn, a critical mean trapped hydrogen monolayer coverage, $\theta_{T\text{-}crit}$, greater than 0.5 is calculated for 99.98% Ni aged 1 h at 550°C using the trapping model of Equation 3 at the observed value of $C_{H\text{-}crit}$ (i.e., $\theta_{L\text{-}crit} = 0.0003$). This value of θ_T can be seen in Fig. 2. A critical trapped hydrogen monolayer coverage was obtained assuming a mean grain boundary trap binding energy of 20 kJ/mole[*61*] and an interstitial hydrogen concentration that depends on hydrogen overpotential, as is often observed in cathodic hydrogen charging. However, variations in grain boundary trap binding energies likely exist due to variations in boundary properties as strongly suggested by Kirchheim's analysis[*45,46*]. Very high interstitial hydrogen concentrations are required to produce grain boundary hydrogen monolayer coverages greater than 0.5 on low angle, special CSL boundaries, or any other type of boundary possessing a lower trap binding energy. This is seen in Fig. 2 when a low value of E_B is assumed. The presence of special boundaries that do not trap hydrogen would help explain regions of polycrystalline Ni

that significantly resist intergranular separation and fail by ductile transgranular processes even at the highest bulk interstitial hydrogen concentrations and levels of applied stresses[*61*]. If it is assumed that grains have different trapping properties, producing a distribution of binding energies due to the observed distribution in boundary orientations as shown in Fig. 4[3] and chemistries, then boundaries with lower binding energies will reach the critical coverage of 0.5 more gradually, or not at all, as interstitial hydrogen coverage is increased. This is seen in Fig. 5 where an assumed broad normal distribution in trap binding energies renders it more difficult to obtain a large percentage of boundaries with a high hydrogen coverage.

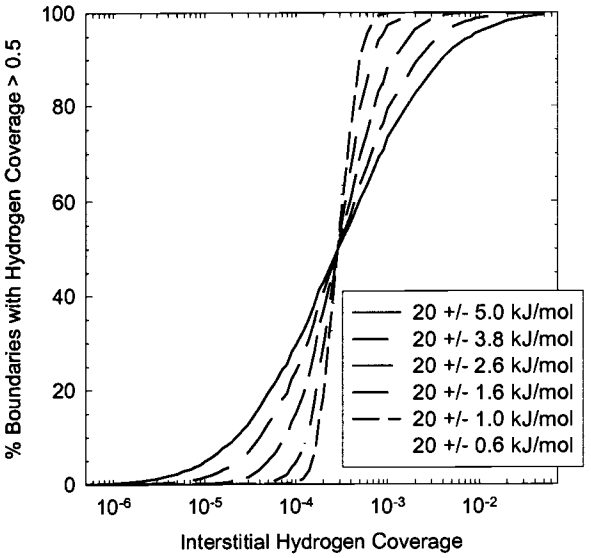


Figure 5 - Fraction of active boundaries defined by a hydrogen monolayer coverage > 0.5 as a function of interstitial hydrogen coverage for indicated statistical distributions of grain boundary trap binding energies with a 20 kJ/mole mean.

This occurs because the remaining low binding energy boundaries resist filling with trapped hydrogen despite increases in lattice hydrogen concentration. However, boundaries with binding energies higher than the mean can achieve a critical coverage ≥ 0.5 more easily with increasing interstitial hydrogen concentration assuming a large population of grains boundaries described by various assumed Gaussian distributions in trap binding energies (Fig. 5). In the limit of small standard deviations in trap binding energies approaching zero, every grain boundary abruptly reaches the critical hydrogen coverage of 0.5 at a single value of θ_L. Hence, the percentage of "*active*" boundaries defined by a selected hydrogen monolayer coverage (e.g., 0.5) can be determined for known interstitial hydrogen concentrations and known distributions of grain boundary trap binding energies (Fig. 5). In summary, the methods described above can be used to rationalize variations in the chemical description of whether a grain boundary is *active* from the hydrogen trapping perspective.

[3] The assumption of Gaussian distributions in trap binding energies is consistent with thermal desorption spectroscopy measurements of trap binding energies.

Grain Boundary Chromium Depletion Levels in Sensitized AISI 304 Stainless Steel

In order to extend bond percolation theory to anodic dissolution controlled IGSCC a chemical description of grain boundary sensitization is required. The metric for sensitization must correlate to grain boundary susceptibility. Recall the significance of the 13% Cr level in relation to the passivation of Fe-Cr-Ni alloys[(4)]. Instead of electron microscopy[*62*], an electrochemical method has been utilized to obtain Cr depletion levels from many boundaries simultaneously[*63-65*]. The resulting cumulative percentage of grain boundaries that possess a minimum Cr content below the bulk concentration are shown for sensitized AISI 304 stainless steel in Fig. 6[*65*]. The distribution reveals an expected trend; longer sensitizing heat-treatment times extend the range of Cr contents to lower concentrations along selected boundaries. Approximately 30% of all boundaries in the 100 h heat-treatment are depleted to below 13% Cr.

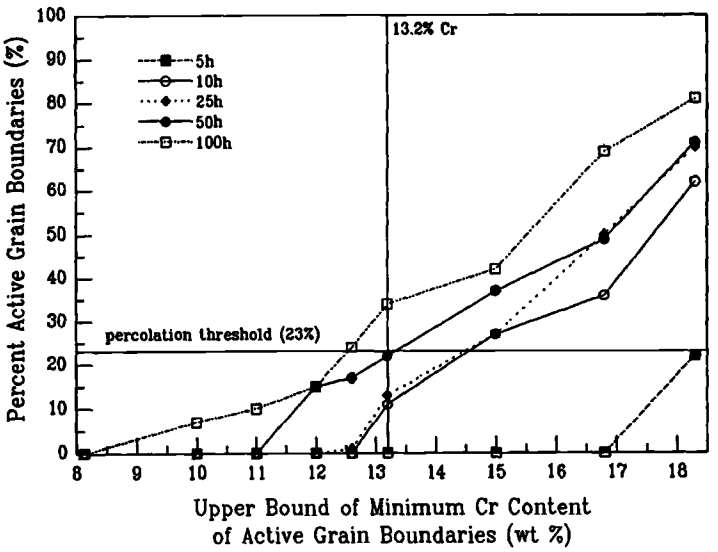


Figure 6 - *Percent active grain boundaries from Cr depletion. Each symbol represents the % of boundaries that possess Cr contents equal to or less than the Cr content given on the abscissa for the given sensitization time at 600 °C. Grain boundaries with a Cr content equal to the bulk alloy Cr content are not shown. The line at 13% represents the minimum Cr content required for passivation [ref. 65].*

(4) Bruemmer *et al*[25,26] determined the relationship between the minimum Cr content of the sensitized grain boundaries and the extent of IGSCC damage that occurs in 288°C aerated water relevant to commercial nuclear reactors. A sharp decrease in IGSCC resistance was observed at a critical grain boundary Cr content of approximately 13.5 wt. %.

Intergranular Cracking: a Bond Percolation Phenomenon?

Case 1: Sensitized AISI 304 Stainless Steel with Grain Boundary Cr Depletion

Sensitized AISI 304 stainless steel subjected to an increasing tensile stress cracks intergranularly in a variety of environments including sulfuric acid[*25*]. The percentage of *active* grain boundaries was varied by varying the isothermal heat treatment time for Cr depletion at 600°C and by exploiting the strong potential dependency of depassivation on Cr content[*65*]. Fig. 7a shows the percent reduction of area (a measure of tensile ductility) as a function of the percentage of *actively* corroding grain boundaries.

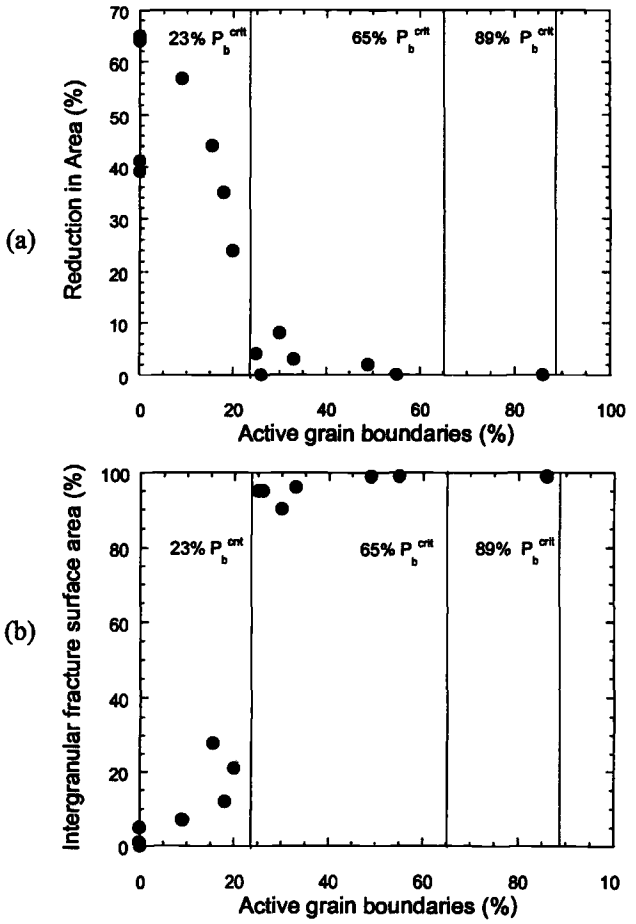


Figure 7 - *Ductility (a) and percentage of intergranular fracture surface area (b) normal to the cross-sectional plane of the tensile specimen versus the percentage of active boundaries defined from the standpoint of Cr depletion below the bulk volume concentration in AISI 304 stainless steel. Three possible bond percolation thresholds, P_b^{crit}, are given by vertical lines at 23, 65, and 89 % active boundaries.*

Low ductility indicates widespread IGSCC. A large decrease in ductility can be seen between 20 and 25 % *active* grain boundaries. The percent of intergranular fracture surface is also a sharp function of the population of *active* grain boundaries prone to IGSCC (Fig. 7b)[*66*]. Wells and coworkers also found a critical percentage of *active* grain boundary "bonds" of approximately 23 % for IGSCC in sensitized AISI 304 stainless steel[*52*]. These results confirm the significance of the 23 % bond percolation threshold described by the tetrakaidecahedral grain model. Very small clusters of connected active grain facets exist at a percentage of *active* bonds below 23 %. These small clusters may form cracks but do not allow widespread IGSCC. At a percentage of *active* grain boundaries at or above the 23 % bond percolation threshold, a well-connected path of *active* grain facets forms large connected clusters of grain boundaries. Consequently, an intergranular crack can continue to propagate over many grains in an aggressive electrolyte. This behavior is reflected by the low % reduction in area and high degree of intergranular cracking.

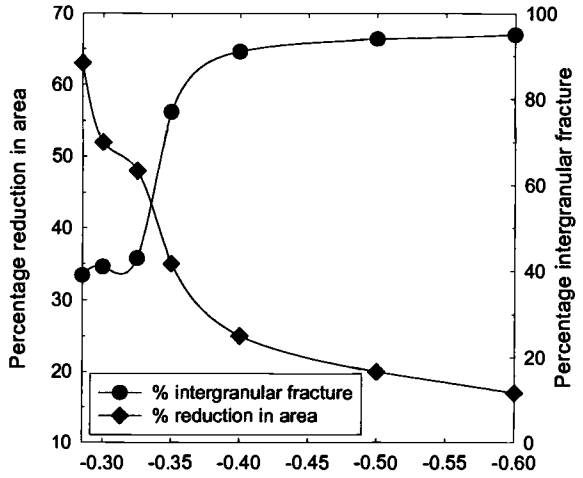
Case 2: Nickel with Grain Boundary Sulfur and Hhydrogen Segregation

Polycrystalline nickel cracks intergranularly when subjected to environments that enable hydrogen production and entry[*7-10,12*]. Bulk interstitial hydrogen concentration and, therefore, interstitial coverage, θ_L, can be controlled by adjusting electrochemical parameters such as hydrogen overpotential. Sulfur co-segregation to boundaries is controlled by nickel purity and segregating heat treatment[*4-11*]. Intergranular cracking susceptibility can then be examined as a function of the percentage of *active* grain boundaries using the notion that a certain critical hydrogen trap coverage describes an *active* grain boundary that promotes intergranular fracture under a certain state of stress. This exercise creates a test of whether a bond percolation threshold exists for intergranular cracking in polycrystalline nickel containing high coverages of grain boundary hydrogen and sulfur. This case differs from IGSCC of sensitized stainless steel in a number of respects. First, both hydrogen and sulfur can be trapped on grain boundaries ahead of any crack tip as a result of solid state diffusion and trapping in the alloy. This enables intergranular separation of *active* grains facets that are not in direct contact with external corrosive aqueous solutions or hydrogen gas. Hydrogen embrittlement controlled intergranular cracking is also a strong function of the resolved component of the applied tensile stress field normal to the planar interface of the grain facet. Intergranular corrosion, stress-assisted corrosion, or stress corrosion depend on stress, such as to produce a strain that ruptures oxide films, but are otherwise driven by electrochemical driving forces.

Constant extension rate tests on tensile specimens of cathodically polarized polycrystalline 99.98% Ni (aged 1h at 550°C) conducted under cathodic polarization in 0.1 M H_2SO_4[*61*] show clear evidence of embrittlement as indicated by the percentage reduction of area and the percentage of the primary fracture surface indicating intergranular separation (Fig. 8a). Test conducted in air failed with more than 70% of the fracture surface exhibiting ductile transgranular fracture characterized by microvoid initiation, growth and coalescence. The decrease in % reduction in area with increasing cathodic potential is indicative of a transition from specimen failure by ductile necking

and void growth to failure by intergranular separation with little necking. The applied cathodic potential in Fig. 8a was converted to interstitial hydrogen coverage (Fig. 8b) using known relationship between hydrogen overpotential, η, and interstitial hydrogen coverage, θ_L obtained from hydrogen permeation experiments on high purity nickel cathodically charged in H_2SO_4[*67*].

(a)



(b)

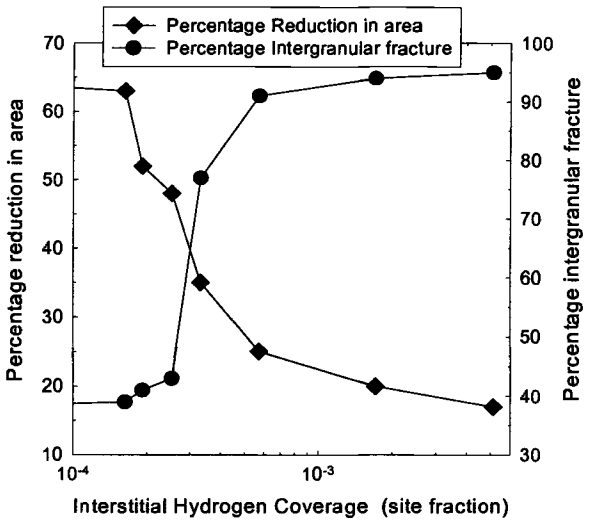


Figure 8 - *Ductility expressed as %RA and percentage of intergranular fracture surface area when examined normal to the cross-sectional plane of the tensile specimen vs. (a) hydrogen overpotential and (b) interstitial hydrogen coverage. Experimental results for 99.98% nickel with both sulfur and hydrogen grain boundary segregation. Cathodic charging was performed in 0.1 M H_2SO_4.*

The general form of the relationship between cathodic hydrogen evolution reaction overpotential, η, and steady state interstitial hydrogen coverage that applies to many metals is

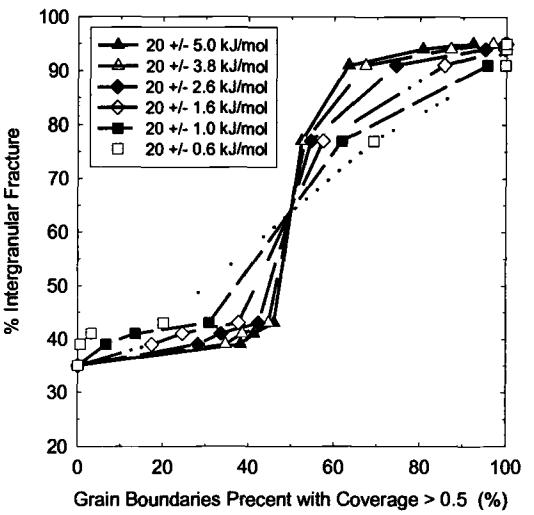
$$\left(\frac{\theta_L}{\theta_{L_{\eta=0}}}\right) = k \exp\left[\left(-\frac{b\eta F}{RT}\right)\right] \tag{4}$$

where $\theta_{L\eta=0}$ describes the interstitial hydrogen coverage at η=0, F is Faraday's constant, k and b are constants. The Langmuir isotherm is assumed to apply and the surface coverage of hydrogen is assumed to be low. The constant b is not necessarily equivalent to the transfer coefficient. Specific values of k, b, and $\theta_{L\eta=0}$ must be determined for each alloy electrolyte combination. A critical cathodic potential of -.035 V_{SCE} and θ_L of .0003 are seen to produce experimentally greater than 50% intergranular fracture (Figs. 8a and 8b) for 99.98% Ni. The trapped coverage is more informative since it is the trapped hydrogen coverage at grain boundaries that defines whether boundaries are *active* from the embrittlement standpoint (Equation 2). A critical mean trapped hydrogen monolayer coverage greater than 0.5 is calculated using equation 3 for 99.98% Ni assuming a mean trap binding energy, E_b, of 20 kJ/mole at $C_{H\text{-}crit}$ (i.e., θ_L ~.0003). It is reasonable to assume that 0.5 is the necessary mean grain boundary coverage to decrease the critical decohesion fracture stress below the stress associated with ductile transgranular fracture as discussed above since this coverage produced the condition where greater than 50% intergranular separation was observed. However, the effect of variations in trap binding energy should be considered given the variations in grain structure depicted in Fig. 4 for the same material used in the CERT tests. Various distributions in E_B that reflect different grain properties produce interesting dependencies of both the percentage reduction of area and percentage of intergranular cracking on the percentage of *active* grain boundaries (e.g., define as those boundaries with $\theta_T > 0.5$).

Figs. 9a and 9b illustrate the effect of the % of active boundaries possessing greater than the critical coverage on these embrittlement parameters. When a distribution of E_B values is imposed to account for variable trapping, an abrupt transition between ductile and brittle intergranular fracture behavior is seen when approximately 50% of the grain boundaries are active from the trapping perspective. Note that Figs. 9a and 9b differ significantly from Figs. 8a and 8b in the information conveyed. The former reveal the abrupt threshold at conditions where widespread intergranular fracture can be triggered in place of ductile fracture. In this regard, they indicate a transition based upon the global mean properties. In contrast, Figs. 9a and 9b indicate how the % reduction in area and percentage of intergranular fracture changes with the fraction of *active* boundaries that can undergo intergranular cracking. A continuous decline indicates no percolation threshold. A more gradual decrease in these parameters versus the % *active* boundaries is seen when all grain boundaries approach the physically unrealistic condition of almost identical trapping tendencies. A more abrupt transition is observed when a distribution of grain boundary properties is considered. One explanation for an abrupt threshold can be explained by the notion that a well-connected intergranular crack path can be formed when a critical threshold % active boundaries is reached. The fraction of active grain boundaries required can be compared to the bond percolation thresholds described above.

Recall that bond percolation thresholds at 23, 65 or 89% active bonds have all been proposed[*49,50,52*].

(a)



(b)

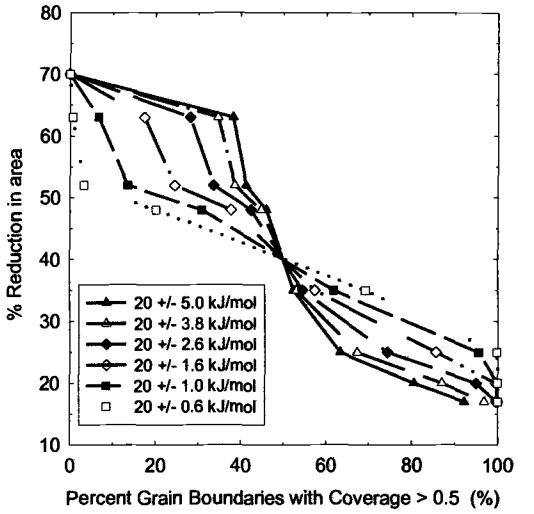


Figure 9 - *Percentage of fracture surface area that is intergranular (a) and ductility expressed as %RA (b) when examined normal to the cross-sectional plane of the tensile specimen versus the percentage of active boundaries defined from the standpoint of grain boundary hydrogen trapping. Experimental results for 99.98% nickel with a combination of sulfur and hydrogen grain boundary segregation.*

Note that the need in Figs. 9a-b for 50% active grain boundaries is greater than the 23% active grains required to produce widespread IGSCC in AISI 304 stainless steel. (Fig. 7) but less than the 65 and 89% thresholds. The exact reasons for this unexpected threshold are presently unclear. It may be a result of the strong dependency of fracture in the case of stress-dependent hydrogen embrittlement on the applied tensile stress. In order to form a connected intergranular path, this stress must exceed the critical grain boundary fracture stress despite grain facets that are unfavorably geometrically oriented relative to the applied tensile stress axis. Alternatively, a larger number of active boundaries and/or a higher coverage per boundary would be required to form a connected path, compensating for the fact that some of the active boundaries are unfavorably geometrically oriented with respect to the tensile stress direction. Hence, even if these boundaries possess $\theta_T >$ the critical coverage of 0.5, they might not crack unless θ_T, the hydrostatic stress, or both were very high. If this were the case, then a larger % of active boundaries than the simple 23% threshold would be required. Recall that the 23% threshold of active boundaries calculated from Monte Carlo simulations[*52*] did not specify grain facet orientation relative to stress axis. The reason the 23% threshold was found to apply for IGSCC of sensitized stainless steel may be related to the lack of sensitivity of the anodic dissolution-controlled phenomenon discussed in case 1 on stress. The section below discusses the effects of microgeometrical grain orientation considerations and the need for hydrostatic stress in intergranular hydrogen embrittlement.

Effects of Stress on Active Grain Boundary Connectivity During Intergranular Embrittlement

High hydrostatic tensile stress under conditions of small scale yielding and plane strain has various effects on intergranular embrittlement[*68,69*]. All of the effects cited in the literature are too numerous to cover here. Two aspects are discussed in the context of how stress would serve to increase the connectivity of the grain boundary crack path. These are (a) to increase the resolved normal tensile stress on unfavorable geometrically oriented grains relative to the applied tensile stress, and (b) to provide local enhancement of hydrogen concentration brought about by a tensile hydrostatic stress field. In decohesion models of grain boundary fracture, the applied local stress must equal or exceed the critical fracture stress of the grain boundary over some distance associated with microstructural features as described by Equation (2) [*13,68,69*]. This critical fracture stress is reduced as a function of sulfur and hydrogen coverage as shown by Equation 2. The local applied tensile stress within a region of material is elevated by crack or notch shape. It is also raised by high yield strength, plastic work hardening and by plastic constraint[*69,70*]. The conditions for grain boundary separation are assumed to involve attainment of a critical tensile stress normal to the macroscopic plane of the crack over some critical distance associated with microstructural features[*71*]. However, grain orientation at an angle relative to the crack plane dictates that the applied tensile stress normal to the macroscopic crack plane becomes even greater, or that a three dimensional tensile stress state exists so that the resolved component of tensile stress perpendicular to

a misoriented grain facet is large enough to trigger fracture on such an unfavorably geometrically oriented boundary. Clearly, development of hydrostatic tensile stress is helpful in raising such a resolved normal tensile stress. It could be argued that a crack in any specimen creates a triaxial state of tensile stresses that helps to provide the necessary resolved tensile stress normal to any boundary. However, it is unclear whether a crack in polycrystalline high purity Ni tensile specimens containing a blunt notch contains a sufficient three dimensional tensile stress state to overcome the geometric grain misorientation effect. Relaxation of the triaxial stress state could create the need for more active boundaries to compensate for unfavorable geometrically oriented boundaries. It would be interesting to observe whether a three dimensional state of tensile stress forces the percolation threshold from the observed 50% towards 23% active grain boundaries for 99.98% nickel. This would require repeating the tests shown in Figs. 8-9 using, for instance, a pre-cracked specimen under plane strain conditions.

Gerberich and Wright advanced a proposal on the effect of geometric grain misorientation on intergranular fracture[*72*]. The model was originally applied to unfavorable orientation of crystallographic cleavage planes[*73*]. The case treated involved an uncracked grain adjacent to an existing cleavage crack and addressed the issue of unfavorable grain orientation relative to the macroscopic crack tip plane. Unfavorable geometric grain orientation was characterized by the angles of either tilt (Fig. 10) or twist (Fig. 11) associated with uncracked grains ahead of the existing crack.

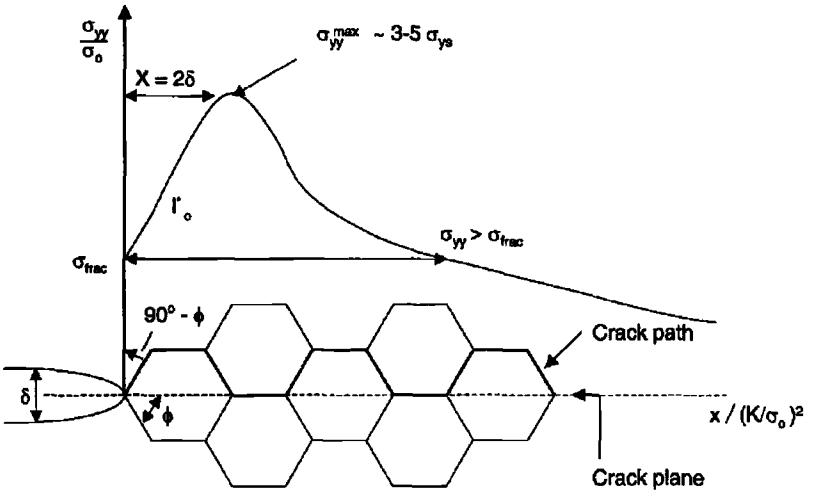


Figure 10 – *Depiction of a stress-controlled intergranular fracture process at a crack tip. The angle of grain boundary tilt is shown for unfavorable geometrically oriented grain boundaries with respect to the axis of applied stress,* σ_{yy}. *[After Ritchie, ref. 71]*

According to the proposal, the applied mode I stress intensity required to nucleate cracking along unfavorable geometrically oriented grain must exceed the minimal mode I stress intensity required to promoted cracking of perfectly oriented active grain boundaries. The following relationship[*72*] describes the effect for the twist orientation associated with an uncracked grain as depicted in Fig. 11

$$K_{I_\psi SCC} = K_{I_o scc} \sec^2 \psi \tag{5}$$

Here, $K_{I_0 scc}$ is the minimum stress intensity for intergranular cracking on ideally geometrically oriented grain boundaries and the angle Ψ represents the twist angle. A geometric twist misorientation between cleavage plane and existing crack plane was found to create a more difficult nucleation condition that a tilt geometric grain misorientation.

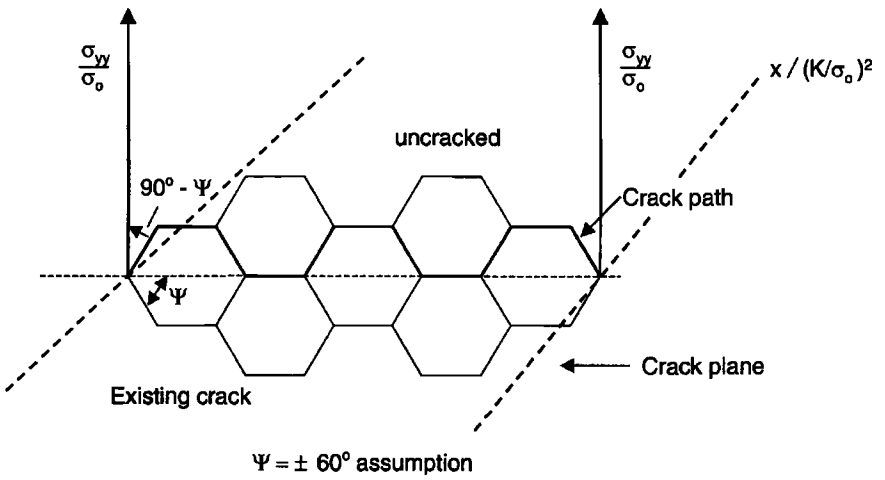


Figure 11 – *Depiction of a stress-controlled intergranular fracture process at a crack tip. The angle of grain boundary twist is shown for unfavorable geometrically oriented grain boundaries with respect to the axis of applied stress,* σ_{yy}. *[After Gerberich and Wright, ref. 72]*

The unfavorably oriented grains at angle Ψ with respect to the macroscopic plane of the crack will not crack unless the stress intensity factor is raised to $K_{I\Psi scc}$. When Ψ approaches 90 degrees, $K_{I\Psi scc}$ approaches a very high value. Extending this idea to intergranular fracture, the need for "chemically *active*" nickel grain boundaries is a necessary but not a sufficient condition to trigger intergranular fracture in a decohesion-type hydrogen embrittlement model. The concept is validated by K_{Iscc} data for 7075-

T7351 with pancake-shaped grains in the ST, TL and LT orientations[*72*]. Moreover, Smith and Scully observed a similar effect when hydrogen-induced cracking was investigated in under-aged alloy 2090 that was hydrogen charged, fatigue precracked and tested in an LT orientation[*74*]. When the alloy contained pancake shaped grains with the long axis of these grains parallel to the L orientation of the applied stress, such that the angle Ψ between the flat face of the grains and the precrack was large, K_{ISCC} was 37 MPa $(m)^{1/2}$. This was a minimal reduction from the air fracture toughness of 38 MPa $(m)^{1/2}$. $K_{I\Psi scc}$ was presumably increased because of the angle Ψ and, in fact, intergranular cracking was not observed. K_{ISCC} was lower {e.g., 20 MPa $(m)^{1/2}$ versus 35 MPa $(m)^{1/2}$ in laboratory air} for a recrystallized alloy of same composition and same charging conditions. Here the alloy contained small equaixed grains where the twist angle was limited (e.g., ~60 degrees). Intergranular cracking was observed in this case.

The second effect of high hydrostatic tensile stress is that a higher grain boundary trap coverage may be created[*68*]. This could further depress the critical fracture stress that opposes the applied tensile stress on all grains including unfavorably oriented grains such that a lower resolved normal tensile stress would still trigger intergranular cracking on an unfavorable geometrically oriented boundary. Hydrostatic tensile stress can raise the trapped grain boundary hydrogen coverage through the influence of lattice dilation on the equilibrium solubility of interstitial hydrogen. The following equation describes the trapped hydrogen coverage at grain boundaries accounting for hydrostatic tensile stress for conditions where $(1-\theta_L \sim 1)$. This expression assumes that hydrogen negligibly effects the elastic modulus of the material

$$\frac{\theta_T}{1-\theta_T} = \left(\frac{C_L}{N_L}\right)\exp\left(\frac{E_B + \sigma_H v_H}{RT}\right) \tag{6}$$

Here, C_L and N_L are the unstressed interstitial hydrogen concentration and perfect lattice interstitial site concentrations, respectively. σ_H and v_H are the hydrostatic stress and partial molar volume of the hydrogen interstitial in the metal lattice. The maximum value of σ_H at the peak stress at a crack tip has been proposed to be between 2.4-3 times the uniaxial yield strength of steels depending on work hardening. Thus, the grain boundary coverage within the region of high triaxial stress would be raised, which would further depress σ_{frac} such that it might be decreased to the level of the applied tensile stress normal to a unfavorably geometrically oriented grain boundary.

These stress related issues complicate the simple "chemical" description of "*active*" versus "*inactive*" grain boundaries applicable for dissolution-controlled IGSCC. Clearly, a "directed" bond percolation model where connections of clusters can propagate more readily in one direction than another may be more appropriate for describing environment-assisted intergranular cracking in such systems if they lack a three dimensional stress state[*75-77*].

Summary and Future Directions

Environment-assisted intergranular cracking occurs in many alloys as well as in high purity metals containing foreign atoms in dilute solid solution. Such species may segregate to homo- and heterophase interfaces and can be potent embrittling agents. A better understanding of the atomistic processes causing homophase interface weakening has been achieved through both atomic modeling and experimental bicrystal studies. Further progress has occurred through consideration of large populations of weakened boundaries using statistical theories of fracture and bond percolation theory. A catastrophic increase in IGSCC was observed at a bond percolation threshold of 23% *active* grain boundaries for sensitized AISI stainless steel undergoing anodic dissolution-controlled IGSCC. Here, a chemically *active* description of grain facets (bonds) defined by Cr depletion adequately predicts severe IGSCC. In the case of polycrystalline 99.98% nickel, a higher percolation threshold was seen when a distribution of grain boundary trap binding energies was imposed. However, polycrystalline nickel subjected to hydrogen-induced intergranular separation may depend on more than just the chemical description of *active* grain facets. Geometric grain facet orientation and the three dimensional nature of the stress state must be considered as well. Further advances in understanding the role of active grain boundary connectivity in IGSCC and intergranular hydrogen embrittlement will likely require more advanced bond percolation models of fracture involving easy crack propagation along clusters of defects situated along specific directions.

Acknowledgments

The authors acknowledge the financial support of the National Science Foundation (DMR-9357463) and the ongoing support of electrochemical instrumentation and software by E.G. &G. Princeton Applied Research and Scribner Associates, Inc.

References

[1] Howe, J.M, *Interfaces in Materials*, John Wiley& Sons, 1997.

[2] Read, W.T. and Shockley, W., *Physical Review,* Vol. 78, 1950, p. 275.

[3] Wolf, D. and Merkle, K.R. in *Material Interfaces: Atomic Level Structure and Properties*, D. Wolf and S. Yip, Eds., Chapman and Hall, London, 1992, pp. 87-150.

[4] Hondros, E.D. and Seah, M.P., *International Metals Reviews*, Vol. 222, No. 22, 1977, p. 262.

[5] Hondros, E.D. and Seah, M.P., *Metallurgical Transactions A,* Vol. 8A, 1977, p. 1363.

[6] Marcus, P. and Oudar, J., *Materials Science and Engineering,* Vol. 42, 1980, pp. 191-197.

[7] Latanision, R.M. and Opperhauser, Jr., H., *Metallurgical Transactions A,* Vol. 14A, 1974, pp. 483-492.

[8] Bruemmer, S.M., Jones, R.H., Thomas, M.T., and Baer, D.R, *Metallurgical and Materials Transactions A*, Vol. 14A, 1983, pp. 223-232.

[9] Jones, R.H., Bruemmer, S.M., Thomas, M.T., and Baer, D.R., *Metallurgical and Materials Transactions A*, Vol. 14A, 1983, pp. 1729-1736.

[10] Lassila, D.H., and Birnbaum, H.K., *Acta Metallurgica,* Vol. 35, 1987, pp. 1815-1822.

[11] Fukushima, H. and Birnbaum, H.K., *Acta Metallurgica,* Vol. 32, 1984, pp. 851-859.

[12] Mulford, R. A., *Treatise of Materials Science and Technology*, Vol. 25, Academic Press, 1983.

[13] Oriani, R.A. and Josephic, P.H., *Acta Metallurgica,* Vol. 22, 1974, p. 1065.

[14] Messmer, R.P. and Briant, C.L., *Acta Metallurgica,* Vol. 30, 1982, pp. 457-467.

[15] Moody, N.R. and Foiles, S.M., *Materials Research Society Symposium Proceedings,* Vol. 238, 1992, p. 381.

[16] Briant, C.L., Feng, H.C., McMahon, Jr., S.J., *Metallurgical Transactions A,* Vol. 9A, 1978, p. 625.

[17] Robertson, I.M. and Birnbaum, H.K., *Acta Metallurgica,* Vol. 34, 1986, p. 353.

[18] Sirois, E. and Birnbaum, H.K., *Acta Metallurgica,* Vol. 40, 1992, p. 1377.

[19] Aaron, H.B. and Aronson, H.I., *Acta Metallurgica,* Vol. 16, 1968, p. 789.

[20] Galvele, J.R. and de De Micheli, S.M.,*Corrosion Science,* Vol. 10, 1970, pp. 795-807.

[21] Muller, I.L. and Galvele, J.R., *Corrosion Science,* Vol. 17, 1977, pp. 179-193.

[22] Urushino, K. and Sugimoto, K., *Corrosion Science,* Vol. 19, 1979, pp. 225-236.

[23] Kumai, C., Kusinski, J., Thomas, G., and Devine, T., *Corrosion,* Vol. 45, 1989, pp. 94-302.

[24] Bain, E.C., Aborn, R.H., and Rutherford, J.J.B., *Transactions of the American Steel Treating Society,* Vol. 21, 1933, 481.

[25] Bruemmer, S.M., Arey, B.W., and Charlot, L.A., *Corrosion,* Vol. 48, 1992, p. 42.

[26] Bruemmer, S.M. and Charlot, L.A., *Scripta Metallurgica,* Vol. 20, 1986, p. 1019.

[27] Hall, E.L. and Briant, C.L., *Metallurgical Transactions.,* Vol. 15A, 1984, p. 793.

[28] Hondros, E.D. and McLean, D., *Philosophy. Magazine A,* Vol. 29, 1974, p. 771.

[29] Wantanabe, T. and Davies, P.W., *Philosophy Magazine A*, Vol. 37, 1978, p. 649.

[30] Don, J. and Majumdar, S., *Acta Metallurgica*, Vol. 34, 1986, p. 961.

[31] Wantanabe, T., Yamada, M., Shima, S., and Karashima, S., *Philosophy Magazine A*, Vol. 40, 1979, p. 667.

[32] Kargol, J.A. and Albright, D.L., *Metallurgical Transactions A*, Vol. 8, 1977, p. 27.

[33] Arora, O.P. and Metzger, M., *Transactions of the Metallurgical Society AIME*, Vol. 236, 1966, p. 1205.

[34] Hasson, G., Boos, J.-Y., Herbeuval, I., Biscondi, M., and Goux, C., *Surface Science*, Vol. 31, 1972, p. 115.

[35] Yamashita, M., Mikaki, T., Hashimoto, S., and Miura, S., *Philosophy Mangazine A*, Vol. 63, 1991, pp. 695-705.

[36] Yamashita, M., Mikaki, T., Hashimoto, S., and Miura, S., *Philosophy Magazine A*, Vol. 63, 1991, pp. 707-726.

[37] Palumbo, G. and Aust, K.T., *Acta Metallurgica*, Vol. 38, 1990, p. 2343.

[38] Crawford, D.C. and Was, G.S., *Metallurgical Transactions A*, Vol. 23A, 1992, p. 1195.

[39] Mason, T.A. and Adams, B.L., JOM, Oct. 1994, p. 43.

[40] Vermilyea, D.A., *This Journal*, Vol. 119, 1972, p. 405.

[41] Newman, R.C. and Sieradzki, K., *Corrosion Science*, Vol. 23, 1983, p. 363.

[42] Ortner, S.R. and Randle, V., *Scripta Metallurgica*, Vol. 23, 1989, p. 1903.

[43] Bennett, B.W. and Pickering, H.W., *Acta Metallurgica*, Vol. 36, 1988, p. 539.

[44] Bourcier, R.J., Scully, J.R. and Jones, W.B.: *A Probabilistic Model of IGSCC*, Symposium Proceedings on Lifetime Prediction of Corrodible Structures, National Association of Corrosion Engineers, Kauai, HI, 1991.

[45] Kirchheim, R. and Stolz, U., *Journal of Non-Crystalline Solids*, Vol. 70, 1985, pp. 323-341.

[46] Kirchheim, R., *Progress in Materials Science*, Vol. 32, 1988, pp. 261-325.

[47] Angelo, J.E., Moody, N.R. and Baskes, M.I., *Modeling and Simulation in Materials Science Engineering*, Vol. 3, 1995, pp. 289-307.

[48] Herrmann, H.J. and Roux, S., *Statistical Models for the Fracture of Disordered Media*, North-Holland, NY, 1990.

[49] Stauffer, D., *Introduction to Percolation Theory*, Taylor and Francis, London, 1985.

[50] Shante, V.K.S. and Kirkpatrick, S., *Advances In Physics*, Vol. 20, 1991, p. 325.

[51] McLean, D., *Grain Boundaries in Metals*, Clarendon Press, Oxford, UK, 1957.

[52] Wells, D.B., Stewart, J., Herbert, A.W., Scott, P.M. and Williams, P.E.: *Corrosion*, Vol. 45, 1989, pp. 649-60.

[53] Pan, Y. and Adams, B.L., *Scripta Metallurgica*, Vol. 30, No. 8, 1994, p. 1055-160.

[54] Schober, T. and Dieker, C., *Metallurgical and Materials Transactions A*, Vol. 14A, 1983, pp. 2440-2442.

[55] Yao, J. and Cahoon, J.R., *Metallurgical and Materials Transactions A*, Vol. 21A, 1990, pp. 603-608.

[56] Woodruff, D.P. and Delcher, T.A., Desorption-Spectroscopies, *Modern Techniques in Surface Science*, 1986, pp. 279-299.

[57] Choo, W.Y. and Lee, J.Y., *Metallurgical Transactions A*, Vol. 13A, No. 2, 1982, pp. 135-140.

[58] Lee, H.G. and Lee, J.-Y., *Acta Metallurgica*, Vol. 32, No. 1, 1984, pp. 131-136.

[59] Young, G.A. and Scully, J.R., *Scripta Metallurgica*, Vol. 36, 1997, pp.713-719.

[60] Lee, S. and Lee, J., *Metallurgical and Materials Transactions A*, Vol. 17A, 1986, pp. 181-187.

[61] Johnson, J.T., "Does a Bond Percolation Threshold Exist for Intergranular Cracking in Polycrystalline Nickel," Masters Thesis, University of Virginia, Jan. 1998.

[62] Chen, J.-S., Radmilovic, V., and Devine, T.M., *Corrosion Science*, Vol. 30, 1990, p. 477.

[63] Frankenthal, R.P. and Pickering, H.W., *This Journal*, Vol. 120, 1973, p. 23.

[64] Devine, T.M., *Acta Metallurgica*, Vol. 36, 1988, p. 1491.

[65] Gaudett, M.A. and Scully, J.R., *Journal of the Electrochemical Society*, Vol. 140, 1994, p. 3425.

[66] Gaudett, M.A. and Scully, J.R., *Metallurgical and Materials Transactions A*, Vol. 25A, 1994, pp. 775-787.

[67] Latanision, R.M., and Kurkela, M., Corrosion Journal, Vol. 39, 1983, pp. 174-181.

[68] Oriani, R.A., *Corrosion Journal*, Vol. 43, 1987, pp. 390-397.

[69] Akhurst, K.N., Baker, T.J., *Metallurgical Transactions A*, Vol. 12A, 1981, p. 1059.

[70] Hertzberg, R.W., Deformation and Fracture Mechanics of Engineering Materials, 4th Addition, John Wiley & Sons, Inc., 1996.

[71] Ritchie, R.O., Knott, J.F., Rice, J.R., Journal of Mechanical Physical Solids, Vol. 21, 1973, p. 395.

[72] Gerberich, W.W., Wright, A.G., In Environmental Degradation of Engineering Materials in Hydrogen, M.R. Louthan, R.P. McNitt and R.D. Sisson, eds., VPI Press, Blacksburg, 1981.

[73] Gell, M. and Smith, E., *Acta Metallurgica*, Vol. 15, 1967, pp. 253-258.

[74] Smith, S.W. and Scully, J.R., "*Hydrogen Trapping and its Correlation to the Hydrogen Embrittlement Susceptibility of Al-Li-Cu-Zr Alloys*," in Hydrogen Effects in Materials, edited by A.W. Thompson and N.R. Moody, The Minerals, Metals & Materials Society, 1996.

[75] Durrett, R. and Schonmann, R.H., *Annals of Probability,* Vol. 77,1988, p. 583.

[76] Efros, A.L., *Physics and Geometry of Disorder:, Percolation Theory* Mir Publishers, Moscow, 1986.

[77] Scully, J.R., MRS Bulletin, Vol. 24, 1999, pp. 36-42.

P. Sofronis[1] and A. Taha[2]

Micromechanical Modeling of Hydrogen Transport—A Review

Reference: Sofronis, P. and Taha, A., **"Micromechanical Modeling of Hydrogen Transport—A Review,"** *Environmentally Assisted Cracking: Predictive Methods for Risk Assessment and Evaluation of Materials, Equipment, and Structures, ASTM STP 1401*, R. D. Kane, Ed., American Society for Testing and Materials, West Conshohocken, PA, 2000.

Abstract: Reviewing the mechanical aspects of stress corrosion cracking and hydrogen embrittlement almost 25 years ago, Rice [*1, 2*] indicated that an accurate analysis of hydrogen transport as affected by local stresses and strains is of primary importance toward understanding the conditions under which the mechanisms causing hydrogen embrittlement operate [*3*]. In 1980, Hirth in a review article [*4*] made it clear that trapping of hydrogen is a very important part of hydrogen embrittlement, and its significance lies behind the embrittling mechanisms. The purpose of this study is to review the models of hydrogen transport in non-hydride forming systems, and draw conclusions as regards to the hydrogen degradation effect. It should be pointed out that this review does not aim at identifying and quoting the entire literature on the subject, which is voluminous. In fact, there is a number of recent articles devoted on various specific issues of hydrogen transport, and related issues of trapping [*5-12*]. Rather, the effort will be directed toward providing the status of our current understanding of hydrogen transport, and in particular how solid mechanics methodology can help in this direction.

Keywords: hydrogen, diffusion, transport, embrittlement, plasticity, fracture

Introduction

It is well-known that the manifestations and kinetics of hydrogen induced fracture are affected by the source of hydrogen, namely internal or solute and external (gaseous or corrosion environments) [*13-16*]. There is no evidence, however, that for a given alloy the fracture mechanism depends on the hydrogen source [*13, 17-19*]. Furthermore, it has been established experimentally that the interaction of hydrogen with the lattice and defects in the vicinity of a major macrocrack [*20*] is the common feature of the hydrogen

[1] Associate Professor, Department of Theoretical and Applied Mechanics and Materials Research Laboratory, University of Illinois at Urbana-Champaign, 104 S. Wright Street, Urbana, IL 61081.

[2] Graduate Research Assistant, Department of Theoretical and Applied Mechanics, University of Illinois at Urbana-Champaign, 104 S. Wright Street, Urbana, IL 61081.

Copyright© 2000 by ASTM International www.astm.org

degradation phenomena [*6, 7, 16, 21-24*]. The ductility minimum versus temperature (at low temperatures hydrogen diffusion slows whereas at high temperatures stress levels and thermodynamics do not allow for the degradation reaction of hydrogen to dominate), the increase in ductility with increased strain rate (hydrogen cannot diffuse effectively), the incubation period, and possible critical concentration build-up before fracture are all common features in the hydrogen embrittlement phenomenology. They reflect the hydrogen transport kinetics rather the mechanisms of embrittlement, as Birnbaum [*13*] points out.

The purpose of this work is to review the progress to date in analyzing hydrogen transport and trapping coupled with material mechanical behavior at a crack tip [*1, 2, 25*] or a rounded notch [*25, 26*]. Hydrogen concentrations predicted in conjunction with a continuum plasticity viewpoint can then be used to correlate experimental observations on crack initiation. In the interest of clarity and economy, the systems that are investigated do not form hydrides (e.g., steels, Fe and Ni). A detailed presentation of the micromechanical treatment of hydrogen transport and diffusion in the presence of hydride formation can be found in the recent work of Lufrano *et al.* [*27, 28*].

Hydrogen Transport Modes

Hydrogen adsorption, transport, accumulation, and the resulting degradation effect on the material behavior can best be visualized by the standard road map of Thompson and Bernstein [*29*]. Following that map, one may distinguish the following modes of hydrogen transport.

Transport by Lattice Diffusion

Once hydrogen is adsorbed and absorbed in a metal or an alloy, it may reside in normal interstitial sites (NILS) [*30-32*]. The number of hydrogen atoms that a given lattice can accommodate depends on its crystal structure [*31*]. In bcc and fcc systems hydrogen can occupy either tetrahedral or octahedral site positions [*32, 33*]. It is relevant here to say that the exact kind of interstitial site occupancy in various solid solutions has not yet been established with certainty [*4, 23*].

Troiano [*34*] reported that hydrostatic stress affects the hydrogen distribution in a material under stress. The interaction [*35-39*] between solute hydrogen atoms and an applied stress field results from the hydrogen-induced volume [*32, 40*] and local moduli changes [*41, 42*] that accompany the introduction of the solute hydrogen in the lattice [*34, 43*]. In regions of tensile hydrostatic stress and softened elastic moduli [*44*], interstitial hydrogen has a lower chemical potential [*45, 46*]. As a consequence, diffusion through normal interstitial lattice sites (NILS) is generated toward these regions, tending to eliminate the gradients of the chemical potential. Regions with compressive hydrostatic stress or hardened elastic moduli are depleted [*44*]. Diffusion of hydrogen atoms through the lattice is rapid [*47, 48*] and is characterized by low activation enthalpies, as a result of which hydrogen remains mobile even at very low temperatures. Johnson [*49*] points out that even though hydrogen diffusivity varies among metals, it is several orders of magnitude larger than the diffusivity in metals of other species.

In the discussion above, it was considered that the hydrogen solute does not interact with a deviatoric stress field. This assumption is in agreement with direct experimental evidence from studies using neutron scattering, channeling, diffuse and quasi-elastic neutron scattering, and neutron spectroscopy reviewed in the article by Hirth [*4*]. These studies indicate that the hydrogen induced lattice distortion is essentially dilatational. In a review of the elastic interactions of hydrogen with the lattice of iron alloys [*50*], Puls states that experimental evidence of impurity interstitials in metals with bcc crystal structure supports tetrahedral site occupancy associated with either a very small or negligible amount of tetragonality. It should be mentioned though that both Hirth and Puls maintain that site occupancy, dipole tensor symmetry, and elastic moduli are subjects that need to be further investigated. Contrary to this direct experimental evidence associated with the crystalline lattice behavior, Hsiao and co-workers [*51-54*] interpreting permeation measurements, claim that hydrogen in the lattice causes a strong tetragonal distortion. In addition, they state that the observed hydrogen-induced cracking at torsion smooth samples [*55*] or torsion of notched round bars [*56*] (termed as Type III specimens) suggests indirectly that the hydrogen strain field in α-Fe is non-spherical. The idea underlying this thesis is that the deviatoric stress field in a torsion test could not result in hydrogen concentration enhancement if the hydrogen strain field were purely dilatational, and as a result, no hydrogen induced cracking should have been observed in those tests. With regard to the interpretation of the results from the torsion test, the following can be mentioned: i) clearly, the rounded notch torsion specimen does not reproduce the conditions of mode III type of antiplane shear, especially if the diameter of the specimen is not large enough and the notch root radius not small enough [*57, 58*]; ii) the conclusions are derived on the supposition that hydrogen induced cracking is due to the development of a critical hydrogen concentration, which is only an assertion; iii) grain boundaries, inclusions and precipitates perturb locally the stress field and in general introduce non-pure mode III components [*57*]; iv) the elastic stress fields of dislocations near the specimen surface and their trapping capabilities, the presence of plastic flow, and the role of plasticity in hydrogen delayed cracking are ignored altogether, despite the fact that it is reported that hydrogen cracking in the rounded notch torsion specimen occurs only when the applied torque is larger than the yield torque [*56*].

Trapping

Transported hydrogen through NILS diffusion can interact with and accumulate at various microstructural heterogeneities such as dislocations, grain boundaries, inclusions, voids, surfaces and impurity atoms described as traps [*7, 8, 59, 60*] and from there initiate fracture [*6*]. Wert and Frank [*8*] note that trapping characterizes the fact that interstitial solute atoms often find interstices associated with lattice imperfections to be energetically preferable to NILS [*7*]. It has been well established that trapping is a very important part of hydrogen embrittlement and its significance lies behind the embrittling mechanisms [*4, 6, 7, 22-24, 29, 61, 62*]. By a way of example, Gibala and Kumnick [*7*] state that the susceptibility to hydrogen embrittlement of a given steel is characterized by the fact that it must be stressed at temperatures high enough so that lattice diffusion is assisted but low enough so that substantial hydrogen goes to trap sites to lead to embrittlement.

Characterization of the trap density, (the number per unit volume), binding energy and occupancy in a given system is a difficult problem and much research has been carried out in this direction [*60, 63-68*]. Identifying the type of traps in a given system is also a stubborn issue [*67-74*]. To measure the trap density and binding energy, the most direct approach is to correlate experimental results on measured permeation transients and time lags with full numerical solutions of the hydrogen diffusion equation [*9, 75*]. In a recent work, Turnbull *et al.* [*76*] reviewed hydrogen desorption models and proposed a model for the calculation of the trap binding energy. A graphical approach based on the McNabb and Foster formalism [*77*], when traps are nearly saturated or dilutely occupied, has been used by Kumnick and Johnson [*64, 67*] to make trap parameter measurements on high purity polycrystalline iron. For pure iron, Kumnick and Johnson [*67*] identified the traps with the imperfection structure, dislocations and point defect aggregates and calculated the trap binding energy equal to 60 kJ/mole independent of temperature and plastic deformation. The measured trapped densities ranged from 10^{20} traps/m^3 for annealed iron to 10^{23} for heavily deformed iron. Hirth [*4*] pointed out that a binding energy value of the order of 60 kJ/mole could well correspond to trap sites of the standard mixed or screw dislocation cores. Tien *et al.* in their dislocation sweep-in model [*78*] assume that there exists one hydrogen atom site per atomic plane threaded by a dislocation. The same assumption was introduced by McLellan [*48*]. Chou and Li [*79*] assigned five trapping sites per dislocation per atomic plane. In the case of hydrogen atoms associated with a dislocation, Hirth and Carnahan [*33*] calculated the number of hydrogen atoms adsorbed per unit dislocation line in bcc iron by the dislocation stress field. They report numbers of several powers of 10 and their result corrects the corresponding numbers reported by Bockris *et al.* [*80*].

Studying hydrogen transport in the alloy X-750, Lufrano *et al.* [*26*] considered that the hydrogen trap sites are associated with dislocations in the deforming metal [*65, 81*]. Assuming one trap site per atomic plane threaded by a dislocation [*48, 65, 78*], one finds that the trap site density in traps per cubic meter is given by $N_T = \sqrt{2}\rho/a$, where ρ is the dislocation density and a is the lattice parameter. This assumption is consistent with the experimental work of Thomas [*65*] in which the best fit to the experimental data was obtained with a trapping radius of only 1 to 2 atomic spacings. This equation can be used to determine the trap site density once the dislocation density is known as a function of a measure of the plastic deformation, e.g., the equivalent plastic strain ε^p [*26*]. On the other hand, if one considers that hydrogen is trapped at the octahedral sites on the interface of the γ' precipitates [*82*], a density of 6.0×10^{26} sites per cubic meter and a binding energy of 15.1 kJ/mole are calculated. This is in contrast to a value of 31 kJ/mole for the trapping binding energy which has also been reported in the literature for the alloy X-750 [*83*].

Reviewing the role of traps in hydrogen embrittlement of steels, Bernstein and Pressouyre [*6*] emphasize that trap characteristics are not fixed properties. Many traps, such as dislocations, vacancies and interstitials can move through the lattice and interact with other traps, coalesce to form new traps etc. Thus the evolutionary nature of traps adds an additional complexity to the issues of hydrogen embrittlement as affected by trapped hydrogen populations. Indeed, deformation affects dislocation density and structure, changes the void population and size, and influences the behavior of inclusions and grain boundaries in their activity as traps.

Dislocation Transport

In iron and its alloys, researchers comment on anomalous values of solubility and diffusivity at temperatures near and below 300K [*60, 64*]. Crack growth kinetic models [*84-87*] based on lattice diffusion times furnished crack growth rates faster than the diffusion rates [*88*]. Diffusivity values at room temperature [*47*] are less than the corresponding values obtained from extrapolation of high temperature data. On the other hand, room temperature solubilities are found to be enhanced [*89*] compared to those predicted theoretically by Sievert's law [*15*]. Also, at slow strain rates and low temperatures hydrogen embrittlement is suppressed [*3, 13, 90*]. Such observations led researchers to recognize that there are additional transport mechanisms besides lattice diffusion.

Hydrogen transport with mobile dislocations (sweep-in model) has been suggested as a possible mechanism for hydrogen lattice supersaturation first by Bastien and Azou [*91*]. The concept has been supported by observations of serrated yielding [*92-94*] and accelerated hydrogen release or uptake [*95-101*] during plastic deformation. Kurkela and Latanision [*102*] and Latanision *et al.* [*101*] have shown through direct hydrogen permeation measurements that mobile dislocations in nickel transport hydrogen at rates far in excess of lattice diffusion. Hwang and Bernstein [*103*], analyzing their experimental measurements on hydrogen flux behavior during plastic deformation in iron single crystals, suggested that hydrogen is transported by edge, screw and mixed dislocations. The same authors [*104*] attributed peaking behavior of the flux during straining of pure iron single crystals to hydrogen transport by screw dislocations. Luthan [*105*] discusses that hydrogen embrittlement results from highly localized hydrogen concentrations developed primarily because of hydrogen transport by dislocations.

Contrary to the evidence supporting the sweep-in model, Donovan [*106*] saw no direct evidence of hydrogen transport by dislocations in a study on tritium uptake into a nickel specimen under tension, even though the apparent diffusivity of tritium decreased due to trapping. Kurkela *et al.* [*107*] carried out permeation measurements in a fully bainitic steel, and found out that dislocations act as traps of hydrogen and decrease the rate of hydrogen transport. They rationalized this behavior in bcc ferrous alloys, which is opposite to that of fcc nickel, with the extremely high binding energy of hydrogen to dislocations in comparison to the low activation energy for lattice diffusion. Investigating trapping by dislocation and dislocation transport in plastically deforming polycrystalline nickel, Frankel and Latanision [*108*] concluded that dislocation transport to great depths is unlikely to occur while dynamic trapping by newly created dislocations causes measured permeation flux to be decreased. Using a model for hydrogen diffusion based on dislocation transport [*109*], Hashimoto and Latanision [*110*] concluded that hydrogen transport is important only at small hydrogen lattice concentrations, a case in which the majority of hydrogen is trapped in dislocation. The same authors [*111*] suggested that hydrogen trapped at dislocations at saturation levels is responsible for the cracking process due to hydrogen in iron. Ladna and Birnbaum [*112*] studied hydrogen transport during plastic deformation in 304 and 310 stainless steels and in nickels from a cathodically charged surface using secondary ion mass spectrometry (SIMS). It was found that transport of D did not make a significant contribution to hydrogen diffusion under the conditions for which transport of D atmospheres by individual dislocations is

expected to take place. They attributed this absence of D transport by dislocation to a probable lack of a net flux of dislocations in from the surface.

Tien *et al.* [*78, 86, 113*] developed a model for dislocation transport that yields much faster diffusion rates than lattice diffusion and showed that dislocations can carry hydrogen deep into a specimen gage section or plastic zone, even at ambient temperatures. According to this model hydrogen supersaturations develop through *stripping* of the solutes off the moving dislocations by traps. On the other hand, Johnson and Hirth [*114*] developed a continuum model to analyze supersaturation produced at random dislocation *annihilation* sites. Numerical results for ferritic and austenitic steels indicate that kinetic supersaturation was negligible for both smooth and cracked geometries. Revisiting the model of Tien *et al.* [*78*] for the case of steels, Tien, Nair and Jensen [*115*] reaffirmed their previous estimate of large hydrogen supersaturation induced by dislocation transport. In 1983, Johnson and Hirth [*116*] indicated some simplifications in the Tien *et al.* [*78, 115*] model, and then presented an overview of hydrogen transport by dislocations. The theoretical analysis of Johnson and Hirth [*116*] points out that transport of hydrogen by dislocations in iron or steel at room temperature produces only small supersaturations at internal trap sites; larger supersaturations by dislocation transport are predicted to be possible in metals with much smaller diffusivities for hydrogen, e.g. nickel; and hydrogen transport occurs in the form of a core atmosphere at a velocity considerably smaller than the critical velocity for breakaway. Reviewing the stripping and annihilation models, Nair, Jensen and Tien [*117*] reaffirm that both models can result in enrichment of hydrogen at voids and grain boundaries. Enrichment by the stripping mechanism occurs when unsaturated traps are present and by the annihilation mechanism when traps exist at the annihilation site. It should be mentioned that saturated traps were assumed in the original stripping model and no traps in the original annihilation model.

Summarizing the above discussion, one may say that the matter of hydrogen transport by dislocations is unsettled. The experimental evidence is inconclusive since there are experiments in favor of the mechanism [*103, 104*] and experiments that are against the mechanism [*108, 112*].

Grain Boundary Transport

Latanision *et al.* [*118*] report that fast grain boundary diffusion of hydrogen in nickel base alloys is unlikely. Permeation experiments by Robertson [*119*] in nickel and Latanision and Kurkela [*120*] in nickel and nickel-base alloys indicate that there is no measurable effect of grain size on hydrogen diffusivity. Thus, one might infer that hydrogen embrittlement in these systems is essentially controlled by bulk diffusion of hydrogen.

On the other hand, Brass *et al.* [*121*] and Harris and Latanision [*122*], interpreting permeation experiments in nickel, suggest enhanced hydrogen diffusion through grain boundaries. Tsuru and Latanision [*123*] used SIMS analysis of hydrogen at the exit surface of Ni through which H permeated and interpreted the results as enhanced H diffusion through grain boundaries. Ladna and Birnbaum [*124*] using SIMS studied the distribution of hydrogen at grain boundaries of nickel bicrystals. They observed enhanced hydrogen diffusion along high energy 39^0 <110> symmetrical tilt boundaries

($\Sigma = 9$) but not along low energy 129^0 <110> symmetric tilt boundaries ($\Sigma = 11$). Kimura and Birnbaum [*125*] pointed out that the kinetics of intergranular embrittlement of Ni from an external hydrogen source is controlled by grain boundary diffusion of hydrogen. Lastly, Mutschele and Kircheim [*126*] and Kircheim *et al.* [*127*], studying hydrogen segregation at grain boundaries and interfaces in palladium, concluded that the grain boundary diffusion coefficient is smaller than the value for the single crystal at low hydrogen concentration, and vice-versa at high hydrogen concentration.

Latanision and Opperhauser [*128*] and Latanision *et al.* [*101*] suggest that one might expect metalloid-segregated grain boundaries to act as preferential paths for the absorption of atomic hydrogen into polycrystalline metal matrices. Conversely, noble elements and catalytic poisons [*129*] reduce the preferential motion of atomic hydrogen through grain boundaries. Here the work of McMahon and his co-workers [*130-140*] should be mentioned according to which hydrogen induced cracking along grain boundary is due to the synergistic action of hydrogen and other impurities in reducing grain boundary cohesion. An overview of grain boundary diffusion theory with emphasis on the interpretation of concentration profiles measured in diffusion experiments can be found in the work of Mishin and Herzig [*141*]. In order to understand the role of hydrogen in promoting grain boundary embrittlement, it is essential that detailed studies on surface structure, electronic structure and bonding of adsorbed hydrogen on strained metal surfaces be carried out [*101*].

Models of Hydrogen Transport

Neglecting trapping at microstructural defects, Van Leeuwen [*142*] and Hippsley and Briant [*143*] calculated the solute hydrogen distribution at a crack tip in an isotropic linearly elastic solid under non-steady state conditions of hydrogen diffusion. Similar calculations of hydrogen atmospheres at a crack tip in equilibrium with local stresses were done by Liu [*144*] in an isotropic linearly elastic material and by Tong-Yi *et al.* [*145, 146*], and Tong-Yi and Hack [*147*] in single crystals of elastically anisotropic iron. Van Leeuwen [*148*] calculated the material fracture toughness as it depends on hydrogen induced microcracking at inclusion-matrix interfaces, and subsequent build-up of pressure. One dimensional hydrogen transport at a crack tip and the associated crack propagation in an elastic material was studied by Unger [*149*]. The interaction of dilatational impurities with the stress field of a crack was analyzed in Fe alloy crystals by Narita *et al.* [*150*]. Their calculations verified the result of McMeeking and Evans [*151*] that purely dilatant transformation centers distributed isobarically around the crack tip do not change the applied stress intensity factor. A detailed and complete analysis of crack tip shielding/antishielding by impurity atoms can be found in the work by Weertman and Hack [*152, 153*]. Calculations on NILS populations at a crack tip in equilibrium with local stress were recently carried out by Lufrano and Sofronis [*154*] in the absence of trapping. In this work the effects of hydrogen induced volume change and modulus softening on the standard crack tip singular elastic solution were investigated. Other mathematical models for hydrogen diffusion that account for the stress effect on hydrogen distribution but neglect material elastoplasticity are those by Yokobori *et al.* [155], Kitajima [*156*], Hirose and Mura [*157, 158*], and Maier *et al.* [*159*]. Most recently, Sun *et al.* [*160*] found experimentally that the distribution of dissolved hydrogen

ahead of a crack tip in a nickel single crystal under load exhibited two peaks that were correlated with the maxima in the plastic strain and the hydrostatic stress.

Hydrogen transport accounting for trap behavior has been modeled according to formulations presented by Oriani [*60*] and McNabb and Foster [*77*]. The latter formulation is mainly pertinent to the trapping and untrapping kinetics whereas the former is concerned with equilibrium conditions. Also, the McNabb and Foster formalism includes probabilistic considerations and places no constraint on the trapping mechanism, thus being more generally applicable. However, this feature constitutes a source of indefiniteness because the parameters are difficult to measure and make the mechanism hard to model in a given system. Turnbull *et al.* [*161*] developed a model to predict the distribution of hydrogen at a crack tip by using boundary conditions that account realistically for the electrochemical phenomena at the crack faces. The model employed trapping and untrapping kinetics between reversible and irreversible traps. The hydrostatic stress drift was calculated by using the stress field associated with elastoplastic deformation in the neighborhood of a blunting crack. An important conclusion of that work is that for ferritic steels the hydrogen concentrations ahead of the crack tip are significantly lower than predicted from constant concentration boundary conditions and that transport of hydrogen is surface reaction controlled rather than diffusion controlled.

In the formulation of Oriani [*60*], it is assumed that hydrogen can reside in the interior of the materials either at normal interstitial lattice sites or at lattice imperfections-trapping sites. Then Oriani postulated that at any stage of hydrogen diffusion, the hydrogen populations in reversible traps [*4, 6, 7, 61-63, 162*], and those in NILS are in local equilibrium. This equilibrium argument is realistic when the lattice diffusion relaxation times are relatively long compared to the time required to replenish or deplete the traps. Oriani concluded that at temperatures around 300K all systems of interest meet the condition for equilibrium because their binding energies are less than a critical binding energy, which he identified to be 67 kJ / mole. It is worth mentioning that most of the earlier numerical solutions to the hydrogen diffusion equation accounting for trapping [*163-168*] are based on the McNabb and Foster formalism [*77, 163*], and they do not account for the interactions between hydrogen concentration, plastic straining and stress. Notable exceptions are found in the work of Ellebrook *et al.* [*169*] and Allen-booth *et al.* [*170*]. Neglecting hydrostatic stress drift, Liu *et al.* [*171, 172*] used the boundary element method to solve transient hydrogen diffusion in a standard steel compact tension specimen under constant load. In the diffusion equation, the unknown concentration was qualified to account for trapping at dislocations through the accumulated plastic strain, which was separately calculated by the finite element method under fixed load. Toribio *et al.* [*173, 174*] used finite element analysis to model stress driven hydrogen diffusion in notched specimens of 316L austenitic stainless steel, and concluded that bulk diffusion is not important for hydrogen embrittlement of this specific steel. They suggested that it is rather the hydrogen residing at the notch surface that triggers the onset of micro-damage and microcracking there. On the other hand, Toribio [*175*], examining the size of the plastic zone in notched specimens from finite element calculations in comparison to the size of microdamaged zone from SEM fractography, maintains that it is hydrogen transported by stress driven diffusion that is responsible for hydrogen induced cracking of hot rolled perlitic steel.

Pressouyre and Bernstein [*176*], extending their model on hydrogen trapping [*61*], studied hydrogen induced intergranular cracking in Fe-Ti alloys. In the model, Oriani's theory was employed to calculate the hydrogen populations in trapping sites, and a critical concentration of hydrogen necessary to nucleate a grain boundary crack was assumed. The model results indicated that increasing the density of reversible traps (e.g. grain boundaries, dislocations, titanium substitutional atoms) decreases the maximum extent of grain boundary cracking, whereas irreversible trapping (e.g. at titanium carbide particles) controls the cracking kinetics. Transient hydrogen motion with mobile dislocations was studied by Fuentes-Samaniego and Hirth [*177, 178*], who obtained analytical expressions for the transient and steady state solute distribution around dislocations moving at constant velocity. In the work by Han *et al.* [*179*] a drift diffusion model was used to calculate hydrogen accumulation at the tip of an edge superdislocation pile-up at a grain boundary in polycrystalline Ni_3Al. Hashimoto and Latanision [*109*] calculated numerically that most of the dragged hydrogen resides at the core of the moving dislocations during plastic deformation in iron. They also modified the McNab-Foster model [*77*] to account for the so called dynamic trapping effect, that is, hydrogen trapping at newly created dislocations by plastic deformation apart from that trapped in the already existing and moving dislocations.

Coupling stress driven diffusion with elastoplastic material deformation was first attempted by Kitagawa and Kojima [*180*]. Sofronis and McMeeking [*181*] analyzed transient diffusion of hydrogen and hydrogen trapping at microstructural defects in iron and steel in the area around a blunting crack tip. The diffusion model accounted for drift due to hydrostatic stress and trapping generated by plastic straining continuously changing with deformation. Modeling the interaction of hydrogen with local elastoplasticity at cracked and rounded—notched geometries, Lufrano and Sofronis [*25*] extended the model of Sofronis and McMeeking by including the effect of hydrogen induced dilatation on the material constitutive law. Krom *et al.* [*182*] modified the model of Sofronis and McMeeking by introducing in the diffusion equation a strain rate factor to account accurately for the hydrogen balance in NILS and trapping sites. This strain rate factor is particularly important in transient calculations of hydrogen at high strain rates.

In the following, the transport model of Sofronis and McMeeking will be presented as modified by Krom *et al.* The model is based on Oriani's equilibrium theory between hydrogen populations in reversible traps and NILS. The model can easily be extended [*183*] and recast to treat hydrogen diffusion according to the McNab and Foster formalism. However, Sofronis [*183*] has demonstrated that in the circumstances of hydrogen diffusion and trapping in iron at room temperature there is little difference in the results between the two formulations.

Stress Driven Hydrogen Diffusion in a Material Undergoing Elastic-Plastic Straining

Following Johnson and Lin [*9*] and Sofronis and McMeeking [*181*], one can state Oriani's equilibrium between reversible traps and NILS through

$$\frac{\theta_T}{1-\theta_T} = \frac{\theta_L}{1-\theta_L} K \tag{1}$$

where θ_L denotes the occupancy of the NILS, θ_T denotes the occupancy of the trapping sites,

$$K = \exp(W_B/RT) \tag{2}$$

represents the equilibrium constant, W_B is the trap binding energy, R is the gas constant equal to $8.31\text{J}/\text{mole K}$, and T is the absolute temperature. The hydrogen concentration per unit volume in trapping sites, C_T, can be phrased as

$$C_T = \theta_T \alpha N_T \tag{3}$$

where α denotes the number of sites per trap and N_T, which is a function of the local effective plastic strain, i.e., $N_T = N_T(\varepsilon^p)$, denotes the trap density measured in number of traps per unit volume. The hydrogen concentration in NILS, C_L, can be stated as

$$C_L = \theta_L \beta N_L \tag{4}$$

where β denotes the number of NILS per solvent atom and N_L denotes the number of solvent lattice atoms per unit lattice volume. If the available number of trapping sites per unit volume, αN_T, is small compared with the available NILS per unit volume, βN_L,

$$N_L = N_A/V_M \tag{5}$$

where $N_A = 6.0232 \times 10^{23}$ atoms per mole is Avogadro's number and V_M is the molar volume of the host lattice measured in units of volume per lattice mole.

Hydrogen conservation in any arbitrary material volume combined with Eqs. (1) through (5) yields the governing equation for transient hydrogen diffusion accounting for trapping and hydrostatic drift as [*9, 181, 182*]

$$\frac{D}{D_{eff}}\frac{dC_L}{dt} = DC_{L,ii} - \left(\frac{DV_H C_L}{3RT}\sigma_{kk,i}\right)_{,i} - \alpha\theta_T \frac{\partial N_T}{\partial \varepsilon^p}\frac{d\varepsilon^p}{dt} \tag{6}$$

where $(\ )_{,i} = \partial(\ )/\partial x_i$, d/dt is the time derivative, D is the hydrogen diffusion constant through NILS, D_{eff} is an effective diffusion constant given by

$$D_{eff} = D/(1 + \partial C_T/\partial C_L), \tag{7}$$

V_H is the partial molar volume of hydrogen in solid solution, σ_{ij} is the Cauchy stress, and the standard summation convention over the range is implied for a repeated index. The second term in the right-hand side of Eq. (6) denotes the hydrostatic stress drift effect, whereas the last term is the strain rate factor due to Krom *et al.* [*182*] that accounts for the effect of trap population change with plastic strain. It is implicit in the Oriani's model that trap filling kinetics is very rapid. Consequently the effective diffusion constant is less than the normal NILS diffusion constant as long as the traps are not saturated or as plastic straining continues and new traps are created. Another important observation is that NILS hydrogen populations can achieve equilibrium with local stress only when plastic straining terminates and new traps are no longer created. Clearly, Eq. (6) demonstrates that the calculation of the hydrogen distribution within a solid is coupled to the fields of the hydrostatic stress and effective plastic strain as they continuously evolve during loading.

Elastic-Plastic Deformation in the Presence of Hydrogen

The hydrogen effect on dislocation behavior is ignored and the flow stress is assumed independent of hydrogen concentration. However, the hydrogen induced lattice

deformation is modeled through the dilatational distortion that accompanies the introduction of the hydrogen solutes into the lattice. Thus, the material is considered to harden isotropically under plastic straining, and flow according to von Mises J_2 flow theory. In the case of small strain formulation, the associated flow law is given by the classical Prandtl-Reuss equations appropriately modified to account for the hydrogen induced dilatational strain:

$$\dot{\sigma}_{ij} = 2G\left[\delta_{ik}\delta_{jl} + \frac{\nu}{1-2\nu}\delta_{ij}\delta_{kl} - \frac{3}{2}\frac{\sigma'_{ij}\sigma'_{kl}}{\left(\frac{h}{3G}+1\right)\sigma_e^2}\right]\left(\dot{\varepsilon}_{kl} - \dot{\varepsilon}^h_{kl}\right) \tag{8}$$

for plastic loading and

$$\dot{\sigma}_{ij} = 2G\left(\delta_{ik}\delta_{jl} + \frac{\nu}{1-2\nu}\delta_{ij}\delta_{kl}\right)\left(\dot{\varepsilon}_{kl} - \dot{\varepsilon}^h_{kl}\right) \tag{9}$$

for elastic loading or any unloading, where a superposed dot denotes time derivative, $\dot{\varepsilon}_{ij} = (v_{i,j} + v_{j,i})/2$ is the strain rate, v_i is the velocity, δ_{ij} is the Kronecker delta, $\sigma'_{ij} = \sigma_{ij} - \sigma_{kk}\delta_{ij}/3$ is the deviatoric stress, $\sigma_e^2 = 3\sigma'_{ij}\sigma'_{ij}/2$ is the equivalent stress, G and ν are the shear modulus and Poisson's ratio respectively, and $h = d\sigma_e/d\varepsilon^p$ is the slope of the uniaxial Cauchy stress versus logarithmic plastic strain, ε^p. In multiaxial deformation ε^p is defined as $\varepsilon^p = \int\sqrt{2\dot{\varepsilon}^p_{ij}\dot{\varepsilon}^p_{ij}/3}\,dt$, where $\dot{\varepsilon}^p_{ij}$ is the plastic strain rate. The strain rate $\dot{\varepsilon}_{ij}$ is given by $\dot{\varepsilon}_{ij} = \dot{\varepsilon}^e_{ij} + \dot{\varepsilon}^p_{ij} + \dot{\varepsilon}^h_{ij}$, where $\dot{\varepsilon}^e_{ij}$ denotes the elastic part and $\dot{\varepsilon}^h_{ij}$ the part due to lattice straining by the solute hydrogen. The hydrogen induced deformation rate $\dot{\varepsilon}^h_{ij}$ is purely dilatational [*40*] and is given by

$$\dot{\varepsilon}^h_{ij} = (\dot{c}\Delta v/3\Omega)\delta_{ij} \tag{10}$$

where c is total hydrogen concentration (in NILS and trapping sites) measured in hydrogen atoms per solvent atom, c_0 is the initial hydrogen concentration in the absence of any straining, Δv is the volume change per atom of hydrogen introduced into solution that is directly related to the partial molar volume of hydrogen $V_H = \Delta v N_A$ in solution, and Ω is the mean atomic volume of the host metal atom.

Lufrano *et al.* [*28*] demonstrated that in high solubility systems (e.g. niobium) and at relatively high initial concentrations (e.g. 0.3 atoms of hydrogen per metal atom), the stress induced enhancement in the local hydrogen concentration is large enough to cause stress relaxation in front of a crack tip by as much as 20%. They concluded though that the hydrogen induced dilatation strain has no effect on the material constitutive behavior when the initial hydrogen concentration is small, that is, approximately less than 0.01 hydrogen atoms per metal atom.

The governing equations for rate equilibrium are expressed in terms of the principle of virtual velocities

$$\int_V \dot{\sigma}_{ij}\,\dot{\varepsilon}^*_{ij}dV = \int_S \dot{T}_i v^*_i dS + \int_V \dot{b}_i v^*_i dV \tag{11}$$

where V is the volume of the material bounded by the surface S, T_i is the traction which is specified on the part S_T of the surface where tractions are prescribed, b_i is the body

force per unit volume, $\dot{\varepsilon}_{ij}^{*}$ and v_i^{*} are arbitrary fields associated through $\dot{\varepsilon}_{ij}^{*} = (v_{i,j}^{*} + v_{j,i}^{*})/2$, with v_i^{*} vanishing on the part S_u of the surface where velocities are prescribed.

Again, it is evident from Eqs. (6-11) that the hydrogen diffusion initial boundary value problem and the elastic-plastic boundary problem are fully coupled. Therefore the problem of calculating the velocity field and the local distribution of hydrogen is coupled in a non-linear sense and the solution procedure involves iteration [*26, 44, 181*]. The finite element procedures, in the most general case involving large strains, for the solution of the coupled problems are outlined in the work by Sofronis and McMeeking [*181*] and Lufrano *et al.* [*26*]. Incompressibility of the plastic deformation is enforced by the method of Nagtegaal *et al.* [*184*].

Numerical Results

In the work of Lufrano *et al.* [*25, 26*], as reviewed and extended in the recent paper of Taha and Sofronis [*20*], one can find: a) a detailed presentation of numerical solution methodologies and solutions for various material systems; b) parametric studies of the effect of strain rate, temperature, nature of boundary conditions, and yield strength on hydrogen populations; and c) an investigation of the competition between hydrostatic stress and plastic strain in the enhancement of the hydrogen concentration in the neighborhood of a stress raiser. In this section, only typical solutions to the initial boundary value problem of transient hydrogen diffusion coupled with material elastoplasticity will be presented: a) in the neighborhood of a blunting crack tip still under small scale yielding conditions; and b) in a four-point rounded-notch bend specimen. The materials used in the simulations were high strength steel and nickel base alloy X-750 as these systems suffer from embrittlement at room temperature and experimental data are readily available [*4, 26, 41, 42, 82, 181*]. In both cases plane strain conditions were assumed, and the system's temperature was 300 K for the steel specimen and 25 and 285 C for the X-750 specimen. At the time $t = 0$, all specimens were under a uniform initial NILS hydrogen concentration, $C_L = C_0$. The trapping site concentrations C_T follow from the NILS populations through Eq. (1). Calculations were carried out either with a constant concentration boundary condition $C_L = C_0$ enforced on the boundary of the domain at all times (open system), or with all external surfaces including those of the crack or the notch assumed insulated (zero hydrogen flux, closed system).

Blunting Crack in a High Strength Steel

The specimen was loaded under constant displacement rate, $\dot{K}_I$, during loading time t_l, at the end of which the applied stress intensity factor was $K_A = t_l \dot{K}_I$. The uniaxial stress strain law of the material was $(\sigma_e/\sigma_0)^{1/N} = (\sigma_e/\sigma_0) + (3G/\sigma_0)\varepsilon^p$, where the yield stress σ_0 was equal to 1200MPa, the work hardening exponent 0.2, Poisson's ratio 0.3, and Young's modulus 207MPa. The lattice diffusion constant of hydrogen at 300K was $D = 1.27 \times 10^{-8}\ \mathrm{m}^2/\mathrm{s}$ [*47*]. The interstitial hydrogen expands the lattice isotropically [*40*] and its partial molar volume in solution was $2.0 \times 10^{-6}\ \mathrm{m}^3$ / mole [*4*]. The molar volume

of iron was $7.116\times10^{-6}\,m^3$ / mole and hence $N_L = 8.46\times10^{28}$ solvent lattice atoms per m^3. Uniform hydrogen concentration in the unstressed lattice, $C_0 = 2.084\times10^{21}$ atoms per m^3 (2.46×10^{-8} atoms per solvent atom) in equilibrium with gas at one atmosphere pressure was used as initial condition. The parameter α was taken equal to 1. The parameter β was set equal to 1 and this corresponds to a maximum NILS concentration of 1 hydrogen atom per solvent lattice atom. The trap density N_T was assumed to increase with plastic straining, ε^p, according to the experimental results of Kumnick and Johnson [*20, 67*], and the trap binding energy was 60 kJ / mole. It should be pointed out that the function $N_T(\varepsilon^p)$ interpolating the experimental data increases monotonically with ε^p [*20*] and no trapping site saturation level exists, as was the case in the calculations of Sofronis and McMeeking [*181*]. The load times were $t_l = 0.4$, 4, and 40 s. The final value of the stress intensity factor was $K_A = 132\,MPa\sqrt{m}$, and the corresponding crack opening displacement b was equal to 3.5 times the initial crack opening displacement b_0 in the undeformed configuration of the body.

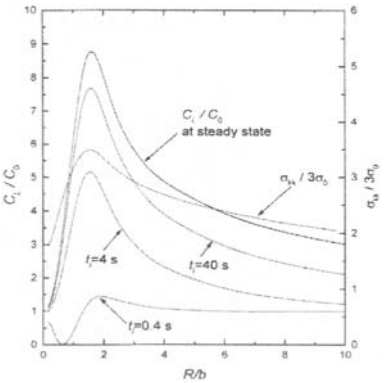


FIG. 1 - *Plot of hydrogen concentration C_L/C_0 in NILS and hydrostatic stress $\sigma_{kk}/3\sigma_0$ vs distance R/b from the crack tip for high strength steel ($\sigma_0 = 1200$ MPa) at a blunting crack tip upon the completion of loading at time t_l and at steady state under constant concentration boundary conditions. The parameter b is the crack opening displacement.*

In Fig. 1 the normalized concentration C_L/C_0 and hydrostatic stress $\sigma_{kk}/3\sigma_0$ and in Fig. 2 the corresponding normalized total concentration $(C_L + C_T)/C_0$ are plotted against distance R/b on the axis of symmetry ($\theta = 0$) ahead of the crack tip for constant concentration boundary conditions at the end of loading ($b = 3.5b_0$) for the three loading courses. Also shown plotted respectively in Figs. 1 and 2 are the steady state concentrations C_L/C_0 and $(C_L + C_T)/C_0$ achieved after approximately 500 s. The site of accumulation of trapped hydrogen is near the crack surface and the profile of the concentration C_T follows closely that of the plastic strain. At the crack surface, where the effective plastic strain is maximum, concentration C_T assumes its maximum value which is equal to 86 times as large as the initial concentration C_0. Diffusion of hydrogen

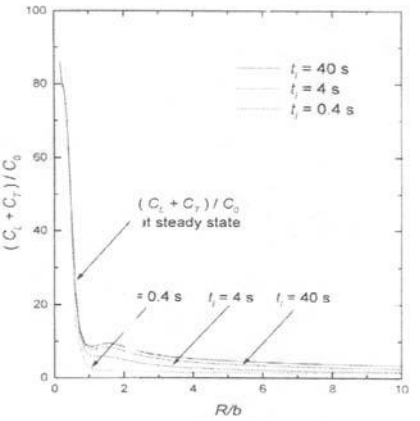


FIG. 2 - *Plot of total hydrogen concentration* $(C_L + C_T)/C_0$ *vs distance* R/b *for high strength steel* ($\sigma_0 = 1200$MPa*) at a blunting crack tip upon the completion of loading at time* t_l *and at steady state under constant concentration boundary conditions.*

through NILS delivers hydrogen to trapping sites at a rate faster than the rate at which traps are generated by plastic straining. As a result, the loading rate has no effect on the trapped hydrogen populations and the trapping sites are always saturated due to the high binding energy, with the exception of the traps in a small segment of size 0.3b centered at $R/b = 0.7$ from the tip when the rate of loading is very fast, ($t_l = 0.4$s). The trap occupancy in that segment though is not less than 75%. Therefore, once loading has ceased and traps are no longer created by plastic straining, there is almost no change in the trapped concentration. As a result, trapped hydrogen concentrations C_T reach their steady state values (saturated traps) upon load termination. While the trapped hydrogen concentration profiles are loading rate independent, the accumulation of hydrogen in NILS decreases with increasing loading rate. At slow strain rates ($t_l = 4,40$s), the distribution of concentration C_L varies with distance from the notch root in accordance with the hydrostatic stress and it attains its maximum at $R/b = 1.6$. However, at higher strain rates ($t_l = 0.4$s), a trough is established in the NILS population profile somewhere between the notch surface and the site of the hydrostatic stress peak location. Trap generation rate close to the notch surface increases with strain rate causing more demand for hydrogen at the crack tip. On the other hand, hydrostatic stress gradients pull hydrogen away from the tip toward the hydrostatic stress peak at $R/b = 1.6$. In addition, the crack tip concentration C_L is kept constant at the value of C_0 at all times (open system). The competition between these three processes dictates the shape of the NILS concentration profiles. Thus, at high strain rates the trap generation rate is "ahead" of hydrogen diffusion. As a result, hydrogen in the region $0 \le R/b \le 1.6$ is depleted from NILS sites to satisfy the elevated demands for hydrogen in the trapping sites close to the notch surface and the hydrostatic stress peak location. As a consequence, a trough is established in the NILS hydrogen distribution somewhere in between the notch surface

and the site of the hydrostatic stress peak. In addition, the crack tip concentration C_L is maintained at the constant value C_0 by hydrogen ingress through the crack surface. In contrast, at slow strain rates the demand for trapping hydrogen is less severe and traps are saturated by the end of loading. Hence, diffusion through NILS and the ingress of hydrogen through the crack surface can supply hydrogen to the trapping sites close to the crack tip and the hydrostatic stress peak location without the establishment of a trough.

Unlike the trapping site concentrations, the NILS concentrations by the end of loading are away from their steady state values (see Fig. 1). Obviously the most dramatic departure from steady state occurs with loading at high strain rates. As a result, the total hydrogen concentration profiles $C_L + C_T$, shown plotted against R/b on Fig. 2, are also away from steady state by the end of loading. It is notable that even at steady state, NILS concentration C_L is only mildly elevated at the peak of the hydrostatic stress location at some distance from the tip. The maximum NILS concentration C_L is attained at distance $R/b = 1.6$ from the notch surface, and its value is nine times the initial concentration C_0. Figure 2 indicates that the hydrostatic stress effect beyond the high trap density region at the notch surface is drawing hydrogen toward the site of the hydrostatic stress peak in large quantities. At that location, the plastic strain and therefore the density of traps is low. As a result, most of the hydrogen there resides in NILS since the demand for trap filling hydrogen is zero (due to saturation at all times). As a consequence, a local minimum is observed in the total hydrogen concentration profile in the segment $0 \le R/b \le 2$ (Fig. 2) when the local chemical potential gradients are neutralized with time.

Four-Point Rounded-Notch Bend Specimen of High Strength Steel

A specimen similar to the four-point bend-specimen of Griffiths and Owen [*185*] was employed in the analysis [*20, 25*]. Uniform initial NILS concentration of 2.46×10^{-8} atoms per solvent atom was used throughout as an initial condition. The loading was performed at constant displacement rates of $0.1\,\text{mm/s}$ until time t_l at which the loading displacements were held constant and hydrogen diffusion continued under fixed held displacements. The extent of deformation and loading in the specimen was measured in terms of a nominal stress defined as $\sigma_{\text{nom}} = 6M/wa^2$, where M is the bending moment, a is the unnotched ligament, and w is the specimen thickness. In the following the hydrogen concentration profiles are plotted vs normalized distance R/r_0 along the axis of symmetry directly beneath the notch, where R is measured from the tip of the notch, and r_0 is the undeformed notch root radius.

Two loading courses with load times $t_l = 1.65$ and 3.8s respectively were simulated. At the end of loading, the corresponding normalized nominal stresses $\sigma_{\text{nom}}/\sigma_0$ were 1.0 and 2.0; and the corresponding plastic strains at the root of the notch were 2.4 and 8.8%. The peak hydrostatic stresses $\sigma_{kk}/3\sigma_0$ were respectively 1.3 and 1.94, and they were achieved at a distance $R/r_0 = 0.8$ and 1.3 from the tip of the notch, where $r_0 = 0.25\,\text{mm}$. Plastic straining at the notch root commences when $\sigma_{\text{nom}}/\sigma_0 = 0.32$, whereas on the other side of the specimen across from the notch root, it commences at

$\sigma_{nom}/\sigma_0 = 1.42$. Hence, when the load time was $t_l = 1.65$s, yielding was contained. In the other case, when $t_l = 3.8$s, general yielding was not established by the end of loading.

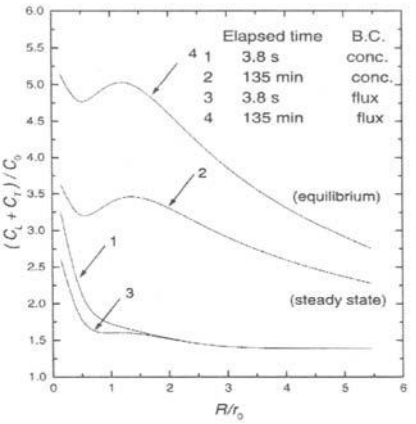


FIG. 3 - *Plot of total hydrogen concentration* $(C_L + C_T)/C_0$ *vs normalized distance* R/r_0 *from the rounded-notch tip in high strength steel* ($\sigma_0 = 1200$MPa) *at the end of loading at time* t_l *at which the nominal stress* σ_{nom}/σ_0 *is equal to* 1.0 *for both constant concentration and zero flux boundary conditions. Also shown are the corresponding steady state and equilibrium concentrations while loads are held constant at* $\sigma_{nom}/\sigma_0 = 1.0$.

Unlike the case of low strength steels [*20*], the results shown in Figs. 3 and 4 indicate that in high strength steels the hydrostatic stress dictates the shape of the equilibrium and steady hydrogen concentration profiles at least up to plastic strains equal to 2.4% ($\sigma_{nom}/\sigma_0 = 1.0$) at the notch root (see Fig. 3). The hydrostatic stress continues to influence the profiles even at strains as large as 8.8% ($\sigma_{nom}/\sigma_0 = 2.0$) (see Fig. 4). This is due to the large magnitude of the peak hydrostatic stress ($\sigma_{kk}/3 = 1560$MPa) in comparison with the corresponding small hydrostatic stress ($\sigma_{kk}/3 = 325$MPa) in low strength steel ($\sigma_0 = 250$MPa) under the same normalized nominal stress of 1.0. However, when $\sigma_{nom}/\sigma_0 = 2.0$, the trapping sites close to the surface of the notch begin to strongly compete with the hydrostatic stress peak location for trap filling hydrogen. As a result, a minimum in the total concentration is observed in the region $0 \le R/b \le 2$. Lastly, the maximum total hydrogen concentration for all loading cases studied is less than 5.2 times the initial concentration C_0.

At the end of loading, Figures 3 and 4 show that hydrogen concentrations under constant concentration conditions are larger than those under zero flux boundary conditions. The reason is that the traps close to the notch surface are not fully saturated for the high strength steel under zero flux boundary conditions since they compete for hydrogen with the large hydrostatic stress away from the notch root. On the other hand, under constant concentration boundary conditions, the traps are saturated due to the hydrogen ingress through the notch root. When equilibrium or steady state is reached,

the traps have saturated and the total hydrogen concentration is larger for flux boundary conditions than for constant concentration boundary conditions. Hydrogen diffuses out of the specimen in the former case in order for the tip concentration to be kept constant.

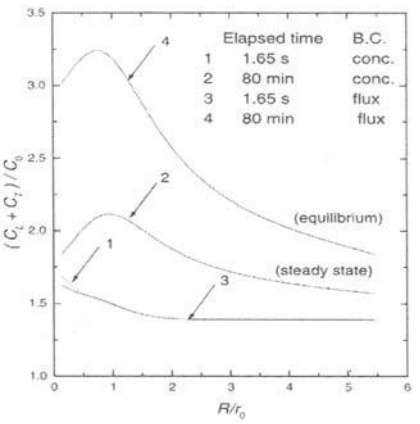


FIG. 4 - *Plot of total hydrogen concentration* $(C_L + C_T)/C_0$ *vs normalized distance* R/r_0 *from the rounded-notch tip in high strength steel* ($\sigma_0 = 1200$MPa) *at the end of loading at time* t_l *at which the nominal stress* σ_{nom}/σ_0 *is equal to* 2.0 *for both constant concentration and zero flux boundary conditions. Also shown are the corresponding steady state and equilibrium concentrations while loads are held constant at* $\sigma_{nom}/\sigma_0 = 2.0$.

Four-Point Rounded-Notch Bend Specimen of Alloy X-750

The calculations were carried out with an initially uniform concentration of 0.003 hydrogen atoms per metal atom, trap binding energy equal to 15.1kJ / mole [*82*], and constant trap density $N_T = 6.0\times10^{26}$ traps / m^3. It was assumed that hydrogen is trapped at the octahedral sites on the interface of the γ' precipitates [*82*] which are saturable traps. The loading was performed at constant displacement rate, as in the case of high strength steel, representing macroscopic strain rates of 4.7×10^{-6}, 4.7×10^{-5}, and 4.7×10^{-4} per second, until loading was completed at time t_l, and thereafter hydrogen diffusion continued under fixed displacements. The diffusion constant was given as function of temperature by $D = 0.016\exp(-49\,\text{kJ/mole}/RT)\text{cm}^2\,\text{s}^{-1}$. The partial molar volume of hydrogen in solution with the metal was 1.72cm^3 / mole and the molar volume of the host lattice was 6.87cm^3 / mole. The Poisson's ratio of alloy X-750 is 0.29 and Young's moduli are 213 and 200MPa, respectively at temperatures 25 and 285C. The uniaxial stress-strain curve is given in the work of Lufrano *et al.* [*26*].

Figure 5 shows that, for the stress levels relevant to four-point bending of notched specimens, the maximum increase in the equilibrium interstitial hydrogen concentration

in X-750 is less then 60 percent of the initial interstitial hydrogen concentration. Also, any transient increase with load in the interstitial hydrogen concentration, which may take place during a load-to-failure test, results in less than a 50% concentration enhancement. Calculations at 285C yielded peak equilibrium hydrogen concentrations in a closed system that are higher than those for an open system, although the difference in the transient hydrogen concentration as loads are increased for an open or closed system is negligible. Therefore the modeling of environmental and internal embrittlement could be accomplished with key experiments, chosen at the discretion of the experimenter. Furthermore, increased understanding of stress corrosion cracking behavior of materials, where determination of the local hydrogen fugacity may only be inferred, may be developed. For instance, Symons and Thompson [*186*] reported on the effect of hydrogen concentration between 0 and 3.0×10^{-3} atomic fraction on the fracture toughness of alloy X-750. Also Kerns *et al.* [*187*] reported that in hydrogenated water below 150 C the fracture toughness of X-750 falls to 40 MPa$\sqrt{\text{m}}$. A comparison of the hydrogen charged data and the measured fracture toughness in water could lead to a determination of the hydrogen concentration at the crack tip in the water environment.

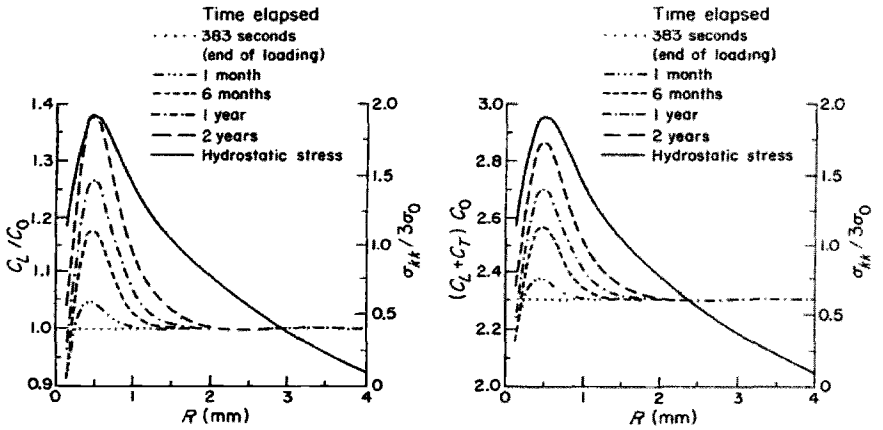


FIG. 5 - *Plot of the normalized interstitial hydrogen concentration, C_L/C_0, and the normalized total hydrogen concentration, $(C_L + C_T)/C_0$, directly ahead of the notch root in a closed system versus the distance, R, from the notch root at and after the completion of a loading at time $t_l = 383$s. The loading strain rate was 4.7×10^{-5} per second, and the temperature 25C. For reference, the normalized hydrostatic stress, $\sigma_{kk}/3\sigma_0$, directly ahead of the notch root is also plotted versus the distance from the notch root.*

As seen in Fig. 6, at a temperature of 285 C, there is a definite loading rate effect on the transient hydrogen concentrations. For a specimen loaded in 4400 seconds, i.e., at a strain rate of 4.7×10^{-6} per second, there is approximately a 14 percent rise in the interstitial hydrogen concentration, while for a specimen loaded in 44 seconds, i.e., at a strain rate of 4.7×10^{-4} per second, there is less than a one percent rise in the interstitial hydrogen concentration. On the other hand, it is clearly shown in Fig. 6 that because of

the relatively slow rate of hydrogen diffusion in X-750 at 25 C, there is no discernible loading rate effect on the transient hydrogen concentration. It is this result in particular, that may portend a disturbing implication for the common interpretation that the observed rate sensitivities in hydrogen embrittlement are entirely due to the ability of large scale diffusion to deliver hydrogen to the region of high stress. Although it should be noted that these results pertain to the geometry and deformation conditions of the rounded notch specimen, there are indications that for the geometry and strain levels of a cracked specimen there exists a loading rate effect on the transient hydrogen concentration even at temperatures as low as 25 C [*188*]. Also, the analysis by Lassila and Birnbaum [*189*] showed that local diffusion to the grain boundary traps may control the intergranular fracture in tensile specimens. That, in conjunction with this work, suggests that hydrostatic stress may not play a large role in the fracture behavior in nickel-base alloys at temperatures of concern for hydrogen embrittlement. This strong temperature dependence and hence, rate sensitivity of hydrogen diffusion suggests that physical experiments conducted at different temperatures are needed to examine the need for available hydrogen in the embrittlement phenomena.

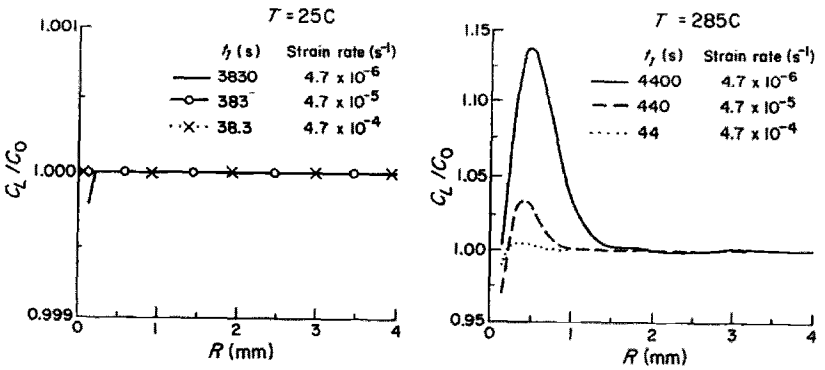


FIG. 6 - *Plot of the normalized interstitial hydrogen concentration, C_L/C_0, and the normalized total hydrogen concentration, $(C_L + C_T)/C_0$, directly ahead of the notch root in a closed system versus the distance, R, from the notch root at the completion of loading at time t_l, strain rates of 4.7×10^{-6}, 4.7×10^{-5}, and 4.7×10^{-4} per second, and temperature of 25 and 285C.*

Implications of Numerical Results on Hydrogen Embrittlement

Typical finite element studies of the interaction between hydrogen diffusion and large strain elastoplasticity near stress raisers in high strength steel and alloy X-750 have been presented. The parameters used in the solutions of the governing equations were based on experimental evidence. Hence, the numerical results may be considered as realistically reflecting real-world mechanical behavior of the material.

In pre-cracked steel specimens strained under small scale yielding conditions, hydrogen trapping dominates the hydrogen populations regardless of the strength level of steel. As a result, hydrogen accumulates at the surface at the crack tip and not at the hydrostatic stress peak location further inside from the tip. In four-point bend specimens of high strength steels $\sigma_0 \leq 250\,\text{MPa}$, NILS populations dominate if the plastic strains at the notch are small (less than ~2.3%, $\sigma_{nom}/\sigma_0 \sim 1.0$). At larger strains, trapping populations dominate as in the case of pre-cracked specimens under small scale yielding conditions. In general, for both low and high strength steels trapped populations dominate when the load is raised to values close and beyond the general yield load [*20*]. In experimental studies [*20, 25*] with four-point bend specimens hydrogen induced cracking at the surface of the notch occurred under large strains and microcracking inside from the notch was the case at very small strains. These results, in conjunction with the finite element calculations of the hydrogen concentration, point to the direction that most of the hydrogen was residing at the microcrack initiation site prior to the onset of fracture.

It has been found that at the temperatures of interest for hydrogen embrittlement of the alloy X-750, hydrogen concentration enhancement due to the elastoplasticity of the notch is surprisingly small according to the model presented in this paper. The conclusion one can draw from this observation is that embrittlement of the alloy can be caused by just a few atomic ppm of hydrogen.

The present hydrogen transport model results, although very helpful in understanding the interaction of hydrogen with local elastoplasticity, do not reveal the role of hydrogen in promoting material degradation. As discussed in the next section, further research is needed in the direction of coupling the present model results with the actual embrittling mechanism(s) (localization or decohesion) operating in the microscale. For instance, incorporation of the shielding mechanism for embrittlement [*44*] in the present calculations may help to elucidate the role of hydrogen in promoting shear localization of the plastic flow under certain temperature and strain rate conditions.

A Case Study: Evaluation of Alloy X-750 through Coupling of Experimental Procedures with Finite Element Analysis

The first step in understanding and modeling the hydrogen embrittlement of a material is to characterize thoroughly the microstructure of the material. Microstructure plays a key role in the embrittlement of engineering alloys [*29*]. For instance, the microstructure controls the degree of slip localization, the local stress concentrators (e.g. grain boundary carbides), and the overall solubility of hydrogen. This analysis normally requires characterization through light optical metallography, scanning electron microscopy, and transmission electron microscopy. This analysis will also identify and provide information on key parameters in the transport model. For instance, it is well known that under certain conditions the nickel base alloys fail by an intergranular fracture mode. Therefore, in developing a model for the hydrogen embrittlement of these alloys, it is important to quantify the segregation of hydrogen to these boundaries, that is, the trapping behavior of grain boundaries. Since in alloy X-750, the grain boundaries have extensive carbide precipitation, the trapping on both the grain boundaries and the carbide matrix interface should be studied first. The alloy, for which numerical results

have been presented in the previous section, was previously characterized [*190*]. The mean intercept grain size was 125 μm with small discrete $M_{23}C_6$ carbide precipitates decorating the grain boundaries. The alloy was strengthened by 20 nm γ' precipitates with rounded cuboidal shape and a weight fraction of 0.126. Primary carbides and carbonitrides, M(C,N), were observed to be aligned along the rolling direction. The trapping at grain boundary carbides in a similar nickel-base alloy has also been examined using thermal desorption spectroscopy on Alloy 600 [*191*]. Alloy 600 is similar to the X-750 though there is no aluminum or titanium to cause precipitation of strengthening γ' precipitates. The trapping at the grain boundaries in nickel was determined by Lassila and Birnbaum [*189*]. Hydrogen diffusivity which also is an important parameter in the model, was measured by using isothermal desorption measurements [*82*]. Cylinders uniformly charged with hydrogen were inserted into a vacuum environment for various periods of time at multiple temperatures. These cylinders were analyzed to determine the basic diffusion equation $D = D_0 \exp(-Q/RT)$.

Fracture mechanics testing was performed on either hydrogen precharged specimens or in hydrogen gas [*186,192*]. Compact tension specimens were machined in an L-R orientation. The specimens were fatigue precracked prior to insertion into the hydrogen autoclave for either hydrogen charging or fracture toughness testing. Hydrogen gas testing was performed at 54 C and at a loading rate of 4.4 MPa$\sqrt{\text{m}}$ / hr. It was found that at this loading rate and below, the loading rate did not affect the behavior of the material. The hydrogen precharged specimens were tested at 25 C at rates between 42 and 1980 42 MPa$\sqrt{\text{m}}$ / hr. The test results demonstrated that alloy X-750 is susceptible to both internal and environmental hydrogen embrittlement. Scanning electron microscopy showed an intergranular fracture morphology and the matrix appeared decohered at the carbide matrix interface. Therefore, it is evident that the finite element calculations presented for the alloy in the previous section should be extended to account for the local stress and hydrogen concentration at the particle/matrix interfaces.

The testing described above used linear elastic fracture mechanics to describe cracking. Many engineering alloys are not sufficiently brittle to allow for this methodology. J-integral testing is required in the elastic-plastic regime. While environmental testing is time consuming, the multiple specimen technique may not be feasible. On the other hand, the simple specimen technique with use of electric potential drop (EPD) or compliance may also not be applicable. The compliance may alter the local stress field ahead of the crack during the environmental test which would then alter the local hydrogen concentration. The EPD may not be adequate when extensive crack tip blunting occurs. The new normalization technique as has been used by others [*193*] evaluating the effects of environment on material behavior provides a single specimen J_{IC} test without the need to unload.

With all the data (fracture toughness, tensile behavior, hydrogen diffusion and hydrogen trapping), the material behavior at the macroscale (specimen) and microscale (matrix/carbide interfaces) can be modeled. The ideal method of analyzing the fracture process is to model both the stress and strain distribution as the specimen is loaded to fracture. A key advantage of the finite element analysis is the ability to model the boundary conditions, such as constant concentration or flux, or possibly even a decrease in the surface hydrogen concentration along the crack flanks as may be expected as the

material undergoes cracking. The controlling fracture criterion may then be determined from the finite element analysis [*194*] by considering the values of the model parameters in conjunction with information extracted from the analysis of the microstructure at the moment of fracture initiation.

Closure

An overview of our current understanding of the mechanisms of hydrogen transport and the related models has been presented. The numerical results for the interaction of hydrogen solutes with the elastoplastic deformation indicate that the existing methodologies of analysis of the hydrogen transport problem are capable of providing a fairly reliable and detailed picture of the hydrogen distribution in a material. Of course, the present models need to be refined to account for more realistic material response, e.g. single crystal or anisotropic plasticity, hydrogen entry in the material, role of trapping hydrogen in the fracture process. However, in order for the models to be used in prediction and evaluation of material response in the presence of hydrogen, they should be augmented to include the specific mechanisms of embrittlement. Thus analysis of transport properties at the microscale in conjunction with experimental evidence about the material microstructure seems to be an area in which further research is needed.

Acknowledgements

This work was supported by the Department of Energy under grant DEFGO2-91ER45439. The authors would like to thank Ms. M. C. Schlembach, Assistant Engineering Librarian for Digital Services, for her help in searching through the hydrogen literature. They would also like to thank Dr. D. M. Symons for many helpful discussions on the effect of hydrogen on the mechanical behavior of materials.

References

[1] Rice, J. R., "Mechanics Aspects of Stress Corrosion Cracking and Hydrogen Embritllement," *Stress Corrosion Cracking and Hydrogen embrittlement of Iron Base Alloys*, R. W. Staehle, J. Hochmann, R. D. McCright and J. E. Slater, Eds., NACE, TX, NACE-5, 1977, pp. 11-15.

[2] Rice, J. R., "Some Mechanics Research Topics Related to the Hydrogen Embrittlement of Metals," *Corrosion,* Vol. 32, 1976, pp. 22-26.

[3] Birnbaum, H. K. and Sofronis, P., "Hydrogen-Enhanced Localized Plasticity-A Mechanism for Hydrogen Related Fracture," *Materials Science and Engineering*, Vol. A176, 1994, pp. 191-202.

[4] Hirth, J. P., "Effects of Hydrogen on the Properties of Iron and Steel," *Metallurgical Transactions,* Vol. 11A, 1980, pp. 861-890.

[5] Kedzierzawski, P., "Hydrogen Trapping in Iron and Iron Alloys," *Hydrogen Degradation in Ferrous Alloys*, R. A. Oriani, J. P. Hirth, M. Smialowski, Eds., Noyes Publications, New Jersey, 1985, pp. 271-288.

[6] Bernstein, I. M., and Pressouyre, G. M., "The Role of Traps in the Microstructural Control of Hydrogen Embrittlement of Steels," *Hydrogen Degradation in Ferrous*

Alloys, R. A. Oriani, J. P. Hirth, M. Smialowski, Eds., Noyes Publications, New Jersey, 1985, pp. 641-685.

[7] Gibala, R. and Kumnick, A. J., "Hydrogen Trapping in Iron and Steels," *Hydrogen Embrittlement and Stress Corrosion Cracking*, (Proceedings of a Troiano Festschrift Symposium, Case Western Reserve University, June 1-3, 1980), R. Gibala and R. F. Hehemann, Eds., ASM Ohio, 1984, pp. 61-77.

[8] Wert, C. A. and Frank, R. C., "Trapping of Interstitials in Metals," *Annual Review of Materials Science*, Vol. 13, 1983, pp. 139-172.

[9] Johnson, H. H. and Lin, R. W., "Hydrogen and deuterium trapping in iron," *Hydrogen Effects in Metals*, I. M. Bernstein and A. W. Thompson, Eds., Metallurgical Society of AIME, New York, 1981, pp. 3-23.

[10] Pound, B. G., "The Role of Traps in Determining the Resistance to Hydrogen Embrittlement," *Hydrogen Effects in Materials*, A. W. Thompson and N. R. Moody, Eds., The Minerals, Metals & Materials Society, 1996, pp. 115-124.

[11] Wipf, H., "Diffusion of Hydrogen in Metals," *Hydrogen in Metals III, Properties and Applications*, H. Wipf, Ed., Springer, Vol. 73, 1997, pp. 51-91.

[12] Vehoff, H., "Hydrogen Related Problems," *Hydrogen in Metals III, Properties and Applications*, H. Wipf, Ed., Springer, Vol. 73, 1997, pp. 215-278.

[13] Birnbaum, H. K., "Hydrogen related fracture of metals," *Atomistics of Fracture* (Proceedings of a NATO Advanced Research Institute on Atomistics of Fracture, Calcatoggio, Corsica, France, May 22-31, 1981), R. A. Latanision and J. R. Pickens, Eds., Plenum Press, New York, 1983, pp. 733-765.

[14] Birnbaum, H. K., "Hydrogen related second phase embrittlement of solids," *Hydrogen Embrittlement and Stress Corrosion Cracking*, (Proceedings of a Troiano Festschrift Symposium, Case Western Reserve University, June 1-3, 1980), R. Gibala and R. F. Hehemann, Eds., ASM Ohio, 1984, pp. 153-177.

[15] Johnson, H. H., "Hydrogen Gas Embrittlement," *Hydrogen in Metals*, I. M. Bernstein and A. W. Thompson, Eds., ASM, 1974, pp. 35-49.

[16] Nelson, H. G., "Hydrogen Embrittlement," *Treatise on Materials Science and Technology, Embrittlement of Engineering Alloys*, C. L. Briant, S. K. Banerji, Eds., Academic Press, New York, Vol. 25, 1983, pp. 275-359.

[17] Gerberich, W. W., Garry, J. and Lessar, J. F., "Grain Size and Concentration Effects in Internal and External Hydrogen Embrittlement," *Effects of Hydrogen on Behavior of Materials*, I. M. Bernstein and A. W. Thompson, Eds., Metallurgical Society of AIME, New York, 1976, pp. 71-81.

[18] Viswamathan, R. and Hudak, S. J., "The effect of impurities and Strength Level on Hydrogen Induced Cracking in Low Alloy Turbine Steel, *Metallurgical Transactions*, Vol. 8A, 1977, pp. 1633-1637.

[19] Oriani, R. A. "Hydrogen Embrittlement of Steels," *Annual Review Materials Science*, Vol. 8, 1978, pp. 327-357

[20] Taha, A. and Sofronis, P., "A Micromechanics Approach to the Study of Hydrogen Transport and Embrittlement," *Engineering Fracture Mechanics*, To appear.

[21] Smialowski, M., "Initiation of Hydrogen-Induced Cracking in Iron and Iron Alloys," *Hydrogen Degradation in Ferrous Alloys*, R. A. Oriani, J. P. Hirth, M. Smialowski, Eds., Noyes Publications, New Jersey, 1985, pp. 561-578.

[22] Bernstein, I. M., Garber, R. and Pressouyre, G. M., "Effects of dissolved Hydrogen on Mechanical Behavior of Metals," *Effects of Hydrogen on Behavior of Materials*, I. M. Bernstein and A. W. Thompson, Eds., Metallurgical Society of AIME, New York, 1976, pp. 37-57.

[23] Gibala, R., "Hydrogen-Defect Interactions in Iron-Base Alloys," *Stress Corrosion Cracking and Hydrogen Embrittlement of Iron Base Alloys*, R. W. Staehle, J. Hochmann, R. D. McCright and J. E. Slater, Eds., Texas, NACE-5, 1977, pp. 244-271.

[24] Pressouyre, G. M., "Trap Theory of Hydrogen embrittlement," *Acta Metallurgica*, Vol. 28, 1980, pp. 895-911.

[25] Lufrano, J. and Sofronis, P., "Enhanced Hydrogen Concentrations Ahead of Rounded Notches and Cracks—Competition Between Plastic Strain and Hydrostatic Stress," *Acta Materialia*, Vol. 46, 1998, pp. 1519-1526.

[26] Lufrano, J., Symons, D. and Sofronis, P., "Hydrogen Transport and Large Strain Elastoplasticity Near a Notch in Alloy X-750, *Engineering Fracture Mechanics*, Vol. 59, 1998, pp. 827-845.

[27] Lufrano, J., Sofronis, P. and Birnbaum, H. K., "Modeling of Hydrogen Transport and Elastically Accommodated Hydride Formation Near a Crack Tip," *Journal of the Mechanics and Physics of Solids*, Vol. 44, 1996, pp. 179-205.

[28] Lufrano, J., Sofronis, P. and Birnbaum, H. K., "Elastoplastically Accommodated Hydride Formation and Embrittlement," *Journal of the Mechanics and Physics of Solids*, Vol. 46, 1998, pp. 1497-1520.

[29] Thompson, A. W. and Bernstein, I. M., "The Role of Metallurgical Variables in Hydrogen-Assisted Environmental Fracture," *Advances of Corrosion Science and Technology*, R. W. Staehle and M. Fontana, Eds., Vol. 7, 1980, pp. 83-175.

[30] Piercy, G. R. "The Physical and Chemical Behavior of Hydrogen in Metals," *Metallurgical Society of CIM Annual Volume*, Vol. 16, 1978, pp. 11-15.

[31] Speiser, R., "Hydrogen in Metals," *Stress Corrosion Cracking and Hydrogen Embrittlement of Iron Base Alloys*, R. W. Staehle, J. Hochmann, R. D. McCright and J. E. Slater, Eds., Texas, NACE-5, 1977, pp. 226-242.

[32] Oriani, R. A., "Hydrogen in Metals," *Fundamental Aspects of Stress Corrosion Cracking*, R. W. Staehle, A. J. Forty and D. VanRooyen, Eds., NACE, Texas, 1969, pp. 32-49.

[33] Hirth, J. P. and Carnahan, B., "Hydrogen Adsorption at Dislocations and Cracks in Fe," *Acta Materiallia*, Vol. 26, 1978, pp. 1795-1803.

[34] Troiano, A. R., "The Role of Hydrogen and Other Interstitials in the Mechanical Behavior of Metals." *Transactions* ASM, Vol. 52, 1960, pp. 54-80.

[35] Cottrell, H. A., "Effects of Solute Atoms on the Behavior of Dislocations," *Report of a Conference on Strength of Solids*, The Physical Society, London, 1948, pp. 30-36.

[36] Eshelby, J. D., "The Elastic Interaction of Point Defects," *Acta Metallurgica*, Vol. 3, 1955, pp. 487-490.

[37] Eshelby, J. D., "The Continuum Theory of Lattice Defects," *Solid State Physics*, F. Seitz and D. Turnbull, Eds., Academic Press, New York, Vol. 3, 1956, pp. 79-144.

[38] Eshelby, J. D., "The Determination of the Elastic Field of an Ellipsoidal Inclusion and Related Problems," *Proceedings of the Royal Society,* London, Vol. 241A, 1957, pp. 376-396.

[39] Hirth, J. P. and Lothe, J., *Theory of Dislocations*, John Wiley & Sons Inc., New York, 1982, pp. 487-530.

[40] Peisl, H., "Lattice Strains due to Hydrogen in Metals," *Hydrogen in Metals I, Topics in Applied Physics*, G. Alefeld and J. Volkl, Eds., Springer, New York, Vol. 28, 1978, pp. 53-74.

[41] Mazzolai, F. M. and Birnbaum, H. K., "Elastic Constants and Ultrasonic Attenuation of the 'alpha—alpha' Phase of the Nb-H(D) System. I. Results," *Journal of Physics F: Metal Physics*, Vol. 15, 1985, pp. 507-523,

[42] Mazzolai, F. M. and Birnbaum, H. K., "Elastic Constants and Ultrasonic Attenuation of the 'alpha—alpha' Phase of the Nb-H(D) System. II. Interpretation of Results," *Journal of Physics F: Metal Physics*, Vol. 15, 1985, pp. 525-542.

[43] Li, J. C. M., Oriani, R. A. and Darken, L. S., "The Thermodynamics of Stressed Solids," *Zeitschhrift fur Physik Chemische Neue Folge*, Vol. 49, 1966, pp. 271-291.

[44] Sofronis, P. and Birnbaum, H. K., "Mechanics of the Hydrogen-Dislocation-Impurity Interaction—I. Increasing Shear Modulus," *Journal of the Mechanics and Physics of Solids*, Vol. 43, 1995, pp. 49-90.

[45] Larche, F. C. and Cahn, J. W., "The Interaction of Composition and Stress in Crystalline Solids," *Acta Metallurgica*, Vol. 33, 1985, pp. 331-357.

[46] Sofronis, P., "The Influence of Mobility of Dissolved Hydrogen on the Elastic Response of a Metal," *Journal of the Mechanics and Physics of Solids*, Vol. 43, 1995, pp. 1385-1407.

[47] Völkl, J. and Alefeld, G., "Diffusion of Hydrogen in Metals," *Hydrogen in Metals I, Topics in Applied Physics*, G. Alefeld and J. Volkl, Eds., Springer-Verlag, New York, Vol. 28, 1978, pp. 321-348.

[48] McLellan R. B., "Thermodynamics and Interstitial Behavior of Interstitial solute Atoms in Non-Perfect Solvent Crystals," *Acta Metallurgica*, Vol. 27, 1979, pp. 1655-1663.

[49] Johnson, H. H., "Overview of hydrogen degradation phenomena," *Hydrogen Embrittlement and Stress Corrosion Cracking*, (Proceedings of a Troiano Festschrift Symposium, Case Western Reserve University, June 1-3, 1980), R. Gibala and R. F. Hehemann, Eds., ASM Ohio, 1984, pp. 3-27.

[50] Puls, M. P., "Elastic Interactions of Hydrogen in the lattice of Iron Alloys," *Hydrogen Degradation in Ferrous Alloys*, R. A. Oriani, J. P. Hirth, M. Smialowski, Eds., Noyes Publications, New Jersey, 1985, pp. 114-130.

[51] Bai, Q-X., Chu, W-Y., Hsiao, C-M., "Partial Molar Strain field of Hydrogen in α-Fe," *Scripta Metallurgica*, Vol. 21, 1987, pp. 613-618.

[52] Zhang, T-Y., Chu, W-Y., Hsiao, C-M., "Strain field of Hydrogen in α-Fe under Boltzmann Distribution," *Scripta Metallurgica*, Vol. 19, 1985, pp. 271-274.

[53] Zhang, T-Y., Chu, W-Y., Hsiao, C-M., "Strain Fields of Hydrogen Atoms in Iron," *Scripta Metallurgica*, Vol. 18, 1984, pp. 1421-1426.

[54] Zhang, T-Y., Chu, W-Y., Hsiao, C-M., "Tetragonal Distortion Field of Hydrogen Atoms in Iron," *Metallurgical Transactions*, Vol. 16A, 1985, pp. 1649-1653.

[55] Chu, W-Y., Zhang, T-Y, Hsiao, C-M., "Hydrogen Induced Delayed Cracking of Smooth Torsional Specimens," *Corrosion*, Vol. 40, 1984, pp. 197-199.

[56] Chu, W-Y., Hsiao, C-M., Ju, S-Y., Wang, C., "Hydrogen Induced Delayed Cracking of Type III Steel specimens," *Corrosion*, Vol. 38, 1982, pp. 446-452.

[57] Swanson, R. E., Thompson, A. W., Bernstein, I. M. and Maloney, J. L., "Effect of Stress State on the Stress Corrosion Cracking of 7075 Aluminum," *Hydrogen Effects in Metals*, I. M. Bernstein and A. W. Thompson, Eds., The Metallurgical Society of AIME, Vol. 1981, pp. 459-466.

[58] Malkin, J. and Tetelman, A. S., "Relation Between K_{IC} and Microscopic Strength for Low Alloy Steels," *Engineering Fracture Mechanics*, Vol. 3, 1971, pp. 151-167.

[59] Wert, C. A., "Trapping of Hydrogen in Metals," *Hydrogen in Metals I, Topics in Applied Physics*, G. Alefeld and J. Volkl, Eds., Springer-Verlag, New York, Vol. 29, 1978, pp. 305-330.

[60] Oriani, R. A., "The Diffusion and Trapping of Hydrogen in Steel," *Acta Metallurgica*, Vol. 18, 1970, pp. 147-157.

[61] Pressouyre, G. M., and Bernstein, I. M., "A Quantitative Analysis of Hydrogen Trapping," *Metallurgical Transactions,* Vol. 9A, 1978, pp. 1571-1580.

[62] Pressouyre, G. M., and Bernstein, I. M., "An Example of the Effect of Hydrogen Trapping on Hydrogen Embrittlement," *Metallurgical Transactions*, Vol. 12A, 1981, pp. 835-844.

[63] Tuyen, D. L. and Bernstein, I. M., "Hydrogen trapping of spheroidized steels as a function of plastic strain," *Scripta Metallurgica,* Vol. 20, 1986, pp. 1025-1029.

[64] Kumnick, A. J., and Johnson, H. H., "Hydrogen Transport Through Annealed and Deformed Iron," *Metallurgical Transactions*, Vol. 5A, 1974, pp. 1199-1206.

[65] Thomas, G. J., "Hydrogen Trapping in FCC metals," *Hydrogen Effects in Metals*, A. W. Thompson and I. M. Bernstein, Eds., *Transactions of Metallurgical Society* AIME, New York, NY, 1980, pp. 77-85.

[66] Chaudhari, B. S. and Radhakrishnan, T. P., "A Reexamination of the Trapping of Hydrogen in Iron and Steel," *Materials Transactions*, JIM, Vol. 34, 1993, pp. 443-449.

[67] Kumnick, A. J., and Johnson, H. H., "Deep Trapping States for Hydrogen in Deformed Iron," *Acta Metallurgica,* Vol. 28, 1980, pp. 33-39.

[68] Iino, M., "Evaluation of Hydrogen-Trap Binding Enthalpy I," *Metallurgical Transactions*, Vol. 18A, 1987, pp. 1559-1564.

[69] Pound, B. G., "Hydrogen Trapping in Work-Hardened Alloys, *Acta Materialia*, Vol. 39, 1991, pp. 2099-2105.

[70] Pound, B. G., "Hydrogen Ingress in High-Strength Alloys Exposed to Different Electrolytes," *Corrosion*, Vol. 46, 1990, pp. 50-56.

[71] Pound, B. G., "Hydrogen Ingress in Titanium," *Corrosion*, Vol. 47, 1991, pp. 99-104.

[72] McKibbin, R., Sharp, R. M., Harrington, D. A., Pound, B. G., and Wright, G. A. "A Potentiostatic Double-Step Method for Measuring Hydrogen Atom Diffusion and Trapping in Metal Electrodes-I. Theory," *Acta Metallurgica*, Vol. 35, 1987, pp. 253-262.

[73] Pound, B. G., Wright, G. A., Sharp, R. M., "A Potentiostatic Double-Step Method for Measuring Hydrogen Atom Diffusion and Trapping in Metal Electrodes-II. Experimental," *Acta Metallurgica*, Vol. 35, 1987, pp. 163-270.

[74] Pound, B. G.," Hydrogen Trapping in Precipitation-Hardened Alloys," *Acta Materialia*, Vol. 38, 1990, pp. 2373-2381.

[75] Johnson, H. H., Quick, N. and Kumnick, A. J. "Hydrogen Trapping Mechanisms by Permeation techniques," *Scripta Metallurgica*, Vol. 13, 1979, pp. 67-72.

[76] Turnbull, A., Hutchings, R. B. and Ferriss, D. H. "Modelling of Thermal Desorption of Hydrogen from Metals," *Materials Science and Engineering*, Vol. A238, 1997, pp. 317-328.

[77] McNabb, A. and Foster, P. K., "A New Analysis of the Diffusion of Hydrogen in Iron and Ferritic Steels," *Transactions Metallurgical Society* AIME, Vol. 227, 1963, pp. 618-627.

[78] Tien, J. K., Thompson, A. W., Bernstein, I. M., and Richards, R. J., "Hydrogen Transport by Dislocations," *Metallurgical Transactions*, Vol. 7A, 1976, pp. 821–829.

[79] Chou, Y. T. and Li, J. C. M., "Chemical Interactions Between Interstitial Solutes and Dislocations," *The Interactions Between Dislocations and Point Defects*, B. L. Eyre, Ed., Metallurgy Division, Atomic Energy Research Establishment, Harwell, England, Vol. I, pp. 105-116.

[80] Bockris, J., beck, W., Genshaw, M. A., Subramanyan, P. K., and Williams, F. S., "The effect of Stress on the Chemical Potential of Hydrogen in Iron and Steel," *Acta Metallurgica*, Vol. 19, 1971, pp. 1209-1218.

[81] Angelo, J. E., Moody, N. R. and Baskes, M. I., "Modeling the Segregation of Hydrogen to Lattice Defects in Nickel," *Hydrogen Effects in Materials*, A. W. Thompson and N. R. Moody, Eds., *Transactions Metallurgical Society* AIME, New York, NY, 1996, pp. 161-170.

[82] Symons, D. M. "An Investigation into the Effects of Hydrogen on the Fracture and Deformation Behavior of Alloy-X-750," Ph.D. dissertation, Carnegie Mellon University, Pittsburgh, PA, 1994.

[83] Turnbull, A., Ballinger, R. G., Hwang, Morra, M. M., Psaila-Dombrowski, M. and Gates, R. M., "Hydrogen Transport in Nickel-base Alloys," *Metallurgical Transactions*, Vol. 23A, 1992, pp. 3231-3244.

[84] Frandsen, J. D., Paton, N. E., and Marcus, H. L., "The Influence of Low-Pressure Hydrogen Gas on Crack Growth in T. D.-Nickel and T.D.-Nichrome," *Scripta Metallurgica*, Vol. 7, 1973, pp. 409-414.

[85] Gerberich, W. W, Chen, Y. T. and St. John, C., "A Short-Time Diffusion Correlation for Hydrogen-Induced Crack Growth Kinetics," *Metallurgical Transactions*, Vol. 6A, 1974, pp. 1485-1498.

[86] Tien, J. K., Richards, R. J., Buck, O., Marcus, H. L., "Model of Dislocation Sweep-in of Hydrogen Atoms During fatigue Crack Growth," *Scripta Metallurgica*, Vol. 9, 1975, pp. 1097-1101.

[87] Tien, J. K., Nair, S., Bates, R. C., and Buck, O., "Dislocation Sweeping Model for Hydrogen Assisted subcritical Crack Growth," *Scripta Metallurgica*, Vol. 14, 1980, pp. 591-594.

[88] Scully, J. C., "The Role of Hydrogen in Stress Corrosion Cracking," *Effects of Hydrogen on Behavior of Materials*, I. M. Bernstein and A. W. Thompson, Eds., Metallurgical Society AIME, New York 1976, pp. 129-147.

[89] Louthan, M. R., Derrick, R. G., Donovan, J. A., and Gaskey, G. R., "Hydrogen Transport in Iron and Steel," *Effects of Hydrogen on Behavior of Materials*, I. M. Bernstein and A. W. Thompson, Eds., Metallurgical society of AIME, New York 1976, pp. 337-346.

[90] Brown, J. T. and Balwin, W. M., "Hydrogen Embrittlement of Steels," *Transactions* of AIME, Vol. 200, 1954, pp. 298-303.

[91] Bastien, P. and Azou, P., "Effect of Hydrogen on the Deformation and Fracture of Iron and Steel in Simple Tension," *Proceedings of the First World Metallurgical Congress*, W. M. Baldwin, Ed., American Society for Metals, 1952, pp. 535-552.

[92] Wilcox, B. A. and Smith, G. C., "Intercrystalline Fracture in Hydrogen-Charged Nickel," *Acta Metallurgica*, Vol. 13, 1965, pp. 331-343.

[93] Windle, A. H. and Smith, G. C., "The Effect of Hydrogen on the Deformation and Fracture of Polycrystalline Nickel," *Metal Science Journal*, Vol. 4, 1970, pp. 136-144.

[94] Latanision, R. M. and Staehle, R. W., "The effect of Continuous Hydrogenation on the Deformation of Nickel Single Crystals," *Scripta Metallurgica*, Vol. 2, 1968, pp. 667-672.

[95] Donovan, J. A., "Accelerated Evolution of Hydrogen from Metals During Plastic Deformation," *Metallurgical Transactions*, Vol. 7A, 1976, pp. 1677-1683.

[96] Louthan, M. R., Gaskey, G. R., Donovan, J. A. and Rawl, D. E., " Hydrogen Embrittlement of Metals," *Materials Science and Engineering*, Vol. 10, 1972, pp. 357-368.

[97] Foster, L. M., Jack, T. J. and Hill, W. W., "Structures Revealed in Zone Refined Aluminum by Tritium Decoration," *Metallurgical Transactions*, Vol. 1, 1970, pp. 3117-3124.

[98] Lecoester, F., Chene, J., and Noel, D., "Hydrogen Embrittlement of the NI-base Alloy 600 Correlated with Hydrogen Transport by Dislocations," *Materials Science and Engineering*, Vol. A262, 1999, pp. 173-183.

[99] Walter, R. J., Jewett, R. P. and Chandler, W. T., "On the Mechanism of Hydrogen-Environment Embrittlement of Iron- and Nickel-base Alloys, *Materials Science and Engineering*, Vol. 5, 1969, pp. 98-110.

[100] Vennett, R. M. and Ansell, G. S., "A Study of Gaseous Hydrogen Damage in Certain FCC Metals," *Transactions* ASM, Vol. 62, 1969, pp. 1007-1013.

[101] Latanision, R. M., Kurkela, M., and Lee, F., "The Role of Grain Boundary Chemistry and the Environment on Intergranular Fracture," *Hydrogen Effects in Metals*, I. M. Bernstein and A. W. Thomspon, Eds., The Metallurgical society of AIME, 1981, pp. 379-394.

[102] Latanision, R. M. and Kurkela, M., "The Effects of Plastic Deformation on the Transport of Hydrogen in Nickel," *Scripta Metallurgica*, Vol. 13, 1979, pp. 927-932.

[103] Hwang, C. and Bernstein, I. M., "Dislocation Transport of Hydrogen in Iron Single Crystals," *Acta Metallurgica*, Vol. 34, 1986, pp. 1001-1010.

[104] Hwang, C. and Bernstein, I. M., "A Demonstration of Dislocation Transport of Hydrogen in Iron," *Scripta Metallurgica*, Vol. 17, 1983, pp. 1299-1304.

[105] Louthan, M. R., "Effects of Hydrogen on the Mechanical Properties of Low Carbon and Austenitic Steels," *Hydrogen in Metals*, I. M. Bernstein and A. W. Thompson, Eds., ASM, Ohio, 1974, pp. 53-75.

[106] Donovan, J. A., "Sorption of Tritium by Nickel During Plastic Deformation," *Metallurgical Transactions*, Vol. 7A, 1976, pp. 145-149.

[107] Kurkela, M., Frankel, G. S., Latanision, R. M., and Suresh, S. and Ritchie, R. O., "Influence of Plastic Deformation on Hydrogen Transport in 2 1/4 Cr-1Mo Steel," *Scripta Metallurgica*, Vol. 16, 1982, pp. 455-459.

[108] Frankel, G. S. and Latanision, R. M., "Hydrogen Transport During Deformation in Nickel: Part I Polycrystalline Nickel," *Metallurgical Transactions*, Vol. 17A, 1986, pp. 861-867.

[109] Hashimoto, M. and Latanision, R. M., "Theoretical Study of Hydrogen Transport During Plastic Deformation in Iron," *Acta Metallurgica*, Vol. 36, 1988, pp. 1837-1854.

[110] Hashimoto, M. and Latanision, R. M., "Experimental Study of Hydrogen Transport During Plastic Deformation in Iron," *Metallurgical Transactions*, Vol. 19A, 1988, pp. 2789-2798.

[111] Hashimoto, M. and Latanision, R. M., "The Role of Dislocations During Transport of Hydrogen in Hydrogen embrittlement of Iron," *Metallurgical Transactions*, Vol. 19A, 1988, pp. 2799-2803.

[112] Ladna, B. and Birnbaum, H. K., "A Study of Hydrogen Transport During Plastic Deformation," *Acta Metallurgica*, Vol. 35, 1987, pp. 1775-1778.

[113] Tien, J. K., "Diffusion and the Dislocation Sweeping Mechanism for Hydrogen Transport," *Effects of Hydrogen on Behavior of Materials*, I. M. Bernstein and A. W. Thompson, Eds., Metallurgical society of AIME, New York 1976, pp. 309-325

[114] Johnson, H. H. and Hirth, J. P., "Internal Hydrogen Supersaturation Produced by Dislocation transport," *Metallurgical Transactions*, Vol. 7A, 1976, pp. 1543-1548.

[115] Tien, J. K., Nair, S. V. and Jensen R. R., "Dislocation Sweeping of Hydrogen and Hydrogen Embrittlement," *Hydrogen Effects in Metals,* I. M. Bernstein and A. W. Eds., Thompson, Metallurgical Society of AIME, New York, NY, 1981, pp. 37-56.

[116] Johnson, H. H. and Hirth, J. P., "On the Transport of Hydrogen by Dislocations," *Atomistics of Fracture* (Proceedings of a NATO Advanced Research Institute on Atomistics of Fracture, Calcatoggio, Corsica, France, May 22-31, 1981), R. A. Latanision and J. R. Pickens, Eds., Plenum Press, New York, 1983, pp. 771-785.

[117] Nair, S. V., Tien, J. K., and Jensen R. R., "Kinetic Enrichment of Hydrogen at Interfaces and Voids by Dislocation Sweep-In of Hydrogen," *Metallurgical Transactions*, Vol. 14A, 1983, pp. 385-393.

[118] Latanision, R. M., Compeau, C. R., and Kurkela, M., "Hydrogen Permeation and Embrittlement Studies on Metallic Glasses," *Hydrogen Embrittlement and Stress Corrosion Cracking*, (Proceedings of a Troiano Festschrift Symposium, Case Western Reserve University, June 1-3, 1980), R. Gibala and R. F. Hehemann, Eds., ASM Ohio, 1984, pp. 297-313.

[119] Robertson, W. M., "Hydrogen Permeation, Diffusion and Solution in Nickel," Zeitschrift Fur Metallkunde, Vol. 64, 1973, pp. 436-443.

[120] Latanision, R. M. and Kurkela, M, "Hydrogen Permeability and Diffusivity in Nickel and Ni-Base Alloys," *Corrosion-NACE*, Vol. 39, 1983, pp. 174-181.

[121] Brass, A. M., Chanfreau, A. and Chene, J., "Role of Grain Boundaries and Cold Work on H Permeation in Nickel," *Hydrogen Effects on Material Behavior*, N. R. Moody and A. W. Thompson, Eds., The Minerals, Metals and Materials Society, Warrendale, PA, 1990, pp. 19-30.

[122] Harris, T. M. and Latanision, R. M., "Grain Boundary Diffusion of Hydrogen in Electrodeposited Nickel," *Hydrogen Effects on Material Behavior*, N. R. Moody and A. W. Thompson, Eds., The Minerals, Metals and Materials Society, Warrendale, PA, 1990, pp. 133-142.

[123] Tsuru, T. and Latanision, R. M., "Grain Boundary Transport of Hydrogen in Nickel," *Scripta Metallurgica*, Vol. 16, 1982, pp. 575-578.

[124] Ladna, B. and Birnbaum, H. K., "SIMS Study of Hydrogen at the Surface and Grain Boundaries of Nickel Bicrystals," *Acta Metallurgica*, Vol. 35, 1987, pp. 2537-2542.

[125] Kimura, A. and Birnbaum, H. K., " Hydrogen Induced Grain Boundary Fracture in High Purity Nickel and its Alloys-Enhanced Hydrogen Diffusion Along Grain Boundaries," *Acta Metallurgica*, Vol. 36, 1988, pp. 757-766.

[126] Mutschele, T. and Kircheim, R., "Segregation and Diffusion of Hydrogen in Grain Boundaries of Palladium," Scripta Metallurgica, Vol. 21, 1987, pp. 135-140.

[127] Kircheim, R., Huang, X. Y., and Mutschele, T., "Interaction of Hydrogen with Internal Interfaces," *Hydrogen Effects on Material Behavior*, N. R. Moody and A. W. Thompson, Eds., The Minerals, Metals and Materials Society, Warrendale, PA, 1990, pp. 85-98.

[128] Latanision, R. M. and Opperhauser H. Jr., " The Intergranular Embrittlement of Nickel by Hydrogen: The Effect of Grain Boundary Segregation," *Metallurgical Transactions*, Vol. 5, 1975, pp. 483-492.

[129] Liu, H. W., Hu, Y-L, and Ficalora, P. J., "The Control of Catalytic Poisoning and Stress Corrosion Cracking," *Engineering Fracture Mechanics*, Vol. 5, 1973, pp. 281-292.

[130] Takeda, Y. and McMahon, C. J. Jr., "Strain Controlled vs Stress Controlled Hydrogen Induced Fracture in a Quenched and Tempered Steel," *Metallurgical Transactions*, Vol. 12A, 1981, pp. 1255-1266.

[131] Kameda, J. and McMahon, C. J. Jr., "Solute Segregation and Hydrogen-Induced Intergranular Fracture in an Alloy Steel," *Metallurgical Transactions*, Vol. 14A, 1983, pp. 903-911.

[132] Morgan, M. J., "Grain Boundary Segregation and Embrittlement by Antimony and Hydrogen in a Model Alloy Steel," PhD dissertation, University of Pennsylvania, Philadelphia, PA, 1987.

[133] Yoshino, K. and McMahon, C. J. Jr., "The Cooperative Relation Between Temper Embrittlement and Hydrogen Embrittlement in a High Strength Steel," *Metallurgical Transactions*, Vol. 5, 1974, pp. 363-370.

[134] Banerji, S. K., McMahon, C. J. Jr. and Feng, H. C., "Intergranular Fracture in 4340-Type Steels: Effects of Impurities and Hydrogen," *Metallurgical Transactions*, Vol. 9A, 1978, pp. 237-247.

[135] Briant, C. L, Feng, H. C. and McMahon, C. J. Jr., "Embrittlement of a 5 pct Nickel High Strength Steel by Impurities and their Effects on Hydrogen-Induced Cracking," *Metallurgical Transactions*, Vol. 9A, 1978, pp. 625-633.

[136] Bandyopadhyay, N., Kameda, J. and McMahon, C. J. Jr., "Hydrogen-Induced Cracking in 4340-Type Steel: Effects of Composition, Yield Strength, and H_2 Pressure," *Metallurgical Transactions*, Vol. 14A, 1983, pp. 881-888.

[137] Mahon, C. J. Jr., and Vitek, V., "The Effects of Segregated Impurities on Intergranular Fracture Energy," *Acta Metallurgica,* Vol. 27, 1979, pp. 507-513.

[138] Jokl, M. L., Vitek, V. and McMahon, C. J. Jr., "A Microscopic Theory of Brittle Fracture in Deformable Solids: a Relation Between Ideal Work of Fracture and Plastic Work," *Acta Metallurgica,* Vol. 28, 1980, pp. 1479-1488.

[139] Kameda, J. and McMahon, C. J. Jr., "Solute Segregation and Brittle Fracture in an Alloy Steel," *Metallurgical Transactions,* Vol. 11A, 1980, pp. 91-101.

[140] Kameda, J. and McMahon, C. J. Jr., "The Effects of Sb, Sn, and P on the Strength of Grain Boundaries in a Ni-Cr Steel," *Metallurgical Transactions,* Vol. 12A, 1981, pp. 31-37.

[141] Mishin, Y. and Herzig, Chr., "Grain Boundary Diffusion: Recent Progress and Future Research," *Materials Science and Engineering,* Vol. A260, 1999, pp. 55-71.

[142] Van Leeuwen, H. P., "The Kinetics of Hydrogen Embrittlement: a Quantitative Diffusion Model," *Engineering Fracture Mechanics,* Vol. 6, 1974, pp. 141-161.

[143] Hippsley, C. A. and Briant, C. L., "Application of a Model for Stress Driven Segregation to Hydrogen Embrittlement," *Scripta Metallurgica,* Vol. 19, 1985, pp. 1203-1208.

[144] Liu, H. W., "Stress-Corrosion Cracking and the Interaction Between Crack-Tip Stress Field and Solute Atoms," *Journal of Basic Engineering,* Transactions of ASME, Vol. 92, 1970, pp. 633-638.

[145] Tong-Yi, Z., Mason, T. A. and Hack, J. E., "The Equilibrium Concentration of Hydrogen Atoms Ahead of Mode I Crack Tip Single Crystal Iron," *Scripta Metallurgica,* Vol. 26, 1992, pp. 139-144.

[146] Tong-Yi, Z., Shen, H. and Hack, J. E., "The Influence of Cohesive Forces on the Equilibrium Concentration of Hydrogen Atoms Ahead of a Crack Tip in Single Crystal Iron," *Scripta Metallurgica,* Vol. 27, 1992, pp. 1605-1610.

[147] Tong-Yi, Z., and Hack, J. E., "The Equilibrium Concentration of Hydrogen Atoms Ahead of A Mixed Mode I-Mode III Crack Tip in Single Crystal Iron," *Metallurgical and Materials Transactions,* Vol. 30A, 1999, pp. 155-159.

[148] Van Leeuwen, H. P., A Failure Criterion for Internal hydrogen Embrittlement," *Engineering Fracture Mechanics,* Vol. 9, 1977, pp. 291-296.

[149] Unger, D. J., "A Mathematical Analysis for Impending Hydrogen Assisted Crack Propagation," *Engineering Fracture Mechanics,* Vol. 34, 1989, pp. 657-667.

[150] Narita, N., Shiga, T. and Higashida, K., "Crack-Impurity Interactions and their Role in the Embrittlement of Fe Alloy Crystals Charged with Light Elements," *Materials Science and Engineering,* Vol. A176, 1994, pp. 203-209.

[151] McMeeking, R. M. and Evans, A. G., "Mechanics of Transformation Toughening in Brittle Materials," *Journal of the American Ceramics Society,* Vol. 65, 1982, pp. 242-246.

[152] Weertman, J. and Hack, J. E., "Stress Intensity Factors for Crack Tip Shielding or Anti-shielding by Impurity Atoms," *International Journal of Fracture,* Vol. 30, 1986, pp. 295-299.

[153] Weertman, J. and Hack, J. E., "Crack Tip Shielding/Antishielding by Impurity Atoms," *International Journal of Fracture,* Vol. 36, 1988, pp. 27-34.

[154] Lufrano, J. and Sofronis, P., "Numerical Analysis of the Interaction of Solute Hydrogen Atoms with the Stress Field of a Crack." *International Journal of Solids and Structures*, Vol. 33, 1996, pp. 1709-1723.

[155] Yokobori, T. A, Nemoto, T, Satoh, K., Yamada, T., "Numerical Analysis of Hydrogen Diffusion and Concentration in Solid with Emission Around the Crack Tip," *Engineering Fracture Mechanics*, Vol. 55, 1996, pp. 47-60.

[156] Kitajima, K., "Modelling of Hydrogen-Induced Fracture in Iron," *Materials Science and Engineering*, Vol. A176, 1994, pp. 249-253.

[157] Hirose, Y and Mura, T., "Nucleation Mechanism of Stress Corrosion Cracking from Notches," *Engineering Fracture Mechanics*, Vol. 19, 1984, pp. 317-329.

[158] Hirose, Y and and Mura, T., "Growth Mechanism of Stress Corrosion Cracking in High Strength Steel," *Engineering Fracture Mechanics*, Vol. 19, 1984, pp. 1057-1067.

[159] Maier, H. J., Popp, W. and Kaesche, H., "A Method to Evaluate the Critical Hydrogen Concentration for Hydrogen-Induced Crack propagation," *Acta Metallurgica*, Vol. 35, 1987, pp. 875-880.

[160] Sun, S., Shiozawa, K., Gu, J., and Chen, N., "Investigation of Deformation Field and Hydrogen Partition Around Crack Tip in fcc Single Crystal," *Metallurgical and Materials Transactions*, Vol. 17, 1995, pp. 1213-1220.

[161] Turnbull, A., Ferris, D. H., Anzai, H., "Modelling of the Hydrogen Distribution at a Crack Tip," *Materials Science and Engineering*, Vol. A206, 1996, pp. 1-13.

[162] Pressouyre, G. M., "A Classification of Hydrogen Traps in Steel," *Metallurgical Transactions*, Vol. 10A, 1979, pp. 1571-1573.

[163] Foster, P. K., McNabb, A. and Payne, C. M., "On the Rate of Loss of Hydrogen from Cylinders of Iron and Steel," *Transactions Metallurgical Society AIME*, Vol. 233, 1965, pp. 1022-1031.

[164] Booth, D. M. A., and Hewitt, J., "A Mathematical Model Describing the Effects of Microvoids upon the Diffusion of Hydrogen in Iron and Steel," *Acta Metallurgica*, Vol. 22, 1974, pp. 171-175.

[165] Booth, D. M. A., Atkinson, C. and Bilby B. A., "A Numerical Solution of the Diffusion Equation Resulting from the Void Theory of the Trapping of Hydrogen in Iron and Steel," *Acta Metallurgica,* Vol. 23, 1975, pp. 371-376.

[166] Caskey, G. R. and Pillinger, W. L., "Effect of Trapping on Hydrogen Permeation," *Metallurgical Transactions*, Vol. 6A, 1975, 467-476.

[167] Frank, R. C., Wert, C. W. and Birnbaum, H. K., "Modeling Diffusion Through Non-uniform Concentrations of Traps," *Metallurgical Transactions*, Vol. 10A, 1979, pp. 1627-1630.

[168] Thomas, P. G. and Stern, E. J., "Efficient Numerical Modeling of Hydrogen Diffusion with Trapping," *Journal of Materials Science,* Vol. 16, 1981, pp. 3122-3130.

[169] Ellebrock, Von H. G., Vibrans, G. and Stuwe, H. P., "Diffusion von Wasserstoff in Stahl mit Inneren Hohlraumen," *Acta Metallurgica*, Vol. 20, 1972, pp. 53-60.

[170] Allen-Booth, D. M., Atkinson, C. and Bilby, B. A., "A Numerical Solution of the Diffusion Equation Resulting from the Void Theory of the Trapping of Hydrogen in Iron and Steel," *Acta Metallurgica*, Vol. 23, 1975, pp. 371-376.

[171] Liu, X., Todd, J. A., Wang, J., "Calculations of Hydrogen Concentrations near Crack Tips Using the Boundary Element Method," PVP-Vol. 336, 1996, pp. 69-76, Structural Integrity, NDE, Risk and Material Performance for Petroleum, process and Power, ASME Pressure Vessels and Piping Conference, Montreal, Quebec, Canada.

[172] Liu, X., Todd, J. A., Wang, J., "Effect of Initial and Boundary conditions on the Hydrogen Concentration Distribution near Crack tips," PVP-Vol. 336, 1996, pp. 77-85, Structural Integrity, NDE, Risk and Material Performance for Petroleum, process and Power, ASME Pressure Vessels and Piping Conference, Montreal, Quebec, Canada.

[173] Toribio, J., Valiente, A., Cortes, R., Caballero, L., "Modelling Hydrogen Embrittlement in 316L Austenitic Stainless Steel for the First Wall of the Next European Torus," *Nuclear Engineering and Design*, Vol. 29, 1995, pp. 442-447.

[174] Toribio, J., Cortes, R., Caballero, L., Valiente, A., "An Integrated Approach to the Modelling of Hydrogen Assisted Failure in 316L Steel," *Nuclear Engineering and Design*, Vol. 41, 1998, pp. 91-96.

[175] Toribio, J., "Hydrogen-Plasticity Interactions in Pearlitic Steel: A Fractographic and Numerical Study," *Materials Science and Engineering*, Vol. A219, 1996, pp. 180-191.

[176] Pressouyre, G. M., and Bernstein, I. M., "A Kinetic Model for Hydrogen-Induced Cracking," *Acta Metallurgica*, Vol. 27, 1979, pp. 89-100.

[177] Fuentes-Samaniego, R. and Hirth, J. P. "Diffusion of Interstitial Solute in a Potential Well Characteristic of a Moving Dislocation," *Physica Status Solidi* (b), Vol. 106, 1981, pp. 359-371.

[178] Fuentes-Samaniego, R. and Hirth, J. P. "Excess Solute Atmosphere carried by a Potential Well characteristic of a Moving Dislocation Core," *Physica Status Solidi* (b), Vol. 125, 1984, pp. 147-154.

[179] Han, G. W., Feng, D. and Ye, W. J., "Drift Diffusion Model of Hydrogen Atoms for Hydrogen Embrittlement in Polycrystalline Ni3Al," *Scripta Metallurgica*, Vol. 31, 1994, pp. 559-564.

[180] Kitagawa, H. and Kojima, Y., "Diffusion of Hydrogen Near an Elasto-Plastically Deformed Crack Tip," *Atomistics of Fracture* (Proceedings of a NATO Advanced Research Institute on Atomistics of Fracture, Calcatoggio, Corsica, France, May 22-31, 1981), ed. R. A. Latanision and J. R. Pickens, Plenum Press, New York, 1983, pp. 799-811.

[181] Sofronis, P. and McMeeking, R. M., "Numerical Analysis of Hydrogen Transport Near a Blunting Crack Tip," *Journal of the Mechanics and Physics of Solids*, Vol. 37, 1989, pp. 317-350.

[182] Krom, A. H. M., Koers, R. W. J. and Bakker, A., "Hydrogen Transport Near a Blunting Crack," *Journal of the Mechanics and Physics of Solids*, Vol. 47, 1999, pp. 971-992.

[183] Sofronis, P., "Mechanics of Hydrogen Embrittlement," Ph.D. dissertation, University of Illinois at Urbana-Champaign, Urbana, IL, 1987.

[184] Nagtegaal, J. C., Parks, D. M. and Rice, J. R., "On Numerically Accurate Finite Element Solutions in the Fully Plastic Range," *Computer Methods in Applied Mechanics and Engineering*, Vol. 4, 1974, pp. 153-177.

[185] Griffiths, J. R. and Owen, D. R. J., "An Elastic-Plastic Stress Analysis for a Notched Bar in Plane Strain Bending," *Journal of the Mechanics and Physics of Solids*, Vol. 19, 1971, pp. 419-431.

[186] Symons, D. M. and Thompson A. W., "The Effect of Hydrogen on the Fracture Toughness of Alloy X-750," *Metallurgical Transactions*, Vol. 28A, 1997, pp. 817-823.

[187] Kearns, J. J., Lebo, M. R. and Mills, W. J., "Hydrogen Embrittlement, Grain Boundary Segregation and Stress Corrosion Cracking of alloy X-750 in Low and High Temperature Water," WAPD-T-3149, Bettis Atomic Power Laboratory, 1997 (available through OSTI).

[188] Lufrano, J., Symons, D., and Sofronis, P., "Hydrogen Embrittlement of Alloy X-750," Unpublished research.

[189] Lassila, D. H. and Birnbaum, H. K., "The Effect of Diffusive Segregation on the Fracture of Hydrogen Charged Nickel," *Acta Metallurgica*, Vol. 36, 1988, pp. 2821-2825.

[190] Symons, D. M. and Thompson A. W., "The Effect of Hydrogen on the Fracture of Alloy X-750, *Metallurgical Transactions*, Vol. 27A, 1996, pp. 101-110.

[191] Young, G. A. and Scully, J. R., "Evidence that Carbide Precipitation Produces Hydrogen Traps in Ni-17Cr-8Fe Alloys," *Scripta Materiallia*, Vol. 36, 1997, pp. 713-719.

[192] D. M. Symons, "A Comparison of Internal Hydrogen Embrittlement and Hydrogen Environment Embrittlement of X-750," To appear in *Engineering Fracture Mechanics.*

[193] James, L. A. and Porr, W. C., "The Effect of an Elevated temperature Aqueous Environment Upon the J-Controlled Tearing of a Low Alloy Steel," *International Journal of Pressure Vessels and Piping*, In Press.

[194] Symons, D., Lufrano, J. and Sofronis, P., "An investigation into the fracture criterion in Alloy X-750," Report #WAPD-T-3203, May 1998, Available through DOE Office of Scientific and Technical Information (OSTI).

Edward Richey III and Richard P. Gangloff[1]

Strain Rate Dependent Environment Assisted Cracking of α/β-Ti Alloys in Chloride Solution

Reference: Richey, E. and Gangloff, R. P., **"Strain Rate Dependent Environment Assisted Cracking of α/β-Ti Alloys in Chloride Solution,"** *Environmentally Assisted Cracking: Predictive Methods for Risk Assessment and Evaluation of Materials, Equipment, and Structures, ASTM STP 1401,* R. D. Kane, Ed., American Society for Testing and Materials, West Conshohocken, PA, 2000.

Abstract: Environment assisted cracking (EAC) occurs in annealed-α/β Ti-6Al-4V (ELI) and Ti-6Al-2Zr-2Sn-2Cr-2Mo in aqueous chloride solution, as evidenced by rising-displacement threshold stress intensity factors well below K_{IC} and a mode transition from ductile fracture to transgranular cleavage of α. The acicular-α/α_2 microstructure of Ti-6-2222 is susceptible to severe cracking in 3.5% NaCl compared to the equiaxed-α/α_2 structure of Ti-6-4. Thresholds and growth rates depend on loading rate, and appear most environment sensitive at intermediate crack tip strain rates. EAC is sustained to high loading rates ($dK/dt = 0.3$ MPa$\sqrt{m}$/s for Ti-6-4 and above 10 MPa$\sqrt{m}$/s for Ti-6-2222) and crack growth rates are rapid (10 μm/s). The hydrogen environment embrittlement mechanism is consistent with such rapid cracking kinetics, but only if the process zone is within 0.001 to 1 μm of the crack tip surface. A near-tip process zone may be promoted by high H produced electrochemically on active areas of the crack surface, or by a sharp crack tip.

Keywords: Hydrogen embrittlement, stress corrosion cracking, titanium alloy, fracture mechanics, crack tip strain rate, crack propagation

Introduction

Two-phase α/β titanium alloys are susceptible to transgranular (TG) environment assisted cracking (EAC) when stressed in aqueous solutions with halide anions including Cl^- [*1-5*]. Embrittlement is promoted by an existing crack [*6, 7*] and occurs at a fraction of the fracture toughness with subcritical crack growth rates approaching 50 μm/s. The likely mechanism is hydrogen environment embrittlement (HEE) [*8*], where atomic hydrogen (H) uptake is localized from the crack tip surface into the process zone [*9*]. Transgranular H damage is in the hexagonal-close packed α phase, and involves lattice decohesion or brittle-hydride formation leading to near-basal plane cracking and slip-

[1]Graduate Research Assistant and Professor, respectively; Department of Materials Science and Engineering, University of Virginia, Charlottesville, VA 22903.

Copyright© 2000 by ASTM International www.astm.org

based tubular microvoiding [*2, 4, 8, 10*]. Cracking along α/β interfaces is promoted at high levels of H [*11*]. The body-centered β phase in metastable β-Ti alloys is susceptible to intergranular HEE in chloride solution [*12*] and cleavage at high dissolved H contents [*13*], but may act as a crack arrestor during TG EAC in α/β-Ti alloys [*2, 8, 11*].

Stress intensity factor (K) and crack tip strain rate ($\dot{\varepsilon}_{CT}$) interactively govern EAC propagation in α/β-Ti alloys. The K controls process zone tensile and hydrostatic stresses [*14*]. $\dot{\varepsilon}_{CT}$ affects the stability of the crack tip passive film that governs cathodic H production and uptake [*15-20*], as well as the time for H transport in the process zone. Experimental results are contradictory. Embrittlement appears to be maximized at intermediate $\dot{\varepsilon}_{CT}$ for loading in an electrolyte and eliminated under static or very slow-rate loading [*21-23*]. Other data suggest that EAC is increasingly severe as dK/dt decreases to quasi-static levels for chloride solution [*3, 24*] and H_2 [*8, 25*]. Comparisons are complicated by subtle differences in prestressing of a cracked specimen prior to hydrogen exposure; conditions that promote crack tip creep and reduced $\dot{\varepsilon}_{CT}$ may retard HEE [*26, 27*]. EAC is generally eliminated at high loading rates, but the levels of environmental crack growth rate (da/dt) and applied stress intensity rate (dK/dt) where brittle cracking persists in α/β-Ti alloys are high [*21, 25, 28*]. The process that rate limits HEE was speculated to be either dislocation transport of H in equiaxed α [*21*], short-range diffusion of H in α/TiH for low H concentration-continuous α microstructure conditions [*11, 25*], or long range diffusion of H in β for high crack tip H levels and a continuous β phase [*28*]. The details of these rate-sensitive processes are not understood.

Crack tip strain rate effects on HEE in Ti alloys are uncertain because quantitative fracture mechanics methods have not been employed [*8, 11, 21, 25*]. Experimentation to characterize the effect of $\dot{\varepsilon}_{CT}$ on the threshold K for the onset of EAC and subsequent da/dt must precisely monitor crack growth, and systematically vary loading rate and format to probe a range of $\dot{\varepsilon}_{CT}$. Modeling must define $\dot{\varepsilon}_{CT}$ to establish the factors that rate limit crack tip damage; particularly film rupture, electrochemical hydrogen adsorption, and H transport into the crack tip process zone. Such understanding is a critical element of life prediction to control EAC in a high performance component [*29*].

The objectives of this research are to characterize the aqueous-EAC resistance of two α/β-Ti alloys as a function of crack tip strain rate and to understand the crack tip damage mechanism. Fracture mechanics threshold K and crack growth rate measurements are interpreted to: (1) better characterize alloy susceptibility to EAC, (2) determine if EAC kinetics correlate with crack tip strain rate, and (3) identify the H transport process capable of sustaining high-rate cracking to test the HEE mechanism. Experiments utilize a precracked specimen stressed at a constant crack mouth opening displacement rate ($\dot{\delta}_m$) in neutral NaCl solution at 23°C.

Experimental Methods

Materials

Two α/β-Ti alloys were studied, Ti-6.2Al-4.3V-0.12O (Ti-6-4; extra-low interstitial, ELI) and Ti-5.6Al-1.9Zr-2.0Sn-2.1Cr-2.2Mo-0.11O (Ti-6-2222) in weight pct. Ti-6-4 was obtained as a 12.7 mm thick plate that was α/β rolled, mill-annealed (MA) for 8 h at 760°C, and vacuum-furnace cooled. The optical micrograph in Fig. 1a

shows that the microstructure consists of about 7 volume pct of retained β (dark phase) in a continuous-equiaxed α matrix (light), with an average α grain diameter of 20 to 25 μm.

Ti-6-2222 plate (6.6 mm thick) was hot rolled in the α + β phase field, air cooled, heated at 900°C for 2 h and furnace cooled at 3°C/min. The beta transus (β_T) for Ti-6-2222 is near 950°C. Figure 1b shows that the resulting microstructure consists of coarse acicular α (dark) phase in a continuous β (light) matrix. Globular-recrystallized α is arrayed parallel to the rolling direction (RD) in Fig. 1b. The β phase in each alloy is free of secondary α precipitates [*30*], while silicides are present in the β of Ti-6-2222 but not Ti-6-4 [*31*]. Slow cooling precipitated Ti_3Al (α_2) in the α of both Ti-6-2222 [*32*] and Ti-6-4 [*33*].

Yield strength (σ_{YS} in the T orientation) and plane strain fracture toughness (K_{JIC} in the TL orientation) are 940 MPa and 66 MPa$\sqrt{m}$ for Ti-6-2222, and 940 MPa (L) and 79 MPa$\sqrt{m}$ (LT) for Ti-6-4.[2]

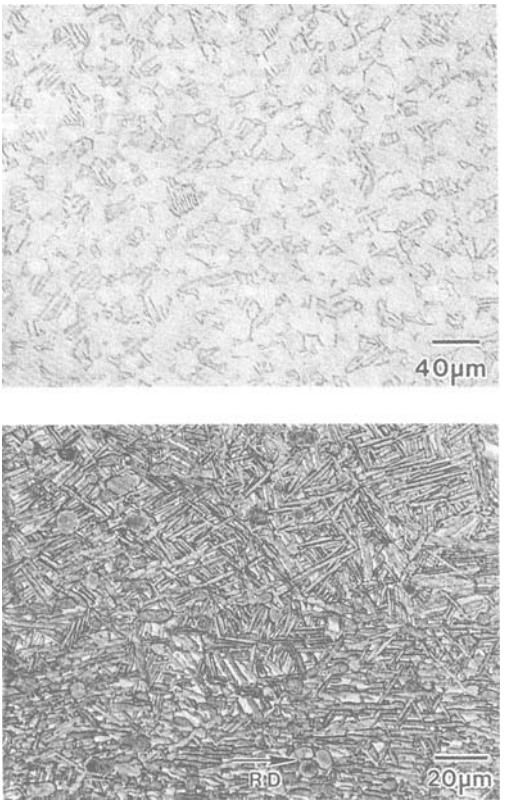


Figure 1 - *Optical micrographs of annealed and furnace cooled Ti-6-4 (top) and Ti-6-2222 plates.*

HEE Characterization

Compact tension (CT) specimens were machined from the mid-planes of the plates. For Ti-6-4, specimens were 6.4 mm thick (B), 63.5 mm wide (W), and in the LT orientation. For Ti-6-2222, B equaled 6.1 mm, W was 50.0 mm, and the orientation was TL.[2] Crack length was determined from measured crack-mouth opening displacement (δ_m) during fatigue cracking and thermal-corrected direct current electrical potential (dcPD) during EAC. The details of compliance and electrical potential measurements are presented elsewhere [*30*], and standard equations were employed to calculate crack length and K [*34*].

[2] The long axis of the tensile specimen was parallel to the transverse (T) or longitudinal (L) direction in the plate, while the Mode I crack was stressed in the first direction with growth parallel to the second direction.

Environment assisted cracking experiments were conducted at 23°C in a near-neutral (pH 6 to 7) and quiescent chloride solution [*30*]. A polymethyl methacrylate environmental cell, was used to selectively immerse the crack tip in 3.5 weight pct NaCl dissolved in deionized water. Elastomeric tubing was inserted in the notch to seal the cell and solution was circulated through the notch at 0.5 ml/s. The grounded CT specimen was maintained at fixed electrode potential with a potentiostat, platinum-mesh counter electrode, and two Ag/AgCl reference electrodes located adjacent to each broad face of the specimen. The counter electrode was positioned in a separate 2-liter reservoir. The electrode potential difference across the specimen notch was always less than 10 mV, as monitored with the two reference electrodes. The selected potential of –500 mV (vs. saturated calomel, SCE) is the value where EAC of several α/β-Ti alloys in chloride was most severe [*2, 35*]. The open circuit potential was –300 mV_{SCE} for ELI Ti-6-4 and –200 mV_{SCE} for Ti-6-2222.

Each specimen was fatigue precracked in the aqueous chloride environment to a final crack length (a) to W ratio of 0.50 utilizing a closed loop servohydraulic test machine operated in load control, a stress ratio ($R = K_{min}/K_{max}$) of 0.1, and frequency of 5-10 Hz. The precracked specimen, controlled with a crack mouth displacement gauge, was loaded at a constant-δ_m rate in aqueous solution to determine the stress intensity at the onset (or threshold) of EAC and subsequent subcritical crack growth rates. Similar experiments in moist air provided a measure of the initiation-fracture toughness at the onset of stable crack growth, K_{JIC} [*36*]. Prior to crack-growth initiation, a fixed $\dot{\delta}_m$ produced constant dK/dt that was determined by linear regression of K vs. time data. For the CT specimen and fatigue crack length, $\dot{\delta}_m$ of 2.3×10^{-6} and 1.2×10^{-2} mm/s produced dK/dt levels of 2.0×10^{-4} and 1.0 MPa$\sqrt{m}$/s; the relationship between these two rates is linear [*30*].

An elastic-plastic analysis was used to account for uncracked-ligament plasticity [*36*]. The plastic part of the J integral was determined using the area method with compliance calculated from the dcPD-measured crack length; the specimen was not unloaded during an experiment. The effective modulus used in this calculation was determined from the δ_m vs. P data prior to crack extension and the measured-final fatigue crack length. Plane strain constraint was substantial at crack initiation, as evidenced by a lack of shear lips, and the crack was in the Mode I orientation without branching. Crack growth rate was calculated as a function of the elastic K from J (K_J) using a modified incremental polynomial method [*30*].

Results

Determination of Environment Assisted Cracking Resistance

Measured load, δ_m, and dcPD were analyzed to characterize the fracture resistance of each Ti alloy in moist-laboratory air and NaCl. For CT specimens loaded at fixed $\dot{\delta}_m$ in air, and in aqueous chloride at faster loading rates, the dcPD signal increased steadily by up to 1 pct prior to crack-growth initiation [*30*]. This rise, due to crack tip plasticity and crack opening, dictated that the δ_i level at the onset of crack growth be determined objectively by regression analysis of pre and post-initiation data [*36*]. For specimens loaded at slower dK/dt in NaCl, δ_i was defined clearly by a sharp increase in dcPD and

decrease in load. These analyses of dcPD vs. δ_m yielded crack length and K vs. time (Fig. 2), as well as da/dt vs. K. The air-initiation fracture toughness was indicated by either K_{JICi} at δ_i or K_{JIC} at the K level after 0.2 mm of crack extension. For EAC, K_{JTHi} and K_{JTH} were defined similarly.

Two propagation behaviors were observed. For moist air and faster loading rates in NaCl, crack length increased monotonically with increasing K during fixed-$\dot{\delta}_m$ loading (Fig. 2b). For slow-rate loading in NaCl, subcritical crack growth occurred with oscillating periods of slow and faster da/dt. As shown in Fig. 2a, each period of slow growth occurred under rising K, while more rapid extension resulted in decreasing K due to falling load.

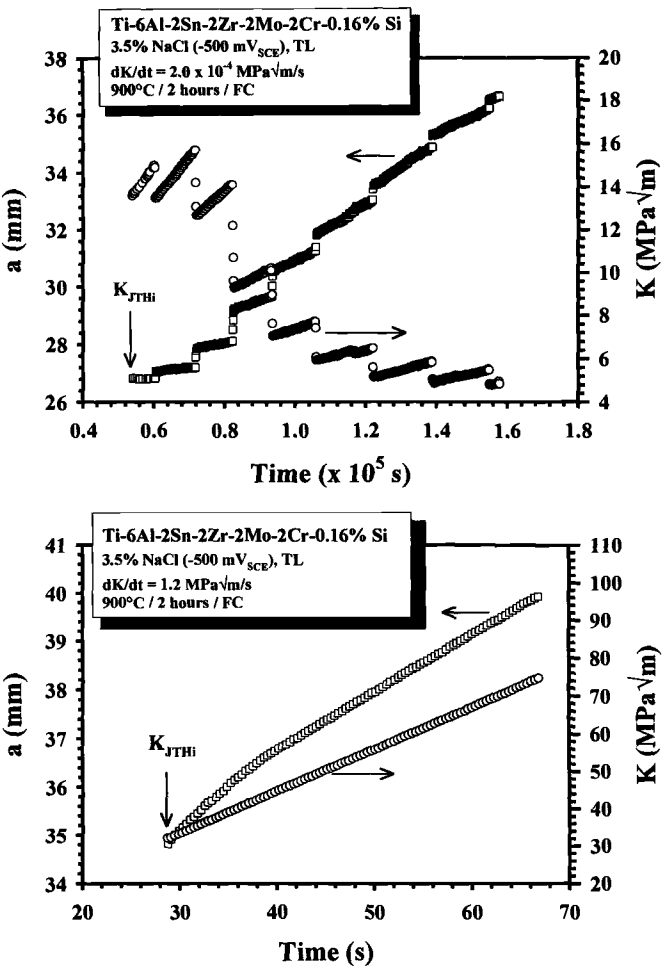


Figure 2 - *Crack length and K vs. time for Ti-6-2222 plate in 3.5% NaCl (-500 mV$_{SCE}$) for: (a) initial dK/dt of 2.0 x 10^{-4} MPa√m/s (top) and (b) 1.2 MPa√m/s (bottom).*

Both Ti-6-4 and Ti-6-2222 were embrittled by rising-δ_m loading in NaCl solution. The threshold stress intensity for crack growth, crack growth rate, and the microscopic cracking path each depended on applied $\dot{\delta}_m$ and dK/dt.

Threshold Stress Intensity for EAC

The threshold stress intensity for EAC in both Ti-6-4 and Ti-6-2222 exposed to 3.5% NaCl solution is less than K_{JIC} and depends on dK/dt, particularly for the latter α/β-Ti alloy, as shown in Figs. 3 and 4.

Mill-annealed Ti-6-4 (ELI, LT) plate exhibits moderate EAC susceptibility. In Fig. 3, K_{JIC} (■) is independent of dK/dt between 4 x 10^{-3} and 0.1 MPa√m/s, and is 79 MPa√m. K_{JICi} equals 66 MPa√m. K_{JTHi} is below K_{JIC} for loading rates below 0.1 to 0.3 MPa√m/s, indicating EAC. K_{JTHi} (o) and K_{JTH} (•) depend on applied dK/dt and are a minimum of 56 MPa√m at 10^{-2} to 0.1 MPa√m/s.

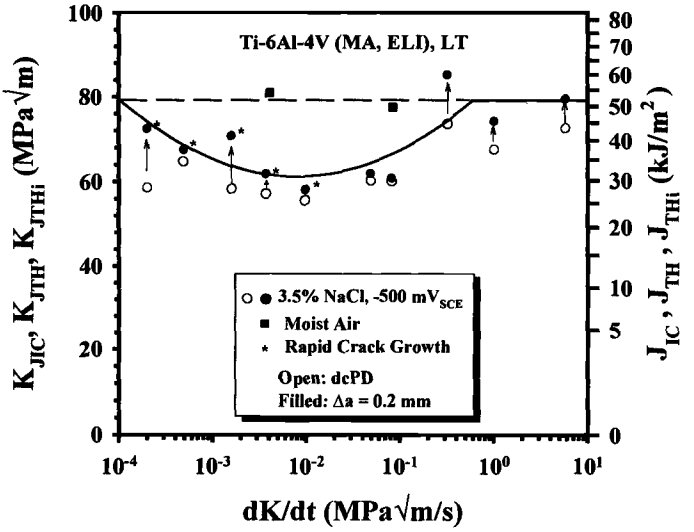


Figure 3 - *K_{JTHi} (o) and K_{JTH} (•) vs. loading rate for Ti-6-4 (ELI, LT) plate in aqueous chloride, compared to K_{JIC} (■).*

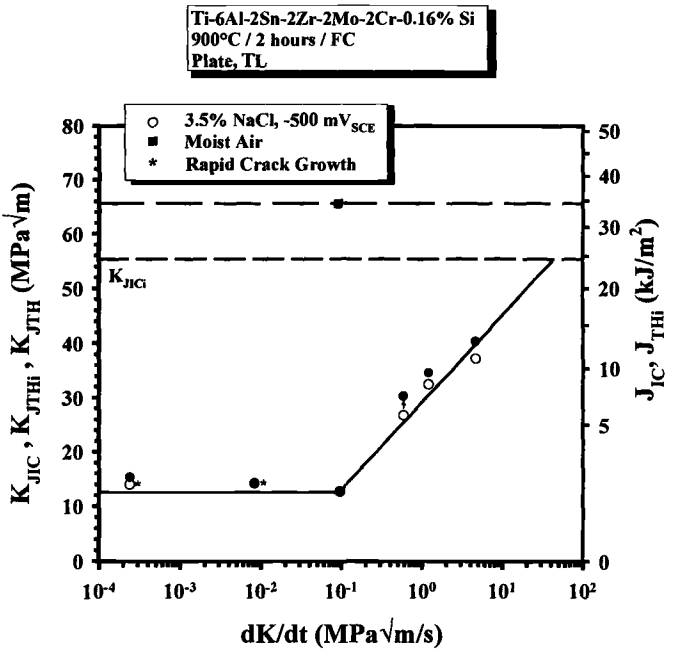


Figure 4 - *K_{JTHi} (o) and K_{JTH} (•) vs. loading rate for Ti-6-2222 plate (TL) in aqueous chloride, compared to K_{JIC} (■).*

The trend in Fig. 3 suggests that fast and slow loading rates eliminate EAC of Ti-6-4 in NaCl. As dK/dt decreases below 10^{-2} MPa√m/s, threshold stress intensities increase toward the moist air fracture toughness. For dK/dt above 0.3 MPa√m/s, mechanical crack tip damage occurs coincident with the onset of EAC, as suggested by equal K_{JTHi} and K_{JICi}. The difference between K_{JTHi} and K_{JTH} is highest at the extreme high and low loading rates. Values of the plane strain

tearing modules over the initial Δa of 0.5 mm [*30*] (10.7, 1.1, 3.1, 2.8, 1.2, 2.5, 0.1, 2.2, 2.8, and 7.0 for the 10 levels of increasing dK/dt in Fig. 3) confirm that the susceptibility to environmental propagation is maximized at the intermediate dK/dt of 0.1 MPa√m/s.

Ti-6-2222 plate exhibits significantly greater EAC susceptibility than Ti-6-4, as indicated by the lower K_{JTHi} values in Fig. 4. While K_{JIC} (■) is 66 MPa√m and K_{JICi} is 56 MPa√m, K_{JTHi} is as low as 13 MPa√m over a range of dK/dt from 2 x 10^{-4} to 0.1 MPa√m/s. K_{JTHi} rises sharply to 37 MPa√m as dK/dt increases to 5 MPa√m/s. The trend line suggests that EAC is eliminated by fast loading rates (dK/dt ≈ 40 MPa√m/s). The threshold stress intensity does not increase with decreasing dK/dt, and the difference between K_{JTHi} and K_{JTH} is small indicating limited resistance to initial-crack growth.

Crack Growth Rate

For both alloys in air, crack growth under rising δ_m was stable, consistent with finite crack growth resistance and positive tearing modulus. Similar behavior was observed for each alloy stressed in NaCl solution, but only at dK/dt levels above 10^{-2} MPa√m/s. For slower loading rates, cracking in NaCl oscillated between periods of slow-stable and faster-stable growth, as illustrated in Fig. 2a. Loading rates that produced slow-fast da/dt are designated by * in Figs. 3 and 4.

The absence of the rapid da/dt regions for dK/dt values greater than 10^{-2} MPa√m/s suggests that specimen-compliance may cause this phenomenon. A CT specimen of Ti-6-2222 was loaded in NaCl at a constant $\dot{\delta}_m$, producing a dK/dt of 6.5 x 10^{-4} MPa√m/s. The measured K_{JTHi} was 12.9 MPa√m and stable crack growth was oscillatory. The specimen was then stressed in load (P) control at a constant dP/dt that produced an initial dK/dt of 7.2 x 10^{-4} MPa√m/s. The resulting K_{JTHi} was 14.4 MPa√m and crack growth above K_{JTHi} did not oscillate. Rather, crack length and K increased steadily with increasing time.

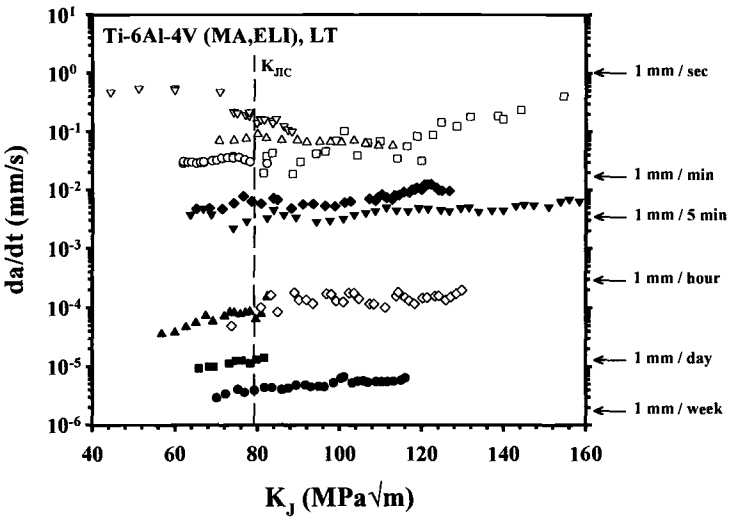


Figure 5 - *da/dt vs K_J for Ti-6-4 (ELI, LT) plate in 3.5% NaCl (-500 mV_{SCE}) and moist air for various loading rates. Values of dK/dt are: 0.2* (•), *0.5* (■), *1.6* (▲), *53* (▼), *82* (O), *320* (□), *1000* (△), *and 5800* (▽) *x 10^{-3} MPa√m/s for NaCl; and 4.1* (◇) *and 85* (◆) *x 10^{-3} MPa√m/s for loading in moist air.*

Figure 5 shows da/dt vs. K_J for Ti-6-4 (ELI, LT) in moist air and NaCl. Data were included for both subcritical crack growth ($K < K_{JIC}$) and stable crack growth above K_{JIC}. The regions of rapid-stable crack extension were not plotted. For all loading rates and both environments, da/dt was independent of K_J for the regions of slow-stable crack extension. As dK/dt increased, the average crack growth rate increased, as shown by the open (NaCl) and filled-circle (moist air) symbols in Fig. 6 for K_J of 60 (□), 70 (○), and 80 (△) MPa√m, as well as the average da/dt (●) for moist air. The trend line in Fig 6 is

$$da/dt = 0.1\ (dK/dt)^{1.13} \qquad (1)$$

for the units shown.

The da/dt corresponding to rapid crack extension in NaCl are included (■) for comparison and were calculated by linear regression of a vs. t data, Fig. 2a. The average da/dt for rapid EAC was 7 μm/s, independent of dK/dt. Below 10^{-1} MPa√m/s, these rates were one to three orders of magnitude faster for chloride solution vs. moist air. The NaCl crack growth rates observed for dK/dt above 10^{-1} MPa√m/s were equal to the air growth rates and cracking did not oscillate.

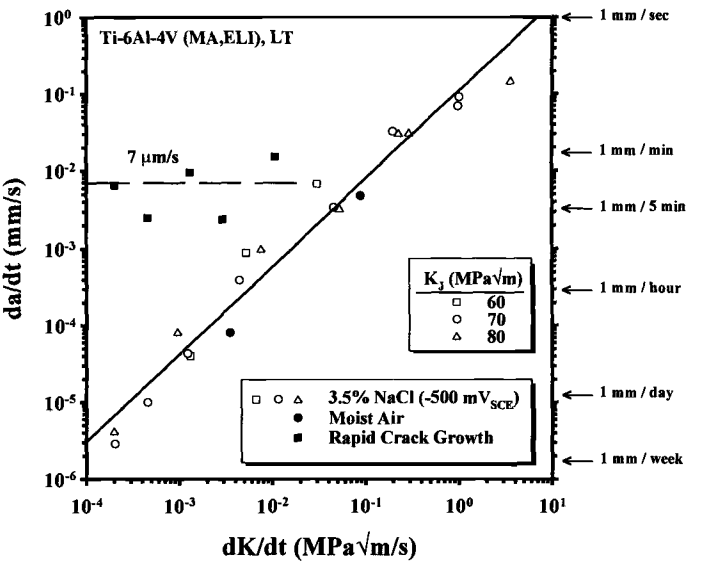


Figure 6 - *da/dt vs. dK/dt for Ti-6-4 (ELI, LT)) plate in 3.5% NaCl (-500 mV_{SCE}) and moist air for various loading rates and K_J levels.*

Similar crack growth behavior was observed for Ti-6-2222, as shown in Fig. 7. The average value of da/dt during rapid-stable crack extension was 11 μm/s, independent of dK/dt. Crack growth rates during the regions of rapid crack extension below 10^{-1} MPa√m/s were orders of magnitude faster than the likely crack growth rates in moist air. The NaCl growth rates observed for loading rates above 10^{-1} MPa√m/s are consistent with the expected air crack growth rates. The average-fast NaCl growth rate for Ti-6-2222 was 60% higher than that observed for Ti-6-4, but similar and environment-independent growth rates were observed for each alloy at dK/dt above 0.1 MPa√m/s.

Fracture Mode

Environment and loading rate effects on the microscopic fracture mode were established by SEM analysis. In all fractographs presented, the crack growth direction is

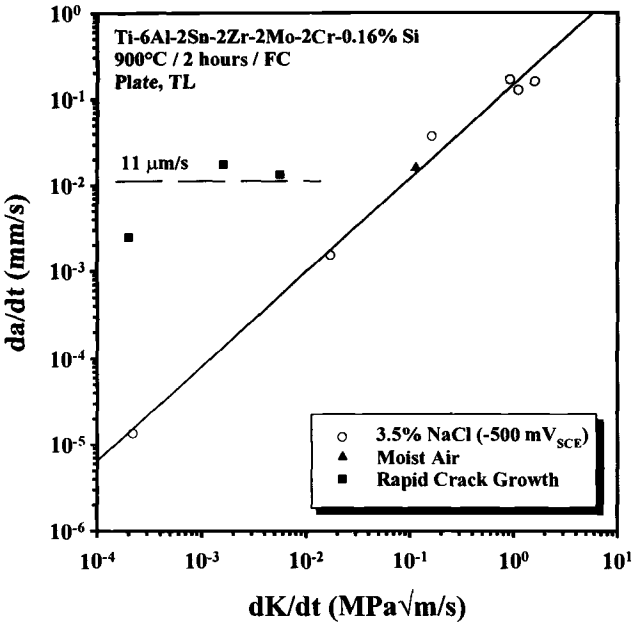


Figure 7 - *da/dt vs. dK/dt for annealed Ti-6-2222 plate (TL) in 3.5% NaCl (-500 mV$_{SCE}$) and moist air for various loading rates. For slow-stable cracking in NaCl, K was 13 MPa√m for loading rates below 10^{-1} MPa√m/s and 35 MPa√m above 10^{-1} MPa√m/s.*

from bottom to top. The fractographs were taken of regions immediately following the fatigue precrack.

Air fracture of Ti-6-4 was by TG-microvoid coalescence (MVC), as illustrated in Fig. 8. Higher magnification analyses established that four features, A through D, constituted this fracture [*30*]. Region A represents the dominant feature of spherical microvoids. Region B is reminiscent of void sheeting linking two regions of different elevation. Region C shows elongated voids probably caused by the intersection of intense-planar slip bands or the intersection of slip bands and grain boundaries. A small amount of cleavage-like features (D) is present on the air fracture surface.

Chloride solution exposure affected a fracture mode change in Ti-6-4, consistent with reduced K_{JTHi} vs. K_{JIC}. Figure 8b shows the Ti-6-4-NaCl fracture surface for a dK/dt of 4 x 10^{-3} MPa√m/s, corresponding to the maximum EAC susceptibility in Fig. 3. Compared to fracture in air, cracking in NaCl involved a substantial amount of cleavage (D). Metallographic sectioning confirmed that EAC in the equiaxed-α microstructure of Ti-6-4 was transgranular [*30*], consistent with literature results [*8*]. Presumably this cleavage is along a high index plane in α, nearly parallel to {0001}[*2, 10, 37-39*]. SEM examination showed that the amount of cleavage decreased with increasing K_{JTHi} as dK/dt both increased and decreased from the minimum in Fig. 3 [*30*]. The crack surfaces created by stressing in NaCl at the fastest and slowest dK/dt levels contained a substantial amount of features A, B, and C. Figure 9 contains the fractograph typical of Ti-6-4 stressed in NaCl at the slowest dK/dt examined. Since microvoid-based features are not environment sensitive, this result confirms that the susceptibility to EAC is reduced at slow loading rates. Similar fractographic results were obtained for fast dK/dt.

Rising-δ_m loading of Ti-6-2222 in NaCl solution produced a fracture mode change corresponding to reduced K_{JTHi} vs. K_{JIC} (Fig. 4). Air fracture was by TG MVC, similar to that for Ti-6-4 (Fig. 8a). Figure 10 shows NaCl fracture surfaces for rapid-stable and

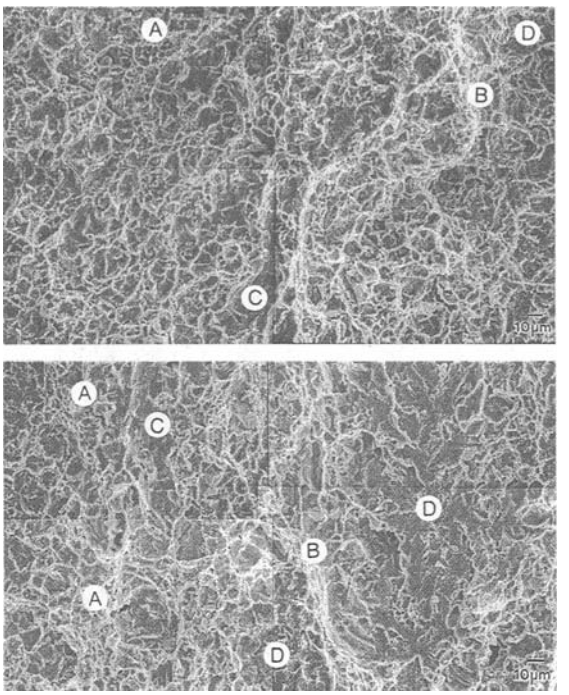


Figure 8 - *Scanning electron fractographs of crack surfaces in Ti-6-4 (LT) produced by rising-δ_m loading in (a-top) moist-laboratory air and (b-bottom) 3.5% NaCl solution at dK/dt of 4 x 10^{-3} MPa√m/s.*

slow-stable EAC in Ti-6-2222. The environmental fracture mode contained extensive TG α-cleavage. This morphology was produced for all loading rates examined, as illustrated by the fractograph of fast-dK/dt EAC in Fig. 11.

Fractographic and metallographic examinations showed that the transition from slow to rapid-stable cracking in NaCl was not accompanied by a crack mode change for either α/β-Ti alloy in NaCl. The fractographs in Fig. 10 show the regions of slow and rapid-stable EAC in Ti-6-2222/NaCl (Fig. 2a). Each regime involved extensive α-cleavage, without a resolvable transition in the crack path when da/dt changed from fast to slow or from slow to fast. Similar results were obtained for Ti-6-4 [*30*].

Discussion

EAC Resistance of Ti-6-2222

The modern α/β-Ti alloy, Ti-6-2222, is susceptible to severe transgranular EAC in chloride solution, as established by the results in Figs. 4, 7, 10, and 11. The threshold stress intensity for the onset of EAC, K_{JTHi}, is reduced to 25% of K_{JIC}, subcritical crack growth rates are as high as 20 μm/s (or one-third of a prior β-Ti grain per second), and a fracture mode

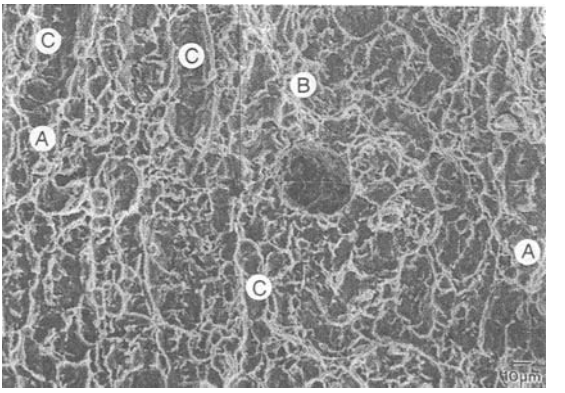


Figure 9 - *SEM fractograph of the NaCl fracture surface of annealed Ti-6-4 (ELI, LT) plate loaded at a slow dK/dt of 2.0 x 10^{-4} MPa√m/s.*

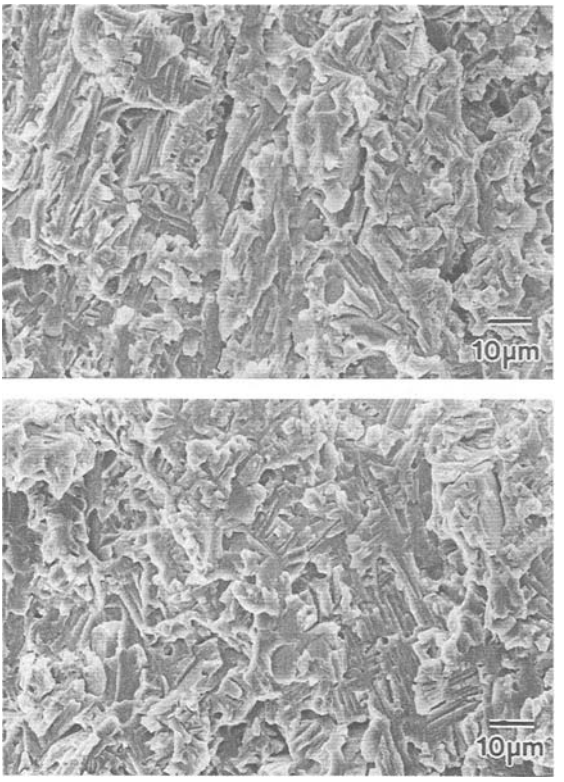


Figure 10 - *Ti-6-2222 (TL) NaCl fracture surfaces depicting regions of (a-top) rapid and (b-bottom) slow-EAC at dK/dt of 2.0 x 10^{-4} MPa √m/s.*

transition is affected by concurrent stress and chloride exposure. Severe EAC persisted over a wide range of applied dK/dt from 2 x 10^{-4} MPa√m/s (or lower) to 0.01 MPa√m/s. Less severe EAC continued to dK/dt levels at least as high as 5 MPa√m/s, and the trend line in Fig. 4 suggests that EAC may be sustained in Ti-6-2222 for dK/dt levels up to 40 MPa√m/s.

EAC may be significant for some applications of Ti-6-2222. The susceptibility of Ti-6-2222 is substantially higher than that exhibited by the ELI grade of Ti-6-4 for identical test conditions. The EAC of Ti-6-2222 was similar in terms of absolute K_{JTH_1} to α/β-Ti alloys with high Al and Sn contents, and heat treated to precipitate α_2 (Ti-8Al-1Mo-1V and Ti-7Al-4Mo [*3, 40*], as well as Ti-5Al-2.5Sn, Ti-6Al-6V-2Sn, Ti-6Al-2Sn-4Zr-2Mo, and Ti-6Al-2Sn-4Zr-6Mo [*21, 40*]).

The microstructure of the α/β-hot rolled plate of Ti-6-2222 (Fig. 1b) was not optimized for yield strength and air-fracture toughness. A so-called Triplex thermomechanical process (solution treat at β_T + 28-42°C for 0.5 h and cool at 20-67°C/min; anneal at β_T - 28-

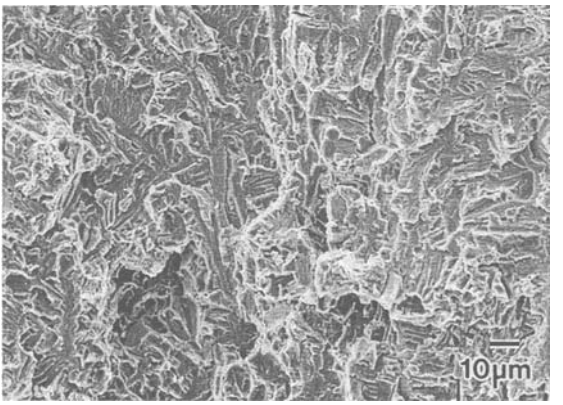


Figure 11 - *SEM fractograph of the environmental fracture surface for annealed Ti-6-2222 (TL) loaded at dK/dt of 1.2 MPa √m/s in NaCl.*

50°C for 1.0 h and cool at 20-67°C/min; age at 496-538°C for 8h and air cool) optimized σ_{YS} (minimum 910 MPa) and plane strain fracture toughness (minimum 77 MPa$\sqrt{m}$) [*41*]. The lower toughness of the Ti-6-2222 microstructure in Fig. 1b (K_{JIC} = 56 MPa$\sqrt{m}$) is likely due to globular-aligned α (Fig. 1b) as well as silicides and α_2 formed during slow cooling from the α/β annealing temperature [*31, 42*].

Ti-6-2222 is generally susceptible to severe TG EAC [*30*]. Several microstructures of both plate and extrusion, including that subjected to the Triplex treatment, were prone to brittle cracking when exposed to NaCl solution under rising δ_m. The effect of microstructure on EAC resistance is considered in detail elsewhere [*43*], where it is established that the critical factor that controls TG EAC is α_2 precipitation in α. This phase formed during furnace cooling of both Ti-6-2222 [*32, 42*] and Ti-6-4 (ELI) [*33*] in the present study. The EAC susceptibility of Ti-6-2222 relative to Ti-6-4 was speculatively ascribed to enhanced α_2-precipitation kinetics due to Si [*43*].

Mechanistic Implications

Each annealed α/β-Ti alloy and aged-metastable β-Ti alloy listed in Table 1 is susceptible to severe environmental cracking for similar chloride solution and cracked-specimen loading conditions. The β-Ti alloys are susceptible to intergranular (IG) cracking, while TG-α cleavage occurs in α/β Ti-6-4 and Ti-6-2222.

Table 1 - *Titanium Alloys Susceptible to EAC in Aqueous Chloride Solution Under Rising Crack-Mouth-Opening Displacement Loading*

	Microstructure	EAC Mode	Minimum K_{JTH}/K_{JIC}	Maximum dK/dt	Maximum da/dt	H Penetration (μm)	
			(MPa$\sqrt{m}$)	(MPa$\sqrt{m}$/s)	(μm/s)	dK/dt	da/dt
Ti-6Al-4V (ELI)	Equiaxed α/α_2 + retained β	TG; α cleavage	56/79	0.1-0.5	7	0.4	0.0004
Ti-6Al-2Zr-2Sn-2Cr-2Mo	Coarse-acicular α/α_2 in β/Ti_xSi_y	TG; α cleavage	14/66	4-40	11	0.03 (α) 7 (β)	0.0003 (α) 0.02 (β)
Ti-8V-6Cr-4Mo-4Zr-3Al [*12, 70*]	Fine α precipitates in β	IG; along β bounds	24/64	>40	20-100	15	0.01
Ti-15Mo-3Nb-3Al [*12, 65*]	Fine α precipitates in β	IG; along β bounds	40/70	0.2-2	≈20	95	---

Background: Hydrogen Environment Embrittlement Mechanism-A body of evidence establishes that both TG EAC in α/β-Ti alloys [*8*] and IG EAC in β/α-Ti alloys [*9, 12*] are caused by HEE local to the crack tip. Qualitatively, EAC in α/β alloys is similar for stressed exposure in H_2 and aqueous-halogen solutions [*8*]. Quantitatively for the β/α-electrolyte system, crack acidification and lowered electrode potential favor electrochemical H production and entry, establishing a crack tip surface H concentration of C_{HS} [*6, 9*]. This H is transported into the process zone where damage occurs when the local tensile stress exceeds a critical level that decreases with increasing concentrated H content. The process zone is typically hypothesized to be located where tensile and hydrostatic stresses are maximum, within the first 20% of the plastic zone [*14, 44*]. Process zone H promotes near-basal cleavage-like cracking through α in α/β-Ti alloys [*2, 4, 10*] and IG cracking along β grain boundaries in β/α-Ti alloys [*12*], Table 1.

Three elements must be understood to model the threshold and kinetics of HEE in Ti alloys; crack electrochemistry, crack tip strain rate, and process zone H diffusion.

Crack Electrochemistry-While bare titanium is extremely reactive, passivity is a critical element of HEE because the surface oxide hinders H supply to damage sites [*17, 45, 46*]. As such, HEE is focused at the crack tip where plastic deformation ruptures the passive film to expose the active and H-diffusion barrier-free alloy [*9, 45, 47, 48*]. Titanium fractured in simulated crack solution repassivates in less than 10^{-3} s [*45*], but net-anodic current transients, with a prolonged decay time of 2 to 20 s, emit from surface reactions on a straining-electrode surface in chloride solution [*47*]. These long-time transients were modeled as comprised of numerous and overlapping-discrete dissolution events, each caused by oxide destabilization due to a superdislocation composed of many single dislocations arriving at the oxide/metal interface in a distribution of time and space [*48*]. Experiments with smooth and notched tensile specimens of a β/α-Ti alloy in NaCl showed that both finite plastic strain and an average strain rate in excess of 10^{-5} s^{-1} were required to produce discrete depassivation events that overlapped to produce a long-term transient [*48*].

From these results, it is hypothesized that the H production step in HEE only occurs above a critical crack tip strain rate that is necessary to mechanically destabilize the tip-passive film for H uptake. It is further speculated that, above a critical strain rate and on average at K_{JTHi}, crack tip deformation conditions are sufficient to provide a quasi-steady state level of film destabilization and H production. Essentially, deformation at this level causes a continued and constant destabilization of a portion of the straining crack tip; as such, a quasi-steady state hydrogen concentration, C_{HS}, is developed. This view is supported by experimental measurements of net-anodic current transients of many seconds duration emitted from a chloride-laden crack subjected to rising K. Such prolonged transients began at about half of K_{JTHi} and increased in frequency to overlap as K approached this threshold [*47*]. The actual H production condition will likely vary about the perimeter of the crack tip due to strain and strain rate variations with position, as well as noncontinuum microscopic plasticity. This model of passive film destabilization should be relevant to α/β-Ti alloys that contain α_2 precipitates that exacerbate localized-planar slip via the particle cutting mechanism and produce large slip offsets at a free surface [*26, 49*].

The rate of supply of electrolyte from the bulk to support crack tip reactions, as well as the removal of ionic reaction products from this region, could rate limit HEE at high loading or crack growth rates [*18*]. For Ti in bulk-neutral chloride solution, the cracking rate limited by Faradic dissolution of a fully-bare crack tip surface is orders of magnitude faster than those encountered in the present study [*50*]. Two uncertainties exist. The limiting rate can be reduced by electrolyte-mass transport that is impeded by either the occluded crack-opening geometry or a precipitated-salt film near the crack tip [*51*]. The anodic and cathodic currents local to the crack tip, and the amount of salt formed, depend on the passive current density vs. crack-solution volume and area of passive surface that is bared by slip step formation. This active area is unknown for Ti alloys in chloride solution [*9, 47, 48, 50*].

Hydrogen Diffusion-If C_{HS} is established rapidly, then the amount of H transported to crack tip damage sites (C_H) should limit the kinetics of HEE. For a stationary-infinite planar surface, maintained at constant C_{HS}, the one-dimensional H-penetration distance is

$$x = A\sqrt{D_H t} \tag{2}$$

where x is distance ahead of the surface, A is a constant that depends on the selected level of C_H/C_{HS}, D_H is the diffusivity of H in α or β Ti, and t is time. For a propagating crack, H penetration distance is estimated from steady-state C_H vs. x profiles for different ratios of da/dt to D_H and with the crack tip acting as a moving line source of H in two dimensions [*52*]. More complex solutions account for stress and plastic strain effects on H diffusion [*53*]. Several issues confound H-transport analysis. The diffusion distance into the process zone is not known [*54*]. Second, H diffusion in a complex α/β-Ti microstructure may occur by parallel lattice and interface paths [*11, 28*]. Third, H may be transported by dislocation sweeping into the process zone [*55*], until H breaks from moving dislocations in α-Ti at a critical strain rate of order 0.01 s^{-1} [*21, 55*].

Crack Tip Strain Rate-In the HEE scenario, $\dot{\varepsilon}_{CT}$ represents a tensile or shear-strain rate component local to the crack tip. Time derivatives of elastic-plastic continuum solutions for strain ahead of a stationary crack show that each component of strain rate depends on alloy deformation properties, position in the crack tip process zone (x ahead of the crack tip and θ above the crack plane), K, and dK/dt [*56-58*]. For the tensile-flow properties of Ti-6-4 (ELI) and Ti-6-2222

$$\dot{\varepsilon}_{CT} = \lambda\left[\frac{1}{E\sigma_o x}\right]^{\gamma} K^{\theta}\left(\frac{dK}{dt}\right) \tag{3}$$

where $\lambda = 0.04$, $\gamma = 1.0$, and $\theta = 1.0$ for a solution based on a small-strain description of the crack tip field [*57*], and $\lambda = 0.20$, $\gamma = 2.2$, and $\theta = 3.4$ derived from a large-strain finite element analysis of crack tip tensile strains [*59*]. Solutions for a propagating crack include an additional term to account for the effect of da/dt on strain rate [*60*]. The crack tip opening displacement rate in the Mode I loading direction, $\dot{\delta}_{CT}$, approximates $\dot{\varepsilon}_{CT}$. A J-integral based description of $\dot{\delta}_{CT}$ is [*60*]

$$\dot{\varepsilon}_{CT} \propto \dot{\delta}_{CT} = 2\alpha \frac{dK}{dt} \frac{K(1-\nu^2)}{E\sigma_{YS}} + \beta \frac{da}{dt} \frac{\sigma_o}{E} \ln\left(0.2 \frac{K^2(1-\nu^2)}{\sigma_{YS}^2 r}\right) \qquad (4)$$

where $\alpha = 0.7$ for low-strain hardening α/β-Ti alloys, $\beta = 5$, r is the distance behind the crack tip, and σ_o is the yield strength or Ramberg-Osgood reference stress.

Crack tip strain rate is difficult to determine. Equation 3 predicts an infinite tip-surface strain rate as x approaches 0, and different strain rate distributions ahead of the crack tip depending on the model chosen. From Eq. 4, $\dot{\varepsilon}_{CT}$ at the blunted-crack tip surface is estimated from $\dot{\delta}_{CT}$ using an uncertain gauge geometry (shear band vs. crack opening displacement) and gauge length [*58, 61*]. The relevant value of r behind this surface is unknown and Eq. 4 does not describe the gradient of $\dot{\varepsilon}_{CT}$ ahead of the crack tip. The continuum approach may not describe $\dot{\varepsilon}_{CT}$ adequately if microscopic deformation is heterogeneous due to slip localization in the two-phase α/β microstructure, accentuated by α_2 precipitates. Equations 3 and 4 do not include a creep contribution. None-the-less, Eqs. 3 and 4 provide the best available description of crack tip strain rate for use in interpreting EAC data and trends.

Hypothesis-The kinetics of EAC of alloys are established by the effect of $\dot{\varepsilon}_{CT}$ on quasi-steady C_{HS} and coupled H diffusion ahead of the crack tip. This notion was consideresd for IG HEE of aged β/α-Ti alloys [*12*] and is tested here for TG HEE of α/β-Ti alloys of two distinctly different microstructures.

Oscillating Environmental Crack Growth-Each of the alloys in Table 1 exhibited EAC that oscillated between periods of slow-stable and fast-stable growth. Analysis of cracking in β-Ti alloys (Table 1) established that this behavior was due to an extrinsic effect of specimen compliance on K and $\dot{\varepsilon}_{CT}$ [*12*] rather than an intrinsically-discontinuous hydrogen embrittlement mechanism [*62, 63*]. The experimental results confirm this conclusion for TG HEE in α/β Ti-6-4 and Ti-6-2222. Each regime of slow or rapid EAC occurred over thousands of micrometers (Fig. 2), well in excess of a typical process zone in a discontinuous cracking process. Crack growth did not arrest during slow growth and occurred at a finite rate during fast-da/dt cracking. Oscillatory EAC was eliminated by either fast dK/dt loading at fixed $\dot{\delta}_m$ (Figs. 2-4) or by load-control at fixed dP/dt. The TG fracture mode was identical for the slow-da/dt and fast-da/dt regions of EAC in Ti-6-4 and Ti-6-2222 (Fig. 10). There was no evidence for striation markings on the fracture surface, or crack-wake ligaments that ruptured by ductile fracture after the environmental crack passed.

Oscillating crack growth and the dK/dt dependence of da/dt (Figs. 6 and 7) are explained by H production governed by crack tip strain rate. Equation 4 shows that the strain rate for a propagating crack depends on dK/dt and da/dt. For slow da/dt or high dK/dt, the loading rate term in Eq. 4 dominates $\dot{\varepsilon}_{CT}$, and da/dt increases with increasing dK/dt, as shown in Figs. 6 and 7 for the regions of slow crack growth. In contrast the growth rates during rapid crack extension are independent of dK/dt. Here, increasing specimen compliance creates negative dK/dt (Fig. 2) and the da/dt term in Eq. 4 controls $\dot{\varepsilon}_{CT}$, independent of the applied δ_m rate. The crack tip strain rates are similar resulting in

crack growth rates that are independent of the initial-applied dK/dt. The rapidly growing crack generates a self-sustaining crack tip strain rate, and rapid crack growth continues until a lower K level is reached which arrests EAC.

Although Eq. 4 qualitatively explains the effect of dK/dt on EAC kinetics, the predicted deformation rates are not consistent with the measured effect of loading on da/dt. During slow crack growth, the calculated da/dt term in Eq. 4 is larger than the dK/dt term for the range of applied displacement rates examined. As concluded for the β-Ti alloys in Table 1 [*12*], existing continuum descriptions of crack tip strain rate with known input parameters are inadequate to explain the experimental observations of HEE in Ti alloys. From the practical perspective, rising crack mouth opening displacement loading is an effective method to characterize the threshold stress intensity for the onset of EAC, but is a complex loading condition for crack growth rate measurement.

HEE at Quasi-Static Crack Tip Strain Rates-Early studies suggested that EAC does not occur in α/β-Ti alloys under either static load [*21-23*] or if crack-tip creep occurs prior to solution exposure [*26, 27*]. The implication is that uptake of H ceases below a critical crack tip strain rate (10^{-5} s^{-1}) due a stable crack tip oxide. The reduction of HEE at low crack tip strain rates was demonstrated for the β-Ti alloys in Table 1 [*12*].

Results suggest that HEE is nearly eliminated in Ti-6-4 at the lower dK/dt examined (Figs. 3, 8 and 9), but not for Ti-6-2222 (Fig. 4). For a slow-applied dK/dt of 10^{-4} MPa$\sqrt{m}$/s, calculated crack tip strain rates are 2 x 10^{-6} s^{-1} (Eq. 3 with $\lambda = 0.04$, $\gamma = 1.0$, and $\theta = 1.0$), 6 x 10^{-6} s^{-1} (Eq. 3 with $\lambda = 0.20$, $\gamma = 2.2$, and $\theta = 3.4$), and 7 x 10^{-5} s^{-1} (Eq. 4 with da/dt = 0); all for x = r = 1 μm and K = 60 MPa$\sqrt{m}$ relevant to Ti-6-4. These strain rates are, with the exception of the propagating crack result, less than the strain rate (1 x 10^{-5} s^{-1}) necessary to stimulate passive film destabilization in the presence of significant plastic strain, as established based on tensile-straining electrode experiments [*47, 48*]. It is reasonable to expect that HEE would not occur in Ti-6-4 at the lowest loading rates examined because crack tip passivity hinders hydrogen uptake.

Considering Ti-6-2222, for dK/dt of 10^{-4} MPa$\sqrt{m}$/s, $\dot{\varepsilon}_{CT}$ is between 5 x 10^{-7} s^{-1} (Eq. 3 with $\lambda = 0.04$, $\gamma = 1.0$, and $\theta = 1.0$), 2 x 10^{-7} s^{-1} (Eq. 3 with $\lambda = 0.20$, $\gamma = 2.2$, and $\theta = 3.4$), and 2 x 10^{-5} s^{-1} (Eq. 4 with da/dt = 0); all for x = r = 1 μm and $K = K_{JTHi} = 14$ MPa$\sqrt{m}$. These strain rates are lower than those predicted for Ti-6-4 due to the lower K at the onset of cracking and suggest that HEE should not occur in Ti-6-2222 at low dK/dt. Since EAC was produced, the strain rate predictions from Eq. 3 and 4 are inconsistent with experimental observations.

The different low-$\dot{\varepsilon}_{CT}$ responses of Ti-6-4 and Ti-6-2222 are not understood quantitatively. The parameters used in the crack tip strain rate equations are uncertain, particularly the distances (x and r). Strain rate models do not account for localized-planar slip at a crack tip. It is reasonable to speculate that the $\dot{\varepsilon}_{CT}$ associated with enhanced-slip localization in Ti-6-2222 vs. Ti-6-4 [*30*] exceeds the continuum predictions to explain severe HEE at the slow dK/dt represented in Fig. 5; even lower dK/dt would be required to mitigate embrittlement in Ti-6-2222.

HEE at Rapid Rates-HEE in α/β-Ti alloys is sustained at high rates, Table 1. If the HEE scenario is correct, then the kinetics of the elemental steps outlined previously must support these rapid environmental cracking kinetics.

Threshold for HEE-It is reasonable to speculate that a quasi-steady level of C_{HS} is produced at the deforming crack tip in Ti-6-4 and Ti-6-2222 stressed in neutral-aqueous chloride at dK/dt of 10^{-2} MPa$\sqrt{m}$/s and faster, conditions that produced severe EAC. Predicted values of crack tip strain rate are between 8 x 10^{-5} s^{-1} (Eq. 3 with $\lambda = 0.04$, $\gamma = 1.0$, and $\theta = 1.0$), 5 x 10^{-5} s^{-1} (Eq. 3 with $\lambda = 0.20$, $\gamma = 2.2$, and $\theta = 3.4$), and 3 x 10^{-3} s^{-1} (Eq. 4 with da/dt = 0); for K = 20 MPa$\sqrt{m}$, dK/dt = 0.01 MPa$\sqrt{m}$/s, and x = r = 1 μm. Each value exceeds the strain rate of 10^{-5} s^{-1} that is necessary for crack tip H production. Faster dK/dt should favor constant or increasing C_{HS} to sustain HEE, and H production and uptake should not be rate limiting for the range of dK/dt considered. It is further assumed that neither electrolyte-mass transport for ion renewal and removal, nor crack-potential drop, limit the cracking kinetics. This speculation is based on the results of occluded-crack electrochemical studies performed on a β/α-Ti alloy [*7, 50*].

The K_{JTH} *vs* dK/dt data in Figs. 3 and 4 provide insight into the location of crack tip damage sites; above a critical dK/dt, HEE is eliminated because time is insufficient for H transport. This location is estimated from the maximum distance of H penetration ahead of the stationary-crack tip surface (x_c) during the time to load to K_{TH} at the maximum dK/dt that produced TG cracking. For diffusion, penetration distances are estimated from Eq. 2. Since the critical level of C_H is not known, C_H/C_{HS} is assumed to equal 0.5 (A = 1.0). Differences in C_H/C_{HS} over a reasonable range exert a second-order effect on the calculation that follows. The time for H transport is less than the duration of solution exposure prior to K_{TH} because H uptake only occurs during film rupture. Assuming that film rupture starts at 50% of K_{TH}/ [*48*], the time for H diffusion ahead of the crack tip is 170 s for Ti-6-4 (HEE terminates at dK/dt ≥ 0.2 MPa$\sqrt{m}$/s where $K_{JTHi} = K_{JICi} = 68$ MPa$\sqrt{m}$), and 1 s for Ti-6-2222 (dK/dt > 20 MPa$\sqrt{m}$/s, $K_{JTHi} = K_{JICi} = 52$ MPa$\sqrt{m}$). Assuming that HEE is controlled by H diffusion in α, with an associated D_H of 1 x 10^{-11} cm^2/s at 25°C [*64*], Eq. 2 shows that x_c is 0.4 μm for Ti-6-4 and 0.03 μm for Ti-6-2222.

These calculated H penetration distances are smaller than the estimated size of the process zone. Continuum modeling of a blunted–stationary crack tip demonstrates that tensile stresses are several times higher than σ_{YS} over a distance from the tip that equals two to four times the blunted crack tip opening displacement (δ_t), where $4\delta_t$ equals $2K^2/\sigma_{YS}E$ [*14*]. This distance is 70 μm for Ti-6-4 and 3 μm for Ti-6-2222, both stressed to K_{JTHi}. Hydrogen trapping by dislocations generated by high crack tip plastic strain may reduce D_H; x_c is further reduced 10-fold for each 100-times decrease in the apparent D_H (Eq. 2). The exact effect of dislocation density on D_H in α-Ti is unknown. These comparisons suggest that diffusion in the α lattice cannot supply H to the location of maximum tensile stress predicted from the blunt-crack model.

Each CT specimen was fatigue cracked in chloride solution prior to rising-δ_m testing. Hydrogen, introduced to the process zone during fatigue, could affect K_{JTHi}. The effect of precrack environment was not defined for Ti-6-4 or Ti-6-2222. Similar experiments with cast Ti-6-2222 in NaCl produced severe transgranular EAC emanating from an air fatigue crack.[3] This cracking exhibited all of the characteristics observed for the plate microstructure of Ti-6-2222 (Figs. 2, 4, 7, 10 and 11). Identically severe IG EAC was produced for air and NaCl-fatigue precracked specimens of a β-Ti alloy [*65*]. Typically, 1 to 12 h elapsed between NaCl fatigue cracking and the beginning of the

[3] Edward Richey III, Unpublished research, University of Virginia, Charlottesville, VA, 1999.

rising-δ_m EAC experiment. The specimen was maintained without stress in the solution during this transition, but H uptake would not occur since crack tip deformation was nil. From Eq. 2, a typical H diffusion distance is 2-7 μm, suggesting that H from fatigue precracking dispersed sufficiently within the process zone, with the residual amount being small compared to C_{Hs} produced during rising δ_m. Possible H trapping in the process zone, and the effect of lapsed time between solution-precracking and rising displacement EAC testing, were not studied.

Crack Propagation Kinetics-The fast rates of TG cracking observed for α/β-Ti alloys in NaCl solution provide further insight into the H-embrittlement site. The ratio of $(da/dt)/D_H$ controls the maximum-H penetration distance [*52*]. For Ti-6-4 (maximum da/dt = 7 μm/s from Fig. 3, an assumed critical C_H/C_S ratio of 0.5, and a D_H of 1.0×10^{-11} cm^2/s [*64*]), the maximum penetration distance is 4×10^{-4} μm. For Ti-6-2222, the maximum da/dt is 11 μm/s (Fig. 4) and the maximum penetration distance is 3×10^{-4} μm.

The opening of a propagating crack tip is less than δ_t estimated for the stationary crack due to elastic unloading of material in the wake. The tip opening predicted from the moving-crack analysis that yielded Eq. 4 is $\delta_t = \{\beta\sigma_o r/E\} ln\{0.2\ K^2/\sigma_o^2 r\}$ [*60*]. Four times this distance, for r = 1 μm behind the crack tip, is 1.0 μm for Ti-6-4 and 0.60 μm for Ti-6-2222, both stressed to the threshold K for HEE. If this multiple of δ_t defines the location of the maximum tensile stresses and process zone ahead of a propagating crack tip, then lattice diffusion cannot supply H at the observed rates of EAC.

Discrepancy between Predicted and Expected Process Zone Distances- Of the four cases in Table 1, the continuum-predicted process zone distance equals the lattice-H diffusion distance only for the static crack in the two β/α Ti alloys. For the static crack in each α/β-Ti alloy, as well as for the propagating cracks in the α/β and β/α-Ti alloys, the calculated H-diffusion distance is substantially smaller than a classic process zone size based on the location of the stress maximum ahead of a blunted crack tip. For HEE to be the correct mechanism, this discrepancy must be explained.

Rapid-Path H Transport-A rapid-path H transport mechanism could augment lattice diffusion of H over the predicted $4\delta_t$. Considering the static crack, D_H for β-Ti is rapid (5×10^{-7} cm^2/s at 25°C [4]) and H transport distances are 90 and 7 μm, respectively, for Ti-6-4 and Ti-6-2222 at the fastest dK/dt that produced TG EAC. While these distances are comparable to the static process zone located at $4\delta_t$, the β phase is sufficiently discontinuous in Ti-6-4 and not a fast-path for H diffusion. The β is sufficiently continuous in Ti-6-2222 to supply H embrittlement of α/β interfaces [*11*]. However, TG-α cleavage is the cracking mechanism for α/β-Ti alloys in chloride solution (Figs. 8, 10 and 11 and Ref. [*8*]). Since the α-plate width is much larger than the lattice diffusion distance, it is unclear how rapid H diffusion in β would supply H to a process zone that is within α. The similar cracking kinetics and transgranular modes for Ti-6-4 and Ti-6-2222 in NaCl solution, in spite of the microstructural differences, suggests that fast-path

[4] George A. Young, Unpublished research, University of Virginia, Charlottesville, VA, 1996.

diffusion does not explain the low K_{JTHi} at the relatively high dK/dt levels represented in Figs. 3 and 4.

If dislocation transport of H is possible in the equiaxed and acicular morphologies of α, then H can be transported rapidly over the distance necessary to reach the blunted crack tip process zone [5] [*21*]. Assuming a density of mobile and H-carrying dislocations of 10^{10} cm^{-2}, H will dissociate from dislocations at a critical velocity of 0.4 $\mu m/s$, corresponding to a critical strain rate of 0.01 s^{-1}. For a static crack and values of x and r in the range from 1 to 10 μm, Eqs. 3 and 4 suggest that this strain rate is achieved at applied dK/dt levels between 0.3 and 20 $MPa\sqrt{m}/s$. Above these rates, H is not carried by dislocations and HEE should not occur. These estimates are of the same order as the loading rates necessary to preclude HEE emanating from the static crack tip. None-theless, these calculations are suspect because of the uncertain values of the model parameters [*21, 55*]. Additionally, the simple model of H association with a dislocation is probably not relevant to the localized-heterogeneous slip structure in α_2-bearing α. Finally, if the α/β interface is a H trap site with a higher binding energy compared to the dislocation, then H could be deposited at the interface as dislocations moved from α to β and fast-path H transport would be mitigated.

Process Zone Location-Stress-based estimates of process zone size, from blunt-crack continuum analyses, may not be relevant to HEE in α/β-Ti alloys. *In situ* SEM measurements showed that the opening of an IG environmental crack tip in the β/α-Ti alloy/NaCl system was less than that of a TG fatigue crack, that was in turn less than the predicted δ_t for a stationary crack at equal K [*12*]. As such, the location of high tensile stresses should be closer to the tip of a sharp IG crack, consistent with a short diffusion distance. High-elastic stresses may exist adjacent to the sharper crack tip [*54,66*]. The origin of the small opening for the IG crack was not understood, but microstructure appears to alter the continuum prediction of crack tip opening and stresses. Considering TG cracking in α/α_2, Curtis *et al.* argued that planar slip constrains blunting to favor a sharper tip with a higher local stress concentration [*26*]. Additionally, interactions between heterogeneous slip bands and α/β boundaries could produce local stress concentrations. In these cases a stress-based process zone distance could be less than a continuum mechanics prediction of δ_t for a stationary or propagating crack.

High C_{HS}-Extremely high levels of H, produced on the crack tip surface, could define the location of the damage zone independent of local tensile stress. The continuum crack tip tensile and hydrostatic stress distributions rise from one to about four times σ_{YS} with distance from the crack tip surface to $4\delta_t$. The C_H decreases from C_{HS}, but is enhanced by hydrostatic tension, and microcracking is usually projected to occur at the subsurface point where stresses are maximized [*14, 44*]. Alternately, C_{HS} may be orders of magnitude higher than expected, as measured for a crack tip in the aluminum alloy/neutral NaCl system and attributed to the high fugacity of H produced on bared Al in contact with an acidified electrolyte [*67*]. It is reasonable to expect a similar high level

[5] Using reasonable parameters in the equations that describe dislocation transport of H [*21*], $D_H = 10^{-11}$ cm^2/s [*64*], and strain rate from Eq. 4, the calculated transport distance is 160 μm for Ti-6-4 and 90 μm for Ti-6-2222 at the dK/dt levels where EAC was eliminated.

of C_{HS} adsorbed at slip-step bared regions of the crack tip surface for the Ti alloy/chloride system. Embrittlement could occur essentially at the crack tip surface, controlled by high C_{HS} and consistent with very short process zone distances.

Environmental cracking under fast dK/dt and da/dt rule out HEE based on TiH fracture. This brittle phase forms by nucleation and growth from a supersaturated solid solution of H in α-Ti, rather than martensitically [*68*]. The growth of TiH on α-Ti contacting H_2 above 100°C was rate limited by H diffusion through the growing hydride; the extrapolated thickening rate was 0.002 to 0.02 μm/s at 25°C [*69*]. This rate is orders of magnitude slower than the EAC rates (7 to 100 μm/s) in Table 1, suggesting that sufficient TiH cannot form during environmental crack propagation. If HEE is the mechanism for environmental cracking in α/β-Ti alloys, then the damage process is reasonably presumed to be lattice or interface decohesion.

Conclusions

1. Annealed Ti-6Al-4V (ELI) and Ti-6Al-2Zr-2Sn-2Cr-2Mo are susceptible to environment assisted cracking (EAC) when stressed under rising crack-opening displacement in aqueous chloride solution. The threshold K_{JTHi} is less than K_{JICi} and the ductile-fracture mode transitions to transgranular cleavage of α.
2. The acicular-α/α_2 microstructure of Ti-6-2222 is susceptible to severe cracking in chloride solution compared to the resistant equiaxed-α structure of Ti-6-4 (ELI).
3. EAC in α/β-Ti alloys depends on loading rate and may be most severe at intermediate crack tip strain rates.
4. EAC is sustained at high loading rates (dK/dt = 0.3 MPa$\sqrt{m}$/s for Ti-6-4 and greater than 10 MPa$\sqrt{m}$/s for Ti-6-2222) and crack growth rates are rapid (10 μm/s).
5. The hydrogen environment embrittlement mechanism is consistent with rapid cracking kinetics in α/β-Ti, but only if the process zone is within 0.001 to 1 μm of the crack tip surface.
6. A near-tip process zone may be promoted by very high H produced on electrochemically active areas of the crack surface, or by a sharp crack tip.
7. Apart from the TG vs. IG crack path, the phenomenological and mechanistic aspects of environmental cracking are similar for annealed α/β and aged-metastable β-Ti alloys stressed actively in aqueous chloride solution.

Acknowledgments

This research was sponsored by the Boeing Company with R. L. Lederich as program monitor, and by the Office of Naval Research (Grant N00014-91-J-4164) with A. John Sedriks as Scientific Officer. Informative discussions were conducted with J. R. Scully and B. P Somerday.

References

[1] Speidel, M. O., Blackburn, M. J., Beck, T. R. and Feeney, J. A., in *Corrosion Fatigue: Chemistry, Mechanics and Microstructure*, O. Devereaux, A. J. McEvily sand R. W. Staehle, Eds., NACE, Houston, TX, 1972, pp. 324-345.

[2] Wanhill, R. J. H., *British Corrosion Journal*, vol. 10, pp. 69-78, 1975.

[3] Czyrklis, W. F. and Levy, M., in *Environment-Sensitive Fracture of Engineering Materials*, Z. A. Foroulis, Ed., TMS-AIME, Warrendale, PA, 1979, pp. 303-313.

[4] Hardie, D., in *Environment-Induced Cracking of Metals*, R. P. Gangloff and M. B. Ives, Eds., NACE, Houston, TX, 1990, pp. 347-361.

[5] Simbi, D. J., *Corrosion Reviews*, vol. 14, pp. 343-374, 1996.

[6] Brown, B. F., in *Materials Research and Standards*, pp. 129-133, 1966.

[7] Kolman, D. G. and Scully, J. R., in *Effects of the Environment on the Initiation of Crack Growth, ASTM STP 1298*, W. A. Van der Sluys, R. S. Piascik and R. Zawierucha, Eds., ASTM, West Conshohocken, PA, 1998, pp. 61-73.

[8] Nelson, H. G., in *Hydrogen in Metals*, I. M. Bernstein and A. W. Thompson, Eds., ASM International, Materials Park, OH, 1974, pp. 445-464.

[9] Kolman, D. G. and Scully, J. R., *Metallurgical and Materials Transactions A*, vol. 28A, pp. 2645-2656, 1997.

[10] Wanhill, R. J. H., *Corrosion*, vol. 29, pp. 435-441, 1973.

[11] Nelson, H. G., *Metallurgical Transactions*, vol. 4, pp. 364-367, 1973.

[12] Somerday, B. P., Young, L. M. and Gangloff, R. P., *Fatigue and Fracture of Engineering Materials and Structures*, vol. 23, pp. 3s9-58, 2000.

[13] Gaudett, M. A. and Scully, J. R., *Metallurgical and Materials Transactions A*, vol. 30A, pp. 65-79, 1999.

[14] Gangloff, R. P., *Materials Science and Engineering A*, vol. A103, pp. 157-166, 1988.

[15] Kolman, D. G., Gaudett, M. A. and Scully, J. R., *Journal of the Electrochemical Society*, vol. 145, pp. 1829-1840, 1998.

[16] Scully, J. C., *Corrosion Science*, vol. 20, pp. 997-1016, 1980.

[17] Scully, J. R. and Moran, P. J., *Journal of the Electrochemical Society*, vol. 135, pp. 1337-1348, 1988.

[18] Ford, F. P., in *Environment-Induced Cracking of Metals*, R. P. Gangloff and M. B. Ives, Eds., NACE, Houston, TX, 1990, pp.139-165.

[19] Parkins, R. N., in *Stress Corrosion Cracking - The Slow Strain-Rate Technique, ASTM STP 665*, G. M. Ugiansky and J. H. Payer, Eds., ASTM, West Conshohocken, PA, 1979, pp. 5-25.

[20] Evans, J. T., *Acta Metallurgica*, vol. 25, pp. 805-808, 1977.

[21] Moskovitz, J. A. and Pelloux, R. M., *Corrosion*, vol. 35, pp. 509-514, 1979.

[22] Buhl, H., in *The Slow Strain Rate Technique, ASTM STP 665*, G. M. Ugiansky and J. H. Payer, Eds., ASTM, West Conshohocken, PA, 1979, pp. 333-346.

[23] Bomberger, H. B., Meyn, D. A. and Fraker, A. C., in *Titanium Science and Technology*, G. Lutjering, U. Zwicker and W. Bunk, Eds., Dt Gesellschaft fur Metallk., Germany, vol. 4, 1985, 2435-2454.

[24] Anderson, D. R. and Gudas, J. P., in *Environment-Sensitive Fracture: Evaluation and Comparison of Test Methods, ASTM STP 821*, S. W. Dean, E. N. Pugh, and G. M. Ugiansky, Eds., ASTM, West Conshohocken, PA, 1984, pp. 98-113.

[25] Nelson, H. G., Williams, D. P. and Stein, J. E., *Metallurgical Transactions*, vol. 3, pp. 469-475, 1972.

[26] Curtis, R. E., Boyer, R. R. and Williams, J. C., *Transactions of the ASM*, vol. 62, pp. 457-469, 1969.

[27] Leckie, H. P., *Corrosion*, vol. 23, pp. 187-191, 1967.

[28] Williams, D. P. and Nelson, H. G., *Metallurgical Transactions*, vol. 3, pp. 2107-2113, 1972.

[29] Andresen, P. L., Gangloff, R. P., Coffin L. F. and Ford, F. P., in *Fatigue 87*, vol. III-A, R. O. Ritchie and E. A. Starke, Jr., Eds., EMAS, West Midlands, UK, 1987, pp. 1723-1751.

[30] Richey, E., *Microstructure and Strain Rate Effects on the Environment Assisted Cracking of α/β-Ti Alloys in Aqueous Chloride*, PhD Dissertation, University of Virginia, Charlottesville, VA, 1999.

[31] Evans, D. J., Broderick, T. F., Woodhouse, J. B. and Hoenigman, J. R., *Materials Science and Engineering A*, vol. A213, pp. 37-44, 1996.

[32] Zhang, X. D., Wiezorek, J. M. K., Baeslack, W. A., Evans, D. J. and Fraser, H. L., *Acta Metallurgica*, vol. 46, pp. 4485-4495, 1998.

[33] Briggs, R. D., in *Advances in the Science and Technology of Titanium Alloy Processing*, TMS-AIME, Warrendale, PA, 1996, pp. 413-420.s

[34] *E647-95a Standard Test Method for Measurement of Fatigue Crack Growth Rates*, in *Annual Book of ASTM Standards*, vol. 03.01, ASTM, West Conshohocken, PA, 1999, pp. 577-613.

[35] Blackburn, M. J., Feeney, J. A. and. Beck, T. R., in *Advances in Corrosion Science and Technology*, M. G. Fontana and R. W. Staehle, Eds., Plenum Publishing, New York, NY, 1972, pp. 67-292.

[36] Haynes, M. J. and Gangloff, R. P., *Journal of Testing and Evaluation*, vol. 25, pp. 82-98, 1997.

[37] Mauney, D. A. and Starke, E. A., *Corrosion*, vol. 25, pp. 177-179, 1969.

[38] Fager, D. N. and Spurr, W. F., *Transactions of the ASM*, vol. 61, pp. 283-292, 1968.

[39] Aitchison, I. and Cox, B., *Corrosion*, vol. 28, pp. 83-87, 1972.

[40] Schutz, R. W., in *Stress Corrosion Cracking*, R. H. Jones, Ed., ASM International, Materials Park, OH, 1992, pp. 265-297.

[41] Ginter, T. J., Cornell, B. L. and Bayha, T. D., *Characterization of Ti-6Al-2Sn-2Zr-2Mo-2Cr*, Report No. WL-TR-4128, Air Force Research Laboratory, Wright Patterson Air Force Base, OH, 1997.

[42] Wilson, A. W. and Howe, J. M., *Metallurgical and Materials Transactions* A, vol. 29A, pp. 1585-1592, 1998.

[43] Richey, E and Gangloff, R. P., "Microstructure-Dependent Environment Assisted Cracking of α/β Ti-6Al-2Sn-2Mo-2Zr-2Cr-Si", *Metallurgical and Materials Transactions*, in review, 2000.

[44] Akhurst, K. N. and Baker T. J., *Metallurgical Transactions. A*, vol. 12A, 1059-1070, 1980.

[45] Kolman, D. G. and Scully, J. R., *Journal of the Electrochemical Society*, vol. 143, pp. 1847-1860, 1996.

[46] Shah, K. K. and Johnson, D. L. in *Hydrogen in Metals*, I. M. Bernstein and A. W. Thompson, Eds., ASM International, Materials Park, OH, 1974, pp. 475-481.

[47] Kolman, D. G., Gaudett, M. A. and Scully, J. R., *Journal of the Electrochemical Society*, vol. 145, pp. 1829-1840, 1998.

[48] Kolman, D. G. and Scully, J. R., *Philosophical Magazine A,* vol. 79, pp. 2313-2338, 1999.

[49] Blackburn, M. J. and Williams, J. C., *Transactions of the ASM*, vol. 62, pp. 398-409, 1969.

[50] Kolman, D. G., *Passivity and Bare Surface Electrode Kinetics on β-Titanium Alloys in Aqueous Chloride Solution and Their Relevancy to Environmentally Assisted Cracking*, Ph.D. Dissertation, University of Virginia, Charlottesville, VA, 1995.

[51] Simonen, E. P., Jones, R. H. and Danielson, M. J., *Corrosion Science*, vol. 34, pp. 899-914, 1993.

[52] Johnson, H. H., in *Hydrogen in Metals*, I. M. Bernstein and A. W. Thompson, Eds., ASM International, Materials Park, OH,1974, pp. 35-49.

[53] Toribio, J. and Kharin, V., *Fatigue and Fracture of Engineering Materials and Structures*, vol. 20, pp. 729-745, 1997.

[54] Pasco, R. W., Sieradzki, K. and Ficalora, P. J., in *Embrittlement by the Localized Crack Environment*, R. P. Gangloff, Ed., TMS-AIME, Warrendale, PA, 1984, pp. 375-381.

[55] Tien, J. K., Nair S. V and Jensen, R. R., in *Hydrogen Effects in Metals*, I. M. Bernstein and A. W. Thompson, Eds., TMS-AIME, Warrendale, PA, 1981, pp. 37-56.

[56] Hutchinson, J. W., *Journal of the Mechanics and Physics of Solids*, vol. 16, pp.13-31, 1968.

[57] Rice, J. R. and Rosengren, G. F., *Journal of the Mechanics and Physics of Solids*, vol. 16, pp. 1-12, 1968.

[58] Lidbury, D. P. G., in *Embrittlement by the Localized Crack Environment*, R. P. Gangloff, Ed., TMS-AIME, Warrendale, PA, 1984, pp. 149-172.

[59] McMeeking, R. M., *Journal of the Mechanics and Physics of Solids*, vol. 25, pp. 357-381, 1977.

[60] Rice, J. R., Drugan W. J.s and Sham T-L., in *Fracture Mechanics: 12th Conference, ASTM STP 700*, P.C. Paris, Ed., ASTM, West Conshohocken, PA, 1980, pp. 189-221.

[61] Mayville, R. A., Warren T. J. and Hilton, P. D., in *Fracture Mechanics: Perspectives and Directions (Twentieth Symposium), ASTM STP 1020*, R. P. Wei and R. P. Gangloff, Eds., ASTM, West Conshohocken, PA, 1989, pp. 605-614.

[62] Sanderson, G., Powell, D. T and Scully, J .C., in *Fundamental Studies of Stress Corrosion Cracking*, R. W. Staehle, A. J. Forty and D. van Rooyen, Eds., NACE, Houston, TX, 1967, pp. 638-649.

[63] Webb, T. W. and Meyn, D. A., in *Fracture Mechanics: 26th Volume, ASTM STP 1256*, W.G. Rueter, J. H. Underwood and J. C. Newman, Eds., ASTM, West Conshohocken, PA, 1997, pp. 678-712.

[64] Tsai, M. M., *Lengthening Kinetics of (0110) γ Hydride Precipitates in α Titanium*, M.S. Thesis, University of Virginia, Charlottesville, VA, 1994.

[65] Young, L. M., *Environment Assisted Cracking in β-Titanium Alloys*, M.S. Thesis, University of Virginia, Charlottesville, VA,1993.

[66] Oriani, R. A. and Josephic, P. H., *Acta Metallurgica*, vol. 22, pp. 1065-1074, 1974.

[67] Young, L. M., *Crack Growth and Hydrogen Uptake in Environment Assisted Cracking in AA 7050*, PhD Dissertation, University of Virginia, Charlottesville, VA, 1999.

[68] Tsai, M. M., *Determination of the Growth Mechanism of γ TiH in α-Ti Using High Resolution and Energy Filtered Transmission Electron Microscopy*, PhD Dissertation, University of Virginia, Charlottesville, VA, 1997.

[69] Efron, A., Lifshitz, Y. and Lewkowicz, I., *Journal of the Less Common Metals*, vol. 153, pp. 23-34, 1989.

[70] Somerday, B. P., *Metallurgical and Crack Tip Mechanics Effects on Environment Assisted Cracking of Beta-Ti Alloys in Aqueous Chloride*, Ph.D. Dissertation, University of Virginia, Charlottesville, VA, 1998.

Plenary Program—II

Roger W. Staehle[1]

Framework for Predicting Stress Corrosion Cracking

Reference: Staehle, R. W., "**Framework for Predicting Stress Corrosion Cracking,**" *Environmentally Assisted Cracking: Predictive Methods for Risk Assessment and Evaluation of Materials, Equipment, and Structures, ASTM STP 1401*, R. D. Kane, Ed., American Society for Testing and Materials, West Conshohocken, PA, 2000.

Abstract: A method for predicting SCC performance is described involving the corrosion based design approach (CBDA) and the locations for analysis matrix (LAM). This method provides bases for considering all the factors that contribute to corrosion-related failure in an orderly framework. The CBDA includes the steps of environmental definition, material definition, mode definition, superposition, failure definition, statistical definition, accelerated testing, prediction, monitoring and feedback, and fix. The LAM is a matrix that applies to a specific subcomponent and provides a framework for explicit actions for each mode of corrosion at each location where conditions are the most aggressive.

Keywords: Corrosion based design approach, locations for analysis matrix, stress corrosion cracking, environmental definition, material definition, mode definition, failure definition, statistical definition, accelerated testing, prediction

Introduction

The purpose of this discussion is to place the prediction of stress corrosion cracking into a perspective of design and to describe a two part method for predicting stress corrosion cracking and other corrosion-related performance from a design point of view. Such an approach is based on the idea that corrosion analysis is fundamentally a design science just as stress analysis is a design science. Emphasis here is placed on stress corrosion cracking (SCC) since it is usually the most virulent of corrosion processes and interacts most directly with design.

In considering prediction as related to this meeting, "Environmentally Assisted Cracking" is a misleading term. It implies that whatever cracking occurs is "assisted" or accelerated by environments. This circumstance where crack propagation is "assisted" by environments actually occurs only in a limited range and in limited circumstances of fatigue where SCC does not contribute. However, SCC occurs in many instances where cyclic stressing is not the dominant mode of applied stress and where SCC initiates from smooth surfaces. In fact, SCC occurs where the applied stresses are not significant and the SCC is influenced by residual stresses alone. There are, in fact, two quite distinguishable conditions: one where environments accelerate the growth of fatigue

[1] Industrial Consultant and Adjunct Professor, Department of Chemical Engineering and Materials Science, University of Minnesota, 22 Red Fox Road, North Oaks, Minnesota, 55127.

Copyright© 2000 by ASTM International www.astm.org

cracks and is of lesser importance; and one where no cracking would occur were it not for SCC that occurs even at static load. In the static load case no cracking occurs if requisite environments are absent. In the cyclic load case cracks grow in the absence of environments and may be accelerated by some environments.

In order to propose a plan for predicting SCC, one has to consider why it has occurred in the past and why it continues to occur in engineering systems. In general, SCC continues to occur because designers do not have a useful conception of how environments affect the mechanical properties of materials nor of the circumstances when SCC occurs. The continued occurrence of SCC has nothing to do with the lack of good models for prediction. Design continues to be effected by using handbook values of strength with no concept that the actual strength of materials depends totally on the environment in which they operate*[1]*. The usable strength of metals in some environments, e.g. stainless steels in dilute chloride environments, may be less than 10% of the yield strength.

One of the fundamental reasons for the occurrence of SCC as well as for many other corrosion phenomena is the lack of appreciation of the fact that all engineering solids are reactive chemicals. The surprise should not be that materials fail; but, rather, the surprise should be that they work at all. The very reactive metals, such as titanium and aluminum are protected only by an insoluble layer that is a few atom layers thick. In view of such an even transparent protection, it may be surprising that there is any protective film at all.

Another reason for the lack of appreciation of the chemical factors that affect SCC is the lack of understanding of the large influences that are produced by small changes in the environment. For example:

- With respect to pH, a change of one unit of pH changes the solubility of oxide by three orders of magnitude for a three valent ion such as Fe^{+3} and by two orders of magnitude for a two valent ion such as Fe^{+2}. Such effects are shown in Fig. 1*[2]*.

- With respect to potential, a change of 250 mV at 300°C changes the solubility of Cr_2O_3 with respect to the soluble Cr^{+6} species by six orders of magnitude.

- The work of Cullen *[3]* shows that the corrosion rate of high nickel alloys as a function of pH in the range of 1 to 6 at 315°C is three orders of magnitude higher when the acidic anion is sulfate rather than chloride.

- In the SCC of pressure vessel steels only the sulfur dissolved from inclusions is required for SCC to propagate.

- Changing the oxygen concentration at 300°C from 1 ppb to 100 ppb in water for stainless steel changes the open circuit potential by 600 mV.

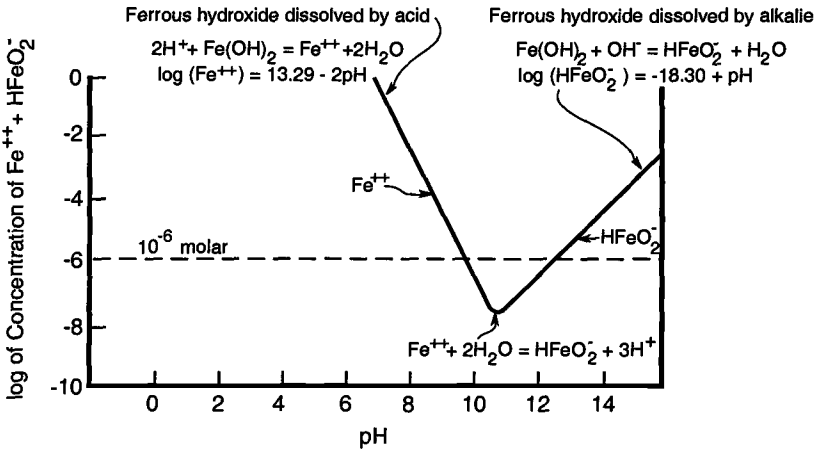


Figure 1 - *Influence of pH on the solubility of $Fe(OH)_2$ in water at 25°C. The 10^{-6} molar line identifies the nominal concentration of iron in water. (Adapted from Pourbaix [4].)*

Such effects as these seem incredible even to people familiar with materials. It is not surprising, then, that designers would be unaware or incredulous. These examples also show why small changes in environments produce large changes in the occurrence and intensity[2] of SCC and why nominally similar environments produce substantially different results.

A further factor that makes SCC incredible to designers is the fact that it can initiate from absolutely smooth surfaces in dilute environments at stresses well below the yield stress. It seems more intuitively credible to assume that some defect is required and that such a defect needs, together with the local stress, to exceed K_{Iscc}. However, such pre-crack geometries are generally not necessary for SCC to initiate.

The fact that more than 70% of SCC failures that occur are related primarily to residual and not applied stresses is also incredible to designers *[5]*.

The fact that the zinc coating used to protect the ordinary steel in auto bodies would lead to the SCC of high strength steel used in high strength applications is also not credible to designers. The zinc lowers the open circuit potential, which reduces the corrosion rate of steel; but in so doing the lowered potential accelerates the reduction of water molecules to hydrogen, which enters the high strength alloys to produce SCC.

It is not credible to designers that very dilute or nominally innocuous environments produce SCC, for example, in the following:

- SCC of high nickel alloys occurs in pure deoxygenated water at 300°C *[6]*.
- SCC of zirconium alloys occurs in iodine gas *[7]*.

[2] The term, "intensity," is used to describe generally various aspects of SCC that include the number of initiation sites per unit area, the time to failure and crack velocity.

- SCC of high strength steels occurs in pure water at RT *[8]*.
- The SCC of high strength steel is 10^3 more rapid in H_2S gas than in hydrogen gas and 10^2 more rapid in chlorine gas than in hydrogen gas *[9]*.
- SCC of mill annealed stainless steels occurs in the ppm range of chlorides above about 200°C *[10]*.

Finally, it is not credible that corrosion products that develop in sequestered geometries can produce stresses above the yield stress. Such a process is well known and was the basis for the constriction of nickel alloy tubes in nuclear steam generators where corrosion products from the surrounding tube supports caused constriction of the tubes and subsequent SCC *[11]*. A clear illustration of the same effect is due to work of Fontana et al. *[12]*, who showed that SCC could propagate in the complete absence of applied stresses using the experiment shown in Fig. 2. Here, a stainless steel insert was placed in a groove of another non-stressed stainless steel piece; the interface between the two pieces produced a crevice where extensive corrosion occurred with the resulting corrosion products expanding and producing stresses that caused SCC at the base of the notch. When the insert was removed, the SCC continued due only to the forces from the corrosion products in the SCC.

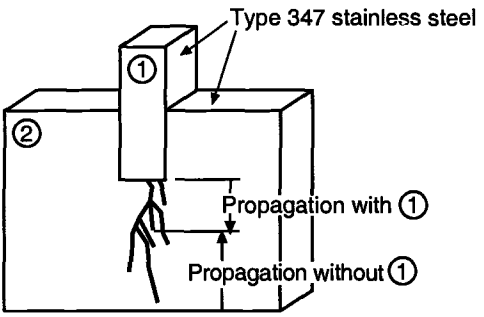


Figure 2 - *Effect of oxide growth on stresses for Type 347 stainless steel exposed to a chloride solution at 206°C. Propagation in stage (1) is due to expansion of corrosion products between insert and groove. Propagation in stage (2) is due to expansion of corrosion products inside SCC of stage (1). (Adapted from Fontana et al. [12].)*

Finally, SCC failures continue to occur because of incorrect assumptions as follows:

- Following the ASME boiler code will insulate the design from corrosion.
- Following well established specifications will prevent corrosion.
- Corrosion allowances account for all foreseeable corrosion.

- Using procedures such as HAZOP or failure modes and effects analysis (FMEA) will obviate corrosion and SCC failures.

- Nominally corrosion resistant alloys such as stainless steels, high alloys, or titanium prevent corrosion.

- Failures occur because of "bad heats" of material (this is almost never the correct interpretation).

- SCC cannot occur at room temperature.

- A fitness for service analysis was conducted and indicated that no SCC would occur.

Modeling work, when it is undertaken, is often misleading or inadequate. As a result, users assume results for which the modeling was simply inadequate. For example, the following apply to the adequacy and applicability of modeling as it presently exists:

- Determinism: It is a vain but a persistent hope that SCC could be modeled in some deterministic way, i.e., the course of SCC can be known exactly if everything could be specified exactly. This is wrong on two counts. First, SCC is inherently statistical as is discussed herein. Second, it is not possible to specify the environment, material, and stress situations with sufficient specificity to predict a precise outcome. Nominally deterministic relationships that are developed incorporate a sufficient number of adjustable constants that they can model any set of results; such models are not predictive *a priori*.

- Atomistics: It is often said that no adequate prediction can be developed that is not based on a precise atomistic model. This is an unrealizable dream in any kind of practical time. Further, not only would the material have to be modeled on an atomistic basis, but the environment would have to meet the same level of atomistic definition.

- Modeling crack growth only is adequate: Available modeling of SCC considers only propagation. Again, this is wrong in general unless the sections are sufficiently thick where crack growth models apply exclusively. Most SCC is dominated by initiation that has yet to be modeled at any useful quantitative level.

- Correlation equations cannot be generalized and are limited to narrow conditions: While this is a popular argument for those proposing modeling research, it is ingenuous. Most of engineering is accomplished using correlation relationships. Correlation equations are often generalized with great success. It is usually clear to experienced engineers where such generalizations are not appropriate.

In general, the design of equipment is dominated by mechanical designers who have little knowledge of the chemical effects described here and who assume that it is adequate to organize the design based on an initial stress analysis including, where appropriate, a cyclic stress dependence for life prediction, e.g. a "40 year life." Generally, stress-based designs provide equipment that is adequate through the warranty period; however, corrosion process usually require several years before even inherently bad designs start to fail by corrosion processes. Thus, the designer is protected, and the user bears the burden of the design which may be initially inadequate from a corrosion point of view.

The domains of time over which the stress-based and corrosion-based concerns are important are illustrated schematically in Fig. 3. Since it is usually not necessary for designers to face up to long-term reliability, it is not implicitly necessary that they inquire about important corrosion issues.

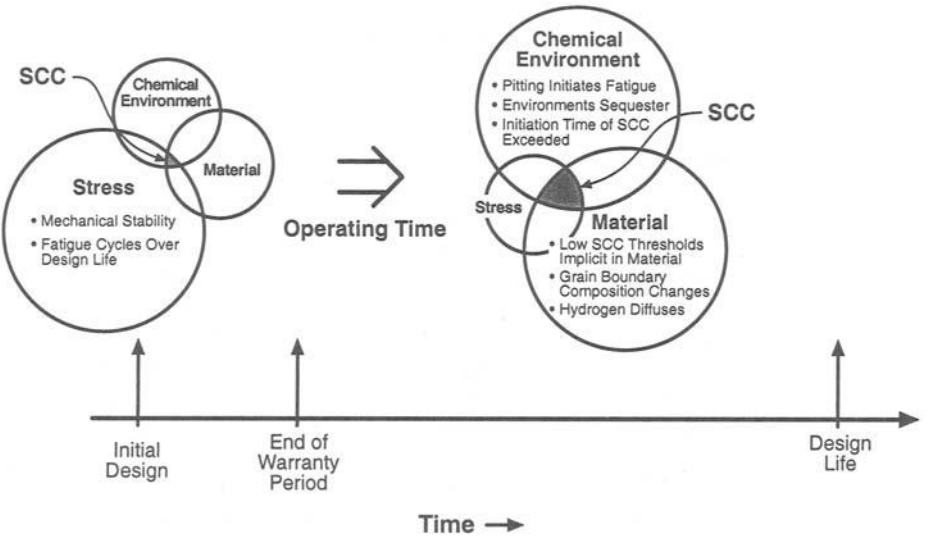


Figure 3 - *Schematic view of the relative importance of chemical environment, stress and material to determining the life of components over time. Times of initial design, end of warranty period, and design life are illustrated schematically. The figure is based on the well-known schematic three ring illustration of the simultaneous importance of chemical environment, stress and material to the occurrence of SCC.*

Problems in Modeling SCC

Modeling of SCC needs to rationalize the following elements:

1. Quantitative relationships for the seven primary variables of temperature, stress, electrochemical potential, pH, species and their concentration, alloy composition and alloy structure.

2. Separate stages of initiation and propagation with their separate dependencies on the primary variables.

3. Multiple locations on components where the modes of corrosion and the local environments are different.

4. Effects of primary variables on statistical dispersion as well as mean value.

There is no modeling available that considers even the quantitative relationships for the seven principal variables that control SCC as shown in Fig. 4. Usually, models deal with mechanics and relegate the chemistry to an inclusive constant. Arguments are variously presented that stress is the dominating variable; these arguments neglect the critical dependencies of SCC on the metallurgy and environmental chemistry.

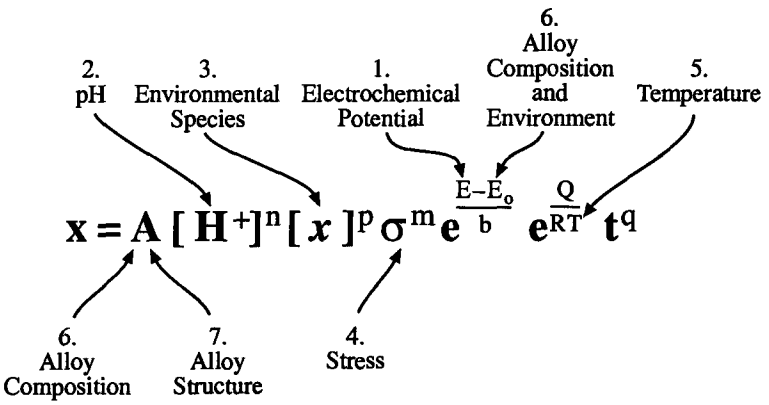


Figure 4 - *General form of an equation describing the penetration "x" of SCC depending on the time "t" and the principal variables of electrochemical potential, pH, environmental species, stress, temperature, alloy composition and alloy structure. (From Staehle [13].)*

Method for Prediction and Design

It is not possible to develop a single basis for modeling owing to the many considerations required in a component unless it is simple and unchallenging. On the other hand, it is necessary to have a well defined basis for predicting performance that can become part of the design record.

Predicting performance from a corrosion point of view has been historically difficult for both designers and materials engineers. Corrosion problems have been regarded as "too complex" and intractable. Engineers have been searching for a single analytical approach and have been frustrated that this hoped for result has not been forthcoming. It

seems that what has been missed is the need for multiple models since most components have multiple locations where aggressive corrosion may occur. Whatever modeling approach is developed, then, must account for these multiple locations and multiple corrosion processes. Further, it is well known that environments change with time so that modeling SCC for a single environment at one location may be useful only for a limited time.

Over the many years that engineers have struggled with design in applications where corrosion is an important consideration, certain rule of thumb approaches have been developed. Somehow engineers have "gotten along" in some applications. From such experience including a rigorous review of the principal factors that need to be considered, a single approach involving two parts has been developed. The first of these is the "Corrosion Based Design Approach (CBDA)" and the second of these is the "Location for Analysis Matrix (LAM)." These are described here in sufficient detail to understand the main ideas and utility of this two part approach. They have been described in more detail elsewhere *[13,14]*. Avoiding corrosion-related failures is not solved by a single mathematical relationship nor by using only engineering experience. Predicting performance, in general, is a "bookkeeping" problem wherein a set of issues has to be accounted for and sometimes quantified; this approach to prediction is the essence of the CBDA and LAM.

Corrosion Based Design Approach (CBDA)

The CBDA was developed *[15]* to identify an orderly set of steps for designing, predicting and assuring performance with respect to effects of corrosion on the performance of materials and components. This same set of steps identifies the questions that need to be considered in analyzing corrosion-related failures. The term, "corrosion-related design," is the generic term that applies here to design, prediction, assurance and failure analysis. In corrosion-related design the essential challenge is not to develop mathematical relationships but rather to determine where it is appropriate to direct attention. The CBDA is a framework for deciding (a) what decisions have to be made and (b) where to focus attention. Once these have been decided, the necessary mathematical relationships can be developed and applied.

In corrosion-related design, the first consideration is associated with the chronology, i.e., at what time in the life of the component is corrosion to be considered? It may be important for all stages in life, but these need to be explicit. The stages for possible chronological analysis of corrosion are shown in Table 1.

[1] Environmental Definition[3]

Defining the environments in which materials and components must operate is the first step in predicting their corrosion-related performance. Specifying environments is

[3] In this article and in the CBDA and LAM the bracket convention, **[x]**, is used to denote action or check off items. These brackets are used as bold face to avoid confusion with referencing where brackets are used but not in bold face.

the most important consideration in corrosion-related design. The environments of specific interest are those that occur specifically on the surface of the materials of the component as opposed to the bulk environments, although the former usually are derived from the latter. Great care has to be used in specifying these local environments for at least the following reasons:

- There may be more than one aggressive environment on the surface of a subcomponent but at different locations.
- Environments accumulate and change with time so that the early environment, which may be dominated by bulk chemistry, may change to being dominated by deposits which are later saturated.
- Environments on surfaces are greatly affected by the state of the surface (intergranular grooves that result from prior cleaning), heat transfer, geometry (crevices and deposits) and flow.
- Large changes in corrosion reactions are inherent in small changes in environments.

Table 1 - *Stages for analysis.*

Before Startup	After Startup
• Manufacture	• Startup
• Testing (e.g. hydrotest)	• Steady State Operation
• Storage at Manufacturer	• Shutdown (planned and forced)
• Shipping	• Maintenance During Shutdown
• Site Storage	• Cleaning During Shutdown
• Installation	• Inspection During Shutdown
• Pre-Start Testing	• Startup After Shutdown
	• Long Time Operation

Fig. 5 is a "dot diagram,"[4] which identifies the main considerations in specifying environments at a specific location, i.e. a Location for Analysis,[5] that is discussed in connection with Fig. 17. For the purpose of the present discussion, discussing a specific location for analysis, LA_i, means a specific location on a subcomponent with its associated environments that occur directly on the surface.

[4] The "dot diagram" as used here provides a map for guiding analysis of the various considerations. The end point of these dot diagrams is the set of factors that need to be considered at the "Locations for Analysis."

[5] The term, "Location for Analysis," is used in this discussion as a specific location on a subcomponent where the intensity of corrosion is considered in detail since such a location is likely to sustain early or rapid and undesirable corrosion. This is the location where mathematical modeling might be focused. There may be many such locations, and each one is given the designation, LA_i (where i = 1, 2 ...n).

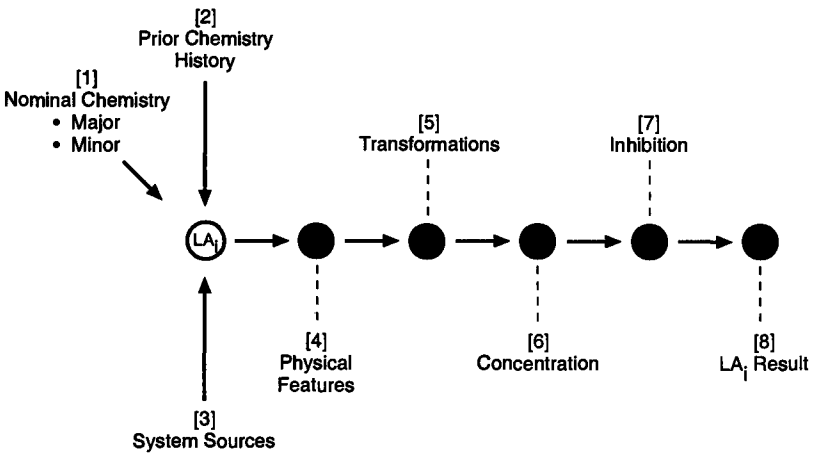


Figure 5 - *Steps in the analysis of chemical environments that occur at a Location for Analysis, LA_i. The use of bold face brackets here, [ ], indicates actions that need to be considered or acted upon. (From Staehle [13].)*

Following are explanations and descriptions of the actions and considerations at each of the dots in Fig. 5; these are correlated with their respective bracket number in the Figure:

[1] Nominal Chemistry, Major and Minor - The first step in defining environments involves defining the nominal chemistry of the surroundings including major and minor nominal species. For an industrial atmosphere the major nominal species are oxygen and nitrogen; the minor nominal species are industrial gases containing sulfur, nitrogen and carbon.

[2] Prior Chemistry History - In some systems contaminants remain from prior use as might have been involved with pickling, cleaning solutions, prior operation, shutdown conditions and accident circumstances. These species may be dried on surfaces or sequestered in crevices or in intergranular surface penetrations. Hydrofluoric acid (HF) from prior pickling is a good example here.

[3] System Sources - Species are released from some components that contaminate others. Resin beads sometimes are released and deposit reduced sulfur species on heat transfer surfaces. Copper alloy heat exchangers release soluble copper that is an oxidizer and also a catalytic substrate for pitting corrosion. Leaks in turbines allow oxygen contamination. Catalytic beds manufactured with the reduction of chloroplatinate produce chloride contamination.

[4] Physical Features - Physical features affect corrosion and include crevices, heat transfer surfaces (sequestered and/or boiling), deposits, low (produce deposits) and high flow (accelerate electrochemical kinetics).

[5] Transformations - Certain species may transform their chemical identity during operation or exposure. For example, sulfur added as sulfate may be reduced to lower valence species (when hydrazine is added in order to lower oxygen concentration), which in turn accelerate SCC or other corrosion processes. Microbiological species metabolize the same environments to produce acidity, alkalinity, complexants or aggressive lower valence species such as sulfur. Retrograde solubility with increasing temperature causes phosphates used in water treatment to form phosphoric acid. At separated anodic and cathodic sites, acidic and alkaline species, respectively, may form. When water is reduced in the deaerated oxidation of iron or more active metals such a zinc or zirconium, hydrogen is formed and some fraction of that produced can enter metals to produce embrittlement.

[6] Concentration - Species may concentrate as a result of wetting and drying, boiling, wicking, and evaporation. In each of these cases, what may have originally been a dilute solution becomes a saturated solution

[7] Inhibition - Corrosion processes are often inhibited by adding agents that reduce the oxygen, change the pH, produce insoluble compounds, or block anodic or cathodic reactions. These species may be effective where they are added but may accelerate corrosion at other locations, e.g. the decomposition of hydrazine produces ammonia which accelerates the corrosion of copper base alloys.

[8] LA_i Result - When items [1] through [7] are integrated, the final result identifies the environment that affects the corrosion of a specific material at a specific location.

The environment considered here is only the aqueous chemical and electrochemical environment. In more general terms the subject of environments includes at least the following:

- Stress in its various frameworks of cyclic frequency, mean stress, R ratio, slow constant straining and static residual.
- Thermal including thermal shock, gradients, thermal cycling.
- Microbiological species.
- Surface coatings.
- Flow with its reaction rate and erosive effects.
- Phase including gas, liquid or solid as well as two phase such as water-steam.
- Geometrical environments including gravity, crevices, galvanic effects, area ratios and others,
- Relative motion leading to wear, fretting, galling and seizing.

- Radiations including neutrons, gamma rays, electromagnetic including solar, charged particles.

Rather than considering a single environment, most engineering subcomponents sustain several aggressive local environments requiring the designation of multiple LA_i, e.g. LA_1, LA_2, LA_3, ... This is illustrated in Fig. 6 where multiple LA_i and modes of corrosion are identified for a steam generator. Figure 6 shows that a proper analysis of corrosion in a complex component, like the steam generator for a pressurized water reactor, should consider several locations as well as several modes of corrosion. Any of these combinations or all of them could be sufficiently aggressive to cause failure of the component.

[2] Material Definition

Materials of the same average composition but with different histories may, at the same yield strength, sustain quite different responses in SCC. Figure 7 shows that different heat treatments for the same steel produce significantly different crack growth behaviors *[16]*; materials are affected differently by their major and minor alloying species and by impurities in the 10^{-5} a/o concentration range. The dot diagram by which materials are defined in the CBDA is shown in Fig. 8 and the basis for each of these dots is:

[1] Major Nominal Alloy Composition - Major alloy species, for example, in brass are copper and zinc; in austenitic stainless steels, the major alloy species are iron, chromium and nickel. The occurrence of SCC depends generally in gradual and regular ways upon such major alloy species as shown in Fig. 9.

[2] Minor Nominal Alloy Composition - Minor alloy species include those in low concentrations but which are present or added intentionally. Well-known minor alloy species include carbon in steels and oxygen in titanium. Minor nominal alloy species often exert substantial influences on the occurrence of SCC, especially in terms of the magnitude of the effect per atom relative to the major alloy species.

[3] Impurities - Certain species exist or are imbibed in alloys either as a result of processing or during the melting. For example, in the welding of titanium and zirconium, oxygen and nitrogen can be absorbed from the air and exert decisive effects on the occurrence of SCC.

[4] Processing - With the alloy composition in place, properties of materials are affected mainly by the results of processing. Processing exerts generally large effects on both initiation and propagation of SCC. The influences of processing on SCC are well known. Processing generally includes hot and cold working, heat treatments, joining (e.g. welding and its associated heating), and surface conditioning such as associated with surface grinding. Thus, the alloy composition by itself does not control uniquely the occurrence and intensity of SCC. Processing, e.g., the items **[5]** through **[8]**, often determines the occurrence of SCC.

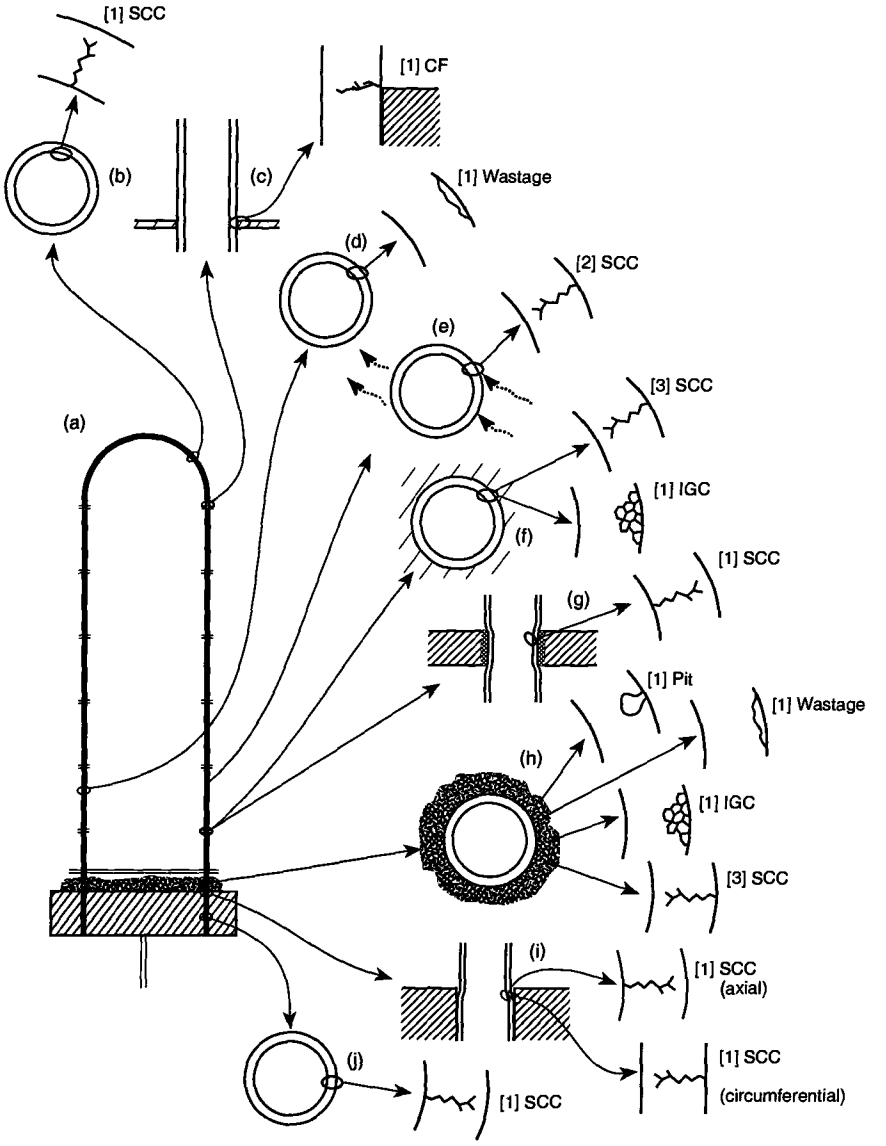


Figure 6 - *Schematic relationship of location to possible mode-location cases of corrosion for a U-tube steam generator used in pressurized water nuclear reactor systems. The modes of corrosion and the locations are based on observed occurrences. Tube sheet shown at bottom. Full width tube support shown above the tube sheet; other periodic locations of tube supports noted. (a) Single tube of U-tube in steam generator of pressurized water reactor systems. (Numbers in [brackets] indicate similar submodes although they may occur at different stresses or temperatures; curved vignettes indicate that the view is parallel to the axis of the tube; straight vignettes indicate that the view is*

Figure 6 caption (continued): *... perpendicular to the axis of the tube.) (b) High stress from bending and forming in U-bend produces axial SCC [1] from primary side. (c) Immediately above the tube support with circumferential corrosion fatigue [1] from secondary side. (d) Free span from secondary side with [1] wastage on cold leg. (e) Free span from secondary side with axial SCC on hot leg side [1]. (f) Tube at tube support with axial SCC [3] and IGC [2]. (g) Denting at intersection of tube support and tube produces stresses in tube which cause axial SCC [1] from the primary side. (h) Tube inside sludge pile above the tube sheet with corrosion on secondary side: pitting [1], wastage [2], IGC [1], axial SCC [1]. (i) Roll transition with circumferential SCC [3] on secondary side and axial SCC [1] on primary side. (j) Expanded tube in tube sheet with axial SCC [1] from primary side. (From Staehle [15].)*

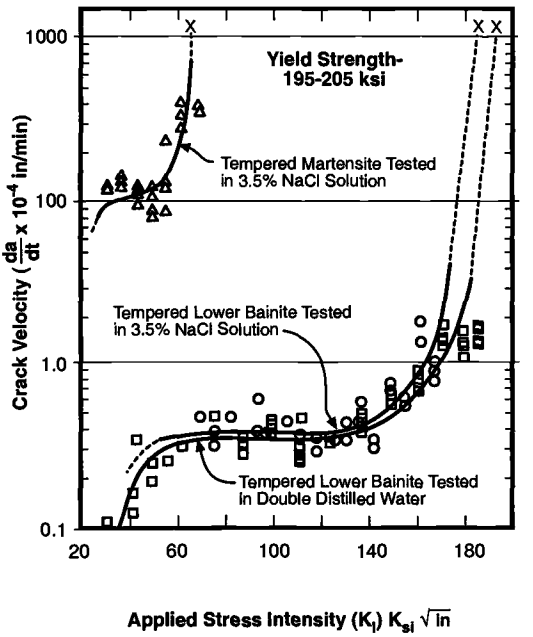


Figure 7 - *Crack velocity versus stress intensity for a 4340 steel heat treated to produce two different structures, but with approximately the same yield strength, and exposed to two different environments. (From Wang and Staehle [16].)*

[5] Structure - Alloy structure identifies the influence of processing on grain size, cold work, anisotropy, distribution of phases (e.g. duplex or inclusions) transformations and metastabilities. In addition, processing affects the distribution of species at grain boundaries. Each of these influences affects the occurrence of SCC

[6] Embrittlement - Certain processing produces embrittlements. Temper embrittlement is well-known to affect SCC. For higher chromium alloys, sigma phase embrittlement is sometimes observed.

[7] Surface - The effects of processing on the surface are particularly important since the initiation of SCC is totally influenced by the metallurgical state of the surface as well as its local environmental chemistry. Such effects have been described by Berge *[19]*.

[8] Mechanical - The combination of the alloy chemistry and the subsequent processing affects mechanical properties including the tensile and fracture properties. These, in turn, influence the SCC behavior.

[9] LA_i Result - The combined influences of the eight steps in defining materials exert decisive influences on the intensity of SCC. Considering items **[1]** - **[8]** together defines a specific LA_i, **[9]** just as the same consideration of the dot diagram in Fig. 5 defines the environments at specific LA_is.

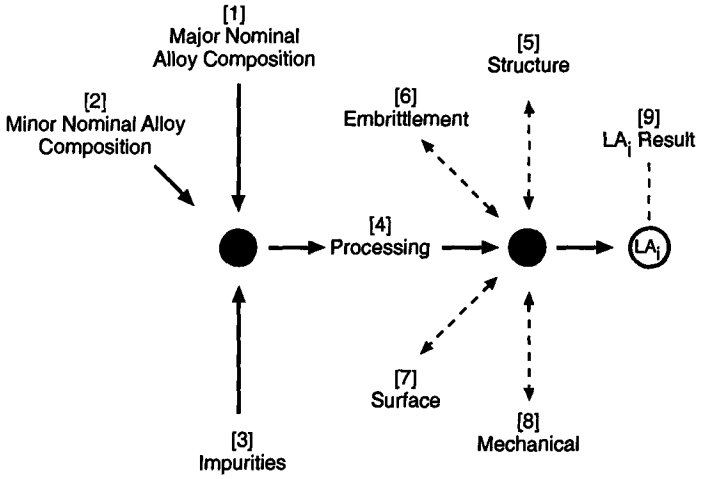


Figure 8 - *Steps in the analysis of materials at a particular LA_i (From Staehle [13].)*

[3] Mode Definition

While the thermodynamic stability of metals in environments can be well defined in a thermodynamic framework such as Pourbaix diagrams, the morphology of corrosion cannot be derived from such a framework. The principal "modes" or morphology of corrosion are identified in Fig. 10. These modes of corrosion have been called "forms" of corrosion in earlier texts; but this was misleading since the array of forms included terms like "crevice corrosion" and "galvanic corrosion" both of which are not intrinsic modes but rather describe environments that are a part of Environmental Definition.

In considering the subject of "Mode" a subcategory of "Submode" is considered. A submode is the same morphology of a particular mode, e.g. SCC, but it depends differently on the seven principal variables. A good example of several submodes for

high nickel alloys are alkaline SCC, acidic SCC, low potential SCC, high potential SCC, lead SCC and possibly others. Each of these depends differently upon the seven principal variables while at the same time occur in a single alloy in aqueous solutions usually in the range of 300°C. Similar arrays of submodes occur for stainless steels, copper alloys, titanium alloys and others.

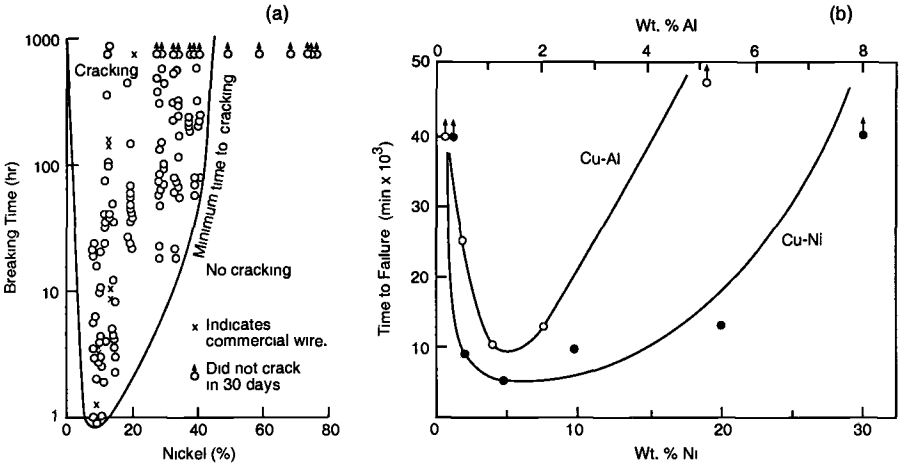


Figure 9 - *Effects of alloy composition on the stress corrosion cracking of Fe-Cr-Ni alloys exposed to boiling 42% $MgCl_2$ (a) and Cu-Al and Cu-Ni alloys in moist ammonia vapor. (Adapted from the work of Copson [17] and Thompson and Tracy [18], respectively.)*

"Mode Definition" includes the following:

- Defining the morphology of corrosion as shown in Fig. 10.
- Defining the submode that operates.
- Defining the extent to which initiation, propagation and other similar stages are involved.
- Identifying the quantitative dependencies of the specific submode.

An example of submodes of SCC is shown for Alloy 600 (78Ni-15Cr-7Fe) in Fig. 11. Here, there are four submodes of SCC: alkaline SCC, acidic SCC, low potential SCC and high potential SCC. There are additional submodes related to impurities such as chloride, copper and dissolved lead, but these are not discussed here. Each of these submodes depends differently upon the seven principal variables. Differences in the dependencies on pH and potential are evident and the other data show that these submodes differ also in dependencies on the other variables.

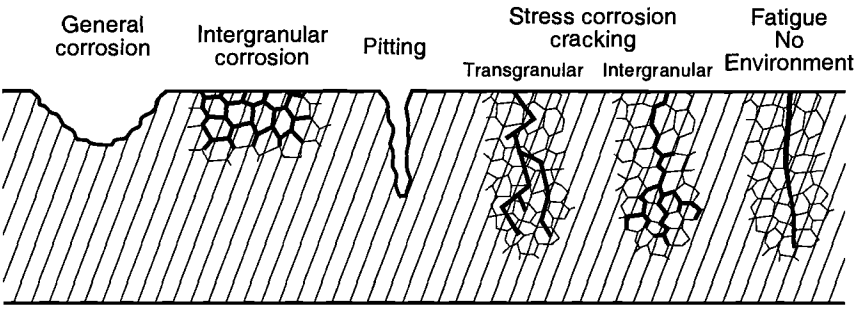


Figure 10 - *Intrinsic modes of corrosion. (From Staehle [15].)*

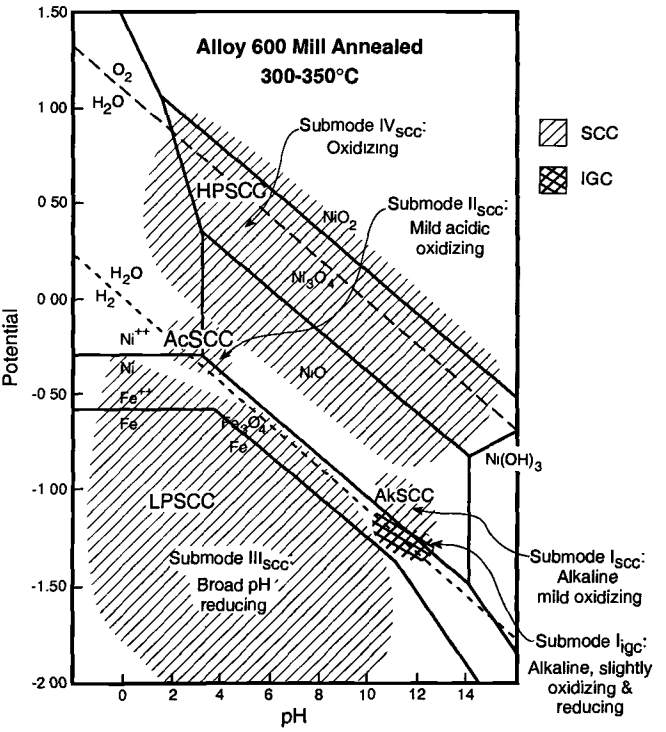


Figure 11 - *Occurrence of modes, MD_j, and submodes, SD_j, of SCC and IGC for mill annealed Alloy 600 in the range of 300-350°C plotted with respect aqueous equilibria for nickel and iron. Submodes included are alkaline SCC, acidic SCC, low potential SCC, high potential SCC. (Diagram originally from Staehle and Gorman [20] and modified in Staehle [13].)*

The morphology of SCC differs completely from the normal mechanical failure of ductile alloys. The normal fracture of ductile alloys involves extensive ductility; whereas, SCC exhibits virtually no large scale ductility. Thus, in no way does the environment "assist" the SCC or fracture as implied in the terminology of "Environmentally Assisted Cracking."

In the ideal circumstance, it would be possible to specify the submode of SCC that applies at an LA_i. However, in many cases it is not known whether SCC actually occurs, and preliminary experiments may be required to determine whether SCC can occur in the range of environments specified in the LA_i.

In defining the mode/submode of SCC, dependencies of the stages of initiation and propagation upon the principal variables have to be defined separately. These stages and their dependencies upon stress are shown schematically in Fig. 12. The stage of initiation depends on the surface stress and SCC continues to apply until some threshold stress is reached. Below this threshold, SCC does not occur although these thresholds sometimes lower gradually with time; but, to a first approximation, it can be assumed that the threshold occurs at a constant stress as shown in Fig. 12a.

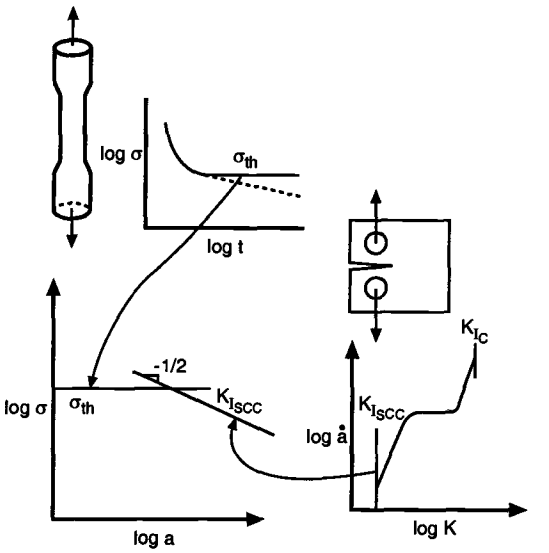
The propagation stage, as shown in Fig. 12, depends both on the stress and size of initial defect. Propagation depends differently from initiation upon the principal variables, and this is evident intuitively from the fact that propagation depends more on the chemistry of the advancing tip of the SCC.

The relative extents of the initiation and propagation stages can be estimated from Fig. 12b showing stress versus depth of defect. If an appropriate stress is selected as the threshold stress, e.g. 100 MPa, which is typical of alkaline SCC for Alloy 600, this defines an horizontal line. If a value of K_{Iscc} is selected, e.g. 5 $MPam^{1/2}$ which is typical for Alloy 600 in alkaline environments, this defines a line with slope -1/2 that depends jointly on the stress and the depth of defect. The intersection of these two lines, as illustrated in Fig. 12a, identifies the depth of defect at which initiation changes to propagation. For the case of the threshold being 100 MPa and the K_{Iscc} being 5 $MPam^{1/2}$ this depth of transition is about 0.7 mm.

Finally, in defining a mode, the dependencies upon principal variables must be defined. The means that a quantitative relationship such as in Fig. 4 should be developed. The extent of such quantification depends on needs of the project. In some cases, it may be adequate to determine whether SCC occurs, or not, since the mere occurrence may not be acceptable. In other cases it may be desirable to determine the dependencies on some or all of the principal variables so that avoiding the occurrence of the submode can be assured.

[4] Superposition

After the environment and modes of corrosion are identified for a specified LA_i and a given material, they can be compared to determine the possibility and intensity of failure. For example, the extent of the environment in potential and pH space is shown schematically in Fig. 13b. The extent of a relevant submode of corrosion is shown in Fig. 13a also in potential-pH space. Since these have been defined in similar coordinates, they can be compared directly. Figure 13c indicates an overlap with the implication that SCC will occur.



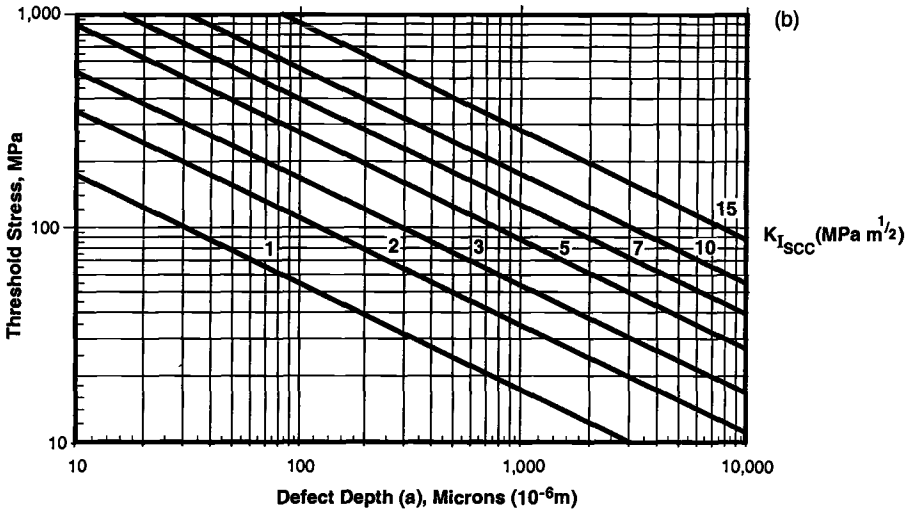


Figure 12 - *(a) Schematic view of log stress versus log of defect depth for smooth surface and pre-cracked specimens. (From Staehle [15]) (b) Threshold stress versus defect depth including various loci of K_{Iscc}. (From Staehle [13].)*

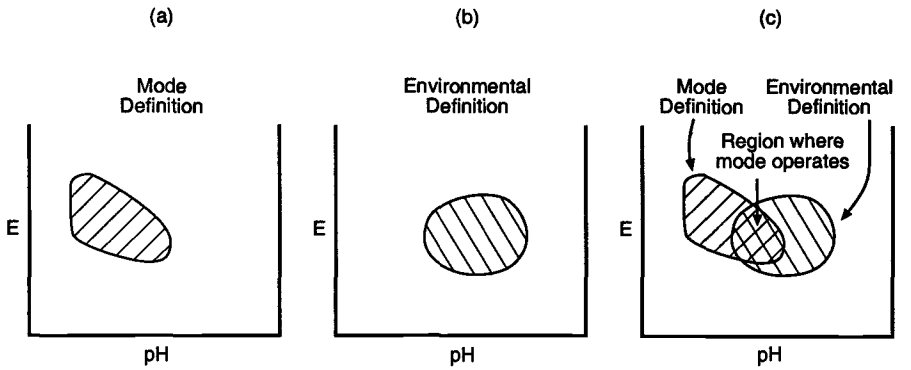


Figure 13 - *(a) Mode definition, (b) environmental definition, and (c) overlap shown schematically in the coordinates of potential and pH. (From Staehle [21].)*

In view of an overlap as shown in Fig. 13c, some action would be required. Such an overlap is nominally not desirable, and changes would be required in some aspects of the environment, material and design.

[5] Failure Definition

Prediction, assurance and design all have a common objective of avoiding "failure." "Failure" is defined as not meeting the design life. The extent of failures may be minimal, as for small leaks or minor rusting, or may be severe in the case of catastrophic explosions.

What constitutes failure varies among industries, for different components, and over time. Failures, on the one hand, may affect only the economy of operation e.g., a shutdown for repair is required or parts require replacement. On the other hand, failures may be inherently dangerous or may lead to dangerous circumstances. Important considerations in considering failure are:

- Criticality. If an SCC occurs generally on a surface where the fracture toughness is typical of wrought material, a leak may result; however, if the same SCC occurs at a weld where the fracture toughness might be significantly lower than the adjacent wrought material, the same SCC would become a critical event. Similarly, if an SCC is longitudinal, it may produce a leak, but in the transverse direction it could lead to double ended fracture. Thus, the location and orientation of SCC affects its "criticality" with respect to whether a relatively innocuous leak occurs or whether a catastrophic event is produced from the same extent of corrosion damage.

- Inspection Interval. SCC may progress sufficiently slowly that the extent may not be critical immediately, and it would be judged acceptable to

examine the progress at the next inspection interval. This "wait and see" would be continued until it could be ascertained that penetration would occur before the next inspection. On the other hand, the inherent variability of SCC together with the lack of definition of residual stresses through the thickness, could lead to unacceptable risk if SCC identified in an inspection is not acted upon.

- BBL vs. LBB. It is often the practice to assume that SCC will produce leaks before any catastrophic fracture occurs. Such a practice assumes "leak before break" or LBB. While this is widely regarded as an acceptable approach, such reliance is not well founded when there are, for example, continuous peripheral paths. Such continuous peripheral paths include circumferential welds, continuous circumferential crevices such as with thermal shields, and continuous circumferential deposits. Such continuous circumferential features produce paths of similar metallurgy, constant stresses or constant chemistry, which, when capable of producing SCC, may produce it uniformly with the result of BBL.

- Hazardous to Life. Certain failures may not be consequential in terms of extent, but they may be hazardous to life. Such failures might include the release of radioactivity, failures of devices inside the human body, release of noxious chemicals, or explosion in a populated region.

The concept of failure varies with the industry:

- Simple rusting would indicate failure in some architectural and food applications. In these cases, the appearance of rust is highly undesirable but the extent of corrosive penetration is minor.

- In a heat exchanger, leaking of a tube or heat exchange element may not be considered a failure since many of these can be repaired during operation or during minor or partial shutdowns. Such leaking is regarded as part of the trade-off for using more corrodible materials.

- On the surfaces of turbine shafts, a pit may require removal by grinding to prevent such a pit from initiating a fatigue failure.

- In some piping applications no failures are permissible so that one failure in a thousand or ten thousand welds would be cause for action.

- In some pipeline applications the mere appearance of clusters of SCC is not cause for action since such clusters of SCC are often observed but do not propagate until some of the adjacent small cracks coalesce. Until such clusters produce propagating SCC, they are not regarded as problems.

- In post tension applications in building construction, up to 30% loss of tendons, most likely by SCC or corrosion, may be acceptable depending on the design of the post tensioning system.

- Inspectability also influences the extent of failure that may be acceptable. The ease with which components can be inspected affects the extent of SCC that can be accepted either as an inherent possibility or as an occurring phenomenon.

Regardless of what is considered failure, some explicit definition of failure is required in order to provide a quantitative objective for prediction and assurance that the design life will be achieved.

[6] Statistical Definition

In predicting performance little attention is usually given to the statistical aspect of failure. For example in the step of "Failure Definition" there is often little quantification of whether failure occurs when the first element fails or 0.01, 1 or 50% of the elements fail. When designers are asked, it is common to respond that "no failure is acceptable." This is not a realistic objective; rather, failure should be specified in statistical terms.

The response of materials to environments is an inherently a statistical process. While the thermodynamic boundaries of corrosion are well-defined, the rate at which degradation occurs, its morphology and the state of environments are inherently statistical. While there are occasional wishes for determinism, as people often wish for more certainty, all corrosion phenomena are inherently statistical.

There are three levels of variability of materials:

- Inherent variability: Under the best, well controlled, and maximally similar conditions, the occurrence and intensity of corrosion phenomena are variable. This can be argued formally as the contributions to inherent variability are considered including: variable surface stresses, variable grain orientations, variable grain boundary angles, variable grain boundary compositions and coverages, variable stresses at crack tips, variable filling of advancing cracks with corrosion products, and variable migration and diffusion of species in advancing cracks. Consideration of such elements yields an inherent variability to the initiation processes and to the velocity of advancing SCC.

- Variability among the same nominal materials: This, simply, is the "heat to heat" variability. Among different heats of material as they are reduced to final shapes, there is a range of variability associated with processing temperatures, heat treatments, hot working and cold working.

- Variability of fabrication of components: Starting with the inherently variable nominal materials, they are welded, cleaned, bent, cut, surface ground, and coated in nominally similar but inherently different ways.

Such fabrication processes, especially as they affect surfaces, e.g. surface grinding, exert decisive effects differently on initiation and propagation.

This variability of materials then interacts with the variability of environments including the following:

- Chemical variability: The composition of the chemistry of the local environments adjacent to corroding sites at the LA_i is inevitably variable as it depends on concentrations, identity of species, pH, and oxidizing species. Further, these factors exert such great leverage with small changes as shown in Fig. 1 that relatively small changes in the chemical state is likely to produce decisive differences in the intensity of SCC.

- Flow variability. Flows at low magnitudes produce deposits at various rates and of varying depth depending on the concentrations of insoluble species; high flows affect kinetics of both oxidation and reduction processes as well as erosive effects. All of these flow effects, again, are highly leveraged as small changes in flow produce large effects.

- Accumulation: Species accumulate and the local environment changes over time at an LA_i. Such changes occur both on free surfaces and in crevices. Heat transfer often accelerates and stimulates such accumulations. As these local chemical conditions change, their leverage on corrosion processes change. Again, small changes in chemistry produce large effects on corrosion.

- Stress and temperature: Both stress and temperature have high leverages on corrosion through their geometric and exponential influences. Stress and temperature interact with other aspects of the environments at an LA_i to produce possibly synergistic effects.

Finally, other factors relate to the variability of occurrence or the measurement of corrosion:

- Different factors affect variability of initiation and propagation, and the total failure time depends on both stages.

- Values of K_{Iscc} are both variable, where measured, and uncertain at best in many cases.

- Results from inspection and monitoring are sometimes not reliable.

The factors of materials, environmental, and physical variables that are identified here may be an overstatement of the total variability that actually occurs although each

element is an undeniable consideration. Regardless, such variability needs to be considered in all aspects of the CBDA.

Having thus considered such variability in the overall combination of materials and environments, it is necessary to develop a practical response in which the nature of variability does not overwhelm the need for decisive engineering actions.

However, considering the implications of these variabilities rationalizes the occasional occurrence of a single failure in a large array of many elements. Such a single occurrence often is surprising to engineers who are not familiar with corrosion and the highly leveraged effects of environments.

Having recognized the nature of variability in SCC and corrosion in general, some method of characterizing such variability is necessary. Such a characterization is necessary both to describe the mean failure behavior and the dispersion of the data which in turn provides a basis for assessing when the earliest failures would occur. The choice of methods to approach such variability is discussed in other references including works by Shibata *[22]*, Nelson *[23]* and Abernethy *[24]*. Approaches to considering statistical implications of SCC are discussed also by Staehle and Gorman *[25]* and Staehle *[13]*.

[7] Accelerated Testing

When the expected performance is uncertain and a design life for reliable performance is specified, it is often necessary to conduct testing to determine whether the design will be adequate for the design life. Since design lives are typically long with respect to the available time for development and design, accelerated tests are organized with the objective of assessing long term design life using short term but accelerated testing.

There are many possible accelerated tests used for various applications. For example, the salt spray test is widely used to assess performance in sea water and in road salt conditions. Typically, variables of temperature, stress or temperature are used to provide acceleration for accelerated tests. For example, Fig. 14 shows the effect of temperature on the SCC of Alloy 600 in pure water. Here, testing at 400°C can be extrapolated to operating temperatures of about 320°C for the application of Alloy 600 in steam generators used in pressurized water nuclear reactors.

Accelerated tests such as that shown in Fig. 14 are well known and widely used. However, there are certain precautions that need to be considered in organizing accelerated testing.

- The mode of failure that is being measured in the accelerated test should be the same as that affecting the long term operation.

- Accelerated testing should account for all the LA_i's that can be sufficiently aggressive to produce failure before or in the range of the design life.

A major problem with accelerated tests is the difference between their statistical dispersion and that of the application. Figure 15 shows the occurrence of SCC failures at welds in stainless steel pipes used in boiling water nuclear reactors (BWR) exposed to

water in the temperature range of 280 to 290°C *[27]*. Here, the earliest failures occurred in about 80 days and accounted for fractions failed of about 0.00001 and 0.0001 (depending on the pipe size); on the other hand, the characteristic time for failures (the Weibull characteristic being θ which is similar to the mean value) is 1675 and 144 years, respectively. These data have been correlated using Weibull statistics such as those described in detail by Abernethy *[24]*. These data show that the earliest failures occur substantially earlier than the characteristic values. This means that accelerated testing needs to consider both the earliest failures, as indicated by the dispersion of data, and the mean values. Rarely does accelerated testing in corrosion obtain such data.

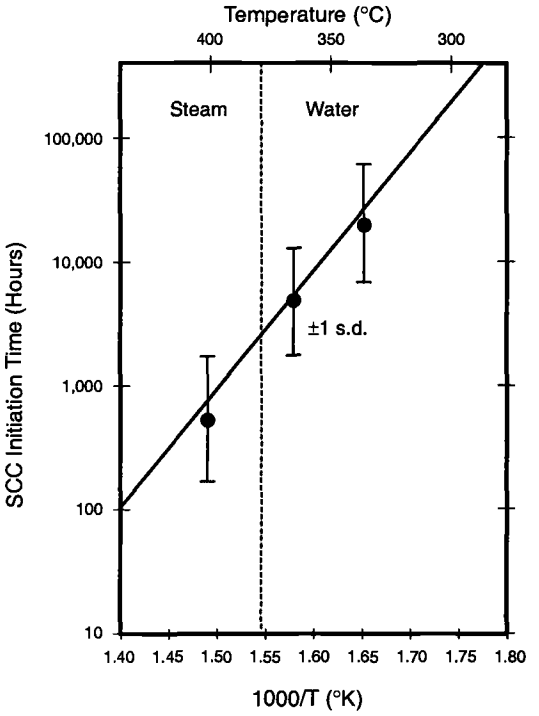


Figure 14 - *Time to failure versus 1/T for the low potential SCC of Alloy 600 exposed to pure water and steam. (From Jacko [26].)*

If it is supposed that the mean value of the accelerated tests is less than the application by a factor of 10 to 1000, it does not follow that the dispersions of data for the accelerated testing and the application are the same. The problem is illustrated in Fig. 16. Figure 16 shows schematically that the dispersion of results from the accelerated test is steeper than that of the application. The more narrow dispersion (a higher value of the Weibull slope i.e. decreasing dispersion of data) occurs usually when the intensity of the stressors is increased relative to the application.

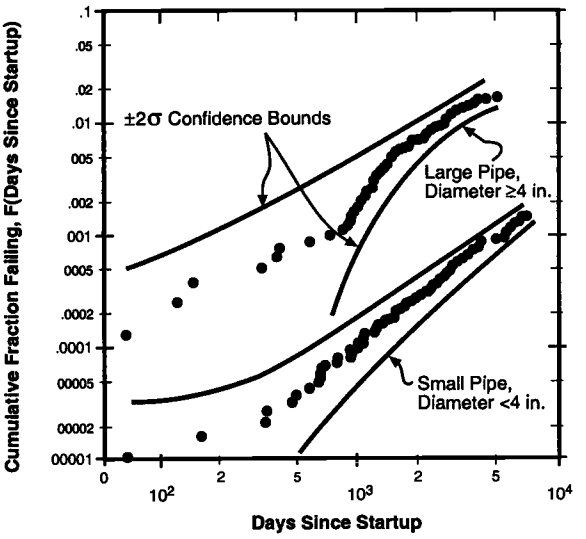


Figure 15 - *Cumulative fraction failed versus time for piping of two ranges of diameters exposed in boiling water nuclear reactors where the environments are pure water. The larger diameter pipes include only IGSCC, and the smaller pipes include all failure modes although they are mainly IGSCC. The Weibull characteristics, θ, and slopes, b, are 144 years and 1.2 and 1675 years and 1.4, respectively, for the large and small pipes. (Adapted from Eason and Shusto [27].)*

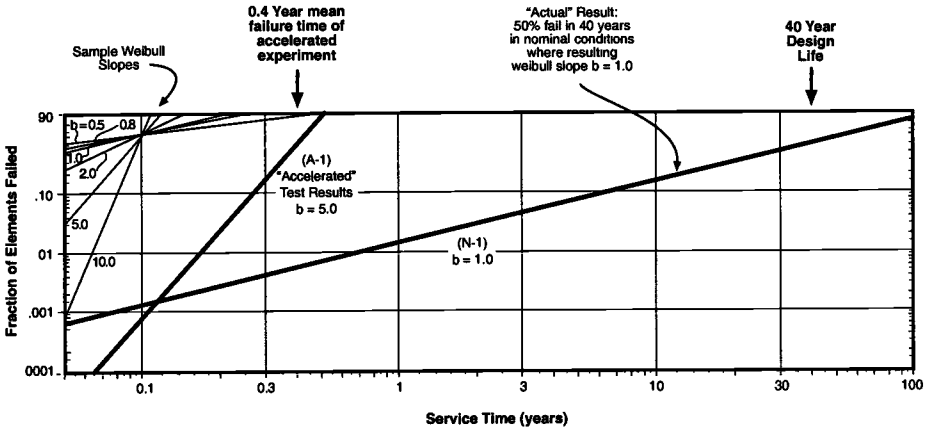


Figure 16 - *Schematic plot for fraction failed versus time for field data and for accelerated tests. Weibull coordinates used.*

In general, as the magnitude of the stressors used in accelerated tests increases (e.g. stress, temperature, and concentration) the dispersion of data decreases. The result of the difference in dispersion of the accelerated test and the application is that, while the mean values may be quite different, the values at 0.001 fraction failed may be about the same with no acceleration as illustrated in Fig. 16. Thus, the accelerated test has provided no insight into the earliest failures. While such a difference as a function of fraction failed can be accounted for by conducting tests with intermediate stressors, the possibility that such a problem may occur first has to be recognized.

[8] Prediction

The set of steps **[1]** through **[7]** provide the bases for predicting corrosion-related performance or for providing assurance that the design life objectives can be achieved. The information in these steps is integrated for the various LA_is to predict the occurrence of failure for each. The aggregation of predictions for the separate LA_is is considered explicitly in connection with the LAM of Fig. 17.

Predictions are developed essentially at two times. One is in the course of the initial design. The second occurs when the components are evaluated throughout their life as data are accumulated from inspections. Such evaluations are also part of the Fitness for Service (FFS) evaluations.

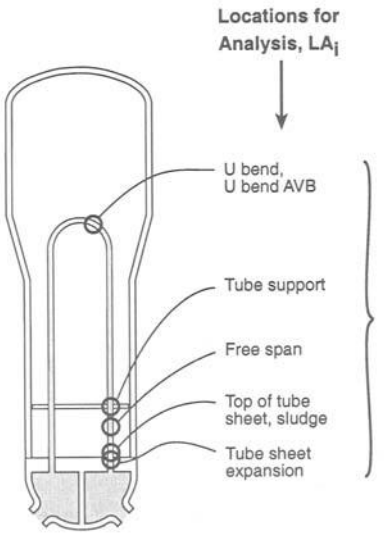
[9] Monitoring and Feedback

At the stage of monitoring and feedback, there are essentially two kinds of information that are developed. One set of information is obtained from instrumentation or periodic analyses that monitors chemistry (conductivity, pH, concentration, impurity species) at various locations in an operating system. Similar types of information are obtained for other important performance parameters including temperature, power, flow, and pressure. Much of such information is obtained continuously. The other set of information is obtained from periodic inspections where LA_is and other useful indicators are measured or monitored. Such information is compared from successive inspections, and trend lines are developed to anticipate conditions at the next inspection and to identify needs for replacement and repair.

The information developed from continuous monitoring and inspections is fed back to operators and designers so that modifications can be developed to minimize damage or to direct the development of replacements or new designs.

[10] Fix

With the information developed in predictions as compared with monitoring, equipment can be repaired or redesigned; operating and shutdown/startup procedures can be modified to minimize the rate of damage. Various remedial operations such as cleaning can be accomplished at shutdowns. Also, improvements in monitoring systems or procedures can be instituted.



(a)

(b)

Locations for Analysis, LA$_i$	Modes (MD$_j$) and Submodes (SD$_j$) To Be Considered														
	Tube Side		Submodes of SCC						Submodes of IGC			Other Modes			
	ID	OD	LPSCC (j=1)	HPSCC (j=2)	AcSCC (j=3)	MRSCC (j=4)	AkSCC (j=5)	PbSCC (j=6)	HPIGC (j=7)	AcIGC (j=8)	AkIGC (j=9)	Wastage (j=10)	Pitting (j=11)	Fatigue (j=12)	Wear (j=13)
Tubesheet Expansion (i=1)	x														
Tubesheet Expansion (i=2)		x													
Top of tubesheet (i=3)	x														
Top of tubesheet (i=4)		x													
Sludge (i=5)		x													
Free span (i=6)	x														
Free span (i=7)		x													
Tube support (hot leg) (i=8)		x													
Tube support (cold leg) (i=9)		x													
U-bend (i=10)	x														
U-bend AVB (i=11)		x													

Figure 17 - *Location for analysis matrix shown in (b). (a) shows the locations for analysis, LA$_i$, that are typical of steam generators used in pressurized water nuclear reactors. The possible modes and submodes of corrosion that can occur at these LA$_i$s are shown at the right. Locations for analysis and modes and submodes from the steam generator are shown in the matrix. (From Staehle [13].)*

Location for Analysis Matrix (LAM)

The CBDA identifies the ten steps which need to be considered. However, it is necessary to utilize a format whereby the information can be brought together and analyzed. A means for accomplishing this objective is the LAM. Such a matrix, as applied to analyzing the corrosion in a steam generator used in pressurized water nuclear reactors, is shown in Fig. 17 *[13]*.

A "Location for Analysis (LA_i)" is the end point of the dot diagrams such as shown in Figs. 5 and 8. An LA_i is a specific location on a material in a component that should be analyzed because it embraces a set of conditions that are likely to produce the earliest and or most intense failures.

Specific features of the LAM in Fig. 17 are the following:

- The LAM itself applies to a specific subcomponent and its constituent materials. The LAM can be executed only where it is possible to be specific about materials and environments.
- In the first vertical column are specific LA_is taken from the steam generator application shown in Figs. 6 and 17 and specifically for the tubing subcomponent. These locations are taken, where appropriate, from inside and outside surfaces, and the ID and OD are designated in the second and third columns.
- Modes and submodes of corrosion are identified and listed in the top three rows.
- The LA are identified with the "i" subscript.
- The Modes, MD_j, and Submodes SD_j are identified with the "j" subscript.
- The open boxes are the locations where the information for the respective cells, LA_i - MD_j/SD_j combinations, is required. More space may be required (an appropriate response may require a several page analysis) depending on the information used to respond to specific LA_i - MD_j/SD_j combinations.
- The individual cells demand a response and identify where some action should be taken. The response may be as simple as a decision that there is no response or no action, e.g. the cell may be omitted, but is done so explicitly. Such actions then become part of the overall design record.
- The individual cells are the locations where specific mathematical analyses can be applied.

Steps in developing the LAM are as follows:

[1] Chronological Stage

Table 1 identifies the stages that equipment and components sustain from their manufacturing to their operation and shutdowns. Since failures have been observed and are extensively documented at every one of these stages, any analysis has to consider each of these stages. While it is natural to consider the steady state condition as the focus for analysis, this stage is not always the one in which failures occur. It may be necessary to account for inputs to the LAM from several chronological stages.

[2] Reference Subcomponents

The second step is to select a subcomponent for analysis. A "subcomponent" in this framework would be the tubes or the vessel wall in a heat exchanger, rebars or the concrete in concrete construction, the engine block material or the valves in an internal combustion engine.

It is at the subcomponent level that specific judgments can be developed for materials and local environments.

[3] Identify Location for Analysis, LA_i

The LA_is, as noted in the left column of Fig. 17b, are where specific analyses are conducted. These LA_is are selected primarily because they epitomize locations where corrosion is the most intense and the most rapid. It is at these locations where the factors of environment, stress, and materials combine to produce the most aggressive total conditions.

Such locations would be selected by experienced engineers based on the steps **[1]** (Environmental Definition, including chemistry, temperature, stress) and **[2]** (Material Definition) of the CBDA.

[4] Identify Modes, MD_j, and Submodes, SD_j

This step is based on steps **[3]** (Mode Definition) and **[4]** (Superposition) of the CBDA. The objective of this step is to determine what modes and submodes are most likely to occur over the range of LA_is of the subcomponent. These become the entries into the row at the top of the LAM shown in Fig. 17. With these entries come the quantitative description of the rates of the modes and their dependencies upon the primary variables.

[5] Develop Location for Analysis Matrix, LAM

With the LA_i and MD_j/SD_j identified in **[3]** and **[4]** the LAM can be developed with specific entries into the columns and rows. This is now the working matrix that provides the framework for prediction.

[6] Take Explicit Actions on the i-j Cells

The specific LAM contains i x j cells that have to be considered and acted upon. Actions that can be taken for each of the cells are the following:

- The cell can be eliminated as not relevant. Eliminating a cell would be easily justified if one of the modes or submodes was clearly irrelevant to the LA_i.
- The cell might be neglected if the result would be inconsequential. Such a decision might be based on the local tensile stress (applied or residual) being too low or compressive.
- Prior engineering knowledge or field performance of a similar LA_i would be used to evaluate the cell.
- A fundamental analysis would be conducted to determine the dependencies upon applicable primary variables.
- Go/no go experiments would be conducted to determine whether and to what extent the cell is significant.
- Accelerated tests would be conducted to obtain the necessary experimental dependencies of relevant principal variables.
- Some cells would be similar or identical and could be modeled with the same information.

The explicit actions taken for each i-j cell become a part of the design record of a subcomponent. The fact that such an action has to be considered makes each cell a reminder to designers that cannot be neglected.

[7] Develop Quantitative Relationships

For some i-j cells it may be necessary to develop quantitative relationships that account for environmental definition **[1]**[6], material definition **[2]**, mode definition **[3]**, failure definition **[5]** and statistical definition **[6]**. The core of whatever quantitative relationships are developed will account for whatever of the principal variables are necessary.

These quantitative relationships can be developed in any or a combination of the ways identified in **[6]**[7] (Take Explicit Actions on the i-j Cells).

[6]These bracketed items are from the discussion of the CBDA.

[7] From LAM discussion.

[8] Identify Work to be Done

Additional work may be required to obtain data or information that is necessary to develop quantitative relationships. This information would be obtained by analysis, experiments or by collecting information from engineering performance or from the technical literature.

[9] Integration of Results for Subcomponent

Once the individual cells of the LAM for single subcomponents have been evaluated, then the overall performance of the component and then the system can be predicted. The overall performance of a single subcomponent may be determined by identifying the overall failure probability from a standard equation that gives the overall failure probability in terms of the individual failure probabilities of the individual LA_is *[13]*.

[10] Integration of Results for Component

In the steam generator of Fig. 6 the tubes are a subcomponent. Other subcomponents of the steam generator include tube supports, anti-vibration bars, the tubesheet, and the vessel. The overall reliability of the steam generator depends on the performance of each of the subcomponents. Each of these would be analyzed in the same terms as those for the tubes as described in Fig. 17.

[11] Assess Need for Modifications

When the quantitative assessments are completed, the need for certain modifications of the subcomponents and components will become apparent. This point is the same as step 10 of the CBDA.

Conclusions

1. The corrosion-related performance of subcomponents can be analyzed explicitly in terms of the CBDA/LAM method. This approach integrates all the important contributions from corrosion.

2. The CBDA/LAM method provides frameworks within which mathematical expressions can be utilized to quantify corrosion at specific LA_is.

3. This CBDA/LAM approach provides a basis for the explicit considerations of corrosion in such a way that they can become part of the design record and are not omitted in the apparent complexity of corrosion-related phenomena.

4. The CBDA/LAM approach provides an approach that can be understood and utilized by both materials and design organizations.

Acknowledgments

I appreciate the encouragement of Dr. R. Kane, Chairman of this meeting and President of Intercorr, in preparing this paper. I appreciate also the support of my staff in assembling the necessary information including M. Ilg, B. Lea, T. Springfield and J. Ilg. Dr. Z. Fang reviewed the manuscript and provided important suggestions. I am indebted to many of my colleagues for suggestions and past discussions that have been used here.

References

[1] Staehle, R. W., "Understanding 'Situation-Dependent Strength' : A Fundamental Objective in Assessing the History of Stress Corrosion Cracking," *Environment Induced Cracking of Metals, NACE-10,* B. E. Ives and R. Gangloff, Eds., NACE International, Houston, 1990, pp. 561-612.

[2] Staehle, R. W. "Environmental Definition," *Materials Performance Maintenance,* R. W. Revie, V. S. Sastri, M. Elboujdaini, E. Ghali, D. L. Piron, P. R. Roberge and P. Mayer, Eds., Pergamon Press, Ottawa, 1991, pp. 3-43.

[3] Cullen, W. H., "Review of IGA, IGSCC and Wastage of Alloys 600 and 690 in High-Temperature Acidified Solutions," *Control of Corrosion on the Secondary Side of Steam Generators,* R. W. Staehle, J. A. Gorman and A. R. McIlree, Eds., NACE International, Houston, 1996, pp. 273-304.

[4] Pourbaix, M. J. N., *Thermodynamics of Dilute Aqueous Solutions,* Edward Arnold, London, 1949.

[5] Spähn, H., Wagner, G. H., and Steinhoff, U., "Stress Corrosion Cracking and Cathodic Hydrogen Embrittlement in the Chemical Industry," *Stress Corrosion Cracking and Hydrogen Embrittlement of Iron Base Alloys, NACE-5,* R. W. Staehle, J. Hochmann, R. D. McCright and J. E. Slater, Eds., NACE International, Houston, 1977, pp. 80-110.

[6] Coriou, H., Grall, L., Olivier, P., and Willermoz, H., "Influence of Carbon and Nickel Content on Stress Corrosion Cracking of Austenitic Stainless Alloys in Pure or Chlorinated Water at 350° C.," *Fundamental Aspects of Stress Corrosion Cracking, NACE-1,* R. W. Staehle, A. J. Forty, and D. van Rooyen, Eds., NACE International, Houston, 1969, pp. 352-359.

[7] Cox, B., "Environmentally Induced Cracking of Zirconium Alloys – A Review," *Journal of Nuclear Materials,* Vol. 170, No. 1, 1990, pp. 1-23.

[8] Speidel, M. O. and Atrens, A., "Stress Corrosion Cracking and Corrosion Fatigue Fracture Mechanics," *Corrosion in Power Generating Equipment,* Plenum Press, New York, 1984, pp. 85-132.

[9] Kerns, G. E., Wang, M., and Staehle, R. W., "Stress Corrosion Cracking and Hydrogen Embrittlement in High Strength Steels," *Stress Corrosion Cracking and Hydrogen Embrittlement of Iron Base Alloys, NACE-5,* R. W. Staehle, J. Hochmann, R. D. McCright and J. E. Slater, Eds., NACE International, Houston, 1977, pp. 700-735.

[10] Latanision, R. M. and Staehle, R. W., "Stress Corrosion Cracking of Iron Nickel Chromium Alloys," *Fundamental Aspects of Stress Corrosion Cracking, NACE-1,* R. W. Staehle, A. J. Forty and D. van Rooyen, Eds., NACE International, Houston, 1969, pp. 214-307.

[11] Steam Generator Owners Group, *Steam Generator Reference Book,* EPRI, Palo Alto, 1985.

[12] Pickering, H. W., Beck, F. H., and Fontana, M. G., "Wedging Action of Solid Corrosion Product During Stress Corrosion of Austenitic Stainless Steels," *Corrosion Journal,* Vol. 18, 1962, pp. 230-239.

[13] Staehle, R. W. "Lifetime Prediction of Materials in Environments," *Uhlig's Corrosion Handbook,* 2nd edition, R. W. Revie, Ed., John Wiley and Sons, New York, 2000.

[14] Staehle, R. W., "Lifetime Prediction," *Proceedings: Corrosion and Its Control in the New Millennium,* R. W. Revie and I. Al-Tai, Meeting Chairmen, NACE International Northern Area Eastern Conference and Exhibition, Ottawa, Ontario, Canada, October 24-27, 1999.

[15] Staehle, R. W., "Combining Design and Corrosion for Predicting Life," presented as a plenary lecture at *Life Prediction of Corrodible Structures*, NACE International, Houston, 1994, pp. 138-291.

[16] Wang , M. T. and Staehle, R. W., "Effect of Heat Treatment and Stress Intensity Parameters on Crack Velocity and Fractography of AISI 4340 Steel," *L'Hydrogene Dans Les Metaux*, Vol. 2, Editions Science et Industrie, Paris, 1972, pp. 342-349.

[17] Copson, H. R., "Effect of Composition on Stress Corrosion Cracking of Some Alloys Containing Nickel," *Physical Metallurgy of Stress Corrosion Fracture,* T. Rhodin, Ed., Interscience, New York, 1959, pp. 247-269.

[18] Thompson, D. H. and Tracy, A. W., "Influence of Composition on Stress-Corrosion Cracking of Some Copper-Base Alloys," *Journal of Metals,* Vol. 1, No. 2, 1949, pp. 100-109.

[19] Berge, P., "Importance of Surface Preparation for Corrosion Control in Nuclear Power Stations," *Materials Performance,* Vol. 11, 1997, pp. 56-62.

[20] Staehle, R. W. and Gorman, J. A., "Development and Application of Intensity and Operating Diagrams for Predicting the Occurrence and Extent of Stress Corrosion Cracking," *Corrosion Science and Engineering: Proceedings of an International Symposium in Honour of Marcel Pourbaix's 85th birthday,* Rapports Techniques Vol. 157-158, CEBELCOR, Brussels, 1989, pp. 199-209.

[21] Staehle, R. W., "Development and Application of Corrosion Mode Diagrams," *Parkins Symposium on Stress Corrosion Cracking,* S. M. Bruemmer, E. I. Meletis, R. H. Jones, W. W. Gerberich, F. P. Ford, and R. W. Staehle, Eds., TMS, Warrendale, Pennsylvania, 1992, pp. 199-209.

[22] Shibata, T., "1996 W. R. Whitney Award Lecture: Statistical and Stochastic Approaches to Localized Corrosion," *Corrosion Journal,* Vol. 52, No. 11, 1996, pp. 813-830.

[23] Nelson, W., *Accelerated Testing: Statistical Models, Test Plans, and Data Analyses,* John Wiley and Sons, New York, 1990.

[24] Abernethy, R. B., *The New Weibull Handbook, Second Edition,* R. B. Abernethy Publisher, North Palm Beach, Florida, 1996.

[25] Staehle, R. W., Gorman, J. A., Stavropoulos, K. D., and Welty, C. S., Jr., "Application of Statistical Distributions to Characterizing and Predicting Corrosion of Tubing in Steam Generators of Pressurized Water Reactors," *Life Prediction of Corrodible Structures, Proceedings of the 3rd International Relations Committee Symposium,* NACE International, Houston, 1994, pp. 1374-1399.

[26] Jacko, R. J., "Corrosion Evaluation of Thermally Treated Alloy 600 in Primary and Faulted Secondary Water Environments," *EPRI NP-6721-SD,* EPRI, Palo Alto, 1990.

[27] Eason, E. D. and Shusto, L. M., *Analysis of Cracking in Small-Diameter BWR Piping,* NP-4394, EPRI, Palo Alto, 1986.

Digby D. Macdonald[1] and George R. Engelhardt[2]

Deterministic Prediction of Localized Corrosion Damage in Power Plant Coolant Circuits

Reference: Macdonald, D. D. and Engelhardt, G. R, **"Deterministic Prediction of Localized Corrosion Damage in Power Plant Coolant Circuits,"** *Environmentally Assisted Cracking: Predictive Methods for Risk Assessment and Evaluation of Materials, Equipment, and Structures, ASTM STP 1401*, R. D. Kane, Ed., American Society for Testing and Materials, West Conshohocken, PA, 2000.

Abstract: The accumulation of damage due to localized corrosion [pitting, stress corrosion cracking (SCC), corrosion fatigue (CF), crevice corrosion (CC), and erosion-corrosion (EC)] in complex industrial systems, such as power plants, refineries, desalination systems, etc., poses a threat to continued safe and economic operation, primarily because of the sudden, catastrophic nature of the resulting failures. Of particular interest in managing these forms of damage is the development of robust algorithms that can be used to predict the integrated damage as a function of time and as a function of the operating conditions of the system. Because complex systems of the same design rapidly become unique, due to differences in operating histories, and because failures are rare events, there is generally insufficient data available on any given system to derive reliable empirical models that capture the impact of all (or even some) of the important independent variables. Accordingly, the models should be, to the greatest extent possible, deterministic with the output being constrained by the natural laws. In this paper, the theory of the initiation of damage, in the form of pitting, is briefly outlined. We then describe the deterministic prediction of the accumulation of damage from SCC and CF in Type 304 SS components in the primary coolant circuits of Boiling Water (Nuclear) Reactors (BWRs) and from pitting and SCC in low-pressure steam turbine disks. These cases have been selected to illustrate the various phases through which localized corrosion damage occurs.

Keywords: Deterministic, prediction, corrosion damage, pitting, stress corrosion cracking, corrosion fatigue.

[1] Professor of Materials Science and Engineering, Pennsylvania State University, 517 Deike Building, University Park, PA 16802.

[2] Sr. Research Engineer, Pure and Applied Physical Sciences Division, Poulter Laboratory, SRI International, 333 Ravenswood Avenue, Menlo Park, CA 94025.

Copyright© 2000 by ASTM International www.astm.org

Introduction

Over the past decade, we have developed powerful, deterministic models and algorithms for predicting the accumulation of damage due to localized corrosion, including pitting, stress corrosion cracking (SCC), crevice corrosion (CC), and corrosion fatigue (CF) in complex industrial systems. Systems that have been modeled to date include electrical power generating facilities [*1-8*], among others. These models and algorithms are "deterministic" because their predictions are constrained by the relevant natural laws. Because corrosion is essentially an electrochemical phenomenon, the primary constraints are the conservation of charge and Faraday's Law. The advantage of determinism, as opposed to empiricism, is that deterministic models require minimal calibration (for example, a single crack growth rate for a given set of environmental and mechanical conditions, in the case of SCC). Accordingly, deterministic models may be used to predict damage in systems that are unique (as are all industrial systems, including power plants, once they have operated for any significant time), for which failure databases do not exist. The "coupled environment" models [coupled environment pitting model (CEPM), coupled environment crevice model (CECM), coupled environment fracture model (CEFM), and the coupled environment corrosion fatigue model (CECFM)] that have been used in this work are, to our knowledge, the only currently available deterministic models for predicting the evolution of damage due to localized corrosion [*2-4, 9-15*]. Furthermore, when coupled with the point defect model (PDM) for passivity breakdown, and hence for the nucleation of damage, the resulting algorithms provide a comprehensive theoretical basis for predicting localized corrosion damage [*14-16*]. The algorithms have been used to predict damage due to stress corrosion cracking in BWRs (the DAMAGE-PREDICTOR and ALERT codes, eleven reactors being modeled to date) [*1*], pitting damage in condensing heat exchangers [*2*], pitting/SCC in LP steam turbine disks [*3*], pitting in CVD nickel detector tubes in the US/Canada neutrino detection experiment, pitting of boiler tubes in fossil-fueled power stations under wet lay-up conditions, and pitting of high strength bearings in helicopter rotor hubs. Currently, the models are being used to predict the nucleation and accumulation of SCC and CF damage in aluminum aircraft alloys and in low-pressure steam turbine blades. The underlying component models in the algorithm referred to above together with their functions, underlying mechanisms, and constraining natural laws are summarized in Table 1.

The progressive development of damage caused by the nucleation and growth of pits and stress corrosion cracks in various components in the heat transport circuits of water-cooled thermal power plants is recognized as a major contributor to unscheduled down time and hence to operating losses. The key issue is that damage forces unscheduled shutdowns, resulting in lost production and often in the need for the utility to purchase replacement power for its customers. It has been estimated that, depending on the extent of failure and damage to the turbine and surrounding machinery, equipment replacement costs in the United States range from $2 million for extensive repair to more than $6 million for replacement of an entire turbine rotor. If the development of damage could be predicted accurately, then preventive maintenance might be carried out during scheduled

Table 1: Summary of Deterministic Models for Predicting Localized Corrosion Damage

Algorithm	Component Models *	Function (calculates)	Underlying Mechanism	Constraining Natural Laws
Damage Function Analysis (DFA)	1.CHEM	1. Chemical composition of environment	1. Mass action/equilibrium thermodynamics	1. Conservation of mass and charge
	2. PDM	2. Pit nucleation rate	2.Cation vacancy condensation	2. Conservation of mass and charge
	3. MPM	3. Corrosion potential	3.Charge/mass transfer and mixed potential theory	3.Conservation of mass and charge
	4. CEPM	4. Pit Growth rate	4. Dissolution with coupling between pit internal and external environments	4. Conservation of mass and charge
Damage-Predictor REMAIN ALERT	1.RADIOCHEM	1. Radiolytic species concentrations	1. Water radiolysis	1. Conservation of mass and change
	2. MPM	2. Corrosion potential	2. Charge/mass transfer and mixed potential theory	2. Conservation of mass and charge
	3. CEFM	3. Crack growth rate	3. Dissolution with coupling between crack internal and external environments	3. Conservation of mass and charge
Miscellaneous	1. CECM	1. Crevice corrosion rate	1. Dissolution with coupling between crevice internal and external environments	1. Conservation of mass and charge
	2. CECFM	2. Fatigue crack growth rate	2. Dissolution with coupling between crevice internal and external environments.	2. Conservation of mass and charge

* PDM= Point Defect Model; CHEM= Chemistry Model; MPM= Mixed Potential Model; CEPM=Coupled Environment Pitting Model; RADIOCHEM= Water Radiolysis Model; CEFM= Coupled Environment Fracture Model; CECM= Coupled Environment Crevice Model; CECFM= Coupled Environment Corrosion Fatigue Model.

shutdowns, thereby greatly decreasing the impact of corrosion on tne economics of operation. Similarly, the economics of extending the operating lives of power generating facilities depends heavily on our ability to predict the development of corrosion damage that might occur in the future.

The development of effective localized corrosion damage prediction technologies is not only essential for the successful avoidance of unscheduled downtime, but it is vital for the successful implementation of life extension strategies. Currently, corrosion damage is extrapolated to future times by using various empirical models coupled with damage tolerance analysis (DTA). In this strategy, known damage is surveyed during each subsequent outage, and the damage is extrapolated to the next inspection period allowing for a suitable safety margin. One of the present authors has argued that this strategy is inaccurate and inefficient, and that in many instances it is too conservative [*17*]. Instead, we suggest that damage function analysis (DFA) [*14*, *16-18*] is a more effective method for predicting the progression of damage, particularly when combined with periodic inspection. Although corrosion is generally complicated mechanistically, a high level of determinism has been achieved in various treatments of both general and localized corrosion, and the resulting deterministic models can be used to predict accumulated damage in the absence of large calibrating databases.

In this paper, the foundations of the deterministic predictions of damage due to localized corrosion are outlined. The application of damage function analysis (DFA) is illustrated with reference to the prediction of the time to failure of condensing heat exchangers due to pitting, of the time to failure of low pressure steam turbine disks due to stress corrosion cracking, and to the accumulation of damage due to stress corrosion cracking (SCC) and corrosion fatigue (CF) in water-cooled nuclear power reactors.

Nucleation of Localized Corrosion Damage

All localized corrosion on passive metals and alloys (e.g., stainless steels) begins with passivity breakdown. Accordingly, any viable, mechanistically based model for the initiation of localized corrosion must address that issue. A commonly observed scenario is that stress corrosion and corrosion fatigue cracks nucleate from pits, so that any viable theoretical treatment for the accumulation of localized corrosion damage on a surface must begin by addressing not only passivity breakdown but also the transition from metastable pitting to stable pitting, pit growth, and the transition of a pit into a crack. This must be done while recognizing that the nucleation of damage is a progressive phenomenon, in that new damage nucleates while existing damage grows and dies. The theory that has been developed to account for the nucleation of localized corrosion damage forms the basis of damage function analysis (DFA) [*16-18*], which has now been developed to the point where damage due to pitting, SCC, and CF may be predicted with considerable accuracy in actual industrial systems [*2*, *3*]. Space does not allow a comprehensive discussion of all aspects of the theory of initiation here, so only a brief outline will be given.

The point defect model (PDM) [*14*, *18*] for the growth and breakdown of passive films attributes passivity breakdown at a single site on a surface to the condensation of cation

vacancies at the metal/film interface. This process is postulated to occur at a structural inhomogeneity within the barrier layer of the passive film (e.g. at the edge of an inclusion), which is characterized by high cation vacancy diffusivity. Condensation occurs because some environmental stress (e.g. the absorption of chloride ions into surface oxygen vacancies) results in the generation of cation vacancies at the film/solution (f/s) interface and hence in an enhanced flux of cation vacancies across the barrier layer from the (f/s) interface to the metal/film (m/f) interface. If the flux is sufficiently high so that all of the vacancies arriving at the m/f interface cannot be annihilated by cation injection from the underlying metal, the excess vacancies condense to form a void. The void represents a local separation of the barrier layer from the underlying metal so that the barrier layer ceases to grow into the metal while dissolution at the f/s interface continues to occur. However, growth of the barrier layer into the metal continues to take place at the surrounding areas, where detachment of the film has not occurred, at a rate in the steady state that matches the film dissolution rate. Accordingly, the film over the cation vacancy condensate thins and eventually ruptures to mark a passivity breakdown event. The resulting pit nucleus may repassivate "promptly" due to its failure to achieve the required separation between the local anode (in the forming cavity) and the local cathode (on the external surface), as demanded by the differential aeration hypothesis. If prompt repassivation occurs, the event is termed "metastable", and it is detected as a current pulse in the external circuit when the system is under potential control. If the nucleus survives, by establishing the required anode/cathode separation, it exists as a stable pit, which will continue to grow until it dies due to "delayed" repassivation. One reason that has been postulated [*18*] for delayed repassivation is the inability of a pit to obtain the necessary resources (oxygen reduction) from the external surfaces to meet the growth demands. This may happen either because of an inherent limitation in the rate of oxygen reduction or because neighboring pits compete for the same resources. This latter scenario results in the "survival of the fittest", and hence is Darwinian in nature [*18*]. One inescapable result of delayed repassivation is that eventually *all* pits must die.

On any real surface, there exists a distribution in potential breakdown sites. In the present version of the PDM [*14-18*], it is assumed that the sites are normally distributed with respect to the cation vacancy diffusivity. That assumption leads to an analytical expression for the metastable pit nucleation rate at an observation time of τ as [*16*]

$$n(r) = A\frac{exp\left[-\left(\frac{a}{\tau}+b\right)^2\right]}{\tau^2} \tag{1}$$

where

$$a = \frac{\xi}{\sqrt{2}\sigma_D B} \tag{2}$$

$$b = \frac{J_m}{\sqrt{2}\sigma_D B} - \frac{\overline{D}}{\sqrt{2}\sigma_D} \tag{3}$$

and

$$B = \frac{\chi F \varepsilon N_A a_x^{\chi/2}}{\Omega RT} \exp\left(\frac{\chi F(\beta.pH + \alpha.E_{corr}) + 2w}{2RT}\right) \tag{4}$$

The parameter a_x is the activity of the aggressive ion (e.g. Cl^-) that adsorbs into a surface oxygen vacancy, α is the polarizability of the f/s interface, and β is the dependence of the potential drop across the f/s interface upon the applied voltage (the corrosion potential, E_{corr}). $\overline{D}$ is the mean cation vacancy diffusivity, σ_D is the standard deviation in D, ξ is the critical (areal) concentration of cation vacancies in the condensate, and Ω is the mole volume of the barrier layer per cation. The parameter J_m is the rate of annihilation of the cation vacancies at the m/f interface, where the film is attached, χ is the barrier layer stoichiometry ($MO_{\chi/2}$), ε is the electric field strength within the film, and F is Faraday's constant. The quantity N_A is Avogadro's number, R is the gas constant, and T is the Kelvin temperature. The parameter w is an energy term related to absorption of aggressive anions into oxygen vacancies at the film/solution interface and the subsequent generation of cation vacancies. All of the parameters contained in Equations (1) to (4) can be measured, with the exception of w, either directly or indirectly. In the case of w, the value must be determined by calibration.

Parameter A is determined by normalization with respect to the finite density of potential breakdown sites on the surface. This quantity does not depend upon the time τ. Accordingly, normalization of the nucleated pit population using the condition

$$N(\infty) = \int_0^\infty n(\tau) d\tau = N_0 \tag{5}$$

requires that

$$A = N_0 / \int_0^\infty \frac{exp\left[-\left(\frac{a}{\tau} + b\right)^2\right]}{\tau^2} d\tau = \frac{N_0 2a}{\sqrt{\pi} erfc(b)} \tag{6}$$

N_0 is the maximum number density of breakdown sites (per cm^2) that can exist on the metal surface (regardless of whether metastable or stable pitting occurs) and erfc(x) is the complementary error function. Accordingly, the metastable pit nucleation rate per unit area of the surface becomes [16]

$$N(\tau) = \frac{N_0}{erfc(b)} erfc\left(\frac{a}{\tau} + b\right) \tag{7}$$

Only stable pits can act as sites for the nucleation of cracks because the cavity must be sufficiently deep for the stress intensity factor to exceed the critical value for crack nucleation (K_{ISCC} and ΔK_{th} for SCC and CF, respectively). Accordingly, we must modify the above theory to calculate the rate of nucleation of stable pits as

$$N_{SP} = \lambda . N_{MS} \tag{8}$$

where λ is the probability that a breakdown event will survive prompt repassivation to form a stable pit. The theory for calculating λ from first principles is currently being developed. However, experiment shows that for stainless steels in chloride containing solutions at ambient temperature, λ has a value of about 10^{-4}; that is only about one in ten thousand breakdown events survives to become a stable pit. Of course, those that survive prompt repassivation are subject to delayed repassivation, so that a pit that grows to a size that can nucleate a crack is, indeed, a rare event.

By combining Equation (8) with a pit growth model, and by assuming that delayed repassivation is a first order process that is characterized by a decay constant γ, it is a relatively straightforward task to calculate the damage function (DF). The DF is the histogram of (stable) pit density on the surface versus pit depth in preselected increments. The value of the DF is that it corresponds to the measured pit depth distribution, and hence represents a vital link between experiment and theory. In order to illustrate some of the properties of the DF, we plot in Figure 1 three predicted damage functions for different values of the delayed repassivation constant, γ. The quantity plotted on the ordinate is $\Delta F(L_1, L_2)/N_o\lambda$, where $\Delta F(L_1, L_2)$ is the number of pits having depths between L_1 and L_2 per unit area for a given observation time. The DFs shown in Figure 1 were actually calculated for aluminum under the conditions given in the caption, and while they will differ from those predicted for stainless steels in power plant coolant circuits they provide a basis for exploring a number of important properties. Thus, for the parameter values chosen, nucleation occurs "instantaneously"; that is, all of the pits nucleate within the first time increment. In the absence of delayed repassivation ($\gamma = 0$), all of the pits grow in unison and the DF takes the form of a single vertical bar. However, when delayed repassivation occurs, pits die at various times that are less than the observation time and hence populate depths that are less than the maximum depth. Thus, for $\gamma = 3$ year^{-1}, only a small number of pits are still alive after an observation time of one year. In the case of more intense repassivation ($\gamma = 5$ year^{-1}), essentially all pits are predicted to be dead. Damage functions of the type shown in Figure 1 have been calculated for different observation times, chloride concentrations, temperatures, and oxygen concentrations (and hence E_{corr}). As expected, each of these independent variables has an important impact on the depth of the predicted damage and on its distribution. For example, reducing $[Cl^-]$ or E_{corr} induces a transition from instantaneous nucleation to progressive nucleation, where new damage nucleates while existing pits grow and die. This, too, has a profound impact on the form of the DF.

Another important advantage of damage function analysis (DFA) is that the DF expresses the "integral damage" (i.e., the penetration depth for a given observation time), and hence leads to a natural definition of failure. Thus, with reference to Figure 1, no failure would have occurred if the critical dimension (h_{crit}, e.g. thickness of a steam generator tube) was 0.15 cm, but failure would have occurred if $h_{crit} = 0.1$ cm. In the present discussion, we are particularly interested in defining the critical dimension for the nucleation of stress corrosion and corrosion fatigue cracks.

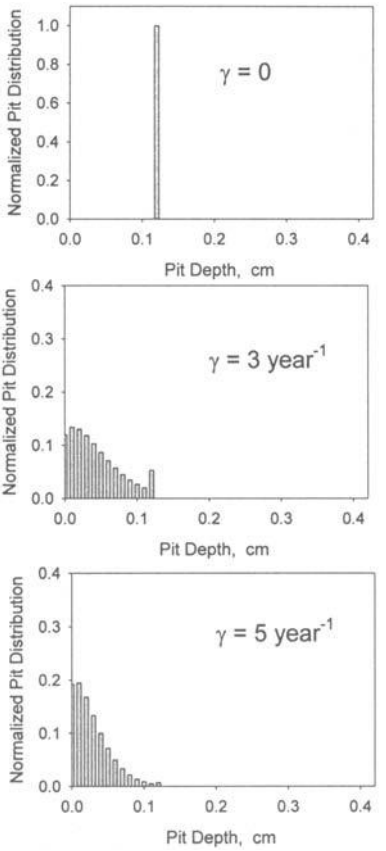


Figure 1. Influence of the value of γ on normalized pit distribution for C_{NaCl} = 0.1 mol/L, E_{corr} = -0. 384 V (SHE), $_{pH}$ = 7, T = 25 ℃, and t_{obs} = 1 year.

According to Chen, et. al., [*19*], two conditions must be satisfied for crack nucleation to take place; namely, $K_I > K_{ISCC}$ (for SCC) or $\Delta K_I > \Delta K_{I,th}$ (CF) and $(dL/dt)_{crack\ growth} > (dL/dt)_{pit\ growth}$. The first requirement defines the mechanical (fracture mechanics) condition that must be met for the prevailing stress and geometry while the second simply says that the nucleating crack must be able to "out run" the pit. Thus, we may define the critical pit depth for the nucleation of a crack as

$$h_{crit} = \left(\frac{K_{ISCC}}{A' \sigma} \right)^2 \tag{9}$$

where σ is the stress and A' is a geometry dependent parameter that also incorporates short crevice factors. An equivalent expression can be written for the nucleation of a corrosion fatigue crack. Note that Eq (*9*) is a necessary, but not a sufficient condition because the velocity constraint must also be satisfied. Comparison of h_{crit} with the DF provides a measure of the probability that a pit exists on the surface of sufficient depth to satisfy the fracture mechanics condition. Alternatively, by calculating the DF for different observation times, it is possible to determine that time at which Eq (*9*) is satisfied to a preselected level of probability. The resulting time is termed the *crack initiation time*. An example of this type of calculation is given later in this paper. Note that the DF provides a *probability* that a super critical pit will exist. In order to determine whether a super critical pit *actually* exists, it is necessary to multiply the probability given by the DF by the number of potential breakdown sites and by the survival probability. Clearly, the resulting product must be greater than one (pits can exist only as integers).

The concept of *integral damage* introduced above through the damage function is exceedingly important in any discussion of the prediction of corrosion damage. This is because the "integral damage" is determined by integrating over the prior history, within which conditions may have changed at various times. This feature has not yet been incorporated into DFA, but it has been included in our predictions of accumulated damage in BWR primary coolant circuits from pre-existing cracks, as discussed below.

Integral (Accumulated) Damage and Life Time Assessment

In the first case that we will discuss, it is assumed that a crack already exists in the structure and that the initial crack length is known by inspection. This is a common scenario, because most power plant operators perform inspections during scheduled outages. To use the inspection data effectively, it is necessary to extrapolate the damage to the next inspection time, taking into account the expected operating conditions. Extrapolation has been performed, in the past, mostly upon the basis of fracture mechanics models and techniques, which incorporate environmental data only inadvertently. However, the increasing demand for higher availability has led to the development of various radiolysis models for calculating the concentrations of electroactive species, such as H_2, O_2, and H_2O_2, as functions of the reactor operating parameters and the concentration of hydrogen added to the feedwater [*4-7, 20-22*]. One such model, ALERT, combines deterministic water chemistry and corrosion models for calculating radiolytic species concentrations in the HTCs of BWRs and for predicting the damage that accumulates from the corrosion processes (SCC) [*1, 4-7, 9-13*]. Because some of the radiolysis species are electroactive, they are instrumental in establishing the electrochemical corrosion potential (ECP) of components within the HTC [*1, 4-7, 13*]. Extensive work in many laboratories worldwide has established that sensitized Type 304SS becomes increasingly susceptible to intergranular stress corrosion cracking in high

temperature aqueous solutions as the ECP is increased above a critical value [*23*]. Constant extension rate tests (CERTs), using round tensile specimens in actual BWR coolant at 288 °C [24], has led the Nuclear Regulatory Commission (NRC) to adopt a value for the critical ECP (E_{crit}) of –0.23 V (SHE). However, we note that critical potentials as negative as –0.4V (SHE) have been observed in laboratory studies [*23*]. A distribution in E_{crit} in an operating reactor is expected, because of the variability in the degree of sensitization (DOS) of the steel at welds and because of differences in neutron fluence experienced by in-vessel components. Because SCC occurs only when ECP>E_{crit} [*23*], the goal of any water chemistry control protocol for inhibiting cracking in BWR coolant circuits is to displace the ECP to a value that is more negative than the critical value for the component of interest under the prevailing conditions. In hydrogen water chemistry (HWC), which is a mitigation technique that is now being applied to operating reactors, molecular hydrogen is added to the feedwater with the objective of reducing the concentrations of oxidizing species (e.g. O_2, H_2O_2) and of displacing the ECP in the negative direction. One of the primary objectives in developing the chemistry/damage simulation codes was to provide a deterministically based technology for assessing the efficacies of various mitigation technologies without incurring the expense of extensive in-plant testing.

The original code (DAMAGE-PREDICTOR) [*4-7*], from which ALERT was developed, incorporates deterministic modules for estimating the specie concentrations [*8*], the ECP [*13*], and crack growth rate (CGR) [*9-12*] for stainless steel components at closely spaced points around the coolant circuit, as a function of coolant pathway geometry, reactor operating parameters (power level, flow velocity, dose rates, etc.), coolant conductivity, and the concentration of hydrogen added to the feedwater. The radiolytic species concentrations are calculated in the steady state using the radiolysis module, RADIOCHEM, which is based on a model that was originally developed to describe the corrosion of high-level nuclear waste containers [*8*]. Calculation of the ECP was affected by the mixed potential model (MPM) [*13, 25*], which makes use of the fact that, for a system undergoing general corrosion (which is the process that establishes the ECP), the sum of the current densities due to all charge transfer reactions at the steel surface must be zero. By expressing the redox reaction currents in terms of the generalized Butler-Volmer equation, which incorporates thermodynamic equilibrium, kinetic, and hydrodynamic effects, and by expressing the corrosion current in terms of either the point defect model or as an experimentally derived function (both have been used), it is possible to solve the charge conservation constraint for the corrosion potential (ECP). The MPM has been extensively tested against experimental and field data and has been found to provide accurate estimates of the ECP [*1, 25*].

The deterministic crack growth model (the CEFM) [*9-11*] estimates the rate of growth of a crack at any point in the coolant circuit. The CEFM is deterministic, in that it satisfies the relevant natural law; the conservation of charge. Furthermore, a basic premise of the CEFM, that current flows from the crack and is consumed on the external surface, has been demonstrated experimentally [*26, 27*]. To our knowledge, the CEFM and variants thereof (e.g. the CECFM) are the *only currently available models that satisfy the conservation of charge constraint explicitly.* The high degree of determinism is demonstrated by the fact that the models require calibration against only a single

CGR/ECP/conductivity/temperature/stress intensity datum for a given degree of sensitization (DOS) of the steel [*11*].

The MPM and CEFM contain the necessary facilities for modeling noble metal enhanced hydrogen water chemistry (NMEHWC), as affected by the use of catalytic coatings (i.e. noble metals), and for modeling other advanced remedial measures such as dielectric coatings and ultra-low conductivity operation. A considerable achievement of the MPM and CEFM was the prediction that dielectric coatings represented a viable, and indeed an advantageous, alternative to noble metal coatings; a prediction that has been confirmed experimentally by the authors [*28*]. The effectiveness of both strategies arises from modification of the exchange current densities for the redox reactions (oxidation of hydrogen and the reduction of oxygen and hydrogen peroxide) that occur on the steel surface [*6,29*]. In the case of the noble metal coatings, the exchange current densities are increased, with the greatest increase occurring for the hydrogen electrode reaction. This renders hydrogen to be a much more effective reducing agent than it is in the absence of the noble metal, thereby making it much more effective in displacing the ECP in the negative direction. In the case of dielectric coatings, the lower exchange current densities render the metal less susceptible to the ECP-raising oxidizing species, with the result that the ECP is also displaced in the negative direction, even in the absence of hydrogen added to the feedwater.

DAMAGE-PREDICTOR has been used to model eleven operating BWRs, including Duane-Arnold, Dresden-2, Grand-Gulf, River-Bend, Susquehanna, Hamaoka-2, Leibstadt, Perry, and Fermi-2. Additionally, the code has been installed in computers at Fermi-2 and has been provided to researchers at the Argonne National Laboratory for use in their NRC-sponsored program on environmentally influenced cracking of reactor alloys in simulated BWR coolant environments. A "second-generation" code, REMAIN [*30*], has been developed for a German vendor to model BWRs with internal coolant pumps and a third generation code, ALERT, is now used to model BWRs with external pumps. All three generations of code have been validated by direct comparison with plant data (e.g. at the Leibstadt BWR in Switzerland), and are found to simulate accurately hydrogen water chemistry. The codes have also been used to explore various enhanced versions of HWC and to model completely new strategies, such as those that employ noble metal coatings and dielectric coatings. Two of the component models of these codes, in fact, *predicted* quantitatively the effectiveness of dielectric coatings for inhibiting crack growth in stainless steels in high temperature water, and these predictions have been validated by direct experiment [*27, 28*].

The speed afforded by the enhanced ALERT code, which employs optimized mathematical algorithms and C++ programming language, permits near "real time" prediction of the accumulated damage (the crack length vs. time for a preconceived operating history). The accumulated damage is the *expected* crack length, L, which is calculated on a component-by-component basis as a function of the observation time, T, for an envisioned future operating protocol

$$L = \int_0^T \frac{\partial L}{\partial t} dt \tag{10}$$

Crack growth rates are calculated from the coupled environment fracture model as

$$\frac{\partial L}{\partial t} = f[power(t), chemistry(t), L(t)] \tag{11}$$

in which the dependencies on the first two independent variables arise from the impact of radiolysis, temperature, flow rate, and impurity concentration on the water chemistry experienced by the crack. However, it is extremely important that any model that is used in calculations of this type incorporates the impact of changing crack geometry, L(t), on the crack growth rate, as discussed below. The CEFM and variants thereof satisfy this condition.

The ALERT code calculates crack length, L, over the anticipated service life(T) of a component, as the accumulation of incremental crack advances over N periods of time $\Delta t_1,...,\Delta t_i,...\Delta t_N$

$$L_i = L_{i-1} + \left(\frac{\partial L}{\partial t}\right)_i \Delta t_i \tag{12}$$

$$T = \sum_{i=1}^{N} \Delta t_i \tag{13}$$

The crack growth rate is assumed to be time-independent for each interval, Δt_i, which is a reasonable assumption provided that the increments are sufficiently small. The initial crack length, L_0, corresponds to the depth of a pre-existing crack (as may have been detected during an inspection or assumed for a safety analysis scenario). The running time for simulating a typical ten-year operating period is less than 10 minutes on a desktop computer or on a notebook PC, and is less than a minute for simulating a single state point {water radiolysis + corrosion potential + crack growth rate}.

The importance of recognizing the impact of crack length on crack growth rate is illustrated by the following analysis. Thus, for an occluded crack under constant load, the crack growth rate is predicted to decrease with crack length (and hence time) as noted above. This is due to the fact that, as the crack length increases, a greater IR potential drop occurs down the crack and smaller potential drops occur across the crack tip and across the interfaces external to the crack, where the principal charge transfer reactions take place. Lower potential drops at these locations imply lower rates of reaction and hence lower crack propagation rate than what would be observed in the absence of the increase in the IR potential drop due to the increase in crack length. If this factor is ignored and a "linear" (or constant crack growth rate) approach is used to estimate L(t) as

$$L(t) = L_0 + \left(\frac{\partial L}{\partial t}\right)_{t=0} t \tag{14}$$

the predicted crack length is significantly overestimated. As an example, we compare the predictions of ALERT and a "linear" approach for the propagation of the same 0.5 cm

deep crack in a BWR core shroud over 24 calendar months of operation (two fuel cycles including outages), as shown in Figure 2. The accumulated crack depth, as estimated by the ALERT algorithm, is about 1.5 cm (which is in excellent accord with actual in service inspection data reported recently in Ref 31). On the other hand, the linear extrapolation of the crack propagation yields 2.9 cm or twice that estimated by ALERT. This difference is significant, and it is not surprising that reactor operators lose confidence in models that predict "failure" well before it actually occurs.

As an example of the prediction of accumulated damage in an operating BWR, we show in Figure 3 predicted crack depth versus time for a crack in the core shroud inner surface above the core midplane. The crack was assumed to have an initial depth of 0.5 cm and to be characterized by an initial stress intensity factor of 27.5 MPa.$\sqrt{m}$ (a constant stress is also assumed, so that K_I increases as the crack grows). Once the length of a crack at a given location exceeds the physical dimension of the component or exceeds the critical value corresponding to $K_I > K_{IC}$, failure of the component is deemed to have occurred. We refer to these two cases as being "damage-controlled" and "stress-controlled" failures, respectively. It is important to note that, even when the stress intensity increases with time, the crack growth rate is predicted to decrease over the same period. This is a consequence of the negative impact of increasing crack length on the current and potential distributions within the internal and external crack environments, and hence on the crack growth rate, as predicted by the CEFM [*11*], being more important than the small positive impact of K_I on the crack growth rate in the Stage II region.

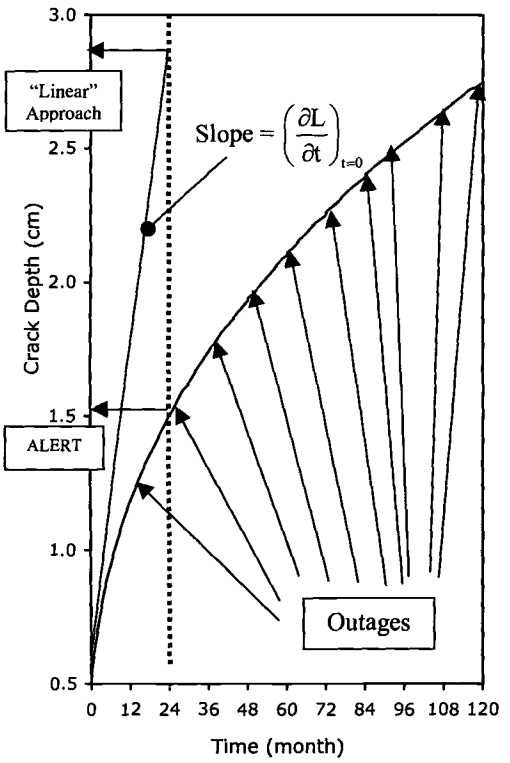


Figure 2: Illustration of the nonlinearity of the accumulated damage and inadequacy of the linear approach for extrapolating crack propagation for future operating periods (regular and identical outages and fuel cycles).

The actual impact that increasing crack length has on the crack growth rate is predicted to be a function of conductivity, ECP, flow rate (even for a high aspect ratio crack), and stress intensity [*11*, *27*]. Accordingly, the predicted accumulated damage becomes a sensitive, nonlinear function of the operating history of the reactor, in a manner that is unlikely to be captured by empirical models.

The impact that hydrogen water chemistry (HWC) is predicted to have on the accumulated damage is illustrated in Figure 3. Thus, an immediate addition of 1 ppm (0.5×10^{-3} mol/kg) of H_2 to the feedwater is predicted to decrease the increment in accumulated damage in the core shroud after ten years of operation by a factor of about 4, from 2.2 cm to about 0.5 cm. This is a substantial reduction in the extent of damage that could not have been estimated from the crack growth rates at a single state point alone (because of the different, non-linear dependencies of crack growth rate on time), or by

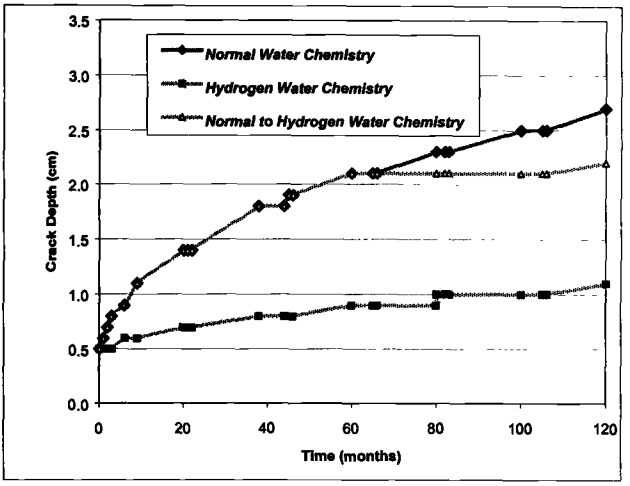


Figure 3: Predicted histories of a growing crack in the core shroud of an operating Boiling Water Reactor as a function of preconceived future operating histories. Note that the discontinuities in the crack length arise from changes in crack growth rate during outages (irregular outages).

using a model that fails to recognize a dependence of crack growth rate on crack length. The same level of hydrogen addition implemented five years later is predicted to yield much smaller benefits for the considered component and location. Thus, an optimal implementation time may be derived for a given reactor by selecting a HWC initiation time that provides for the most cost effective operation in the future in light of other (technical and economic) factors.

As an indication of the accuracy that can be achieved in predicting the accumulation of SCC damage in an operating reactor, we show in Figure 4 a comparison of the calculated increase in length of a crack in the H-3 weld in the inner surface of a BWR core shroud with the observed value, as determined by inspection [*31*]. The level of agreement is considered to be excellent, considering that estimates had to be made of many parameters (e.g. stress and water conductivity).

Our work to date has emphasized BWRs, because that is where the greatest need has been in assisting plant operators to specify the most cost-effective operating protocols. However, we have also employed two of the modules (RADIOCHEM and the MPM) of the three generations of codes that have been developed in our program for modeling the primary coolant of commercial pressurized water reactors (PWRs), with the goal of specifying the coolant conditions ([H_2], [B], [Li], T) under which cracking of steam generator tubes and other susceptible components might be avoided [*32*].

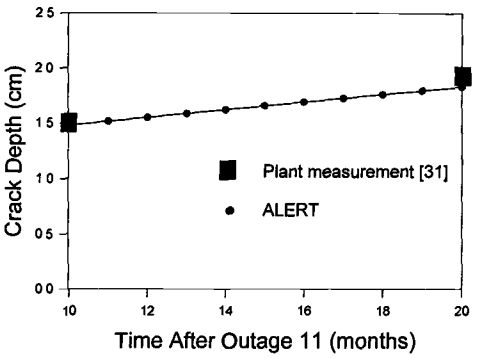


Figure 4. Depth of the crack in the H-3 weld monitored by Tang, et. al. [31] in an operating BWR as a function of time after Outage 11. The calculated and measured depths at ten months were made to coincide by adjusting the initiation time, so that only the comparison at 20 months has value.

Other water chemistry protocols and reactor types may also be modeled using the same basic codes, including CANDUs and various designs from the FSU (e.g. VVER and RBMK). In all of these systems, the coolant chemistry was formulated *before* an adequate understanding of the radiolytic behavior of water in reactor circuits and the electrochemical nature of corrosion damage was understood. The present technology provides that understanding, and hence represents an unprecedented opportunity to optimize the water chemistry to enhance the reliability of reactor operation.

Corrosion Fatigue

Reactor coolant circuits are not subjected to stationary loads but instead experience time dependent loads that arise from a variety of sources. These include, at the extremes, high frequency ($f > 100$ Hz) cyclical loads from rotating machinery (e.g. turbine generators and pumps) to low frequency loads from variations in the operating conditions in the plant. The frequency of these latter loads may be as low as the frequency of the refueling cycle (one cycle every 18 months, or about 0.02 μHz!). In general, because of the high steam pressure in the coolant circuit, the mean load is high (at least for a pressure boundary components) and hence the load is generally characterized by a high R-ratio.

Of particular importance for the prediction of damage in heat transport circuits is the recent development of the corrosion fatigue model, the CECFM [*32*]. This model provides deterministic prediction of crack growth rate for cyclic loading frequencies ranging from zero (static loading, SCC or creep) to infinity (mechanical fatigue), as a function of environmental (ECP, conductivity, temperature) and mechanical (R ratio,

ΔK_I, loading frequency) variables. Typical plots of crack growth rate as a function of loading frequency (sinusoidal load), ΔK_I, and ECP for CF in sensitized Type 304 SS in high temperature water (T = 288°C) are shown in Figures 5 and 6. The bold line in Figure 5 represents the CGR (crack growth rate) under mechanical fatigue conditions (Paris' Law). Environmental effects are manifest at low frequencies but the CGR converges to Paris' law at high frequencies (Figure 5). The CGR is seen to increase with increasing frequency, ΔK_I, and ECP; the latter provided that the frequency is sufficiently low that environmental effects are significant. These predictions are in excellent agreement with the experiment [*33*] (see Figure 7), even though the model is quite crude in that it does not take into account advection induced by the cyclical motion of the sides. A later model that is now being evaluated includes advection, which is shown to have a significant effect on the properties of the crack tip and on the potential distribution down the crack.

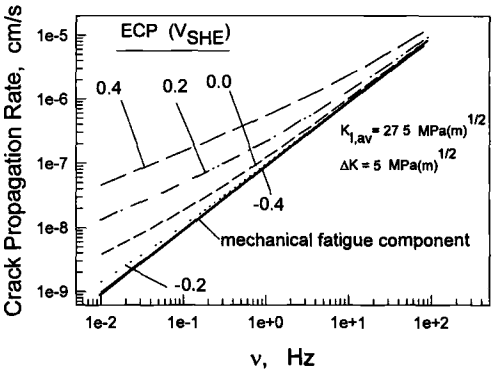


Figure 5: The effect of loading frequency, ν, on crack propagation rate for different corrosion potentials.

Failure of Low Pressure Steam Turbine Disks

The algorithm outlined earlier in this paper for calculating the accumulated damage is essentially identical to that employed recently [*3*] to predict the lifetime of disks in low-pressure steam turbines under conditions where thin electrolyte films precipitate on the steel surface. Thus, we have developed [*3*] a deterministic (mechanistically-based) approach to address SCC initiation and propagation in low-pressure steam turbine disks downstream of the Wilson line, which specifies the temperature and pressure at which steam condenses into a liquid and thus forms a thin electrolyte film on the disk surface. Because of the cyclical shift of the Wilson line during operation, corresponding to changes in the power output of the plant, the thin electrolyte film that forms on the surface concentrates steam impurities, particularly in the creviced locations where impurities cannot easily be "washed" away. Therefore, although the steam in

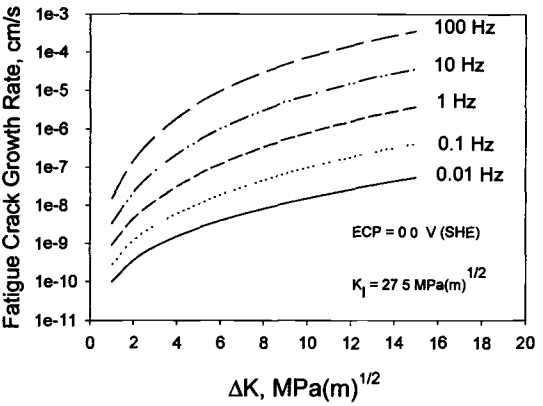


Figure 6: Effect of stress intensity factor range, ΔK, on the fatigue crack growth rate for different frequencies.

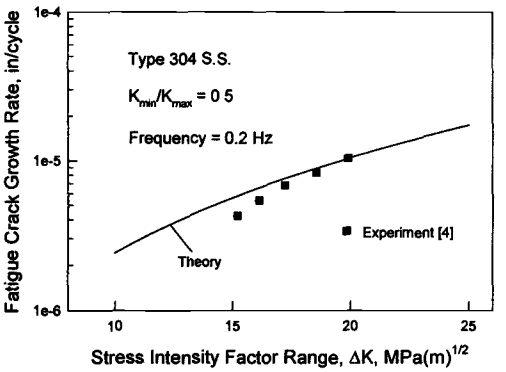


Figure 6: Effect of stress intensity factor range on corrosion fatigue crack growth rates in sensitized AISI 304 SS in 0.01 Na_2SO_4 solution at potential of 35 mV_H. T = 250 °C. The experimental data were taken from Ref. 34.

the heat transport circuit of a power plant is of high purity (contaminants present in the parts per billion level), concentrated electrolytes may form on the steam turbine disk surface. Thus, it has been noted that in some cases, condensates on the surfaces of low-pressure steam turbine disks contain over 20 wt. % NaOH or NaCl, together with deposits of mixed metal oxides. We have chosen to model SCC initiation and propagation on the

surface of steam turbine disks downstream of the Wilson line by recognizing that it is first necessary to describe the chemical properties of the condensed phase, simply because it is in these regions where cracks are frequently observed. Because stress corrosion cracking in steel components frequently initiates from (though not limited to) pits, and because pits have been found to form at very short times, it is assumed that the nucleation of stable pits on the disk surface is "instantaneous". Accordingly, the crack initiation time essentially corresponds to the time required to grow a super critical pit, i.e. a pit having a depth that satisfies Equation (9). The pit growth module used in that study [*3*] was originally developed to calculate pit propagation in gas fired condensing heat exchangers, where the surface in the exit region of the heat exchanger is covered by a thin electrolyte film that condenses from the flue gas [*2*]. By specifying a critical stress intensity (and hence dimension) for SCC initiation (K_{ISCC}=10 MPa$\sqrt{m}$), the pit growth module calculates the time at which the pit depth reaches the required dimension for transition to a crack [for K_I to become equal to K_{ISCC} (Figure 8)]. The module that estimates the crack growth rate, and hence the failure time, is in essence the coupled environment fracture model (CEFM). By specifying the critical stress intensity (K_{IC}) at which fast fracture begins, the module calculates the time at which catastrophic failure occurs. The total time from pit initiation to fast fracture (Figure 8) is defined as the service life of the component. The disk lifetime predictions were found to be in good agreement with laboratory and field data [*3*].

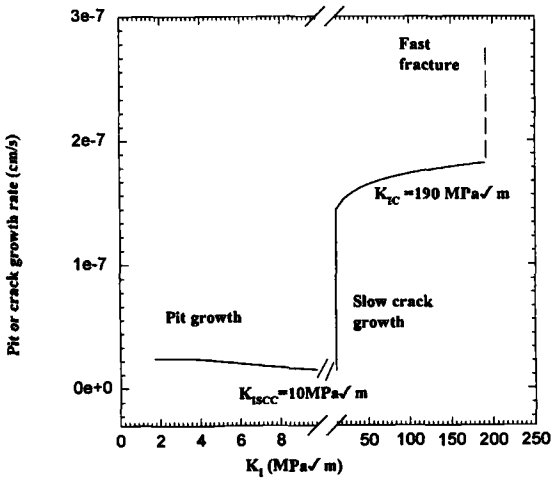


Figure 8: Stages of development of a pit into a crack ultimately resulting in a fast fracture presented as a plot of growth rate versus stress intensity.

The work of Liu and Macdonald [*3*] predicted that the conductivity of the thin electrolyte layer and stress have the greatest impact on the SCC initiation time and the failure time. Interestingly, oxygen concentration was predicted to have only minor effect

on the failure time, even though it was assumed to be the only cathodic depolarizer in the system. The predicted importance of conductivity and stress are consistent with field observations, which dictate that the avoidance of the thin electrolyte layer on the steel surface and minimization of residual stress are the most effective means of enhancing the service life of a low-pressure steam turbine.

Summary and Conclusions

The rate of development of damage is almost always a strong function of the history of operation. Accordingly, industrial systems and plants that are nominally identical quickly become unique, due to unique operating histories and conditions. This uniqueness, coupled with the fact that failures are generally rare events, means that, in most cases, insufficient statistical failure data are available to devise effective empirical models for predicting the onset and evolution of localized corrosion damage. In most cases, one essentially needs to know the answer about the development of damage in advance before predictions can be made. Clearly, in these cases, empirical methods are of marginal value. The alternative philosophy is determinism, in which prediction is made on the basis of mechanism-based physical and chemical models whose outputs are constrained by the natural laws.

In this paper, the foundations of the deterministic prediction of damage due to localized corrosion have been outlined, including the theoretical bases for predicting a complete cycle of damage development: the nucleation, growth, and death of individual events (pits/cracks) and the evolution of damage in an ensemble of events occurring in a progressive manner. Damage is expressed in terms of integral damage functions, which are histograms of event frequency vs. incremental depth. The application of damage function analysis (DFA) has been illustrated with reference to the prediction of the time to failure of low-pressure steam turbine disks due to stress corrosion cracking and to the accumulation of damage due to stress corrosion cracking in water-cooled nuclear power reactors.

Acknowledgments

The authors gratefully acknowledge the support of this work by the U.S. Department of Energy/ Environment Management Science Program under Grant No. DE-FG07-97ER62515 and by SRI International, Menlo Park, CA. In particular, we thank Dr. Iouri Balachov of SRI for performing some of the BWR modeling calculations described in this paper.

References

1. Macdonald, D. D., Balachov, I., and Engelhardt, G. R., "Deterministic Prediction of Localized Corrosion Damage in Power Plant Coolant Circuits", *Power Plant Chemistry*, Vol. 1, 1999, p. 9.

2. Macdonald, D. D., Liu, C., Urquidi-Macdonald, M., Stickford, G., Hindin, B., and Agrawal, A. K., "Prediction and Measurement of Pitting Damage Functions for Condensing Heat Exchangers", *Corrosion*, Vol. 50, 1994, p.761.

3. Liu, C. and Macdonald, D. D., "Prediction of Failures of Low Pressure Steam Turbine Disks", *Journal of Pressure Vessel Technology*, Vol. 119, 1997, p. 393.

4. Yeh, T. K., Macdonald, D. D., and Motta, A. T., "Modeling Water Chemistry, Electrochemical Corrosion Potential and Crack Growth Rate in the Boiling Water Reactor Heat Transport Circuits-Part I: The DAMAGE-PREDICTOR Algorithm", *Nuclear Science and Engineering*, Vol. 121, 1995, p.468.

5. Yeh, T. K., Macdonald, D. D., and Motta, A. T., "Modeling Water Chemistry, Electrochemical Corrosion Potential and Crack Growth Rate in the Boiling Water Reactor Heat Transport Circuits-Part II: Simulation of Operating Reactors", *Nuclear Science and Engineering*, Vol. 123, 1996, p.295.

6. Yeh, T. K., Macdonald, D. D., and Motta, A. T., "Modeling Water Chemistry, Electrochemical Corrosion Potential, and Crack Growth Rate in the Boiling Water Reactor Heat Transport Circuits-Part III: Effect of Reactor Power Level", *Nuclear Science and Engineering*, Vol. 123, 1996, p.305.

7. Macdonald, D. D., M. Urquidi-Macdonald, and P-C. Lu, "Towards Deterministic Methods for Predicting Stress Corrosion Cracking Damage in Reactor Heat Transport Circuits" *Proceedings of the International Conference on Chemistry in Water Reactors: Operating Experience & New Developments*, French Nuclear Society, Nice, France, (1994)

8. Macdonald, D. D. and Urquidi-Macdonald, M., "Thin Layer Mixed Potential Model for the Corrosion of High-Level Nuclear Waste Canisters", *Corrosion*, Vol. 46, 1990, p.380.

9. Macdonald, D. D. and Urquidi-Macdonald, M., "A Coupled Environment Model for Stress Corrosion Cracking in Sensitized Type 304 Stainless Steel in LWR Environments", *Corrosion Science*, Vol. 32, 1991, p.51.

10. Macdonald, D. D. and Urquidi-Macdonald, M., "An Advanced Coupled Environment Fracture Model for Predicting Crack Growth Rates", *Proceedings of the TMS Parkins Symposium on Fundamental Aspects of Stress Corrosion Cracking*, The Materials Society, Warrendale, PA, 1992, p.443

11. Macdonald, D. D., Lu, P.C., Urquidi-Macdonald, M., and Yeh, T.-K., "Theoretical Estimation of Crack Growth Rates in Type 304 Stainless Steel in BWR Coolant Environments", *Corrosion*, Vol. 52, 1996, p.768.

12. Macdonald, D. D., "On the Modeling of Stress Corrosion Cracking in Iron and Nickel Base Alloys in High Temperature Aqueous Environments", *Corrosion Science*, Vol. 38, 1996, p.1003.

13. Macdonald, D. D., "Viability of Hydrogen Water Chemistry for Protecting In-Vessel Components of Boiling Water Reactors", *Corrosion*, Vol. 48, 1992, p.194.

14. Macdonald, D. D., "The Point Defect Model for the Passive State", *Journal of the Electrochemical Society*, Vol. 139, 1992, p.3434.

15. Engelhardt, G. R., Urquidi-Macdonald, M., and Macdonald, D. D., "A Simplified Method for Estimating Corrosion Cavity Growth Rates", *Corrosion Science*, Vol. 39, 1997, p. 419.

16. Engelhardt, G. R. and Macdonald, D. D., "Deterministic Prediction of Pit Depth Distribution", *Corrosion*, Vol. 54, 1998, p. 469.

17. Macdonald, D. D. Urquidi-Macdonald, M., "Corrosion Damage Function Interface Between Corrosion Science and Engineering", *Corrosion*, Vol.48, 1992, p. 354.

18. Macdonald, D. D., "Passivity: The Key to Our Metals-Based Civilization", *Pure and Applied Chemistry*, Vol. 71, 1999, p. 951.

19. Chen, G. S., Wan, K.-C., Gao, M., Wei, R. P., and Flournoy, "Transition from Pitting to Fatigue Crack Growth – Modeling of Fatigue Crack Initiation in a 2024-T3 Aluminum Alloy", *Materials Science and Engineering*, Vol. A219, 1996, p. 126.

20. Ruiz, C. P., Lin, C. C., Wong, T. L., Robinson, R. N., and Law R. J., "Modeling HWC for BWR Applications", *EPRI-NP-6386*, Electric Power Research Institute, Palo Alto, CA, (1989)

21. Ishigure, K., Takagi, J., and Shiraishi, H., "Hydrogen Injection in BWR and Related Radiation Chemistry", *Radiation Physics and Chemistry*, Vol. 29, 1987, p.195.

22. Ibe, E., Nagase, M., Sakagami, M., and Uchida, S. "Radiolytic Environments in Boiling Water Reactor Cores", *Journal of Nuclear Science and Technology*, Vol. 24, 1987, p.220.

23. Macdonald, D. D. and Cragnolino, G., "The Critical Potential for the IGSCC of Sensitized Type 304 SS in High Temperature Aqueous Systems". *Proc. Second International Symposium on the Environmental Degradation of Materials in Nuclear Power Systems. - Water Reactors.* (September 9-12, 1985). Monterey, CA., ANS.

24. Indig, M. E. and Nelson, J. L., "Electrochemical Measurements and Modeling Predictions in Boiling Water Reactors Under Various Operating Conditions", *Corrosion*, Vol. 47, 1991, p.202.

25. Macdonald, D. D., Song, H., Makela, K., and Yoshida, K., "Corrosion Potential Measurements on Type 304SS and Alloy 182 in Simulated BWR Environments", *Corrosion*, Vol. 49, 1993, p.8.

26. Manahan, Sr., M. P., Macdonald, D. D., and Peterson, Jr., A. J., "Determination of the Fate of the Current in the Stress-Corrosion Cracking of Sensitized Type 304SS in High Temperature Aqueous Systems", *Corrosion Science*, Vol. 37, 1995, p.189.

27. Macdonald, D. D. and Kriksunov, L., "Flow Rate Dependence of Localized Corrosion in Thermal Power Plant Materials", *Advances in Electrochemical Science and Engineering*, Vol. 5, John Wiley & Sons, New York, N.Y., 1997, p.125.

28. Zhou, X., Balachov, I., and Macdonald, D. D., "The Effect of Dielectric Coatings on IGSCC in Sensitized Type 304SS in High Temperature Dilute Sodium Sulfate Solution", *Corrosion Science*, Vol. 40, 1998, p.1349.

29. Yeh, T.-K., Yu, M.-S., and Macdonald, D. D., *Proceedings of the 8th International Symposium on Environmental Degradation of Materials in Nuclear Power Systems - Water Reactors*, Amelia Island, GA, NACE Int., Houston, TX, (1997)

30. Balachov, I., Macdonald, D. D., Henzel, N., and Stellwag, B., "Modeling and Prediction of Materials Integrity in Boiling Water Reactors", Proc. Eurocorr98, Utrecht, NL, Sept. 28-Oct. 1, 1998.

31. Tang, J.-R., Kao, L., Shiau, D.-Y., Chou, L.-Y., Yao, C.-C., and Chiang, S.-C., "Thermal-Hydraulic Analysis of Core Shroud Crack for Chinshan BWR/4 Unit 2 Using RETRAN-02/MOD5", *Nuclear Technology*, Vol. 121, 1998, p. 324.

32. Bertuch, A., Pang, J., and Macdonald, D. D., "The Argument for Low Hydrogen and Lithium Operation in PWR Primary Circuits", *Proceedings of the 7th International Symposium on Environmental Degradation of Materials in Nuclear Power Systems - Water Reactors*, Vol. 2, p.687. Breckenridge, CO, NACE, Int., Houston, TX, (1995)

33. Engelhardt, G. R. and Macdonald, D. D., "Deterministic Model for Calculating Fatigue Crack Growth Rate in Stainless Steel in BWR Coolant Environments", *in preparation* (2000).

34. Tsai, W.-T., Moccari, A., Szklarska-Smialowska, Z., and Macdonald, D. D., "Effect of Potential on the Corrosion Fatigue Crack Growth Rate in AISI 304 Stainless Steel in Sodium Sulfate Solution at 250°C", *Corrosion*, Vol. 40, 1984, p. 573.

EPRI Sponsored Session—Prediction of IASCC Performance in Reactor Cooling Water Systems

Yoshiyuki Kaji,[1] Takashi Tsukada,[1] Yukio Miwa,[1] Hirokazu Tsuji,[1] and Hajime Nakajima[1]

Status of JAERI Material Performance Database (JMPD) and Its Use for Analyses of Aqueous Environmentally Assisted Cracking Data

Reference: Kaji, Y., Tsukada, T., Miwa, Y., Tsuji, H., and Nakajima, H., **"Status of JAERI Material Performance Database (JMPD) and Its Use for Analyses of Aqueous Environmentally Assisted Cracking Data,"** *Environmentally Assisted Cracking: Predictive Methods for Risk Assessment and Evaluation of Materials, Equipment, and Structures, ASTM STP 1401,* R. D. Kane, Ed., American Society for Testing and Materials, West Conshohocken, PA, 2000.

Abstract: A material performance database for nuclear applications, which was named the JAERI Material Performance Database (JMPD), has been developed since 1986 with a view to utilizing various kinds of characteristic data of nuclear materials efficiently. The data stored in the JMPD are mainly fatigue crack growth data on low alloy steels, creep data on superalloys, tensile data on aluminum alloys and stress corrosion cracking data (slow strain rate testing (SSRT), crack growth rate, etc.) on austenitic stainless steels.

Irradiation assisted stress corrosion cracking (IASCC) of austenitic stainless steels in high temperature water has been considered as a degradation phenomenon potential not only in the light water reactors (LWRs) but rather common in systems where the materials are exposed simultaneously to radiation and water environments.

This paper describes the present status of the JMPD, which is available through the Internet partially. Furthermore, some trials of utilization of the system focused on the issues relating to IASCC are mentioned as follows: the effect of alloy composition, dissolved oxygen and neutron fluence on IASCC susceptibilities and SCC growth rate could be drawn.

Keywords: materials database, JMPD, IASCC, LWRs, SSRT, crack growth rate, alloy composition, dissolved oxygen, neutron fluence, IASCC susceptibility, SCC growth rate

Introduction

Based on the recent remarkable improvements of the computational environment, it is possible to extract sophisticated information easily and rapidly from complex materials data. Moreover, the World Wide Web (WWW), which is based on hypertext and is capable of moving from one document to another, is the predominant method for accessing the Internet. Many groups are now developing computerized material databases to make available general properties data for metals, alloys, composites etc [*1-5*].

[1] Research Scientists, Japan Atomic Energy Research Institute, Tokai-mura, Naka-gun, Ibaraki-ken, 319-1195, Japan.

Copyright© 2000 by ASTM International www.astm.org

Referring to the critical and technical assessment on the research and development in the field of nuclear technologies, promotion of advanced material research which could bring about technical breakthroughs in many research fields have to be encouraged. In accordance with this new trend, a material performance database, which was named JAERI (Japan Atomic Energy Research Institute) Material Performance Database (JMPD) [*6-8*], has been developed since 1986 focusing on the data stored through research and development promoted by JAERI.

In-core structural materials used in the light water reactors are exposed to high-flux neutron and gamma radiation in a high-temperature water environment. Effects of the radiation, stress and/or water cause various degradation phenomena on structural materials. Irradiation-assisted stress corrosion cracking (IASCC) is known as a degradation phenomenon that occurs due to a synergistic effect of radiation, stress and water [*9*]. IASCC is considered to be one of the key issues for a life assessment of the core internals of nuclear power plants because an accumulation of radiation damage in the material is a primary cause of IASCC. Field experience of IASCC failures indicate that it is a form of intergranular cracking (IG) that occurs in austenitic stainless steels (SS), e.g., type 304 SS. A threshold neutron fluence level has been reported at around $5x10^{24}n/m^2$ (E>1 MeV) in BWR condition [*10*]. In BWR and PWR, some in-core components such as bolts, sheath tubes, etc., have suffered from IASCC.

Welded BWR core shrouds in relatively old plants have also experienced cracking. In case of this failure, fast neutron fluence levels were somewhat lower than the threshold fluence level of IASCC and the failure occurred at thermally sensitized part of the components. Therefore, cracking of the core shroud has been considered as a thermally induced IGSCC. In Japan, core shrouds of old plants were manufactured using type 304 SS and they will be replaced by new components made of type 316L SS that is more resistant to the thermally induced SCC. To confirm an effectiveness of the replacement of material, it is worth while to compare IASCC behavior of type 304 and 316 materials and to investigate factors that cause differences between both materials.

This paper describes the present status of the JMPD, which is partially available through the Internet (http://jmpdsun.tokai.jaeri.go.jp), along with some trials of system utilization focused on the issues relating to IASCC. Based on the knowledge derived from our post-irradiation examinations (PIEs), analysis of IASCC data in JMPD was performed to confirm dependence of IASCC susceptibility on alloy composition and test environment and dependence of crack growth rate on environmental factors.

Outline of JMPD

Fundamental studies of structural materials have been performed at JAERI regarding practical applications for nuclear plants. For the evaluation of reliability and safety of structural materials, various material tests have been conducted. The JMPD was designed for mechanical properties data such as fatigue crack growth, creep, tensile, low-cycle fatigue, SSRT, etc.

Referring to more than ten materials databases which have been already developed in Japan and foreign countries [*11-13*], the data structure for metallic materials in the JMPD was originally determined in a three-level hierarchy. Six categories such as data source, material, specimen, test method & data reduction, test condition, and test result,

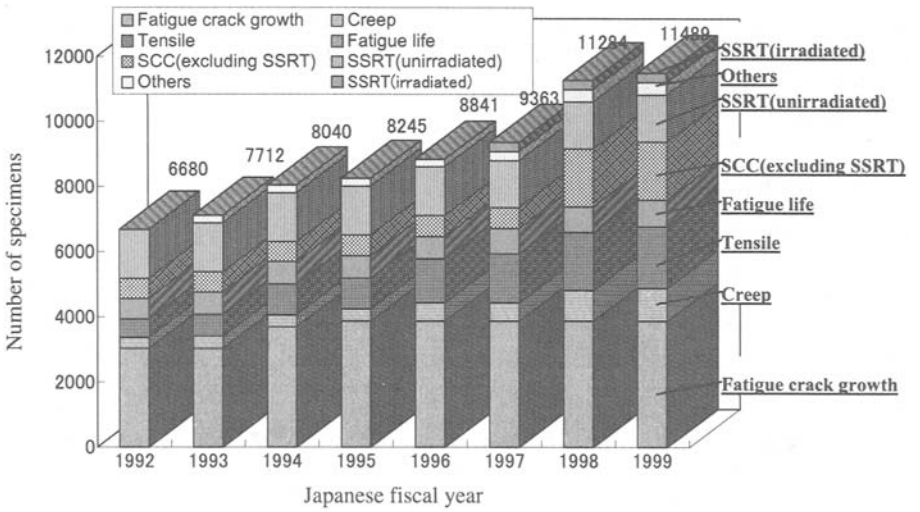


Fig. 1-*Transition of data stored in JMPD at the end of each fiscal year.*

were classified into the primary level. Twenty-five tables were considered to be in the secondary level. More than 420 data items were prepared for the tertiary level.

The JMPD is implemented with Oracle, which is a relational database system on a workstation. A data entry supporting system is implemented with spreadsheet-type software on a personal computer and is connected with the JMPD by middle software through Ethernet. The main features of this system are (a) to design the input sheet by extracting the data item from the data dictionary of the JMPD, and (b) to enter the data by using the guide function. Users can access the Internet through their own computers in the WWW browser, retrieve the required data from JMPD and output the graph.

The data stored in the JMPD by the end of March 1999 are listed in Fig. 1, in which the data from more than 11,000 test pieces are prepared for data evaluation. The data stored were checked through the author's review in order to prevent the unexpected miss-input within the range of possibility. Only the data of the materials whose origin such as chemical compositions and heat treatment conditions as well as experimental methods are clear have been stored.

The JMPD was designed for effective utilization of material data focused on environmentally assisted degradation, e.g., fatigue or SCC behavior in the aqueous or gaseous environments. As for the part of IASCC database, about 300 data of post irradiation SSRT from our experimental work and 20 open published papers [*14-33*] were input. IASCC data consist of those from type 304 and 316 materials and irradiation temperatures are between 333 K and 573 K. Fast neutron fluences exposed to the materials are in a range of $1x10^{22}$ n/m^2 to $8x10^{26}$ n/m^2(E>1MeV). IASCC susceptibilities of the materials had been examined by SSRT at around 573 K in high-temperature water containing various levels of dissolved oxygen concentration. Data analyses were performed based on the knowledge about factors controlling IASCC derived from our results of the post irradiation SSRT [*34-36*].

As for the part of SCC growth rate database, about 1,000 data of SCC growth rate

from 21 open published papers [*37-57*] were input. SCC growth rate data consist of those from thermally sensitized type 304 and 316 alloys under constant load condition at 403-561K in high temperature water containing various levels of dissolved oxygen concentration.

Post Irradiation Examinations

Materials and Irradiation

Chemical compositions of specimen materials are listed in Table 1. Two high-purity base alloys, HP304 and HP316 have similar concentrations of major alloying elements except for molybdenum. Other twelve alloys were doped with minor elements, i.e., C, Si, P, S and Ti, into both base alloys to separate the effect of those elements on IASCC. The alloys were solution annealed and machined to round bar type specimens with the dimensions shown in Fig. 2. Neutron irradiation of the specimens was carried out in helium gas by the Japan Research Reactor No. 3 Modified (JRR-3M), which is a 20MW pool type reactor. A typical neutron fluence of specimens was 6.7×10^{24} n/m^2(E>1MeV) and the irradiation temperature was 513K.

Slow Strain Rate Testing (SSRT) in High Temperature Water

Susceptibility to SCC in high temperature water of the irradiated specimen was evaluated by the SSRT method with a test apparatus installed in a hot cell at the Oarai hot laboratory of JAERI. It consists of a tensile test apparatus, an autoclave and a water circulation system as illustrated in Fig. 3. SSRT tests were carried out in high-temperature water at 573K in 9.3MPa and at an initial strain rate of 1.7×10^{-7} s^{-1}. Degassed demineralized water was pumped to the autoclave with a high pressure pump. Dissolved oxygen (DO) level was controlled at 32ppm by bubbling pure oxygen gas into a water make-up tank of the high-pressure water supply system connected with the SSRT test machine. A flow rate of water into the autoclave was 5l/h. Electric conductivity of inlet water to the autoclave was kept below 0.2μS/cm.

Table 1-*Chemical compositions of model stainless steels (unit: wt%).*

Alloy ID	C	Si	P	S	Mn	Cr	Ni	Mo	Ti	Fe
HP304	**0.003**	**0.01**	**0.001**	**0.001**	**1.36**	**18.17**	**12.27**	**—**	**0.01**	**bal.**
HP304/Si	0.003	0.69	0.001	0.001	1.36	18.01	12.24	—	0.01	bal.
HP304/P	0.006	0.03	0.017	0.001	1.40	18.60	12.56	—	0.01	bal.
HP304/S	0.002	0.03	0.001	0.032	1.41	18.32	12.47	—	0.01	bal.
HP304/C	0.098	0.03	0.001	0.002	1.39	18.30	12.50	—	0.01	bal.
HP304/C/Ti	0.099	0.03	0.001	0.002	1.39	18.50	12.47	—	0.31	bal.
HP304/All	0.107	0.72	0.019	0.036	1.41	18.66	12.68	—	0.29	bal.
HP316	**0.004**	**0.02**	**0.001**	**0.001**	**1.40**	**17.21**	**13.50**	**2.50**	**0.01**	**bal.**
HP316/C	0.061	0.03	0.001	0.001	1.40	17.28	13.50	2.49	0.01	bal.
HP316/C/Ti	0.062	0.04	0.001	0.001	1.39	17.05	13.47	2.48	0.29	bal.
HP316/C/Ti/Si	0.065	0.70	0.001	0.001	1.39	17.16	13.53	2.44	0.30	bal.
HP316/C/Ti/P	0.061	0.05	0.019	0.002	1.40	16.95	13.53	2.48	0.29	bal.
HP316/C/Ti/S	0.061	0.03	0.001	0.037	1.41	17.82	13.60	2.47	0.30	bal.
HP316/All	0.063	0.76	0.018	0.037	1.42	17.32	13.56	2.43	0.30	bal.

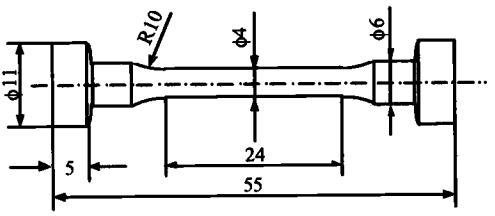


Fig. 2-*SSRT specimen (unit: mm).*

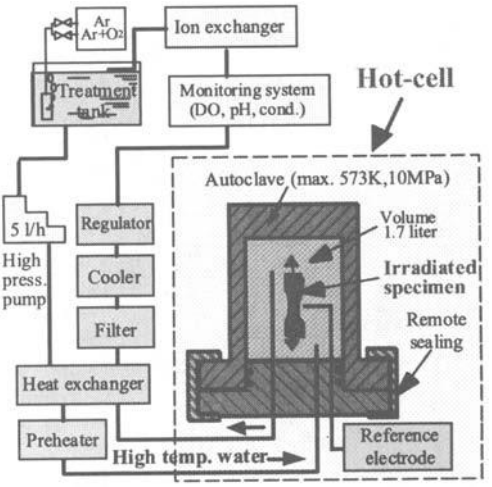
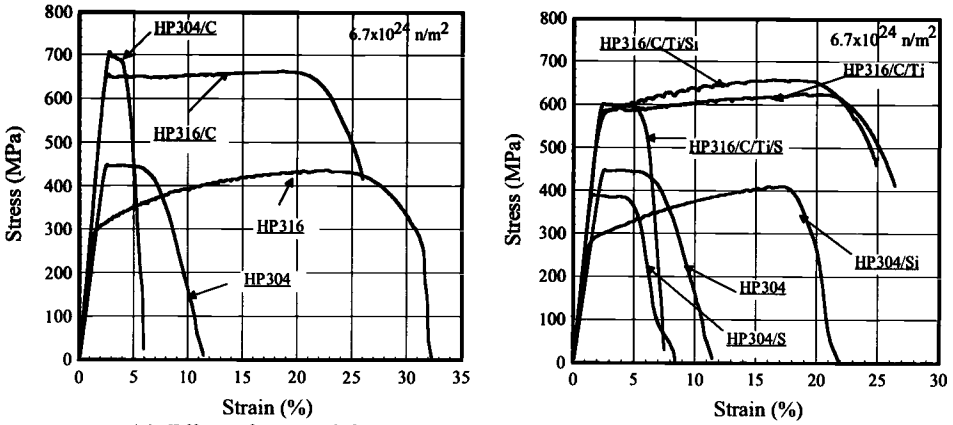


Fig. 3-*SSRT test machine at hot laboratory.*

SEM and TEM Analyses

After the SSRT tests, all specimens are examined by the scanning electron microscope (SEM) and fractions of SCC area on the fracture surfaces were evaluated as IASCC susceptibility.

Though change of deformation mechanism by radiation hardening is one of important factors, radiation induced segregation (RIS) of alloy elements at the grain boundaries may be the most important process affecting IASCC. However, since the compositional profiles by RIS in the vicinity to grain boundaries are very narrow, around 5 nm in width, qualitative analyses of profiles were not possible using the conventional type of transmission electron microscope (TEM). At JAERI, microstructural analyses of irradiated specimen were performed with a field emission gun type TEM to examine the radiation-induced microstructural and microchemical effects [*58,59*]. To reduce a detrimental effect of gamma radiation from TEM specimen for the compositional analysis using energy dispersive spectrometer (EDS), the specimen was miniatured to about 1/50 volume of conventional TEM specimens by using composite specimen technique [*60*].



(a) *Effect of Mo and C* (b) *Effect of S and Si*

Fig. 4-*Stress-strain behavior of irradiated specimen during SSRT in high temperature water at 573 K.[36]*

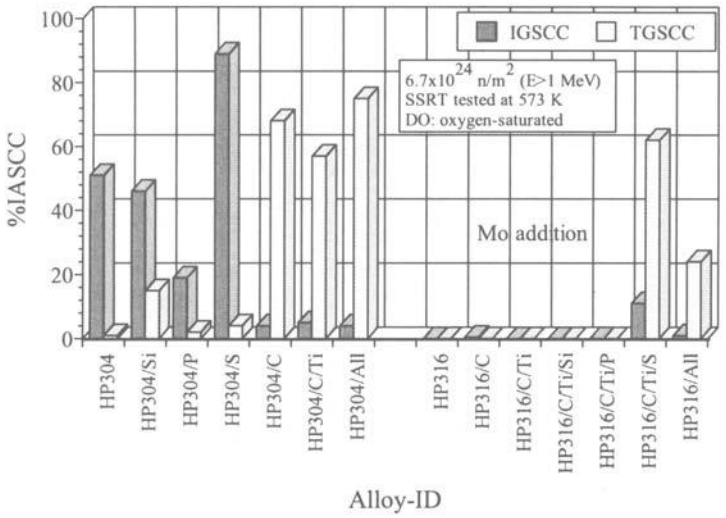


Fig. 5-*IASCC susceptibility of the alloys irradiated up to 6.7x10^24 n/m^2 at 513 K.*

Experimental Results of Post Irradiation SSRT

Examples of engineering stress-strain curves during SSRTs are shown in Fig. 4 for type 304 and 316 alloys [*36*]. In Fig. 4(a), the results for HP304, HP304/C, HP316 and HP316/C are presented. Alloy HP316 doped with molybdenum showed a lower yield stress than that of HP304 alloys, but the maximum stresses were nearly same on the both alloys. Carbon addition to the both HP304 and HP316 alloys caused a fairly large

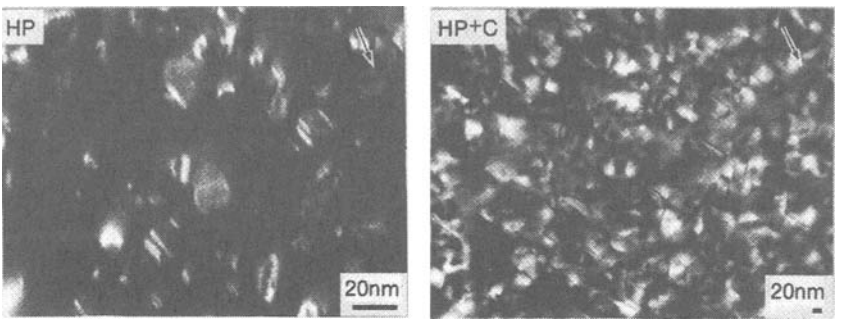


Fig. 6-*Typical transmission electron micrographs of HP304 and HP304/C.*

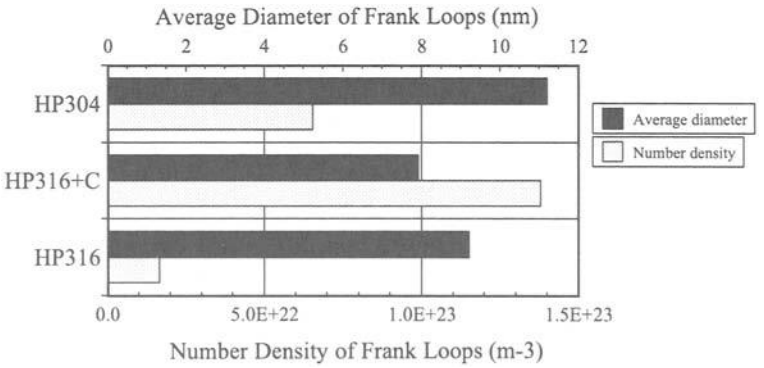


Fig. 7-*Number density and average diameter of Frank Loops.*

radiation hardening. Total elongation of the specimens doped with molybdenum is larger than those of HP304 and HP304/C alloys because the latter alloys failed by a large fraction of IGSCC and TGSCC. Fig. 4(b) shows stress-strain curves for alloys doped with silicon and sulfur where three alloys doped with molybdenum showed higher strength because carbon was added into those alloys in 0.06 wt% but not into the type 304 alloys. In each series of alloys of type 304 and 316 alloys, two alloys doped with silicon, HP304/Si and HP316/C/Ti/Si, showed the largest total elongation. Total elongations of alloys doped with sulfur, HP304/S and HP316/C/Ti/S, were smaller than those of the other alloys. There is little difference in the stress-strain curves among alloys doped with carbon and titanium and with carbon, titanium and silicon for type 316 alloys.

In Fig. 5, IASCC susceptibilities of the irradiated materials are summarized where ratios of intergranular (IG) or transgranular (TG) cracking area to whole fracture area are illustrated in terms of IASCC fractions [*35,36*]. It is known from the field experience that IASCC in power plants appears as IG cracking, therefore, a comparison of susceptibilities to IG type IASCC is more important in Fig. 5. In case of SCC test by SSRT, frequently an appearance of TGSCC has been reported, and it is probably due to the severe loading condition by SSRT method to maintain a constant strain rate.

Effects of C, Mo and S additions on IASCC behavior can be derived from the results shown in Fig. 5. In a series of type 304 alloys, an effect of C addition can be seen

clearly on fracture morphology. A dominant fracture mode of alloys without C addition was IGSCC and C addition of about 0.1 wt% changed it to TGSCC. Comparing HP304 with HP316, or HP304/C with HP316/C, we can conclude that addition of Mo entirely suppressed IASCC susceptibility. Only two alloys, i.e., HP316/C/Ti/S and HP316/All, showed susceptibilities to TGSCC and IGSCC of all the type 316 alloys. The element commonly doped for both alloys is S (0.037 wt%). In addition, type 304 alloys doped with S, i.e., HP304/S, showed the highest susceptibility to IASCC in 513 K pure water. It can be concluded that S addition of about 0.04 wt% is very injurious to IASCC. On the other hand, effects of Si, P and Ti on IASCC susceptibility are not clear from Fig. 5, though it seems that an addition of P reduced IASCC susceptibility in HP304/P.

HP304 alloys irradiated at JRR-3M were analyzed using the FEG-TEM [*58,59*]. Major radiation defects were Frank loops in all alloys and additionally small defect clusters were observed as black dots. Examples of weak-beam dark-field images of HP304 and HP304/C are shown in Fig. 6. In all alloys, Frank loops and small defect clusters were the dominant microstructural features, while neither precipitates nor cavities were observed. The number density of small defect clusters in HP316 seemed to be lower than that in HP304. Fig. 7 shows the number density and average diameter of Frank loops in these alloys. The number density and the average diameter in HP316 were smaller than those in HP304. Addition of Mo decreased the average diameter and the number density of Frank loops, because chemical compositions between these alloys were slightly different except for molybdenum content. By the addition of C in HP316, the number density of Frank loops drastically increased and the average diameter decreased.

Analyses and Evaluations of Material Data through JMPD

SSRT Data Analyses

In Fig. 8, data of IASCC susceptibilities compiled into the JMPD are plotted against fast neutron fluence (E>1MeV). Though the percent IG cracking in the SSRT is a

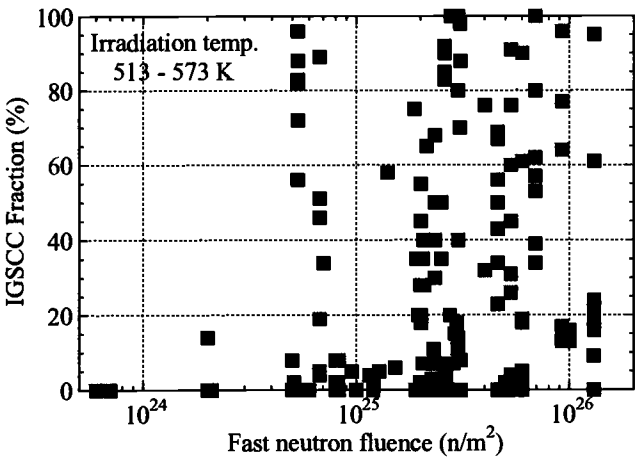


Fig. 8-*SSRT database in JMPD (all data).*

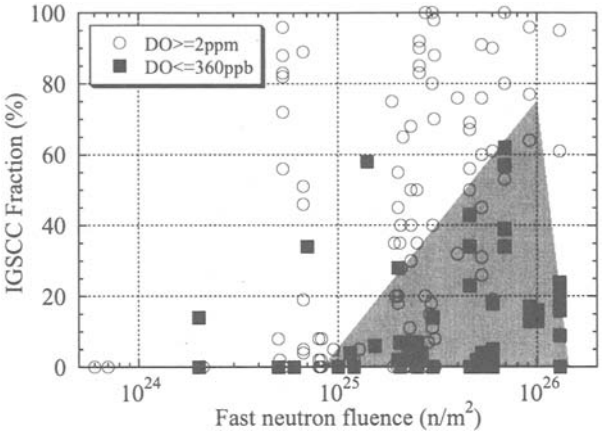


Fig. 9-*Effect of dissolved oxygen (DO).*

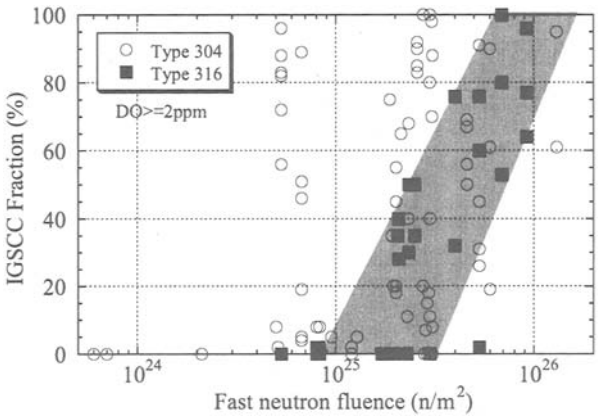


Fig. 10-*Effect of molybdenum addition.*

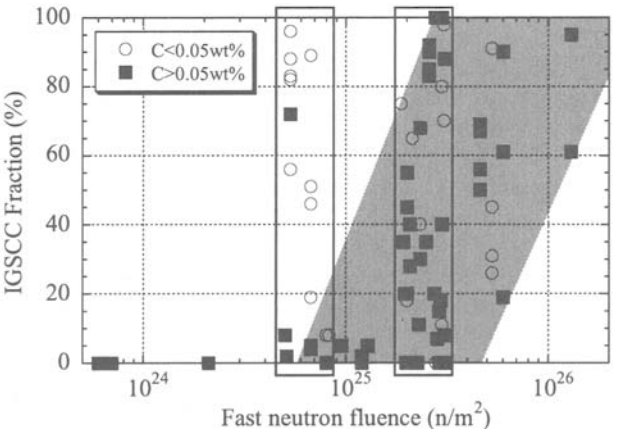


Fig. 11-*Effect of carbon content.*

variable parameter, susceptibility was evaluated in terms of the IG cracking area in the SSRT for the common indicator in these database analyses. The data scattered over a wide range of susceptibility through the neutron fluence and it is difficult to deduce any relation between the susceptibility and the fluence level from Fig. 8. Since the dissolved oxygen (DO) content in high-temperature water is an essential factor for SCC phenomenon all data are classified into two groups by levels of DO content during SSRT in Fig. 9. A tendency is observed that the percent IG cracking of alloys tested in lower DO environment is smaller. According to the results of the post irradiation SSRT, an addition of Mo to 304 SS caused a drastic suppression of IASCC [*34*]. In Fig. 10, therefore, the data from the higher DO environment are plotted separately for type 304 and 316 alloys to confirm the effect of Mo. As seen in Fig. 10, at a lower fluence level around $1x10^{25}$ n/m^2, type 316 alloys show smaller susceptibility compared with type 304 alloys and the tendency may be due to Mo addition. However, at higher fluence level, susceptibilities of type 316 alloys are increasing with the fluence and differences seem to be diminished with increasing neutron fluence. In Fig. 11, the data from type 304 alloys in Fig. 10 are plotted into two ranges of bulk C content. Some data discussed here are for uncontrolled 304 SSs, that is, C is not the only variable changing, but also Ni and N etc. are variable changing. The authors had found that addition of C appeared to promote TGSCC and suppress IGSCC by means of post-irradiation SSRT experiments of type 304 alloys with single-addition of C [*34-36*]. Therefore by combination of the PIEs and database analysis, it is found that at lower fluence levels around $5x10^{24}$-$9x10^{24}$ n/m^2(E>1MeV), an effect of C addition to suppress IASCC appeared, but at higher fluence levels around $2x10^{25}$-$3x10^{25}$ n/m^2 the effect seems to be lost as seen in two boxes shown in Fig. 11.

Comparing IASCC behavior of the materials, we derived effects of C and Mo on IASCC susceptibility and its fracture morphology. In the case of SCC of unirradiated thermally sensitized stainless steels, a significance of the effect of C on IGSCC has been recognized distinctly, because thermal sensitization primarily depends on precipitation of Cr-carbide and consequent Cr depletion at grain boundaries (GBs). However, in the case of IASCC an effect of C has not been suggested clearly. This study, however, showed an effect of C addition at a lower neutron fluence level around "threshold" fluence of IASCC, where the addition of C caused a suppression of IG type IASCC. This effect of C can be discussed from two viewpoints that are relating to the mechanical property and microchemistry of irradiated alloys.

The authors had found that the addition of C enhanced radiation hardening [*35,36*] and increased the number density of Frank loops [*58*]. These findings are consistent and it may be suggested that an addition of C enhances a radiation hardening of alloy matrix, consequently it suppresses a plastic deformation or slip deformation near GBs that is necessary for a crack propagation through the slip dissolution mechanism [*38,61,62*], in which environmentally assisted crack advance is attributed to repetitive rupture of the passive film at the crack tip by intersection of slip bands and following film rupture, rapid metal reaction occurs with eventual film repair, at lower fluence levels. In addition, it is expected that an addition of C reduces the Cr depletion at GBs because it increases a number density of Frank loops that act as trapping site for point defects, therefore a flow of point defects and a subsequent radiation induced depletion of Cr at GBs will be reduced. These two effects of C addition may suppress a susceptibility to IG type IASCC.

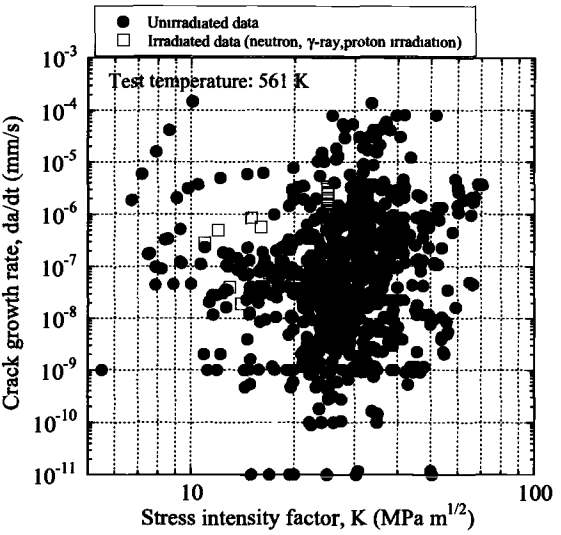


Fig. 12-*SCC growth rate database in JMPD (all data).*

Analysis of IASCC database in JMPD revealed that the above-mentioned effect of C addition became indistinct at higher fluence levels of the mid of 10^{25} n/m^2 (E>1 MeV) as seen in Fig. 11. It is speculated that at these fluence levels effects of C addition become relatively small, because the radiation hardening and Cr depletion due to the radiation induced segregation (RIS) nearly saturate regardless of C addition. It appears that other factors are affecting IASCC behavior and are more essential at the higher fluence levels in BWR condition.

Importance of Mo on IASCC has been suggested [*63,64*], but we made it clear by means of post-irradiation SSRT experiments of the alloy with single-addition of Mo [*34-36*]. An effect of Mo addition was very remarkable to suppress IASCC, though its effect gradually decreased at higher fluence levels above about $2x10^{25}$ n/m^2 (E>1 MeV) according to our results of database analysis as seen in Fig. 10. It is obvious that in the case of SCC due to thermal sensitization, addition of Mo is very effective to mitigate SCC and it has been suggested that Mo stabilizes a passive film formed on stainless steels. A similar process can be suggested for the case of IASCC, because Mo addition decreased the number density of Frank loops as the authors reported [*59*] and it is not expected to reduce RIS at GBs.

In BWRs, the fast neutron fluence of core shroud at the end-of-life is estimated as about $2x10^{25}$ n/m^2; the present results from post irradiation SSRT and database analysis support an effectiveness of replacement of type 304 by type 316L. At the lower neutron fluence levels, a reduction of C content may cause an enhancement of IASCC of type 304 alloys.

Crack Growth Data Analyses

Data analyses were performed based on the knowledge about factors controlling SCC. In

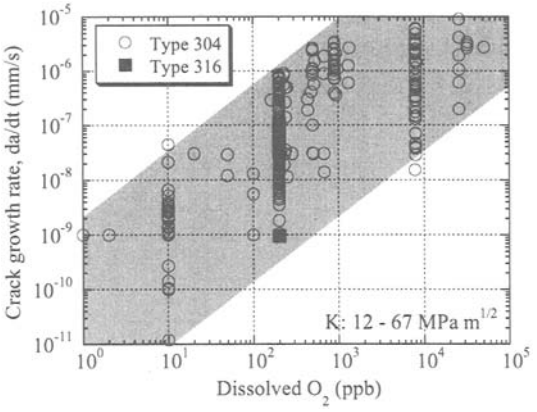


Fig. 13-*Relationship between da/dt and dissolved oxygen (DO) level.*

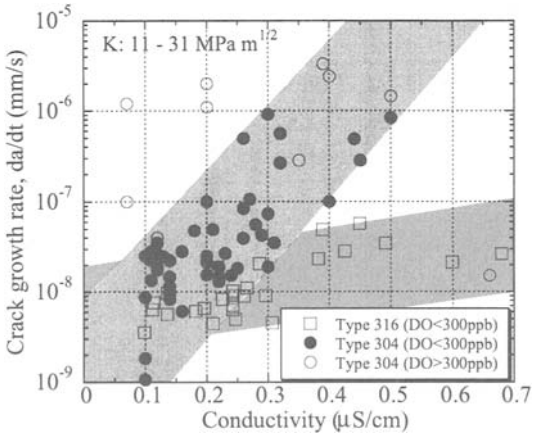


Fig. 14-*Relationship between da/dt and conductivity.*

Fig. 12, all data of SCC growth rate, da/dt at 561K, for unirradiated and irradiated type 304 and 316 alloys compiled into the JMPD from the literature are plotted against stress intensity factor, K. The data including the irradiated data scattered over a wide range of crack growth rate through the stress intensity factor, and it is difficult to deduce an effect of radiation on the relation between da/dt and K from Fig. 12. Therefore hereafter, data analyses were carried out for sensitized type 304 and 316 alloys including the irradiated data. Suzuki et al. [*65*] reported that crack growth rates of SCC are affected by specimen thickness, and thicker specimens show slower crack growth rates for sensitized 304 SS. Though the size effect of SCC growth rate is one of key factors on SCC growth behavior, we can not extract a size effect of the specimens on SCC growth rate in these database analyses, because there is a little SCC growth data for 1/4TCT specimen and most of SCC growth data is for 1TCT specimen in JMPD.

Figure 13 shows relationship between da/dt and dissolved oxygen level for type

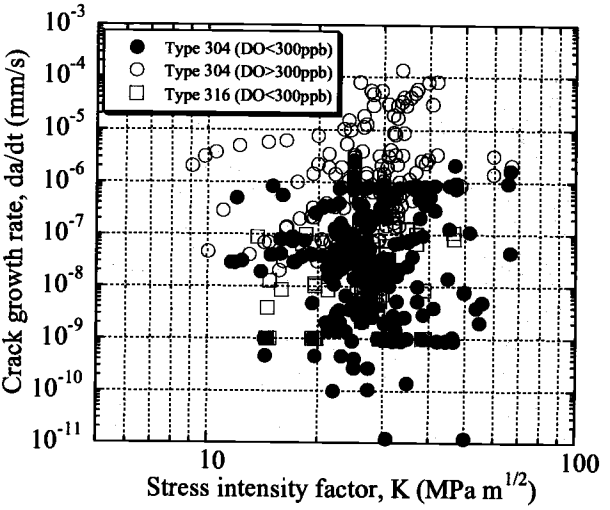


Fig. 15-*Effect of dissolved oxygen on da/dt-K relationship.*

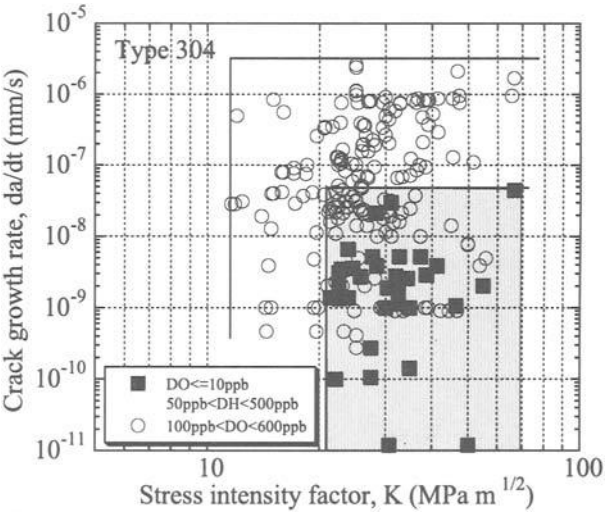


Fig. 16-*Effect of hydrogen addition on da/dt-K relationship.*

304 and 316 alloys. It is confirmed that SCC crack growth rate increase with increasing the dissolved oxygen level for both type 304 and 316 alloys.

Figure 14 shows the relationship between da/dt and conductivity of the water and the data are classified into three groups by levels of dissolved oxygen and alloy type. It is found that da/dt in lower DO environment is smaller for type 304 alloys and that da/dt for type 316 alloys is lower than that for type 304 alloys in the same DO condition.

Since the DO content in high temperature water is an essential factor for SCC growth rate, as shown in Fig. 13, all data are classified into three groups by levels of DO content and alloy type on da/dt-K relationship in Fig. 15. A tendency is observed that da/dt of both type 304 and 316 alloys tested in lower DO environment are smaller than ones in higher DO environment in Fig. 15. It is difficult to deduce any relation between type 304 and 316 alloys on da/dt-K relationship in lower DO condition, because the data scatter over wide range of da/dt through the K for type 304 alloys.

In Fig. 16, therefore, the data from type 304 alloys are plotted separately to confirm the effect of dissolved hydrogen (DH) on the da/dt-K relationship. The range of DH is from 50 to 500ppb for BWR condition in Fig. 16. As shown in Fig. 16, da/dt in lower DO and DH environments show smaller da/dt compared with ones in normal DO environments and it can be attributed to DH addition.

On the future subjects, it is necessary to get and store sufficient reliable data of SCC crack growth for irradiated type 304 and 316 alloys in the JMPD, because it is important to confirm the effect of irradiation and the size effect of the specimen on crack growth data in the sufficient controlled high temperature water.

Conclusions

The present status of the system of JMPD and some trials of sophisticated utilization of the system focused on the issues relating to IASCC were described briefly. From analyses of IASCC data in JMPD based on the knowledge derived from our results of the PIEs, the following conclusions were obtained.

- SSRT data analyses

  (1) By means of a combination of the post irradiation SSRT and database analysis, the dependence of IASCC susceptibilities on alloy composition, neutron fluence and dissolved oxygen level could be drawn.

- SCC growth rate data analyses

  (2) Crack growth rate in high temperature water containing lower dissolved oxygen and conductivity is smaller under the same stress intensity factor.

  (3) Addition of hydrogen to normal DO environments remarkably suppresses crack growth rate.

Acknowledgment

The authors are grateful to Mr. T. Sakino and Ms. T. Yoshikawa of JAERI for their assistance in the data search procedure from the JMPD.

References

[1] Doyama, M., Suzuki, T., Kihara, J., Yamamoto, R., ed., *Computer Aided Innovation of New Materials*, Elsevier Sci. Publ., Netherlands 1991.

[2] Doyama, M., Kihara, J., Tanaka, M., Yamamoto, R., ed., *Computer Aided Innovation of New Materials (II)*, Elsevier Sci. Publ., Netherlands 1993.

[3] Glazman, J.S. and Rumble, J. R., ed., *ASTM-STP 1017*, 1989.

[4] Barry, T. and Reynard, K. W., ed., *ASTM-STP 1140*, 1992.

[5] Nishijima, S. and Iwata, S., ed., *ASTM-STP 1311*, 1997.
[6] Yokoyama, N., Tsukada, T. and Nakajima, H., "JAERI Material Performance Database (JMPD): Outline of the system", JAERI-M90-237, (in Japanese), 1987.
[7] Tsuji, H., Yokoyama, N., Tsukada, T. and Nakajima, H., "Development of Comprehensive Material Performance Database for Nuclear Applications", J. Nucl. Sci. Technol., Vol. 30, No. 12, pp. 1234-1242, 1993.
[8] Yokoyama, N., Tsuji, H., Tsukada, T. and Shindo, M., "Development of Comprehensive Material Performance Database for Nuclear Applications", *Computerization and Networking of Materials Databases: Fifth Volume, ASTM STP 1311*, pp.261-272, 1997.
[9] Scott, P., "A Review of Irradiation Assisted Stress Corrosion Cracking", J. Nucl. Mater. Vol. 211, p.101,1994.
[10] Andresen, P. L., Ford, F. P., Murphy, S. M. and Perks, J. M., "State of Knowledge of Radiation Effects on Environmental Cracking in Light Water Reactor Core Materials", Proc. 4th Int. Symp. on Environmental Degradation of Materials in Nuclear Power Systems - Water Reactors, p.1-83, 1990.
[11] Rumble, J., Northrup, C., Westbrook, J., Grattidge, W. and McCarthy, J., Materials Information for Science and Technology (MIST), Project Overview, US Department of Commerce, 1986.
[12] Mindlin, H., Rungta, R., Koehl, K. and Gubiotti, R., EPRI NP-4485, 1986.
[13] Buchmayr, B. and Krockel, H., High Temperature Materials Databank (HTM-DBC), Comm. of the European Communities, Joint Research Center, 1988.
[14] Fukuya, K., Sima, S., Kayano, H. and Narui, M., "Stress Corrosion Cracking and Intergranular Corrosion of Neutron Irradiated Austenitic Steels", J. Nucl. Mater. Vol.191-194, p.1007, 1992.
[15] Chung, H. M., Ruther, W. E., Sanecki, J. E., Hins, A. G. and Kassner, T. F., "Stress Corrosion Cracking Susceptibility of Irradiated Type 304 Stainless Steels", *Effects of Radiation on Materials, ASTM STP 1175*, 1993.
[16] Kodama, M., Morisawa, J., Nishimura, S., Asano, K., Shima, A. and Nakata, K., Stress Corrosion Cracking and Intergranular Corrosion of Austenitic Stainless Steels Irradiated at 323K", J. Nucl. Mater. Vol.212-215, p.1509, 1994.
[17] Kodama, M., Katsura, R., Morisawa, J., Nishimura, S., Suzuki, S., Takemori, K., Shima, S. and Kato, T., "IASCC Susceptibility of Irradiated Austenitic Stainless Steel under Very Low Dissolved Oxygen", Proc. Seventh Int. Sym. on Environmental Degradation of Materials in Nuclear Power Systems, Breckenridge, Colorado, August 7-10, 1995.
[18] Fukuya, K., Shima, S., Nakata, K., Kasahara, S., Jacobs, A. J., Wozadlo, G. P., Suzuki, S. and Kitamura, M., "Mechanical Properties and IASCC Susceptibility in Irradiated Stainless Steels", Proc. Sixth Int. Sym. on Environmental Degradation of Materials in Nuclear Power Systems, San Diego, California, August 1-5, p.565, 1993.
[19] Jacobs, A. J., Shepherd, C. M., Bell, G. E. C. and Wozadlo, G. P., "High-Temperature Solution Annealing as an IASCC Mitigation Technique", Proc. Fifth Int. Sym. on Environmental Degradation of Materials in Nuclear Power Systems, Monterey, California, August 25-29, 1991.
[20] Jacobs, A. J., Wozadlo, G. P., Nakata, K., Yoshida, T. and Masaoka, I., "Radiation Effects of Stress Corrosion and Other Selected Properties of Type-304 and Type-316

Stainless Steels", Proc. Third Int. Sym. on Environmental Degradation of Materials in Nuclear Power Systems, Traverse City, Michigan, August 30- September 3, p.673, 1987.
[21] Clarke, W. L. and Jacobs, A. J., "Effect of Radiation Environment on SCC of Austenitic Materials", Proc. Int. Sym. on Environmental Degradation of Materials in Nuclear Power Systems, Myrtle Beach, South Carolina, August 22-25, p.451, 1983.
[22] Jacobs, A. J., Clausing, R. E., Heatherly, L. and Kruger, R. M., "Irradiation-Assisted Stress Corrosion Cracking and Grain Boundary Segregation in Heat Treated Type 304 SS", *Effects of Radiation on Materials, ASTM STP 1046*, p.424, 1989.
[23] Jacobs, A. J., Wozadlo, G. P., Nakata, K., Kasahara, S., Okada, T., Kawano, S. and Suzuki, S., "The Correlation of Grain Boundary Composition Irradiated Stainless Steel with IASCC Resitance", Proc. Sixth Int. Sym. on Environmental Degradation of Materials in Nuclear Power Systems, San Diego, California, August 1-5, p.597, 1993.
[24] Nakata, K., Yoshida, T., Masaoka, I., Saito, T., Jacobs, A. J. and Wozadlo, G. P., "Susceptibility to Intergranular Cracking in Pressurized High Temperature Water in Neutron-Irradiated Austenitic Stainless Steels", J. Japan Inst. Metals, Vol.52 No.11, p.1067, 1988.
[25] Nakata, K., Yoshida, T., Masaoka, I., Saito, T., Jacobs, A. J., Wozadlo, G. P. and Yan, W. J. S., "Effect of Neutron-Irradiation at 560K on the Mechanical Properties in Austenitic Stainless Steels", J. Japan Inst. Metals, Vol.52 No.11, p.1023, 1988.
[26] Suzuki, S., Watanabe, M., Iokibe, H., Nishino, A., Fukushima, M., Kanno, M., Shima, S., Saito, T., Nishimura, S. and Kodama, M., "Characterization of Neutron Irradiated Austenitic Stainless Steels (I) Mechanical Properties", Fall Meeting of the Atomic Energy Society of Japan, Hokkaido University, Oct. 2-4, p.119, 1987.
[27]Suzuki, S., Watanabe, M., Iokibe, H., Nishino, A., Fukushima, M., Kanno, M., Shima, S., Saito, T., Nishimura, S. and Kodama, M., "Characterization of Neutron Irradiated Austenitic Stainless Steels (II) Corrosion Resistance", Fall Meeting of the Atomic Energy Society of Japan, Hokkaido University, Oct. 2-4, p.120, 1987.
[28] Kodama, M., Nishimura, S. and Morisawa, J., "Effects of Fluence and Dissolved Oxygen on IASCC in Austenitic Stainless Steels", Proc. Fifth Int. Sym. on Environmental Degradation of Materials in Nuclear Power Systems, Monterey, California, August 25-29, p.948, 1991.
[29] Jacobs, A. J., Wozadlo, G. P. and Gordon, G. M., "Low-Temperature Annealing – A Process to Mitigate IASCC", Corrosion 95, Paper No.418, 1995.
[30] Kodama, M., Fukuya, K. and Kayano, H., "Influence of Inpurities and Alloying Elements on IASCC in Neutron Irradiated Austenitic Stainless Steels", *Effects of Radiation on Materials, ASTM STP 1175*, 1993.
[31] Jones, R. H. and Henager, C. H., "Effect of Gamma Irradiation on Stress Corrosion Behavior of Austenitic Stainless Steel under ITER – Relevant Conditions", J. Nucl. Mater. Vol.191-194, p.1012, 1992.
[32] Jacobs, A. J. and Dumbill, S., "Effects of Low-Temperature Annealing on Microstructure and Grain Boundary Chemistry of Irradiated Type 304SS and Correlations with IASCC Resistance", Environmental Degradation of Materials in Nuclear Power Systems – Water Reactors.
[33] Suzuki, I., Kanasaki, H., Mimaki, H., Akiyama, M., Okubo, T., Mishima, Y. and Mager, T. R., "Slow Strain Rate Tensile (SSRT) Test on Cold-Worked 316 Stainless Steel (S.S) and 304 S.S Irradiated to 3E+21n/cm^2(E>0.1MeV)", Proc. Stress Corrosion

Cracking of Irradiated The Stainless Steel in Simulated PWR Primary Water, ASME, 1996.
[34] Tsukada, T., Miwa, Y., Tsuji, H., Mimura, H., Goto, I., Hoshiya, T. and Nakajima, H., "Stress Corrosion Cracking Susceptibility of Neutron Irradiated Stainless Steels in Aqueous Environment", Proc. 7th Int. Conf. on Nucl. Engng. (ICONE-7), L4-3, 1999.
[35] Tsukada, T., Miwa, Y. and Nakajima, H., "Stress Corrosion Cracking of Irradiated Type 304 Stainless Steels", Proc. 7th Int. Symp. on Environmental Degradation of Materials in Nuclear Power Systems - Water Reactors, Vol. B, p.1009, 1995.
[36] Tsukada, T., Miwa, Y., Nakajima, H. and Kondo, T., "Effects of Minor Elements on IASCC of Type 316 Model Stainless Steels", Proc. 8th Int. Symp. on Environmental Degradation of Materials in Nuclear Power Systems - Water Reactors. Vol. B, p.795, 1997.
[37] Ford, F. P. et al., "Application of Water Chemistry Control, On-line Monitering and Crack Growth Rate Models for Improved BWR Materials Performance", Proc. 4th Int. Symp. on Environmental Degradation of Materials in Nuclear Power Systems - Water Reactors, p.4-26, 1990.
[38] Andresen, P. L. and Ford, F. P., "Life Prediction by Mechanistic Modeling and System Monitoring of Environmental Cracking of Iron and Nickel Alloys in Aqueous Systems", Mat. Sci. and Eng. A103, p.167, 1988.
[39] Schmidt, C. G., Caligiuri, R. D. and Eiselstein, L. E., "Intergranular Stress Corrosion Cracking of Low Temperature Sensitized Type 304 Stainless Steel Pipe Welds", Proc. Int. Sym. on Environmental Degradation of Materials in Nuclear Power Systems, Myrtle Beach, South Carolina, August 22-25, p.423, 1983.
[40] Macdonald, D. D. and Cragnolino, G., "The Critical Potential for the IGSCC of Sensitized Type 304 SS in High Temperature Aqueous Systems", Proc. Second Int. Sym. on Environmental Degradation of Materials in Nuclear Power Systems, Monterey, CA, September 9-12. p.426, 1985.
[41] Brown, K. S. and Gordon, G. M., "Effects of BWR Coolant Chemistry on the Propensity for IGSCC Initiation and Growth in Creviced Reactor Internals Components", Proc. Third Int. Sym. on Environmental Degradation of Materials in Nuclear Power Systems, Traverse City, Michigan, August 30- September 3, p.243, 1987.
[42] Itow, M. and Sudo, A., "SCC Growth Behavior on DCB Specimen of Type 304 Stainless Steel in High Temperature Water", Proc. Fifth Int. Sym. on Environmental Degradation of Materials in Nuclear Power Systems, Monterey, California, August 25-29, p.112, 1991.
[43] Sudo, A. and Itow, M., "SCC Growth and Intergranular Corrosion Behavior of Type 316L Stainless Steel in High Temperature Water", Proc. Fifth Int. Sym. on Environmental Degradation of Materials in Nuclear Power Systems, Monterey, California, August 25-29, p.251, 1991.
[44] Nakata, K., Shimanuki, S., Anzai, H., Mabuchi, K., Fuse, M. and Shigenaka, N., "Stress Corrosion Crack Growth of Sensitized Type 304 Stainless Steel during High Flux Gamma-Ray Irradiation in 288°C Water", Proc. Fifth Int. Sym. on Environmental Degradation of Materials in Nuclear Power Systems, Monterey, California, August 25-29, p.955, 1991.
[45] Katsura, R., Morisawa, J., Kodama, M., Nishimura, S., Suzuki, S., Shima, S. and Yamamoto, M., "Effect of Stress on IASCC in Irradiated Austenitic Stainless Steels",

Proc. Sixth Int. Sym. on Environmental Degradation of Materials in Nuclear Power Systems, San Diego, California, August 1-5, p.625, 1993.
[46] Weinstein, D., "Real Time In-Reactor Monitoring of Double Cantilever Beam Crack Growth Sensors", Proc. Sixth Int. Sym. on Environmental Degradation of Materials in Nuclear Power Systems, San Diego, California, August 1-5, p.645, 1993.
[47] Jenssen, A., Bengtsson, B., Morin, U. and Jansson, C., "Crack Propagation in Stainless Steels and Nickel Base Alloys in a Commercial Operating BWR", Proc. Seventh Int. Sym. on Environmental Degradation of Materials in Nuclear Power Systems, Breckenridge, Colorado, August 7-10, p.553, 1995.
[48] Lidar, P., "Influence of Sulfate Transients on Crack Growth in Type 304 Stainless Steel in Water at 288°C", Proc. Seventh Int. Sym. on Environmental Degradation of Materials in Nuclear Power Systems, Breckenridge, Colorado, August 7-10, p.597, 1995.
[49] Jansson, C. and Morin, U., "Assessment of Crack Growth Rates in Austenitic Stainless Steels in Operating BWRs", Proc. Eighth Int. Sym. on Environmental Degradation of Materials in Nuclear Power Systems, Amelia Island, Florida, August 25-29, p.667, 1997.
[50] Suzuki, S. and Shoji, T., "Characteristics of the SCC Surface Crack Propagation in the Low K Region in Oxygenated High Temperature Water", Proc. Eighth Int. Sym. on Environmental Degradation of Materials in Nuclear Power Systems, Amelia Island, Florida, August 25-29, p.685, 1997.
[51] Anzai, H., Nakata, K., Kuniya, J. and Hattori, S., "The Effect of Hydrogen Peroxide on the Stress Corrosion Cracking of 304 Stainless Steel in High Temperature Water", Corrosion Science, Vol.36, No.7, p.1201, 1994.
[52] Speidel, M. O., "Stress Corrosion Crack Growth in Austenitic Stainless Steel", Corrosion, Vol.33, No.6, p.199, 1977.
[53] Kikuchi, E., Itow, M., Kuniya, J., Sakamoto, H., Yamamoto, M., Sudo, A., Suzuki, S. and Kitamura, M., "Intergranular Stress Corrosion Crack Growth of Sensitized Type 304 Stainless Steel in a Simulated Boiling-Water Reactor Environment", Corrosion, Vol.53, No.4, p.306, 1997.
[54] Hazelton, W. S. and Koo, W. H., "Technical Report on Material Selection and Processing Guidelines for BWR Coolant Pressure Boundary Piping", NUREG-0313-Rev.2-Final, 1988.
[55] Jacobs, A. J., Wozadlo, G. P. and Wilson, S. A., "Stress Corrosion Testing of Irradiated Type 304 SS Under Constant Load", Corrosion, Vol.49, No.2, p.145, 1993.
[56] Nakata, K., Shimanuki, S., Anzai, H., Fuse, M. and Hattori, S., "Effects of γ-ray Irradiation on Crack Growth of Sensitized Type 304 Stainless Steel in 288°C Water", Corrosion, Vol.49, No.11, p.903, 1993.
[57] Andresen, P., Ford, F., Higgins, J., Suzuki, I., Koyama, M., Akiyama, M., Mishima, Y., Okubo, T., Hattori, S., Anzai, H., Chujo, H. and Kanazawa, Y., "Life Prediction of Boiling Water Reactor Internals", Proc. Of The ASME-JSME 4th Int. Conf. on Nuclear Engineering ICONE-4, Vol. 5, p. 461, New Orleans, ASME, 1996.
[58] Miwa, Y., Tsukada, T., Jitsukawa, S., Kita, S., Hamada, S., Matsui, Y. and Shindo, M., "Effect of Minor Elements on Irradiation Assisted Stress Corrosion Cracking of Model Austenitic Stainless Steels", J. Nucl. Mater., Vol. 233-237, p.1393, 1996.
[59] Miwa, Y., Tsukada, T., Tsuji, H. and Nakajima, H., "Microstructures of Type 316 Model Alloys Neutron-Irradiated at 513K to 1dpa", J. Nucl. Mater. Vol. 271 & 272,

p.316, 1999.
[60] Hamada, S. and Hojou, K., J. Nucl. Mater. 200, p.149, 1993.
[61] Ford, F. P., Taylor, D. E., Andresen, P. L. and Ballinger, R. G., "Corrosion Assisted Cracking of Stainless and Low Alloy Steels in LWR Environments", EPRI Contract RP2006-6, Report NP5064M, Feb. 1987.
[62] Ford, F. P. and Andresen, P. L., "Development and Use of a Predictive Model of Crack Propagation in 304/316L, A533B/A508 and Inconel 600/182 in 288°C Water", Proc. Third Int. Sym. on Environmental Degradation of Materials in Nuclear Power Systems, Traverse City, Michigan, August 30- September 3, p.789, 1987.
[63] Jenssen, A., and Ljungberg, L. G., "The Importance of Molybdenum on Irradiation Assisted Stress Corrosion Cracking in Austenitic Stainless Steels", CORROSION/96, Paper No. 101, 1996.
[64] Kasahara, S. et al., "The Effects of Minor Elements on IASCC Susceptibility in Austenitic Stainless Steels Irradiated with Neutrons", Proc. 6th Int. Symp. on Environmental Degradation of Materials in Nuclear Power Systems - Water Reactors, p.615, 1994.
[65] Suzuki, S. and Itoh, W., "Effect of Stress Biaxiality on SCC Growth Rate", Proc. of the 76th JSME annual meeting, Vol.1, Sendai, Japan, p.145, 1998.

Peter M. Scott,[1] Marie-Christine Meunier,[1] Denis Deydier,[2] Sarah Silvestre,[2] and Alain Trenty [3]

An Analysis of Baffle/Former Bolt Cracking in French PWRs

Reference: Scott, P. M., Meunier, M.-C., Deydier D., Silvestre, S., and Trenty, A., **"An Analysis of Baffle/Former Bolt Cracking in French PWRs,"** *Environmentally Assisted Cracking: Predictive Methods for Risk Assessment and Evaluation of Materials, Equipment, and Structures, ASTM 1401,* R. D. Kane, Ed., American Society for Testing and Materials, West Conshohocken, PA, 2000.

Abstract: Irradiation-assisted stress corrosion cracking (IASCC) has been observed in various highly irradiated, stainless steel core components of both Boiling Water and Pressurized Water nuclear reactors. This phenomenon is believed to be responsible for cracking detected by ultrasonic nondestructive examination of some Type 316L stainless steel baffle/former bolts in six first generation CP0 series PWRs operating in France. Similar bolt failures in PWR core structures have been confirmed more recently in other countries. This paper describes a statistical analysis of the French observations. The objective was to determine whether any of the known fabrication and operating characteristics of the baffle/former bolts could be identified as having an important influence on the extent of bolt cracking. This information has been used to aid decisions concerning inspection frequency, possible replacement of cracked bolts, and selection of more resistant materials.

Keywords: PWR, irradiation-assisted stress corrosion cracking, austenitic stainless steel, baffle/former bolts

Introduction

Baffle/former bolt cracking was first detected by non-destructive examination of the core internals of French CP0 series Pressurized Water Reactors (PWR) in 1989 [*1,2*]. The intergranular nature of the cracking between the head and the shank of the bolts was confirmed by metallographic examination after five bolts were removed from one plant in 1991 [*1*]. The most likely cause was deduced to be intergranular stress corrosion cracking. Due to the apparent importance of neutron irradiation damage as a precursor to the cracking, the phenomenon is now generally called Irradiation-Assisted Stress

[1] Principal consultant and assistant engineer respectively, Materials Technology Department, Framatome, Tour Framatome, 92084 Paris La Défense, France.
[2] Engineer, Reactor Branch, SEPTEN, Electricité de France, 12-14 Avenue Dutriévoz, 69628 Villeurbanne, France.
[3] Engineer, Reactor Vessel Department, DPN, Electricité de France, Site Cap Ampère, 1 Place Pleyel, 93207 Saint-Denis, France.

Copyright© 2000 by ASTM International www.astm.org

Corrosion Cracking (IASCC). Similar baffle/former bolt cracking has since been detected in PWRs in other countries [*3,4*].

The six plants in the CP0 series of three loop 900 MWe PWRs were the first to be built in France according to a Westinghouse licensed design. A cutaway drawing of the pressure vessel and core of a PWR is shown in Figure 1 while a more detailed sketch of the core baffle structure for CP0 plants is shown in Figure 2. An inset in Figure 2 shows a detail of the bolts that fix the vertical core baffle plates to eight horizontal formers. There are 120 bolts on each former level so that the total number of baffle/former bolts for the CP0 design is 960. This total represents a very large safety margin by comparison with the number strictly necessary for structural integrity. The core baffle structure is fabricated from Type 304L stainless steel while the bolts are fabricated from strain hardened (12 to 20%) Type 316L stainless steel. The heads of the bolts and the baffle plates are adjacent to the peripheral fuel elements of the core and are consequently highly irradiated in normal service for a design life of up to 40 years.

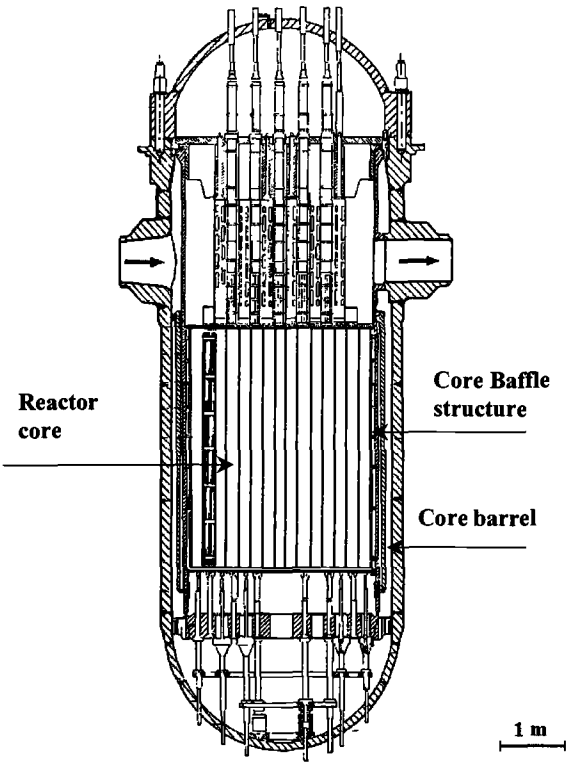


Figure 1 – *Pressure vessel and internal core components of a PWR.*

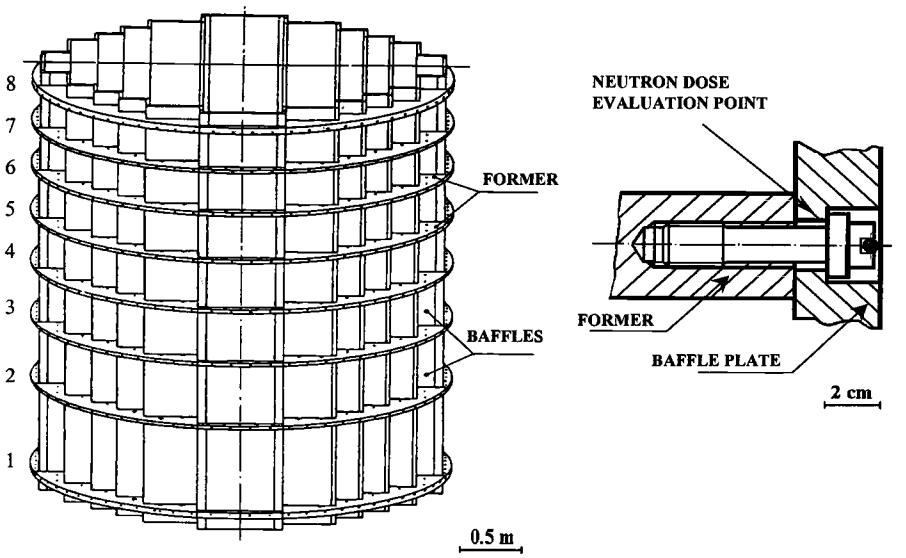


Figure 2 – *Core baffle structure of CP0 series PWRs.*

The primary coolant in a PWR enters the pressure vessel at a temperature of 286°C, flows down the inter-space between the pressure vessel and the core barrel, and then up through the fuel elements where it is heated to 323°C (Figure 1). The primary coolant is sub-cooled and therefore, with minor exceptions on highly rated fuel pins, does not boil during its passage over the nuclear fuel. A small bypass flow also passes through the space between the core barrel and the core baffle plates and cools those components that are subject to significant γ heating. In the original CP0 design, this bypass flow was downwards through the core barrel/baffle plate inter-space but was modified in the early nineties to flow upwards. This gives rise to plants being called "Downflow" or "Upflow" respectively, and is important because it influences the normal operating temperatures of the baffle/former bolts.

Attention was first drawn to the possibility of baffle/former bolt cracking when fuel pin failures in peripheral fuel elements were observed [*1*]. These fuel pin failures were caused by flow-induced vibration due to water jetting through gaps between the baffle plates. This problem was quickly resolved by the "Downflow" to "Upflow" conversion described above, which significantly reduced the differential pressure between the core barrel/baffle plate inter-space and the core itself. In due course, the origin of the gaps developing between the baffle plates was investigated. One potential reason identified was baffle/former bolt cracking and this gave rise to the ultrasonic inspections referred to earlier even though no correlation was eventually established between the occurrence of peripheral fuel pin failures and baffle/former bolt cracking.

The purpose of this paper is to describe the results of an analysis of the baffle/former bolt inspection data obtained over the last nine years. The objective was to determine those factors known about the fabrication and operating conditions of the bolts that

influence the observed extent of cracking. The ultimate aim was to aid decisions concerning inspection frequency, possible replacement of cracked bolts and selection of more resistant materials.

Database

Inspection Data

The total numbers of baffle/former bolts with reportable indications for each of the French CP0 plants after almost twenty years of operation have been reported previously (Figure 3) [*1,2*]. During the early inspections, a rather large number of bolts with uninterpretable indications were observed, but their number was sharply reduced by improvements in the inspection technique. Only the numbers of bolts deemed "defective" by the inspections are plotted in Figure 3. In addition, the published results for inspections carried out at Tihange 1, which is located in Belgium, are also plotted in Figure 3 [*3*]. This Belgian plant has the same design as the French CP0 series.

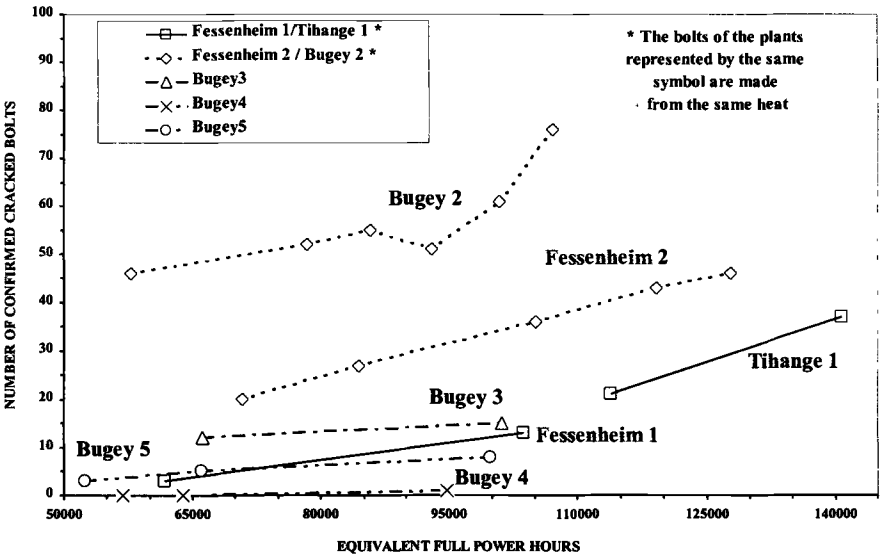


Figure 3 – *Summary of inspection results for baffle/former bolts for CP0 PWRs that have been confirmed defective.*

A striking feature of the data in Figure 3 is the variation in the percentage of affected bolts from practically zero to nearly 10% between different plants with the same design and no immediately apparent differences in the way they are operated. Of particular interest is the observation that plants with bolts fabricated from the same heat of Type 316L stainless steel show rather similar behavior suggesting a strong material dependent contribution to cracking sensitivity. Another interesting feature is the tendency in one

notable case (Bugey 2) for a rather erratic progression in the extent of bolt cracking that seems unlikely to be entirely due to inspection uncertainty.

The distribution of cracking among the different former levels and among the different baffle plates was observed to be far from uniform. Bolts with reportable indications tend to be concentrated on Level 2 with a lesser number on Levels 1 and 3 and occasionally on Levels 4 and 5. (The former levels are numbered from the bottom to the top of the core in Figure 2). Tihange 1 is an interesting exception to these generalizations in that the observed bolt cracking was much more evenly distributed with only a slight tendency to concentrate on level 2 [*3*]. In addition, it was observed in the French plants that certain baffle plates have significantly more cracked bolts than others, notably those that are subject to higher irradiation doses in service.

Chemical Composition and Mechanical Properties

Only five heats of material equivalent to Type 316L stainless steel were used to fabricate the baffle/former bolts of the French CP0 plants plus Tihange 1, as indicated in Figure 3. They were strain hardened between 12 and 20% to generate the required mechanical properties. The chemical compositions and mechanical properties are given in Table 1. For the purposes of this investigation, a number of other parameters were derived from these data using standard formulas from the literature. These included the martensitic transformation temperature Md_{30}, the stacking fault energy, and the nickel and chromium equivalents. A lack of a data concerning free nitrogen content for some heats prevented this parameter being included in these calculations.

Table 1 - *Chemical composition and mechanical properties of the baffle/former bolts as manufactured.*

Heat	C, %	Cr, %	Ni, %	Si, %	Mn, %	S, %	P, %	Mo, %	Cu, %	Co, %	N_2, %
AA016	0.026	16.80	12.10	0.64	1.81	0.016	0.017	2.56	0.100	<0.05	0.042
AA400	0.028	16.90	12.20	0.62	1.77	0.013	0.015	2.60	0.100	0.070	—
AM776	0.030	17.40	11.75	0.50	1.66	0.017	0.023	2.46	<0.10	<0.10	0.052
E4827	0.025	17.40	11.63	0.47	1.64	0.017	0.030	2.48	0.180	0.130	0.059
E5844	0.033	17.55	12.18	0.62	1.65	0.010	0.032	2.51	—	0.140	0.070

Heat	Ni_{eq}	Cr_{eq}	YS, MPa	UTS, MPa	El, %	Plant
AA016	13.785	21.92	513	676	34.3	Fessenheim 1 & Tihange 1
AA400	13.925	22.04	514	659	39.2	Fessenheim 2 & Bugey 2
AM776	13.48	22.09	456	637	40.0	Bugey 3
E4827	13.2	22.06	480	637	40.2	Bugey 4
E5844	13.995	22.555	513	667	37.7	Bugey 5

Ni_{eq} = % Ni + % Co + 0.5(% Mn) + 30(%C)+0.3(% Cu) + 25 (%N) [*5*]

Cr_{eq} = % Cr + 2(% Si) + 1.5(% Mo) + 5.5(% Al) + 1.75 (%Nb) + 1.5(% Ti) + 0.75(% W) [*5*]

Radiation Doses

Since it was strongly suspected that irradiation damage of the bolting materials was implicated in baffle/former bolt cracking, the neutron doses to the bolts were calculated for every bolt position on Levels 1 to 7. The uppermost level (8) is so little irradiated by at least an order of magnitude compared to the other levels that the calculation was not carried out for this case. The neutron dose was specifically evaluated at a depth corresponding to the bolt head to shank junction where the cracking was observed on the extracted bolts (Figure 2).

The basis for these calculations was two separate studies carried out independently by Framatome and EDF using the neutronic code DOT. The neutron fluxes to the bolts were evaluated for a specific reference case, fuel cycle 9 of Fessenheim 2, which had been especially well-instrumented in order to verify the neutronic codes. The two codes were found to give results in good agreement with each other. The fluxes at the head to shank junction of the baffle/former bolts ranged from 6.8×10^{12} to 2.7×10^{13} n/cm^{2}s ($E > 1.0$ MeV), the highest fluxes being associated with the re-entrant corners into the core and former Levels 2 to 6. These neutron fluxes were then scaled to account for the different fuel cycles of Fessenheim 2 and the other plants from available information on relative neutron doses to the pressure vessels. Changes in fuel management of the CP0 plants influenced the neutron fluxes to the internals (and pressure vessels) by up to a factor of two in the period relevant to this study. Then, from the known effective full power hours at each inspection, the neutron doses to the bolts were calculated. The doses at the head to shank junctions at all the bolt positions on Levels 1 to 7 were thus evaluated for each plant in the study at the time of each inspection.

Temperatures

The above-mentioned Framatome study of the neutron fluxes to the core internal structure also enabled the γ heating load to be evaluated and thence, via a thermalhydraulic study, the temperatures at various points in the core internals. Unfortunately, these studies were not sufficiently comprehensive to allow the temperatures to be evaluated at every baffle/former bolt position. Nevertheless, sufficient data were available to allow linear interpolation to be used to fill in the gaps. At the bolt head to shank junction, the surface metal temperatures for the "Upflow" condition vary from 295 to 344°C and are up to 12°C higher at the hottest positions for the "Downflow" condition. Thus, for the "Upflow" condition that applied to the CP0 plants during the inspection campaign, the surface temperature at the crack initiation point rarely exceeded the primary circuit pressurizer temperature of 342°C. This would seem to exclude local boiling of the fluid trapped in the crevice between the bolt and its hole (Figure 2) as contributing to baffle/former bolt cracking. It should be noted, however, that the internal metal temperatures have been estimated to be as high as ~370°C due to γ heating.

Bolt Stresses

The initial torquing of the baffle bolts leads to pre-loads between about 20 and 37.5 kN. These values take into account the effects of stress relaxation by primary creep

during the first increase in temperature to the operating value. The bolt stresses evolve subsequently due to the action of isothermal relaxation, irradiation creep and, possibly, irradiation induced swelling of the baffle plates (even if very small). These phenomena and their effect on bolt stresses have been neglected in this study.

The unbolting torques of about 80 baffle bolts were measured at Tihange 1 during the baffle bolt replacement campaign conducted in 1995. The results appear to indicate that some modest degree of relaxation had occurred. The uncoupling torques were on average smaller for the most irradiated former levels (levels 2 to 6) than the least irradiated former levels (levels 1, 7 and 8), consistent with the expected influence of irradiation creep.

Differential thermal expansion between the core barrel and the baffle plates applies shear loads on the bolted joints and induces cyclic bending in the baffle bolts. No three-dimensional stress analysis of the baffle/former structure is available to evaluate these stresses, although a simplified method was applied in another Framatome study of three separate baffle plate types for both the "Upflow" and "Downflow" conditions. The results showed a consistent trend for all three types of baffle plate with very similar values at the same former levels and for the two directions of flow in the core barrel/baffle plate inter-space. Thus, an average value of shear stress due to differential thermal expansion was assumed to apply to all the bolts on the same former level independent of the identity of the baffle plate. These average values for the "Upflow" condition varied from 20.6 kN for the former levels at the top and bottom of the core (1 and 8) to 3.8 kN for the middle levels (4 and 5).

The above results should be considered as indicating the relative magnitudes of the baffle bolt loads in order to compare stresses between different bolts. They are linked to the distribution of heat in the core baffle structure and therefore vary with fuel management. For this reason, they can only be considered to be approximate values. The true values of the stresses at the junction of the head and the shank of the baffle bolts are difficult to determine. Local stress concentrations, plastic deformation and structural relaxation modify the initial torque and differential thermal expansion loads. In summary, the only available parameter which enables a distinction to be made in the evaluation of baffle/former bolt loads is that due to differential thermal expansion although this gives only a simplified view of the state of the stresses in the bolts.

Transients

An assessment was carried out by EDF of the operating transients affecting the CP0 plants since start-up. Some of these transients can potentially stress cycle the baffle/former bolts. Summarizing the plant records is not an easy task and envelope conditions are often used to characterize particular types of transient. Nevertheless, these summaries provided a quantitative guide, albeit subject to some uncertainty, to the CP0 plant transients. It was particularly noted that the number of transients defined by a power envelope of 15 to 100% full power varied significantly between the plants due to their use from time to time at full power during the working week and on hot stand-by during the weekends. This factor turned out to be an important one in the subsequent analysis.

Analysis of Baffle/Former Bolt Cracking

As a Function of Neutron Dose

The preliminary analysis of the extent of baffle bolt cracking was in the form of histograms of the fraction of bolts classified as "defective" as a function of neutron dose. Only five French CP0 plants were analyzed in this way because Bugey 4 had too few indications at the last examination. An example is shown in Figure 4 based on the 1997 inspection of the most affected plant, Bugey 2, which shares the most sensitive heat of material with Fessenheim 2. The histogram is in steps of $2x10^{21}$ n/cm^2, E >1.0 MeV, the bolt doses being rounded to the lower limit of each step. Also indicated in Figure 4 are the maximum neutron doses attained by the bolts at each former level at the 1997 inspection. The results are shown separately for each former level because the bolt stresses (loads), which are nearly constant for each former level, were assumed to have an important influence on the extent of cracking. It should also be noted in Figure 4 that the normal order of former Levels 1 and 2 has been reversed in order not to hide the results of former Level 1 behind those of former Level 2. In addition, former Level 8 is ignored because of the very low neutron flux at this level.

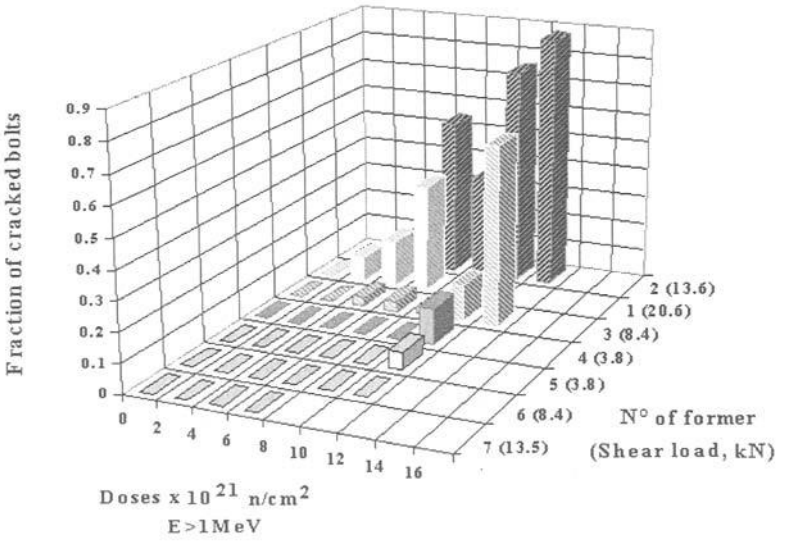


Figure 4 – *Histogram showing the fraction of defective baffle/former bolts observed in 1997 as a function of neutron dose for the Bugey 2 plant.*

It is important to note that the dose axis of Figure 4 should not be interpreted as being directly proportional to time. The dose axis reflects the combined effect of time and flux profile at the time of the inspection. At any point in time, bolts on a given former level will have a range of neutron doses that for this purpose have been classified in "bins" increasing in units of $2x10^{21}$ n/cm^2, E >1.0 MeV. In addition, the ordinate of Figure 4

shows the fraction of bolts that have cracked of the total number that have attained a given neutron dose. The total numbers of bolts in each dose "bin" cannot be deduced from this figure.

Figure 4 shows that the fraction of cracked bolts increases significantly with cumulative neutron dose and differential thermal loading (defined approximately by the former level). Thus, in spite of neutron doses which are as high for former Levels 4 and 5 as for Levels 2 and 3, for example, the lower stresses at Levels 4 and 5 seem to have caused much less bolt cracking. At the more highly stressed Levels 2 and 3, the start of bolt cracking coincides with the apparent threshold dose of $2x10^{21}$ n/cm^2, E >1.0 MeV observed in laboratory studies of IASCC in PWR primary water [*6,7*]. Baffle/former bolt cracking at the lower stressed Levels 4 and 5 reveals a much higher apparent neutron dose threshold. It can also be anticipated from Figure 4 that cracking may initiate in the near future at former Levels 6 and 7 since these are comparable to former Levels 2 and 3 from the point of view of bolt stresses, but are presently only just approaching the apparent threshold dose for those stress levels (6 to $8x10^{21}$ n/cm^2, E >1.0 MeV). This conclusion is, of course, only true if there are no other unknown parameters that vary between former levels and affect the cracking phenomenon. Moreover, the approximate nature of the average bolt loads characterizing each former level make precise comparisons difficult.

Due to the distributed or stochastic character of most material aging phenomena, including stress corrosion cracking, it can be helpful to fit the observed failure rate of a given type of component or test specimen to an appropriate distribution. In the case of stress corrosion cracking, the Weibull distribution is often found suitable for this purpose [*8,9*]. In principle, the core baffle bolt inspection data can be fitted to the Weibull distribution where the cumulative neutron dose rather than time is used as the principal parameter governing sensitivity to IASCC. For this study, the "rank regression" method was used to fit the Weibull equation to the inspection data in the form of the histograms described earlier.

The Weibull distribution was fitted to the fraction of baffle bolts declared "defective" by ultrasonic inspection as a function of the neutron dose at each former level for each CP0 plant. This was based on the hypothesis that it is necessary to separate the influence of stress as well as neutron fluence on the phenomenon of IASCC. Unfortunately, the scatter observed on the Weibull plots for the results of each inspection for the same plant was often unsatisfactory although it appeared to be random. This suggests that the width of the error band is mainly linked to scatter in the original data rather than a fundamental error in the hypothesis that the extent of cracking depends only on the cumulative neutron dose for each former level for a given heat of material.

In an attempt to reduce the impact of the scatter in the original database, all the inspection results after the first observation of a "defective" bolt at each former level (for each plant) were grouped together. Thus, all the bolts in each histogram step (in units of $2x10^{21}$ n/cm^2, E>1.0 MeV) were added together as were the corresponding numbers of bolts with reportable indications, independently of the time of inspection, before calculating the fraction of cracked bolts. In this way, the sample size is multiplied by the number of inspections carried out after the first observation of a "defective" bolt at each former level, and the range of neutron doses taken into account is thereby also increased. This approach is clearly permissible only if the cumulative neutron dose controls the rate

of cracking independent of the time of each inspection. The results of the Weibull analyses carried out on this basis are shown in Figure 5 for Bugey 2.

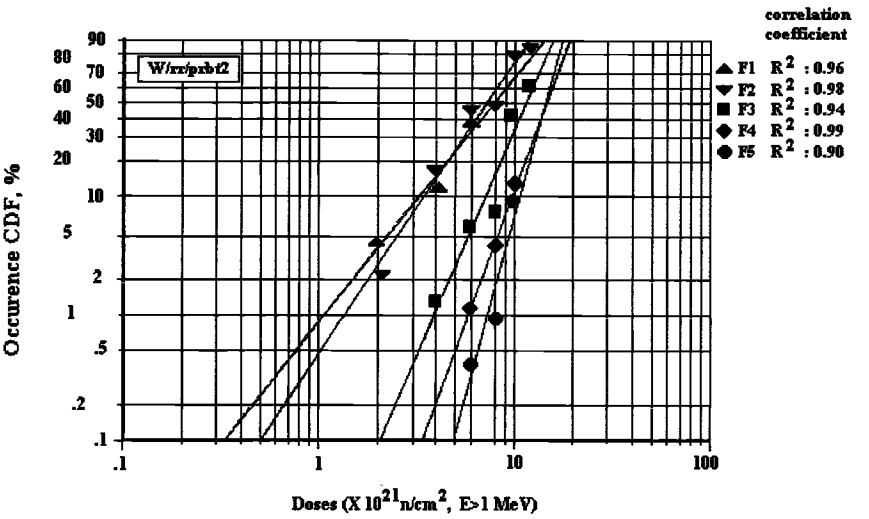


Figure 5 – *Weibull plot of the percentage of defective baffle/former bolts as a function of neutron dose based on the data for all inspections combined for the Bugey 2 plant.*

The quality of the Weibull distributions based on all the inspection data grouped together (by former level of each plant) was particularly satisfactory for Bugey 2, but not really acceptable from a statistical point of view for the other CP0 plants. It is noteworthy that the number of inspections is particularly high for Bugey 2. This observation supports the approach taken here, which also does not seem to have disturbed significantly the values of the Weibull parameters compared to those deduced from the more scattered plots for each individual inspection.

As a Function of Bolt Loads and Temperatures

Since the core baffle structure has effectively eightfold symmetry, it is sufficient to define the positions of all the baffle bolts on a one eighth plan. It is then possible to examine the correlation between the extent of cracking by bolt position (of a total of 8) as a function of the parameters neutron dose, stress (or load due to differential thermal effects) and characteristic temperature. The loads and temperatures used here apply to the "Upflow" condition as described earlier.

The statistical correlation analysis of the last two inspections of each CP0 plant was carried out using a commercial statistical analysis program. It showed that the rate of cracking by bolt position depended very significantly on the neutron dose, with the exception of Fessenheim 2. The correlation with the bolt loads was, in general, less significant than that with the neutron dose, but nevertheless important for Fessenheim 2

and Bugey 2. A similar observation was made for the bolt temperature, which always exerted the weakest influence of the three parameters.

It should also be noted, however, that the neutron doses were always strongly inter-correlated with the loads and temperatures, and therefore these three parameters were not statistically independent variables. Nevertheless, it is recalled that in the Weibull study it was necessary to analyze the data by former level because the bolt loads that are characteristic of each level seem to exert a strong influence on the rate of cracking for any given neutron dose.

An attempt to define a quantitative parametric correlation for the extent of baffle bolt cracking by multi-parametric regression on the parameters described above failed to give a satisfactory result. The correlation coefficients never exceeded 50 %. No significant improvement was obtained by using an equation dependent on stress to integral powers up to six, an exponential inverse temperature dependence, and an exponential function for the neutron dose. These functions were chosen as the best approximations likely to be most physically realistic from the point of view of their influence on IASCC.

The influence of power transients for each French CP0 plant on the extent of baffle bolt cracking was also examined. However, because all bolt positions for any given plant experience the same number of power transients, this aspect was integrated into the task devoted to the influence of material heat, which is also unique to each plant.

As a Function of Metallurgical Data and Plant Transients

In order not to confuse the influence of either material heat or plant transients with the other potentially important parameters (neutron dose, bolt load, temperature), the inspection results for this analysis were selected for a specific and comparable maximum cumulative neutron dose for each plant. This procedure was equivalent to taking a vertical cut through Figure 3 at about 100, 000 hours.

It is possible to distinguish three distinct groups of plants in Figure 3. In the first group, the most affected, are found Fessenheim 2 and Bugey 2, which share the same heat of material. The second group comprises Fessenheim 1 and Tihange 1, which also share a common heat of material, plus Bugey 3. The final, least-affected group, comprises Bugey 4 and 5. There are, however, no immediately obvious trends in the metallurgical database to explain these apparent differences in cracking behavior.

A statistical correlation analysis was carried out between the observed extent of baffle bolt cracking at each French CP0 plant and the metallurgical parameters shown in Table 1. In addition, some derived parameters such as the martensitic transformation temperature Md_{30}, the stacking fault energy and the nickel and chromium equivalents were also examined (Table 1). It showed that only the concentrations of chromium and phosphorus had any significant effect (at or better than the 90% confidence level) on the behavior of the different heats of material and that higher concentrations of both were beneficial. The correlation with chromium was rather weak compared to that of phosphorus and, moreover, both parameters were surprisingly inter-correlated. These metallurgical parameters were, however, insufficient in themselves to enable a quantitative parametric correlation to be derived. The physical significance of these trends should also be treated with caution due to the small ranges of values available for each metallurgical parameter for only one generic type of stainless steel. Nevertheless, it

is noted that phosphorus has been cited as a favorable element with regard to neutron irradiation damage in experimental studies for fast reactors [7]. This element in solid solution is an efficient trap for point defects induced by neutron irradiation and, in this way, it can potentially slow the microstructural changes occurring as point defects diffuse towards grain boundaries.

Concerning the transients affecting baffle/former bolt cracking of French CP0 plants, their effect was studied after the metallurgical parameters influencing the rate of cracking per plant had been identified. When the two effects were examined together, a statistically significant correlation (at or better than the 90% confidence level) was found between the extent of baffle/former bolt cracking and the cumulative number of transients corresponding to the normal increase and decrease of power between 15 and 100%. No other transients were statistically significant.

By combining the metallurgical and transient effects on baffle/former bolt cracking, a satisfactory quantitative parametric correlation was found that rationalized the plant-to-plant behavior observed in Figure 3 at approximately 100, 000 hours. The two variables used were the phosphorus concentrations and the cumulative totals of the major (15 to 100%) power transients. The parametric correlation derived for the total fraction of bolts affected per plant had a regression coefficient of 92%. The p-values for the coefficients were less than 0.05 so that the terms were statistically significant to better than the 95% confidence level.

A further check on the importance of the major power transients was carried out by comparing the results of the above parametric correlation with the rather discontinuous development of baffle/former bolt cracking observed at Bugey 2. Thus, the correlation developed from a vertical cut through Figure 3 at about 100, 000 hours was tested in the orthogonal direction as a function of time. This comparison is shown in Figure 6 where the time axis is expressed in terms of reactor fuel cycles. Despite the fact that the (non-linear) effect of increasing neutron dose was ignored by this procedure, the comparison in Figure 6 would seem to confirm the importance of the major power transients for baffle/former bolt cracking.

These observations provoked a more detailed study before too much physical importance was attributed to the parameters identified as having a statistically significant effect on the extent of baffle/former bolt cracking. As stated earlier, the classification and counting of transients were not straightforward and a re-examination gave rise to a slightly different database. The statistical significance of the metallurgical variables in Table 1 plus derived parameters such as Md_{30}, stacking fault energy and nickel and chromium equivalents was then re-examined together with the revised list of transients. It was observed that some additional power transients other than the normal 15 to 100% power variations were now statistically significant for enhancing the extent of cracking. Moreover, a high Cr_{eq}/Ni_{eq} ratio had a favorable effect on the incidence of baffle/former bolt cracking.

A second quantitative parametric correlation including a constant was then derived as a function of the major (15 to 100%) power transients and the ratio of the chromium and nickel equivalents. In this case, the regression coefficient was 97.5% and the p-values of the coefficients were less than 0.01 implying a statistically significant relationship between the variables at the 99% confidence level.

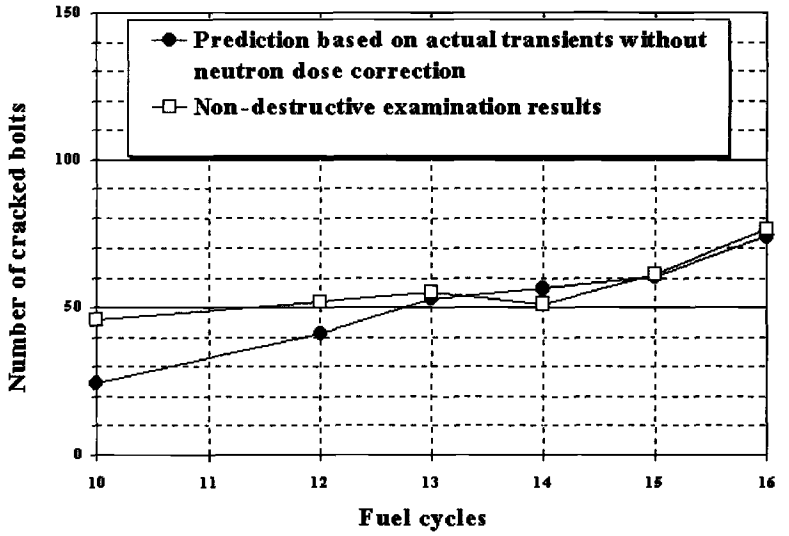


Figure 6 – *Parametric correlation showing the influence of major power transients on the development of baffle/former bolt cracking at Bugey 2.*

The results above underline the fact that a combination of heat to heat variability and plant transients are certainly linked to the great differences in the extent of baffle/former bolt cracking observed in French CP0 plants. However, the precise physical nature of these effects still remains to be determined and is the subject of ongoing studies.

Conclusions

An analysis has been carried out of the cracking detected by nondestructive examination of the baffle/former bolts of French CP0 plants.

It is observed that the extent of cracking is principally a function of the neutron dose. The heat of stainless steel used to fabricate the bolts, the number of major power transients (between 15 and 100%) and the differential thermal expansion loads applied to the bolts are additional important influencing parameters.

The increase in the extent of cracking as a function of the neutron dose can be fitted to a Weibull distribution. This was carried out for each former level of each plant because the differential thermal expansion loading of the bolts is approximately constant for each former level but varies significantly between the former levels. However, only the Weibull distributions deduced for former Levels 1 to 5 of Bugey 2 (based on the non-destructive examination data for five inspections grouped together) are statistically acceptable.

The combination of one parameter representing the metallurgical differences between the heats of Type 316L stainless steel (the phosphorus content or the ratio Cr_{eq}/Ni_{eq}) with the numbers of major power transients is sufficient to describe parametrically the differences in the extent of baffle bolt cracking observed between French CP0 plants at

around 100, 000 effective full power hours of operation. This same parametric correlation also successfully explains the rather discontinuous development of baffle/former bolt cracking observed at Bugey 2, which underlines the significance of power cycling. Nevertheless, the precise physical nature of these effects still remains to be determined and is the subject of ongoing studies.

References

[1] Cauvin, R., Goltrant, O., Rouillon, Y., Verzaux, E. Cazus, A., Dubuisson, P., Poitrenaud and P., Bellet, S., "Endommagement des structure internes inférieures soumises à fortes fluence: apports de l'expertise," *Proceedings of the International Symposium Fontevraud III*, Société Française d'Energie Nucléaire, 1994, pp. 54-65.

[2] Trenty, A. and Deydier, D., "Maintenance of the Lower Internal Structures in EDF PWRs," *Proceedings of an IAEA Specialists Meeting on Behaviour of Core Materials*, October 6-8, 1998, Rez, Czech Republic.

[3] Pironet, G., Heuzé, A., Goltrant, O. and Cauvin, R., "Expertise des vis de liaison cloison-renfort de la centrale de Tihange 1," *Proceedings of the International Symposium Fontevraud IV*, Société Française d'Energie Nucléaire, 1998, pp. 195-206.

[4] Pfefferle, J. R., Saporito, M., Mignogna, G. M. and Hacker, M. G., "Investigation program on Irradiated Reactor Vessel Internals Bolting," *Eurocorr '99*, August 30 - September 2, 1999, Aachen, Germany.

[5] Lacombe, P., Baroux, B., Beranger, G., *Les Aciers Inoxydables*, Les Editions de Physique, 1990.

[6] Scott, P., " A Review of Irradiation Assisted Stress Corrosion Cracking ," *Journal of Nuclear Materials*, Vol. 211, 1994, pp. 101-122.

[7] Bruemmer, S. M., Simonen, E. P., Scott, P. M., Andresen, P. L., Was, G. S. and Nelson, J. L., "Radiation-Induced Material Changes and Susceptibility to Intergranular Failure of Light-Water-Reactor Core Internals," *Journal of Nuclear Materials*, Vol. 274, 1999, pp. 299-314.

[8] Scott, P., Meyzaud, Y. and Benhamou, C., "Prediction of Stress Corrosion Cracking of Alloy 600 Components exposed to PWR Primary Water," *Proceedings of Plant Aging and Life Prediction of Corrodible Structures*, NACE International, 1995, pp. 285-292.

[9] Abernethy, R.B., *The New Weibull Handbook*, 1st edition, Dr. Robert B. Abernethy, 1993.

Toshio Yonezawa,[1] Koji Fujimoto,[1] Toshihiko Iwamura,[1] and Seishi Nishida[2]

Improvement of IASCC Resistance for Austenitic Stainless Steels in PWR Environment

Reference: Yonezawa, T., Fujimoto, K., Iwamura, T., and Nishida, S., **"Improvement of IASCC Resistance for Austenitic Stainless Steels in PWR Environment,"** *Environmentally Assisted Cracking: Predictive Methods for Risk Assessment and Evaluation of Materials, Equipment, and Structures, ASTM 1401,* R. D. Kane, Ed, American Society for Testing and Materials, West Conshohocken, PA, 2000.

Abstract: In recent years, irradiation-assisted stress-corrosion cracking (IASCC) of austenitic stainless steels for core internal component materials became a subject of concern for in light water reactors (LWRs). Intergranular cracking of baffle former bolts has been found in pressurized water reactors (PWRs) after long operating periods. Therefore, the authors investigated the possibility of IASCC in austenitic stainless steels used for core internal materials of PWRs in order to estimate the degradation of PWR plants up to the end of their lifetime. In this study, in order to verify the hypothesis that the IASCC in PWRs can be caused by the primary water stress-corrosion cracking (PWSCC) as a result of radiation-induced segregation (RIS) at grain boundaries, the authors melted materials whose bulk compositions simulated the grain boundary compositions of irradiated austenitic stainless steels. The effects of chromium, nickel and silicon content on PWSCC susceptibility was studied by slow strain-rate tensile (SSRT) tests. In order to improve the IASCC resistance of austenitic stainless steels for PWRs, authors developed modified 316CW(cold worked) and high chromium stainless steels. The former steel has high chromium content and ultra low impurity elements within the specification of chemical composition for ASTM A193 B8M Type 316 stainless steel. The latter steel has high chromium content of up to 30% chromium and ultra low impurity elements. Both materials are aged after solution annealing, in order to precipitate the $M_{23}C_6$ carbides coherent with the austenitic matrices along the grain boundaries and to recover the sensitization.

Keywords: irradiation-assisted stress-corrosion cracking, stainless steel, PWR, slow strain-rate tensile test, irradiation-induced segregation, aging, cold working, coherency

Introduction

Austenitic stainless steels are widely used for the core internals of pressurized water reactors (PWRs) and boiling water reactors (BWRs) due to their resistance to corrosion in high temperature water and to irradiation embrittlement. However, intergranular cracking of core shrouds [1] of BWRs was reported as due to irradiation-assisted stress

[1] Chief staff engineer, engineer, acting manager, respectively, Takasago R & D Center, Mitsubishi Heavy Industries, Ltd. 2-1-1, Shinhama, Arai-Cho, Takasago-City, Hyogo Pref., 676-8686, Japan.

[2] Technical project manager, Kobe Shipyard & Machinery Works, Mitsubishi Heavy Industries, Ltd., 1-1-1, Wadasaki-Cho, Hyogo-Ku, Kobe-City, Hyogo Pref., 652-8585, Japan.

Copyright© 2000 by ASTM International www.astm.org

corrosion cracking (IASCC) as well as the cracking of baffle former bolts (BFBs) in PWRs.

IASCC of stainless steel components has recently become an important aging issue in light water reactors (LWRs) [2].

A combination of the following phenomena has been proposed as the possible cause of IASCC in the literature [2-6].

(1) Irradiation-induced segregation of alloying elements and impurities at the grain boundaries.
(Depletion of chromium and molybdenum, and enrichment of nickel, silicon, sulfur, etc..)

(2) Micro-structural changes due to irradiation.
(Transformation to martensitic phase, increase of dislocation loops, etc..)

(3) Mechanical property changes due to irradiation.
(Increases in tensile strength, yield strength, and hardness, and decreases in elongation and toughness.)

(4) Generation of oxidants due to radiolysis by neutron and gamma rays in the water.

In PWRs, the production of oxidants (radicals, ions, and molecules) due to radiolysis is believed to be suppressed by including from 25 to 35 cc/kg STP (standard temperature and pressure)$\cdot H_2O$ (about 2-3 ppm) of hydrogen in the primary water environment. Although, IASCC has only been observed occasionally in PWRs, the authors have estimated the susceptibility of IASCC for PWRs, after high irradiation dose and under high stress.

In the authors' previous studies [6] slow strain-rate tensile (SSRT) test in simulated PWR primary water have been carried out as well as energy dispersive X-ray spectroscopy (EDS) analyses of the grain boundaries for irradiated Type 304, Type 316 CW, and Type 347 stainless steels. In addition, out of pile SSRT tests were conducted on laboratory melted low chromium, high nickel, and high silicon alloys simulating grain boundary chemical compositions of Type 316 stainless steel after irradiation of 2×10^{22} n/cm^2 (E>0.1MeV). It was conducted that the intergranular cracking in BFBs of PWRs [7] seemed to be caused by the primary water stress corrosion cracking (PWSCC) due to changes in grain boundary chemical compositions, characterized by depletion of chromium concentration and enrichment of nickel and silicon concentration under irradiation [6, 8, 9].

The authors' previous studies [8, 9] also reported that the PWSCC susceptibility of austenitic stainless steels increase with reduced chromium composition and increased nickel and silicon composition. In addition, susceptibility to PWSCC is decreased by precipitation of the coherent carbides with the matrices at grain boundaries.

From these data, it was estimated that if IASCC occurs in the core components of PWRs in future, radiation-induced segregation (RIS) near grain boundaries and high stress would be the main cause of IASCC in PWRs.

In this study, the authors evaluated PWSCC susceptibility of the austenitic alloys, of which the chemical compositions simulated the grain boundary chemical compositions after irradiation. SSRT tests in simulated PWR primary water were carried out in order to verify our hypothesis that IASCC in PWRs can be caused by PWSCC due to RIS. Moreover, in this study the authors investigated the optimized chemical compositions and heat treatment conditions of Type 316 CW and a high chromium austenitic stainless steels to develop IASCC resistant alloys for alternative BFB materials. Also, the cold working process has been studied in further detail in order to meet to required mechanical property for bolting materials.

To assist in the development of a modified 316 CW stainless steel that meets the requirements of ASTM A193 B8M, the authors examined the effects of carbon, nickel, chromium, and molybdenum compositions on grain boundary precipitation and intergranular corrosion behavior. In the case of 300 series austenitic stainless steels, recovery of grain boundary chromium depletion is observed typically after aging at about

750 °C for periods longer than 1,000 hours [10]. Therefore, precipitation of coherent grain boundary carbides without grain boundary chromium depletion will be achieved by aging at about 750 °C for longer than 1,000 hours after solution treatment. To reduce the aging time, the effects of carbon content and cold working before aging on chromium depletion and the precipitation of grain boundary carbides were examined in this study. From the authors' calculation of RIS in Type 304 and Type 316 CW stainless steels, the chromium content of the austenitic stainless steels before irradiation should be higher than 30% in order to ensure a chromium composition higher than 15% at the grain boundaries of BFBs after 40 years of operation. Thus, to aid in the development of a high chromium stainless steel, the authors examined the effects of carbon, nickel, and silicon contents in 30% chromium stainless steels on the grain boundary precipitation and intergranular corrosion behavior.

Experimental Procedures

Test Materials

PWSCC Susceptibility of Simulated Materials-Chromium and molybdenum depletion and nickel, silicon, sulfur, phosphorus enrichment are commonly observed at grain boundaries of irradiated Type 316 CW and Type 304 stainless steels. In this study, the chemical compositions of the alloys investigated have simulated grain boundary chemical compositions of irradiated Type 304 and Type 316 CW stainless steels, as shown in Table 1. Thus, the simulated materials contain less chromium and more nickel, silicon and phosphorus than normal Type 304 and Type 316 CW stainless steels. In order to confirm the effect of individual alloying elements on the PWSCC susceptibility of irradiated stainless steels, these simulated materials were evaluated by SSRT test in simulated PWR primary water in this study.

Table 1-*Chemical composition of simulated RIS materials.*

Alloy No.	Feature	Chemical Composition (mass%)								
		C	Si	Mn	P	S	Mo	Ni	Cr	Fe
1	Low Cr-High Ni-High Si	0.040	2.74	0.94	<0.001	0.001	-	27.80	11.70	Bal.
2	Low Cr-High Ni	0.030	0.02	0.89	<0.001	0.001	-	27.70	11.70	Bal.
5	High Si	0.030	2.96	0.99	0.001	0.001	-	11.90	16.90	Bal.
6	High P	0.040	0.02	0.97	0.140	0.001	-	12.80	16.80	Bal.
A5	Med. Cr- Med. Ni-High Si	0.039	2.94	1.00	<0.001	<0.001		19.74	14.94	Bal.
A6	Med. Cr-High Ni-High Si	0.039	2.96	0.99	<0.001	0.001	-	29.84	15.06	Bal.
A8	Med. Ni-High Si	0.039	3.00	1.01	<0.001	0.001	-	20.09	19.95	Bal.
A9	High Ni-High Si	0.039	3.03	1.01	<0.001	0.001	-	30.10	20.08	Bal.
A12	Low Cr-High Ni-High P	0.038	0.01	1.02	0.130	0.001	-	27.52	11.99	Bal.
A13	Low Cr-High Ni-High S	0.035	0.02	0.95	<0.001	0.300	-	27.95	11.90	Bal.
A14	Low Cr-High Ni- High Si-Mo	0.041	3.04	1.01	<0.001	0.001	2.49	28.14	12.11	Bal.
A16	Low Cr-High Ni-High Si	0.009	3.02	1.01	<0.001	0.001	-	27.68	11.79	Bal.
A24	Ultra Low Cr-High Ni-Mo	0.033	0.03	0.97	0.001	0.001	2.43	28.43	5.10	Bal.
A25	Ultra Low Cr-High Ni	0.037	0.02	1.01	0.001	0.001	-	28.31	5.17	Bal.
M1	Med. Cr- Ultra High Ni -Low Si	0.035	0.53	0.99	<0.001	0.002	-	48.89	14.74	Bal.
M3	Med. Cr- Ultra High Ni- Med. Si	0.033	1.03	0.99	<0.001	0.002	-	48.88	14.75	Bal.
M5	Med. Cr- Ultra High Ni- Med. Si	0.040	1.99	1.00	<0.001	0.001	-	48.94	15.03	Bal.
M7	Low Cr- Med. Ni-High Si	0.040	2.79	0.99	<0.001	0.002	-	14.75	9.83	Bal.
M8	Med. Cr- Ultra High Ni-High Si	0.038	2.96	0.99	<0.001	0.002	-	48.77	14.99	Bal.
C1	Ultra Low Cr-High Ni-High Si	0.0095	3.04	1.02	<0.001	0.001	-	30.18	5.98	Bal.
304	304 stainless steel	0.060	0.56	0.83	0.025	0.004	-	8.80	18.40	Bal.

Med.: Medium

The above simulated materials were solution annealed at 1,100 °C for 1 hour and water-quenched. Alloys 1, 2, 5, A14, and C1 were aged at 650 °C for 20 hours (alloys 1S, 2S,

A14S, C1S) after solution annealing in order to precipitate coherent $M_{23}C_6$ carbides with the matrices at the grain boundaries. The aged Type 304 stainless steel (alloy 304S) was also tested as a reference material.

Alternative IASCC-Resistant Materials for Baffle Former Bolts-Using the results from the above work, modified 316 CW and high chromium austenitic stainless steels were developed for this study in order to select the optimum chemical compositions for PWR alternative BFB materials.

These test materials were melted using a laboratory 17 to 75 kg vacuum induction melting furnace and formed to a 30 mm diameter round bar by forging. The chemical compositions of these test materials are shown in Tables 2 to 4. To obtain the optimum microstructure of grain boundary carbides and the required mechanical properties, various conditions of solution heat treatment, aging, and cold working processes were attempted with these test materials. Using the modified 316 CW stainless steel, solution heat treatment, cold working, and aging processes were examined under the conditions shown in Fig. 1. Cold working was conducted by cold rolling.

Table 2-*Chemical compositions of test 316 stainless steels.*

Steel	Chemical Composition (mass%)								
	C	Si	Mn	P	S	Ni	Cr	Mo	Fe
K1	0.060	0.01	0.01	0.001	0.001	13.61	17.54	2.44	Bal.
K2	0.041	0.01	0.03	0.001	0.001	13.82	17.77	2.14	Bal.
K3	0.058	0.01	0.03	0.001	0.001	13.75	17.86	2.11	Bal.
K4	0.073	0.01	0.02	0.001	0.001	13.93	16.36	2.17	Bal.
K5	0.073	0.01	0.03	0.001	0.001	13.85	17.10	2.14	Bal.
K6	0.068	0.01	0.03	0.001	0.001	10.30	17.83	2.15	Bal.
K7	0.074	0.01	0.02	0.001	0.001	12.07	17.89	2.15	Bal.
K8	0.072	0.01	0.02	0.001	0.001	13.79	17.78	2.44	Bal.
K9	0.072	0.01	0.03	0.001	0.001	13.86	17.71	2.83	Bal.
K11	0.071	0.01	0.03	0.001	0.001	13.75	17.69	2.10	Bal.
ASTM A193 B8M	≦0.08	≦1.00	≦2.00	≦0.045	≦0.030	10.00/ 14.00	16.00/ 18.00	2.00/ 3.00	–

Table 3-*Chemical compositions of high-chromium stainless steels tested.*

Steel	Chemical Composition (mass%)							
	C	Si	Mn	P	S	Ni	Cr	Fe
A (30Cr-20Ni)	0.040	0.03	1.51	0.001	0.002	20.59	30.20	Bal.
B (30Cr-25Ni)	0.039	0.03	0.18	0.001	0.001	25.97	30.28	Bal.
C (30Cr-30Ni)	0.037	0.05	0.19	0.001	0.001	30.46	30.18	Bal.
D (35Cr-35Ni)	0.021	0.03	1.51	0.001	0.001	35.39	35.07	Bal.

Table 4-*Chemical compositions of 30%Cr-30%Ni stainless steels.*

Steel	Chemical Composition (mass%)							
	C	Si	Mn	P	S	Ni	Cr	Fe
C1 (0.01%C)	0.012	<0.01	0.20	<0.001	0.001	29.84	30.14	Bal.
C2 (0.025%C)	0.024	0.01	≦0.01	≦0.001	0.001	30.00	30.01	Bal.
C3 (0.04%C)	0.040	0.01	≦0.01	≦0.001	0.001	29.86	29.99	Bal.
C4 (0.06%C)	0.057	0.01	≦0.01	≦0.001	0.001	30.10	30.08	Bal.
C5 (0.08%C)	0.082	<0.01	0.19	<0.001	0.001	30.22	30.19	Bal.

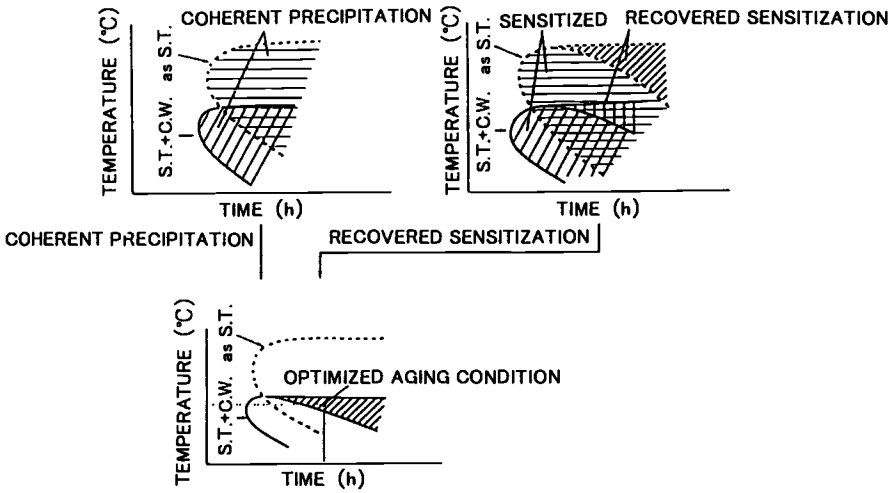


Figure 1-*The effect of cold working before aging on the precipitation time of coherent carbides at grain boundary and on the recovery of grain boundary chromium depletion by aging.*

SSRT Tests

SSRT tests on the simulated grain boundary materials were performed with an initial strain-rate of $1x10^{-7}$/s. The water chemistry of the SSRT test loop was simulated PWR primary water. In these tests, a test temperature of 360 °C was adopted to accelerate the SCC of the test alloys in the simulated PWR primary water. The fracture surfaces of specimens after SSRT tests were analyzed using scanning electron microscope (SEM) and the fracture mode was characterized. The area ratio of IGSCC fracture was estimated after SSRT tests in order to evaluate IGSCC susceptibility.

Intergranular Corrosion Tests

In order to select the optimum chemical compositions and heat treatment conditions from the viewpoint of chromium depletion and recovery of the grain boundary chromium depletion, an intergranular corrosion test was conducted on each test material. The intergranular corrosion test was conducted in a ferric sulfate-sulfuric acid solution according to ASTM A262 Practice B.

Microscopy

Grain boundary carbides and grain boundary chemical compositions were characterized via optical microscopy, scanning electron microscopy (SEM), and transmission electron microscopy (TEM). The TEM was conducted using a JEOL JEM-2010F field emission gun type with TRACOR NORTHERN SERIES-II energy dispersive X-ray spectroscopy (EDS) analyzer.

Tensile Test

Tensile properties were conducted to the requirement for the mechanical properties in

ASTM A193 B8M and ASME Code Case N-60 SA163 B8M.

Results and Discussion

PWSCC Susceptibility of Simulated Materials

The SSRT test results are shown in Table 5. The correlation between the chromium content of materials and IGSCC susceptibility is shown in Fig. 2. Effects of chromium, nickel, and silicon contents on PWSCC susceptibility are illustrated in Figs. 3-5. From these data, IGSCC susceptibility of the austenitic alloys is greatly enhanced at lower than about 15% chromium and with an increase in nickel content. The effect of silicon on IGSCC susceptibility was evaluated for the high nickel materials. IGSCC susceptibility increased with an increase in silicon content; the threshold for IGSCC susceptibility was about 1% silicon in these high nickel materials.

Table 5-*SSRT test results of simulated RIS materials.*

Alloy No.	Feature	Heat Condition	Tensile Strength	Elong-ation	IGSCC Ratio
			MPa	%	%
1-1	Low Cr-High Ni-High Si	1100°C,1hr W.Q.	361	28	98
1-2			352	27	97
2-1	Low Cr-High Ni	1100°C,1hr W.Q.	425	57	1
2-2			428	59	0
5	High Si	1100°C,1hr W.Q.	463	70	5
6	High P	1100°C,1hr W.Q.	417	59	5
A5	Med. Cr- Med. Ni-High Si	1100°C,1hr W.Q.	506	68	2
A6	Med. Cr-High Ni-High Si	1100°C,1hr W.Q.	458	65	10
A8	Med. Ni-High Si	1100°C,1hr W.Q.	521	91	0
A9	High Ni-High Si	1100°C,1hr W.Q.	516	80	0
A12	Low Cr-High Ni-High P	1100°C,1hr W.Q.	489	71	0
A13	Low Cr-High Ni-High S	1100°C,1hr W.Q.	476	56	0
A14	Low Cr-High Ni- High Si-Mo	1100°C,1hr W.Q.	424	36	95
A16	Low Cr-High Ni-High Si	1100°C,1hr W.Q.	402	40	100
A24	Ultra Low Cr-High Ni-Mo	1100°C,1hr W.Q.	483	63	0
A25	Ultra Low Cr-High Ni	1100°C,1hr W.Q.	389	54	14
M1	Med. Cr- Ultra High Ni -Low Si	1100°C,1hr W.Q.	515	79	0
M3	Med. Cr- Ultra High Ni- Med. Si	1100°C,1hr W.Q.	500	62	6
M5	Med. Cr- Ultra High Ni- Med. Si	1100°C,1hr W.Q.	295	18	100
M7	Low Cr- Med. Ni-High Si	1100°C,1hr W.Q.	314	22	100
M8	Med. Cr- Ultra High Ni-High Si	1100°C,1hr W.Q.	235	9	100
1S	Anneled+Aged No.1	1100°C,1hr W.Q.+650°C,20hrs A.C.	483	72	3
2S	Anneled+Aged No.2	1100°C,1hr W.Q.+650°C,20hrs A.C.	427	68	0
5S	Anneled+Aged No.5	1100°C,1hr W.Q.+650°C,20hrs A.C.	470	76	0
A14S	Anneled+Aged No.A14	1100°C,1hr W.Q.+650°C,20hrs A.C.	559	33	18
C1S	Anneled+Aged No.C1	1100°C,1hr W.Q.+650°C,20hrs A.C.	—	—	90
304S	Anneled+Aged 304	1100°C,1hr W.Q.+650°C,20hrs A.C.	471	38	0

Med.: Medium

An aging treatment at 650 °C for 20 hours was performed for alloy 1 that was initially solution treated (12%Cr-28%Ni-3%Si) and this revealed the highest IGSCC susceptibility among the test materials. The SSRT test on alloy 1S revealed low IGSCC susceptibility, in spite of the presence of chromium depletion at the grain boundary of

less than 5% chromium. Alloy A14S also showed decreasing IGSCC susceptibility after aging treatment at 650 °C for 20 hours. However, the area ratio of IGSCC fracture in alloy A14S was higher than that of alloy 1S. The difference between A14S and 1S is only the molybdenum content. Addition of molybdenum is harmful for the precipitation of coherent $M_{23}C_6$ carbides with the matrices at grain boundaries. No IGSCC was observed in the aged Type 304 stainless steel with precipitates of coherent $M_{23}C_6$ carbides with matrix at grain boundaries following the SSRT test in simulated PWR primary water. Aged alloys show coherent $M_{23}C_6$ carbides with the matrices at grain boundaries. This tendency is comparable with the increase of PWSCC resistance due to precipitation of coherent $M_{23}C_6$ carbides at the grain boundaries in alloy X-750 and alloy 690 [11,12].

In case of those alloys with 3% silicon, PWSCC susceptibility was observed at lower than at least about 15% of chromium and higher than about 20% nickel. The threshold chromium composition for PWSCC susceptibility increases with an increase in nickel

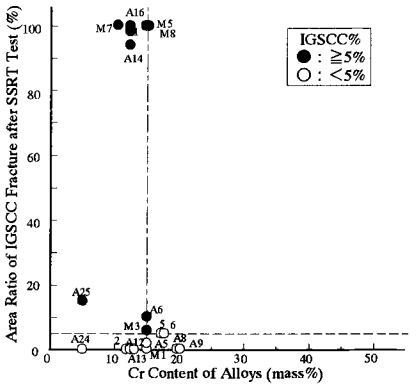


Figure 2-*The correlation between chromium content and IGSCC susceptibility by SSRT test in simulated PWR primary water at 360°C for simulated RIS materials.*

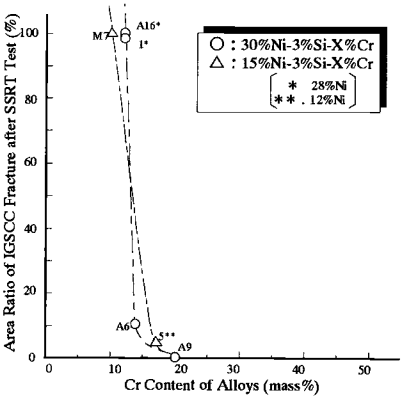


Figure 3-*The correlation between chromium content and IGSCC susceptibility by SSRT test in simulated PWR primary water at 360°C for 15%Ni-3%Si and 30%Ni-3%Si materials.*

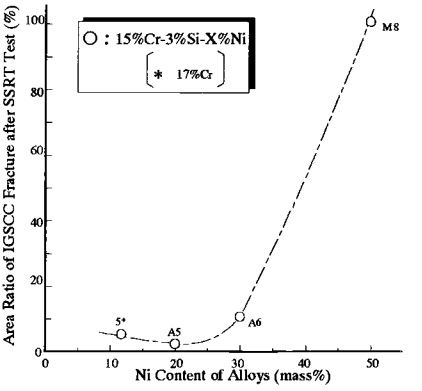


Figure 4-*The correlation between nickel content and IGSCC susceptibility by SSRT test in simulated PWR primary water at 360°C for 15%Cr-3%Si materials.*

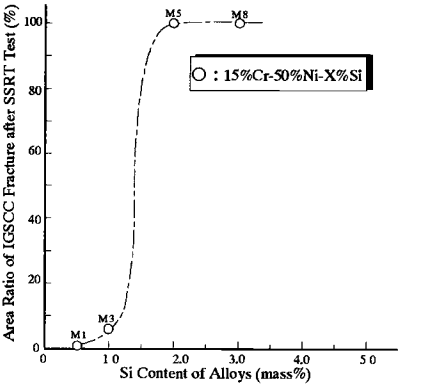


Figure 5-*The correlation between silicon content and IGSCC susceptibility by SSRT test in simulated PWR primary water at 360°C for 15%Cr-50%Ni materials.*

composition. However, in case of low silicon and aged materials with coherent $M_{23}C_6$ carbides at grain boundaries, the threshold chromium and nickel compositions for PWSCC susceptibility decrease.

Optimized Chemical Composition and Heat Treatment Conditions of Modified 316 CW Stainless Steel

In order to improve the IASCC resistance of Type 316 CW stainless steel, optimized chemical compositions and heat treatment conditions within the requirements of ASTM A193 B8M were investigated.

It is well known that the standard 300 series austenitic stainless steels have no SCC susceptibility in normal PWR primary water. Thus, the SCC test cannot be used to evaluate optimized chemical compositions within the requirements of ASTM A193 B8M in the good quality, simulated PWR primary water. The authors' previous study showed that the precipitation of the grain boundary coherent carbides might be a good countermeasure to improve the IASCC resistance of Type 316 CW stainless steel. The precipitation of the grain boundary coherent carbides without chromium depletion due to thermal sensitization is considered especially desirable for preventing the intergranular corrosion in unexpected off-normal PWR primary water chemistry environments. It was also concluded in the same study [7-9] that higher chromium content before irradiation is better for chromium depletion due to RIS at the grain boundaries after irradiation. Therefore, a higher chromium content within the requirements of ASTM A193 B8M is recommended for the improvement of IASCC resistance of Type 316 CW stainless steel. Also, the precipitation of the grain boundary coherent carbides is desirable for improvement of the IASCC resistance.

Working on this knowledge, this study looked at the effects of chemical composition and heat treatment conditions on the time-temperature-precipitation (TTP) behavior and time-temperature-sensitization (TTS) behavior using TEM and the intergranular corrosion tests.

The TTS curve of Type 316 stainless steel seems to shift towards the shorter times direction with increases in the carbon, chromium, nickel, and molybdenum contents, as shown qualitatively in Fig. 6. However, high molybdenum content is undesirable for the stability of the austenitic phase during aging.

The corrosion rate of these materials decreases when cold working is applied after the solution annealing and before aging, as shown schematically in Fig. 1. This tendency is thought to be caused by the acceleration of recovery due to the cold working before aging.

The above evidence suggests that recovery of chromium depletion can be accelerated by applying cold working before aging and by the addition of higher carbon, chromium, and nickel contents. Lower molybdenum content is recommended to ensure the stability of the austenitic phase.

Fig. 7 shows the microstructure of the low and high carbon Type 316 stainless steels with and without cold working before aging. The density of the grain boundary carbides is not sufficient in the low carbon material with cold working before aging due to the additional precipitation of carbides at deformation twin boundaries. Thus, a higher carbon content is recommended for the cold-worked and aged Type 316 CW stainless steel to increase the amount available for precipitating grain boundary carbides.

The coherency of the grain boundary carbides with matrix was identified by TEM. All carbides at the grain boundaries in the above modified 316 CW stainless steel have the same orientation with the matrix and were identified as $M_{23}C_6$.

Fig. 8 shows the effect of cold working before aging on the TTS curve of the 0.06% carbon and high chromium Type 316 stainless steel. In the case of 10% cold working before aging, the recovery of grain boundary chromium depletion was observed after

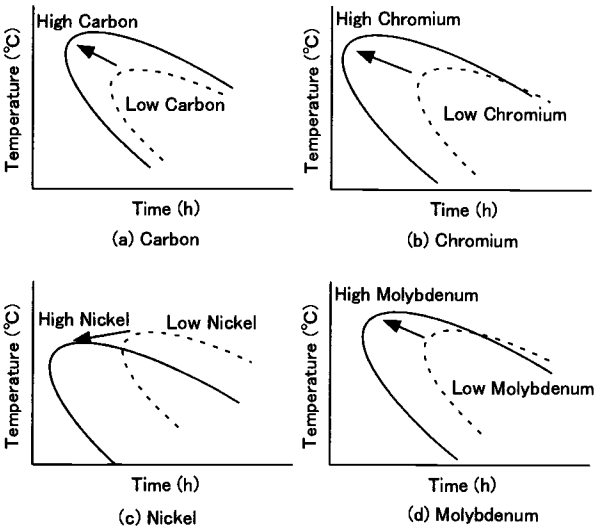


Figure 6-*The estimated TTS curves for carbon, chromium, nickel, and molybdenum contents of Type 316 stainless steel.*

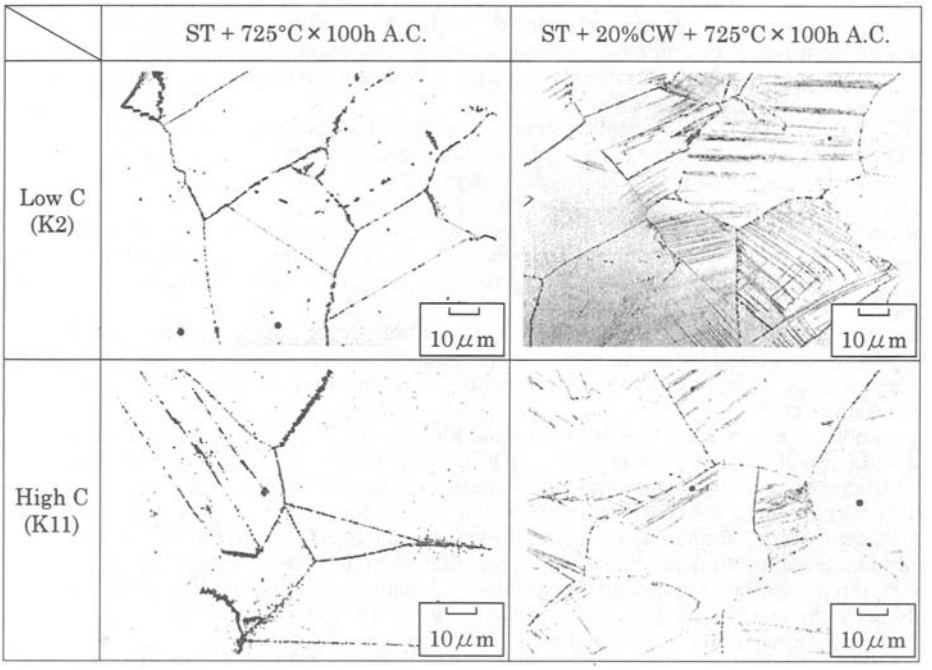


Figure 7-*Microstructure of the low- and high-carbon 316 CW stainless steels with and without cold working before aging at 725 °C for 100 hours.*

aging at 700 °C for over 100 hours. In the case of 30% cold working before aging, recrystallization was observed after aging at temperatures higher than 750 °C. Therefore, in order to conduct economical and proper aging for the precipitation of grain boundary carbides without chromium depletion, these data suggest that aging at 700 to 725 °C for 20 hours to 50 hours after cold working of about 20% should be recommended for the modified 316 stainless steel containing more than 0.06% carbon. For the application of the above modified 316 stainless steel to BFBs, a satisfactory cold working process after aging to meet the requirements of the mechanical properties in ASTM A193 B8M and ASME Code Case N-60 SA163 B8M was investigated. Fig. 9 shows tensile properties at room temperature and 350 °C, respectively. From these data, the recommended cold working after aging for the above modified 316 CW stainless steel is from 5% to 10%.

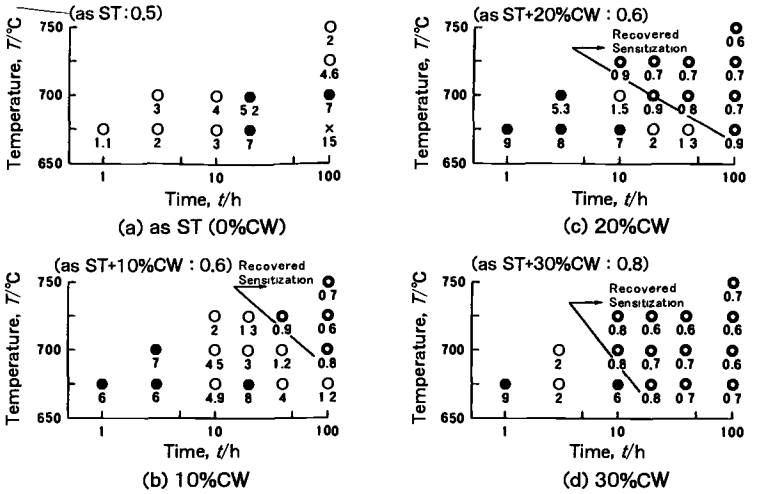
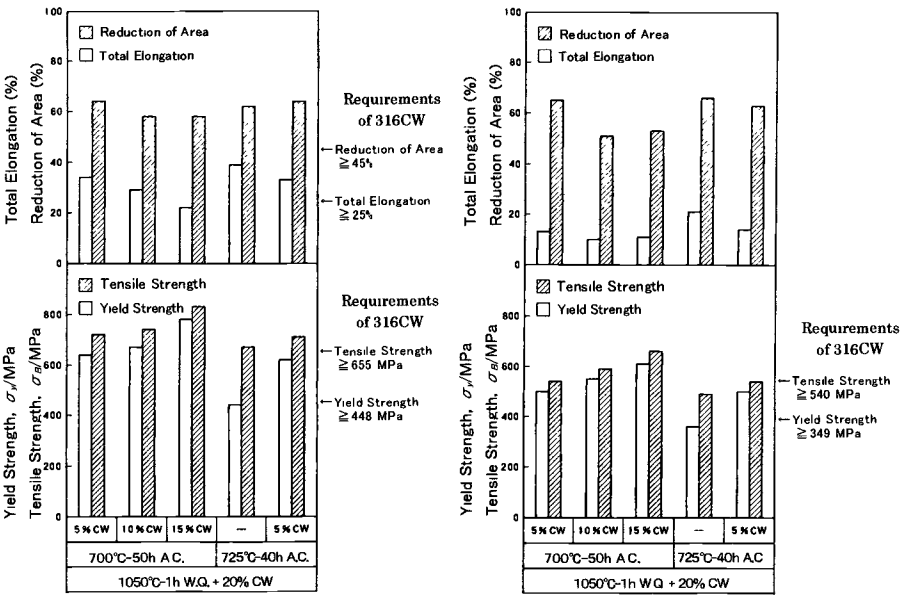


Figure 8-*The corrosion rate measured by the ferric sulfate-sulfuric acid solution corrosion test for modified 316 CW stainless steel.*

Optimized Chemical Composition and Heat Treatment Conditions of High Chromium Austenitic Stainless Steel

From the authors' previous studies [8, 9], it was concluded that increases in the chromium composition of the coherent grain boundary carbides and their purification and precipitation must all be highly effective in order to improve the IASCC resistance of austenitic stainless steels for PWR BFBs. In addition the chromium content of austenitic stainless steels before irradiation must be higher than 30% in order to reduce of RIS. In this study, the optimized chemical composition and heat treatment conditions were evaluated from these viewpoints.

The effects of chromium and nickel contents on the austenitic phase stability were evaluated for high purity austenitic stainless steels using the test steels shown in Table 3. For these steels, the solution annealing was conducted at 1,050 °C. In the case of steels A (30%Cr-20%Ni), B (30%Cr-25%Ni), and D (35%Cr-35%Ni), ferritic phase and sigma phase were observed after solution annealing, as shown in Fig. 10. The steel C (30%Cr-



(a) R.T. (b) 350°C

Figure 9-*The effect of the final cold working ratio on the tensile properties of modified 316 CW stainless steel at R.T. and 350℃. The thermo-mechanical process was conducted in the following order: cold working, aging, and final cold working.*

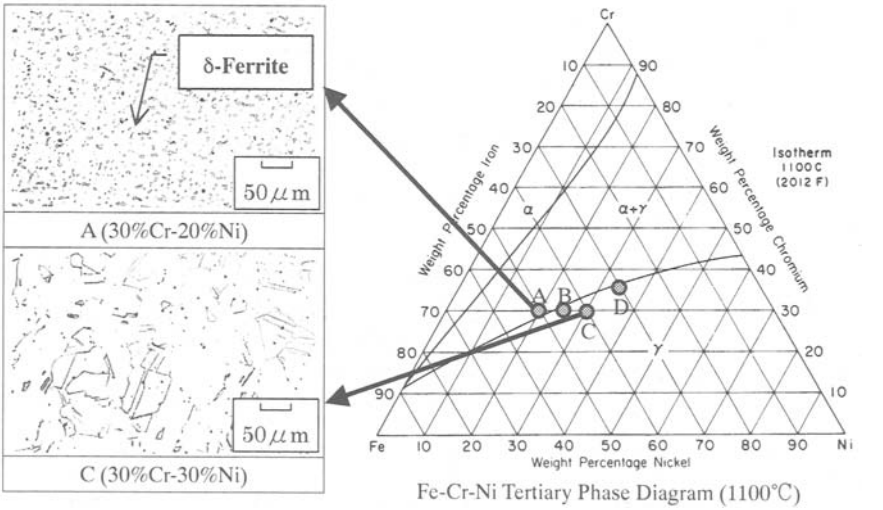


Figure 10-*Microstructure of the cross section of high chromium stainless steels water-quenched after solution treatment at 1100℃ for 1 hour.*

30%Ni) revealed only the austenitic phase. Moreover, the thermal expansion coefficient of the steel C was close to that of a Type 304 stainless steel used for baffle plates in PWR core structures.

The effects of carbon content and solution heat treatment condition for the 30% chromium and 30% nickel austenitic high purity stainless steel were evaluated using the test steels shown in Table 4. The quantity of undissolved carbides increased with an increase in the carbon content after solution treatment. In the case of the steels containing more than 0.06% carbon, undissolved carbides were observed after solution treatment at 1,100 °C.

The effects of aging temperature and time on the precipitation of coherent grain boundary carbides without chromium depletion were evaluated using the test steel containing 0.04% carbon, 30% chromium, and 30% nickel. Fig. 11 shows the microstructure observed by SEM and the chromium composition at the grain boundaries analyzed by TEM/EDS in the test specimens after aging under various conditions. When the specimens were aged at temperatures lower than 675 °C, the aging time had to be longer than about 100 hours in order to recover the grain boundary chromium depletion. With aging at temperatures higher than 750 °C, an aging time of about 20 hours was sufficient to recover the grain boundary chromium depletion. However, the particle sizes of the grain boundary carbides were relatively large and were precipitated discretely along the grain boundaries.

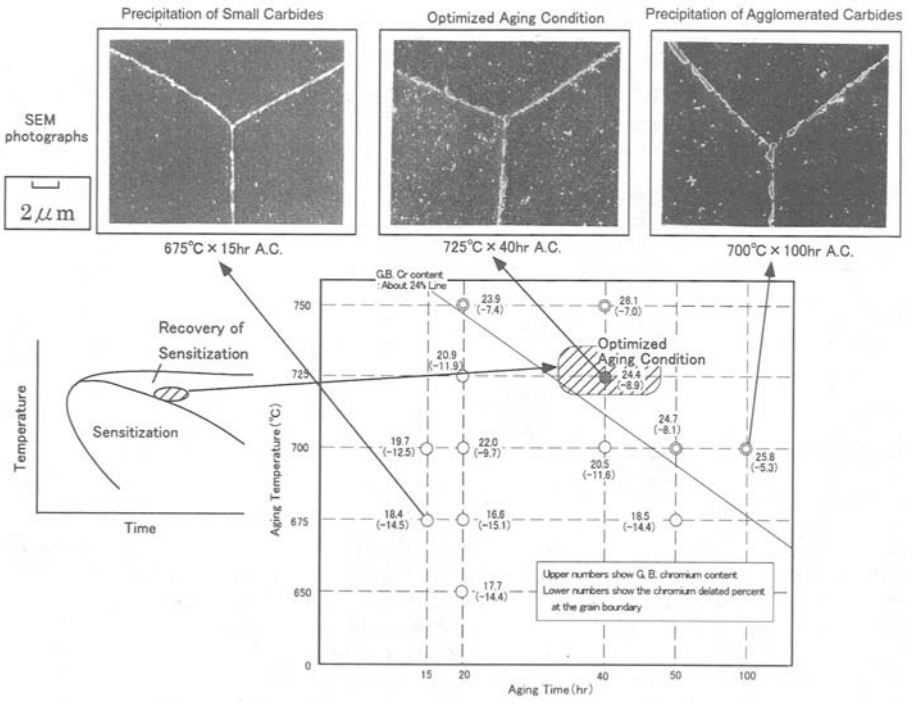


Figure 11-*Microstructure observed by SEM and grain boundary chromium content measured by TEM/EDS for 30%Cr-30%Ni stainless steels after aging under various conditions.*

It was concluded from our earlier work [8, 9], firstly, that there is a good correlation between the PWSCC resistance and the type, morphology, and coherency of precipitates along the grain boundary, and secondly, that the $M_{23}C_6$ carbides which are coherent with the matrix and are precipitated semi continuously along the grain boundaries, also give good resistance against PWSCC in nickel-based alloys [13]. Thus, the grain boundaries of the IASCC resistant alloys should be semi continuously decorated by the coherent grain boundary carbides when choosing optimized heat treatment conditions for IASCC resistant PWR BFB materials.

Therefore, aging at 700 to 725 °C for longer than 40 hours after solution treating at 1,100 °C is recommended as the heat treatment condition for the high chromium austenitic stainless steel used for alternative BFB materials.

The cold working for this steel was evaluated to meet the mechanical properties of ASTM A193 B8M and ASME Code Case N-60 SA163 B8M. Table 6 shows the tensile properties at room temperature and 350 °C of the high chromium austenitic stainless steel after cold working under various conditions. In order to meet the mechanical properties of ASTM A193 B8M and the ASME Code Case N-60 SA163 B8M, 10 to 15% cold working is needed after aging for the high chromium austenitic stainless steel. The coherency of the grain boundary carbides in this steel does not change even after the cold working.

Table 6-*Tensile properties of 30%Cr-30%Ni stainless steels after cold working.*

(a) R.T.

Ratio of Cold Working	Yield Strength σ_y		Tensile Strength σ_B		σ_y / σ_B	Total Elongation	Reduction of Area
	kg/mm²	MPa	kg/mm²	MPa		%	%
10%	53.8	528	63.8	626	0.84	32	66
15%	64.2	630	69.3	680	0.93	26	64
20%	73.0	716	77.9	764	0.94	18	62
25%	76.4	749	82.2	806	0.93	15	60
Requirements	≧45.7	≧448	≧66.8	≧655	—	≧25	≧45

(b) 350°C

Ratio of Cold Working	Yield Strength σ_y		Tensile Strength σ_B		σ_y / σ_B	Total Elongation	Reduction of Area
	kg/mm²	MPa	kg/mm²	MPa		%	%
10%	42 4	416	48.3	474	0.88	20	64
15%	52 2	512	55.2	541	0.95	12	59
20%	60.2	590	63.9	627	0.94	11	58
25%	64.3	631	67.7	664	0.95	11	56
Requirements	≧35.6	≧349	≧55.1	≧540	—	—	—

Conclusions

In this study, the potential of IASCC susceptibility in austenitic stainless steels for PWRs was investigated by SSRT tests in simulated PWR primary water using test materials whose composition simulated that of grain boundary after induced grain boundary segregation. Such knowledge is required to estimate the degradation of PWR plants to the end of their operating lifetime. The authors have investigated optimized chemical compositions and heat treatment conditions of Type 316 CW and high chromium austenitic stainless steels in order to develop IASCC resistant austenitic stainless steels for PWR BFBs.

(1) In case of steels containing 3% silicon, PWSCC susceptibility was observed for chromium concentrations lower than about 15% and nickel composition higher than about 20%. The threshold chromium composition for PWSCC susceptibility

increases with an increase of nickel composition. However, in case of steels with low silicon composition and aged materials with coherent $M_{23}C_6$ carbides at grain boundaries, the threshold chromium and nickel concentrations for PWSCC susceptibility decrease.

(2) It is concluded that IASCC of austenitic stainless steels in PWRs may be caused by PWSCC as a result of irradiation induced grain boundary segregation. Coherent carbide precipitation with the austenitic matrices at the grain boundary could be very effective for decreasing the IASCC susceptibility of austenitic stainless steels in PWRs in future.

(3) An optimized chemical composition of Type 316 CW stainless steel with ultra low impurities and high chromium content has been recommended within the requirements of ASTM A193 B8M. About 20% cold working before aging and after solution treatment is also recommended for this steel in order to precipitate coherent $M_{23}C_6$ carbides with the matrix at grain boundaries and recover the grain boundary chromium depletion. Heating at 700 to 725 °C for 20 to 50 hours was selected as a suitable aging condition. Cold working at 5 to 10% for this steel after aging was selected to meet the requirements for mechanical properties of PWR BFBs.

(4) An optimized chemical composition for a high chromium austenitic stainless steel with ultra low impurities, 30% chromium, and 30% nickel has been recommended in order to increase PWSCC resistance and assure a thermal expansion coefficient close to that of a Type 304 stainless steel which is used for baffle plates. In addition, heating at 700 to 725 °C for longer than 40 hours was selected as the suitable aging condition. Cold working at 10 to 15% after aging is recommended to meet the requirements for the mechanical properties of PWR BFBs.

References

[1] Wacher, O., Bruns, J., Wesseling, U., Kilian, R., and Roth, A., "Crack Initiation in the Nb-stabilized Austenitic Stainless Steel (A347) in the Core Shroud and Top Core Guide of a German Boiling Water Reactor – Description of the Extent of the Damage and Explanation of its Causes, "*Proceedings of the 8th International Symposium on Environmental Degradation of Materials in Nuclear Power Systems - Water Reactors,* Myrtle Beach, SC, American Nuclear Society, 1997, pp. 812-822.

[2] Andresen, P. L., Ford, F. P., Murphy, S. M., and Perks, J. M., "State of Knowledge of Radiation Effects on Environmental Cracking in Light Water Reactor Core Materials," *Proceedings of the 4th International Symposium on Environmental Degradation of Materials in Nuclear Power Systems-Water Reactors-,* Jekyll Island, Georgia, American Nuclear Society, 1989, pp. 1-83-120.

[3] P. Scott et al., *NEA / UNIPEDE Specialists Mtg. on Life Limiting & Regulatory Aspects of Core Internals and Pressure Vessels, Stockholm,* 1987.

[4] Jacobs, A. J., Letter Report and Literature Search, GE Nuclear Energy, San Jose, CA, 1979.

[5] Kodama, M., Nishimura, S., Morisawa, J., Suzuki, S., Shima, S., and Yamamoto, M., "Effect of Fluence and Dissolved Oxygen on IASCC in Austenitic Stainless Steels," *Proceedings of the 5th International Symposium on Environmental Degradation of Materials in Nuclear Power Systems-Water Reactors-,* Monterey, California, American Nuclear Society, 1991, pp. 948-959.

[6] Suzuki, I., Fukuya, K., Kanasaki, H., Akiyama, M., Mishima, Y. and Mager, T. R., "Stress Corrosion Cracking of Irradiated Stainless Steels in Simulated PWR Primary

Water" *International Conference on Nuclear Engineering Vol. 5 ASME*, 1996, pp. 205-213.

[7] Cauvin, R., Golyrant, O., Rouillon, Y., Verzaux, E., Cazus, A., Dubuisson, P., Poitrenaud, P., and Bellet S., "Endommagement des Structures Internes Inferieures Soumises a Forte Fluence: Apports de L'Expertise," *Proceedings of the International Symposium on FONTEVRAUD III*, French Nuclear Energy Society, Vol. 1, 12-16, 1994, pp. 54-65.

[8] Yonezawa, T., Fujimoto, K., Kanasaki, H., Iwamura, T., Nakada, S. Nakada, Ajiki, K., Sakai, K., "SCC Susceptibility of Irradiated Austenitic Stainless Steels for PWR," *Proceedings of the 8th International Symposium on Environmental Degradation of Materials in Nuclear Power Systems-Water Reactors-,* Amelia Island, American Nuclear Society, 1997, pp. 823-830.

[9] Yonezawa, T., Arioka, K., Kanasaki, H., Fujimoto, K., Otsuka, E., Urata, S., and Mizuta, H., "IASCC Susceptibility and It's Improvement of Austenitic Stainless Steels for Core Internals of PWR," *Proceedings of the International Symposium on FONTEVRAUD III*, French Nuclear Energy Society, Vol. 1, 1998, pp. 237-248.

[10] Kowaka, M., Kobayashi, D., and Kudo, T., *Sumitomo Kinzoku*, Vol. 30, 1978, p.93.

[11] Yonezawa, T., Onimura, K., Sakamoto, N., Sasaguri, N., and Susukida, H., "Effect of Heat Treatment Conditions on Stress Corrosion Cracking Resistance of Alloy X-750 in High Temperature Water," *J. Japan Inst. Metals,* Vol. 48, No. 3, 1984, pp. 283-247.

[12] Yonezawa, T., Yamaguchi, Y., and Iijima, Y., "Electron Micro Autoradiographic Observation of Tritium Distribution on Alloy X750," *Proceedings of the 6th International Symposium on Environmental Degradation of Materials in Nuclear Power Systems -Water Reactors-,* San Diego, California, August, American Nuclear Society, 1993, pp. 799-804.

[13] Yonezawa, T., Onimura, K., Sakamoto, N., Sasaguri, N., Nakata, H., and Susukida, H. "Effect of Heat Treatment on Stress Corrosion Cracking resistance of High Nickel Alloys in High Temperature Water," *Proceedings of the International Symposium on Environmental Degradation of Materials in Nuclear Power Systems-Water Reactors-,* Myrtle Beach, American Nuclear Society, 1987, pp. 345-366.

NACE Sponsored Session—
Understanding and Predicting EAC Performance in Industrial Applications

Narasi Sridhar,[1] Darrell S. Dunn,[1] and Andrzej Anderko[2]

Prediction of Conditions Leading to Stress Corrosion Cracking of Gas Transmission Lines

Reference: Sridhar, N., Dunn, D. S., and Anderko, A., **"Prediction of Conditions Leading to Stress Corrosion Cracking of Gas Transmission Lines,"** *Environmentally Assisted Cracking: Predictive Methods for Risk Assessment and Evaluation of Materials, Equipment, and Structures, ASTM STP 1401*, R. D. Kane, Ed., American Society for Testing and Materials, West Conshohocken, PA, 2000.

Abstract: Corrosion, including stress corrosion cracking (SCC), constitutes about 12% of the failures of gas transmission lines. Two types of SCC have been observed: intergranular SCC (IGSCC) under alkaline conditions and transgranular SCC (TGSCC) under near-neutral conditions. The environmental and electrochemical conditions under which these types of SCC can be produced in the laboratory have been reasonably well established. However, a quantitative relationship between the laboratory environments in which SCC can be reproducibly observed and the chemistry of trapped water under disbonded coatings has not been established. The purpose of this paper is to review the state of knowledge of the environmental conditions leading to either type of SCC and relate this to the evolution of the actual environment under disbonded coating. The relationship between SCC and chemistry of trapped water is examined through the use of a comprehensive thermodynamic model. The temporal and spatial evolution of the trapped water chemistry is examined as a function of external conditions through the use of a reactive-transport model.

Keywords: Pipeline, disbonded coating, SCC, cathodic protection, trapped water, steel

Introduction

Buried pipelines carrying natural gas or gas liquids are made of various grades of C-Mn steels. They are usually protected from external corrosion by a combination of polymeric coating and cathodic protection (CP). The polymeric coating limits the exposed area of bare steel and the CP protects the steel in locations where the coating is ruptured (termed a holiday). Unfortunately, coatings can disbond and lift off from the steel in addition to developing holidays. The susceptibility to disbondment is a function of coating type, coating application procedures, operating temperature, soil stresses, and level of CP.

The evolution of the environment under the disbonded coating is a complex function of disbondment geometry, coating type, external environment, and applied CP. Localized corrosion and SCC have been observed essentially under the disbonded coatings. These two phenomena are interconnected in that localized corrosion is observed along with SCC as evidenced by various iron corrosion products as well as small pits near cracks [1]. Both intergranular (IGSCC) and transgranular (TGSCC) stress corrosion cracking have been observed, depending upon environmental conditions [2-5]. The research on IGSCC, triggered by the rupture of a high pressure gas pipeline near Natchotoches, Louisiana in

[1] Manager and senior research engineer respectively, CNWRA, Southwest Research Institute, 6220 Culebra Rd., San Antonio, TX, 78238-5166.

[2] Vice President, OLI Systems, Inc., 108 American Rd., Morris Plains, NJ, 07950.

Copyright© 2000 by ASTM International www.astm.org

1965, has shown that it occurs over a relatively wide range of pH from about 7 to 10.5, narrow potential range of about 100 millivolts (mV) that depends on the pH, and in a concentrated mixture of carbonate (CO_3^{2-}) and bicarbonate (HCO_3^-) [2]. The laboratory environments in which IGSCC has been observed are usually much more concentrated than field environments and the temperature used (75°C) is higher than expected, even near compressor stations. The TGSCC research was initiated after a number of failures of Canadian pipeline [3] and has been shown to occur in relatively dilute solutions, under near-neutral conditions, and ambient temperatures.

The risk assessment of pipelines from SCC has focused on a combination of qualitative ranking of risk factors, such as soil and coating types, that could lead to cracking and quantitative estimation of fracture probability through the use of crack growth rates and fracture mechanics approaches [3]. However, a completely quantitative risk assessment, incorporating both the initiation and propagation of cracks, has not yet been attained. The main disadvantage of a qualitative ranking system is that risk assessment is limited to pipelines for which extensive field data has already been obtained [3]. The cost of accumulation of such a field database has been estimated to be about $1200 (Canadian) per kilometer, and there is over 500 000 Km of pipeline in Canada alone. While the accumulation of such a database has dramatically improved the probability of detecting SCC [3], it will not be completely useful for new soil or coating conditions. The limitation of quantitative crack growth models is that crack initiation conditions are not considered. Therefore, these models rely on the detection of existing cracks through sensitive pigs or excavation.

One of the main limitations in the current methods of risk assessment of pipelines is the lack of a quantitative understanding of the relationship between the external conditions prevailing around a pipe and the environmental conditions under the disbonded coating that may lead to SCC. The purpose of this paper is to briefly review the state of knowledge of environmental conditions leading to SCC and present some results of computer modeling that analyzes the relationship between external environment and SCC conditions.

A Brief of Survey of the Literature

Conditions Leading to IGSCC

Reviews of SCC research activities funded by Pipeline Research Committee International (PRCI) and others suggest that the conditions for generating IGSCC in the laboratory are well established, but understanding of the relationship between laboratory and field environments is still qualitative at best [2,5]. Typical compositions of water trapped under disbonded coatings near IGSCC sites are shown in Table 1. Unfortunately, SCC could not be induced in the laboratory in these environments. Laboratory tests [2], using slow strain rate and fatigue pre-cracked, fracture mechanics specimens have shown that IGSCC can be induced in environments ranging from 0.125M $NaHCO_3$ + 0.062M Na_2CO_3 to 0.75M Na_2CO_3 + 1M $NaHCO_3$ and at temperatures ranging from 20 to about 75°C. The crack velocity increases with temperature, with the activation energy increasing with a decrease in solution concentration [2].

In contrast to the analyses reported in Table 1, recent analyses of solutions under disbonded coatings adjacent to IGSCC sites have indicated the presence of concentrated electrolytes as evidenced by the deposition of various sodium carbonate and bicarbonate

Table 1 – Typical compositions of trapped waters under disbonded coating found near IGSCC sites. concentrations in moles/liter. the predominant cation was sodium [2].

State	pH	CO_3^{2-}	HCO_3^-	OH^-	Cl^-	NO_3^-
Alabama	9.7	0.083	0.082	-	-	-
Arizona	12.3	0.17	-	0.06	0.003	0.001
Mississippi	10	0.23	0.082	-	0.034	0.0006
Mississippi	10	0.15	0.13	-	0.034	-
Mississippi	9.6	0.083	0.1	-	-	-
N. Carolina	10.5	0.12	0.066	-	-	-

salts [6]. Two mechanisms have been proposed for the generation of concentrated, alkaline environment under disbonded coating [5,6]. In the first mechanism [6], the application of cathodic polarization leads to the generation of hydroxyl ions. The permeation of carbon dioxide through the coating results in the formation of carbonate and bicarbonate ions in the disbonded region. The electromigration of positively charged species, such as Na^+, leads to the formation of concentrated sodium carbonate and bicarbonate solutions. In the second mechanism, the application of cathodic polarization, which generates the alkaline conditions, is combined with thermally induced evaporation to produce concentrated carbonate-bicarbonate solutions [5,6]. The increased frequency of IGSCC near compressor stations [2], where adiabatic heating of the gas occurs, may support the second mechanism.

Laboratory testing has indicated that anions such as chloride and nitrate do not have a significant effect on IGSCC [2]. The potentials at which SCC occurs increase with a decrease in pH, and at a pH of 10, the susceptible potentials range from –0.5V vs. saturated calomel electrode (SCE) to – 0.65V (SCE). IGSCC has generally not been observed when the pH is greater than about 11. The range of potential for SCC is wider at higher temperatures and shifts to a more negative value as the temperature is raised from ambient to 75°C. SCC is enhanced by the presence of low frequency, cyclic loading engendered mainly by pressure fluctuations in the pipe. The threshold stress for cracking decreased with a decrease in the ratio of minimum stress to maximum stress (called, R ratio), suggesting that increased fluctuations exacerbated the SCC [2].

The corrosion products around IGSCC sites and on the fracture faces are predominantly magnetite (Fe_3O_4) with some siderite ($FeCO_3$) [2,5]. Although significant lateral corrosion of crack walls is not observed, the presence of these corrosion products suggests that some corrosion must occur at a local level. In addition, the range of potential for cracking is more positive than that required to create a high pH environment. This apparent discrepancy between conditions required to generate suitable chemistry and potential for cracking is attributed to seasonal variations in the external environment [4,6]. For example, during wet period CP can penetrate to the disbonded region creating an alkaline condition. During the subsequent dry period, CP is not able to be applied and the potential in the disbonded region rises to the critical potential range for SCC.

Conditions Leading to TGSCC

The compositions of typical environments used to simulate trapped water under disbonded coatings near TGSCC sites are shown in Table 2. The pH and ionic composition of these solutions are calculated using OLI Systems Environment Simulation Program, Version 6.2. In contrast to the IGSCC environments, the TGSCC environments are dilute, the composition difference between the groundwater and trapped water are small, and the maximum pH is close to neutral [2,6]. The actual pH may well be more acidic because gas bubbles (presumably CO_2) were found to be released upon extracting these trapped waters [2]. In laboratory tests[4], up to 15% CO_2 (total pressure of 0.1 MPa or 1 atm) is bubbled through these solutions to lower the pH to about 6.5.

Table 2 – Components used to prepare simulated trapped waters near TGSCC sites and calculated pH and ionic compositions [2].

Sample	Input Compounds, g/liter				Calculated		
	KCl	$NaHCO_3$	$CaCl_2$.$2H_2O$	$MgSO_4$.$7H_2O$	pH	HCO_3^- M	CO_2 M
NS3	0.337	0.559	0.008	0.089	7.96	0.006	$1.4x10^{-4}$
NS4	0.122	0.483	0.181	0.131	7.15	0.004	$6.2x10^{-4}$

The TGSCC has been found predominantly under polyethylene (PE) tape coating and to a lesser extent under asphalt and coal tar enamel coatings [2,7]. Thus far, no cracking has been observed under fusion bonded epoxy (FBE) and extruded PE coatings. It is believed that the ability of the PE tape coating to shield cathodic protection, exclude water from disbonded regions, and permeate gases such as CO_2 is responsible for its high tendency to induce TGSCC. The crack colonies, which may appear similar to IGSCC colonies, are usually oriented longitudinally and near stress raisers such as weld toes, gouges, or pits. The tenting of the tape coating over the weld crown and along overlapping seams of spiral wrapping also create disbonded regions and help localize SCC to these areas.

In addition to the fracture path, several differences between IGSCC and TGSCC have been noted. TGSCC is typically associated with much greater corrosion of fracture faces and the presence of iron carbonate. TGSCC does not seem to exhibit a significant dependence on temperature in laboratory tests [8]. In the field, TGSCC has been observed as far as 63 Km from compressors [5,7], whereas the probability of occurrence of IGSCC decreases greatly away from compressor stations [2]. Whereas IGSCC occurs over a narrow potential range of about 150 millivolts, there appears to be no critical potential regime for TGSCC. Parkins et al. [8], using slow strain tests on X-65 steel in NS4 solution (Table 2) saturated with CO_2, observed that the SCC susceptibility increased with more negative potential, the effect being more pronounced at lower pH values (about 5.8). Gu et al. [9] also found that TGSCC susceptibility of X-80 steel in NS-4 solution generally increased as the potential was made more negative, and the effect was much more pronounced when the solution was purged with CO_2. Johnson et al. [10] have shown that the TGSCC growth increased when the CO_2 increased from 0 to 15% in the sparging gas, with the most pronounced effect occurring between 0 and 5%.

Mechanistic Considerations

The IGSCC has been shown to be associated with enhanced crack tip dissolution due to plastic deformation, which disrupts the passive film locally. SCC in such a case occurs under a set of finely tuned environmental conditions. The environment should be capable of promoting passive film formation, which in the case of carbon steel occurs under alkaline conditions. The passive film protects the walls of the crack from dissolution and helps maintain a crack geometry. However, the pH should be such that a large active-passive transition current density is present. At pH values higher than about 11, such a large transition is not present and hence IGSCC does not occur. At low pH values, only active dissolution is observed. Too positive a potential promotes either passivity or active corrosion, whereas too negative a potential prevents anodic dissolution even when passive film is disrupted. The crack velocity in IGSCC compares reasonably well with the peak anodic dissolution rates measured by rapid scan polarization curves [2]. In contrast, the TGSCC crack growth rates are typically much higher than calculated by anodic dissolution rates [4]. This observation combined with greater propensity to crack at more negative potentials has led to the suggestion that TGSCC occurs by a hydrogen embrittlement mechanism [4,6,9-11]. The presence of increased hydrogen at stressed notch tips of X-52 and X-80 steels at open-circuit and cathodic potentials in NS-4 solution was demonstrated by Qiao et al. [11]. More recently, Beavers and Jaske [12] and Johnson et al. [10] have shown that the presence of carbonic acid in solution or CO_2 in the gas phase increases the concentration of hydrogen absorbed by the steel.

Potential Distribution under Disbonded Coatings

In both IGSCC and TGSCC, the potentials required for SCC are not conducive to the generation of the chemical environments needed for cracking. In IGSCC, the cracking potentials are in the range of –0.5 to –0.65 V (SCE), whereas the pH of the environment at these potentials is not sufficiently alkaline for IGSCC [2]. In TGSCC, the potential required for cracking are more negative than the open-circuit potential [4,8,9]. However, the pH increases with the application of negative potentials. The near-neutral pH in the case of TGSCC is attributed to the lack of penetration of CP in the disbonded coating and the presence of CO_2. However, there is disagreement in the literature regarding the distribution of potential within the disbonded coating in low conductivity solutions.

Fessler et al. [13] found that the potential gradient inside a crevice between steel and polymer immersed in a moderately concentrated solution of 1N $NaHCO_3$ + 1N Na_2CO_3 decreased with time in an exponential fashion given by

$$E(x) = A_0 + (E_{applied} - A_0) \exp\left(\frac{-x}{\sqrt{A_1 \sigma t}}\right) \qquad (1)$$

Where $E(x)$ is the potential at any distance inside the crevice, A_0 and A_1 are constants to be determined experimentally, σ is the solution conductivity, and t is the time. Equation 1 suggests that the crevice potential will approach the externally applied potential at long time periods. Parkins [2,5] showed that the rate of change of potential is a function of steel surface condition and that sufficient residence time in a critical potential regime for SCC may be necessary for initiating SCC in some pipelines. Gan et al. [14] examined the potential distribution under crevices in NaCl solutions ranging in

conductivity from 0.24 to 6.3 mS/cm (0.002 to 0.06M NaCl). They showed that the potential at a distance of 7.4 cm from the mouth of the crevice became continually more negative, in qualitative agreement with Fessler et al. [13].

Jack et al. [15] conducted disbonded coating experiments using thermoplastic coating and disbondment gaps ranging from 1 to 5 mm. The test solutions contained varying concentrations of KCl to obtain conductivities ranging from 0.56 to 4.18 mS/cm. They found that the potential distribution inside the disbonded region fit the equation

$$E(x) = E_{corr} + (E_{corr} - E_{applied}) \exp\left(\frac{-x}{(2.086\ G + 0.826\ S)}\right) \quad (2)$$

Where E_{corr} is the corrosion potential of the steel in the solution, $E_{applied}$ is the applied cathodic potential at the mouth of the disbondment, G is the crevice gap in centimeters, and S is the conductivity of the solution in mS/cm. Their results, obtained over a relatively short period of time (24 hours), indicate that in these relatively low conductivity solutions, the potential at the far end of the crevice never approaches the protection potential. Brusseau and Qian [16] also measured the potential distribution under an artificial disbondment exposed to a relatively dilute solution (5×10^{-4}M $NaHCO_3 + 5 \times 10^{-4}$M $CaCl_2 + 5 \times 10^{-4}$M $Ca_3(PO_4)_2$) and came to the conclusion that the potential at the deepest point in the crevice (38 cm) remains at corrosion potential after 250 hours of cathodic polarization. They also found that the pH at the deepest point remains near neutral, while locations closer to the mouth attain quite alkaline pH values. It is not clear whether hydrogen bubble formation due to high cathodic potentials employed by these investigators resulted in lack of penetration of cathodic polarization deep in the crevice.

Lara and Klechka [17] discussed the evolution of potential under a plexiglas-steel crevice exposed to a saturated soil with conductivity ranging from 5.56μS/cm to 0.17 mS/cm. The crevice gap was 1.1 mm, the total length of the crevice region was 24 cm, crevice width was 10.8 cm, and there was a rectangular holiday region with an area of 48.4 cm^2. They concluded that regardless of the conductivity, the potential 17.8-cm deep into the crevice was close to the externally applied potential and the pH attained a value close to 12. The pH inside the crevice only depended on the potential at the holiday, not on solution conductivity. The total duration of their test was 162 days, but the CP "on" time ranged from 21 to 61 days.

From the above investigations, it appears that the absence of cathodic polarization in the disbonded region, even in dilute solutions, is a transient phenomenon. Therefore, presence of potential in the –0.6 V (SCE) regime required for IGSCC and near-neutral pH required for TGSCC are also transient features. This is consistent with the measurements made by Parkins [2] using segmented crevice electrode. As pointed out by Beavers and Harle [4] and Jack et al. [6], seasonal variation introduced by wet-dry periods may create transient conditions of susceptibility to SCC many times during the life of the pipe.

Modeling Approaches

Thermodynamic Model

To establish whether thermodynamic analysis of phase stability can give insights into the conditions that are conducive to IGSCC, thermodynamic simulations have been performed. Establishing the SCC susceptibility regions within a potential-pH framework in the form of the classic Pourbaix diagrams is not new [18]. Since it is recognized that other anionic and cationic species may affect SCC, additional frames of reference, in the form of stability diagrams are necessary. Additionally, electrolytes under disbonded coatings have been characterized as being concentrated by slow evaporation. In such cases, the dilute solution approximation will no longer be accurate. For these reasons, the OLI model of multicomponent, multiphase solutions [19,20] has been used and the results have been collected and visualized in the form of stability diagrams [21,22].

The thermodynamic analysis consists of the following steps:

- Identification of independent variables for thermodynamic analysis,
- Stability analysis, including the prediction of stability ranges for various solid phases,
- Identification of the ranges of independent variables that are conducive to IG SCC from experiments and field experience,
- Comparison of the predicted conditions with experimental analyses, including hypothetical samples that are obtained by concentrating experimental samples,
- Analysis of the effect of solution ions that may result from the dissolution of soil minerals, and
- Independent variables for thermodynamic analysis

For stability analysis, the following independent variables can be assumed:

- Generation of alkalinity as a result of cathodic protection,
- Migration of cations, such as Na^+ or Ca^{2+} from the outside to maintain electroneutrality, which can be simulated thermodynamically as increased amounts of NaOH,
- Migration of CO_2 from the outside, either from the atmosphere or as a result of biological activity,
- Migration of O_2 from the outside, and
- Dissolution of Fe in the crevice, which may result in the formation of sparingly soluble solids or ions in solution.

Reactive-Transport Modeling of the Disbonded Region

In order to calculate the variation of environment chemistry over time and space inside the disbonded region, a computer model, Transient Electrochemical Transport (TECTRAN) code, which couples the kinetics of various chemical and electrochemical reactions with transport of species in and out of the disbonded region is employed. Modeling crevice corrosion by solving a coupled reactive transport equation is not new in corrosion science [23-28]. However, the following are some of the features that distinguish TECTRAN from previous computer models of crevice corrosion:

- The chemical species and the kinetic reactions can be specified through an input file rather than requiring modification of the code;

- A large number of chemical species, limited only by the computer memory and thermodynamic data can be specified enabling a wide variety of problem to be solved. Additionally, the code can be coupled to a speciation module, developed by OLI Systems [19,20], that can consider aqueous concentrations up to 50 molal;
- A wide range of electrochemical and non-electrochemical reactions can be included, with several parallel steps. Different electrochemical reactions can be specified at different spatial locations of a system as desired by the user;
- The code considers mineral precipitation, but the current version does not include change in crevice geometry due to mineral formation;
- A variety of boundary conditions (constant concentration, zero flux etc.) can be applied at any spatial location specified by the user; and
- The fully implicit formulation enables the code to execute even relatively large 3-D problems in a reasonable time period.

The details of this model has been described elsewhere [29]. The model was used to calculate the effects of external CO_2 and applied potential on the crevice pH. bicarbonate, and carbonate concentrations.

Results and Discussion

Stability Diagrams in Systems with Sodium

The potential-pH diagram for iron in a system consisting of 1M $NaHCO_3$ + 1M Na_2CO_3 at 60°C is shown in Figure 1. The proportion of bicarbonate and carbonate will

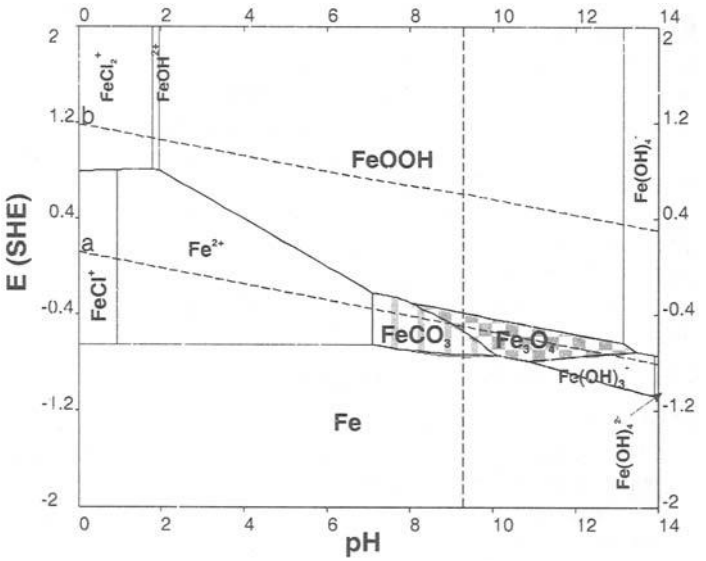


Figure 1. Potential-pH diagram for iron in 1N carbonate- 1N bicarbonate system at 60°C

change with pH, but the total molality of Na is maintained at 3m. The dashed vertical line indicates the pH of this type of environment (about 9.5). Lines (a) and (b) represent the hydrogen ion and oxygen reduction reactions respectively. The lines demarcating the regions of stability of various ionic species indicate a concentration of 10^{-6} molal of the species. Regions of stability of aqueous complexes are not shown in this figure for clarity. It can be seen that at the natural pH of this environment and a potential of –0.65 V (SCE) or –0.4 V(SHE), both $FeCO_3$ and Fe_3O_4 can be present together, which is consistent with experimental observations of fractures.

It has been determined that the formation of $FeCO_3$, which is known to exist on fracture faces [2], is sensitive to the amounts of CO_2 and dissolved Fe. Figure 2 shows a stability diagram with the molalities of NaOH and O_2 as independent variables. The total dissolved concentrations of CO_2 and Fe have been assumed to be 0.17 molal (moles/kg of

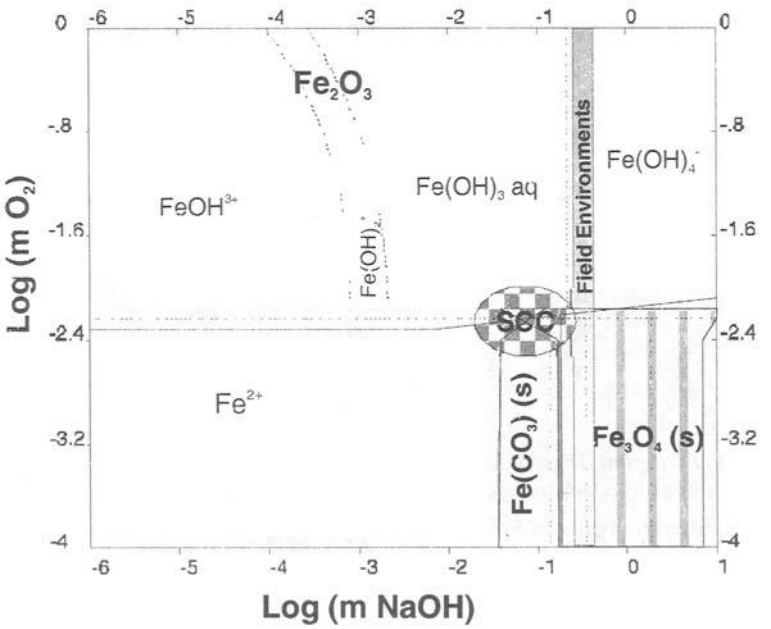


Figure 2. Stability diagram for steel exposed to an environment containing 10^{-2} molal Fe and 0.17 molal CO_2 at 25°C. Shaded rectangle corresponds to conditions in Table 1

water) and 0.01 molal, respectively, and were kept constant while the molalities of NaOH and O_2 were varied. The assumed CO_2 amount is an average of several samples examined by Parkins [2]. The amount of Fe was assumed arbitrarily and many different values were tested. In the case of CO_2 and O_2, the molalities refer to the total molality of the component, which partitions between the gas and liquid phases. As shown in Figure 2, the amount of oxygen determines whether iron is in the 2+ or 3+ oxidation state. As long as the amount of oxygen is sufficiently low to maintain iron in the 2+ oxidation state, the alkalinity of the system (i.e., the molality of NaOH) determines whether $FeCO_3$ or Fe_3O_4 (magnetite) are the most stable phases. The relative magnitude of the $FeCO_3$ and

magnetite fields depends on the amount of reacted iron. For example, Figure 3 shows a similar stability diagram in which the amount of reacted Fe is 0.1m. In this case, the stability fields of both $FeCO_3$ and Fe_3O_4 are larger and overlap to a significant extent.

Parkins and Zhou [30] attributed the limits of IG SCC to the stability of certain solids. With respect to pH, the IG SCC domain is bracketed by the dissolution of $FeCO_3$ in weakly acidic solutions and equilibrium between $FeCO_3$ and $Fe(OH)_2$ at moderately alkaline conditions (pH = ca. 11). Although $Fe(OH)_2$ is a metastable phase, the latter limit

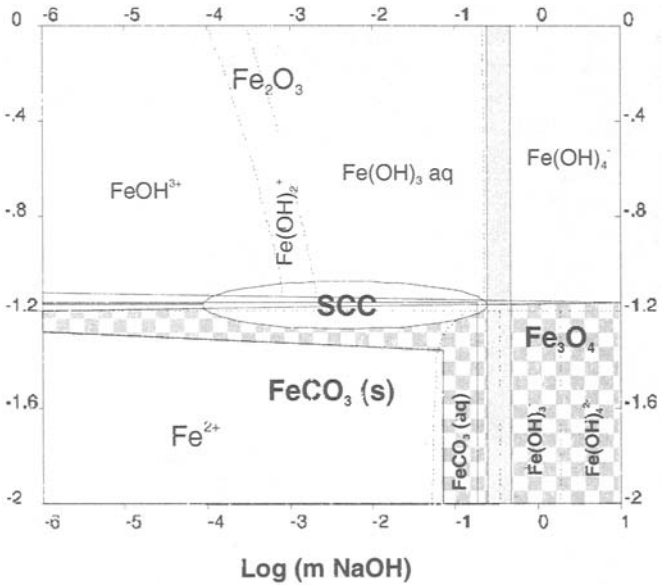


Figure 3. Stability diagram calculated for 0.1m Fe, 0.17 m CO_2 at 60°C. Shaded rectangle corresponds to conditions in Table 1.

is close to the equilibrium between $FeCO_3$ and Fe_3O_4. The lower potential limit of SCC was attributed to a redox equilibrium between $FeCO_3$ and γ-Fe_2O_3. The upper potential limit was identified with the equilibrium between Fe_3O_4 and α-Fe_2O_3. Unlike the pH range, the potential range is very narrow. It should be noted that the equilibrium line between Fe_3O_4 and α-Fe_2O_3 lies within the stability field of $FeCO_3$, which indicates an equilibrium between metastable phases. To satisfy both the upper and lower potential limits, it is necessary to be in the area of overlap between the stability fields of $FeCO_3$ and Fe_3O_4. At the same time, this region lies close to the transformation of both $FeCO_3$ and Fe_3O_4 to oxides of Fe(III). The regions that satisfy these conditions are approximately marked by the shaded "ellipses" in Figures 2 and 3.

The experimental conditions have been placed in Figures 2 and 3 in the form of a shaded rectangle. The rectangle spans the whole range of oxygen concentrations because experimental analyses do not include oxygen. The width of the rectangle corresponds to the range of pH, represented by NaOH amounts that are given in Table 1. It should be noted that Figures 2 and 3 were generated on the assumption that the molality of CO_2 is 0.17, which is an average amount from Table 1. As shown in Figures 2 and 3, the sample analyses lie at NaOH amounts that are within the stability field of Fe_3O_4. Irrespective of

the amount of reacted Fe, the samples correspond to a higher alkalinity than that for the boundary between $FeCO_3$ and Fe_3O_4. This indicates that the system is slightly outside of the conditions that are conducive to SCC. Since SCC is not observed for the conditions given in Table 1, this analysis is consistent with experimental observations.

Effect of Evaporation

Parkins [2] postulated that evaporative concentration of the samples may lead to compositions that cause SCC. Therefore, simulations have been performed in which the

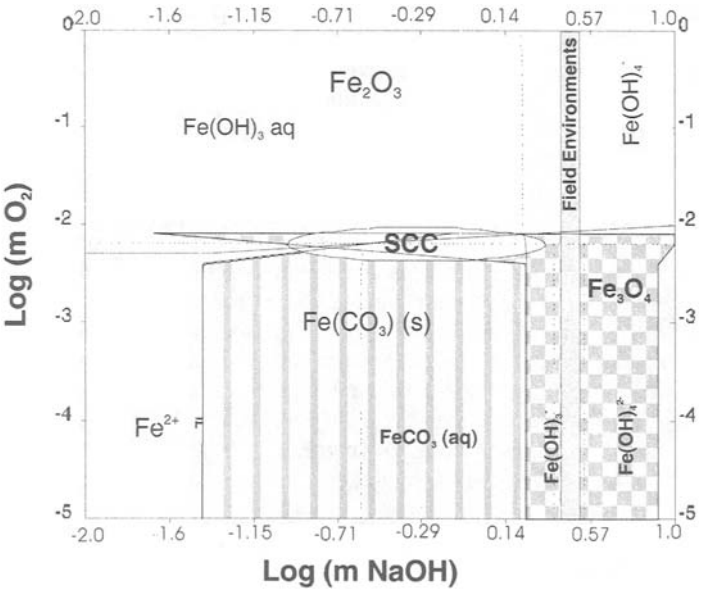


Figure 4. Stability diagram with 0.01m Fe and 1.21 m CO_2 at 25 °C. The shaded rectangle represents the NaOH concentration after 90 percent evaporation.

samples from Table 1 were evaporated at 75 °C. Thermodynamically, the extent of evaporation depends on the amount of the vapor phase (including neutral gases) that is in contact with the aqueous phase. Thus, various scenarios of evaporation were tried. An example of such calculations is shown in Figure 4. Here, the Alabama sample (Table 1) was evaporated and the conditions were adjusted so that 90% of H_2O was removed. Since the solution was alkaline, most of CO_2 remained in the liquid phase. After evaporation, the conditions changed to $m_{NaOH} = 2.36$ and $m_{CO2} = 1.21$. The new conditions are shown in Figure 4 as a shaded rectangle. It is noteworthy that the shaded rectangle is still in the stability field of magnetite and corresponds to higher alkalinity than the $FeCO_3/Fe_3O_4$ boundary. Thus, evaporation does not seem to change the relative stability of solid phases even though the concentration of the solution changes very significantly.

To achieve conditions at the $FeCO_3/Fe_3O_4$ boundary (or the overlap region for higher amounts of dissolved Fe), the solution composition would have to be somewhat changed, i.e., either the alkalinity would have to be slightly reduced or the amount of CO_2 would have to be somewhat increased. These two options are essentially equivalent and involve

shifting the balance between HCO_3^- and CO_3^{2-} ions towards the predominance of HCO_3^-. Since the bicarbonate/carbonate system is a buffer, the pH would be then changed by only a small amount.

Thus, the thermodynamic analysis leads us to two possible conclusions:

1. Assuming that the thermodynamic analysis is strictly valid, the concentration of the solution through evaporation is not likely to result in conditions that have been associated with SCC. Instead, a somewhat reduced alkalinity or increased CO_2 content is necessary; or
2. The formation of the solid phases proceeds through some metastable steps. Stabilization of such a metastable phase would be favored by more concentrated solutions (e.g., in the presence of solid $NaHCO_3$). Although we are not aware of experimental data regarding a $FeCO_3$ to Fe_3O_4 transformation, similar process are known for other iron compounds [31].

The necessity for less alkalinization is consistent with the observation that IGSCC occurs at less negative potentials (-0.65 V SCE) than the externally applied CP.

Effect of Other Cations on Stability Fields

Thermodynamic simulations have also been performed to examine the effect of calcium and magnesium ions. For the quantitative analysis, it was assumed that the system contains 0.17 m CO_2 and 0.1 m of dissolved Fe. The amount of oxygen and OH^- ions was varied. To examine the effect of alkaline earth cations, fixed concentrations of $CaCl_2$ or $MgCl_2$ were added to the system while keeping other variables as described above. The presence of Ca^{2+} results in the formation of $CaCO_3$, which is stable in the whole range of independent variables that are shown in Figure 5. Therefore, a stability field of $CaCO_3$ is not shown explicitly in the figure.

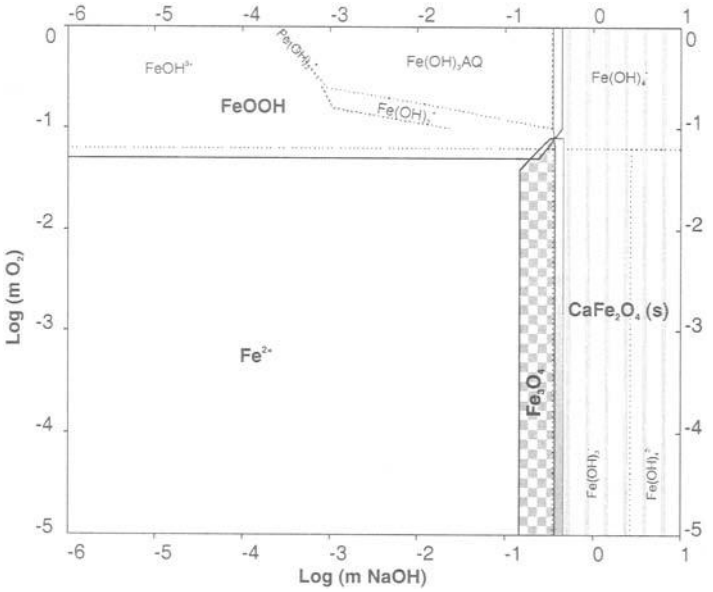


Figure 5. Stability diagram for 0.1 m Fe, 0.17m CO_2, and 1 m $CaCl_2$ at 60°C. $CaCO_3$ is not shown for clarity.

The important phenomenon here is the competition between the precipitation of $CaCO_3$ and $FeCO_3$. $CaCO_3$ is much less soluble than $FeCO_3$, especially at low and moderate temperatures. Therefore, the available CO_2 is consumed mostly by the formation of $CaCO_3$. Only the remainder of CO_2 may yield $FeCO_3$. This results in the shrinkage of the $FeCO_3$ stability field. Additionally, the presence of calcium ions results in the formation of calcium ferrate ($CaFe_2O_4$) in the region of high alkalinity. As the amount of Ca^{2+} ions is increased above the available amount of CO_2 (here, 0.17 m), $FeCO_3$ is predicted to disappear. This is shown in Figure 5 for a solution containing 1 m Ca^{2+}. For such concentrations of calcium, there is no $FeCO_3$ stability field and, therefore, no conditions that would be conducive to IG SCC. Magnesium has a qualitatively similar effect as calcium because of the formation of magnesium carbonate. However, the effect of Mg^{2+} is quantitatively weaker because of the relative stability of magnesium and iron carbonates. Finally, stability diagrams have been generated for systems containing both Ca^{2+} and Mg^{2+} ions. It is known that Ca^{2+} and Mg^{2+} show some synergy in the formation of mixed carbonates (e.g. dolomite). However, very little synergy is observed when it comes to the competition between iron carbonate and alkaline earth carbonates because calcium plays the dominant role. Thus, the simulations predict that the presence of sufficient concentrations of Ca^{2+} ions and, to a lesser extent, Mg^{2+} ions may prevent IG SCC because of the destabilization of $FeCO_3$.

Reactive Transport Calculation of the Effect of Potential

The experiments of Turnbull and May [32] on the effects of cathodic polarization on crevice pH were simulated using a 1-D geometry. Because of the symmetry, the simulation assumes a crevice length of 120 mm (with one closed end) and a gap of about 0.4 mm. It was assumed that the end open to bulk solution was maintained at a constant potential for each simulation. The bulk solution was assumed to be constant in concentration just outside the crevice. The temperature was assumed to be 25°C, although the experiments were performed at temperatures of 18 and 5°C. Equilibrium with atmosphere (0.21 atm. O_2 and $10^{-3.5}$ atm. CO_2) was assumed. The end opposite to the open end was assumed to be a zero-flux boundary.

The results of a simulation are shown in Figure 6. As expected, the pH inside the crevice increases as the externally applied potential becomes more negative. It can be seen that t higher potentials, the agreement between experiments and calculation is quite good. At externally applied potentials below about –0.9V (SCE), the calculated pH reaches a maximum value of about 11.2, whereas Turnbull and May [32] observed that the pH in the crevice attain a constant value at lower potentials (-1.1V SCE) and the value is higher (about 12.5). This is the result of the assumed electrochemical reaction rate law for water reduction, which attains a constant value beyond a certain negative potential. Although not shown in Figure 6, the model calculations indicate that the crevice pH under cathodic polarization is relatively independent of crevice gap/length ratio, as confirmed by experiments. The dependence of crevice pH on external potential is also consistent with the results of Lara and Klechka [17] in groundwater of varying conductivity. At potentials lower than –0.5V vs. SHE (-0.75V vs. SCE), no significant gradient in potential is calculated. This is consistent with the experimental observation of Turnbull and May [32]. Lack of potential gradient in such a highly conductive solution is not surprising.

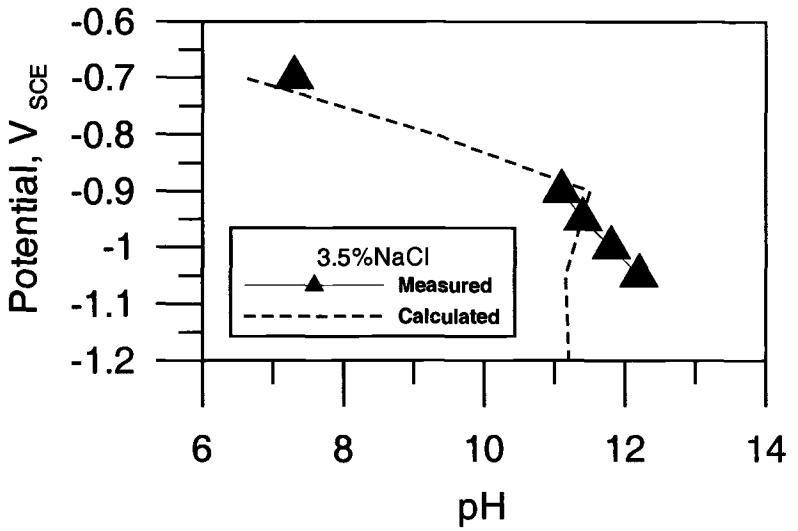


Figure 6. Comparison between calculated and measured pH at the deepest point in the crevice. Experiments were performed by Turnbull and May[18].

Most analyses of disbonded coating environment suggest that dissolved CO_2 is responsible for the acidification of the environment. However, under open-circuit conditions, significant dissolution of iron occurs and the hydrolysis of the ferrous species can also contribute to local acidification. This is consistent with the observation of magnetite in the disbonded region.

Effect of Carbon Dioxide

The simulation of CO_2 effect was done by varying the CO_2 partial pressure in the gas phase and assuming that this is in equilibrium with the dissolved CO_2 in solution. The solution composition and applied potential were the same as those used in the SwRI experiments [29] (10^{-2}M NaCl + 10^{-2}M Na_2SO_4; -0.9V SCE). A 1-D simulation was conducted and the results are shown in Figure 7. The atmospheric partial pressure of CO_2 is approximately 0.032 kPa (3.16×10^{-4} atm.). If this partial pressure is increased by one order of magnitude, no substantial change in pH at the tip of the crevice is predicted despite an increase in the dissolved CO_2. However, if the partial pressure is increased by three orders of magnitude (roughly twice the highest partial pressure of CO_2 used in laboratory experiments investigating TGSCC) , then the crevice pH at the tip remains near-neutral for a considerable length of time before attaining an alkaline value due to CP. These results are consistent with the experimental findings reported by Charles and Parkins [33]. This suggests that the transient effects are important to consider in understanding the role of environmental factors on SCC.

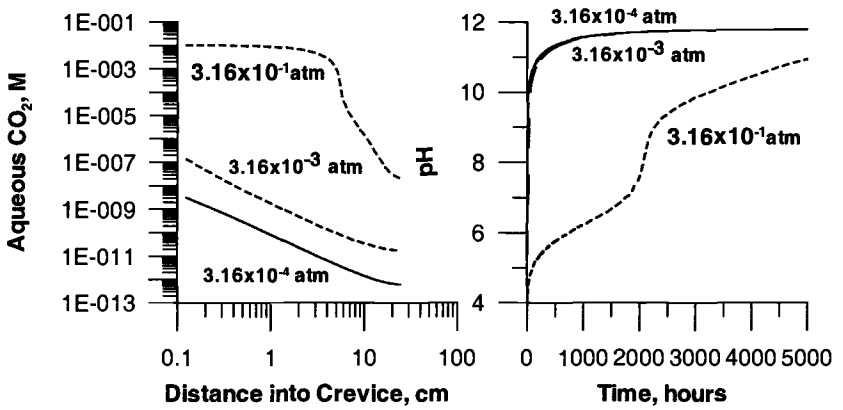


Figure 7. Effect of increasing CO_2 in the gas phase on environment inside the crevice. Solution was 10^{-2} M Cl^- + 10^{-2} M SO_4^{2-}. Potential: -0.9V SCE

Summary

The environmental conditions leading to high-pH (IGSCC) and near-neutral pH (TGSCC) cracking was reviewed. While laboratory experiments have defined the solution compositions, potentials, and temperatures for cracking relatively well, the relationship of these laboratory test conditions to conditions present under disbonded coatings in the field is still unclear. Of specific importance is the dichotomy in the potential required for cracking and the chemistry of the environment compatible with the potential. For high-pH SCC, potentials in the range of –0.65 V SCE are necessary, but the solution pH at these potentials would not be alkaline. Similarly, for near-neutral pH SCC, negative potentials are not compatible with relatively low pH needed for cracking.

Thermodynamic modeling predicts the conditions under which the solid corrosion products observed on fracture surfaces are stable. Based on a thermodynamic analysis, the nominal environments found trapped under disbonded coating near IGSCC sites are not predicted to lead to SCC, which is consistent with experimental observations. Thermodynamic analysis also suggests that evaporation of such trapped waters alone is not likely to result in generating conditions for IGSCC. Reduction in alkalinization (less negative potentials) or penetration of CO_2 may be necessary to generate IGSCC environments.

The beneficial effect of calcium and, to a lesser extent, magnesium was predicted by the stability diagrams through the competitive formation of calcium carbonate or dolomite.

Reactive transport modeling show that even in relatively dilute environments, the pH under cathodic protection potentials eventually reaches high values. The potential gradient also decreases with time. The rate of increase of pH with time is lower for environments containing high CO_2. These are consistent with experimental observations. These observations suggest that transient conditions lead to SCC and there may be periods during which the environmental conditions and potential are out side the

windows of susceptibility to SCC. Such transient periods may be related to seasonal fluctuations in water table or freeze-thaw cycles. Further correlation of field observations of SCC with soil conditions and local hydrology is needed.

Acknowledgment

The authors acknowledge the technical discussions with G. Cragnolino and O. Moghissi. The project is funded by GRI under Contract No. 5097-260-3784, with Phil Dusek as the project manager. The authors acknowledge the helpful discussions with Kevin Krist, GRI during the course of the project.

References

[1] M. Eiboujdaini, Wang,Y.-Z., Revie, R.W., Parkins, R.N., and M.T. Shehata, "Stress Corrosion Crack Initiation Processes: Pitting and Microcrack Coalescence," *Corrosion/2000,* NACE International, Houston, TX, 2000, Paper 379.

[2] Parkins, R.N., *"Overview of Intergranular Stress Corrosion Cracking Research Activities,"* Report PR-232-9401, Pipeline Research Committee International, Arlington, VA, 1994.

[3] National Energy Board, *"Public Enquiry Concerning Stress Corrosion Cracking on Canadian Oil and Gas Pipelines,"* MH-2-95, National Energy Board, Calgary. Alberta, Canada, November, 1996.

[4] Beavers, J.A. and Harle, B.A., "Mechanisms of High-pH and Near Neutral-pH SCC of Underground Pipelines," *International Pipeline Conference*, V. 1, American Society of Mechanical Engineers, New York, 1996, p. 555.

[5] Parkins, R.N., "A review of stress corrosion cracking of high pressure gas pipelines," *Corrosion/2000,* NACE International, Houston, TX, 2000, Paper 363.

[6] Jack, T.R., Erno, B., Krist, K., and Fessler, R.R., "Generation of Near-Neutral pH and High pH SCC Environments on Buried Pipelines," *Corrosion/2000*, NACE International, Houston, TX, 2000, Paper 362.

[7] Dupuis, B.R., "The Canadian Energy Pipeline Association Stress Corrosion Cracking Database," *International Pipeline Conference*, V.1, The American Society of Mechanical Engineers, New York, 1998, p. 589.

[8] Parkins, R.N., Blanchard, Jr., W.K., Delanty, B.S., *Corrosion*, "Transgranular stress corrosion cracking of high-pressure pipelines in contact with solutions of near neutral pH," V.50, 1994, p. 394.

[9] Gu, B., Yu, W.Z., Luo, J.L., and Mao, X., "Transgranular stress corrosion cracking of X-80 and X-52 pipeline steels in dilute aqueous solution with near-neutral pH," *Corrosion*, V. 55, 1999, p. 312.

[10] Johnson, J.T., Durr, C.L., Beavers, J.A., and Delanty, B.S., "Effects of O_2 and CO_2 on Near-Neutral pH Stress Corrosion Crack Propagation," *Corrosion/2000*, NACE International, Houston, TX, 2000, Paper 356.

[11] Qiao, L, Luo, J.L., and Mao, X., "Hydrogen evolution and enrichment around stress corrosion crack tips of pipeline steels in dilute bicarbonate solution," *Corrosion*, V. 54, 1998, p. 115.

[12] Beavers, J.A and Jaske, C.E., "SCC of Underground Pipelines: A History of the Development of Test Techniques," *Corrosion/99*, NACE International, Houston, TX, 1999, Paper 142.

[13] Fessler, R.R., Markworth, A.J., and Parkins, R.N., "Cathodic protection levels under disbonded coatings," *Corrosion*, V.39, 1983, pp. 20-25.
[14] Gan, F., Sun, Z.-W., Sabde, G., and Chin, D.-T., "Cathodic protection to mitigate external corrosion of underground steel pipe beneath disbonded coating," *Corrosion* V. 50, 1994, pp. 804-816.
[15] Jack, T.R., Van Booven, G., Willmott, M., Sutherby, R.L., and Worthingham, R.G., "Cathodic protection potential penetration under disbonded pipeline coating," *Materials Performance,* V.34, 1994, pp. 17-21.
[16] Brousseau, R. and Qian, S., "Distribution of steady-state cathodic currents underneath a disbonded coating," *Corrosion,* V. 50, 1994, pp. 907-911.
[17] Lara, P.F. and Klechka, E., "Corrosion mitigation under disbonded coating," *Materials Performance* V. 38, No. 6, 1999, pp. 30-36.
[18] Staehle, R.W., "Combining design and corrosion for predicting life," *Life Prediction of corrodible Structures*, R.N. Parkins (ed.), Volume I, NACE International, Houston, 1994, pp. 138-291.
[19] Zemaitis, J.F., Clark, D.M., Rafal, M., Scrivner, N.C., *Handbook of Aqueous Electrolyte Thermodynamics*, American Institute of Chemical Engineers, New York, 1986.
[20] Rafal, M, Berthold, J.W., Scrivner, N.C. and Grise, S.L., "Models for Electrolyte Solutions," *Models for Thermodynamic and Phase Equilibria Calculations*, ed. by S.I. Sandler, Marcel Dekker, New York, 1995.
[21] Anderko, A, Sanders, S.J. and Young, R.D., "Real-solution stability diagrams: A thermodynamic tool for modeling corrosion in wide temperature and concentration ranges," *Corrosion*, V. 53, 1997, 43.
[22] Lencka, M.M, Nielsen, E., Anderko, A. and Riman, R.E., "Hydrothermal synthesis of carbonate-free strontium zirconate: thermodynamic modeling and experimental verification," *Chemistry of Materials*, V. 9, 1997, p.1116.
[23] Gartland, P.O., "Modeling Crevice Corrosion of Fe-Ni-Cr-Mo Alloys in Chloride Solutions,", *Proceedings of the 12th International Corrosion Congress*, Vol 3B, NACE International, Houston, TX, 1993, pp 1901-1914.
[24] Sharland, S.M., "A mathematical model for the initiation of crevice corrosion in metals," *Corrosion Science* V. 33, No. 2, 1992, pp. 183-201.
[25] Watson, M. and Postlethwaite, J., "Numerical simulation of crevice corrosion of stainless steels and nickel alloys in chloride solutions," *Corrosion,* V. 46, No. 7, 1990, pp. 522-530.
[26] Stewart, K., Ph.D. Thesis, University of Virginia, (1999).
[27] Walton, J.C., Cragnolino, G., and Kalandros, S.K., "A numerical model of crevice corrosion for passive and active metals," *Corrosion Science,* V.38, No.1, 1996, pp. 1-18.
[28] Gravano, S.M. and Galvele, J.R., "Transport processes in passivity breakdown – III. Full hydrolysis plus ion migration plus buffers," *Corrosion Science*, V.24, No. 6, 1984, pp. 517-534.
[29] Sridhar, N, Dunn, D.S., and Seth, M., "Application Of A General Reactive Transport Model To Predict Environment Under Disbonded Coatings," *Corrosion/2000*, NACE International, Houston, TX, 2000, Paper No.366.

[30] Parkins, R.N. and Zhou, S., "The stress corrosion cracking of C-Mn steel in CO_2-HCO_3^--CO_3^{2-} solutions. I: stress corrosion data," *Corrosion Science*, V. 39, 1997, p. 175.

[31] Anderko, A and Shuler, P.J., "A computational approach to predicting the formation of iron sulfide species using stability diagrams," *Computers and Geosciences*, 23, 647 (1997).

[32] Turnbull, A. and May, A.T., "Cathodic protection of crevices in BS 4360 50D structural steel in 3.5% NaCl and in seawater," *Materials Performance,* V. 22, No. 10, 1983, pp. 34-38.

[33] Charles, E.A. and Parkins, R.N., "Generation of stress corrosion cracking environments at pipeline surfaces," *Corrosion*, V. 51, 1995, p. 518.

Russell H. Jones[1]

Considerations in Using Laboratory Test Data as an Indicator of Field Performance: Stress Corrosion Cracking

Reference: Jones, R. H., **"Considerations in Using Laboratory Test Data as an Indicator of Field Performance: Stress Corrosion Cracking,"** *Environmentally Assisted Cracking: Predictive Methods for Risk Assessment and Evaluation of Materials, Equipment, and Structures, ASTM STP 1401,* R. D. Kane, Ed., American Society for Testing and Materials, West Conshohocken, PA, 2000.

Abstract: Correlations between laboratory stress corrosion test data and field performance and data are done for the express purpose of demonstrating the validity of the laboratory data for use in component design and performance. Improved component performance and life-prediction is the primary goal of developing correlations between the laboratory and field performance. It is not sufficient to merely obtain data from a standard test and assume this will suffice. The purpose of this paper is to summarize the role of standardized tests, specialized tests, full-size component tests, the impact of the quality of field data, inability to match field conditions in the laboratory, and role of modeling in developing a high confidence laboratory-field correlation.

Keywords: Stress-corrosion, laboratory tests, field performance, standard tests, non-standard tests, correlation, validation.

Introduction

There are many scenarios where laboratory data must be used as either an indicator of performance or to predict field performance. The rigor needed and approaches available for obtaining the laboratory data depends to some extent on the application. There may be situations where analysis of field data is sufficient to identify mitigation routes such that laboratory data isn't required. However, the quality of field data as obtained by failure analysis or other means may not be sufficiently accurate to delineate clearly the causes of cracking and therefore the mitigation pathway. Also, data may be needed for a new component or material without field data. These scenarios are where laboratory testing can be used to separate effects and clearly identify causes. Factors such as capital cost associated with an application, expected component life-time, and license requirements are also factors in developing the laboratory testing program. Clearly, the implications of a component failure in a low-cost, consumer item such as the exhaust system in an automobile are vastly different than those associated with failure of a nuclear component or natural gas pipeline.

[1]Senior Staff Scientist, Structural Materials Research, Pacific Northwest National Laboratory, PO Box 999, Richland, WA, 99352.

Copyright© 2000 by ASTM International www.astm.org

Development of a new material or application for which there is no existing field experience will likely require a different testing regime than where a mitigation route is being sought for an existing field problem. In the former case, the testing regime will likely be a series of standardized tests while in the latter case it may be necessary to develop specialized tests that give laboratory failures that match field failures. Of course, standardized tests should be employed whenever possible but there are occasions when specialized testing may be necessary. In some cases such as nuclear piping and natural gas pipeline steels, it has been necessary to perform full-scale testing. Another choice must be made as to whether susceptibility testing will be sufficient, such as determining threshold values, or whether it is necessary to determine crack growth rates. There is often the need to accelerate rates by altering the environment, electrochemical potential or loading condition but care must be taken to ensure that the stress corrosion cracking (SCC) mechanism matches those observed in the field. Modeling can be useful in bridging the gap between laboratory and field performance especially where extrapolations in time, environment or loading are necessary. The corrosion performance of nuclear waste packaging materials is an example where modeling is crucial for extrapolating to the very long storage times.

Test Selection Considerations

Any application that requires a material to perform within some design envelope without failure requires accurate data for the design. A desirable goal for SCC testing is to provide life-prediction guidelines or conditions for which SCC does not or cannot occur. The key question is how much data and what type. For instance, in the aerospace industry [*1*], it is common to use the building block approach with data obtained from a range of tests from coupon, element, subcomponent, component and full scale components. This very rigorous testing approach reflects the critical nature of the component performance requirement and the consequences of a failure. At the other extreme is a design that relies primarily on material data obtained from coupon testing. There are a number of standard tests for stress corrosion testing including: 1) bent beam (ASTM G-39), 2) C-ring (ASTM G-38), 3) U-bend (ASTM G-30), 4) tensile (ASTM G-49), 5) pre-crack wedge open load , 6) compact tension-crack growth rate and more generally crack velocity measurements using pre-cracked specimens. The selection of a test technique is often based on which correlates best with the field conditions and result in SCC process that mimics the field results. A complication to this approach is that it is often difficult to collect unambiguous information from field samples. The sample surfaces may be damaged during removal from a component making crack path analysis difficult, the stresses may not be well-described, and the crack growth rates will only be estimates because the crack initiation time is unknown. Correctly defining the environment in the field is perhaps the most difficult aspect. Clearly, for buried pipeline steels covered with a wrap or other coating, the definition of the environment at the pipe surface is very difficult [*2*]. In contrast, the chemical environment in a nuclear power plant has been carefully measured, monitored and recorded [*3*]. Even with quantitative water chemistry data, Andresen [*3*] suggests that care must be taken in interpreting field data.

There are numerous examples in the literature on the use of standard tests for evaluating the SCC while examples of direct correlation with field results are somewhat limited. One example is that reported by Jones et al. [*4*] for the evaluation of SCC in a spent fuel pool system pipe at Three Mile Island. In this case, a failure analysis was conducted to evaluate the SCC process and causes, followed by a laboratory study to elucidate further the SCC mechanism and causes and to identify routes to alleviate further SCC. The failure analysis revealed that the Type 304 SS pipe was sensitized in the heat affected zone (HAZ) and that SCC was intergranular and occurred only in the HAZ. The service environment was boric acid, with a pH ranging from 4.5 to 7.0 and temperatures ranging from 7 to 33°C. There was evidence of elemental sulfur on the intergranular SCC surface and evidence for the presence of $Na_2S_2O_3$. Transmission electron microscopy revealed that the HAZ material was heavily deformed with a high dislocation density. This deformation resulted from the high stresses generated by the pipe constraint during welding. The ASTM G-49 test (constant extension rate test- CERT) was chosen to perform SCC evaluation of samples removed from the pipe because the deformation induced during the CERT testing would mimic the extensive deformation and high residual stresses in the HAZ. Tests were performed in water at 33°C with boric acid with and without Cl^-. Further tests were performed by Bruemmer and Johnson [*5*] on plate material at these same conditions with the addition of thiosulfate and fluoride concentrations in the water. The tests performed on samples removed from the pipe and the plate material demonstrated a match in crack growth mode and identified the role of water impurities such as chloride, thiosulfate and fluoride in promoting SCC in these samples at low temperatures, Figs. 1 and 2.

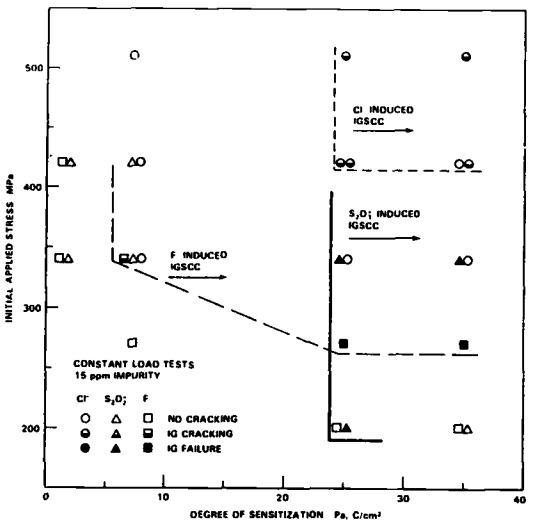


Fig. 1. *Constant load test results for four steel alloys in 32°C water with 15 ppm impurity additions of chloride, thiosulfate or fluoride ions* [*Ref. 5*].

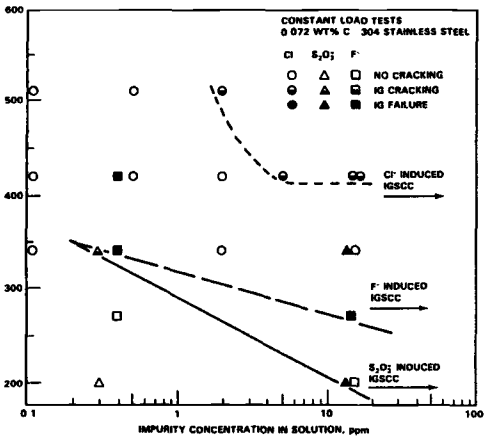


Fig. 2. *The effect of impurity concentration in solution on the stress necessary to promote IGSCC in furnace sensitized, high carbon 304 SS [Ref. 5].*

Speidel and Magdowski [*6*] have presented a second example where crack growth rate data for Alloy 600, stabilized austenitic stainless steel and high-strength austenitic steel obtained using pre-cracked samples was compared to field results. The laboratory field correlation for the alloy 600 consisted of the development of a crack growth rate equation for stage II cracking given below and the correlation of field data with this laboratory equation.

$$da/dt = 6 \times 10^{-7} \times S^3 \times e^{-Q/RT} \qquad (1)$$

where S is the yield strength, Q the activation energy of 130 kJ/mole, R is the gas constant and T the temperature in °K. The correlation with field results for Alloy 600 vessel head penetrations in PWR's demonstrates that the laboratory data and model provide an upper bound for the field crack growth rates. Speidel and Magdowski [*6*] concluded, for all three materials and applications, that the laboratory data correlated best with the fastest crack growth rates obtained from the field data and that the laboratory data predicted the worst case scenario for in-service conditions. This correlation results from the laboratory test data being obtained with pre-cracked specimens, which bypasses crack initiation and early crack growth processes that occur in the field and therefore result in slower average crack growth rates. The instantaneous crack growth rates, i.e. long crack-steady Stage II crack growth rates, are likely similar for cracks in components and laboratory samples for the same conditions. It is also necessary to obtain a statistically significant data set in the laboratory because of the inherent variability of the SCC process.

Selection of a Specialized Testing Technique

Occasionally it is necessary to modify a standard test or devise a whole new one to obtain SCC data that is field relevant. This has been the case for gas pipeline SCC testing as summarized by Beavers and Jaske [*7*] and for corrosion tests as summarized by

Kane [*8*]. Kane evaluated several important parameters that must be chosen to represent the field conditions best and then controlled in laboratory tests. It was necessary to modify existing tests and develop new ones for gas pipeline applications in order to duplicate field results and to provide useful data for identifying routes to mitigate SCC in buried pipelines. An early technique that later became a standard (ASTM G-49) is the slow strain rate technique. This work was done by Parkins and coworkers [*9*] for the purpose of screening environments and conditions that cause SCC prior to development of a significant field of databases. This technique has a number of limitations with the most severe being the resulting high crack velocities and the lack of material sensitivity, i.e. all heats crack similarly in this test while this is not the case in the field. This test also does not provide much information on crack initiation. Therefore, this test is of little value for life-prediction or remaining life predictions.

The tapered tensile test technique was developed [*7*] to help provide better information on crack initiation in buried pipelines. In early developmental work, samples were taken directly from the pipeline and a tapered gage section machined into the sample with the inner and outer diameter of the pipe left intact. Tests are conducted to 110% of the minimum yield strength of the material and as with many pipeline SCC tests, the load is cycled at an R (P_{min}/P_{max}) of 0.9 at a frequency of 10^{-4} to 10^{-5} Hz. While this test can provide information on stress thresholds for crack initiation it has some of the same limitations as the slow strain rate test with the primary one being that the cracks formed in these samples are in the circumferential direction of the pipe and not the longitudinal direction as observed in service.

To solve the crack orientation issue for gas pipelines associated with the slow strain rate and tapered tensile specimens, a test where a sample is removed in the circumferential direction and loaded in bending was devised. This is a modification of the bent beam test, ASTM G-39, but with the sample loaded as a cantilever although there it is also possible to load the sample in three or four point bending as in ASTM G-39. This test provides information on the initiation in the longitudinal direction, as observed in service, with the original pipe surface intact and can include crack colonies formed on pipe surfaces in the field. Multiple tests must be conducted to determine stress thresholds. Quantitative crack growth rates cannot be determined with this, the slow strain rate or tapered tensile specimens. Precracked compact tension samples or related test geometries must be used to obtain this information.

The slow strain rate test is conducted with smooth or original component surfaces under conditions of dynamic sample strain to accelerate crack initiation and propagation but with only a qualitative measure of the crack velocity. Precracked tests are conducted with nominally constant loads with notched specimens to obtain more quantitative crack velocities, but stress corrosion cracks often exhibit decreasing crack velocities with time unless the load is cycled or increased slightly. Abramson, Evans and Parkins [*10*] devised a test that combines the use of precracked samples and the constant extension rate of the slow strain rate test. This approach allowed for accurate crack length measurements using potential drop techniques while obtaining a dynamic crack tip as with the slow strain rate technique. The results are presented as energy release rate versus crack length or J-contour integral versus crack length. Just as the slow strain rate test will result in sample failure (either ductile or brittle) the rising load J test will result in crack extension. The degree to which SCC accelerates this crack extension is the key

aspect of this test. This effect is clearly reflected in the changes in the tearing modulus, which is a dimensionless parameter that measures the resistance to crack growth. The tearing modulus showed a strong dependence on the displacement rate and the environment (i.e. concentration of NaCl in a chromate solution) with a minimum value at intermediate displacement rates. Abramson, Evans, and Parkins [*10*] concluded that this test is useful for measuring SCC although the test has not been widely adopted.

Electrochemical Tests for Predicting the Occurrence of SCC

Electrochemical tests are occasionally used to identify susceptibility to SCC and even estimate the crack growth rates of materials. There are few correlations to field results although Parkins has utilized electrochemical polarization to identify SCC susceptibility in gas pipeline steels [*11*]. This technique utilizes the difference in current during fast and slow potentiodynamic scans to provide an estimate of the susceptibility to SCC. The fast scan rate is a measure of the bare surface dissolution kinetics over a range of potentials and is therefore representative of the crack tip corrosion rate. The slow scan rate is a measure of the passive dissolution kinetics and is therefore representative of the crack wall corrosion rate. This test was developed specifically for underground gas pipeline steels and was useful for identifying the electrochemical potential at which SCC occurs in these steels. This test is effective with the gas pipeline steels in the carbonate/bicarbonate environment because passivation is very slow so that the fast scan rate polarization dissolution kinetics measure relatively film free dissolution kinetics. This test would not work with materials with rapid passivation kinetics such as austenitic stainless steel.

Scratch repassivation is another electrochemical test used to identify susceptibility to SCC. With this technique, an in situ scratch is produced that disrupts the passive film and the total charge passed between the sample and counter electrode between the time of the scratch event and repassivation. This approach is used to estimate the crack velocity by the following equation

$$da/dt = (E.W./\rho F)\,(Q_f e_{ct}/e_f) \qquad (2)$$

where

da/dt is the crack velocity,
E.W. = the equivalent weight,
ρ = material density,
F = Faraday's constant,
Q_f = the anodic charge density (coulombs/cm^2) integrated over the time from the scratch to repassivation,
e_f = the fracture strain of the film, and
e_{ct} = the crack tip strain rate (s^{-1}).

The value of da/dt determined from Eq. 2 is clearly an estimate since values for the fracture strain of the film and crack tip strain rate are usually not well known for any given condition. Also, there is some uncertainty about how much of the anodic charge density goes to establishing the charge double layer and the capacitance of the system relative to anodic dissolution. Therefore, this approach can best be used for relative

comparisons of the effects of minor compositional changes in materials, changes in heat treatments and environment where the fracture strain of the film and crack tip strain rate are relatively constant.

The degree of sensitization (DOS) in austenitic stainless steel induced by the precipitation of chromium rich carbides at grain boundaries can be used as a measure of the susceptibility of austenitic stainless steels to intergranular stress corrosion cracking (IGSCC). The electrochemical reactivation test, ASTM G108, developed by Novak et al. [*12*] and Clarke et al. [*13*] and the double loop electrokinetic repassivation test developed by Streicher and coworkers [*14*] are two tests used to determine the DOS of austenitic stainless steels such as Type 304 SS. These techniques measure the anodic current associated with the incomplete passivation adjacent to a grain boundary containing chromium rich carbides. These tests can provide a measure of susceptibility given that the chemical environment and stress fall within the parameters that cause IGSCC at the measured DOS. Correlations of the DOS grain boundary chromium concentration and %IGSCC have been made by Bruemmer et al. [*15*], and it was shown that as the grain boundary Cr concentration decreased below 14% the DOS value increased sharply rising to 100 C/cm^2 at 10% Cr at the grain boundary, Fig. 3.

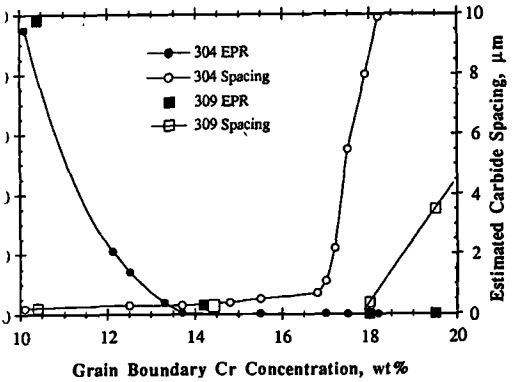


Fig. 3. *Interdependence of chromium depletion, EPR-DOS and carbide spacing at grain boundaries after various desensitization heat treatments. Near-continuous boundary carbides are maintained to higher chromium levels in the 309 SS [Ref. 15].*

However, the % IGSCC and strain to failure of sensitized Type 304 SS for tests at a strain rate of 1 x 10^{-7} s^{-1} in aerated water at 288°C began to show marked evidence of SCC at grain boundary concentrations as high as 17% Cr, Fig. 4. Therefore, the DOS is not a conservative measure of susceptibility to IGSCC.

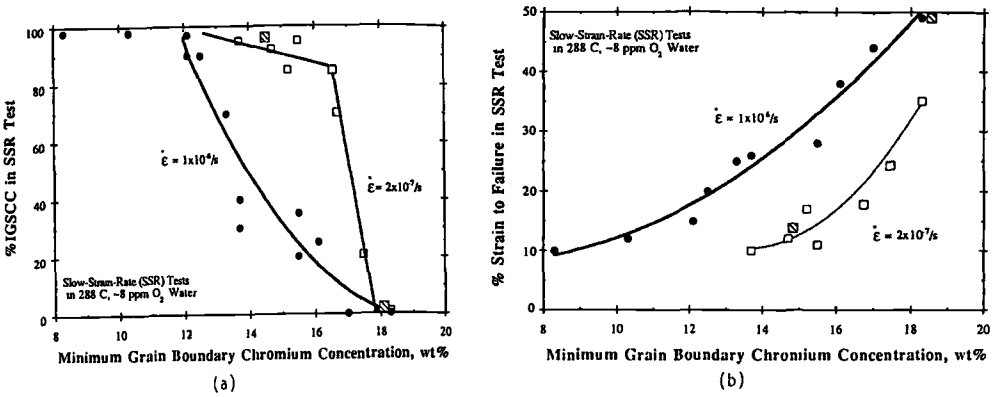


Fig. 4. *The influence of grain boundary chromium concentration on the %IGSCC (a) and the strain to failure (b) during SSR testing in aerated 288°C water [Ref. 15].*

Laboratory vs. Full Size Component Testing

Perhaps the extreme example of modifying a standard test to improve the correlation with the field conditions is that conducted by Zheng et al. *[16]*, where a full sized 61 cm diameter gas pipeline pipe was tested in soil in the laboratory. This is an extreme attempt to bring the field to the laboratory rather than the laboratory to the field. In this test, the pipes were loaded hydrostatically and buried in a wet clay type soil. Stress corrosion cracks were observed to grow in this full scale test and the crack growth rates measured although no direct correlation was made to field values. However, the reported crack growth rates from the pipe test were between 1 and 2 x 10^{-9} cm/s which is similar to that reported in laboratory tests and estimated from field results.

Another example of a full-sized pipe test is that reported by Kass et al. *[17]* for 10 cm, by Hughes for 25 cm *[18]* and by Olson et al. *[19, 20]* on 60 cm diameter boiling water reactor piping. These tests were developed to simulate better the nuclear reactor pipe conditions and to develop weld repair techniques. The system developed by Olson et al. *[19, 20]* allowed the pipe to be internally pressurized with water to a temperature of 288°C while an external tensile or compressive load was applied.

One aspect of full size testing in lieu of standard laboratory tests is the ability to test field repairs or conditions on SCC. For example, Zheng et al. *[16]* evaluated the effect of hydrotesting done in the field to pressures over the operating pressure on stress corrosion cracking. They found that the SCC velocity of all cracks in the pipe decreased following hydrotesting. Similarly, Olson et al. *[20]* were able to evaluate the effects of welding and repair welding parameters such as last pass heat sink welding on SCC. These effects could not be measured with laboratory size coupons so full sized testing was required.

Role of Modeling/Mechanistic Information

Modeling environment-induced crack growth may seem like the last tool to choose when developing a correlation between laboratory and field results. However, there are a few instances where this may be the best approach. These cases are: 1) when a phenomenon is not readily measurable in either the laboratory or the field, 2) when the field data may be of low quality but high-quality laboratory data is available, or 3) there

is a need to extrapolate beyond current field experience. Crack initiation or early stages of cracking is an example of Case #1, since quantitative data on the growth rates of very short cracks is very difficult to obtain in the laboratory and impossible to obtain in the field. Yet, there is a tremendous need to predict when cracking begins not just when a component is about to fail by SCC. An example of Case #2 includes SCC in a very complex environment such as a nuclear reactor while Case #3 includes life-prediction modeling where the goal is to predict component failure beyond current experience or there is a desire to modify a design but insufficient time to develop a complete set of laboratory data.

The behavior of short stress corrosion cracks (sometimes referred to as crack initiation) is a clear example of Case #1. In some systems the transition from a short to long crack behavior may be a smooth transition as noted by Andresen [*21*] where cracks of length longer than 20-50 um acquired steady state or "mature" crack conditions, i.e. crack velocities in sensitized Type 304 SS in a BWR water environment, Fig. 5.

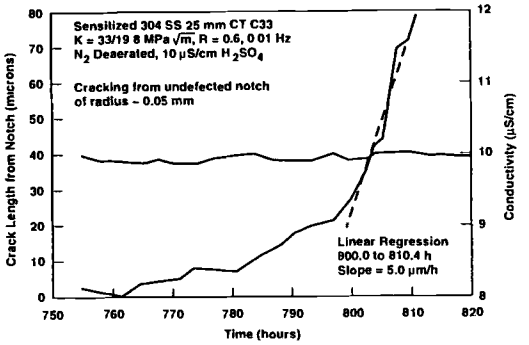


Fig. 5. *Crack length vs. time for compact tension specimen C33 (sensitized type 304 SS) exposed to deaerated 288°C water* [*Ref. 21*].

This result suggests that there would be a relatively small uncertainty in component failure prediction based on the growth of long cracks because the transition occurs at a relatively short length. However, there is a greater uncertainty in predicting when a short crack begins growing so that life prediction would require a stochastic approach based on the probability that a crack begins to grow along any of the population of grain boundaries interfacing with the aqueous environment. Therefore, while there may be an ability to model some aspects of short crack and long crack growth rates in Type 304 SS in BWR environments, the ability to predict component life based on the total process of initiation, short crack growth and long crack growth is still not well-developed.

Simonen et al. [*22*] also developed a model for short crack behavior which describes the transition from short to long behavior for a material in which intergranular stress corrosion cracking is occurring along a grain boundary where active corrosion is occurring. Examples where active corrosion may be occur include segregation of an impurity that is easily oxidized or the precipitation of an anodically active phase at the grain boundary. A key feature of this model is that short cracks begin growing very fast and may decelerate depending on the applied stress or stress-intensity. A notable feature

is the small increase in stress-intensity needed to reinitiate a crack that has retarded, Fig. 6.

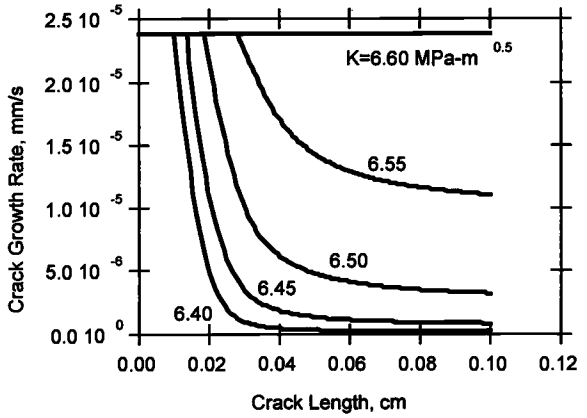


Fig. 6. *Calculated crack growth rate as a function of crack length for selected values of stress intensity. Reducing the stress intensity below 6.6 MPa-m$^{0.5}$ result in inhibited crack growth [Ref. 22].*

Andresen [*21*] makes a strong point on use of laboratory data to predict BWR plant component behavior because the complexity of stress corrosion and uncertainties in plant inspection data. This is an example of Case #2 where the field data is of insufficient quality to make a quantitative comparison between laboratory and field results. He further states that a much more comprehensive predictive capability is possible only with the development of a model that incorporates all the complexities associated with stress corrosion with verification from laboratory data. Andresen [*21*] gives examples where modeling has been used to predict stress corrosion in BWR environments. These include: 1) crack growth rates of Type 304 SS as a function of corrosion potential, 2) crack growth rate versus solution conductivity, 3) fraction of wall thickness penetrated versus time and solution conductivity for schedule 80 stainless steel piping, 4) crack depths in a core shroud, and 5) frequency of cracking versus average plant conductivity for Alloy 600 shroud bolts.

The goal of the work by Andresen [*21*] is to provide some measure of life-prediction for BWR reactor components. Other examples where life-prediction of components subjected to environmental effects include that by Parkins [*23*] for gas pipeline steels and those for corrosion fatigue as summarized by L. Hagn [*24*]. Parkins has proposed four stages for pipeline cracking and the time to failure model based on these four stages. Stage 1 is the period from when the pipeline is put into service and the beginning of cracking, Stage 2 occurs over a relatively short time period with decreasing crack velocity because of an increasing number of cracks in a crack colony, Stage 3 exhibits a constant crack velocity where the cracks are still below K_{ISCC} and short cracks are coalescing to reach a size long enough to achieve K_{ISCC} conditions and Stage 4 is growth of these cracks leading to failure. Parkins has developed equations describing Stages 3 and 4 but not Stages 1 and 2. Therefore, considerable uncertainty remains in the life

prediction capability for gas pipeline steels because Stage 1 can be a very long and variable period of time. Hagn [*24*] has provided an extensive review of life-prediction models for corrosion-fatigue but this subject is outside of the topic of this paper. In summary, these models all rely on environmental affects on S-N or da/dn vs delta K curves without a clear definition of the crack initiation period. This aspect is very similar to that noted above for life-prediction models for stress corrosion cracking. He concludes that empirical approaches relying on the superposition concept can be useful that without a good mechanistic basis these models are limited.

Summary

Correlations between laboratory stress corrosion test data and field performance and data are done for the express purpose of demonstrating the validity of the laboratory data for use in component design and performance. There are a number of examples where direct correlations have been made with some success, but in many cases these correlations are hampered by the quality of the field data or the difficulty of obtaining the relevant laboratory conditions. Laboratory-field correlations may be as simple as duplicating the crack growth mode observed in failure analysis of a component so as to study effects of various factors on SCC or it may a more quantitative measure where crack velocities obtained in the laboratory are compared to those estimated from field results.

Standardized tests should be the first choice in developing a laboratory test to correlate with field observations. However, it is sometimes necessary to develop specialized tests that mimic field conditions. The slow strain rate, tapered tensile specimen and rising J tests are examples of tests developed to represent better gas pipeline cracking. There are also electrochemical tests such as the double scan rate potentiodynamic test developed by Parkins for predicting gas pipeline SCC and the double loop electrokinetic repassivation test for degree of sensitization and SCC in austenitic stainless steels. Full size component testing is an extreme example of a specialized test. Examples include full pipe testing of boiling water reactor and natural gas pipeline pipe testing. There are also times when modeling may the best route to providing guidance for component design or life prediction because of the inability to obtain the needed laboratory data or an inability to obtain the needed field data.

Improved component performance and life prediction is the primary goal of developing correlations between the laboratory and field performance. It is not sufficient merely to obtain data from a standard test and assume this will suffice. It is important that the data be correlated with field performance to the fullest extent possible.

References

[1] "Quantifying Qualification: The Building-Block Approach to Designing Composite Structures," *High Performance Composites*, July/August 1999, p. 20.

[2] Rebak, R. B., Xia, Z, Safruddin, R., and Szklarska-Smialowska, Z, "Effect of Solution Composition and Electrochemical Potential on Stress Corrosion Cracking of X-52 P:peline Steel," *Corrosion*, Vol. 52, 1996, p. 396.

[3] Andresen, P. L., "Factors Governing the Prediction of LWR Component SCC Behavior from Laboratory Data," paper 145, *NACE/99*, National Association of Corrosion Engineers, Houston, TX.

[4] Jones, R. H., Johnson, Jr., A. B., and Bruemmer, S. M.,1982, "An Evaluation of Stress Corrosion Cracking of Sensitized Type 304SS in Low Temperature Borated Water," *Proceedings of the 2nd International Conference on Environmental Degradation in Engineering Materials*, Blacksburg, Virginia, September 1981, p. 321.

[5] Bruemmer, S. M. and Johnson, Jr., A. B., "Effect of Chloride, Thiosulfate and Fluoride Additions on the IGSCC Resistance of Type 304 Stainless Steel in Low Temperature Water," P*roceedings of the International Symposium on Environmental Degradation of Materials in Nuclear Power Systems-Water Reactors*, Myrtle Beach, South Carolina, August, National Association of Corrosion Engineers, Houston, TX, 1983, p.571.

[6] Speidel, M. O. and Magdowski, R., "Correlation of Laboratory and Field Stress Corrosion Results in the Power Generation Industry," paper 146, *Corrosion/99*, Paper National Association of Corrosion Engineers, Houston, TX , 1999.

[7] Beavers, J. A. and Jaske, C. E., "SCC of Underground Pipelines: A History of the Development of Test Techniques," paper 142, *Corrosion/99*, National Association of Corrosion Engineers, Houston, TX , 1999.

[8] Kane, R. D., "Relevance of Laboratory Corrosion Tests," *Materials Performance*, October 1996, p. 67.

[9] Humphries, M. J. and Parkins, R. N., "Stress-Corrosion Cracking of Mild Steels in Sodium Hydroxide Solutions Containing Various Additional Substances," *Corrosion Science*, Vol. 7, 1967, p. 747.

[10] Abramson, G., Evans, J. T., and Parkins, R. N., "Investigation of Stress Corrosion Crack Growth in Mg Alloys Using J-Integral Estimations," *Metallurgical Transactions A*, Vol. 16A , 1985, p. 101.

[11] Parkins, R. N., "Predictive Approaches to Stress Corrosion Cracking Failure," *Corrosion Science*, Vol. 20, 1980, p. 147.

[12] Novak, P., Stefec, R., and Franz, F., "Testing the Susceptibility of Stainless Steels to Intergranular Corrosion by Reactivation Method," *Corrosion*, Vol. 31, No. 10, 1975, p. 344.

[13] Clarke,W.L., Cowan, R. L., and Walker, W. L., "In Intergranular Corrosion of Stainless Alloys," ASTM STP 656, R. F. Steigerwald, Ed. *American Society for Testing Materials*, Philadelphia, PA, 1978, p. 99.

[14] Majidi, A.P. and Streicher, M.A., "The Double Loop Reactivation Method to Detecting Sensitization in AISI 304 Stainless Steel," *Corrosion*, Vol. 40, No. 11, 1984, p. 584.

[15] Bruemmer, S. M., Arey, B. W., and Charlot, L. A., "Grain Boundary Chromium Concentration Effects on the IGSCC and IASCC of Austenitic Stainless Steels," in *Proceedings of the Sixth International Symposium on Environmental Degradation of Materials in Nuclear Power Systems-Water Reactors*, August 1-5, 1993, San Diego, CA, TMS, Warrendale, PA, p. 277.

[16] Zheng, W., Tyson, W. R., Revie, R.W., Shen, G., and Braid, J. E. M., "Effects of Hydrostatic Testing on the Growth of Stress-Corrosion Cracks," *Proceedings of the International Pipeline Conference*, Calgary, Alberta, Canada, June, 1998, American Society of Mechanical Engineers, New York, NY, p. 459.

[17] Kass, J. N., Walker, W. L., and Giannuzzi, A. J., "Stress Corrosion Cracking of Welded Type 304 and 304L Stainless Steel Under Cyclic Loading," *Corrosion*, 36, 1980, p. 299.

[18] Hughes, N., paper 17, *Proceedings Sem. Countermeasures for Pipe Cracking in BWR's*, EPRI WS-79-174, Electric Power Research Institute, May 1980.

[19] Olson, N. J., Anderson, W.C., and Gilman, J.D., "Testing of Larger Diameter Pipe in a Simulated BWR Environment to Evaluate Stress Corrosion Cracking Resistance," *Transactions of ANS*, Vol. 39,1981, p. 453.

[20] Gilman, J. D. and Olson, N. J., "Full Scale Testing of a Residual Stress Modification to Control BWR Pipe Cracking," *Proceedings of the International Symposium on Environmental Degradation of Materials in Nuclear Power Systems-Water Reactors*, Myrtle Beach, National Association of Corrosion Engineers, Houston, TX, August 1983, p. 876.

[21] Andresen, P. L., Vasatis, I. P., and Ford, F. P., "Behavior of Short Cracks in Stainless Steel at 288°C," paper 495, *Corrosion/90*, NACE, Houston, 1990.

[22] Simonen, E. P., Jones, R. H., and Windisch, Jr., C. F., "A Transport Model for Characterizing Crack Tip Chemistry and Mechanics During Stress Corrosion Cracking," *New Techniques for Characterizing Corrosion and Stress Corrosion*, R. H. Jones and D. R. Baer, Eds., TMS, Warrendale, PA, 1996, p. 141.

[23] Parkins, R. N., "Localized Corrosion and Crack Initiation," in Mechanics and Physics of Crack Growth: Application to Life Prediction, Thompson, Ritchie, Bassani and Jones, *Materials Science and Engineering*, A103, 1988, p. 143.

[24] Hagn, L., "Life Prediction Methods in Aqueous Environments," in Mechanics and Physics of Crack Growth: Application to Life Prediction, Thompson, Ritchie, Bassani and Jones, *Materials Science and Engineering*, A103,1988, p. 193.

Yi-Ming Pan,[1] Darrell S. Dunn,[1] and Gustavo A. Cragnolino[1]

Effects of Environmental Factors and Potential on Stress Corrosion Cracking of Fe-Ni-Cr-Mo Alloys in Chloride Solutions

Reference: Pan, Y.-M., Dunn, D. S., and Cragnolino, G. A., **"Effects of Environmental Factors and Potential on Stress Corrosion Cracking of Fe-Ni-Cr-Mo Alloys in Chloride Solutions,"** *Environmentally Assisted Cracking: Predictive Methods for Risk Assessment and Evaluation of Materials, Equipment, and Structures, ASTM STP 1401*, R. D. Kane, Ed., American Society for Testing and Materials, West Conshohocken, PA, 2000.

Abstract: The stress corrosion cracking (SCC) susceptibility of several Fe-Ni-Cr-Mo alloys, which are candidate materials for high-level radioactive waste containers, was evaluated using slow strain rate and fracture mechanics testing. Slow strain rate tests of type 316L stainless steel (SS) and alloy 825 were performed in hot, concentrated chloride solutions (6.2 to 14.0 molal Cl^-). SCC of type 316L SS was observed at chloride concentrations equal to or greater than 7.2 molal and temperatures above 95°C, whereas, alloy 825 experienced SCC only in a 14.0 molal Cl^- solution at 120 °C. In both materials, SCC does not occur at potentials below the repassivation potential for pitting corrosion (E_{rp}). In fracture mechanics tests using wedge-loaded specimens, alloy 22 was found to be resistant to SCC when tested in 14.0 molal Cl^- solutions at 110°C. On the contrary, crack growth was observed in type 316L SS specimens exposed to concentrated chloride solutions at potentials above the E_{rp}. These results suggest that E_{rp} constitutes a lower limit for the critical potential for SCC that can be used for assessing material performance.

Keywords: Stress corrosion cracking, nickel-base alloys, stainless steel, repassivation potential, chloride solutions, slow strain rate testing, fracture mechanics testing, high-level radioactive waste disposal

Introduction

Stress corrosion cracking is one of the most important modes of degradation of the Fe-Ni-Cr-Mo alloys selected as candidate container materials for the disposal of high-

[1] Senior research engineer, senior research engineer, and staff scientist, respectively, Center for Nuclear Waste Regulatory Analyses, Southwest Research Institute, 6220 Culebra Road, San Antonio, TX 78238.

Copyright© 2000 by ASTM International www.astm.org

level nuclear waste. Environmental factors such as temperature, chloride concentration, pH, redox potential, and other variables that could be relevant to the long-term performance in the high-level nuclear waste repository, are critical in determining the susceptibility of these materials to SCC. Additionally, there is a need for identifying experimental parameters that can be used as suitable parameters in performance assessment codes for the long-term prediction of material degradation due to SCC.

The concept of a critical or threshold potential for SCC has been applied to several alloy-environment combinations and was reviewed by Cragnolino and Sridhar [*1*]. As first noted by Hines and Hoar [*2*], transgranular SCC of solution-annealed type 304 SS in boiling, concentrated magnesium chloride ($MgCl_2$) solutions occurs only above a critical potential. The critical potential concept was also applied to the intergranular SCC of sensitized type 304 SS in high-temperature aqueous environments characteristic of recirculating lines in boiling water reactors [*3*]. In addition, Tsujikawa and coworkers [*4*] have identified the critical potential for austenitic SSs in hot chloride solutions as the repassivation potential for crevice corrosion (E_{rcrev}), above which the environment inside crevices could promote SCC initiation in the presence of applied stresses. However, there are few data for the alloys and environments of interest to the proposed Yucca Mountain repository [*5*].

Suitable experimental techniques are essential to define the range of environmental and mechanical conditions for SCC susceptibility of candidate container materials. The advantages and limitations of several accelerated SCC tests for determining suitable bounding parameters for long-term life prediction have been evaluated previously [*1*]. In this study, the effects of environmental factors and potential on the SCC susceptibility of type 316L SS and alloys 825 and 22 were evaluated by using slow strain rate and fracture mechanics testing techniques. The ultimate goal is to determine whether a critical potential for SCC exists for these three alloys, to define the relationship between this potential and the repassivation potential for pitting/crevice corrosion, and to determine the minimum chloride concentration required to promote SCC.

Experimental Methods

Specimens

The chemical compositions of the heats of type 316L SS, and alloys 825, and 22 used in this study are given in Table 1. Slow strain rate test (SSRT) specimens of both type 316L SS and alloy 825, with a diameter of 6.3 mm, were machined from mill-annealed, 12.7 mm thick plates with the tensile axis perpendicular to the rolling direction. Two types of specimens were used. One of them was a round, smooth tensile specimen with a waisted section having a gage length of 12.7 mm and a diameter of 3.2 mm. The other one was a round, notched specimen, in which a circumferential notch, with a depth of 1.6 mm, an included angle of 60°, and a radius of 51 μm, was machined. The notched specimens were intended to facilitate crack initiation.

For fracture mechanics SCC tests, wedge-loaded double cantilever beam (DCB) specimens were machined from mill-annealed alloy 22 plates, 12.7 mm (heat A) and 25.4 mm (heat B) in thickness. The 12.7-mm plate was used for specimens with a long

Table 1 - *Chemical compositions of the materials used in this study (in weight percent)*

Alloy/Heat	Fe	Ni	Cr	Mo	W	Co	Mn	Si	C	Others
316L SS	Bal.	10.04	16.35	2.07	—	—	1.58	0.49	0.014	Cu:0.27 N:0.06
825	30.41	41.06	22.09	3.21	—	—	0.35	0.19	0.016	Cu:1.79 Ti:0.82
22/A	4.01	Bal.	21.79	13.42	2.97	1.62	0.20	0.024	0.003	P:0.008 V:0.13
22/B	5.17	Bal.	21.57	13.39	2.90	0.37	0.26	0.023	0.003	P:0.011 V:0.16

transverse-longitudinal direction (T-L) orientation where the crack plane is perpendicular to the width direction (T direction) of the rolled plate and the crack propagation is in the longitudinal rolling direction (L direction). The 25.4-mm plate was used for the S-L orientation specimens where the fracture plane is perpendicular to the short transverse direction (S direction) and the crack propagation is also in the L direction. Type 316L SS DCB specimens with a T-L orientation were machined from the 12.7-mm thick plate. These specimen orientation designations are listed in ASTM Test Method for Plain-Strain Fracture Toughness of Metallic Materials (E 399-90). The DCB specimen dimensions are 25.4 × 9.5 × 101.6 mm in accordance with NACE Test Method for Laboratory Testing of Metals for Resistance to Sulfide Stress Cracking in H_2S Environments (TM0177-90 Method D). In addition, modified wedge-opening-loaded (WOL) specimens [6] with a T-L orientation were also machined from the 12.7-mm thick type 316L SS plate. The WOL specimens have dimensions of 61.0 x 12.7 x 63.5 mm, and a specimen width/thickness ratio of 4.

Slow Strain Rate Testing

The SSRTs were conducted in electrochemical cells made of glass and polytetrafluoroethylene, and equipped with a fritted gas bubbler, platinum counter electrode, temperature probe, and a water cooled Luggin probe with a saturated calomel electrode (SCE). A series of SSRTs was performed in concentrated chloride solutions, prepared with salts of different cations [magnesium (Mg^{2+}), lithium (Li^+), and sodium (Na^+)] but without the presence of additional anions. The solutions in this set of tests were fully deaerated with nitrogen. Tests were also conducted in concentrated sodium chloride (NaCl) solutions with the addition of sodium thiosulfate ($Na_2S_2O_3$) or acidified to pH 4.0. An extension rate of 1.27×10^{-5} mm/s, which represents an initial strain rate of 1.0×10^{-6} s^{-1} for the smooth tensile specimens, was used in the first series of SSRT. The extension rate was reduced to 4.6×10^{-6} mm/s and 2.8×10^{-6} mm/s, respectively, in several tests to increase the sensitivity of the slow strain rate technique. After failure, the fracture and side surfaces of all specimens tested were examined with an optical microscope. Selected specimens were further examined in the scanning electron

microscope (SEM). Additional experimental details were presented elsewhere [5].

Fracture Mechanics Testing

The SCC tests using DCB specimens were conducted according to NACE TM0177-90 Method D DCB Test. The initial stress intensity, K_I, for the side grooved DCB specimen can be expressed as follows [7]:

$$K_I = \frac{P\,a\,(2\sqrt{3} + 2.38\,h/a)\,(b/b_n)^{1/\sqrt{3}}}{b\,h^{3/2}} \quad (1)$$

where P is the wedge load, a is the crack length, h is the specimen arm height (or half of the specimen height), b is the specimen thickness, and b_n is the net thickness of the specimen at the side grooves. The DCB specimens were fatigue-precracked under load control at 20 Hz, with a load ratio of 0.10, and a maximum stress intensity of 19.6 MPa·m$^{1/2}$ for alloy 22 and 17.6 MPa·m$^{1/2}$ for type 316L SS. The initial crack length for all specimens was approximately 32.8 mm. Double-tapered wedges were used to load the specimens to the selected stress intensities. An initial stress intensity of 25.0 MPa·m$^{1/2}$ was selected for type 316L SS specimens. Alloy 22 specimens were tested using a stress intensity of 32.7 MPa·m$^{1/2}$. The selection of these initial conditions was based on calculations of the DCB arm bending stress and K_I, which is close to the highest stress intensity that can be attained without deforming the arms of the DCB specimens.

The SCC susceptibility of both type 316L SS and alloy 22 was evaluated in 0.9 molal Cl^- (5% NaCl) solution, acidified to pH 2.7 by the addition of HCl, at 90°C and in 9.1 and 14.0 molal Cl^- (30 and 40% $MgCl_2$) solutions at 110°C under open-circuit conditions. In the tests in 0.9 molal NaCl solution, high-purity N_2 gas was bubbled into the solution to remove the dissolved oxygen. In addition, a series of SCC propagation tests of type 316L SS were conducted in 9.1 molal Cl^- (30% $MgCl_2$) solutions at 110°C under potentiostatic conditions to measure crack growth rates as a function of potential. The specimens were periodically removed from the test cells and inspected with an optical microscope at low magnification. SEM photographs were used to document the starting condition of the specimens and changes in surface features and/or signs of crack growth along the grooves. At the end of each test, the wedge was removed by loading the specimen in a servo-hydraulic load frame. The final wedge load was also determined. The stress at which the crack is arrested, expressed in terms of a threshold stress intensity, K_{ISCC}, can then be calculated. Specimens were then heat-tinted in air at 371°C for 2.5 h inside a furnace and broken open to reveal the fracture surfaces, which were examined with the SEM to determine the final crack length.

Precracking of the type 316L SS WOL specimens was made in accordance with ASTM E 399-90. The initial crack length was about 16.5 mm. The initial stress intensities, ranging from 21.8 to 54.5 MPa·m$^{1/2}$, were achieved through wedge loading by engaging a pair of tapered wedges with the adjustment of two pin spacers. SCC susceptibility was evaluated in both 0.028 molal Cl^- (0.165% NaCl) and 9.1 molal Cl^- solutions (27.8% LiCl) at 95°C under both open-circuit and potentiostatic conditions.

Evidence of SCC and final crack length was determined by inspecting the specimens either along the side grooves or on the fracture surfaces.

Results

Slow Strain Rate Testing

Type 316L Stainless Steel - Fig. 1 summarizes the SSRT results obtained using smooth tensile specimens of type 316L SS in various concentrated chloride solutions of different cations. Pit initiation potential (E_p) and repassivation potential (E_{rp}) are plotted in Fig. 1 as a function of chloride concentration using data obtained in cyclic potentiodynamic polarization (CPP) tests with a scan rate of 0.167 mV/s [*8*]. As previously reported [5], an initial set of tests were conducted at 120°C in 14.0 molal Cl^- (40% $MgCl_2$) solution at the corrosion potential (approximately -300 mV_{SCE}) and at a slightly anodic potential (-280 mV_{SCE}). SCC was observed under both conditions, in which elongation values of 7.4 and 4.6% were obtained, respectively. Similar results were obtained at a lower temperature (110°C) in 9.1 molal Cl^- (30% $MgCl_2$) solution. A decrease in the elongation to failure from 49.4 to 15.2% was observed by increasing the potential to slightly anodic values with respect to the open-circuit potential. SCC was also observed under open-circuit conditions (-370 to -300 mV_{SCE}) at temperatures ranging from 120 to 95°C in concentrated LiCl (≥7.2 molal) solutions acidified to pH 4.0 by the addition of HCl. The effect of potential on the elongation to failure ratio (the elongation to failure in the solution to that in an inert environment) in 9.1 molal LiCl solutions at 95°C is shown in Fig. 2. An increase in the applied potential promoted cracking as indicated by the decrease in the elongation to failure ratio. Under such conditions, SCC only occurs at potentials above E_{rp}. Fractographic examination revealed that, besides the "cleavage-like" features typical of the transgranular cracking of austenitic SSs in boiling chloride solutions [*9*], intergranular cracking occurred over a large proportion of the fracture surface.

Several tests were conducted at 95°C in concentrated NaCl and LiCl solutions (6.2 molal Cl^-) in which the pH was adjusted to 2.6 by the addition of HCl. Since SCC was not observed in these tests, additional tests were conducted at a strain rate of 2.2×10^{-7} s^{-1} to increase the sensitivity of the technique. No SCC was observed in this series of tests in which open-circuit and anodic conditions were investigated under both potentiostatic and galvanostatic control. Smooth tensile specimens of type 316L SS were also tested in concentrated NaCl solutions (5.8 and 6.2 molal Cl^-) containing 0.01 M $Na_2S_2O_3$ with the pH adjusted to 4.0 by the addition of HCl. SCC of mill-annealed type 316L SS was observed at the open-circuit potential (-390 mV_{SCE}) and also at low-anodic potentials (-420 to -390 mV_{SCE}). The elongation to failure in these two tests, 12.2 and 18.0%, was very low, indicating a significant susceptibility to SCC in this environment. For comparison, a solution-annealed and quenched specimen of type 316L SS was tested at the open-circuit potential in the same solution. The elongation to failure, 11.4%, was similar to that for the mill-annealed specimen.

Alloy 825 - The SSRT results for alloy 825 in concentrated chloride solutions are

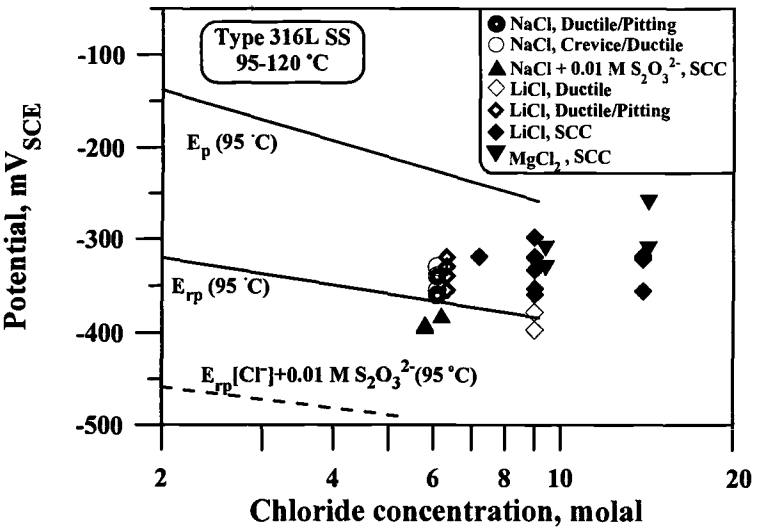


Figure 1 - *Slow strain rate test results of type 316L SS*

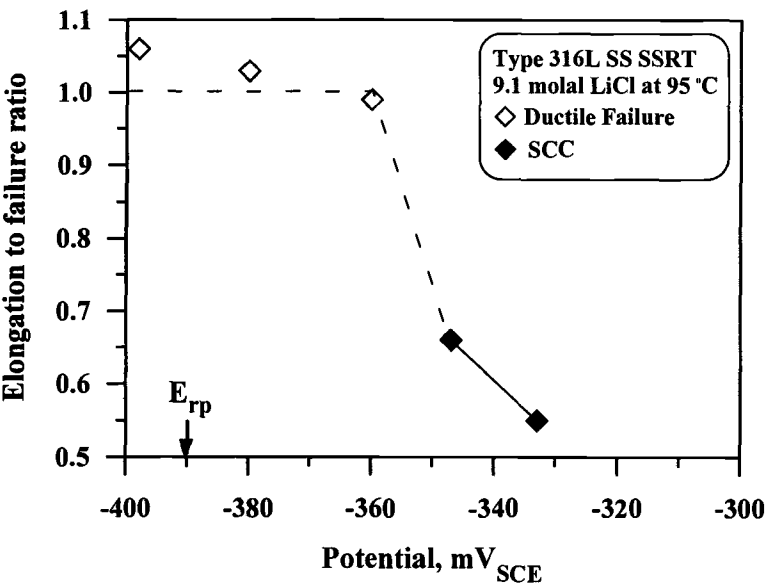


Figure 2 - *Effect of potential on elongation of failure ratio of type 316L SS*

presented in Fig. 3. As in the case of type 316L SS, E_p and E_{rp} for alloy 825 [*8*] are plotted in the same figure. SCC was observed, both at an anodic potential as well as at the E_{corr}, only in 14.0 molal Cl^- (40% $MgCl_2$) solution at 120°C. The elongation to failure was 44% at the E_{corr} (approximately -270 mV_{SCE}) and decreased to 36% at a slightly anodic potential (-260 mV_{SCE}) whereas the elongation to failure corresponding to a purely ductile fracture was approximately 53%. No SCC was observed in 9.1 molal LiCl solutions at 110°C or 5.8 molal NaCl with the addition of 0.01 M $Na_2S_2O_3$ at 95°C under both open-circuit and anodic-applied potentials. In these tests, ductile failure promoted by coalescence of microvoids and signs of pitting corrosion were detected on the fracture surface. Failure by SCC did not occur in either of these solutions in additional tests in which a circumferentially notched specimens were used and the strain rate was decreased five times with respect to that applied for smooth tensile specimens. However, the addition of a crevice on the gage length of the smooth specimens results in an increase in susceptibility to SCC for the as-received material as shown in Fig. 4. In contrast to the results presented in Fig. 3 for smooth tensile specimens without a crevice, significant SCC of creviced specimens was observed in 9.1 molal LiCl at 110°C and 6.2 molal NaCl with the addition of 0.01 M $Na_2S_2O_3$ at 95°C. The occurrence of SCC was confirmed by fractographic examination of the failed smooth tensile specimens using the SEM. Several thumbnail-shaped areas exhibiting transgranular quasi-cleavage features were observed along the periphery of the fracture surface.

Fracture Mechanics Testing

Type 316L Stainless Steel - The SCC susceptibility of type 316L SS was investigated in chloride solutions using the test conditions shown in Table 2. No evidence of SCC propagation was observed in a DCB specimen in deaerated, acidified (pH 2.7) 0.9 molal NaCl solution at 90°C over a cumulative test time of 386 days. It is apparent that the test conditions, including chloride concentration, temperature, and initial stress intensity, were not sufficiently severe for SCC to occur. In contrast, significant crack growth was observed in a type 316L SS specimen after a 5.6-day exposure under open-circuit conditions in 14.0 molal Cl^- (40% $MgCl_2$) solutions at 110°C. After three weeks, many transverse cracks almost perpendicular to the direction of the fatigue precrack were observed on the arms of the DCB specimen. To reduce the occurrence of these transverse cracks, a lower initial stress intensity (21.8 $MPa \cdot m^{1/2}$) and a less concentrated solution (9.1 molal Cl^- or 30% $MgCl_2$) were selected for the following tests. In spite of the lower stress intensity and reduced chloride concentration, transverse cracks were again observed on the arms of the DCB specimen when tested under open-circuit conditions ($E_{corr} \approx$ -330 to -320 mV_{SCE}). Nevertheless, the effect of transverse cracks on the final equilibrium wedge load was evaluated to be negligible by comparing compliance measurements performed before and after exposure. From a final wedge load measurement of 890 N, K_{ISCC} = 13.1 $MPa \cdot m^{1/2}$ was calculated for type 316L SS in 9.1 molal Cl^- (30% $MgCl_2$) at 110°C using Equation (1). Although SCC was clearly identified, the fracture surface does not exhibit the quasi-cleavage features typical of transgranular SCC of austenitic SS in hot concentrated chloride solutions nor the

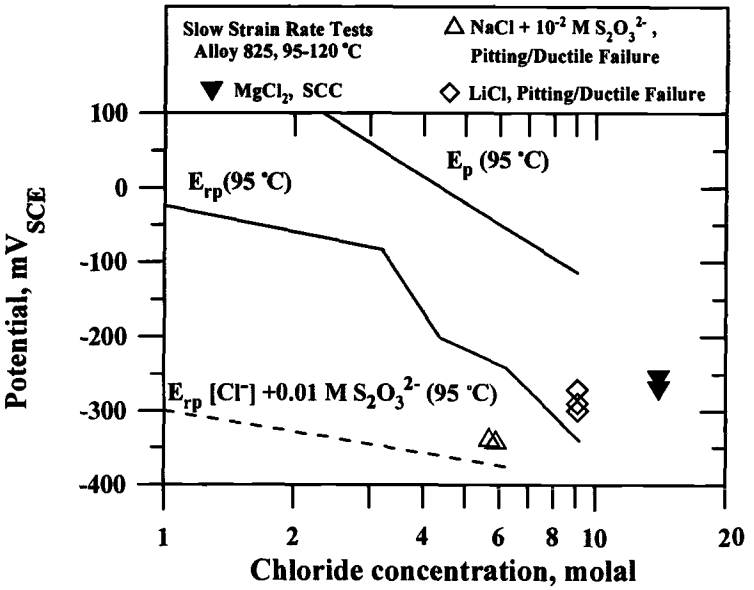


Figure 3 - *Slow strain rate test results of alloy 825*

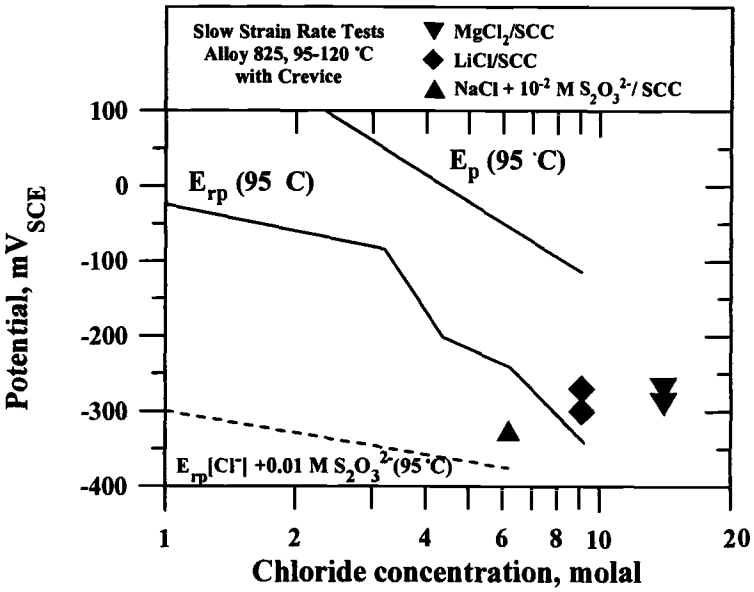


Figure 4 - *Slow strain rate test results of alloy 825 with crevice*

Table 2 - *Fracture mechanics SCC test results of type 316L SS and alloy 22*

Specimen ID (Orientation)	Initial K_I ($MPa \cdot m^{1/2}$)	Test Solution	Potential (mV_{SCE})	Result (Crack Growth Rate)
316L-DCB1(T-L)	25.0	0.9 molal Cl^- (5% NaCl), pH 2.7, 90°C	-340 to -320 (O.C.)	No SCC
316L-DCB2(T-L)	25.0	14.0 molal Cl^- (40% $MgCl_2$), 110°C	-320 to -300 (O.C.)	SCC - Extensive Transverse Cracks
316L-DCB6(T-L)	21.8	9.1 molal Cl^- (30% $MgCl_2$), 110°C	-330 to -320 (O.C.)	SCC (1.0×10^{-8} m/s)
316L-DCB5(T-L)	21.8	9.1 molal Cl^- (30% $MgCl_2$), 110°C	-340	SCC (2.5×10^{-9} m/s)
316L-DCB7(T-L)	21.8	9.1 molal Cl^- (30% $MgCl_2$), 110°C	-360	SCC (2.0×10^{-9} m/s)
316L-DCB8(T-L)	21.8	9.1 molal Cl^- (30% $MgCl_2$), 110°C	-380	SCC (7.3×10^{-10} m/s)
316L-WOL5(T-L)	21.8	9.1 molal Cl^- (27.8% LiCl), 95°C	-405	No SCC
316L-WOL6(T-L)	21.8	9.1 molal Cl^- (27.8% LiCl), 95°C	-345 to -335 (O.C.)	SCC (2.7×10^{-9} m/s)
316L-WOL7(T-L)	32.7	9.1 molal Cl^- (27.8% LiCl), 95°C	-405	No SCC
316L-WOL8(T-L)	32.7	9.1 molal Cl^- (27.8% LiCl), 95°C	-350 to -340 (O.C.)	SCC (2.9×10^{-9} m/s)
22-DCB1(T-L)	32.7	0.9 molal Cl^- (5% NaCl), pH 2.7, 90°C	-330 to -310 (O.C.)	No SCC
22-DCB2(T-L)	32.7	14.0 molal Cl^- (40% $MgCl_2$), 110°C	-280 to -260 (O.C.)	No SCC - Grain Boundary Attack
22-DCB7(S-L)	32.7	14.0 molal Cl^- (40% $MgCl_2$), 110°C	-270 to -250 (O.C.)	No SCC - Minor Secondary Cracks

O.C. - Open-Circuit

intergranular cracking observed in SSRT. An average crack growth rate of 1.0×10^{-8} m/s was calculated by dividing the final crack length by the total test time. Table 2 provides initial stress intensity values because the stress intensity decreases with time as a result of total relaxation due to crack growth.

For SCC tests using WOL specimens, a set of tests was conducted in 0.028 molal Cl^- (0.165% NaCl) solution at 95°C under both open-circuit and potentiostatic conditions with stress intensities of 32.7 and 54.4 $MPa \cdot m^{1/2}$. No SCC was detected in these tests along the side grooves of the type 316L SS specimens after an exposure period of about four months. In addition, no evidence of SCC was observed in the tests in 9.1 molal LiCl solution at 95°C under an applied potential of -405 mV_{SCE}, which is below E_{rp}, at applied stress intensities of 21.8 and 32.7 $MPa \cdot m^{1/2}$. In contrast, SCC propagation was observed at $K_I = 21.8$ and 32.7 $MPa \cdot m^{1/2}$ under open-circuit conditions ($E_{corr} \approx -350$ to -335 mV_{SCE}). Average crack growth rates were measured to be 2.7×10^{-9} and 2.9×10^{-9} m/s,

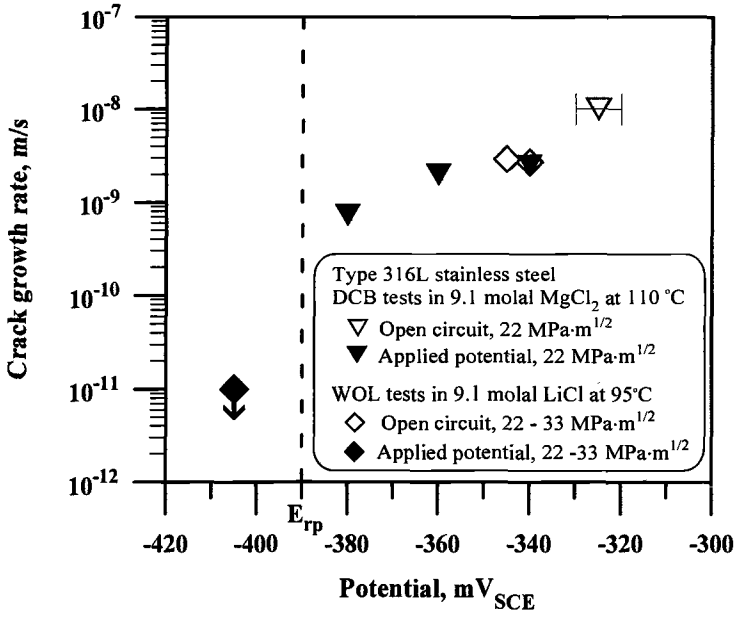


Figure 5 - *Effect of potential on crack growth rate of type 316L SS*

respectively. The experimental conditions and results of the tests in 9.1 molal LiCl are summarized in Table 2.

One of the main objectives of the SCC tests conducted with fracture mechanics specimens was to determine the effect of potential on the SCC propagation rate. The effect of applied potential on the SCC propagation of type 316L SS is also summarized in Table 2. From the crack growth rate versus potential curve as shown in Fig. 5, it is apparent that the SCC propagation decreased as the potential was decreased. No SCC propagation was observed below E_{rp}, which is approximately -390 mV_{SCE} for type 316L SS in 9.1 molal Cl^- (30% $MgCl_2$) [*8*]. With the current technique using an optical microscope, the lowest crack propagation rate that can be detected in one-month inspection periods is approximately 1×10^{-11} m/s.

Alloy 22 - The SCC susceptibility of alloy 22 was also investigated in chloride solutions using the test conditions shown in Table 2. Similar to type 316L SS, no evidence of SCC propagation was observed for alloy 22 in 0.9 molal NaCl solution at 90°C over a cumulative test time of 386 days. In addition, no crack growth was observed after the same period for both T-L and S-L specimens tested in 14.0 molal Cl^- (40% $MgCl_2$) solutions at 110°C under open-circuit conditions ($E_{corr} \approx -280$ to -250 mV_{SCE}). Periodic examination of the specimen surfaces using the SEM revealed that grain boundary attack occurred in the T-L specimen after testing for 21 weeks. Minor

secondary cracking near the main precrack, perhaps indicative of SCC initiation, was observed in the S-L specimen tested for ten weeks. However, after continued exposure, these secondary cracks observed near the tip of the fatigue precrack did not propagate. Grain boundary attack may be attributed to the lower corrosion resistance along the grain boundaries and the formation of the secondary cracks may be related to near-surface defects in the test specimen. Regardless of the presence of these minor cracks, alloy 22 appears to be extremely resistant to SCC in concentrated $MgCl_2$ solutions.

Discussion

Slow Strain Rate Testing

Type 316L Stainless Steel - The results plotted in Fig. 1 clearly indicate that mill-annealed type 316L SS failed by SCC in SSRTs when exposed to $MgCl_2$ and LiCl solutions at chloride concentrations equal to or greater than 7.2 molal and temperatures above 95°C. Although SCC was observed under open-circuit conditions, it was significantly enhanced at slightly anodic potentials. The potential range for SCC is bounded by the E_p and E_{rp} measured in CPP tests. The important effects of chloride concentration, temperature, and potential on the SCC susceptibility are reflected in the elongation to failure values. A significant decrease in these values is observed above 7.2 molal of chloride concentration and temperatures above 95°C. As shown in Fig. 2, at potentials just above the E_{rp} the elongation to failure ratios decrease significantly. In contrast, even at high Cl^- concentrations, SCC was not observed when the potential of the specimen was maintained below the E_{rp}.

On the contrary, as also shown in Fig. 1, SCC did not occur at 95°C in plain NaCl solutions in which the chloride concentration was 6.2 molal. This is close to the maximum concentration attainable in NaCl due to solubility limitations. The same results were obtained in LiCl solutions of equivalent chloride concentration. These results indicate that under the experimental conditions used in these tests, particularly in terms of temperature and strain rate, no SCC can be promoted regardless of the cation at chloride concentrations equal to or lower than 6.2 molal, even at acidic pHs. However, the addition of $Na_2S_2O_3$ to the NaCl solutions promoted SCC at slightly lower chloride concentrations (5.8 and 6.2 molal) both at the open-circuit and anodic-applied potentials, as shown in Fig. 1. SCC occurred in the presence of thiosulfate at potentials lower than the corrosion potential in plain chloride solutions and, therefore, below the extrapolation of the E_{rp} line plotted in Fig. 1. This effect of $Na_2S_2O_3$ is due to the fact that E_{rp} decreases significantly by the addition of $Na_2S_2O_3$ with respect to that in plain chloride solutions. Indeed, Nakayama et al. [*10*] have observed that the E_{rcrev} of type 304 SS decreased by approximately 400 mV when 10 ppm $S_2O_3^{2-}$ was added to a 100 ppm Cl^- solution.

Alloy 825 - The results shown in Fig. 3 clearly indicate that mill-annealed alloy 825 only failed by SCC in SSRTs when exposed to $MgCl_2$ solutions at a chloride concentration of 14.0 molal and a temperature of 120°C. However, SCC did not occur in LiCl solutions in which the chloride concentration was equal to 9.1 molal at 110°C.

These results indicate that under the experimental conditions used in these tests, particularly in terms of temperature and strain rate, SCC cannot be promoted regardless of the cation at chloride concentrations less than or equal to 9.1 molal, even at acidic pHs. Instead of SCC, the dominant failure mode was ductile failure, accompanied by pitting corrosion. No SCC was observed on alloy 825 with the addition of $Na_2S_2O_3$ to a 5.8 molal NaCl solution or under more severe conditions prompted by the use of a notched specimen at a lower extension rate over a very extended period. Tsujikawa et al. [*11*] reported that alloy 825 did not exhibit SCC in solution 4.3 molal Cl^- (20% NaCl) containing 0.001 to 0.1 M $Na_2S_2O_3$ (pH 4.0) at 80 °C by conducting slow strain rate tests and constant load tests at applied stresses above the yield strength of the alloy. As indicated in Fig. 3, pitting was observed in the $Na_2S_2O_3$-containing solution.

The presence of a crevice on the smooth tensile specimen resulted in a substantial increase in the SCC susceptibility of alloy 825. As shown in Fig. 4, significant cracking was observed in SSRTs in 6.2 molal NaCl with the addition of 0.01 M $Na_2S_2O_3$ under an anodic applied potential and in 9.1 molal LiCl under both open-circuit and an anodic-applied potential. Since the chloride concentration in these solutions is very high, it seems unlikely that the increase in SCC susceptibility is simply a result of an increase in the Cl^- concentration of the occluded region. Substantial decreases in pH in the creviced region may have also been detrimental. Nevertheless, the potentials at which the specimens were found to be susceptible to SCC are still bounded by the E_{rp} with the addition of 0.01 M $Na_2S_2O_3$, as shown in Fig. 4.

Fracture Mechanics Testing

Although it has been argued that fracture mechanics specimens such as DCB specimens provide a preexisting flaw to facilitate the initiation of SCC [*12*], the main advantage over other specimen configurations is the possibility of measuring crack growth rates under well defined stress intensities. Several authors have reported the effect of stress intensity on crack growth rate of austenitic SS under open-circuit conditions in chloride containing solutions. Speidel [*13*] reported crack growth rate versus K_I curves for austenitic type 304L SS exposed to 15.2 molal Cl (42% $MgCl_2$) solution at 130 °C and to 4.8 molal Cl^- (22% NaCl) solution at 105 °C. The crack growth rate at the plateau was found to be almost one order of magnitude higher in $MgCl_2$ (5×10^{-8} m/s) than that in NaCl (5×10^{-9} m/s). In addition, the threshold stress intensity, K_{ISCC}, was significantly lower in the higher temperature $MgCl_2$ solution. Eremias and Marichev [*14*] reported a K_{ISCC} value of 14 MPa·$m^{1/2}$ for Fe-18Cr-10Ni-0.5Ti SS in a 16.8 molal Cl^- (44.5% $MgCl_2$) solution at 115 °C, whereas 10 MPa·$m^{1/2}$ was measured by Lefakis and Rostoker [*15*] for type 304 SS in boiling $MgCl_2$. The K_{ISCC} (13.1 MPa·$m^{1/2}$) and crack growth rate (1.0×10^{-8} m/s) obtained in this work for type 316L SS under open-circuit conditions in a 9.1 molal Cl^- (30% $MgCl_2$) solution at 110°C are consistent with those reported in the literature.

The effect of temperature on the SCC propagation of type 316L SS has been previously studied in similar test environments. Russell and Tromans [*16*] tested type 316L SS T-double notch DCB specimens, cold worked 25 and 50%, in 17.0 molal Cl^-(44.7% $MgCl_2$) solutions at temperatures ranging from 116 to 154°C and initial stress

intensities ranging from 12 to 100 $MPa \cdot m^{1/2}$. At 116°C, the SCC propagation rates were 6×10^{-8} m/s for specimens with K_I greater than 20 $MPa \cdot m^{1/2}$ at potentials more noble than −280 mV_{SCE}. The rate increased to almost 5×10^{-7} m/s at 154°C. An apparent activation energy of approximately 65 kJ/mol was reported by plotting crack growth rates as a function of the reciprocal of temperature [*16*]. A similar temperature effect was observed in the present study. The average crack growth rates measured at 110 and 95°C, respectively, using two different fracture mechanics specimens were 1.0×10^{-8} m/s (DCB specimen) and 2.8×10^{-9} m/s (WOL specimen). An apparent activation energy of approximately 98 kJ/mol can be estimated from these results higher than that reported for cold-worked type 316L SSs [*16*]. Since the average crack growth rates were calculated by dividing the final crack length by the total test time, the rates may be underestimated due to the inclusion of the crack initiation time, particularly at long total test times. Multiple rate measurements through short exposure times were adopted in the tests using DCB specimens, whereas, the rates for the WOL tests were obtained over a cumulative test time of about four months. This may result in an underestimation of crack growth rates in the WOL tests leading to a high apparent activation energy value. Additional data are needed to attain a better estimate of the activation energy.

The effect of potential on SCC of type 316L SS was also reported by Russell and Tromans [*16*]. No SCC was observed on the specimens tested with 30 $MPa \cdot m^{1/2} < K_I < 35$ $MPa \cdot m^{1/2}$ at 154°C when the potential was reduced below −350 mV_{SCE}. Additionally, work performed by Silcock [*17*] using type 316L SS specimens in boiling 15.2 molal Cl^- (42% $MgCl_2$) solutions at 154°C shows that the SCC propagation rate decreased as the potential was decreased. The repassivation potential for type 316L SS in 9.1 molal Cl^- (30% $MgCl_2$) at 95°C was measured to be approximately −390 mV_{SCE} [*8*]. The SCC propagation rates plotted in Fig. 5 clearly indicate that at potentials greater than the repassivation potential, the crack growth rate increases as the potential increases. In addition, SCC is not initiated at potentials below the repassivation potential. Our observations on the effect of potential on the SCC propagation rate agree with the results of Russell and Tromans [*16*] and Silcock [*17*].

Final Remarks

The effects of waste package fabrication processes (i.e., welding and heat treatments) on corrosion and SCC of candidate container materials still remain as major concerns. Residual stresses from waste package fabrication or applied stresses resulting from seismic events combined with the necessary electrochemical conditions may be sufficient to cause SCC. Residual stress measurements conducted after waste package mock up fabrication have shown that high residual stresses could be present in the vicinity of the welds [*18*]. While fabrication welds can be annealed, it may not be practical to adequately anneal the closure welds without heating the spent nuclear fuel inside the waste packages to temperatures above 350°C. Short-term tests conducted in this study as well as those reported by Speidel [*13*] suggest that high Ni alloys are not susceptible to SCC even in concentrated chloride solutions at temperatures up to the boiling point of water and high stress intensities. However, the long-term initiation and propagation of SCC for high Ni alloys in chloride solutions has not been adequately investigated. High residual stresses

from fabrication processes suggest that the mechanical component necessary for SCC will be present in every waste package placed in the repository. Cragnolino et al. [5] observed severe SCC adjacent to spot welds on the otherwise unstressed legs of U-bend type 316L SS specimens exposed to chloride solutions.

In the present investigation, critical potentials for SCC of both base type 316L SS and alloy 825 were determined to be bounded by the repassivation potentials for pitting corrosion. Thus, the repassivation potential can be used as a bounding parameter for the prediction of long-term SCC behavior. This critical potential approach can also be applied to evaluate the SCC performance of the weld container materials.

Conclusions

1. Results of this investigation using both slow strain rate and fracture mechanics type specimens showed that the repassivation potential for pitting corrosion constitutes a lower limit for the critical potential for SCC. Although SCC occurred in different ranges of chloride concentrations depending on the material, no SCC was observed at potentials below the repassivation potential.

2. Using the slow strain rate testing technique, a minimum chloride concentration of 7.2 molal was required to promote SCC of type 316L SS in the absence of thiosulfate. In the presence of 0.01 M thiosulfate, SCC was observed in solutions containing 5.8 molal Cl^-. In contrast, SCC of alloy 825 was not observed in chloride solutions over a wide range of chloride concentrations, except in 14.0 molal Cl^- (40% $MgCl_2$) solution at 120°C. The presence of an artificial crevice promoted the SCC susceptibility of alloy 825 at lower chloride concentrations.

3. The crack propagation rate on type 316L SS fracture mechanics specimens was found to be strongly dependent on potential. A substantial decrease in the propagation rate was observed when the potential of the specimen was reduced approaching the repassivation potential. The K_{ISCC} and crack growth rate of type 316L SS tested in 9.1 molal Cl^- (30% $MgCl_2$) solution at 110°C under open circuit conditions were measured to be 13.1 $MPa \cdot m^{1/2}$ and 1.0×10^{-8} m/s, respectively. In contrast, precracked alloy 22 specimens do not exhibit crack growth when tested in concentrated $MgCl_2$ solutions at temperatures up to 110°C.

Acknowledgments

This paper was prepared to document the work performed by the Center for Nuclear Waste Regulatory Analyses (CNWRA) for the Nuclear Regulatory Commission (NRC) under contract No. NRC-02-97-009. This paper is an independent product of the CNWRA and does not necessarily reflect the views or the regulatory position of the NRC.

References

[1] Cragnolino, G.A., and Sridhar, N., "A Review of Stress Corrosion Cracking

of High-Level Nuclear Waste Container Materials - I," CNWRA 92-021, Center for Nuclear Waste Regulatory Analyses, San Antonio, TX, 1992.

[2] Hines, J.G., and Hoar, T.P., "Stress Corrosion Cracking of Austenitic Chromium-Nickel Stainless Steels at Ambient Temperature," *Journal of Applied Chemistry*, Vol. 8, 1958, pp. 764-776.

[3] Cragnolino, G.A., "The Significance of a Critical Potential in the Intergranular Stress Corrosion Cracking of Stainless Steel Piping in BWR Environments," *Predictive Capabilities in Environmentally Assisted Cracking, ASME PVP-99*, R. Rungta, Ed., American Society of Mechanical Engineers, New York, NY, 1985, pp. 293-318.

[4] Tsujikawa, S., Shinohara, T., and Hisamatsu, Y., "The Role of Crevices in Comparison to Pits in Initiating Stress Corrosion Cracks of Type 310 Stainless Steel in Different Concentrations of $MgCl_2$ Solutions at 80 °C," *Corrosion Cracking*, V.S. Goel, Ed., American Society for Metals (ASM), Metals Park, OH, 1985, pp. 35-42.

[5] Cragnolino, G.A., Dunn, D., and Sridhar, N., "Environmental Factors in the Stress Corrosion Cracking of Type 316L Stainless Steel and Alloy 825 in Chloride Solutions," *Corrosion*, Vol. 52, No. 3, 1996, pp. 194-203.

[6] Sedriks, A.J., *Stress Corrosion Cracking Test Methods*, National Association of Corrosion Engineers (NACE), Houston, TX, 1989, pp. 47-52.

[7] Heady, R.B., "Evaluation of Sulfide Corrosion Cracking Resistance in Low Alloy Steels," *Corrosion*, Vol. 33, No. 3, 1977, pp. 98-107.

[8] Dunn, D.S., Cragnolino, G.A., and Sridhar, N., "An Electrochemical Approach to Predicting Long-Term Localized Corrosion of Corrosion-Resistant High-Level Nuclear Waste Container Materials," *Corrosion*, Vol. 56, No. 1, 2000, pp.90-104.

[9] Scully, J.C., "Fractographic Aspects of Stress Corrosion Cracking," *Theory of Stress Corrosion Cracking in Alloys*, J.C. Scully, Ed., North Atlantic Treaty Organization, Brussels, Belgium, 1971, pp. 127-166.

[10] Nakayama, G., Wakamatsu, H., and Akashi, M., "Effects of Chloride, Bromide, and Thiosulfate ions on the Critical Conditions for Crevice Corrosion of Several Stainless Alloys as a Material for Geological Disposal Packages for Nuclear Waste," *Scientific Basis for Nuclear Waste Management XVI*, MRS Symposium Proceeding Vol. 294, C.G. Interrante, and R.T. Pabalan, Eds., Materials Research Society, Pittsburgh, PA, 1993, pp. 323-328.

[11] Tsujikawa, S., Miyasaka, A., Uedo, M., Ando, S., Shibata, T., Haruna, T.,

Katahira, M., Yamane, Y., Aoki, T., and Yamada, T., "Alternative for Evaluating Sour Gas Resistance of Low-Alloy Steels and Corrosion-Resistant Alloys," *Corrosion*, Vol. 49, 1993, pp. 409-419.

[12] Brown, B.F., "The Application of Fracture Mechanics to Stress-Corrosion Cracking," *Metallurgical Reviews*, Vol. 13, 1968, pp. 171-183.

[13] Speidel, M.O., "Stress Corrosion Cracking on Stainless Steels in NaCl Solutions," *Metallurgical Transactions*, Vol. 12A, 1981, pp. 779-789.

[14] Eremias, B., and Marichev, M.A., "Environmental Aspects of Stress Corrosion Crack Growth in Austenitic Stainless Steel," *Corrosion Science*, Vol. 28, 1979, pp. 1 003-1 018.

[15] Lefakis, H., and Rostoker, W., "Stress Corrosion Crack Growth Rates of Brass and Austenitic Stainless Steels at Low Stress Intensity Factors," *Corrosion*, Vol. 33, No. 5, 1977, pp. 178-181.

[16] Russell, A.J., and Tromans, D., "A Fracture Mechanics Study of Stress Corrosion Cracking of Type-316L Austenitic Steel," *Metallurgical Transactions*, Vol. 10A, 1979, pp. 1 229-1 238.

[17] Silcock, J.M., "Nucleation and Growth of Stress Corrosion Cracks in Austenitic Steels with Varying Ni and Mo Contents," *Corrosion*, Vol. 38, No. 3, 1982, pp. 144-156.

[18] "Waste Package Phase II Closure Methods Report," TRW BBA000000-01717-5705-00016, Revision 00, TRW Environmental Safety Systems, Inc., Las Vegas, NV, 1998.

Raúl B. Rebak[1]

Environmentally Assisted Cracking in the Chemical Process Industry. Stress Corrosion Cracking of Iron, Nickel, and Cobalt Based Alloys in Chloride and Wet HF Services

---

Reference: Rebak, R. B., **"Environmentally Assisted Cracking in the Chemical Process Industry: Stress Corrosion Cracking of Iron, Nickel, and Cobalt Based Alloys in Chloride and Wet HF Services,"** *Environmentally Assisted Cracking: Predictive Methods for Risk Assessment and Evaluation of Materials, Equipment, and Structures, ASTM STP 1401*, R. D. Kane, Ed., American Society for Testing and Materials, West Conshohocken, PA, 2000.

Abstract: Many different alloys are used in the fabrication equipment for the chemical process industry (CPI) and the most common of these alloys are iron base (stainless steels). During service, the primary cause of failure of engineering alloys is stress corrosion cracking (SCC). Although the occurrence of environmentally induced cracking might be prevented by reducing the level of tensile stresses on components, this approach is seldom practiced. In some cases, failure can be avoided through a proper alloy selection based on results from laboratory testing. The aim of this paper is to assess the predictive capabilities of laboratory testing for cases of SCC in the CPI. Instances of chloride cracking and wet hydrofluoric acid (HF) cracking in the field are analyzed based on results from laboratory testing.

Keywords: Stress corrosion cracking, stainless steel, nickel alloys, cobalt alloys, chloride cracking, wet HF cracking, U-bend specimens, temperature

Introduction

The Materials Technology Institute of the Chemical Process Industries (MTI) recently conducted a survey to determine the corrosion failure modes in the equipment of process industries [*1*]. The most common mode of failure (with an average incidence rate of 36%) was stress corrosion cracking, followed by general corrosion (26%) and localized attack,

[1] Senior Staff Corrosion Engineer, Haynes International Inc., 1020 West Park Ave., Kokomo, IN 46901.

Copyright© 2000 by ASTM International www.astm.org

such as pitting and intergranular corrosion (20%). Regarding material classification, the highest incidence rate of SCC was for stainless steels (61.4%) followed by steel (30.4%), copper alloys (4.3%), nickel alloys (2.8%), titanium (0.7%) and tantalum (0.3%) [*1*]. Regarding the causes of cracking, for steels the majority of the failures were attributed to caustic solutions, for stainless steels the majority of the failures were attributed to chlorides, and for nickel alloys the majority of the failures were attributed to hydrofluoric acid (HF) [*1*].

Stress corrosion cracking is a type of failure by which a normally ductile alloy develops cracks or suffers embrittlement when it is subjected to tensile stresses in the presence of an aggressive environment. That is, for stress corrosion cracking to occur, the existence of three factors is necessary simultaneously: (1) a susceptible microstructure, (2) a specific aggressive environment and (3) tensile stresses. If one of these factors is eliminated, SCC will not occur. The aggressive species and the susceptible alloy are different from application to application; however, the common denominator for all cases of SCC is the presence of tensile stresses. There are many ways by which tensile stresses might be applied to a piece of equipment that is in service. The most common tensile stresses are residual stresses introduced during fabrication of the equipment (e.g. welding and cold forming). Tensile stresses might also be generated by expansion due to temperature gradients or applied pressure and, to a lesser extent, due to constant loads such as supporting weight.

The occurrence of stress corrosion cracking in service may be predicted by testing in the laboratory or by testing in situ, that is, by introducing coupons into the actual service stream according to Standard Guide for Conducting Corrosion Coupon Tests in Field Applications (ASTM G 4). Testing in the laboratory can be carried out in the presence of aggressive species that simulate the service conditions or by using the actual chemical mixture that can be carried from the plant to the laboratory. Testing will be more representative when it is conducted in situ, since it is difficult to simulate in the laboratory the actual service conditions, such as start ups or shut downs, fluctuations in the temperature, the presence of different types of impurities at different times of service, etc.

The aim of this paper is to describe cases of SCC found in service and to discuss their occurrence based on knowledge acquired through laboratory testing.

Stress Corrosion Cracking Induced by Chlorides

Stress Cracking of an Auger

A cobalt alloy was selected in the fabrication of the flights or spiral vanes of an auger (screw conveyor) that was used to move salt (NaCl) in a mining/processing plant. The auger was 41 cm in diameter and was fabricated by welding a 6 mm thick vane plate to a central shaft. The shaft was fabricated using a Ni-Cr-Mo alloy. This auger moved 40 tons per hour of crystalline salt at 121°C. Two times a week, the auger was in contact with spilled water and steam when a salt dryer unit above the auger was washed. After five years of service, cracks were found in the cobalt alloy vane. Figure 1 shows the typical transgranular cracking found on the vanes of the cobalt alloy. The cracks progressed due

to residual fabrication stresses and were probably induced by the presence of chlorides under high temperature conditions.



Figure 1 - *Transgranular Chloride Cracking of a Cobalt Base Alloy. Mag. X200.*

Cobalt based alloys are resistant to wear, erosion and galling. For most aggressive applications, cobalt based alloys are not as resistant to corrosion as certain nickel alloys (e.g. Ni-Cr-Mo alloys). However, many applications such as valves, pumps, nozzles and screw conveyors require alloys that are resistant both to corrosion and wear. During the alloy selection process a decision has to be made if the environmental resistance factor is more important than the wear factor. A few cobalt based alloys, such as alloy R31233 (Table 1), were designed to provide moderate corrosion resistance while providing at the same time resistance to wear.

Table 1 - *Corrosion Resistant Cobalt Alloys*

Alloy	UNS Number	Co	Cr	Mo	Ni	Others
Co-Cr-Ni-Mo	R31233	54	26	5	9	3Fe, 2W, 0.08N

Stress Cracking of an Evaporator

It is a fact that up to 99% of hazardous waste is actually water; therefore, it is logical

to reduce the volume of the waste before sending it to disposal sites. Evaporators are generally used to eliminate the water of dilute solutions such as machining coolants, photographic solutions, plating rinses, ion exchange regenerates, etc. Evaporation is accomplished by heating the solution in a retort using electricity or natural gas. Evaporators are commonly designed using Type 304 SS for the cabinet and Type 316 SS (Table 2) for the evaporation retort. Even though most of the waste solutions are neutralized and the bulk chloride content is well below 100 ppm, the retorts, and even the external cabinets, are prone to chloride induced cracking. Failure analysis of stainless steel evaporators showed typical transgranular chloride cracking. In these evaporators the tensile stresses are fabrication stresses, such as residual stresses present along the weld seams, or thermal stresses. Cracking is generally observed at the liquid level interface where evaporation can produce the highest concentration of chlorides at near normal boiling temperatures and where a high availability of oxygen exists. Some cases of chloride induced cracking in evaporators can be avoided by upgrading the alloy to super austenitic stainless steels such as alloys N08367 or S32654 (Table 2) or to duplex stainless steels. However, the alloys that offer the highest resistance to chloride cracking are nickel alloys (Table 3).

Table 2 - *Chemical Composition of Stainless Steels*

Alloy	UNS Number	Fe	Cr	Ni	Mo	Other
AISI 304	S30400	Bal.	18-20	8-10.5	---	---
AISI 316L	S31603	Bal.	16-18	10-14	2-3	---
Alloy 20	N08020	Bal.	19-21	30-38	2-3	3-4Cu
6-Moly SS	N08367	Bal.	20-22	23.5-25.5	6-7	0.18-0.25N
7-Moly SS	S32654	Bal.	24-25	21-23	7-8	0.45-0.55N

Laboratory Testing

To correlate better the results from laboratory testing with failures in service, the tests in the laboratory should reproduce the conditions in service as closely as possible. The amount of chlorides in service is rarely known, especially under evaporative conditions. The way how tensile stresses are applied to the laboratory coupons is also important. It is common to use slow strain rate tests or notched and fatigue pre-cracked specimens; however, these types of specimens would not reproduce conditions in service. Constant deformation specimens such as U-bend produced according to Standard Practice for Making U-bend Stress-Corrosion Test Specimens (ASTM G 30) generally best reproduce the fabrication or residual tensile stresses in service. Regarding the testing environment, the susceptibility of engineering alloys to chloride cracking is primarily determined using the Standard Test Method for Evaluating Stress-Corrosion Cracking of Stainless Alloys with Different Nickel Content in Boiling Acidified Sodium Chloride Solution (ASTM G 123) or the Standard Practice for Evaluating Stress-Corrosion-Cracking Resistance of Metals and Alloys in a Boiling Magnesium Chloride Solution (ASTM G 36).

Table 3 - *Chemical Composition of Nickel Alloys*

Alloy	UNS Number	Ni	Cr	Mo	Fe	Other
825	N08825	Bal.	21	3	30	2.2Cu, 1Ti
400	N04400	Bal.	---	---	1.2	31.5Cu
C-276	N10276	Bal.	16	16	5	4W
Ni-Cr-Mo-W	N06022	Bal.	22	13	3	3W
Ni-Cr-Mo-Cu	N06200	Bal.	23	16	---	1.6Cu
Ni-Mo-Cr	N06242	Bal.	8	25		---
B-2	N10665	Bal.	---	28	---	---
Ni-Mo	N10675	Bal.	1.5	28.5	1.5	---

Table 4 - *Susceptibility of Iron, Nickel and Cobalt Alloys to Chloride Cracking*

Alloy	UNS Number	Number of U-bend specimens that cracked/Total Specimens, Time at which they cracked or test terminated
		30% $MgCl_2$ at 118°C
304 SS	S30400	2/3, 24 h
316L SS	S31603	2/5, 125 h; 4/5, 175 h; 5/5, 715 h
Alloy 20	N08020	0/4, 1008 h
		35% $MgCl_2$ at 126°C
316L SS	S31603	1/1, 72 h
Alloy 20	N08020	2/5, 336 h; 4/5, 672 h; 5/5, 840 h
6-Moly SS	N08367	1/1, 164 h
Co-Cr-Ni-Mo	R31233	2/2, 96 h
		45% $MgCl_2$ at 154°C
304 SS	S30400	1/1, 1 h
316L SS	S31603	1/3, 1 h; 3/3, 24 h
Alloy 20	N08020	2/5, 8 h; 4/6, 26 h; 5/5, 120 h
6-Moly SS	N08367	1/1, 24 h
7-Moly SS	S32654	1/1, 120 h
C-276	N10276	0/4, 1008 h
Ni-Cr-Mo-W	N06022	0/3, 1008 h
Ni-Cr-Mo-Cu	N06200	0/1, 1008 h
B-2	N10665	0/2, 1008 h

Table 4 shows results of U-bend testing in magnesium chloride solutions (ASTM G 36). As the chloride concentration and temperature increases, the resistance of the alloys to cracking decreases. For example, 100% of 316L SS specimens cracked within 24 h when exposed to a 45% $MgCl_2$ solution at 154°C; however, an exposure time of 715 h was necessary for the entire population of 316L SS specimens to crack in 30% $MgCl_2$ solution at 118°C. Table 4 also shows that the higher alloyed stainless steels such as N08367 and S32654 are more resistant to SCC than 316L SS. A cobalt alloy such as R31233 is more resistant than 316L SS to chloride induced cracking; however, it appears to be less resistant than the higher alloyed stainless steels such as alloys N08367 or

S32654. The alloys that offer the highest resistance to chloride induced cracking are Ni-Cr-Mo alloys such as alloy N06022 or N06200 (Table 3).

Stress Corrosion Cracking in Hydrofluoric Acid Environments

Failure During Commercial Production of HF

Hydrofluoric acid is produced by the reaction of fluorspar or calcium fluoride and concentrated sulfuric acid in externally heated horizontal kilns. The temperature of the kiln is approximately 150°C. These rotary kilns can be up to 3.5 m diameter and over 45 m long. The kilns are usually made of carbon steel and are internally lined with nickel based alloys. Reactor internals such as baffles, lifters and chutes are also made of nickel alloys. A lifter screw flange made of a Ni-Cr-Fe-Mo alloy (N06030) was in service inside one of these kilns for an unknown period of time and suffered thinning by general corrosion as well as stress corrosion cracking. Figure 2 shows the typical transgranular cracking that propagated in the Ni-Cr-Fe-Mo flange while in operation in a kiln. It is not clear which type of stresses promoted the cracking shown in Fig. 2, but they were probably operational stresses. In another part of the production line, a valve bellows connector made of a Ni-Cr-Mo alloy was in service in presence of hydrofluoric acid at 40°C for approximately eight months when failed due to transgranular stress corrosion cracking. The environment was supposed to be anhydrous hydrogen fluoride; however, a failure analysis showed that the bellows material was in contact with wet HF. The triple foils of the bellows were heavily cold worked and the transgranular cracks nucleated at the point of maximum operational tensile stress.

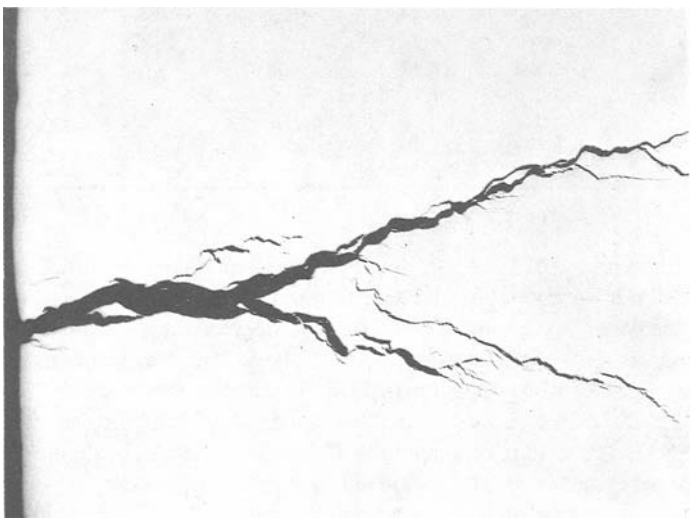


Figure 2 - *Transgranular HF Cracking of a Ni-Cr-Fe-Mo Alloy. Mag. X20*

Laboratory Testing in HF Environments

U-bend specimens (ASTM G 30) were used to determine the susceptibility of several nickel alloys to SCC in wet HF environments. Specimens were exposed to aqueous solutions containing 20% HF and to the corresponding vapor spaces for 240 h (10 days) at 66°C, 79°C and 93°C. The testing retorts were open to the atmosphere through a condenser; that is, the ingress of air was not restricted. The specimens were removed after 10 days and were metallographically sectioned. The average crack or preferential penetration rate was calculated by dividing the deepest crack or penetration length by the total testing time of 240 h (i.e. induction time was not considered). The detection limit for crack rate was 1.5×10^{-11} m/s. Table 5 shows the experimental results.

Table 5 - *SCC Laboratory Testing of Nickel Alloys in Wet HF Environments*

Alloy	U-bend Specimens in 20% HF, 240 h	Average General Corrosion Rate (Weight Loss), mpy (mm/year)	Average Crack or Preferential Penetration Rate, m/s	Observations
400	66°C, Liquid	6.5 (0.165)	$<1.5 \times 10^{-11}$	Shiny metallic. Shallow IGA.
	66°C, Vapor	255 (6.48)	1.6×10^{-9}	Black. Severe IGA, Fissures.
	79°C, Liquid	<0.1 (<0.003)	$<1.5 \times 10^{-11}$	Intense Cu color. 0.05 mm thick layer of Cu on surface.
	79°C, Vapor	267 (6.78)	1.5×10^{-10}	Dark gray. IGA.
	93°C, Liquid	<0.1 (<0.003)	$<1.5 \times 10^{-11}$	Cu color. Crystalline lumps of Cu on the surface.
	93°C, Vapor	150 (3.81)	$<1.5 \times 10^{-11}$	Ni plated appearance. Shallow IGA.
C-276	66°C, Liquid	116 (2.95)	$<1.5 \times 10^{-11}$	Ni plated appearance. Uniform corrosion.
	66°C, Vapor	42.6 (1.08)	$<1.5 \times 10^{-11}$	Light gray. Small corrosion pits. Green corrosion product ($NiCrF_5.7H_2O$).
	79°C, Liquid	239 (6.07)	1.2×10^{-10}	Dark gray. Uneven general corrosion especially in stressed areas. Crevice corrosion.
	79°C, Vapor	94 (2.39)	3.0×10^{-11}	Light gray. Uneven penetration. Small corrosion pits. Green corrosion product ($NiCrF_5.7H_2O$).
	93°C, Liquid	28.8 (0.732)	6.8×10^{-10}	Ni plated appearance. SCC, pitting and crevice corrosion. Cr Rich black deposits in creviced area. Compressive side attack.
	93°C, Vapor	31.4 (0.798)	2.4×10^{-10}	Ni plated appearance. SCC. Green corrosion products ($NiCrF_5.7H_2O$).

Table 5 Continued

N06200	66°C, Liquid	33.7 (0.856)	$<1.5 \times 10^{-11}$	Dark gray. Shallow sponge like surface appearance.
	66°C, Vapor	34 (0.864)	$<1.5 \times 10^{-11}$	Ni plated appearance. Uniform corrosion. Green corrosion products ($NiCrF_5.7H_2O$).
	79°C, Liquid	16.2 (0.411)	1.3×10^{-10}	Light Cu color. Small crevice corrosion. Thin band of forest like penetration.
	79°C, Vapor	14.3 (0.363)	5.9×10^{-11}	Bluish color with dotted areas of Cu color. Small crevice corrosion. Thin hair like penetration.
	93°C, Liquid	13.9 (0.353)	3.2×10^{-10}	SCC. In compressive side cracks parallel to surface.
	93°C, Vapor	14.8 (0.376)	$<1.5 \times 10^{-11}$	Ni plated appearance. Small crevice corrosion. <1 μm Cu granules on surface.
N06242	66°C, Liquid	71.6 (1.82)	$<1.5 \times 10^{-11}$	Light gray. Sponge-like surface (metal flaking). Crevice corrosion.
	66°C, Vapor	26.9 (0.683)	2.0×10^{-11}	Sponge-like appearance. Uneven corrosion in the stressed areas.
	79°C, Liquid	65.4 (1.66)	1.3×10^{-10}	Dark gray. Uneven sponge-like corrosion in stressed areas. Small crevice corrosion. Pitting.
	79°C, Vapor	19.8 (0.503)	3.5×10^{-11}	Bluish. Small crevice corrosion. SCC.
	93°C, Liquid	17.1 (0.434)	4.3×10^{-10}	Dark gray. SCC, pitting and crevice corrosion.
	93°C, Vapor	24.2 (0.615)	1.6×10^{-10}	Ni plated appearance. Shallow crevice and pitting corrosion.
N10675	66°C, Liquid	112 (2.84)	8.8×10^{-11}	Dark gray. Uneven sponge-like corrosion. Small crevice and pitting corrosion.
	66°C, Vapor	73.6 (1.87)	5.9×10^{-11}	Dark gray. Uneven sponge-like corrosion especially in the stressed area. Crevice corrosion.
	79°C, Liquid	393 (9.98)	7.3×10^{-11}	Dark gray. Uneven sponge-like corrosion especially in the stressed area. Crevice corrosion.
	79°C, Vapor	179 (4.55)	1.2×10^{-10}	Dark gray. Uneven sponge-like corrosion especially in the stressed area. Crevice corrosion.
	93°C, Liquid	103 (2.62)	6.5×10^{-10}	Dark gray. Fissures, crevice and pitting corrosion.
	93°C, Vapor	94.2 (2.39)	2.5×10^{-10}	Ni plated appearance. Fissures, crevice and pitting corrosion.

IGA = Intergranular attack.

Figure 3 shows the influence of the temperature on the corrosion behavior of stressed nickel alloy samples in the vapor phase of a 20% HF aqueous solution. The intergranular attack and fissures in alloy 400 were the deepest at 66°C (Figs. 3 and 4), probably because at this temperature a higher amount of oxygen was available. As the temperature increased the depth of the preferential attack in alloy 400 decreased (Fig. 3). The behavior of C-276 alloy was just the opposite. The tested coupon suffered just general corrosion at 66°C; however, as the temperature increased, the depth of stress corrosion cracking increased. Figure 5 shows transgranular cracks that nucleated in C-276 alloy at 93°C. It appears that the SCC process (C-276) depended more on the temperature and the IGA process (alloy 400) depended more on the available level of oxygen. Under the tested conditions, alloy 400 did not suffer IGA or SCC in the liquid phase of aqueous 20% HF (Table 5). C-276 alloy was susceptible to SCC in the liquid phase and the behavior was similar to that of the vapor phase, that is, the process was thermally activated (Table 5 and Fig. 3). Under the same tested conditions, alloy N06200 was more resistant than C-276 alloy to localized corrosion (SCC, crevice and pitting) both in the liquid and vapor phases (Table 5). For alloys N06242 and N10675 (Table 3), the effect of the temperature on their susceptibility to localized attack is less defined (Table 5); probably because the attack was dominated by both availability of oxygen and temperature.

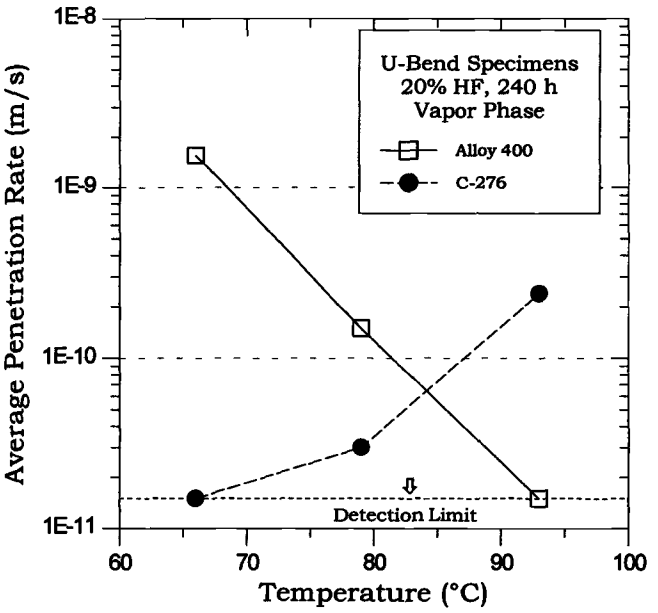


Figure 3 - *Effect of Temperature on the SCC/IGA behavior of Nickel Alloys*

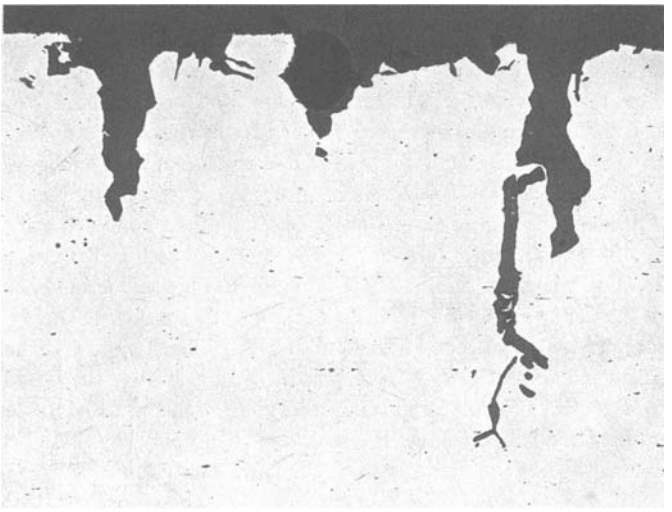


Figure 4 - *Fissuring of Alloy 400 in the vapor phase of 20% HF at 66°C. Mag. X100*

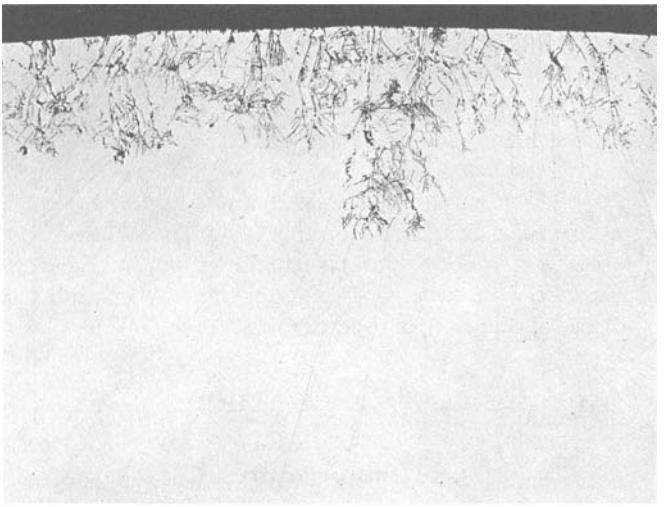


Figure 5 - *SCC of C-276 alloy in the vapor phase of 20% HF at 93°C. Mag. X100*

Factors Controlling Stress Corrosion Cracking

The factors that control SCC can be divided between metallurgical factors and environmental factors. Metallurgical factors are: (a) Alloy composition and (b) Metallurgical state or condition of the alloy, that is, for the same chemical composition, an alloy that is cold worked is generally more susceptible to SCC than an annealed alloy. Similarly, an alloy that is 'sensitized' could be more susceptible than an annealed alloy. Environmental factors are: (c) Electrochemical potential, (c) Electrolyte composition (aggressive species, pH, etc.), (d) Temperature, (e) Type and amount of applied load, etc.

At a given level of stress and in the presence of the same aggressive species, alloys of different composition have different susceptibility to SCC. For example, Table 4 shows that stainless steels containing higher amounts of Mo and nitrogen (Table 2) have higher resistance to chloride cracking. This effect has been previously reported in the literature [*2-3*]. For example, Andersen et al. stated that elements such as Ni, Cr, Mo and N are beneficial in the resistance of stainless steels against SCC [*2*]. It has been reported that the cobalt alloy R31233 is more resistant to chloride cracking than the stainless steel alloy N08020 [*4*]. The fact that alloy R31233 is less resistant to chloride cracking than Ni-Cr-Mo alloys such as C-276 alloy (Table 4) could be the consequence of the different amounts of beneficial alloying elements in the cobalt alloy but also an effect of the intrinsic metallurgical characteristic of cobalt alloys as compared to nickel alloys. Results from laboratory testing (Table 4) and evidences from failures in service (evaporator and screw conveyor) seem to indicate that a nickel alloy would offer the best performance in a high temperature, high chloride concentration environment.

The choices of material for hydrofluoric acid service are limited. The reactive metals (titanium, zirconium, niobium, tantalum), for example, and glass are readily attacked by hydrofluoric acid and the stainless steels generally exhibit high corrosion rates. Nickel based alloys seem to be the best choice for this type of application since they exhibit low to moderate corrosion rates in hydrofluoric acid. However, nickel alloys are prone to stress corrosion cracking or localized corrosion, such as pitting corrosion and intergranular attack. Cracking was found in HF service (lifter and bellows) and in laboratory testing (Table 5). Cracking of nickel alloys in HF environments has also been reported in the literature [*5-7*]. Table 5 shows that not all nickel alloys are equally susceptible to stress cracking in presence of HF and that environmental factors such as temperature or level of oxygen have a definitive influence on their cracking susceptibility. Failures in service of nickel alloys can be minimized by eliminating one or more of the factors that control SCC (e.g. the presence of cold work or residual stresses).

Predictive Capabilities of Laboratory Testing for CPI Applications

Since many of the environments used in the chemical process industries are aggressive, it can be assumed that most of SCC failures in plant would be predicted through laboratory or plant testing. In most cases, as it happens with other branches of industry, laboratory testing in CPI environments will provide the upper limit of incidence

rate; that is, it is unlikely that failures will occur in service at a rate higher that the one measured in the laboratory. After a first screening through laboratory testing, it is recommended to have testing performed in situ, using the actual variables of the process stream. This testing would allow the assessment of unaccounted variables in the laboratory such as temperature overruns, batch process cycles, presence of impurities, etc.

Conclusions

(1) Results from failure analyses of components made of iron, cobalt and nickel alloys and which suffered stress corrosion cracking during field service in chloride and wet HF are presented.

(2) Laboratory testing confirmed that nickel alloys are more resistant alloys to chloride cracking that iron or cobalt based alloys.

(3) The susceptibility of five nickel alloys to environmentally induced cracking in wet HF are presented. Effects of temperature, alloying elements and presence of oxygen are discussed.

Acknowledgments

The author is thankful to J. R. Dillman, J. P. Cotner and M. Richeson for their laboratory work and to Dr. P. Crook for his insightful comments.

References

[1] Puyear, R. B., *Corrosion Failure Mechanisms in Process Industries: A Compilation of Experiences, MTI Report R-4*, Materials Technology Institute of the Chemical Process Industries, Inc., St. Louis, MO, 1997.

[2] Andersen, H., Arnvig, P.-E., Wasielewska, W., Wegrelius, L. and Wolfe, C., "SCC of Stainless Steel under Evaporative Conditions," *Corrosion/98*, Paper 251, NACE International, Houston, TX, 1998.

[3] Sedricks, A. J., "Stress-Corrosion Cracking of Stainless Steels," *Stress-Corrosion Cracking - Materials Performance and Evaluation*, ASM International, Materials Park, OH, 1992, pp. 91-130.

[4] Crook, P., "Cobalt-Base Alloys," *Corrosion Tests and Standards, Application and Interpretation, ASTM Manual Series MNL 20,* Philadelphia, PA, 1995.

[5] Ciaraldi, S. W., Berry, M. R., and Johnson J. M., "Corrosion of Austenitic Stainless Steels and Nickel Based Alloys in Dilute Hydrofluoric Acid Solutions," *Corrosion/82*, Paper 98, NACE International, Houston, TX, 1982.

[6] Pawel, S. J., "Corrosion of High-Alloy Materials in Aqueous Hydrofluoric Acid Environments," *Corrosion*, Vol. 50, 1994, pp. 963-971.

[7] Crum, J. R., Smith, G. D., McNallan, M. J. and Hirnyj, S., "Characterization of Corrosion Resistant Materials in Low and High Temperature HF Environments," *Corrosion/99*, Paper 382, NACE International, Houston, TX, 1999.

ESIS Sponsored Session—EAC Testing and In-Service Experiences

Ronald W. J. Koers,[1] Alfons H. M. Krom,[2] and Ad Bakker[3]

Hydrogen Embrittlement - Loading Rate Effects in Fracture Mechanics Testing

Reference: Koers, R. W. J., Krom, A. H. M., and Bakker, A., **"Hydrogen Embrittlement-Loading Rate Effects in Fracture Mechanics Testing,"** *Environmentally Assisted Cracking: Predictive Methods for Risk Assessment and Evaluation of Materials, Equipment, and Structures, ASTM STP 1401,* R. D. Kane, Ed., American Society for Testing and Materials, West Conshohocken, PA, 2000.

Abstract: The fitness for purpose methodology is more and more used in the oil and gas industry to evaluate the significance of pre-existing flaws and material deficiencies with regard to the suitability of continued operation of equipment. In this methodology, traditional fracture mechanics is integrated with expertise in inspection technology, material evaluation, and corrosion damage assessment, stress analysis and the mechanics of materials. Application of the fitness for purpose methodology for equipment operating in hydrogenation environments or in sour service is rather complex, in particular, due to the uncertainty in the reduction of the fracture toughness caused by hydrogen embrittlement. Hydrogen embrittlement is a time-dependent fracture process caused by the absorption and diffusion of atomic hydrogen into the steel, which results in a loss of ductility.
An experimental study has been performed to quantify the reduction of fracture toughness of an API 5L grade X56 pipeline steel, and a numerical model has been presented to understand the experimental results.

Keywords: API 5L grade X56 line pipe steel, hydrogen embrittlement, hydrogen diffusion, rising load fracture mechanics tests, fracture toughness, double cantilever beam (DCB).

[1] Research scientist, Shell Global Solutions, Shell Global Solutions International B.V. Badhuisweg 3 1031 CM Amsterdam, The Netherlands.

[2] Research scientist, TNO Institute for Industrial Technology, Laan van Westenenk 501, P.O. Box 541, 7300 AM Apeldoorn, The Netherlands.

[3] Professor, Delft University of Technology, Laboratory of Material Science, Rotterdamseweg 137, 2628, AL Delft, The Netherlands.

Copyright© 2000 by ASTM International www.astm.org

Introduction

The fitness for purpose methodology is more and more used in the oil and gas industry to evaluate the significance of pre-existing flaws and material deficiencies with regard to the suitability of continued operation of equipment. In this methodology, traditional fracture mechanics is integrated with expertise in inspection technology, material evaluation and corrosion damage assessment, stress analysis, and the mechanics of materials. Application of the fitness for purpose methodology for equipment operating in hydrogenation environments or in sour service is rather complex, in particular, due to the uncertainty in reduction of the fracture toughness caused by hydrogen embrittlement. Hydrogen embrittlement is a time-dependent fracture process caused by the absorption and diffusion of atomic hydrogen into the steel, which results in a loss of ductility. In tensile testing this results in a smaller reduction of area and, in the fracture mechanics testing this results in a lower fracture toughness. The time-dependence of the hydrogen embrittlement process results in loading rate dependent test data. In this paper the term fracture toughness is used which is also commonly reffered to as the threshold stress intensity factor value for environmentally assisted cracking.

To determine the effect of the degree of sourness of the test environment, both tensile and fracture toughness tests were carried out in air and in four aqueous environments. The effect of applied loading rate and test environment on the measured fracture toughness is presented in this paper. Secondly a numerical model is developed that gives opportunity to study the effect of loading rate on the hydrogen distribution in the specimen. The model takes into account the effects of the stress-state and the level of plastic deformation on the time dependence of the hydrogen diffusion process.

Material and Environment

The material tested is an API 5L carbon steel pipe, grade X56 with a yield stress is equal to 399 MPa and ultimate tensile strength is 558 MPa, the chemical composition is given in Table 1.

Table 1 - *Chemical composition of the tested API 5L grade X56 steel (wt%)*

C	S	P	Si	Mn	Ni	Cr	Mo	V
0.15	0.005	0.0017	0.30	1.32	0.02	0.03	0.005	0.06
Cu	Nb	Ti	Al	B	Sn	Co	As	
0.03	<0.002	<0.002	0.048	<0.0003	<0.005	<0.005	<0.005	

To determine the effect of the environment on the fracture resistance, the tests were performed in four environments, namely:

Solution A: A 5% NaCl solution in H_2O buffered with 1% natriumacetate and soured with acetic acid to pH of 4.1. Hydrogen charging was performed under a partial H_2S pressure of 300 mbar (300 000 N/m^2) using nitrogen as balance

gas. The equilibrium concentration of H_2S in the solution was approximately 1093 mg H_2S/L.

Solution B: A 5% NaCl solution in H_2O buffered with 1% natriumacetate and soured with acetic acid to pH of 5.5. Partial H_2S pressure was 35 mbar (35 000 N/m^2) and nitrogen as balance gas. The equilibrium concentration of H_2S in the solution was approximately 128 mg H_2S/L.

Solution C: Artifical seawater according to ASTM 1121-75-6 buffered with 1 % sodium acetate resulting in pH of 5.5

Solution D: Artifical seawater according to ASTM 1121-75-6 (pH = 8.0).

Before testing in the solutions A, B, and C all the specimens were pre-charged with hydrogen for a period of 150 hours or longer to achieve the equilibrium hydrogen concentration in the specimen at the beginning of the mechanical testing.

Test Specimens

Two kinds of tests have been performed, namely rising load tests on standard fracture mechanics specimens and constant wedge opening tests on double cantilever beam specimens.

The rising load fracture mechanics tests were performed on three point bending single edge notched fracture mechanics specimens, see ASTM Standard Test Method for Measurement of Fracture Toughness (ASTM 1820-96). The specimen width and thickness were equal to 20 mm and the specimen contained 2 mm side grooves, resulting in a net section thickness equal to 16 mm. The specimens contained a pre-fatigue crack with a depth of approximately 6 mm. The specimens were tested using the unloading compliance technique.

The constant wedge opening tests were performed using double cantilever beam (DCB) specimens as described in NACE standard on Laboratory Testing of Metals for Resistance to Specifiec Forms of Environmental Cracking in H_2S Environments (NACE TM0177-96). The specimen dimensions were in accordance with TM0177, further the test environment was modified and the wedge sizes have been varried. The applied DCB specimen thickness is 12.7 mm.

Rising Load Fracture Mechanics Tests

To determine the effect of the loading rate in rising load experiments, tests were carried out for a range of loading rates (load point displacement rates). The specimens were tested in Solution A. The highest applied loading rate corresponded to the rate that is normally applied in standard fracture mechanics testing, and the lower rates were used to find the loading rate at which a threshold fracture toughness level could be obtained. The results are given in Fig. 1 and Table 2. In all tests no unstable brittle fracture was observed. From the tests performed in air it was found that the fracture toughness reduced

with lowering the loading rate. This is attributed to strain hardening effects, analogue to the strain rate sensitivity observed in the tensile tesing of carbon manganese steels. Under sour conditions with H_2S charging, the loading rate sensitivity of the fracture toughness was found to be much larger than observed under ambient conditions. The loading rate below which no further reduction of fracture toughness is observed could be established as 10^{-5} mm/s. A qualitative explanation of the loading rate effect on the measured fracture toughness is described as follows. The presence of hydrogen in the crack tip process zone is responsible for hydrogen embrittlement. Hydrogen at the crack tip proces zone is supplied by the hydrogen atoms present in the bulk material and by hydrogen originating from the corrosion reactions at the crack surfaces, and the crack growth mechanism is expected to be diffusion-controlled. This would explain the loading rate sensitivity of the fracture toughness: the hydrogen diffusion to the crack tip process zone must be sufficient to create a critical condition before fracture occurs. At high testing rates, the hydrogen diffusion is too slow to supply sufficient amount of hydrogen for hydrogen embrittlement.

To investigate the effect of the environment on the measured fracture toughness, the tests were performed in four different environments (solutions A, B, C and D). All these tests were performed at a loading rate equal to 10^{-5} mm/s. The results are given in Fig. 2. It is shown that the fracture toughness significantly reduces under both sour and seawater test conditions. Even under non-acidic seawater conditions (test solution D with pH of 8.0) the fracture toughness reduced dramatically to approximately 50 % of the value measured in air. The lower toughness is most probably caused not by hydrogen embrittlment but due to anodic stress corrosion cracking. The specimens tested under both sour and seawater conditions showed all a reduction in the initiation fracture toughness and reduced resistance to stable cracking (reduced slope the fracture resistance versus crack growth curve). In all tests no unstable brittle fracture was observed.

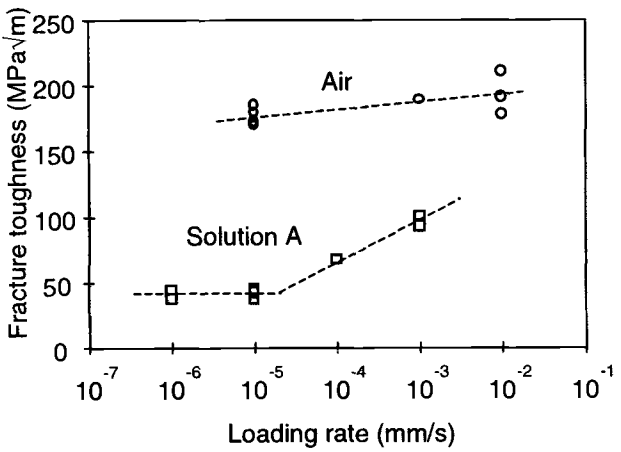


Figure 1 – *Fracture toughness as a function of loading rate in air and solution A.*

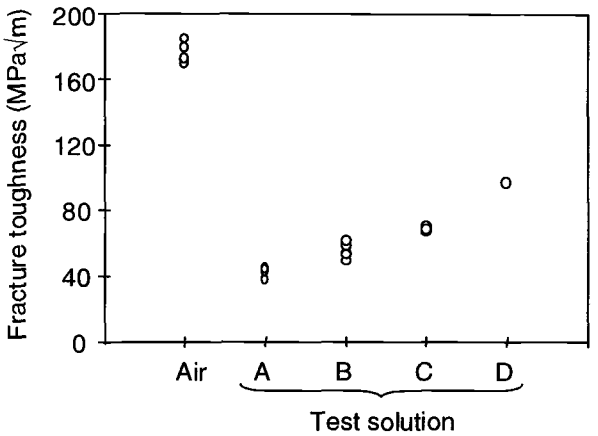


Figure 2 – *Fracture toughness as a function of environment. All the specimens were tested at a loading rate equal to 10^{-5} mm/s.*

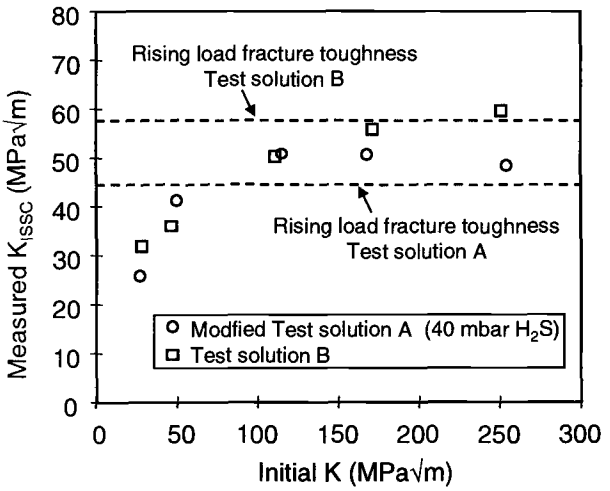


Figure 3 - *Comparison of the DCB test results with rising load fracture toughness test (loading rate is equal to 10^{-5} mm/s).*

Constant Displacement DCB Tests

In addition to the rising load experiments, non-rising load tests were carried out. The objective was to investigate whether the threshold fracture toughness obtained in the rising load experiments agrees with the data of so called crack arrest tests. According to

NACE these specimens were tested in a prescribed environment with a fixed wedge opening. To determine the effect of wedge opening on the arrest toughness, tests were performed using different wedge thicknesses resulting in different initial stress intensity factors at the beginning of the test. When the initial stress intensity factor was high enough, the crack started to grow until its arrest due to the load decay with crack growth. The measured arrest toughness as a function of initial loading is given in Fig. 3 and Table 3. The mean threshold fracture toughness values obtained from the rising load experiments are also plotted in Fig. 3. The DCB specimens tested in solution B were exposed for a period of 22 days while the specimens tested in a modified test solution A (40 mbar H_2S) were exposed during 15 days. There seems to be a reasonable agreement between the threshold fracture toughness obtained from the rising load experiments and the arrest toughness obtained from the DCB tests, except for those where the amount of crack growth was minimal (less than 0.4 mm). These tests, three in total, have a K_{ISSC} less than 40 MPa$\sqrt{m}$ and should be considered as invalid since there was no or only marginal crack growth in these test.

Table 2 - *Results of rising load fracture mechanics tests*

Test environment	Loading rate, mm/s	Fracture toughness, MPa$\sqrt{m}$
Air	10^{-2}	190.9, 210.1, 177.5
	10^{-3}	189.2
	10^{-5}	171.3, 179.3, 169.5, 184.6, 179.3, 172.6
Solution A 0.3 bar H2S, pH 4.1	10^{-3}	92.2, 100.7
	10^{-4}	67.6
	10^{-5}	37.6, 42.4, 44.9, 44.2
	10^{-6}	37.0, 37.6, 44.4
Solution B 35 mbar H2S, pH 5.5	10^{-5}	53.0, 53.4, 49.2, 53.0, 58.6, 61.4
Solution C ASTM 1141-75-6 seawater, buffered	10^{-5}	66.9, 70.4, 68.5
Solution D ASTM 1141-75-6 seawater	10^{-5}	97.0

Table 3 - *Results of DCB test*

Initial K, MPa√m	Crack growth, mm	K_{ISSC}, MPa√m Test solution B
29.0	0.10	31.7
47.1	0.38	35.8
112.2	1.54	50.0
172.1	1.37	55.5
251.9	1.31	59.5
Initial K, MPa√m	Crack growth, mm	K_{ISSC}, MPa√m Modified test solution A (40 mbar H_2S)
27.1	0.13	25.6
50.1	2.32	41.1
115.8	3.36	50.7
168.4	4.45	50.6
254.9	5.76	48.3

Hydrogen Embrittlement Model

The experiments showed the measured fracture toughness is loading rate dependent. This was explained earlier in this paper by hydrogen diffusion towards the process zone around the crack tip resulting in high hydrogen concentrations therein. When a critical level of hydrogen concentration at a certain plastic strain is reached, fracture in the process zone is initiated and later it is stopped when the crack enters the bulk material with lower hydrogen concentration. A numerical model has been developed to investigate the mechanism of hydrogen embrittlement in more detail. In the model it is assumed that hydrogen atoms diffuse through lattice sites and that trap sites are filled by lattice diffusion. More trap sites are formed due to plastic deformation. Coupled diffusion-elasto plastic finite element analyses were carried out in order to investigate the hydrogen concentration in the lattice and trap sites near a blunting crack tip under small-scale yielding conditions as a function of the loading rate.

Hydrogen Transport Equations

In the hydrogen transport model, it is assumed that traps are isolated, i.e., that they do not form an extended network. Hence, hydrogen transport between trap sites proceeds by lattice diffusion. Moreover, only one kind of traps is considered, namely those which are

saturable and reversible, such as a dislocation core. Considering a body with volume V and surface S, conservation of mass requires that the rate of change of the total hydrogen content inside V is equal to the flux through S

$$\frac{\partial}{\partial t}\int_V \{C_L + C_T\}dV + \int_S \mathbf{J}\cdot\mathbf{n}dS = 0 \tag{1}$$

where $\partial/\partial t$ is the partial derivative with respect to time, C_L is the hydrogen concentration in lattice sites, C_T is the hydrogen concentration in trap sites, $\mathbf{n}$ is the outward-pointing unit normal vector and $\mathbf{J}$ the hydrogen flux, which depends on the stress state as follows

$$\mathbf{J} = -D_L\nabla C_L + \frac{D_L C_L \overline{V}_H}{RT}\nabla\sigma_h \tag{2}$$

where D_L is the concentration independent lattice diffusivity, $\overline{V}_H$ the partial molar volume of hydrogen, i.e. $2.0\text{x}10^{-6}$ m^3 for α-iron at 293 K [1], R the universal gas constant, T the absolute temperature, and σ_h the hydrostatic stress: $\sigma_h = (\sigma_{xx} + \sigma_{yy} + \sigma_{zz})/3$. Substitution of Eq. 2 in Eq. 1 gives

$$\int_V \left\{\frac{\partial C_L}{\partial t} + \frac{\partial C_T}{\partial t}\right\}dV + \int_S \left\{\left(-D_L\nabla C_L + \frac{D_L C_L \overline{V}_H}{RT}\nabla\sigma_h\right)\cdot\mathbf{n}\right\}dS = 0 \tag{3}$$

Using the divergence theorem we find

$$\int_V \left\{\frac{\partial C_L}{\partial t} + \frac{\partial C_T}{\partial t} - \nabla\cdot\left(D_L\nabla C_L\right) + \nabla\cdot\left(\frac{D_L C_L \overline{V}_H}{RT}\nabla\sigma_h\right)\right\}dV = 0 \tag{4}$$

Since this equation holds for an arbitrary volume V, the integrand must vanish, i.e.

$$\frac{\partial C_L}{\partial t} + \frac{\partial C_T}{\partial t} - \nabla\cdot\left(D_L\nabla C_L\right) + \nabla\cdot\left(\frac{D_L C_L \overline{V}_H}{RT}\nabla\sigma_h\right) = 0 \tag{5}$$

In the case of equilibrium the hydrogen concentration in trap sites can be expressed as a function of the hydrogen concentration in lattice sites

$$C_T = \frac{N_T}{1 + \dfrac{1}{K_T\theta_L}} \tag{6}$$

where N_T is the number of trap sites, θ_L is the occupancy of lattice sites: $\theta_L = C_L/N_L$, N_L is the number of lattice sites per unit volume, K_T is the trap equilibrium constant: $K_T = e^{-\Delta E_T/RT}$, ΔE_T is the trap binding energy. As shown by Kumnick and Johnson [2] the number of trap sites depends on the level of plastic deformation. Hence, the of trap

sites density, N_T, can be expressed as a function of equivalent plastic strain ε_p. Since the number of lattice sites is constant and the temperature will be kept constant, the partial derivative of the hydrogen concentration in trap sites with respect to time becomes

$$\frac{\partial C_T}{\partial t} = \frac{\partial C_T}{\partial C_L}\frac{\partial C_L}{\partial t} + \frac{\partial C_T}{\partial N_T}\frac{dN_T}{d\varepsilon_p}\frac{\partial \varepsilon_p}{\partial t} \tag{7}$$

Finally, using Eq. 7, Eq. 5 becomes

$$\frac{C_L + C_T(1-\theta_T)}{C_L}\frac{\partial C_L}{\partial t} - \nabla\cdot\left(D_L \nabla C_L\right) + \nabla\cdot\left(\frac{D_L C_L \bar{V}_H}{RT}\nabla\sigma_h\right) + \theta_T \frac{dN_T}{d\varepsilon_p}\frac{\partial \varepsilon_p}{\partial t} = 0 \tag{8}$$

where θ_T is the occupancy of trap sites: $\theta_T = C_T/N_T$. More details on the hydrogen transport model including the variational and finite element forms of Eq. 8 can be found in [3].

Simulation of the Effect of the Loading Rate on Hydrogen Distributions near a Blunting Crack Tip

Finite Element Mesh, Boundary Conditions and Material Properties - The boundary layer approach is used in order to investigate the hydrogen distribution around a blunting crack tip with no need to model a complete geometry as far as sufficiently close to the crack tip, stresses and strains are controlled by the Mode I stress intensity factor K_I. The approach is valid as long as the small-scale yielding conditions hold. Due to symmetry, it is sufficient to model a semi-circular region $0 \le \theta \le \pi$ relative to the crack tip. The finite element mesh consists of 960 4-node plane strain elements: 40 elements in the radial direction and 24 elements in the tangential direction. The elements increase in size in the radial direction by a growth factor of 1.29. The only length parameter is the initial crack tip opening displacement which is 10 μm. The radius of the semi-circular mesh is 15 000 times the initial crack tip opening displacement. On the symmetry axis the hydrogen flux is zero while on the circular outer boundary and the crack surface the hydrogen concentration in lattice sites is prescribed to be equal to the the initial hydrogen concentration in lattice sites C_{L0} (the initial conditition for the diffusion problem). On the symmetry axis the displacements in the y-direction are zero, while on the circular boundary the displacements are prescibed from the elastic solution, which is controlled by K_I. The crack surface is stress-free. In each time step a diffusion analysis is carried out followed by an updated Lagrangian stress analysis. The diffusion coefficient D_L at 300 K is $1.27\text{x}10^{-8}$ m^2/s and the initial hydrogen concentration in lattice sites C_{L0} is $2.08\text{x}10^{21}$ m^{-3}, corresponding to hydrogen gas of 1 atmosphere at 300 K, [3]. The uni-axial stress-strain relation is taken in the form of a power law

$$\varepsilon = \begin{cases} \dfrac{\sigma}{E} & \text{if } \varepsilon \le \dfrac{\sigma_y}{E} \\ \dfrac{\sigma_y}{E}\left(\dfrac{\sigma}{\sigma_y}\right)^n & \text{if } \varepsilon > \dfrac{\sigma_y}{E} \end{cases} \tag{9}$$

where $E = 207\,000$ MPa is Young's modulus $\sigma_y = 250$ MPa is the yield stress, and $n = 5$ is the hardening exponent. The Poisson's constant is 0.3.

Results

The effect of the loading rate is investigated by varying the loading time to reach a fixed load of $K_I = 89.2$ MPa$\sqrt{\text{m}}$. Thus, the longer the loading time, the lower is the loading rate and therefore the strain rate around the crack tip. At this load level the crack tip opening displacement, according to 45° intercept definition [4], was 4.7 times the initial crack tip opening displacement. Material parameters are assumed to be strain-rate independent.

First, we discuss the case in which the boundaries, i.e. both the circular outer boundary and the crack surface, have a prescribed hydrogen concentration equal to C_{L0}. In Fig. 4a the hydrogen concentration in lattice sites along the symmetry axis at the end of loading is shown for different loading times. At the loading time of 1.3 s, the strain rate is so high that the diffusion cannot deliver hydrogen for the lattice sites which are emptied of hydrogen due to trapping. There is a small region with high plastic strains at the crack tip, and thereis a high number of trap sites that are filled due to high trap binding energy. Hydrogen for the trap sites is supplied by hydrogen at the lattice sites. Hence the hydrogen concentration in lattice sites becomes lower than its initial value. Since the hydrogen concentration on the crack surface is maintained, the hydrogen concentration in lattice sites rises again to the surface. With increasing loading time, the time for hydrogen diffusion increases, the emptied lattice sites can be filled again with hydrogen and the peak due to the hydrostatic stress appears. Increasing the loading time to more than $1.3\text{x}10^6$ s does not give higher hydrogen concentrations. At a loading time of $1.3\text{x}10^6$ s the lattice sites, which are emptied by trapping, are filled again by hydrogen diffusion. As a consequence, this hydrogen distribution coincides with the steady-state solution, see Fig. 4a. The hydrogen concentration in the trap sites, Fig. 4b, shows a peak at the crack tip that is approximately 86 times the initial hydrogen concentration in the lattice sites.

In the other case, it is assumed that the boundaries, i.e. the outer circular boundary and the crack surface, are insulated. As a result, there is no supply of hydrogen through the boundaries and the total hydrogen content remains constant. In Fig. 5a the hydrogen concentration in lattice sites along the symmetry axis at the end of loading is shown for different loading times. Again, at loading time of 1.3 s the strain rate is so high that diffusion cannot deliver hydrogen to the lattice sites, which are emptied by trapping. Because of the insulated crack surface, the lattice sites at the crack tip are also emptied of hydrogen. With increasing loading time, the time for hydrogen diffusion increases, the

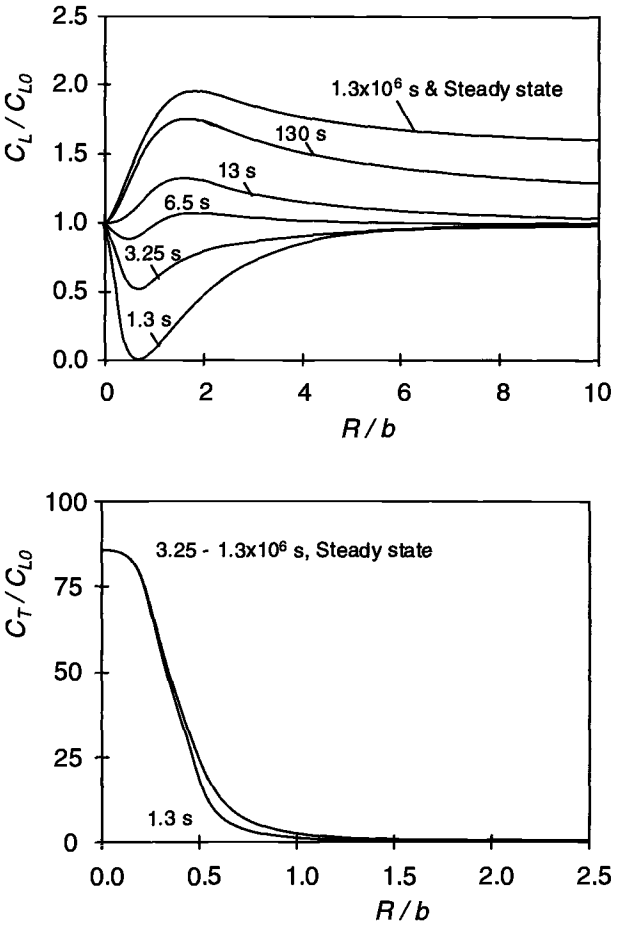


Figure 4 - *The hydrogen concentration in (a) lattice sites and (b) trap sites ahead of the crack tip after loading to K_I = 89.2 MPa$\sqrt{m}$ for different loading times. The hydrogen concentration is prescribed on the crack surface. C_{LO} is the initial hydrogen concentration in the lattice sites, R the distance from the crack tip and b the crack opening displacement.*

emptied lattice sites can be filled again and the peak due to the hydrostatic stress appears. However, the filling of lattice sites is now slower, since hydrogen must be supplied from the bulk metal. Again, increasing the loading time to more than $1.3x10^6$ s does not give a higher hydrogen concentration. At a loading time of $1.3x10^6$ s the lattice sites which are emptied by trapping are filled again by hydrogen diffusion. But the steady state condition could not be reached due to insulated boundary conditions.

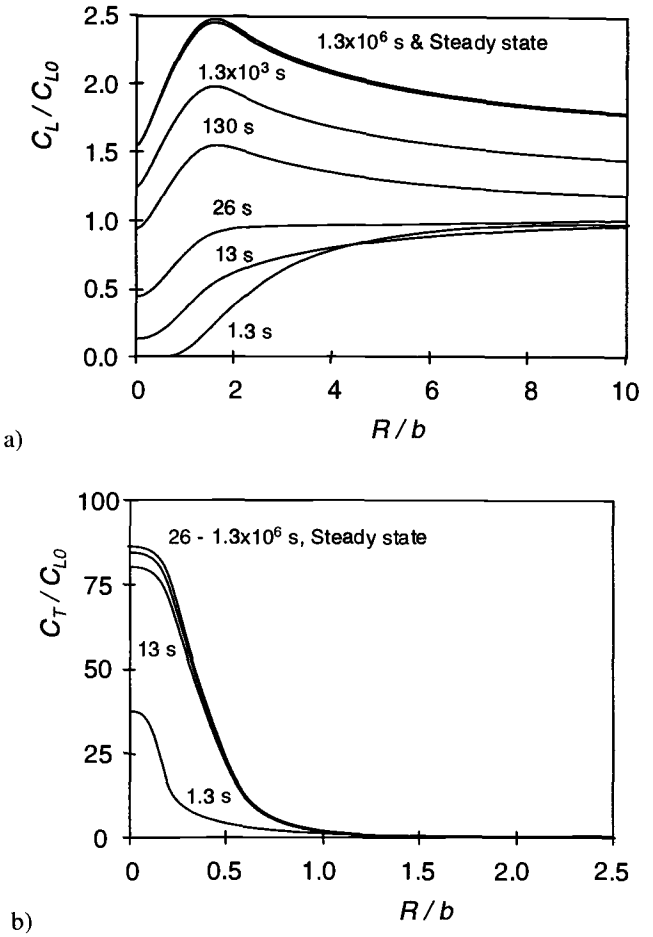


Figure 5 - *The hydrogen concentration in (a) lattice sites and (b) trap sites ahead of the crack tip after loading to K_I = 89.2 MPa$\sqrt{m}$ for different loading times. The crack surface is insulated. C_{L0} is the initial hydrogen concentration in the lattice sites, R the distance from the crack tip and b the crack opening displacement.*

The hydrogen distribution in trap sites shows again a high peak at the crack tip, see Fig. 5b. The height of this peak is approximately 86 times the initial hydrogen concentration in lattice sites. Only when the loading time is 1.3 s, this height reduces to 38 C_{L0}. This is a result of the assumption of the equilibrium between hydrogen in lattice and trap sites which is still valid despite the high strain rates. Near the crack tip the hydrogen concentration in lattice sites is extremely low compared with its initial value. As a result, the hydrogen concentration in traps is somewhat lower than at longer loading

times. However compared with the hydrogen distribution in lattice sites, the effect of the strain rate on the hydrogen concentration in traps is still slight.

Discussion of the Numerical Results - The analysis shows that, given the material parameters, the plastic strain rate has a considerable influence on the hydrogen concentration in lattice sites as a result of the creation of traps created during plastic deformation. The effect of the traps depends on the temperature, the trap binding energy, the number of trap sites and the initial hydrogen concentration in lattice sites. These parameters are related by Eq. 6. Increasing the parameters that increase the hydrogen concentration in trap sites will result in a greater effect of the strain rate on the hydrogen concentration in lattice sites. Considering the total hydrogen distribution two peaks can be found. The highest one situated at the crack tip approximately 86 times the initial hydrogen concentration in lattice sites and corresponds to the peak in the plastic strain distribution. The height of this peak depends on the number of trap sites. The other peak can be found some distance away from the crack tip: it corresponds to the location of the maximum hydrostatic stress. The height of this peak depends on the temperature and the yield stress. The level of the hydrostatic stress depends on the yield stress. Increasing the initial hydrogen concentration will decrease the relative amount of hydrogen moved to trap sites. Hence the effect of the strain rate on the hydrogen distribution in lattice sites will become weaker as the hydrogen concentration in lattice sites increases. Thus the loading rate independent fracture toughness should be obtained at a higher loading rate for elevated bulk hydrogen concentrations. This is supported by the test results. On the other hand, increasing the number of trap sites due to plastic strains will result in a greater effect of the strain rate. Opposite effects will occur when these parameters decrease.

In the presented calculations two types of boundary conditions were considered: prescribed surface concentration of hydrogen and insulated crack surface. The outer surface, i.e. the radius of the domain is, so far away from the crack tip that it has no influence on crack tip processes. These two boundary conditions can be seen as two extremes: when the surface reactions are slow compared with the hydrogen lattice diffusion, the crack surface can be regarded as insulated. When the surface reactions are fast compared with diffusion, the crack surface can be regarded as a surface with a prescribed hydrogen concentration. When the crack surface is insulated, the effect of strain rate is greater as hydrogen must be supplied from the lattice around the plastic zone. Thus, the diffusion distance is greater. Moreover, the peak in the hydrogen distribution due to the hydrostatic stress is higher when the crack surface is insulated. Nevertheless, the conclusions drawn from the results for both boundary conditions are the same.

Conclusions

- The measured fracture resistance is reduced in the rising load fracture mechanics test when the rate of loading is decreased. However, at the slowest rates of testing the fracture resistance becomes rate independent.

- To quantify the reduction of fracture toughness due to hydrogen embrittlement, the rising load fracture mechanics tests must be performed at a loading rate which is several orders of magnitude lower than applied in standard fracture mechanics testing.
- The fracture resistance determined using the DCB tests is in agreement with that measured in rising load experiments. To determine the fracture resistance using DCB specimens, a number of tests need to be performed with different levels of initial loading. Otherwise a criterion for the minimum amount of crack growth needs to be defined.
- The model predicts that a constant fracture toughness would be obtained at higher loading rates for specimens with high bulk hydrogen concentration than when the tests are performed on specimens with a low bulk hydrogen concentration.
- The hydrogen embrittlement model gives an opportunity to identify/develop a testing methodology to correlate the observed hydrogen embrittlement in mechanical testing with hydrogen charging and loading conditions in practice.

References

[1] Hirth, J.P.: "Effect of hydrogen on the properties of iron and steel", *Metallurgical Transactions* Vol. **A11**, 1980, pp. 881-890.

[2] Kumnick A.J. and Johnson, H.H.: "Deep trapping states for hydrogen in deformed iron", *Acta Metallurgica*, Vol. **28**, 1980, pp. 33-39.

[3] Krom, A.H.M, Koers, R.W.J. and, Bakker, A.: "Hydrogen transport near a blunted crack tip", *Journal of the Mechanics and Physics of Solids*, Vol. **47**, 1999, pp. 971-992.

[4] Tracey, D.M.: "Finite element solutions for crack-tip behavior in small-scale yielding," *Journal of Engineering Materials Tech.*, Vol. **98**, 1976, pp. 146-151.

Wolfgang Dietzel[1]

Standardization of Rising Load/Rising Displacement SCC Testing

Reference: Dietzel, W., **"Standardization of Rising Load/Rising Displacement SCC Testing,"** *Environmentally Assisted Cracking: Predictive Methods for Risk Assessment and Evaluation of Materials, Equipment, and Structures, ASTM STP 1401,* R. D. Kane, Ed., American Society for Testing and Materials, West Conshohocken, PA, 2000.

Abstract: Two new draft standards for fracture mechanics based stress corrosion cracking (SCC) tests have recently been issued by ASTM and ISO committees. Both concern the determination of the threshold stress intensity factor, K_{ISCC}, and the crack growth velocity, $da/dt = f(K_I)$ from rising load or rising displacement tests. One of these drafts, prepared by ASTM Committee G-1 on Corrosion of Metals, is an extension of an existing ASTM standard on slow strain rate testing. The second one was elaborated by ISO TC 156 and is based on a procedure proposed by the European Structural Integrity Society, ESIS. This procedure has been validated in an interlaboratory test program. Results of this research project and issues of both drafts are discussed in the paper.

Keywords: fracture mechanics approach, linear elastic fracture mechanics (LEFM), rising load/rising displacement tests, standardization, slow strain rate tests, stress corrosion cracking (SCC), threshold stress intensity factor, K_{ISCC}

Introduction

In the damage-tolerant approach to the assessment of structural integrity it is assumed that cracks or defects are already existent in a given structure, and fracture mechanics concepts are applied. Investigations of stress corrosion cracking usually apply linear elastic fracture mechanics (LEFM) concepts. This appears justified, since in most cases the plastic deformations caused by the mechanical stresses are confined to a small zone at the crack tip and thus the crack tip stress intensity factor in the opening mode, K_I, can be used to characterize the mechanical driving force which controls the initiation and subsequent growth of environmental cracks from initial defects.

[1]Research associate and head of Corrosion Department, Institute of Materials Research, GKSS-Forschungszentrum Geesthacht GmbH, Max-Planck-Str., D-21 502 Geesthacht, Germany.

Copyright© 2000 by ASTM International www.astm.org

The parameters which are determined from fracture mechanics SCC tests are the threshold value of the stress intensity factor, K_{ISCC}, below which environmentally assisted cracking should not occur, and the crack growth velocity, da/dt, as a function of K_I (Figure 1).

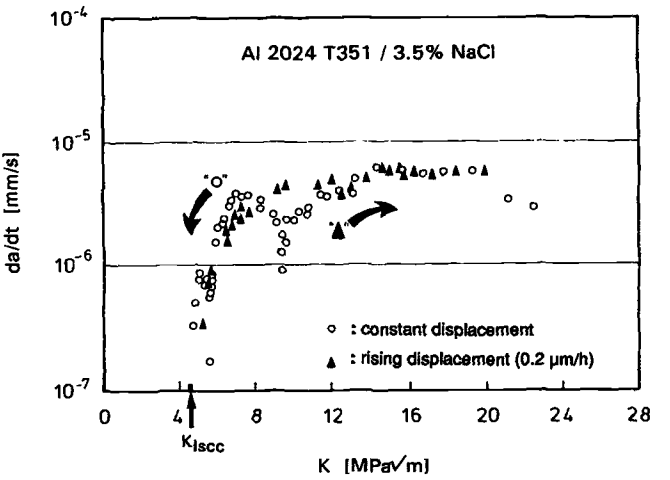


Figure 1 – Experimentally determined relationship between stress intensity factor, K, and crack growth velocity, da/dt, for aluminum alloy 2024 T351 in 3.5% NaCl solution [1].

Standardization Situation

A number of test standards exist that provide guidance for performing fracture mechanics SCC tests. The ASTM Standard Test Method for Determining a Threshold Stress Intensity Factor for Environmentally Assisted Cracking of Metallic Materials Under Constant Load (ASTM E 1681-95), ISO standard on Corrosion of Metals and Alloys - Stress Corrosion Testing; Part 6: Pre-Cracked Specimens (ISO 7539-6), and NACE Standard Test Method Laboratory Testing of Metals for Resistance to Sulphide Stress Cracking in H_2S Environments (NACE TM 0177-90) specify the use of pre-cracked samples in SCC tests aimed at determining K_{ISCC}. According to these standards, K_{ISCC} is evaluated in either constant load or constant deflection experiments. The duration of the tests is usually "left open to the parties concerned," but test times are recommended which in ISO 7539-6 range from 100 hours for titanium alloys to 10 000 hours for aluminum alloys and steels.

A major advantage of these standards is their moderate requirements with respect to the experimental set-up, but they also have some inherent shortcomings:

1. The duration of a static test can be quite long and/or the test is terminated after an arbitrary test time. It sometimes remains uncertain whether the measured K-value really represents the threshold of the material/environment combination under investigation.

2. Discrepancy can exist between laboratory tests performed under static conditions (constant load, constant deflection) and practical situations where dynamic loading and increasing plastic deformation can occur and may be prerequisite for SCC [2].
3. The specimens must satisfy the minimum size requirements imposed by the linear elastic fracture mechanics concept; for lower strength and/or more ductile materials this can lead to large specimen dimensions, particularly the specimen thickness may exceed the thickness of the actual component.

Problems 1 and 2 can be overcome by using dynamic test techniques like the slow strain rate test in which constant extension rates are applied [3]. Because of their accelerating nature these tests usually yield results within an acceptable amount of time, and they can reveal cases of susceptibility to SCC which remain undetected in static tests.

The slow strain rate test on smooth or notched specimens is standardized by ASTM, ISO and NACE. These standards, however, do not explicitly include the use of pre-cracked fracture mechanics specimens, although such tests have been in use for SCC investigations over more than 25 years [*4, 5*]. Hence, no generally accepted standard exists to date which would specify a procedure for fracture mechanics based rising load/rising displacement tests. The major problem encountered is the selection of suitable loading or displacement rates which are to be applied in order to obtain reliable K_{ISCC} values. This problem is particularly addressed in two drafts of new standards which are in preparation by ASTM and ISO committees.

The draft ASTM Standard Practice for Slow Strain Rate Testing to Evaluate the Susceptibility of Metallic Materials to Environmentally Assisted Cracking (ASTM G 129-99) is an extension of ASTM G 129-95, now explicitly including the use of pre-cracked specimens.

The test philosophy of the second draft, ISO Draft International Standard on Corrosion of Metals and Alloys - Stress Corrosion Testing - Part 9: Preparation and Use of Pre-cracked Specimens for Tests Under Rising Load or Rising Displacement (ISO/DIS 7539-9) follows guidelines which were first proposed in 1992 by the European Structural Integrity Society, ESIS, as ESIS Recommendations for Stress Corrosion Testing Using Pre-Cracked Specimens (ESIS P4-92 D).

Principles and Problems of Dynamic SCC Testing

As in constant load and constant deflection SCC experiments, fatigue pre-cracked specimens are used. These specimens are subjected to increasing displacements - usually as constant extension rates - while they are exposed to the corrosion environment. The onset and extent of crack growth are monitored using indirect crack length measuring techniques such as the potential drop or unloading compliance methods [*6, 7*].Testing is thus comparable to fracture toughness tests in air except that the applied extension rates are significantly lower.

The establishment of cracking conditions in SCC tests usually is time-dependent, if they do not exist at the outset of the test. SCC may hence only be observed in a rising load/rising displacement test if the displacement rate is sufficiently slow to ensure that failure due to pure mechanical rupture does not occur before the proper environmental conditions for cracking have been established. Previous investigations have shown that the stress intensity factor at crack initiation, $K_{I\text{-}init}$, in a certain material/environment

combination usually is a function of the applied displacement rate [5, *8-11*]. Figure 2 is a typical example of the influence of the loading rate on $K_{I\text{-}init}$. The threshold value, K_{ISCC}, corresponds to the lower shelf regime in this graph.

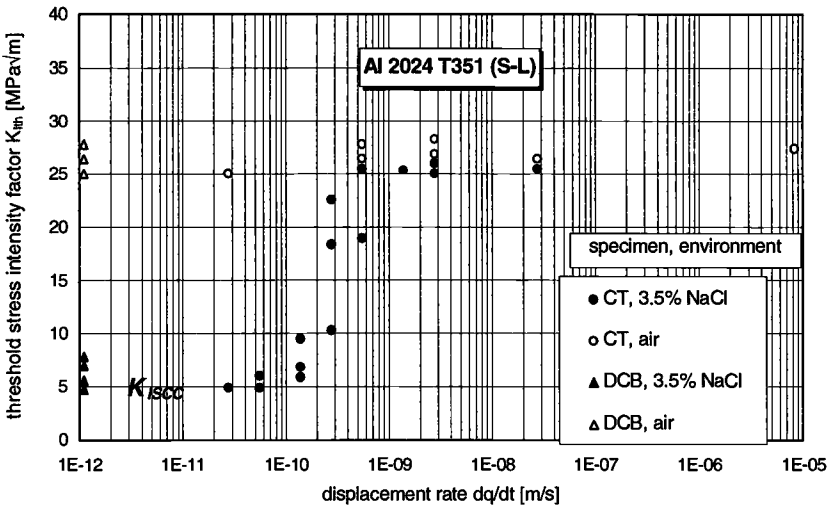


Figure 2 – Influence of the displacement rate, dq/dt, on the stress intensity factor at crack initiation, K_{Ith}, measured in rising displacement tests on CT specimens (circles); the results of long term constant displacement tests (10,000 hours) on DCB specimens are shown for comparison (triangles), [1].

The rate at which the specimens are loaded is therefore the crucial parameter in these tests. Both the ASTM and the ISO drafts recommend that tests should be conducted over a range of displacement rates in order to ensure that a conservative value of K_{ISCC} is obtained. The number of tests, however, that have to be performed for evaluating K_{ISCC} should be kept to an absolute minimum in order to maintain the accelerating nature which is associated with this concept of dynamic SCC testing. This requires that the loading rate at which K_{ISCC} is measured can readily be determined.

ASTM G 129-99 approaches the problem of specifying a suitable extension rate in those cases where no previous data exist which might be used as guidance by recommending a range of extension rates. These should be chosen between 10^{-4} and 10^{-7} in/s ($2.54*10^{-3}$ and $2.54*10^{-6}$ mm/s) for screening tests in which the effect of extension rates on SCC is studied. According to ASTM G 129-99 most tests are conducted in the range of extension rates from 10^{-5} to 10^{-7} in/s ($2.54*10^{-4}$ and $2.54*10^{-6}$ mm/s).

ISO/DIS 7539-9 recommends using an initial displacement rate of $1*10^{-5}$ mm/s for titanium alloys and $1*10^{-6}$ mm/s for higher strength steels and aluminum alloys if no other information is available. At least one additional test should be performed at a lower

displacement rate. The selection of the rate for this second test should, where feasible, be based on an examination of the fracture surface obtained from the first test. Here it is implied that the percentage of environmental cracking measured in the region of stable crack extension adjacent to the initial pre-crack yields an estimate of the factor by which by the displacement rate for the second test should be lowered compared to the first test.

Further guidance for determining an appropriate initial displacement rate is given in an appendix to ISO/DIS 7539-9 (Annex A) which results from previous SCC test experience [*1, 12*]. This approach was adopted from ESIS P4-92 and assumes that the displacement rate, $(dq/dt)_{SCC}$, at which a rising displacement test in a corrosive environment should be performed in order to determine K_{ISCC}, can be estimated from the ratio of the measured crack growth velocity in a rising displacement test in air (or in inert environment), $(da/dt)_{air}$, and the crack growth velocity in the plateau region for environmentally induced cracking, $(da/dt)_{SCC}$, by

$$(dq/dt)_{scc} \leq 0.5 \cdot \frac{(da/dt)_{scc}}{(da/dt)_{air}} \cdot (dq/dt)_{air}. \quad (1)$$

The value of $(da/dt)_{SCC}$ may be obtained within short time from tests that avoid long incubation periods by applying high stress intensity levels. This can be constant deflection tests on self-loaded DCB or WOL specimens, which are interrupted after a sufficient amount of crack propagation has been observed, or step loading tests. Even average crack growth velocity data, $\Delta a/\Delta t$, calculated from tests on smooth specimens according to ISO Standard on Slow Strain Rate Stress Corrosion Tests (ISO 7539-7) may be used as a first estimate [*12, 13*].

Comparison with Results of a Joint European Research Project

An interlaboratory comparison was conducted in order to verify the approach of ESIS P4-92. The project was funded by the European Commission within the framework of the "Standards, Measurements & Testing" program, and 24 laboratories took part [*14*]. SCC tests were performed on three material/environment combinations, i.e., one high strength aluminum alloy (AA 7010) and two steels (AISI 4340, AISI 316H); test environments consisted of aqueous chloride solutions. Rising load/rising displacement tests, experiments under constant load, constant deflection, and step loading tests were carried out. Slow strain rate tests on smooth specimens yielded average crack growth velocities, $\Delta a/\Delta t$. These were used in combination with results from rising displacement tests in air to calculate a suitable initial displacement rate using Eq. (1).

Figure 3 shows results of rising displacement tests on aluminum 7010 in the T651 temper, which is known to be susceptible to SCC. The tests were performed in synthetic seawater according to ASTM Standard Specification for Substitute Ocean Water (ASTM D 1141-90). It should be noted that for all material/environment combinations investigated in the project a considerable scatter of threshold data was observed. This scatter, possibly due to variations in handling of the corrosive environment, was not typical of one particular test method but was observed in all types of SCC experiments.

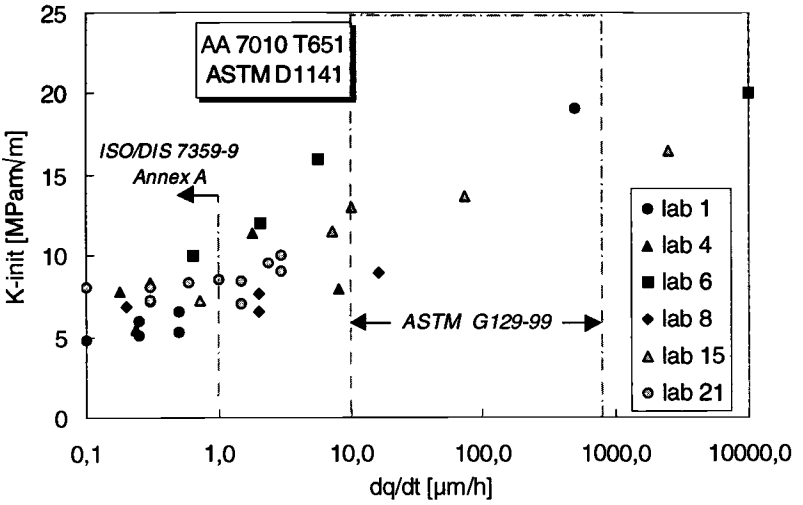


Figure 3 – Stress intensity factor at crack initiation as a function of applied displacement rate, measured for aluminum 7010 T651 in ASTM D1141; the vertical lines indicate displacement rates recommended by ASTM and ISO.

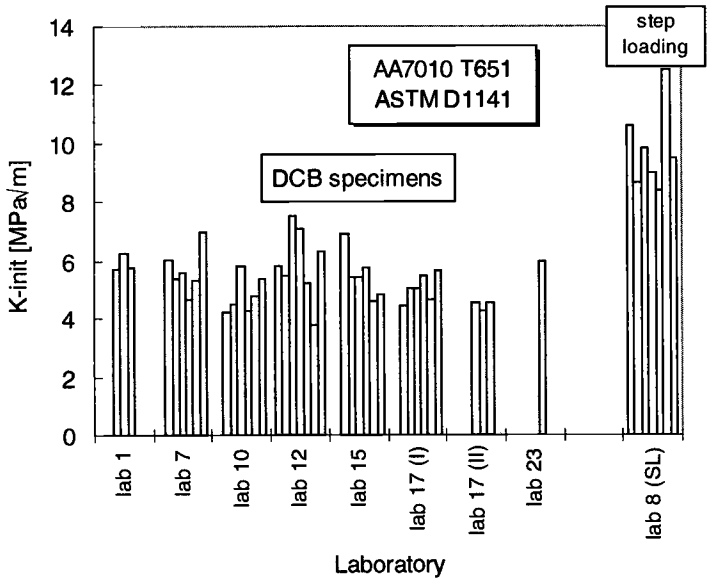


Figure 4 – Results of constant displacement tests on bolt loaded DCB specimens of aluminum 7010 T651 in ASTM D 1141; the data on the right hand side of this diagram were obtained in step loading tests [14].

Using the results of the preliminary slow strain rate tests and the tests in air, Eq. (1) yielded a displacement rate of 1 µm/h or lower as a suitable initial rate for determining K_{ISCC}. In Figure 3, this rate is indicated together with the range of extension rates recommended in ASTM G 129-99 (note that in this figure the scale of the x-axis is in micrometer per hour). Taking into consideration only tests that were performed at or below 1 µm/h, the K_{mat} values range from 4.8 to 10.5 MPa$\sqrt{m}$. The average threshold value calculated from these results is 6.8 MPa$\sqrt{m}$.

Threshold values determined for the same material/environment combination from crack arrest measurements at constantly deflected DCB specimens were slightly lower (Figure 4). Here, minimum values between 3.8 and 6.0 MPa$\sqrt{m}$ were measured. In these experiments the intra-laboratory scatter was almost as pronounced as the interlaboratory scatter. A total of 38 threshold values were reported yielding to an average of 5.4 MPa$\sqrt{m}$. In constant load tests, a threshold of 6.5 MPa$\sqrt{m}$ was measured. With a value of 8.4 MPa$\sqrt{m}$ the step loading tests yielded the highest average threshold of all test methods used in the project.

Similar observations were made for the two other material/environment combinations in the project. In general, the results of rising displacement experiments performed according to ESIS P4-92 were within the scatter range of results that were obtained in static tests following existing ASTM and ISO standards. As a consequence of this, ISO TC/156 WG/2 used ESIS P4-92 as the basis for the first draft of ISO 7539-9 on rising load/rising displacement tests.

Outlook

A major problem of SCC tests for evaluating K_{ISCC} is to decide whether the lowest value measured by a particular test method really represents the threshold, i.e. the lower bound limit of the fracture toughness of a material in a certain environment. This to some extent corresponds to the question whether the fracture was dominated by the corrosive environment or whether it was , at least in part, caused by mechanical rupture. A possible answer to this problem might be the use of fractographical observations of specimens which failed in SCC tests: If the fracture surface exclusively shows features of SCC, it can be assumed that the displacement rate used in a particular test was appropriate and hence that a valid K_{ISCC} was determined.

Another issue is the duration of rising displacement tests, although usually shorter than in static SCC tests. ISO/DIS 7539-9 tries to further reduce this time by pre-exposing the specimens to the test environment prior to the initiation of dynamic strain. The specimens are kept in the corrosion environment under some pre-load for at least 24 hours before starting the test machine. The selection of the initial load essentially determines the length of the subsequent test. A typical pre-load could be a value corresponding to 5 percent of K_{Ic}, the material's fracture toughness in air. Or, the pre-load could be chosen equal to the final maximum load at fatigue pre-cracking. In cases where K_{ISCC} is likely to be high, the initial load may be stepped to an even higher value. In any case the choice of this initial K value should then be refined in the course of the test series. This issue is particularly addressed in ongoing investigations.

Yet another problem arises from the fact that the current standards and drafts for fracture mechanics SCC testing are limited to linear elastic fracture mechanics (LEFM).

This approach imposes minimum requirements with respect to the specimen dimensions and can in some cases lead to a significant disparity of the crack sizes used in SCC tests and the size of cracks, which are typical of practical problems of SCC. In laboratory scale tests on specimens made from lower and medium strength alloys or from alloys with high resistance to SCC, the stress intensities for cracking often are not reached before the plastic zone has grown large relative to the size of the specimens. In these cases, the assumption of small scale yielding which is underlying the linear elastic approach is not justified and the stress intensity factor K may no longer be a meaningful parameter. Instead, elastic-plastic fracture parameters such as the J-integral, the crack tip opening displacement (CTOD) and/or the crack-tip opening angle (CTOA) would better be used to characterize the cracking process.

When comparing threshold data that were generated from specimens of different sizes and/or using different test methods, a generalized parameter presenting the crack driving force is required. Ideally, this would be the crack tip strain rate $d\varepsilon/dt$. Because of the difficulty in determining this variable due to the singularity of the stress strain field at the crack tip, the rate of change of the crack tip opening displacement, d(CTOD)/dt, is expected to be a more appropriate parameter than load line or crack mouth displacement rates.

Future developments of SCC tests procedures may take these issues into account.

Conclusions

The existing ASTM and ISO standards on fracture mechanics based SCC tests combine special merits with inherent drawbacks: The easy handling of experiments under static loading conditions can be impeded by their long duration. Crack growth out of plane or crack branching can occur particularly in constant deflection tests. Rising load/rising displacement tests according to the current drafts of ASTM and ISO may yield results at shorter test times. The validity of the results, however, strongly depends on the proper use of the method, especially on the selection of appropriate displacement rates. Validity criteria are hence required in order to assess the results of rising load/rising displacement tests. Fractographic investigations may provide such criteria.

The experience which has been gained in the project presented here and in a number of other investigations should assist in reaching a consensus about the requirements of rising load/rising displacement K_{ISCC} tests yielding reproducible results and thus lead to a future common ASTM/ISO standard on this subject.

Acknowledgement

The experimental work was carried out within the framework of the *"Measurements and Testing"* (now: *"Standards, Measurements and Testing"*) program of the European Commission (Contract No. MAT1 CT 930038). This financial support is gratefully acknowledged.

References

[1] Dietzel, W., "ESIS Guidelines for Fracture Mechanics Based Stress Corrosion Testing," *Technology, Law and Insurance*, Vol. 1, 1996, pp.151 – 157.

[2] Erlings, J. G., de Groot, H. W., and Nauta, J., "The Effect of Slow Plastic Straining on Sulphide Stress Cracking and Hydrogen Embrittlement of 3.5% Ni Steel and API 5L X60 Pipeline Steel," *Corrosion Science,* Vol. 27, 1987, pp. 1153-1167.

[3 Parkins, R. N., "Development of Strain-Rate Testing and Its Implications," *Stress Corrosion Cracking - The Slow Strain-Rate Technique, ASTM STP 665*, G. M. Ugiansky and J. H. Payer, Eds., American Society for Testing and Materials, West Conshohocken, PA, 1979, pp. 5-25.

[4] McIntyre, P., and Priest, A. H., "Accelerated Test Technique for the Determination of K_{ISCC} in Steels," British Steel Corporation Report MG/31/71, London, 1972.

[5] Clark, W. G., Jr., and Landes, J. D., "An Evaluation of Rising Load K_{ISCC} Testing," *Stress Corrosion - New Approaches, ASTM STP 610*, H. L. Craig Jr. Ed., American Society for Testing and Materials, West Conshohocken, PA, 1976, pp. 108-127.

[6] Johnson, H. H., "Calibrating the Electric Potential Method for Studying Slow Crack Growth," *Materials Research and Standards,* Vol. 5 , 1965, pp. 442-445.

[7] Dietzel, W. and Schwalbe, K.-H., "Monitoring Stable Crack Growth Using a Combined AC/DC Potential Drop Technique," *Zeitschrift für Materialprüfung/Materials Testing*, Vol. 28, No. 11, 1986, pp. 368-372.

[8] Anderson, D. R., and Gudas, J. P., "Stress Corrosion Evaluation of Titanium Alloys Using Ductile Fracture Mechanics Technology," *Environment Sensitive Fracture, Evaluation and Comparison of Tests Methods; ASTM STP 821*, S. W. Dean, E. N. Pugh and G. M. Ugiansky, Eds.; American Society for Testing and Materials, West Conshohocken, PA, 1984, pp. 98-113.

[9] Abramson, G., Evans, J. T., and Parkins, R. N., "Investigation of Stress Corrosion Crack Growth in Mg Alloys Using J-Integral Estimations," *Metallurgical Transactions*, Vol. 16 A, Oct. 1985, pp. 101-108.

[10] Mayville, R. A., Warren, T. J., and Hilton, P. D., "The Influence of Displacement Rate on Environmentally Assisted Cracking of Precracked Ductile Steel Specimens," *Transactions of ASME*, Vol. 109, 1987, pp. 188-193.

[11] Dietzel, W., Schwalbe, K.-H., and Wu, D., "Application of Fracture Mechanics Techniques to the Environmentally Assisted Cracking of Aluminium 2024," *Fatigue and Fracture of Engineering Materials and Structures*, Vol. 12, (6), 1989, pp. 495-510.

[12] Mayville, R. A., Warren, T. J., and Hilton, P. D., "Determination of the Loading Rate Needed to Obtain Environmentally Assisted Cracking in Rising Load Tests," *Journal of Testing and Evaluation*, Vol. 17, 1989, pp. 203-211.

[13] Strieder, K., Daum, K.-H., Dietzel. W. and Müller-Roos, J., "The Use of Slow Strain Rate Tests for Measuring the Velocity of Environmentally Assisted Cracking," *Structural Integrity: Experiments - Models - Applications, Proceedings of the 10th European Conference on Fracture, ECF 10, Berlin, 20-23 September 1994,* K.-H. Schwalbe and C. Berger, Eds., Deutscher Verband für Materialforschung und –prüfung e.V., Berlin, 1994, pp. 715-720.

[14] Dietzel, W., "Characterization of Susceptibility of Metallic Materials to Environmentally Assisted Cracking," Report GKSS 99/E/24, GKSS-Forschungszentrum Geesthacht GmbH, Geesthacht, 1999.

Research Session—Mechanistic Studies for Understanding and Control of EAC

Jesús Toribio[1] and Victor Kharin[2]

Role of Cyclic Pre-Loading in Hydrogen Assisted Cracking

Reference: Toribio, J. and Kharin, V., **"Role of Cyclic Pre-Loading in Hydrogen Assisted Cracking,"** *Environmentally Assisted Cracking: Predictive Methods for Risk Assessment and Evaluation of Materials, Equipment, and Structures, ASTM STP 1401*, R. D. Kane, Ed., American Society for Testing and Materials, West Conshohocken, PA, 2000.

Abstract: A numerical analysis is performed of the effect of cyclic pre-loading regime on the posterior hydrogen assisted cracking behaviour of high-strength steel, considering mechanical items (stress-strain evolution) and chemical aspects (hydrogen diffusion). With regard to mechanical issues, a high resolution numerical modelling is carried out of the elastoplastic stress-strain field in the near-tip area under cyclic loading (to simulate fatigue pre-cracking) and posterior monotonic loading (to simulate a slow strain rate test), considering the role of large near-tip deformations. In the matter of chemical aspects, a quantitative modelling of hydrogen diffusion is performed near the crack tip, accounting for the transient stress-strain field that evolves from the compressive one after pre-cracking to the tensile one during the test. Results show that hydrogen accumulation in fracture sites depends on residual stress distributions produced by cyclic pre-loading.

Keywords: hydrogen assisted cracking, cyclic pre-loading, stress assisted diffusion, slow strain rate testing, pre-cracked specimens, fatigue pre-cracking

Introduction

In the framework of fracture mechanics, experimental evaluation of environmentally assisted cracking (EAC) of materials is commonly performed in a laboratory by testing pre-cracked specimens. In this procedure, a pre-crack in the sample is required for posterior EAC testing, and it is usually generated by fatigue (cyclic) loading in air environment. The procedure of fatigue precracking inevitably produces ambiguous mechanical effects in the near-tip area (cf. [*1*]), since the cyclic loading regime affects the plastic zone development and controls the evolution of stress-strain fields in the close vicinity of the crack tip after loading/unloading the specimens.

This paper analyzes experimental results of slow strain rate (SSR) tests on high-strength steel in aqueous environments under cathodic electrochemical conditions promoting *hydrogen assisted cracking* (HAC). Emphasis is placed on the effect of the fatigue pre-cracking procedure, which influences dramatically the behaviour of the steel in the SSR test.

[1] Professor, Department of Materials Science, University of La Coruña, E.T.S.I. Caminos, Campus de Elviña, 15192 La Coruña, Spain.
[2] Visiting Scientist, Department of Materials Engineering, University of Salamanca, E.P.S. Zamora, Campus Viriato, 49022 Zamora, Spain.

Copyright© 2000 by ASTM International www.astm.org

Experimental

The aim of this paper is to analyze the consequences of fatigue pre-cracking on the posterior stress corrosion behaviour of the high-strength steel. Different zero-to-tension cyclic loading levels were used in the experiments, the key variable being the maximum stress intensity factor at the last stage of the pre-cracking K_{max}, whereas $K_{min} \approx 0$ in all tests. Four different fatigue programs were performed with K_{max}/K_{IC}= 0.28, 0.45, 0.60 and 0.80, where K_{IC} is the standard fracture toughness of the steel in the absence of harsh environment.

A high-strength steel was studied whose chemical composition and mechanical properties are given respectively in Tables 1 and 2. The EAC experiments were SSR tests with pre-cracked specimens in aqueous solution, as described in detail elsewhere [2]. The tests analyzed in this paper were performed at cathodic potentials to evaluate the HAC phenomenon as a key mechanism of EAC. Figure 1 shows the experimental results of the failure load in solution F_{HAC} (divided by the reference value at rupture in air F_C) as a function of the ratio K_{max}/K_{IC}. The mechanical effect of fatigue pre-cracking is beneficial for the HAC resistance of the steel, since the fracture load in aggressive environment is an increasing function of K_{max}.

Table 1 — *Chemical composition (wt %) of the steel.*

C	Mn	Si	P	S	Cr	Ni	Mo
0.74	0.70	0.20	0.016	0.023	0.01	0.01	0.001

Table 2 — *Mechanical properties of the steel.*

Young modulus E (GPa)	Yield strength σ_Y (MPa)	UTS σ_R (MPa)	Fracture toughness K_{IC} (MPam$^{1/2}$)	Ramberg-Osgood $\varepsilon=\varepsilon^e+\varepsilon^p=\sigma/E+(\sigma/P)^n$ I ($\varepsilon^p \leq 1.07$) P_I (MPa)	n_I	II ($\varepsilon^p > 1.07$) P_{II} (MPa)	n_{II}
195	725	1300	53	2120	5.8	2160	17

In the matter of microscopic fracture modes, a special topography associated with hydrogen effects was found in the fractographic analysis: the *tearing topography surface* (TTS), cf [3], so that the size of the TTS region is an indicator of the extension of hydrogen assisted micro-damage. In Figure 2 a plot is given of the TTS depth vs. K_{max}, showing that the fatigue pre-cracking regime also influences clearly the micromechanics of HAC in the steel. The higher the fatigue pre-cracking load, the lower the extension of the TTS domain and, accordingly, the lower the deletereous effect of hydrogen on metal, which is consistent with trend plotted in Figure 1, i.e., the increase of failure load in the hydrogen environment for higher K_{max}-values.

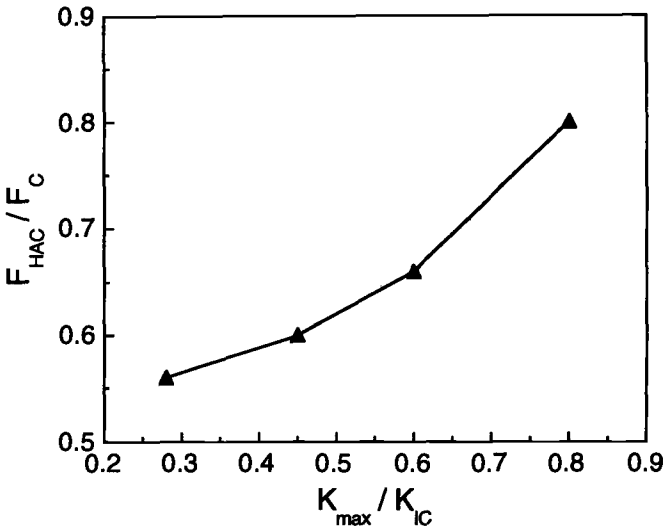


Figure 1 — *SSR test results in terms of respective fracture loads in aggressive (hydrogen) and inert (laboratory air) environments as a function of the maximum stress intensity factor during fatigue pre-cracking* K_{max} (average values, cf. [2]).

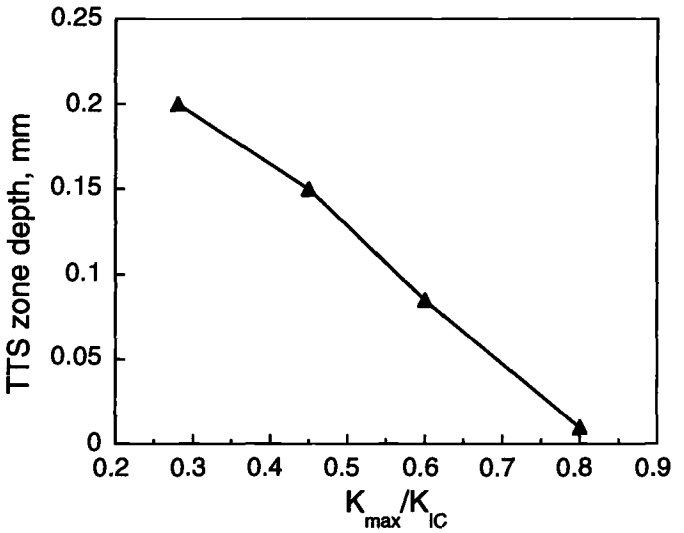


Figure 2 — *Depth of the TTS zone ahead of the crack tip as a function of* K_{max}.

These phenomena may be caused by the development of the cyclic plastic zone and the presence of compressive stresses (cyclic residual stresses) in the vicinity of the crack tip as a consequence of the fatigue pre-cracking procedure. The crack tip is pre-strained (and in a certain sense pre-stressed) by fatigue: the higher the cyclic load level, the more pronounced is the pre-straining/stressing effect, which delays the hydrogen entry into the metal and improves material performance.

To ascertain the mechanical effects of the pre-cracking regime on EAC, it is desired to know the evolution of certain mechanical variables associated with the environmentally assisted cracking processes. The item of primary interest is the stress distribution beyond the crack tip affected by cyclic pre-loading. In particular, hydrostatic stress σ plays a fundamental role in HAC processes driven by stress assisted hydrogen diffusion [*4*].

Mechanical Modelling: Evolution of Near-Tip Stress-Strain Fields

A mechanical approach to the problem of fatigue pre-cracking by cyclic loading in real structural materials is performed by taking into account strain hardening effects in the material and modelling in detail the near-tip area in which the evolution of stress and strain is fundamental. In this section, the effect of fatigue pre-cracking is analyzed by high-resolution numerical modelling of the stress-strain state near the crack tip in a rate-independent elastoplastic material with von Mises yield surface and power-law strain hardening. A combined isotropic-to-kinematic hardening rule is used, which captures the effect of hysteresis loop stabilisation associated with cyclic stress-strain behaviour [*5*]. The mechanical characteristics of the material correspond to the steel used in the experimental program (cf. Table 2).

Stress-strain fields in the close vicinity of the crack tip are known to depend substantially on the crack blunting [*6,7*]. To reveal them, finite deformation analysis of a plane strain crack subjected to mode I (opening) load was performed, confining the study to the small scale yielding situation, which allows a consideration of the stress intensity factor K as the only variable governing the near tip mechanical situation irrespective of a particular geometry of a cracked solid and applied load (cf. [*6,8*]). The crack was modelled as a parallel-sided round-tip slit with initial height (twice the tip radius) $b_0 = 5$ μm, which is in agreement with experimental data reported for fatigue cracks in steels [*9*]. The applied loading history consisted of several (up to ten) zero-to-tension cycles in accordance with two of the experimental fatigue programs, namely, at K_{max}/K_{IC}= 0.45 and 0.80, followed by rising load corresponding to the SSR testing. The nonlinear finite element code MARC [*10*] was used with updated Lagrangian formulation. The modelling peculiarities (solid's geometry, loading, *etc.*) are the same as described elsewhere [*7*]. In particular, after trying several refinements of the finite element mesh near the crack tip, the optimum one was chosen in which the average size of the smallest four-node quadrilateral elements adjacent to the tip was about $0.02b_0$.

Figure 3 shows the evolution of the hydrostatic stress distribution in the plane of the crack beyond the tip, $\sigma = \sigma(x)$, during monotonic loading in the SSR tests after fatigue pre-cracking, where x is the distance from the crack tip in the *deformed configuration* of the solid and thus x=0 represents the crack tip itself, i.e., the surface of the solid which determines the boundary condition for the problem of hydrogen diffusion in the solid. This Figure 3 provides a first insight —based on mechanical considerations— into the consequences of fatigue pre-stressing on the posterior HAC behaviour of the steel. For an intermediate level of externally applied loading in the SSR test (applied K= 0.30 K_{IC}), clear differences may be observed between the two distributions of hydrostatic stress (those associated with fatigue pre-cracking levels of K_{max} = 0.45 and 0.80 K_{IC}), especially in the close vicinity of the crack tip, which implies a different rate of hydrogen transport to prospective fracture nuclei by stress assisted diffusion according to which hydrogen is driven by the hydrostatic stress gradient $d\sigma/dx$ [*4*]. In the case of the

strongest fatigue program (K_{max} = 0.80 K_{IC}) it is seen in Figure 3b that residual stresses remain compressive in an extended area beyond the crack tip and, what is more important, there is a negative gradient of hydrostatic stress $d\sigma/dx<0$ that delays hydrogen diffusion towards the inner points, prevents hydrogen degradation of the material therein, and increases the fracture load in a hydrogen environment.

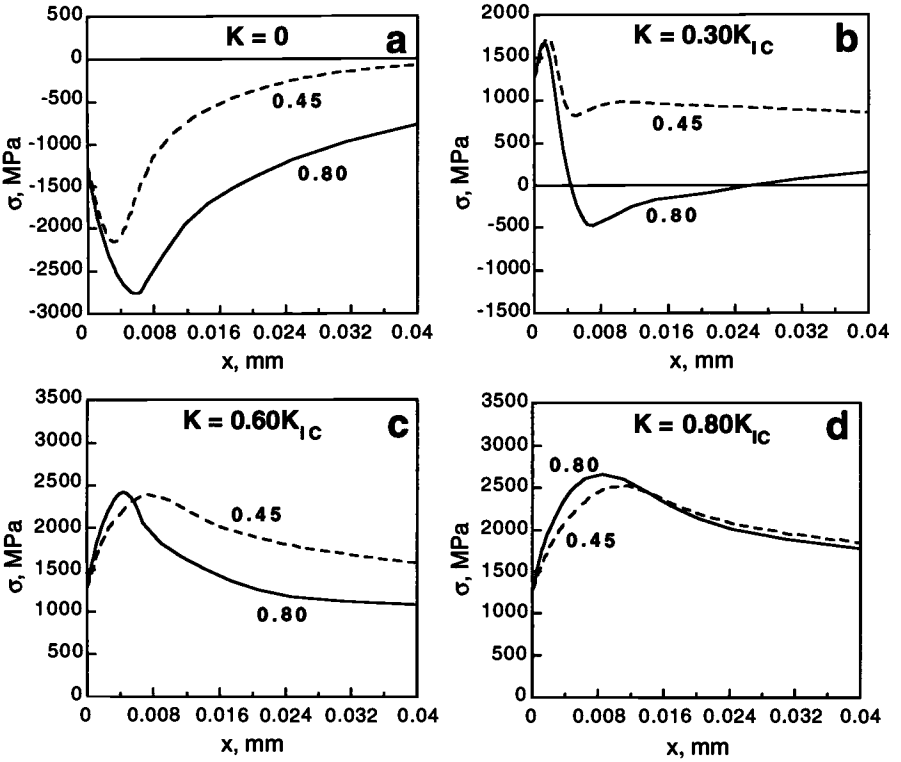


Figure 3 — *Hydrostatic stress distributions ahead of the crack tip during monotonic loading at SSR test after fatigue pre-cracking at K_{max}/K_{IC} = 0.45 (dashed lines) and 0.80 (solid lines) at progressive applied K levels indicated in the figures. The distance x from the crack tip is measured in the deformed configuration and the sequential test instants (load levels) are indicated in the figures in relation to the fracture toughness K_{IC}.*

Another assumption of increasing trapping of hydrogen as a consequence of heavier fatigue pre-cracking is also consistent with the observed beneficial effect of K_{max} on posterior HAC resistance: accumulated mechanical pre-damage in the cyclic plastic zone delays the hydrogen delivery due to an increase of the dislocation density and therefore of the number of potential traps for hydrogen therein [*11*]. Thus the experimental fact of better HAC performance for higher K_{max} (Figure 1) can in part be attributed to this phenomenon of hydrogen trapping. The higher the K_{max}-level, the larger the region of elevated density of traps and the lower the hydrogen permeation rate.

Hydrogen Diffusion Modelling: Evolution on Near-Tip Concentration Distributions

A chemical approach to the problem is performed by numerical modelling of hydrogen diffusion in the vicinity of the deformed crack tip. This section of the paper includes the theoretical fundamentals of the phenomenon (diffusional theory of HAC) and the numerical approach to it (finite element formulation of hydrogen diffusion).

Theoretical Fundamentals: Diffusional Theory of HAC

Hydrogen effect on fracture depends on its amount in prospective rupture sites represented by the value of its volume concentration C which is provided there by hydrogen diffusion from external (environmental) or internal (residual hydrogen) sources. Local rupture occurs when in a relevant material element (cell, or "grain", or whichever point of interest) the concentration achieves the critical value C_{cr} determined, in general [*12,13*], by the principal components of stresses and (plastic) strains, respectively, σ_i and ε_i (i = 1,2,3)

$$C_{cr} = C_{cr}(\sigma_i, \varepsilon_i) \tag{1}$$

The crack situated along the x-axis is supposed to grow provided hydrogen concentration accumulated with time t in a certain responsible location at $x = x_c$ attains the critical level corresponding to the instantaneous stress intensity factor $K(t)$

$$C(x_c,t) = C_{cr}(K(t), x_c) \tag{2}$$

where the value of x_c must be defined associated with the concept of the responsible material cell, i.e., with the worst material unit, weak grain, fixed microstructural length, or other [*4, 12-16*].

Local rupture repeatedly occurs whilst concentration of accumulated hydrogen $C(x,t)$ can satisfy the criterion (2) after finite diffusion times Δt. Then the crack advances by its size increments Δa which render macroscopic crack growth rate $v = \Delta a/\Delta t$. Impossibility to fulfil the criterion (2) with a certain K value at finite time means crack arrest (v = 0). This is associated with the steady-state (obviously, equilibrium) hydrogen concentration distribution in metal $C_\infty(K,x)$ attained at $t \to \infty$. C_∞ defines the extreme hydrogenation at a given stress intensity factor. Then, using this steady-state solution $C_\infty(K,x)$ in the criterion (2), this latter yields the equation to find the upper limit of K with which crack growth rate v= 0. Thus, C_∞ determines the threshold stress intensity factor value K_{IHAC} for the phenomenon of HAC.

The driving force X_D for diffusion is derived as [*12,17*]

$$X_D = -\nabla\left(RT \ln \frac{C}{K_S}\right) \tag{3}$$

where R is the universal gas constant, T the absolute temperature and K_S the solubility. The coefficient of diffusion of hydrogen in metal D defines its mobility equal to D/RT, which together with the driving force (3) yield the diffusion flux $\mathbf{J}$ of hydrogen in metal

$$\mathbf{J} = \frac{D}{RT} C X_D \tag{4}$$

The solubility K_S and the diffusivity D are known to depend on alloy and on density of hydrogen traps in metal lattice [*11*]. Trap density and, in certain alloys, their phase

composition, e.g., like martensite formation in austenitic steels [*18,19*], both depend on plastic deformation, which may be incorporated in terms of the effective plastic strain ε_p [*20*]. In addition, K_S depends on the hydrostatic stress σ and finally is given by [*12,20*]

$$K_S(\sigma, \varepsilon_p, T) = K_{S\varepsilon}(\varepsilon_p, T) \exp(\Omega\sigma) \quad \text{with } \Omega = \frac{V_H}{RT} \tag{5}$$

where $K_{S\varepsilon}$ is the strain-only dependent component of solubility and V_H the partial molar volume of hydrogen in metal. According to eqs. (3)-(5), the gradients of both ε_p and σ turn out to be the governing factors of hydrogen diffusion.

Assuming constant temperature in the system, from eqs. (3)-(5) one can write

$$\mathbf{J} = -D(\varepsilon_p)\left\{\nabla C - C\left[\nabla(\Omega\sigma) + \frac{\nabla K_{S\varepsilon}(\varepsilon_p)}{K_{S\varepsilon}(\varepsilon_p)}\right]\right\} \tag{6}$$

Adopting material (Lagrangian) description of the medium, and referring the equations to the current configuration of a deformed material volume which at time t instantaneously occupies a certain spatial domain ${}_tV$, the obvious consideration of mass balance [*21*] with the flux defined by expression (6) leads to the equation of stress-strain assisted diffusion (cf. [*12,17*])

$$\frac{\partial C}{\partial t} = D\left[\nabla^2 C - \mathbf{M}\bullet\nabla C - NC\right] + \nabla D \bullet \left[\nabla C - \mathbf{M}C\right] \tag{7}$$

where vector and scalar coefficients, respectively, are

$$\mathbf{M} = \nabla \ln K_S \tag{8}$$

$$N = \nabla^2 \ln K_S \tag{9}$$

For most applications where the hydrogen environment effect on crack growth is of interest, hydrogen entry conditions may be characterised by the equilibrium value of concentration on metal surface C_Γ [*12,17*]. Then, with account for relation (5), the boundary condition for diffusion is

$$C_\Gamma = C_0 K_{S\varepsilon}(\varepsilon_p(\Gamma)) \exp(\Omega\,\sigma(\Gamma)) \tag{10}$$

where C_0 is the equilibrium hydrogen concentration provided by the environment in the bare metal (free of stress and plastic strain).

For solids under conditions of uniform environmental hydrogen activity characterised by an equilibrium concentration value $C_0 = const$, it is easy to get the exact *steady-state solution* of eq. (7) of stress-strain assisted diffusion which is asymptotically attained at $t \to \infty$. This corresponds to the equilibrium state when the diffusion flux (6) is zero or, equivalently, when the diffusion driving force (3) is null. This is provided when $C/K_S = const$. Then the steady-state solution is the following

$$C_\infty(K,x,y) = C_0 K_{S\varepsilon}(\varepsilon_p(K,x,y)) \exp(\Omega\,\sigma(K,x,y)) \tag{11}$$

With $\varepsilon_p = 0$, $K_{S\varepsilon} = 1$ and the last expression coincides with the well known one for stress-only driven concentration [*4*].

Numerical Approach: Finite Element Formulation of the Hydrogen Diffusion Problem

With regard to near-tip hydrogen diffusion, accounting for large deformations of the body is essential since they notably change diffusion distances in the zone of interest. The standard weighted residual process [22] to build up the finite element approximation to the initial-boundary value problem (7)-(10) is performed in material (Lagrangian) coordinates taking as the reference one the instantaneous deformed configuration of the solid occupying at the moment t the volume ${}_tV$ bounded by the surface ${}_tS$. In brief, following the Galerkin process for the continuum discretized into a finite element mesh, where the same shape functions family $\{{}_tW_m(x,y);\ m = 1,2,...M\}$, M being the number of nodes, plays the role of both the trial and the weighting functions, the weak form of the weighted residual statement of the problem for any t yields the system of equations with respect to the array of the nodal concentration values $\{C_m(t);\ m = 1,2,...M\}$ as

$$ {}_t\left[\mathbb{M}_{i,j}\right]\left\{\frac{dC_j}{dt}\right\} + {}_t\left[\mathbb{K}_{i,j}\right]\ \{C_j\} = {}_t\{F_i\}\quad (i,j = 1,...,M) \tag{12} $$

where the components of the respective matrices are

$$ {}_tM_{i,j} = \int_{{}_tV} {}_tW_i\ {}_tW_j\ \ dV \tag{13} $$

$$ {}_tK_{i,j} = \int_{{}_tV} D\left\{\nabla\, {}_tW_i \bullet \nabla\, {}_tW_j\ - \left[\left(\frac{V_H}{RT}\nabla\sigma(t) + \frac{\nabla K_{s0}\left(\varepsilon_p(t)\right)}{K_{s0}\left(\varepsilon_p(t)\right)}\right)\bullet \nabla\, {}_tW_j\right] {}_tW_i\right\} dV \tag{14} $$

and for the column in the right-hand part we have

$$ {}_tF_i = -\,J_S \int_{{}_tS_f} {}_tW_i\ \ dS \tag{15} $$

which arises in order to prescribe the flux of hydrogen J_S on the part ${}_tS_f$ of the surface ${}_tS$.

For a given loading history in terms of the applied stress $\sigma_{app}(t)$, or equivalently, stress intensity factor variation $K(t)$, the deformation displacements together with the stress and strain components involved in the diffusion modelling are provided by the MARC finite element code as nodal values after solution of the elastoplastic boundary-value problem. In the implementation of the diffusion problem, they were approximated using the same shape functions family $\{{}_tW_m\}$. The time-domain Galerkin procedure [22] was applied for integration of the finite element equations system (12).

The results of the large-deformation elastoplastic stress-strain field simulations considered in the previous paragraphs (cf. Figure 3) were taken as the input data. Diffusion modelling was performed in one-dimensional (1D) approximation along the x-axis or crack line, as described elsewhere [23]. The calculations were performed for an ambient temperature $T = 293$ K. The following data were considered in the computations [4,11,14]: $V_H = 2{\cdot}10^{-6}$ m^3/mol and $D = 10^{-12}$ m^2/s. The applied loading rate in modelling the rising load SSR tests was taken to be $dK/dt = 0.25$ MPa·m$^{1/2}$/s. The results of the diffusion calculations, shown in Figure 4, are valid for whichever particular value of D provided the loading rate is adjusted to maintain the constant ratio $D/(dK/dt)$, as it

follows from the similitude criteria for the transport eq. (7), so that availability of the exact value of D for the steel under consideration is not a crucial matter. Analysis of the diffusion was performed during the rising load phase from $K = 0$ after pre-cracking to $K = K_{IC}$, i.e., during the diffusion time $t_R = K_{IC}/(dK/dt)$.

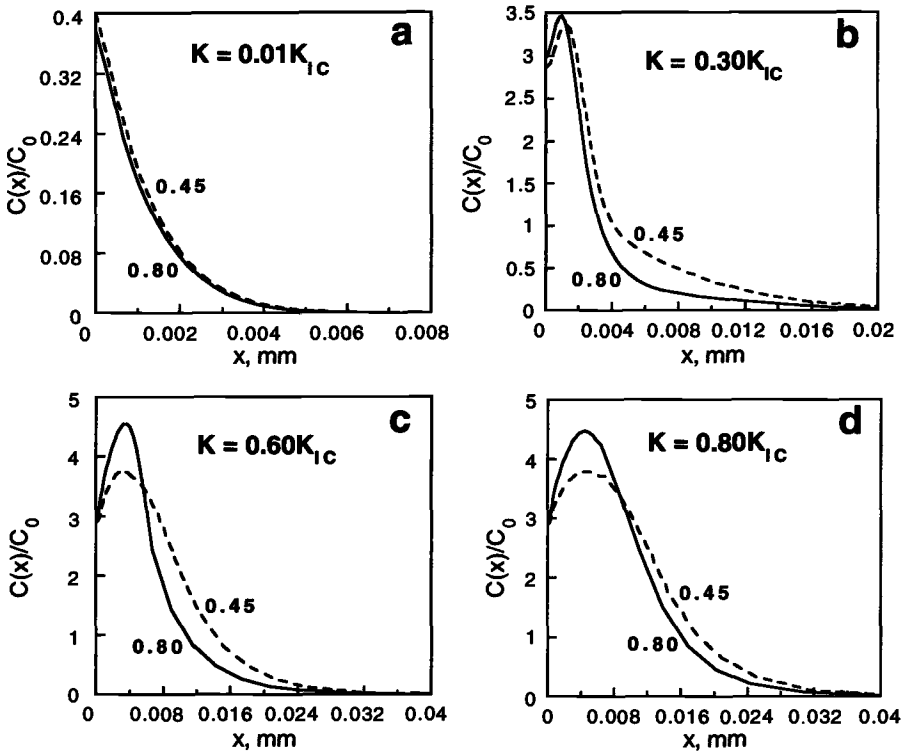


Figure 4 — *Hydrogen concentration distributions ahead of the crack tip during constant-rate monotonic loading at SSR test after fatigue pre-cracking at* $K_{max}/K_{IC} = 0.45$ *(dashed lines) and 0.80 (solid lines) at progressive applied K levels indicated in the figures. The distance x from the crack tip is measured in the deformed configuration and the sequential test instants (load levels) are indicated in the figures in relation to the fracture toughness* K_{IC}.

The generated numerical results about crack tip hydrogen diffusion presented in Figure 4 and complementary stress evolution data in Figure 3 show that in the very close vicinity of the entry surfaces $x \leq 2...4$ μm the concentration patterns $C(x,t)$ for fixed diffusion times t (or applied load levels $K = dK/dt \cdot t$) are quite similar to the respective stress profiles $\sigma(x)$, so that the steady-state equilibrium concentration is approximately achieved at this depths under the tried loading rate. In deeper material points, a more or less significant delay of hydrogenation due to heavier fatigue pre-cracking is observed.

Discussion

Mechanical Aspects

To analyze the results of the SSR tests on the basis of the performed simulation of the crack tip mechanics, it is useful to obtain the critical value of the stress intensity factor for HAC to proceed, K_{QHAC}, from the ratio of the failure load in hydrogen F_{HAC} to the failure load in air F_C (Figure 1) as follows

$$K_{QHAC} = \frac{F_{HAC}}{F_C} K_{IC}(\text{air}) \tag{16}$$

K_{QHAC} may be considered as an upper bound estimate for the threshold stress intensity factor K_{IHAC}. Neglecting subcritical crack growth the two values are the same, and in this case the fracture initiation coincides with the final fracture instant.

The stress-dependent component of the flux (6) provides acceleration of hydrogen diffusion towards the sites of maximum hydrostatic stress and delays it if negative stress gradient $\nabla\sigma < 0$ is met along the penetration path. Considering the evolutions of stress-patterns ahead of the blunting crack tip during rising load SSR tests after various pre-cracking histories (Figure 3), it follows that heavier pre-cracking produces higher residual compressive stress and more negative stress gradient persisting over greater depth ahead of the crack tip during longer portion of the rising-load path or loading time under constant-rate loading, which are both represented by the K/K_{IC} ratio. This way, higher K_{max} during pre-cracking delays crack tip hydrogenation in the rising load SSR tests and improves resistance against hydrogen assisted fracture. This is consistent with the fundamental experimental fact displayed in Figure 1 of HAC behaviour improvement by heavier pre-cracking regimes.

From Figure 3 it follows that the paths of the hydrostatic stress extremum near the crack tip $\sigma^+ = \max\{\sigma(x), x > 0\}$ corresponding to monotonic load route after different pre-cracking regimes K_{max} should proceed too close to each other, so that the maximum value of σ cannot be a cause of the notable effect of pre-cracking on HAC through its influence on diffusion. On the other hand, at the initial stages of the SSR tests (applied $K \lesssim 0.40K_{IC}$) when the local minima of stress $\sigma^- = \min\{\sigma(x), x > 0\}$ still exists in the process zone, the value of $\sigma^-(K)$ goes substantially lower for the pre-cracking at $K_{max2} = 0.80K_{IC}$ than after fatigue at $K_{max1} = 0.45K_{IC}$ (cf. Figure 3). This K_{max}-controlled compression, which produces underdevelopment of tensile hydrostatic stresses, persists over the zone of interest during a considerable portion of a SSR test, which provides a reason for the delay of the near-tip hydrogen accumulation by stress assisted diffusion as a consequence of a more severe pre-cracking program.

As a summary of the discussion on mechanical aspects reflected in the hydrostatic stress profiles plotted in Figure 3, it is possible to say that, during the monotonic loading at the SSR tests in the range $0 \le K \le K_{QHAC}$, the near-tip stress field due to the milder fatigue regime $K_{max} = 0.45K_{IC}$ provides higher hydrogenation of the deeper material cells, whereas the very-near surface region is under the effect of the more elevated stresses arising under heavier pre-cracking procedure $K_{max} = 0.80K_{IC}$.

Chemical Aspects

The equations of *stress-and-strain* assisted diffusion of hydrogen (6)-(7) may be simplified by neglecting the spatial variability of the solubility K_S and of the diffusivity D which are in general dependent on the equivalent plastic strain ε_p, i.e., taking K_S and D as some constant averaged values of $K_S(\varepsilon_p)$ and $D(\varepsilon_p)$ over the zone of interest. It is acceptable as the first approximation, since dislocations and other trap density which

affect hydrogen solubility and mobility attain a certain *saturation level* with rising plastic strain [*24*]. Thus the terms with ∇K_S and ∇D are omitted and eqs. (6) and (7) yield those for *stress-only* assisted diffusion

$$\mathbf{J} = -D\nabla C + DC\Omega\nabla\sigma \tag{17}$$

$$\frac{\partial C}{\partial t} = D\ [\nabla^2 C - \mathbf{M}\bullet\nabla C - NC] \tag{18}$$

The boundary condition condition for diffusion (10) and the equilibrium concentration of hydrogen (11) have an exponential dependence on hydrostatic stress σ. In the 1D case analyzed here they take respectively the form

$$C_\Gamma = A\ e^{\Omega\sigma(\Gamma)} \tag{19}$$

$$C_\infty(x) = A\ e^{\Omega\sigma(x)} \tag{20}$$

According to the results of the near-tip stress-strain field analysis displayed in Figure 3, the evolution of $\sigma(\Gamma)$ during monotonic loading after fatigue pre-cracking is fairly insensitive to K_{max} and the same applies for the boundary condition (19). On the other hand, eq. (20) indicates that the shapes of the hydrostatic stress distributions $\sigma(x)$ in a certain near-tip domain $x > 0$ are important for the crack tip hydrogenation. During load rise in the SSR test up to intermediate levels of applied $K \approx 0.30K_{IC}$, Figure 3 shows substantial differences in the close vicinity of the crack tip between the two distributions of the hydrostatic stress associated with fatigue pre-cracking levels of $K_{max}/K_{IC} = 0.45$ and 0.80. These distinctions imply different rates of hydrogen transport to prospective fracture nuclei by stress assisted diffusion flux (17) driven along the x-axis by the hydrostatic stress gradient $\partial\sigma/\partial x$.

In particular, it is seen in Figures 3a and 3b that, until $K/K_{IC} \approx 0.30$, notably more negative values of both the stress $\sigma < 0$ and its gradient $\partial\sigma/\partial x < 0$ persist ahead of the crack tip for the heavier fatigue program $K_{max} = 0.80K_{IC}$ than those for $K_{max} = 0.45K_{IC}$. This enhances hydrogen diffusion towards the fracture nuclei in the interior according to eq. (18) and explains the different hydrogen concentration profiles obtained in Figures 4a and 4b for $K_{max}/K_{IC} = 0.45$ and 0.80.

Micromechanics of HAC

From the micromechanical point of view, a relevant observation in Figure 3d is that the depth of maximum hydrostatic stress is about 8 μm at the fracture instant $K_{QHAC} = 0.8K_{IC}$ corresponding to the pre-cracking at $K_{max}/K_{IC} = 0.80$, so that such a distance is approximately the same as the respective TTS depth (cf. Figure 2). Therefore, the *theoretical* distance over which the stress field favours hydrogen diffusion is close to the *real physical* dimension of the hydrogen-assisted micro-damaged region. Considering the stress distribution corresponding to the hydrogen assisted fracture event after pre-cracking at $K_{max}/K_{IC} = 0.45$, i.e., for $K_{QHAC} = 0.6K_{IC}$ shown in Figure 3c, the position of maximum hydrostatic stress at fracture turns out to be fairly the same: 8μm in this case too, i.e., $x_{\sigma+}(K_{QHAC}) \approx 8$ μm for both K_{max}. It is confirmed by the stress distributions at load levels when HAC occurs after different pre-cracking regimes: at $K_{QHAC1} = 0.60K_{IC}$ for $K_{max1}/K_{IC} = 0.45$ in Figure 3c, and at $K_{QHAC2} = 0.80K_{IC}$ for $K_{max2}/K_{IC} = 0.80$ in Figure 3d. This draws the supposition that this specific dimension represents some microstructural scale of the local fracture process: the size of a material unit cell or grain that must be hydrogenated in order to advance HAC by one step.

In addition, since the axial σ_{yy} and the hydrostatic σ stresses have their maxima approximately at the same material point, this yields the same location of possible fracture initiation site x_c assuming that a critical stress criterion of local fracture is operative, $x_c = x_\sigma + (K_{QHAC}) = 8$ μm, which again suggests that the distance x_c might be a relevant microstructure scale of local rupture events in HAC.

On the basis of these facts, the role of the fatigue pre-cracking on HAC initiation, which is attributed to the the post-cycling residual stresses near the crack tip, may be examined through concentration evolution data just at the afore-said critical location x_c. Although it may be observed in the plots of Figure 4, the patterns of concentration $C(x_c,t)$ in Figure 5 provide a better resolution of the effect. They confirm a notable delay of hydrogenation of the responsible material unit at x_c just in the domain of interest $K_{QHAC} < K_{IC}$ due to residual stresses produced by the heavier fatigue pre-cracking regime.

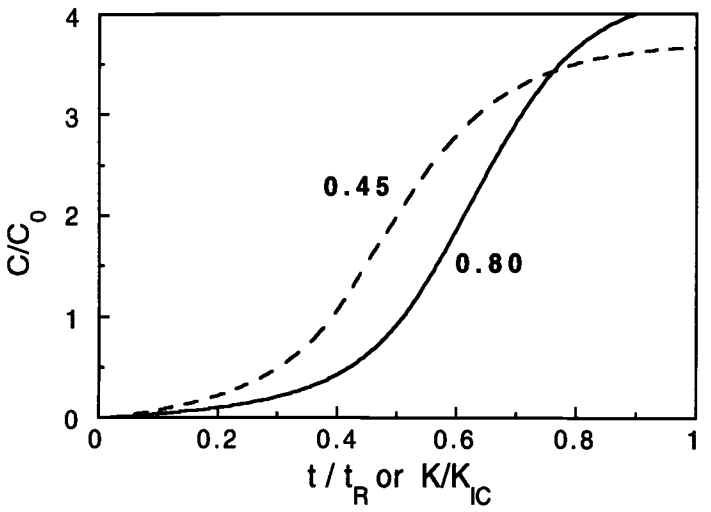


Figure 5 — *Evolutions of the hydrogen concentration at the prospective fracture loci near the crack tip x_c = 8 μm during the constant-rate rising load SSR tests after pre-cracking regimes at K_{max}/K_{IC} = 0.45 (dashed line) and 0.80 (solid line). In this plot t_R represents the diffusion time $t_R = K_{IC}/(dK/dt)$.*

Conclusions

Cyclic accumulation of plastic strain and creation of the domain of compressive residual stresses improve the HAC behaviour through the increase of the failure load in aggressive environment by delaying the entry of hydrogen into the fracture process zone near the crack tip due to the existence of negative gradients of hydrostatic stress in the vicinity of the crack tip in the most severe fatigue pre-cracking program.

From the mechanical point of view, the numerical results of a high-resolution elastic-plastic finite element analysis show that hydrostatic stress distributions depend markedly on the fatigue pre-cracking level K_{max}, and this dependence is stronger at the first stages of the monotonic load phase associated with the SSR test during which the heaviest fatigue program produces compressive residual stresses in the near-tip area.

The depth of the maximum hydrostatic stress point at the fracture instant coincides with the size of the region affected by the hydrogen at the microscopical level. Therefore, the theoretical distance over which the stress field favours hydrogen diffusion is close to the real physical dimension of the hydrogen-assisted micro-damaged region detectable by scanning electron microscopy in the form of a special topography (TTS).

Since the axial and the hydrostatic stresses have their maxima approximately at the same material point, the depth of the maximum tensile (or hydrostatic) stress should be a relevant microstructure scale to mark the prospective fracture loci. This idea is consistent with the previous conclusion based on micromechanics of HAC after fractographic analysis of the broken specimens.

From the chemical point of view, the results of stress assisted hydrogen diffusion computations show that hydrogen accumulation in the vicinity of the crack tip also depends on previous cyclic loading, the effects being clearly detectable in the prospective fracture loci associated with the maximum tensile (and hydrostatic) stress or, accordingly, with the hydrogen-assisted micro-damage region.

Acknowledgments

The financial support of this work by the Spanish CICYT (Grant MAT97-0442) and *Xunta de Galicia* (Grant XUGA 11802B97) is gratefully acknowledged. In addition, the authors wish to express their gratitude to EMESA TREFILERIA S.A. (La Coruña, Spain) for providing the steel used in the experimental program.

References

[1] Judy, R.W., Jr., King, W.E., Jr., Hauser II, J.A., and Crooker, T.W., "Influence of Experimental Variables on the Measurement of Stress Corrosion Cracking Properties of High-Strength Steels," *Environmentally Assisted Cracking: Science and Engineering, ASTM STP 1049*, W.B. Lisagor, T.W. Crooker and B.N. Leis, Eds., American Society for Testing and Materials, Philadelphia, 1990, pp. 410-422.

[2] Toribio, J. and Lancha, A. M., "Overload Retardation Effects on Stress Corrosion Behaviour of Prestressing Steel," *Construction and Building Materials*, Vol. 10, 1996, pp. 501-505.

[3] Toribio, J., Lancha, A. M., and Elices, M. "Characteristics of the New Tearing Topography Surface," *Scripta Metallurgica et Materialia*, Vol. 25, 1991, pp. 2239-2244.

[4] Van Leeuwen, H. P., "The Kinetics of Hydrogen Embrittlement: A Quantitative Diffusion Model," *Engineering Fracture Mechanics*, Vol. 6, 1974, pp. 141-161.

[5] Suresh, S., *Fatigue of Materials*, Cambridge University Press, Cambridge, 1991.

[6] McMeeking, R. M., "Finite Deformation Analysis of Crack-Tip Opening in Elastic-Plastic Materials and Implications for Fracture," *Journal of the Mechanics and Physics of Solids*, Vol. 25, 1977, pp. 357-381.

[7] Toribio, J. and Kharin, V., "High-Resolution Numerical Modelling of Stress-Strain Fields in the Vicinity of a Crack Tip Subjected to Fatigue," *Fracture From Defects (ECF12)*, M.W. Brown, E.R. de los Ríos and K.J. Miller, Eds., EMAS, West Midlands, 1998, pp. 1059-1064.

[8] Kanninen, M. F. and Popelar, C. H., *Advanced Fracture Mechanics*, Oxford University Press, New York , 1985.

[9] Handerhan, K. J. and Garrison, W. M., Jr., "A Study of Crack Tip Blunting and the Influence of Blunting Behavior on the Fracture Toughness of Ultra High Strength Steels," *Acta Metallurgica et Materialia*, Vol. 40, 1992, pp. 1337-1355.

[10] *MARC User Information*, Marc Analysis Research Corporation, Palo Alto, 1994.

[11] Hirth, J. P., "Effects of Hydrogen on the Properties of Iron and Steel," *Metallurgical Transactions*, Vol. 11A, 1980, pp. 861-890.
[12] Toribio, J. and Kharin, V., "Evaluation of Hydrogen Assisted Cracking: The Meaning and Significance of the Fracture Mechanics Approach," *Nuclear Engineering and Design*, Vol. 182, 1998, pp. 149-163.
[13] Panasyuk, V. V., Andreikiv, A. Ye. and Kharin, V. S., "Model of Crack Growth in Deformed Metals under the Action of Hydrogen," *Soviet Materials Science*, Vol. 23, 1987, pp. 111-124.
[14] Gerberich, W. W., Chen, Y. T., and John, C. St., "A Short-time Diffusion Correlation for Hydrogen-induced Crack Growth Kinetics," *Metallurgical Transactions*, Vol. 6A, 1975, pp. 1485-1498.
[15] Panasyuk, V. and Kharin, V., "The Influence of Hydrogenating Environments on Crack Propagation in Metals," *Environment Assisted Fatigue*, P. Scott and R.A. Cottis, Eds., Mechanical Engineering Publications, London, 1990, pp. 123-144.
[16] Kharin, V. S. "Crack Growth in Deformed Metals under the Action of Hydrogen," *Soviet Materials Science*, Vol. 23, 1987, pp. 348-357.
[17] Toribio, J. and Kharin, V., "*K*-dominance Condition in Hydrogen Assisted Cracking: The Role of the Far Field," *Fatigue and Fracture of Engineering Materials and Structures*, Vol. 20, 1997, pp. 729-745.
[18] Itatani, M., Miyoshi, Y., and Ogura, K. C., "A Numerical Analysis of Hydrogen Concentration at the Crack Tip in Austenitic Stainless Steel," *Journal of the Society of Materials Science Japan*, Vol . 40, 1991, pp. 1079-1085.
[19] Perng, T. P. and Altstetter, C. J., "Effects of Deformation on Hydrogen Permeation in Austenitic Stainless Steels," *Acta Metallurgica*, Vol. 34, 1986, pp. 1771-1781.
[20] Kronshtal, O. and Kharin, V., "Influence of Material Inhomogeneity and Variation of Temperature on Hydrogen Diffusion as a Risk Factor of Enhancement of Metals Hydrogen Degradation," *Soviet Materials Science*, Vol. 28, 1992, pp. 475-486.
[21] Malvern, L.E., *Introduction to the Mechanics of a Continuous Medium*, Prentice Hall, Englewood Cliffs, 1969.
[22] Zienkiewicz, O.C. and Morgan, K., *Finite Elements and Approximation*, John Wiley and Sons, New York, 1983.
[23] Toribio, J. and Kharin, V., "Role of Fatigue Crack Closure Stresses in Hydrogen Assisted Cracking. *Advances in Fatigue Crack Closure Measurement and Analysis: Second Volume, ASTM STP 1343*, R.C. McClung and J.C. Newman, Jr., Eds., American Society for Testing and Materials, West Conshohocken, PA, 1999, pp. 440-458.
[24] Kummick, A. J. and Johnson, H. H., "Deep Trapping States for Hydrogen in Deformed Iron," *Acta Metallurgica*, Vol. 28, 1980, pp. 33-39.

Ian de Curiere,[1] Bernard Bayle,[2] and Thierry Magnin[3]

Improvement of Stress Corrosion Cracking (SCC) Resistance by Cyclic Pre-Straining in FCC Materials

Reference: de Curiere, I., Bayle, B., and Magnin, T., **"Improvement of Stress Corrosion Cracking (SCC) Resistance by Cyclic Pre-Straining in FCC Materials,"** *Environmentally Assisted Cracking: Predictive Methods for Risk Assessment and Evaluation of Materials, Equipment, and Structures, ASTM STP 1401,* R. D. Kane, Ed., American Society for Testing and Materials, West Conshohocken, PA, 2000.

Abstract : Improving the materials resistance to SCC has become a topic of wide interest for theoretical, engineering and financial reasons. The aim of this paper is to propose a process to delay the SCC damage. Recent studies of 316L austenitic stainless steel in boiling $MgCl_2$ solutions show an improvement in SCC resistance by cyclic pre-straining in low cycle fatigue [1]. This improvement consists of an increase in both strain to failure and crack initiation strain, during Slow Strain Rate Tensile (SSRT) tests in aqueous solution.

This paper analyses the effect of pre-fatigue in 316L and copper on their mechanical and electrochemical responses to better understand the delay of SCC damage in boiling $MgCl_2$ and nitrite, respectively.

The explanation for this beneficial effect is related to a modification of both surface electrochemical reactions kinetics and corrosion/plasticity interactions at the crack tip, due to the particular fatigue dislocation structure.

Keywords : SCC, low cycle fatigue, SCC damage delay, surface layers, dislocation structure, electrochemical noise analysis.

[1] Ph.D student, Département MPI, centre SMS, URA CNRS 1884, Ecole Nationale Supérieure des Mines de Saint-Etienne, 158 cours FAURIEL, 42023 Saint-Etienne cedex2, FRANCE

[2] Research Engineer, Département MPI, centre SMS, URA CNRS 1884, Ecole Nationale Supérieure des Mines de Saint-Etienne, 158 cours FAURIEL, 42023 Saint-Etienne cedex2, FRANCE

[3] Professor, Département MPI, centre SMS, URA CNRS 1884, Ecole Nationale Supérieure des Mines de Saint-Etienne, 158 cours FAURIEL, 42023 Saint-Etienne cedex2, FRANCE

Copyright© 2000 by ASTM International www.astm.org

Introduction

Resistance to Stress-Corrosion Cracking (SCC) in FCC materials is widely discussed and many models have been proposed in the last ten years. For a review, see [2]. Most of them rely to the corrosion-deformation interactions concept.

Recently, a systematic study on the effect of pre-straining conditions on the SCC behaviour of 316L austenitic stainless steel in a boiling $MgCl_2$ solution at 117°C (30 % weight) [1] has shown that (i) a tensile pre-straining is deleterious for SCC damage during SSRT tests ; (ii) in contrast, a cyclic pre-straining can delay crack initiation and crack propagation and seems to be a very interesting way to improve SCC resistance.

The aim of this paper is to analyse such improvement in terms of mechanisms through the Corrosion Enhanced Plasticity Model (CEPM) developed some years ago by one of the authors [3]. In particular the conditions of pre-cycling will be analysed. It will be shown that only pre-cycling to stress saturation improves the SCC resistance of both 316L in 117°C $MgCl_2$ and Cu in nitrite.

Experimental Process

Two different material/environment couples were tested in this study : 316L austenitic stainless steel in 117°C $MgCl_2$ (30 % weight) solution and copper in 1M $NaNO_2$ solution at a pH of 9.

Square samples (4mm width and 12 mm gauge length) were used for SSRT tests, at a constant applied elongation rate of $4x10^{-7}s^{-1}$ for 316L and $2x10^{-7}s^{-1}$ for copper.

After mechanical polishing, specimens were pre-strained by low cycle fatigue under plastic strain control in tension-compression, at an applied plastic strain amplitude of 10^{-3} for 316L and for Cu. According to the number of cycles, specimens are then tested in SCC without any further polishing. At an applied plastic amplitude of 10^{-3}, for 316L, the cyclic stress increases, till a saturation for N = 50 cycles [3]. For the parameters used for the fatigue of copper, the cyclic stress increases, till a plateau for 1400 cycles. 1400 cycles are applied to reach the saturation plateau.

The electrochemical potentials are measured with respect to an Ag/AgCl electrode for reasons of temperature resistance, for 316L, and with respect to a saturated Calomel electrode, for copper. All the collected transients are analysed by electrochemical noise method, including chaos analysis. This method has been shown to be relevant to quantify another kind of localised corrosion, pitting corrosion [4].

Complementary tests of the post-fatigue surface strain state formed appeared relevant to explain the beneficial effect of pre-fatigue at saturation. These analyses were made by SEM technique.

Results

Evolution of the tensile properties and the corresponding electrochemical potentials.

Figure 1 shows the stress-strain curves for the SSRT SCC tests of the 316L alloy in 117°C in $MgCl_2$ according to the number of cycles during pre-fatigue. Corresponding evolutions of the corrosion potentials during such tests are illustrated in figure 2.

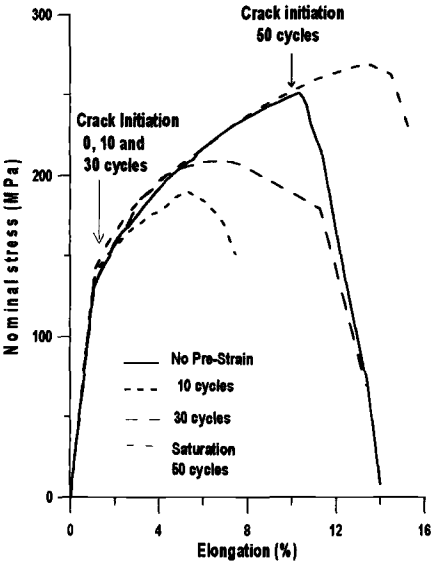


Figure 1 : *Stress-strain curves for the various SCC tests - 316 L in 117°C $MgCl_2$ boiling*

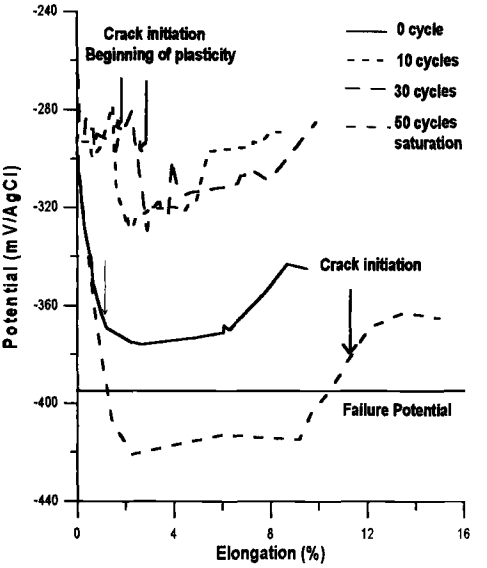


Figure 2 :*Evolutions of the rest potentials*

The following observations can be made :

- Only pre-fatigue at saturation (50 cycles at 10^{-3}) has a beneficial effect on SCC behaviour. Crack initiation resistance increases, as shown on Figure 1. *We shall see in the discussion that crack propagation also decreases.*
- Conversely, cyclic pre-straining can have a deleterious effect on SCC resistance when the number of cycles is less than the one for stress saturation, i.e ,10 and 30 cycles for our applied plastic strain. Cracks initiate earlier and propagate faster than in the case of no pre-cycling, as it will be discussed later on.
- Looking at the evolution of the corrosion potentials during SCC tests, it clearly appears that pre-cycling to saturation allows the potential to decrease below the critical for SCC initiation [5]. This is the potential under which no SCC damage can be noticed.

Samples pre-fatigued before saturation are in fact subject to strong dissolution effects at potentials higher than the above critical potential.

What we define as crack initiation corresponds to the connection between microscopic observations of the specimen surface and corrosion potentials instabilities (indicated by arrows on figure 1 and 2). Indeed, during the first stages, potentials fall down and stabilise. For specimens pre-cycled before saturation (i.e., 0 10 and 30 cycles) the formation of first visible cracks coincide with the stabilisation of the potential above the critical one. Such a correlation is used to detect crack initiation.

Fatigue at saturation leads to delay the crack initiation time and to decrease the crack growth velocity. A beneficial effect is also found on copper single crystals in 1M $NaNO_2$ at pH=9, as shown on Figure 3 [6]

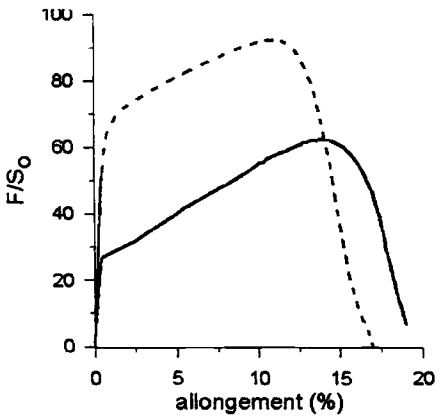


Figure 3 : *Stress-strain curves for a <1 1 0> Cu single crystal in 1M NaNO2 pH 9 solution. [6]. Beneficial effect of pre-fatigue at saturation (non-continuous curve corresponds to pre-fatigued specimen and continuous to non pre-fatigued specimen).*

One can notice a few points

(i) The stress level at which SCC occurs is much higher for a pre-fatigued specimen, even if the strain to failure is quite similar to non-pre-strained ones. The energy to rupture, i.e. the area under the stress-strain curves, increases due to beneficial pre-fatigue to saturation.

(ii) The initial increase of the yield strength due to pre-fatigue partly explains the beneficial effect of pre-fatigue. Cracks initiate at the yield strength by dissolution along slip bands, but at much higher stresses.

Fracture Analysis.

SEM analysis in 316L samples after 10 cycles of pre-straining shows that : (i) cleavage-like fracture is generally observed as for non pre-cycled specimen [7], and (ii) a transition from trans to intergranular is more marked. The figure 4 illustrates such a transition.

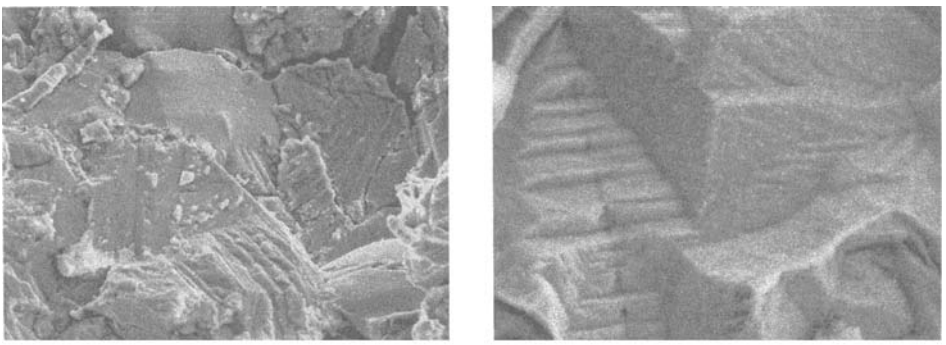


Figure 4 : *Micro-cracks and fracture facies of a 316L sample pre-cycled at 10 cycles before a SCC SSRT test. Illustration of a trans-intergranular transition.*

Such intergranular cracking is promoted by SCC tests for pre-hardened samples, whatever the pre-hardening conditions [7]. It has been related to higher local stresses at the crack tip and to a faster access to a critical stress intensity factor for a transgranular to intergranular cracking transition.

DISCUSSION

Crack Initiation Delay

In this paragraph, we shall mostly discuss the results obtained on the 316L, the study of the OFHC Cu being currently in progress.

The results of figures 1 and 2 show an interesting correlation between the corrosion potentials and the appearance of the first visible cracks. Moreover, rest potentials vary widely according to pre-cycling. Such variations are clearly related to surface fatigue-induced strain, according to the pre-cycling conditions. Examples of surface strain are given in figures 5 and 6.

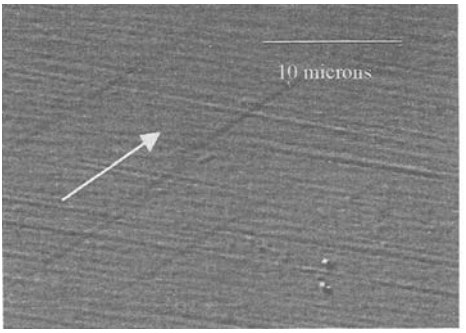


Figure 5 : Surface state after 10 cycles of pre-fatigue. Sparse slip bands at the surface (black lines going up)

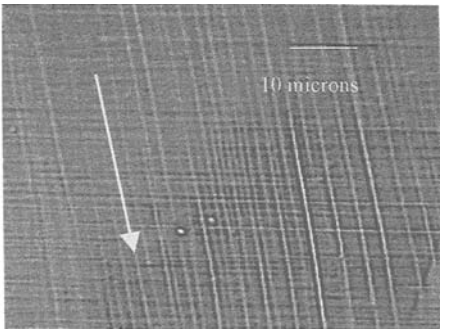


Figure 6 : Surface state at saturation. Fine parallel slip bands, very close.

Arrows indicate the directions of slip bands.

Cracks initiate by a strain-induced local breakdown of the passive layer for 316L in 117°C $MgCl_2$ at free potential. This leads to localised dissolution in the slip bands. Thus, the morphology and the repartition of such bands are important parameters to consider.

Fatigue has in fact two interesting aspects with respect to this point :

(i) It promotes fine parallel slip bands and favours single-glide [3].

(ii) The distance between slip bands decreases with an increasing number of cycles. For 316L, the distance is 15 μm after 10 cycles and about 1 μm after 50 cycles (i.e. at saturation). This is illustrated in figures 5 and 6.

During SCC tests, two different aspects must then be considered :

(i) The distance between slip bands characterises the cathodic surface during the initiation stage. The important parameter is then the cathodic/anodic surface ratio.

(ii) The stability of fatigue slip bands is observed only when saturation is established. This means that specimens pre-cycled at 50 cycles will be able to keep their pre-cycled slip bands much longer than others during SSRT tests. Thus, single glide is longer favoured in this case. SCC crack initiation mainly occurs in slip bands and at slip bands crossing. The crossing occurrence will be delayed for specimens pre-cycled at saturation, not for others which cannot keep the fatigue slip bands during SCC tests.

Both the crossing of slip bands and the distance between slip bands must be considered for crack initiation. Saturation is required to delay crack initiation because crossing of slip bands is delayed during SSRT tests, and because finer homogeneous slip with decreasing slip bands distance reduces the cathodic/anodic surface ratio. When this ratio is low enough, the local dissolution kinetics decreases. The average potential is then below the critical potential for SCC (figure 2) till crossing of slip bands occur due to an important tensile strain. This last situation promotes a transition from trans to intergranular cracking (figure 4) which can be related to SCC at higher stresses level.

Crack growth velocity decrease.

As for crack growth, fatigue at saturation has also a beneficial effect on crack propagation. This can be understood with the help of the Corrosion Enhanced Plasticity Model (CEPM) [3].

It is based on the fact that dissolution-plasticity interactions at the crack tip generates hydrogen and vacancies which enhance locally the dislocation mobility [8]. Thus two different zones can be observed :

- The very near crack tip zone is softened by the enhanced plasticity to the diffusion distance of hydrogen and vacancies.
- Ahead of this zone, a second one corresponds to the "normal" tensile plasticity during SSRT tests.

A kind of mobile obstacle is formed at the interface between the two zones, corresponding to the diffusion front. Dislocations can pile-up at this obstacle where local k_{1c} [9] can be reached because of stress concentration and hydrogen segregation in the pile-up.

Considering this model, one can understand that the dislocation structure of the bulk play an important role on the resistance of the obstacle to pile-up. If a low energy dislocation structure like in fatigue at saturation is established, the resistance of the obstacle decreases and crack propagation rate decreases too. But if the saturation is not reached during pre-cycling, Lomer locks can form easily which promotes crack propagation because of the formation of strong obstacles.

Looking at Figure 1, one can see that crack propagation occurs at stress levels much higher for pre-fatigued specimen. Calculations of crack propagation conditions were performed elsewhere [9]. They show that the importance of the applied stress on crack velocity is such that the elongation after crack initiation would be much less than that observed on Figure 1 when the applied stress is changed from 150 MPa (non pre-strained samples) to 250 MPa (pre-fatigued samples). Moreover, 250 MPa corresponds to rapid bulk propagation on non-pre-strained specimens. The same effect can be taken into account for copper (Figure 3).

According to that effect, one can consider that crack propagation is also decreased by fatigue pre-straining. Such results must be confirmed by SCC tests at applied stress level on CT specimens, with and without pre-straining.

Conclusions

Through this study we propose a process to delay the SCC damage for a classical environment/material couple, the 316L austenitic stainless steel in a boiling chloride solution. This method consists in pre-straining the material by low cycle fatigue, under plastic strain control, until the saturation of the flow stress. This methods seems applicable to another couple : OFHC copper in a nitrite solution.

This beneficial effect is valid for both crack initiation and crack propagation.

First, it induces a homogeneous and fine repartition of strain on the surface, which promotes a modification of the electrochemical reactions kinetics. This leads to a slower dissolution along the slip bands and induces a delay in crack initiation. The latter is delayed as long as the dislocation structure of pre-fatigue is not degraded.

The second is a decrease of the crack growth speed velocity related to the low-energy dislocation structure generated by the pre-fatigue at saturation. These beneficial effects are expected to be more pronounced for SCC tests at imposed stress. This is the subject of further studies.

Acknowledgements

The authors would like to thank the Région Rhône-Alpes for their financial involvement in this study.

References

[1] Chambreuil-Paret, A. and Magnin, Th., "Improvement of the Resistance to Stress-Corrosion Cracking in Austenitic Stainless Steels by Cyclic Prestraining", *Metallurgical and Material transactions A*, vol. 30, May 1999, pp 1327-1331.

[2] "*Corrosion-deformation interactions*", Proceedings of CDI 92, Les éditions de Physique Les Ulis , edited by Th. Magnin and J.M. Gras, 1993.

[3] Magnin, Th., *Advances in Corrosion-Deformation Interactions*, trans. Tech publications Ltd, Zurich, 1995

[4] Baroux, B. and Gorse, D, Chaotic Behaviors in Pitting Corrosion Processes, JECS Montreal, 1997

[5] da Cunha Belo, M., Bergner, J. and Rondot B., "Relationships Between the Critical Potential for SCC of Stainless Steels and the Chemical Composition of the Films Formed in Boiling $MgCl_2$ Solutions", *Corrosion Science*, vol. 21, No.4, pp 273 to 277, 1980

[6] Château, J.P., "Vers une quantification des mécanismes de corrosion sous contrainte : simulations numériques des interactions hydrogène-dislocations en pointe de fissure", Thèse 202 TD, january 1999, Ecolne Nationale Supérieure des Mines de Saint-Etienne.

[7] Chambreuil-Paret, A., "Corrosion sous contrainte de mono et polycristaux d'aciers inoxydables austénitiques en milieu $MgCl_2$: analyse microfractographique et recherche d'améliorations du comportement", Thèse 163 TD, septembre 1997, Ecole Nationale Supérieure des Mines de Saint-Etienne.

[8] Birnbaum, H.K., Robertson, I.M., Sofronis, P., Teter, D., " Mechanisms of Hydrogen Rlated Fracture-a Review", 2nd International Conference on Corrosion-deformation interactions, CDI 96 in conjunction with Eurocorr 96, *European Federation of Corrosion Publications Number 21*, ed. Th. Magnin, 1996, pp172.

[9] Delafosse, D., Château, J.P. and Magnin Th., 'Microfracture by Pile-Up Formation at a Stress Corrosion Crack Tip : Numerical Simulations of Hydrogen/Dislocations Interactions", J. Phys. IV France, vol. 9, pp. 251 to 260, 1999.

P. H. Chou,[1] R. Etien,[1] and T. M. Devine[2]

Influence of Surface Films and Adsorption of Chloride Ions on SCC of Austenitic Stainless Steels in 0.75M HCl at Room Temperature

Reference: Chou, P. H., Etien, R., and Devine, T. M., **"Influence of Surface Films and Adsorption of Chloride Ions on SCC of Austenitic Stainless Steels in 0.75M HCl at Room Temperature,"** *Environmentally Assisted Cracking: Predictive Methods for Risk Assessment and Evaluation of Materials, Equipment, and Structures, ASTM STP 1401,* R. D. Kane, Ed., American Society for Testing and Materials, West Conshohocken, PA, 2000.

Abstract

In situ surface enhanced Raman spectroscopy (SERS) was used to investigate the surface films that form on 304 and 316L stainless steels in a number of acidic solutions that either cause stress corrosion cracking (SCC) at room temperature (0.75M HCl) or do not cause SCC at room temperature (0.75M NaCl (pH3), 0.74M H_2SO_4, 0.87M $HClO_4$ and 0.75M HBr). The results indicate the same film forms on the steels in all solutions except 1M NaCl (pH3). Hence, while a specific surface film may be necessary for SCC, it is not sufficient to cause SCC of tensile stressed stainless steels. It was also determined that adsorption of chloride ions on stainless steel in 0.75M HCl does not occur in the range of potentials in which SCC occurs. Hence, the role of chloride in causing SCC of stainless steels in acidic solutions at room temperature is not associated with either the formation of specific surface films or adsorption of chloride ions.

Introduction

Austenitic stainless steels are the most widely used alloys for structural components

[1]Graduate student, Department of Materials Science and Engineering

[2]Professor, Department of Materials Science and Engineering, University of California, Berkeley, CA 94720

Copyright© 2000 by ASTM International www.astm.org

exposed to aqueous and atmospheric environments. Because of the ubiquitous presence of chloride ions, the stress corrosion cracking (SCC) susceptibility of austenitic stainless steels in aqueous chloride solutions is of great practical interest. At room temperature, chloride SCC of austenitic stainless steels only occurs in low pH solutions [1-3]. Stainless steel components stressed in tension and exposed to neutral and mildly alkaline, chloride-containing solutions at room temperature may fail by SCC in pits and crevices where low pH solutions develop [4,5].

Despite its practical importance, the mechanism of SCC of austenitic stainless steels in acidic chloride solutions at room temperature remains unclear [6]. The present study investigates the possible involvement in the SCC process of two phenomena. The first is the possibility that specific surface films form on stainless steels in acidic chloride solutions at room temperature and that these films induce susceptibility to SCC. Surface films may cause SCC by a variety of mechanisms [6]. Surface films have been strongly implicated as necessary factors of SCC in at least three other systems: SCC of carbon steels in nitrate [7], carbon steels in mildly alkaline carbonate/bicarbonate solutions [8] and IGSCC of sensitized austenitic stainless steel in high purity water at 288°C [9].

The second phenomenon investigated in this study that might possibly play a role in the SCC of austenitic stainless steels in acidic chloride solutions at room temperature is the adsorption of chloride ions. This is one of the mechanisms proposed to explain the TGSCC of austenitic stainless steel in boiling $MgCl_2$ [10].

If particular surface films and/or anion adsorption are found to be necessary for SCC, then their occurrence could be used to predict the SCC susceptibility of stainless steels in a particular environment.

In the present study, in situ surface enhanced Raman spectroscopy (SERS) [11, 12] is used to investigate chloride ion adsorption and the films that form on 304 and 316L stainless steels in a variety of acid solutions in which SCC is known to occur at room temperature (0.75M HCl) as well as solutions in which SCC is known to not occur at room temperature (0.75M NaCl (pH3), 0.74M H_2SO_4, 0.87M $HClO_4$ and 0.75M HBr). By comparing the films that form in solutions in which SCC occurs to the films that form in solutions in which SCC does not occur, it may be possible to infer the role of surface films in SCC of stainless steel in acidic chloride solutions at room temperature.

Procedure

U-bend tests were conducted according to ASTM specifications on 4"x0.25"x0.060" sheet samples of 304 stainless steel immersed 0.75M HCl at room temperature. After machining, the samples were heat treated at 1100°C/1 hr. in quartz capsules filled with 1/6 atm of argon, and quenched in water. The U-bend samples were placed in individual glass cells containing the test electrolyte, which was saturated with nitrogen gas, platinum counter electrodes and standard calomel reference electrodes and were polarized at constant potentials by means of potentiostats. The samples were periodically removed from the solution throughout the test period, which extended up to several weeks, and were examined for evidence of corrosion and cracking with the aid of a stereo-optical microscope and an optical microscope.

In situ surface enhanced Raman spectroscopy (SERS) experiments were conducted on samples of 304 stainless steel immersed in 0.75MHCl and 0.74M H_2SO_4. SER spectra were also obtained from 316L stainless steel samples in 0.75M HCl, 0.75M NaCl (pH3), 0.74M H_2SO_4, 0.87M $HClO_4$ and 0.75M HBr. The SER spectra were obtained during the anodic and cathodic polarization of the steel samples. The rate of polarization was 1 mV/s and aproximately five seconds were required to measure the SER spectrum. SERS was performed by first electrodepositing $\approx$ 50 nm diameter gold particles on the surface of the steel sample, then illuminating the sample with a krypton ion laser (647.1 nm) and collecting the SER scattered light. A detailed description of the procedure for obtaining SER spectra from passive films is provided in reference [13].

Results and Discussion

The influence of applied potential on the SCC behavior of 304 stainless steel U-bends in 0.75M HCl is presented in figure 1. In each test the sample was removed from the solution after two weeks of immersion and its surface was examined with an optical microscope to determine the lowest magnification at which cracks could be seen. The results indicate that the range of potential over which SCC occurs extends from –550 mV to –300 mV vs. SCE.

It is helpful to analyze the SCC results with the aid of the anodic and cathodic polarization curves presented in figure 2. The corrosion potential is near –400 mV, and so SCC occurs at potentials below as well as above the corrosion potential. Of course, significant rates of oxidation can occur at potentials less than the corrosion potential and hydrogen embrittlement is not thought to be the cause of cracking since the amount of cracking decreases with cathodic polarization. At potentials above –300 mV the rate of

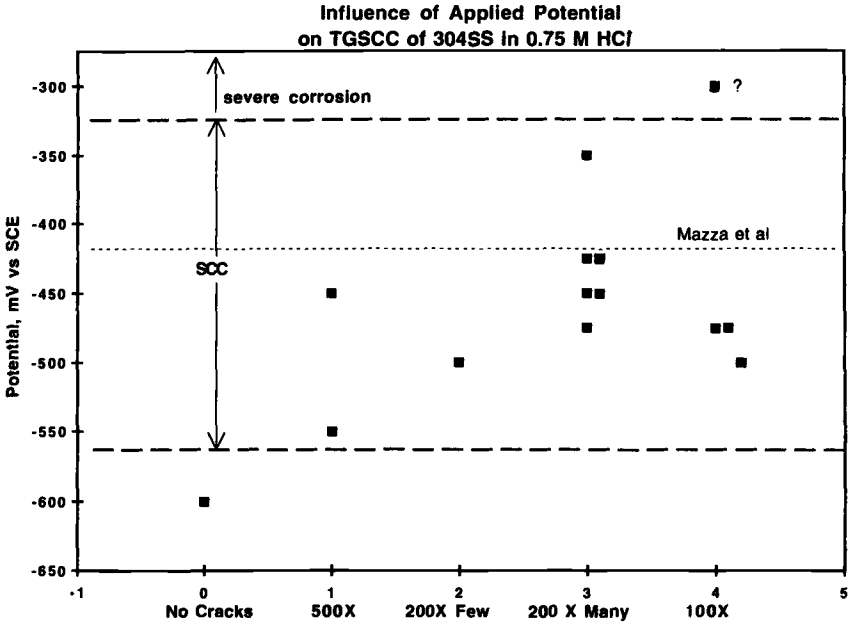


Figure 1. Influence of applied potential on SCC of 304 stainless steel in 0.75M HCl. Each point represents the lowest magnification at which cracks could be observed after two weeks of testing.

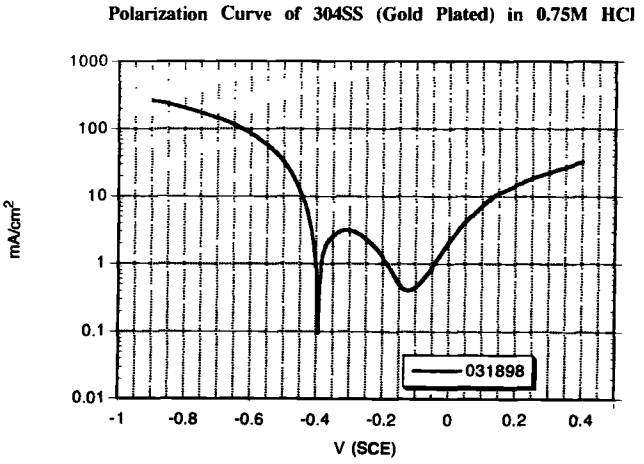


Figure 2. Anodic and cathodic polarization curves of 304 stainless steel (with electrodeposited gold particles) in 0.75M HCl.

corrosion is very high and SCC appears to no longer occur because of corrosion induced blunting of cracks.

The polarization curves in figure 2 were obtained from samples of 304 stainless steel that had been electrodeposited with ≈ 50 nm diameter particles of gold. Scanning electron microscopy indicates that approximately 25% of the steel's surface is covered with gold particles. The gold particles make it possible to obtain SER spectra of the passive films and species adsorbed on the steel's surface [11,12]. The SER spectra, which will be presented further on in this paper reveal whether or not specific surface films or adsorbed species play roles in the mechanism of SCC.

Parenthetically, it should be noted that the gold particles act as inert Raman antennae and serve to enhance the intensities of the Raman spectra of the surface films and adsorbates. In the absence of the gold particles, the intensities of the Raman spectra of the small quantities of surface species are too weak to be measured. The inert nature of the gold particles is demonstrated as follows. First, the gold particles are thermodynamically stable and, hence, are not oxidized at potentials of interest in this study: –550 mV to –300 mV [14]. Second, since in these experiments the potentials of the samples are controlled by a potentiostat, the potentials of the gold particles and the stainless steel electrodes are identical and there is no galvanic effect of the gold on the stainless steel. Third, in earlier experiments it was shown that the SER spectrum of the passive film formed on iron in borate buffer (pH=8.4) was the same independent of whether gold or silver particles were used to provide the enhancement of the Raman spectrum [15]. Hence, if it is postulated that the gold particles affect the identity of the passive film, it must be concluded that the silver particles have the same effect. While not impossible, it seems unlikely that both gold and silver would change the passive film in the same way. Fourth, there is even more compelling evidence for the lack of influence of the gold or silver particles on the identity of the passive film formed on stainless steel. The SER spectrum of the passive film formed on 304 stainless steel with silver particles in borate buffer is the same as that for the passive film formed on a 6 nm thick layer of 304 SS that was deposited by pulse laser deposition onto a roughened surface of silver [16]. The underlying silver provided the enhancement of the Raman spectrum and, as determined by Auger spectroscopy, the silver was completely covered by the stainless steel and was not in contact with the aqueous solution or the passive film.

The SER spectrum of the surface film formed on 304 stainless steel in 0.75M HCl is constant throughout the range of potentials in which SCC occurs. The spectra obtained between –786 mV and –284 mV are presented in Figure 3. There are three peaks of particular interest: 280 cm^{-1}, 410 cm^{-1} and 540 cm^{-1}. The five peaks located at 900 cm^{-1} –

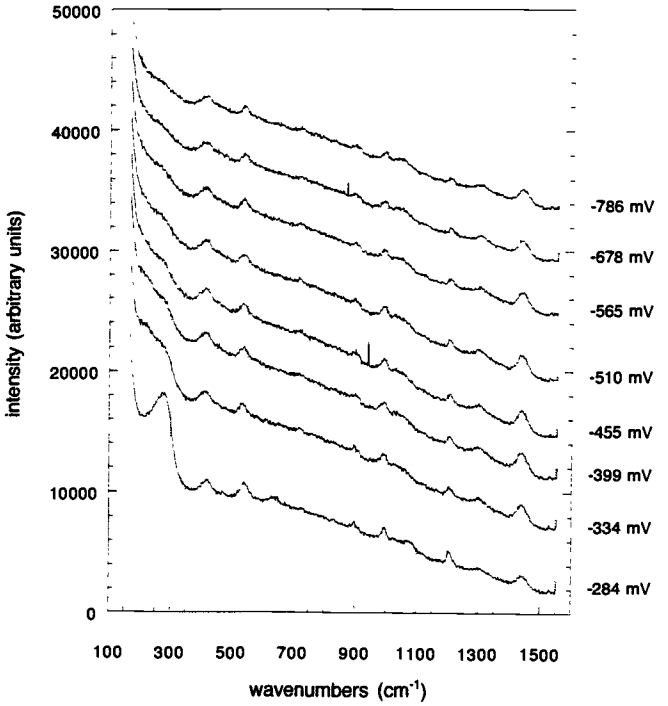


Figure 3. SER spectra obtained during potentiodynamic polarization of 304 in 0.75M HCl.

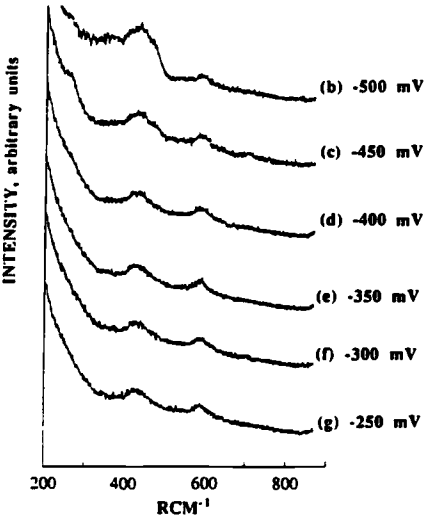


Figure 4. SER spectra obtained during potentiodynamic polarization of 304 in 0.74M H_2SO_4.

1440 cm^{-1} were due to the stop-off lacquer, which was used to define the sample's test area and which started to decompose in the 0.75M HCl. The two peaks at 410 cm^{-1} and 540 cm^{-1} are assigned to the film that forms on 304 stainless steel. The peak at 280 cm^{-1} is assigned to adsorbed chloride. This assignment was confirmed when the test solution was changed to 0.75M HBr and the peak shifted from 280 cm^{-1} to 180 cm^{-1}. This is the shift predicted in the peak location due to the mass difference between chloride and bromide.

SER spectra were also obtained from pure gold electrodes to confirm that the species responsible for the spectra in Figure 3 were located on the surface of the stainless steel and not on the surfaces of the gold particles. The SER spectra of the pure gold electrode was featureless in the range of 400 to 600 cm^{-1} so that the peaks at 410 cm^{-1} and 540 cm^{-1} are indeed due to species on the stainless steel's surface. During anodic polarization chloride ion adsorption on gold first occurred at a potential of –374 mV. The maximum of the peak was located at 230 cm^{-1}. The location of the maximum increased with increasing potential and reached a value of 270 cm^{-1} at +400 mV. The peak associated with chloride ion adsorption on stainless steel was located at 290 cm^{-1} and its position did not shift with potential. Hence, it was possible to use the peak location to distinguuish between adsorption of chloride on gold and on stainless steel.

The SER spectrum of the surface film formed on 304 stainless steel in 0.74M H_2SO_4 was reported in an earlier study and is presented for comparison in Figure 4. The SER spectra obtained in 0.75M HCl and 0.74M H_2SO_4 are clearly different. This is of particular interest since 304 stainless steel is susceptible to SCC in 0.75M HCl at room temperature but not in 0.74M H_2SO_4.

The need for a critical minimum concentration of chloride ions of $\approx$ 1M in order for SCC to occur at room temperature in acidic solutions is true for 301 and 310 stainless steels as well as for 304 stainless steel [17]. Similarly, the work of Nishimura and Kudo indicates that SCC does not occur for 316 stainless steel in 0.82M H_2SO_4 at room temperature [18]. However, 316 stainless steel does SCC in the acidic solutions that develop in pits and crevices [4]. Thus, the requirements of low pH and high chloride ion activity for SCC at room temperature apply to a number of 300 grade austenitic stainless steels. To further explore the roles of anion adsorption and surface films on the mechanism of SCC, SER spectra were obtained as a function of applied potential on samples of 316L stainless steel at room temperature in 0.75M HCl, 0.75M NaCl (pH3), 0.74M H_2SO_4, 0.87M $HClO_4$ and 0.75M HBr. While 316 stainless steel is susceptible to SCC in 0.75M HCl [19], it is immune to SCC in the other four solutions at room temperature.

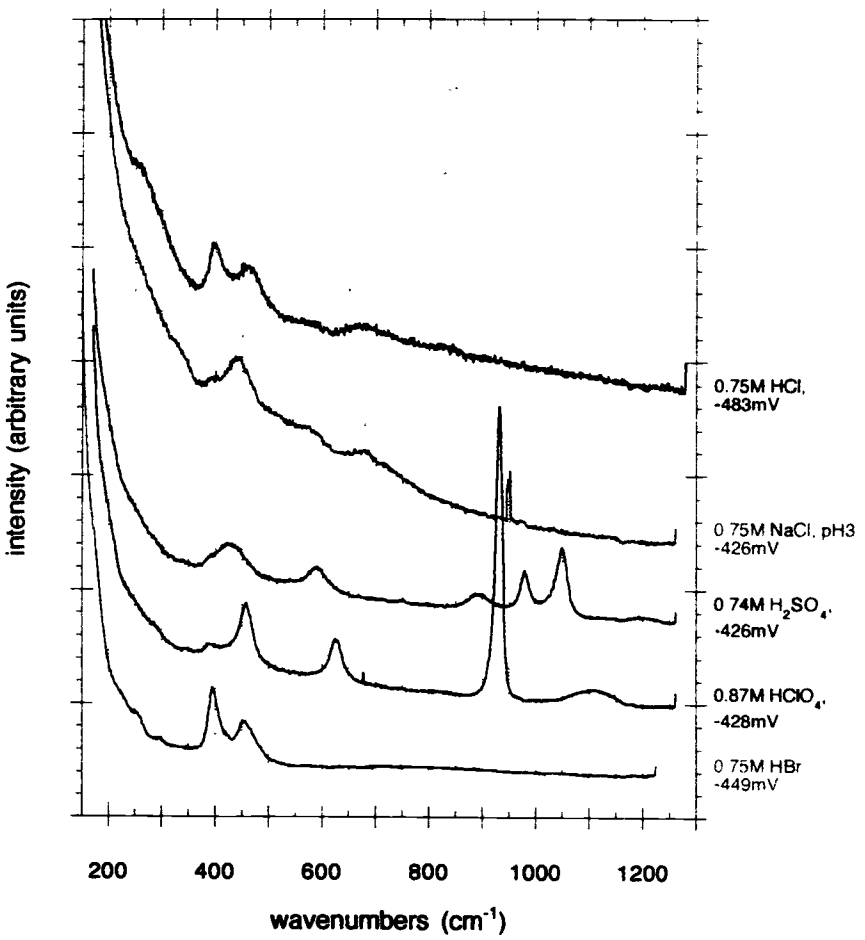


Figure 5. Comparison of the SER spectra of 316L in 0.75M HCl, 0.75M NaCl (pH3), 0.74M H_2SO_4, 0.87M $HClO_4$ and 0.75M HBr.

In the range of ≈ -600 mV to –300 mV, the SER spectra of 316L were independent of potential in the five solutions. The spectra obtained in each solution are presented in Figure 5. The film formed on 316L in 0.75M NaCl (pH3) is similar to that formed in unbuffered 0.17M NaCl [20] and is decidedly different from the film formed in 0.75M HCl. This result is consistent with the concept that a particular surface film is responsible for susceptibility to SCC. However, while the SER spectra obtained in H_2SO_4 and $HClO_4$ are also clearly different from the SER spectrum in 0.75M HCl, this is not due to differences in the spectra of the films formed in these solutions. While Cl^- dissolved in aqueous solutions is not Raman active, both ClO_4^- and $SO_4^=$ are Raman active. ClO_4^- has Raman active modes at 462 cm^{-1}, 692 cm^{-1}, 935 cm^{-1} and 1113 cm^{-1}[21]. The Raman active modes of $SO_4^=$ and HSO_4^- are {451 cm^{-1}, 613 cm^{-1}, 980 cm^{-1} and 1104 cm^{-1}} and {422 cm^{-1}, 585 cm^{-1}, 831 cm^{-1}, 1035 cm^{-1}, 1043 cm^{-1} and 1195 cm^{-1}}, respectively [21]. The Raman peaks associated with these modes contribute significantly to the spectra presented in Figure 5. If their contributions are subtracted from the measured spectra, the results indicate that the same films are formed on 316L in 0.75M HCl, 0.74M H_2SO_4, 0.87M $HClO_4$ and 0.75M HBr.

The differences in the SER spectra of the films formed on 316L in 0.75M HCl, in which SCC occurs, and 0.75M NaCl (pH3), in which SCC does not occur suggest that a specific film may be a necessary condition for SCC. However, the SER spectra obtained in 0.74M H_2SO_4, 0.87M $HClO_4$ and 0.75M HBr indicate that the formation of a specific film is not a sufficient condition (in the presence of a tensile stress) for SCC.

The identity of the film that forms in the very acidic solutions is not known at this time. However, its SER spectrum suggests it is similar to green rust [22].

The SER spectra of species on the surface of 304 obtained as a function of applied potential in 0.75M HCl (Figure 3) indicate that adsorption of chloride ions only occurs at potentials above ≈ -300 mV, which is above the range of potentials that cause SCC. This is a very informative result. It indicates that the mechanism of SCC does not involve the adsorption of chloride ions. Collectively, the results of the present study indicate that the role of chloride ions in causing SCC of austenitic stainless steels in acidic solutions at room temperature may be more subtle or less direct than previously thought. The role of chloride ions in causing SCC of austentitic stainless steels in acidic solutions at room temperature cannot be related to either their adsorption on the surface of the film or to their causing the formation of a particular surface film that induces susceptibility to SCC.

Conclusions

1. Although 304 stainless steel is susceptible to SCC at room temperature in 0.75M HCl but is not susceptible to SCC at room temperature in 0.74M H_2SO_4, in situ surface enhanced Raman spectroscopy (SERS) indicates the same film forms on 304 stainless steel in both solutions.
2. A similar film forms on 316L in 0.75M HCl, 0.74M H_2SO_4, 0.87M$HClO_4$ and 0.75M HBr. Of these four solutions, 316L is susceptible to SCC at room temperature only in 0.75M HCl.
3. The precise identity of the film that forms on 304 and 316L stainless steels in the strong acids investigated in this study has not been determined but its SER spectrum is simialr to that of green rust.
4. 316L stainless steel is not susceptible to SCC at room temperature in 1M NaCl (pH3) and SERS indicates the film that forms in this solution resembles that which forms in mildly alkaline solutions and is markedly different from the films that form in strong acids.
5. Collectively, the results indicate that (in combination with a tensiile stress) a particular film may be a necessary condition for SCC but it is not a sufficient condition.
6. SERS indicates that adsorption of chloride ions in 0.75M HCl occurs at potentials above ≈ -300 mV (SCE), which is above the range of potentials that cause SCC.

The mechanism by which chloride ions cause SCC of 304 and 316L stainless steel at room temperature does not involve either the formation of a unique surface film or chloride ion adsorption on the surface film.

Acknowledgements

We wish to thank Dr. Dave Kolman of Los Alamos National Laboratory for helpful discussions and the Los Alamos National Laboratory for financial support of this research.

References

1. A. Acello and N.D. Greene, Corrosion, v.18, p. (1962).
2. J.D. Harston and J.C. Scully, Corrosion, v. 25, p. 493 (1969).
3. G. Bianchi, F. Mazza and S. Torchio, Corrosion Science, v. 13, p.165 (1973).
4. Tamaki, K., Tsujikawa,S. and Hisamatsu, Y., Development of a New Test Method for Chloride SCC of Stainless Steels in Dilute NaCl Solutions, " *Advances in Localized Corrosion*, Proceedings of the Second International Conference on Localized Corrosion, H.S. Isaacs, U. Bertocci, J. Kruger and S. Smialowska, eds., National Association of Corrosion Engineers, Houston, TX, 1987, p. 207-214.

5. Dana, A., Am. Soc. Testing Mater. Bull., v. 225, 1957, p.46.
6. Newman, R.C., "Stress Corrosion Cracking Mechanisms," *Corrosion Mechanisms in Theory and Practice*, P. Marcus and J.Oudar, eds., Marcel Decker, Inc., New York, 1995, p. 311-372.
7. Flis, J., Corrosion Science, v. 15, 1975, p.553.
8. Odziemkowski, M., Flis, J. and Irish, D.E., Electrochimica Acta, v. 39 1994, p.2225.
9. Cubicciotti, J. Nuclear Materials, v. 167, 1989, p.241.
10. Uhlig, H. and Cook, E., Journal of the Electrochemical Society, v. 116, 1969, p. 173.
11. J. Gui and T.M. Devine, Use of Surface Enhanced Raman Scattering as an *In-Situ* Probe of the Metal-Aqueous Solution Interface, *Corrosion '91*, paper #79, NACE, Houston, TX (1991).
12. T.M. Devine, Use of Raman Spectroscopy in Corrosion Science and Engineering, *Proceedings of Corrosion 97, Advanced Monitoring and Analytical Techniques*, p. 131-162, National Association of Corrosion Engineers, Houston, TX (1997).
13. J. Gui and T.M. Devine, Obtaining SERS from the Passive Film in Iron, *J. Electrochem. Soc.*, v. 138, 1376-1384 (1991).
14. Pourbaix, M. Atlas of Electrochemical Equilibria in Aqueous Solutions, 1966, Pergamon Press, Oxford.
15. Shimizu, T., Oblonsky, L.J. and Devine, T.M., "SERS Study of the Passive Films on Iron and Stainless Steel," *Proceedings of the H.H. Uhlig Memorial Symposium*, Mansfeld, M., Asphahani, A., Bohni, H. and Latanision, R., eds., 1995, The Electrochemical Society, p.114 .
16. Oblonsky, L.J., M.S. Thesis, Department of Materials Science and Engineering, 1992, University of California, Berkeley.
17. Juang, H.K. and Altstetter, C., Corrosion, v. 46, 1990, p.881.
18. Nishimura,R. and Kudo, K., Corrosion, v.45, 1989, p.308.
19. Etien, R., M.S. Thesis, Department of Materials Science and Engineering, August, 2000, University of California, Berkeley.
20. Ferreira, M.G.S., Moura E Silva, T., Catarino, A., Pankuch, M. and Melendres, C.A., Journal of the Electrochemical Society, v. 139, 1992, p.3146.
21. Irish, D.E. and Ozeki, T., "Raman Spectroscopy of Inorganic Species in Solution," in *Analytical Raman Spectroscopy*, Grasselli, J.E. and Bulkin, B.B., eds., J.Wiley & Sons, New York, 1991, p.59.
22. Boucherit, N., Hugot-Le Goff, A. and Joiret, S., Corrosion, v.48, 1992, p.569.

Peter F. Ellis II,[1] Ronald E. Munson,[1] and Jay Cameron[1]

Toward A More Rational Taxonomy For Environmentally Induced Cracking

Reference: Ellis, P. F., Munson, R. E., and Cameron, J., **"Toward A More Rational Taxonomy for Environmentally Induced Cracking,"** *Environmentally Assisted Cracking: Predictive Methods for Risk Assessment and Evaluation of Materials, Equipment, and Structures, ASTM STP 1401*, R. D. Kane, Ed., American Society for Testing and Materials, West Conshohocken, PA, 2000.

Abstract: An improved taxonomy (systematic nomenclature) is proposed for environmentally induced cracking in aqueous systems. This improved taxonomy reduces the number of named environmentally induced cracking phenomena from more than 25 to just 7, and places these in relationship to each other, to cracking phenomena that are independent of environmental factors, and to corrosion processes that are independent of stress.

This improved taxonomy is designed to reduce the confusion inherent in the current *post hoc* nomenclature and to facilitate predictive or anticipatory consideration for the potential for cracking phenomena in materials, equipment, and structures.

Key Words: cathodic hydrogen embrittlement, caustic cracking, chloride stress corrosion cracking, corrosion fatigue, environmentally induced cracking, fatigue, corrosion-fatigue, hydrogen embrittlement, stress corrosion cracking, anodic processes, cathodic processes, atomic hydrogen, electrochemistry, corrosion

Introduction

Regardless of the name assigned—ammonia cracking, arsenical cracking, brittle fracture, cathodic hydrogen embrittlement, caustic cracking, chloride stress corrosion cracking, corrosion-assisted cracking, corrosion fatigue, cyanide cracking, ductile fracture, environmentally induced cracking, fatigue, hydrogen fluoride cracking, hydrogen stress cracking (HSC), hydrogen embrittlement, hydrogen assisted stress corrosion cracking (HSSC), hydrogen assisted cracking (HAC), hydrogen induced cracking (HIC), intergranular stress corrosion cracking (IGSCC), methanol cracking, polythionic acid cracking, season cracking, step-wise cracking, stress corrosion cracking

[1] Principal scientist, Corrosion and Materials Selection: principle engineer, Metallurgy; and senior engineer, Mechanical Engineering, respectively, Mechanical & Materials Engineering, 8501 N. MoPac Blvd, Suite 100, Austin, TX, 78759

Copyright© 2000 by ASTM International www.astm.org

(SCC), stress-oriented hydrogen induced cracking (SOHIC), sulfide stress cracking (SSC), transgranular stress corrosion cracking (TGSCC)—the consequences of in-service cracking are potentially catastrophic, frequently resulting in "sudden unscheduled disassembly" of the affected structure, machinery, or vessel.

Since risk is the product of probability of occurrence and severity of consequence, and the consequences of in-service cracking are frequently catastrophic, the variability in risk of in-service cracking is controlled entirely by the probability of occurrence. Evaluating the probability of occurrence of in-service cracking is therefore critical to predictive risk assessment for machinery or structures.

The current nomenclature associated with in-service cracking is confused and not well suited to predictive evaluation. The confusion begins at a most fundamental level: the very definition of stress corrosion cracking. For example, NACE-International defines stress corrosion cracking as "any cracking resulting from the interaction of tensile stress, a susceptible material, and a specific substance in the corrosive environment [*1*]." This all-inclusive definition corresponds to the term "environmentally induced cracking" used by ASTM, and includes both metals and non-metals and both active-path and hydrogen-induced cracking mechanisms. ASM-International, on the other hand, reserves the term "stress corrosion cracking" for cracking initiating at sites where active corrosion is occurring, i.e., where metal is lost. Under the ASM-International system, mechanisms resulting from the action of atomic hydrogen are collected under a separate heading—hydrogen embrittlement [*2*].

A significant part of the difficulty in understanding the relationship between environmental factors and stress cracking originates from the fact that the nomenclature for the observed phenomena is mostly *post hoc* and descriptive of the observed failure rather than the causative mechanisms. In addition, the current nomenclature attempts to draw discrete boundaries between phenomena on a continuum. The current nomenclature, for example, implies that there is a clear distinction between static stress corrosion, corrosion fatigue, and "pure" fatigue, while in fact the process is a continuum. At one extreme, a component exposed to a corrosive environment is subjected to one-half of a stress cycle (static loading). At the other extreme, the frequency is so high that the contribution of corrosion become negligible and the resulting failure becomes indistinguishable from fatigue in an inert atmosphere [*3-6*].

In many cases, the assigned name is archaic ("season cracking") or simply identifies the perceived causative agent, i.e., caustic cracking, ammonia stress cracking (of brass), chloride stress cracking, and sulfide stress cracking. To add to the confusion, the literature is not consistent in the usage of these terms. For example, some authors use the term "stress corrosion cracking" to refer to any cracking mechanism involving corrosion (the NACE-International usage) as the term "environmentally influenced cracking" is used in this document, while others use the same term to refer specifically to chloride-induced stress corrosion cracking of austenitic stainless steels. ASM-International, for example, draws a clear distinction between "stress corrosion cracking" and "hydrogen embrittlement" (Table 1), but then characterizes the failure of high-strength steels exposed to water and hydrogen sulfide as "sulfide stress cracking" though the known mechanism is hydrogen embrittlement (according to the ASM-International usage). Table 1, a comparison of definitions for selected corrosion terms

by three technical societies, illustrates the inherent confusion in the current nomenclature.

Table 1—*Comparison of definitions.*

Term	Association	Definition
Caustic Cracking	ASTM	Stress corrosion cracking of metals in caustic solutions.
	ASM-International	None offered
	NACE-International	None offered
Caustic Embrittlement	ASTM	None offered
	ASM-International	An *obsolete term* [emphasis original] for a forms of stress corrosion cracking most frequently encountered in carbon steels or iron-chromium-nickel alloys that are exposed to concentrated caustic solutions at temperatures of 200-250°C
	NACE-International	Cracking as a result of the combined actions of tensile stress and corrosion in an alkaline environment.
Corrosion	ASTM	The chemical or electrochemical reaction between a material, usually a metal, and its environment that produces a deterioration of the material and its properties
	ASM-International	The chemical or electrochemical reaction between a material, usually a metal, and its environment that produces a deterioration of the material and its properties.
	NACE-International	The destruction of a substance; usually a metal, or its properties because of a reaction with its (environment) surroundings [parentheses original]
Corrosion Fatigue	ASTM	The process in which a metal fractures prematurely under conditions of simultaneous corrosion and repeated cyclic stress loading at lower stress or fewer cycles than would be required in the absence of the corrosive environment
	ASM-International	The process in which a metal fractures prematurely under conditions of simultaneous corrosion and repeated cyclic stress loading at lower stress or fewer cycles than would be required in the absence of the corrosive environment
	NACE-International	The combined action of corrosion and fatigue (cyclic stressing) in causing metal fracture
Cracking	ASTM	None offered
	ASM-International	None offered
	NACE-International	Fracture of a metal in a brittle manner along a single or branched crack.
Embrittlement	ASTM	The severe loss of ductility or toughness or both of a material, usually an alloy
	ASM-International	Severe loss of ductility of a metal or alloy.
	NACE-International	Severe loss of ductility of a metal or alloy.

Table 1—*Continued.*

Term	Association	Definition
Fatigue	ASTM	A process leading to fracture resulting from repeated stress cycles well below the normal tensile strength. Such fractures start as tiny cracks that grow to cause total failure.
	ASM-International	The phenomena leading to fracture under repeated or fluctuating stresses having a value less than the tensile strength of the material.
	NACE-International	None offered
Hydrogen Blistering	ASTM	Formation of blisters on or below a metal surface from excessive internal hydrogen pressure.
	ASM-International	Formation of blisters on or below a metal surface from excessive internal hydrogen pressure.
	NACE-International	Formation of blister-like bulges on a ductile metal surface caused by internal hydrogen pressures,
Hydrogen Assisted Cracking (HAC)	ASTM	None offered
	ASM-International	See under *Hydrogen embrittlement*
	NACE-International	None offered
Hydrogen Assisted Stress Corrosion Cracking (HSCC)	ASTM	None offered
	ASM-International	See under *Hydrogen embrittlement*
	NACE-International	None offered
Hydrogen Disintegration	ASTM	None offered
	ASM-International	None offered
	NACE-International	Deep internal cracks in a metal caused by hydrogen.
Corrosion Embrittlement	ASTM	None offered
	ASM-International	The severe loss of ductility of a metal due to corrosive attack, usually intergranular without surface signs,
	NACE-International	None offered
Hydrogen Embrittlement	ASTM	Hydrogen-induced cracking or severe loss of ductility caused by the presence of hydrogen in the metal.
	ASM-International	A process resulting in a decrease in the *toughness* or *ductility* [emphases original] due to the presence of atomic hydrogen. *Internal hydrogen embrittlement* [emphasis added] occurs the hydrogen enters molten metal which becomes supersaturated with hydrogen immediately after solidification. *Environmental hydrogen embrittlement* [emphasis added] results from hydrogen being absorbed by solid metals. This can occur during elevated-temperature thermal treatments, and in service during electroplating, contact with maintenance chemicals, corrosion reactions, cathodic protection, and operating in high-pressure hydrogen. (cont)

Table 1—*Continued.*

Term	Association	Definition
(Cont.) Hydrogen Embrittlement	(Cont.) ASM-International	(Cont.) In the absence of residual stress or external loading, environmental hydrogen embrittlement is manifested in various forms, such as blistering, internal cracking, hydride formation, and reduced ductility. With a tensile stress or stress-intensity factor exceeding a specific threshold, the atomic hydrogen interacts with the metal to induce subcritical crack growth. In the absence of a[n anodic] corrosion reaction (i.e., polarized cathodically), the usual term used is *hydrogen assisted cracking (HAC)* or *hydrogen stress cracking (HSC)* [emphases added]. In the presence of active corrosion, usually as pits or crevices (polarized anodically), the cracking is generally called *stress corrosion cracking (SCC)* but should more properly be called *hydrogen- assisted stress corrosion cracking (HSCC).*
	NACE-International	Embrittlement of a metal caused by hydrogen.
Hydrogen-induced cracking (HIC)	ASTM	None offered
	ASM-International	See under *Hydrogen embrittlement*
	NACE-International	None offered
Hydrogen stress cracking (HSC)	ASTM	None offered
	ASM-International	See under *Hydrogen embrittlement*
	NACE-International	None offered
Stress-Accelerated Corrosion	ASTM	None offered
	ASM-International	None offered
	NACE-International	Corrosion which is accelerated by stress
Stress Corrosion	ASTM	None offered
	ASM-International	None offered
	NACE-International	Corrosion which is accelerated by stress
Stress Corrosion Cracking	ASTM	A cracking process that requires the simultaneous action of a corrosive and sustained tensile stress. This excludes corrosion-reduced sections that fail by fast fracture. It also excludes intercrystalline or transcrystalline corrosion which can disintegrate an alloy without applied or residual stress.
	ASM-International	A cracking process that requires the simultaneous action of a corrosive and sustained tensile stress. This excludes corrosion-reduced sections that fail by fast fracture. It also excludes intercrystalline or transcrystalline corrosion which can disintegrate an alloy without applied or residual stress. Stress corrosion cracking may occur in combination with *hydrogen embrittlement* [emphasis original].
	NACE-International	Cracking that results from stress and corrosion.

Table 1—*Continued.*

Term	Association	Definition
Sulfide Stress Cracking (SSC)	ASTM	None offered
	ASM-International	Brittle failure by cracking under the combined action of *tensile stress* and *corrosion* [emphases original] in the presence of water and hydrogen sulfide,
	NACE-International	Stress corrosion cracking of a metal in an environment containing H_2S.
Source of Definitions	ASTM	"Standard Terms Relating to Corrosion and Corrosion Testing" (G 15), Annual Book of ASTM Standards, ASTM, Philadelphia, PA.
	ASM-International	*Metals Handbook, Ninth Edition, Corrosion*, ASM-International, Metals Park, OH
	NACE-International	*NACE Basic Corrosion Course*, NACE-International, Houston, TX

Much of this ambiguity in nomenclature arose because many of the cracking phenomena were named before the underlying mechanisms were understood. In addition to being inherently confusing, the existing nomenclature is not facile for the purposes of anticipating and assessing the potential risk of environmentally induced cracking.

While commonly used to refer to the systematic naming of plants and animals, the term *taxonomy* refers to the process of systematic naming, regardless of the system under consideration. Taxonomies are further divided into *analytic taxonomies* that draw finer and finer distinctions, and *synthetic taxonomies* that seek broader, underlying similarities. This paper presents a synthetic taxonomy of environmentally induced cracking processes designed to facilitate the anticipation of environmentally induced cracking based on the anticipated electrochemical and stress environment of the component under consideration. The discussion is limited to aqueous systems, including condensing steam, but should be expandable to include other systems as well.

Precursor Concepts

Figure 1 shows a precursor diagram that inspired the development of the nomenclature proposed in this paper. This Venn diagram [*6*] is a depiction of the interaction between "hydrogen embrittlement," "stress corrosion cracking," and "corrosion fatigue." This figure, while quite interesting, contains some buried assumptions that are explicit in the proposed taxonomy.

A second precursor concept was the recognition that, at least for aqueous systems including steam, all corrosion-related brittle cracking mechanisms fall into two very broad categories [*3-5, 7-11*].

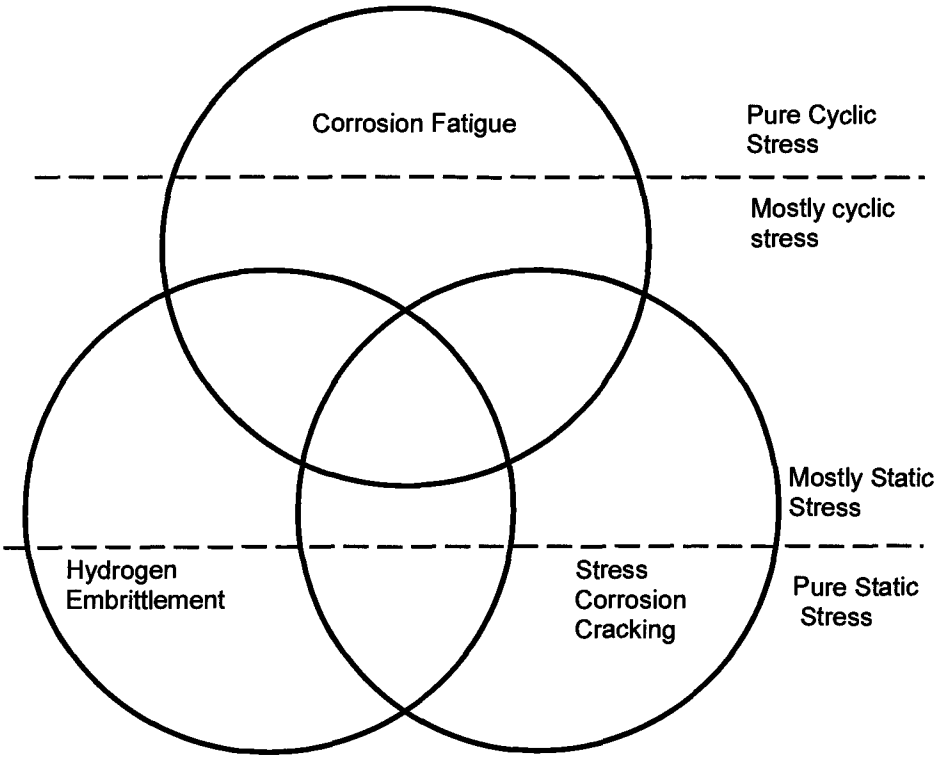


Figure 1—*Venn diagram illustrating the interrelationship between stress corrosion cracking, corrosion fatigue, and hydrogen embrittlement [6].*

- *Active-Path Processes.* The exact mechanism(s) of active-path cracking processes is not known and more that one mechanism may exist. However, it is known that active-path cracking propagates by metal dissolution at the crack tip while the walls of the crack do not corrode significantly. The distinguishing feature of an active path mechanism is that time-to-failure is decreased by polarizing the specimen anodic to the hydrogen ion reduction potential and retarded by polarizing the specimen cathodic to the hydrogen ion reduction potential of the environment to which the material is exposed. Making the specimen anodic to the hydrogen ion reduction potential accelerates the metal dissolution at the crack tip while making the specimen cathodic to the hydrogen ion reduction potential halts the metal dissolution reaction. All active-path processes require the simultaneous action of tensile stress, either applied or residual.

- *Hydrogen-Mediated Processes.* The central commonality of all hydrogen-mediated processes is that they are accelerated by polarization active to the

hydrogen ion reduction potential (because making the specimen cathodic to the hydrogen ion reduction potential increases the rate at which hydrogen enters the metal) and all result from the effect of absorbed atomic (metallic) hydrogen, though the absorbed atomic hydrogen can alter the material in a variety of ways, producing a number of superficially different failure modes. Some of these modes require the simultaneous action of tensile stress, either applied or residual. Some hydrogen-mediated damage processes do not require the simultaneous action of tensile stress.

A third precursor concept is the recognition that cracking due to the synergy of static stress and environmental factors and cracking due to the synergy between cyclic stress and environmental factors are not discretely separate phenomena. In a given corrosive environment, failures under very slow cyclic stress rates become indistinguishable from static load failures. At very high cyclic rates the "corrosion fatigue" failure becomes indistinguishable from fatigue failures in the absence of a corrosive environment [*3-6*]. At intermediate frequencies the resulting fractures show features characteristic of both static stress corrosion cracking and of pure fatigue cracking [*12*].

Proposed Taxonomy

The proposed taxonomy is based on the overlay of a corrosion (electrochemical) axis and a stress axis. Each axis is discussed separately, prior to synthesis into an integrated Venn diagram including both stress related and stress-independent corrosion phenomena.

Corrosion (Electrochemical) Axis

Figure 2 illustrates the corrosion or electrochemical axis of the system. All aqueous corrosion processes consist of a minimum of two electrochemical half-steps that necessarily proceed at the same coulombic rate. The first step in the anodic reaction is the oxidation of a metal atom to the corresponding metal ion of the lowest valence state, for example

$$Fe \rightarrow Fe^{+2} + e^{-} \quad (1)$$

though this reaction may be followed by oxidation to higher valence states. Metal is lost wherever the anodic half reaction occurs.

The electrons liberated by the anodic half reaction must be consumed by one or more cathodic half reactions as rapidly as they are generated. In aqueous systems, all of these reactions involve Lewis acids as the electron receptors. The three most common cathodic half reactions are

$$2H^{+} + 2e^{-} \rightarrow H_2 \quad (2)$$

$$4H^{+} + O_2 + 4e^{-} \rightarrow 2H_2O \quad (3)$$

$$2H_2O + O_2 + 4e^{-} \rightarrow 4OH^{-} \quad (4)$$

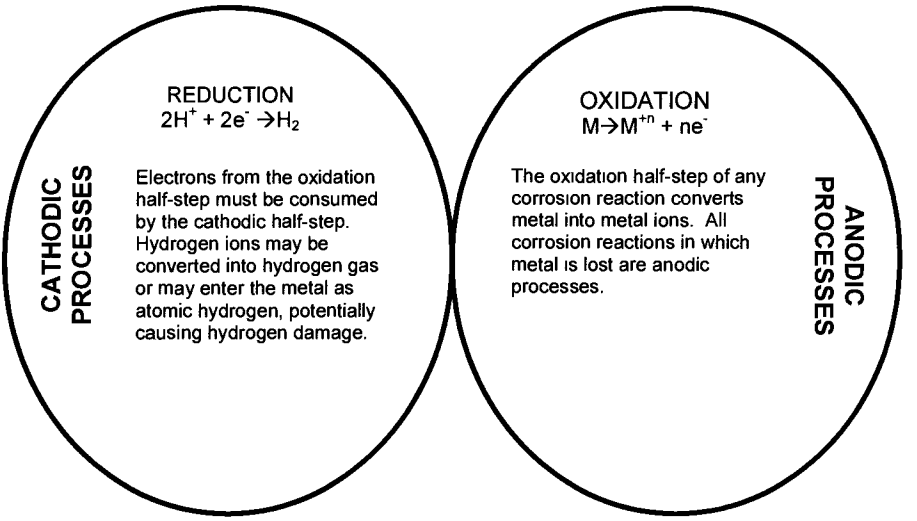
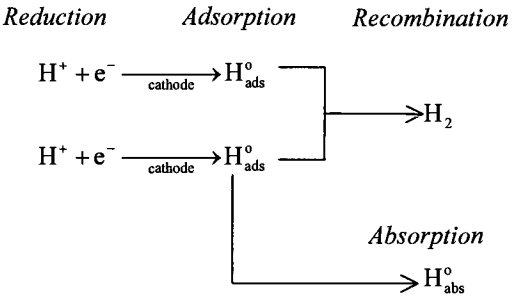


Figure 2—*Electrochemical Axis*

Reaction 2, of primary concern from the standpoint of environmentally induced cracking, is actually a summary of a complex reaction chain illustrated below.



(5)

Hydrogen ions are reduced to adsorbed atomic hydrogen on the metal surface. These adsorbed atomic hydrogen atoms may combine with other adsorbed atomic hydrogen atoms to form molecular hydrogen that diffuses into the corrosive medium. Adsorbed atomic hydrogen can also diffuse into the metal lattice becoming absorbed atomic hydrogen. The rate of the absorption step depends on temperature and the properties of the metal or alloy, while the rate of the recombination reaction is controlled by variables in the corrosive environment. If reduction to adsorbed atomic hydrogen occurs more rapidly than the recombination step can remove the atomic hydrogen from the metal surface, the metal or alloy will become charged with atomic hydrogen. So-called "cathodic poisons" inhibit the recombination reaction step without affecting either the rate of the reduction or absorption steps, resulting in increased rates

of hydrogen absorption (hydrogen charging). Some well-known cathodic poisons include sulfides and selected other sulfur compounds, some arsenic and phosphorus compounds, and cyanide.

Once absorbed, atomic hydrogen is a metal, and can act as an interstitial "alloying" constituent (with highly detrimental effects), reducing the ductility and toughness of the matrix. If the source of atomic hydrogen is removed and the material is held at elevated temperature (greater than 150°C) for several hours, the atomic hydrogen will diffuse out and the mechanical properties will return to normal. Hence, this form of embrittlement is termed reversible hydrogen embrittlement [*7*].

However, if two atomic hydrogens emerge together at an interstitial defect, such as an inclusion boundary, they may recombine to form molecular hydrogen (H_2). Molecular hydrogen cannot diffuse back into the lattice, and the equilibrium pressure between atomic and molecular hydrogen is between 10 and 100 GPa (100-1000 kbar) depending on the temperature [*10*]. The resulting pressures disrupt the microstructure, forming blisters or internal cracks. This damage is irreversible.

At low concentrations, atomic hydrogen produces reversible embrittlement in many titanium, zirconium, tantalum, and niobium alloys. At higher concentrations, atomic hydrogen reacts with these materials to form brittle hydrides. This damage is likewise irreversible [*7, 10*].

The electrochemical axis is bipolar. At any instant in time, any microscopic area on the metal surface is either a cathode or an anode, never both at once. In uniform corrosion, the polarity of any given site reverses on a time frame of seconds or less so that the average metal loss is uniform. In other forms of corrosion, such as pitting and crevice corrosion, certain areas become fixed anodes, where the metal is dissolving, while the adjacent surfaces become fixed cathodes. An active path crack is an extreme case in which the tip of the crack is the anode while the walls of the crack and the surrounding surface are cathodes protected from metal loss.

Stress Axis

Unlike the electrochemical axis, the stress axis (Figure 3) is not bimodal. At one extreme, the top of the stress axis in Figure 3, is purely cyclic stress in which there is no residual stress and the applied stress drops to or passes through zero on each stress cycle (stress ratio $R \leq 0$). At the other extreme, the bottom of the stress axis in Figure 3, the residual plus applied stress is constant (stress ratio $R = 1$), and the stress load is said to be static. In the real world the situation is frequently one of fluctuating stress that does not pass through zero load ($0 < R < 1$), i.e., cyclic stress is superimposed on either residual or applied static stress. Figure 3 illustrates the continuum nature of this relationship.

Integrated Corrosion/Stress Venn Diagram

Figure 4 shows the integrated Venn diagram created by overlying the stress axis diagram on the electrochemical axis diagram divided into 16 domains or *modes*. Eight of these modes require the simultaneous action of stress and environmental factors to produce cracking, two are capable of producing cracking in the absence of stress or

through the application of stress following exposure to the inducing environment. Four modes do not require an inducing environment, and two modes do not produce cracking

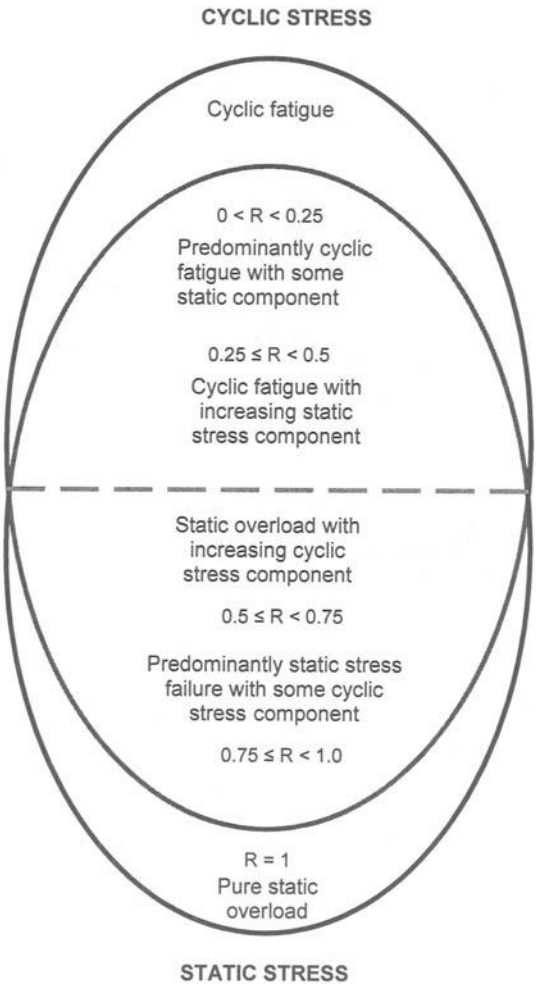


Figure 3—*The Stress Axis*

Non-cracking Modes—There are two modes that contain all of the corrosion processes that do not result in crack formation.

- Mode A, Anodic Corrosion Processes, contains all anodic processes—including uniform corrosion, fretting, erosion corrosion, pitting, crevice corrosion,

intergranular attack, and the anodic halves of galvanic cells—in which metal is lost independent of or in the absence of stress.

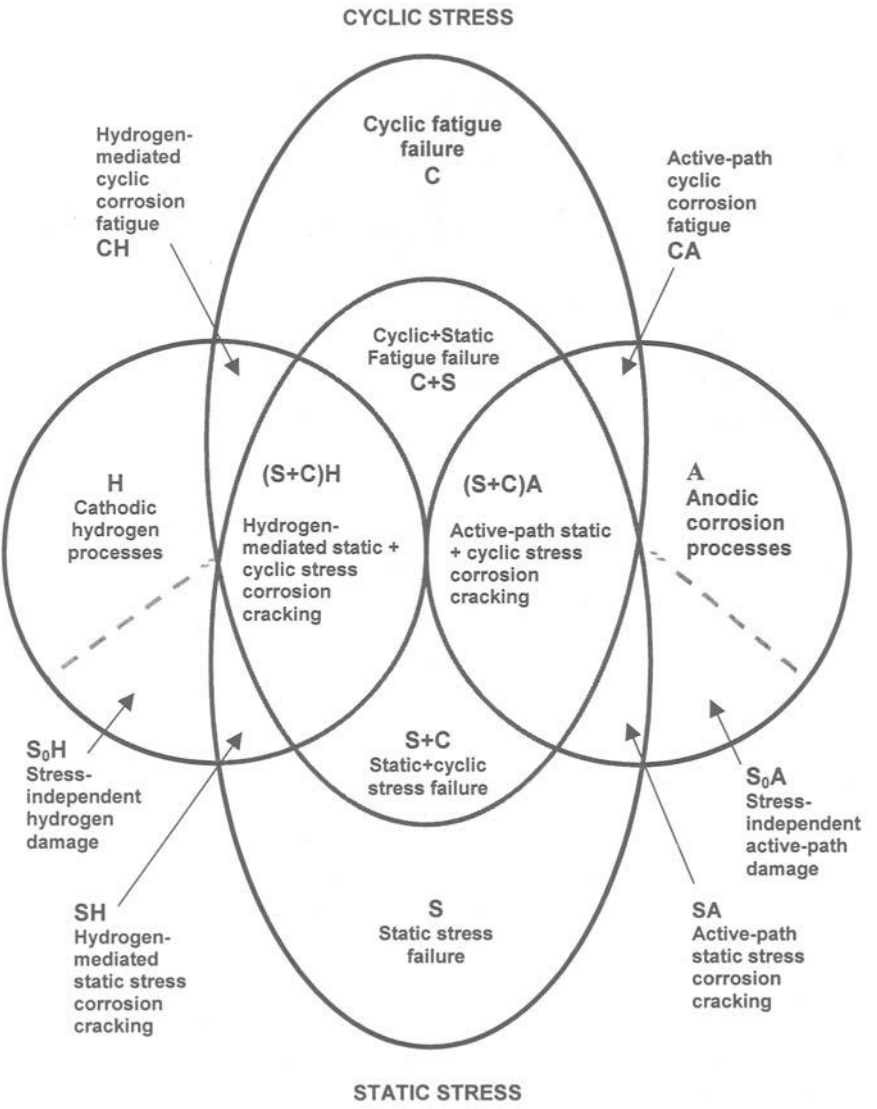


Figure 4—*Superimposed Stress and Electrochemical Axes*

- Mode H, Cathodic Corrosion Processes, contains all corrosion-related cathodic processes where the electrons from the anodic half reactions are accepted by Lewis acids without the induction of brittleness or cracking.

Cracking Modes Independent Of Environmental Factors—Four modes of cracking that do not involve environmental factors form a continuum from pure static loading to pure cyclic loading.

- Mode S, Static Stress Failure, includes all modes of cracking failure (i.e., ductile overload, brittle overload) under purely static tensile stress (R = 1) without any corrosive contribution.

- Mode S fades into Mode S+C, Static/Cyclic Stress Failure, as cyclic stress is impressed on the static stress load and the stress ratio R falls below 1. In this domain, the static stress is more than half of the peak stress.

- Mode C+S fades into Mode S+C, Cyclic/Static Fatigue Failure, when R drops below 0.5 and the static stress is less than half of the peak stress.

- As the static stress contribution approaches zero, Mode S+C merges with Mode C, Cyclic Fatigue Failure. In Mode C there is no static stress component either applied or residual, and $R \leq 0$. The current common name for this domain is fatigue.

Environmental Cracking Modes Requiring Simultaneous Tensile Stress—Six cracking modes result from the simultaneous interaction of tensile stress and a corrosive environment. Three of these modes are active-path processes and three are hydrogen-mediated. Table 2 compares the distinctive features of active-path and hydrogen-mediated cracking.

- Mode SA, Active-Path Static Stress Corrosion Cracking, contains all active path stress corrosion cracking mechanisms occurring under purely static stress. Examples include polythionic acid cracking, chloride stress cracking, season cracking, and caustic cracking.

- Mode CA, Active-Path Cyclic Corrosion Fatigue, contains all cracking mechanisms involving active-path propagation under pure cyclic load (total applied plus residual stress dropping to or passing through zero on each cycle).

- Mode (S+C)A, Active-Path Static + Cyclic Stress Corrosion Cracking, contains all active path stress corrosion cracking mechanisms occurring under combined static and cyclic stresses. Mode (S+C)A fades without clear boundary into mode SA as R approaches 1, and likewise fades without clear boundary into Mode CA as R approaches zero.

Table 2—*Comparison of active-path and hydrogen-mediated cracking mechanisms.*

		Active-path Cracking Processes	Hydrogen-mediated cracking Processes
Commonly used names		Chloride stress cracking, ammonia cracking, season cracking.	Hydrogen embrittlment, cathodic hydrogen damage, hydrogen induced cracking (HIC), stress-oriented hydrogen induced cracking (SOHIC), sulfide stress cracking (SSC).
Mechanism		Active path dissolution (rapid metal dissolution at the crack tip)	Detrimental effects of absorbed corrosion product atomic hydrogen. May alter mechanical properties directly by alloying, may react with carbides forming internal pockets of methane, or may precipitate out in microvoids producing stepwise cracking.
Crack initiation		Crack always initiates at surface and propagates inwards.	Cracks may initiate below the alloy surface.
Mechanical Factors	Threshold stress	No threshold stress below which cracking does not occur.	Threshold stress below which cracking does not occur.
	Threshold hardness	No hardness below which cracking does not occur	Threshold hardness blow which cracking does not occur.
	Notch sensitivity	Generally not sensitive	Sensitive
Environmental Factors	Effect of anodic polarization	Accelerates cracking	Inhibits cracking
	Effect of cathodic polarization	Inhibits cracking	Accelerates cracking
	Causative agent(s)	Alloy dependent (Chloride most common)	Atomic hydrogen
	Effect of atomic hydrogen recombination inhibitors (i.e., sulfide, cyanide, arsenic compounds)	Little if any	Strong accelerators
	Effect of pH	Slight increase in rate with decreasing pH.	Strong increase in rate with decreasing pH.
	Effect of oxygen	May greatly accelerate attack.	Little effect.
	Effect of temperature	Increasing temperature increases severity.	Increasing temperature may decrease severity.

- Mode SH, Hydrogen-Mediated Static Stress Corrosion Cracking, contains the cracking failure modes resulting from absorption of atomic hydrogen into metals or alloys under static stress. Current nomenclature for these processes includes hydrogen stress cracking (HSC), hydrogen induced stress corrosion cracking (HSCC), sulfide stress cracking (SSC), hydrogen fluoride stress cracking (HFSC), and stress oriented hydrogen induced cracking (SOHIC) plus probably others.

- Mode CH, Hydrogen-Mediated Cyclic Corrosion Fatigue, is the compliment to Mode SH, with the difference being that the stress is purely cyclic ($R \leq 0$). Polarization cathodic to the hydrogen ion reduction potential is known to accelerate the corrosion fatigue of many materials, but the diverse nomenclature associated with static hydrogen cracking has not evolved for systems affected by hydrogen-mediated corrosion fatigue.

- Mode (S+C)H, Hydrogen-Mediated Static/Cyclic Stress Corrosion Cracking, contains the cracking failure modes resulting from absorption of atomic hydrogen into metals or alloys under combined static and cyclic stresses. Mode (S+C)H fades without clear boundary into mode SH as R approaches 1, and likewise fades without clear boundary into Mode CH as R approaches zero.

Cracking Processes Independent of Simultaneous Stress—There are two modes of cracking that do not require the simultaneous application of tensile stress.

- Mode S_0A, Intergranular Corrosion, for example of a sensitized austenitic stainless steel, can propagate without the simultaneous application of tensile stress (is independent of simultaneous stress). Subsequent application of stress may produce a fracture with the appearance of intergranular stress corrosion cracking.

- Mode S_0H, Stress-Independent Hydrogen Damage, contains modes of hydrogen-mediated damage that do not require simultaneous tensile strength. These include—
  - -- Hydrogen embrittlement in which a susceptible material charged with hydrogen fails due to reduced ductility and/or toughness when a subsequent tensile load is applied
  - -- Microstructural alteration by hydride formation
  - -- Microstructural disruption due to precipitation of molecular hydrogen (H_2) at interstitial defects in the lattice, producing such effects as hydrogen blistering and hydrogen induced cracking, sometimes designated as step-wise hydrogen cracking.

Inducing Agent Systems

By definition, the inducing agent is the chemical factor in the environment essential for the environmentally induced cracking to occur. The inducing agent may be directly involved in the crack propagation process as is the case with chloride-induced stress corrosion cracking of austenitic stainless steels. However, the inducing agent may be only indirectly involved with the mechanism of crack propagation as is the case with sulfide stress cracking, cyanide cracking, arsenical cracking, and hydrogen fluoride cracking. In each of these cases, the inducing agent, sulfide for example, does not participate in the crack propagation process, but instead promotes the absorption of atomic hydrogen (actually inhibits the recombination step of Eq 5), thus introducing the atomic hydrogen responsible for crack propagation.

Inducing agents are material-specific, meaning that a substance that promotes cracking in one material or category of materials may be harmless to other materials or categories of materials. Table 3 lists a number of known materials/inducing agent systems.

Proposed Naming of Phenomena

It is proposed that the diverse environmental cracking phenomena be named in the pattern *mode-inducing agent.* For example, the cracking of U-bend specimens in boiling magnesium chloride would be designated as *active-path static stress cracking by chloride*, cracking of a component subjected to combined static and cyclic stresses in a hydrogen sulfide environment would be designated as *hydrogen-mediated static + cyclic stress cracking by sulfide.*

Implications for Risk Assessment and Evaluation

Whether or not the proposed nomenclature is adopted, Figure 4 provides an integrated framework for assessing the potential for environmentally induced cracking in aqueous systems. To apply Figure 4:

- Define the stress domain(s) to which the component or materials will be exposed;
- Define the process environment(s) and identify any potential inducing agents;
- Evaluate whether cathodic, anodic, or both cathodic and anodic electrochemical processes may affect the component; and
- Based on the above, consider whether there is a potential for environmentally induced cracking.

Table 3—*Some known material/inducing agent systems.*

Metal or Alloy	Known Inducing Agent(s)
Carbon steels	nitrates
	carbonate/bicarbonate
	concentrated hydroxide (caustic)
	sodium hydroxide-sodium silicate solutions
	acidic hydrogen sulfide solutions
	hydrogen cyanide solutions
High-strength low-alloy steels	aqueous electrolytes, especially those containing hydrogen sulfide, cyanide, or arsenical compounds
Austenitic stainless steels	hot chlorides
	chloride contaminated steam
	hydroxide
High nickel alloys	high-purity steam
	concentrated hydroxide
Copper alloys	ammonia
	ammonia vapor
	amines
	water
	water vapor
Aluminum alloys	aqueous chloride, bromide, or iodide solutions
	sea water
	air
	water vapor
Titanium alloys	aqueous chloride, bromide, or iodide solutions
	some organic solvents
Magnesium alloys	aqueous chloride solutions
Zirconium alloys	aqueous chloride solutions
	some organic solvents
	iodine at 350°C

Conclusions

- An improved nomenclature or taxonomy for environmentally induced stress cracking phenomena has been presented.

- This improved nomenclature relates cracking phenomena in terms of the nature of the stresses involved as well as the underlying electrochemical processes, and relates environmentally induced cracking phenomena to stress-related processes that do not involve corrosion, as well as to corrosive processes that do not involve stress.

References

[1] Brasunas, A. de S. and Hamner, N.E., "Scope and Language of Corrosion," *NACE Basic Corrosion Course,* NACE-International, Houston, TX, 1978.

[2] "Glossary of Terms," *Corrosion, Metals Handbook, Ninth Edition, Vol. 13,* ASM-International, Metals Park, OH, 1987, pp. 1-14.

[3] Glasser, W. and Wright, I. G., "Mechanically Assisted Degradation," *Corrosion, Metals Handbook, Ninth Edition, Vol. 13,* ASM-International, Metals Park, OH, 1987, pp. 142-144.

[4] Jones, R. H. and Ricker, R. E., "Stress Corrosion Cracking," *Corrosion, Metals Handbook, Ninth Edition, Vol. 13,* ASM-International, Metals Park, OH, 1987, pp. 145-163.

[5] Sprowls, D. O., "Evaluation of Corrosion Fatigue," *Corrosion, Metals Handbook, Ninth Edition, Vol. 13,* ASM-International, Metals Park, OH, 1987, pp. 291-302.

[6] Ford, F. P., "Current Understanding of the Mechanism of Stress Corrosion and Corrosion Fatigue," *Environment-Sensitive Fracture: Evaluation and Comparison of Test Methods,* ASTM STP 821, Dean, S. W., Pugh, E. N., and Ugianski, G. M., Ed., American Society for Testing and Materials, West Conshohocken, PA, 1984, pp. 32-51.

[7] Craig, B., "Hydrogen Damage," *Corrosion, Metals Handbook, Ninth Edition, Vol. 13,* ASM-International, Metals Park, OH, 1987, pp. 163-171.

[8] Raymond, L., "Evaluation of Hydrogen Embrittlement," *Corrosion, Metals Handbook, Ninth Edition, Vol. 13,* ASM-International, Metals Park, OH, 1987, pp. 283-290.

[*9*] Sprowls, D. O., "Evaluation of Stress-Corrosion Cracking," *Corrosion, Metals Handbook, Ninth Edition, Vol. 13*, ASM-International, Metals Park, OH, 1987, pp. 245-282.

[*10*] Fontana, M. G. and Greene, N.D., *Corrosion Engineering*, McGraw-Hill Book Company, New York, NY, 1967, pp. 91-115.

[*11*] Brown, B. F., *Stress Corrosion Cracking Control Measures*, NACE-International, Houston, TX, 1981, pp. 1-69.

[*12*] Engel, L., and Klingele, H., *An Atlas of Metal Damage—Surface Examination By Scanning Electron Microscope*, Prentice-Hall, Englewood Cliffs, NJ, 1981, pp. 76-120.

Eun U. Lee,[1] Henry C. Sanders,[2] Kenneth George,[1] and Veena V. Agarwala[1]

Environmentally Influenced Near-Threshold Fatigue Crack Growth in 7075-T651 Aluminum Alloy

Reference: Lee, E. U., Sanders, H. C., George, K., and Agarwala, V. V., **"Environmentally Influenced Near-Threshold Fatigue Crack Growth in 7075-T651 Aluminum Alloy,"** *Environmentally Assisted Cracking: Predictive Methods for Risk Assessment and Evaluation of Materials, Equipment, and Structures, ASTM STP 1401,* R. D. Kane, Ed., American Society for Testing and Materials, West Conshohocken, PA, 2000.

Abstract: The near-threshold fatigue crack growth behavior of the 7075-T651 aluminum alloy was studied in laboratory air, vacuum, and an aqueous 3.5% NaCl solution. Results indicate that a rising stress ratio (R) enhanced the near-threshold fatigue crack growth by increasing the crack growth rate (da/dN) and decreasing the threshold stress intensity range (ΔK_{th}) in both laboratory air and aqueous 3.5% NaCl solution. However, the reverse was observed in vacuum. It was also noticed that the near-threshold fatigue crack growth resistance was greatest in vacuum, intermediate in aqueous 3.5% NaCl solution, and lowest in laboratory air. Conversely, the crack growth rate at given values of ΔK were shown to be greatest in laboratory air, less in 3.5% NaCl solution, and lowest in vacuum. In both laboratory air and aqueous 3.5% NaCl solution, ΔK_{th} initially decreased with increasing R until a critical stress ratio of $R_c = 0.5$ was reached, which it then leveled off or decreased slightly. The ΔK_{th} values for these two environments appear to converge at a higher R. On the other hand, in vacuum, the ΔK_{th} increased linearly with increasing R. In addition, at lower R, a greater resistance to near-threshold fatigue crack growth was detected in aqueous 3.5% NaCl solution than in laboratory air. This is presumably attributed to crack closure that has been induced by accumulation of corrosion product in the crack-tip.

Keywords: fatigue, near-threshold fatigue crack growth, stress ratio, vacuum, laboratory air, 3.5% NaCl solution, threshold stress intensity range, maximum stress intensity

[1]Materials Engineer and [2]Materials Engineering Technician, Naval Air Warfare Center Aircraft Division, Aerospace Materials Division, Code 4.3.4.2, Unit 5, Patuxent River, MD, 20670.

Copyright© 2000 by ASTM International www.astm.org

Due to its high strength, aluminum alloy (AA) 7075-T6 has been widely used in the fabrication of airframe structures. The AA 7075 contains zinc, magnesium, copper, and chromium. The T6 heat-treatment coincides with the peak-aged condition of the material that provides high strength but has drawbacks of low fracture toughness at room and cryogenic temperatures and poor resistance to stress-corrosion cracking. To improve the fracture toughness and stress-corrosion resistance, a T73 temper has been introduced, but this temper lowers the overall tensile and yield strengths. In any case, many in-service aircraft have been fabricated using the T6 temper, therefore necessitating further study.

Recently, a great emphasis is being placed upon the maintenance and integrity of AA 7075-T6 structures to extend the life of aging aircraft. During their long service, many aircraft structures have been subjected to repeated loading in corrosive environments. As a result, it is highly likely that mechanical fatigue and/or corrosion fatigue has been developed in those aging structures. Therefore, it is essential to understand this fatigue behavior for assessing and extending the service life of aging airframe structures of AA 7075-T6. This study was initiated to characterize the fatigue behavior, specifically in the near-threshold regime of fatigue crack growth, in the presence of an inert and corrosive environments.

Experimental Procedure

The material used for this study was an AA 7075-T651 plate with the following dimensions: 279 x 406 x 9.5 mm (11 x 16 x 3/8 in.). Tables 1 and 2 show the chemical composition limits and typical mechanical properties for AA 7075-T651, respectively. Figure 1 depicts the microstructure and orientation of a longitudinal section taken parallel to rolled surface of the specimen material plate. The microstructure consists of grains elongated in the rolling direction with dispersed stringers of precipitated particles of $MgZn_2$, $Cr_2Mg_3Al_{18}$ and (Fe, Mn)Al_6.

TABLE 1-*Chemical composition limits for AA 7075.*

	Weight Percent	
Element	Min	Max
Cu	1.2	2.0
Mg	2.1	2.9
Mn	---	0.3
Fe	---	0.7
Si	---	0.5
Zn	5.1	6.1
Cr	0.18	0.4
Ti	---	0.2
Other Impurities		
Each	---	0.05
Total	---	0.15
Al	Balance	

TABLE 2–*Typical Mechanical properties of AA 7075-T651 plate.* [*1*]

	MPa	ksi	%	MPa√m	ksi√in
Tensile Strength	572	83			
Yield Strength	503	73			
Elongation			11		
Fracture Toughness:					
L-T Orientation				28.6	26
T-L Orientation				24.2	22
S-L Orientation				17.6	16

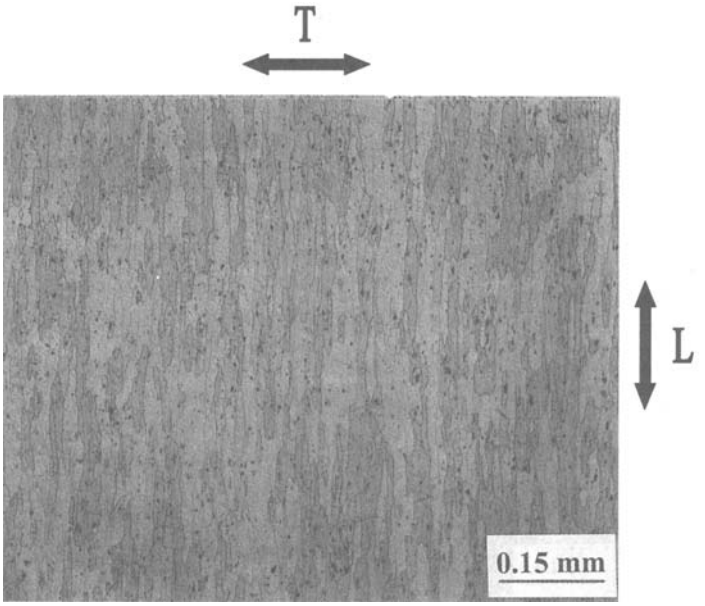


FIG. 1–*Micrograph of specimen material taken at a longitudinal section parallel to the rolled surface revealing a microstructure characteristic of AA 7075-T651.*

Compact tension, C(T), specimens, 9.5 mm (3/8 in.) thick and 38.1 mm (1.5 in.)*, were prepared in the L-T orientation from the plate in accordance with ASTM E 647-95a. (* The C(T) specimen width, 38.1 mm is the "W" in Figure 1 of ASTM E 647-95a.)

For the fatigue tests, two closed-loop servo-hydraulic mechanical test machines were employed: a vertical MTS machine equipped with an environmental chamber was used for testing in air and vacuum; a horizontal mechanical test machine coupled with a liquid container was used for testing specimens with the crack tip fully submersed in an aqueous solution. The liquid was constantly circulated between the container and a 3.8 liter (1 gallon) reservoir by a pump without aerating. Each test machine was interfaced with a computer system for automated monitoring of fatigue load and crack growth.

Fatigue tests were conducted at ambient temperature under load control in tension-tension cycling with a sinusoidal waveform at a frequency of 10 Hz and stress ratios (R = minimum stress/maximum stress) ranging from 0.1 - 0.9. The test environments were laboratory air, vacuum ($2\sim4 \times 10^{-8}$ torr), and an aqueous non-aerating 3.5% NaCl solution of pH 7.3. The loading procedure consisted of K-decreasing (load shedding) with a K-gradient parameter $C = -0.16\ mm^{-1}$ and K-increasing with a $C = +0.16\ mm^{-1}$, for fatigue crack growth rates (da/dN) below and above 2.54×10^{-5} mm/cycle (10^{-6} in./cycle) respectively. The crack length was determined using a compliance measurement technique.

After the fatigue testing, one side of the C(T) specimens was ground and polished, and then etched in Keller's reagent to reveal the microstructure. Micrographs were taken to characterize the crack path resultant of testing in the various environments.

Results and Discussion

Fatigue Crack Growth Rate

In both laboratory air and aqueous 3.5% NaCl solution, ΔK_{th} decreased with increasing R as shown in Figs. 2 and 3. In vacuum, the reverse behavior was observed as shown in Fig. 4. Also, increasing R showed an increase in da/dN for given values of ΔK for tests conducted in laboratory air. This is clearly demonstrated in Fig. 3 by comparison of data taken at R values of 0.8 and 0.5. Similar behavior was observed in tests performed in aqueous 3.5% NaCl solution, however, the effect was more subtle.

With decreasing R, it became impossible to collect fatigue crack growth data in aqueous 3.5% NaCl solution below a certain da/dN due to the occurrence of crack arrest. As shown in Fig. 3, crack arrest occurred at da/dN values of 7×10^{-11}, 1×10^{-10} and 5×10^{-10} mm/cycle at R-values of 0.5, 0.3 and 0.15 respectively. Similar behavior has been reported for underaged, peak-aged, and overaged 7075 aluminum alloys tested in moist air of 95% relative humidity [*2*], 2024-T351 aluminum alloy in dry and wet argon [*3*], Al-3%Mg alloy in dry nitrogen at 298°K and in liquid nitrogen at 77°K [*4*], 7091 aluminum alloy in air of humidity greater than 90% [*5*], and 2024-T3 aluminum alloy in laboratory air at ambient temperature [*6*]. These observations have also been made for low and medium carbon alloys, 2¼ Cr-1 Mo, rotor, 4340, JIS SB42, and AerMet 100 steels [*7-16*].

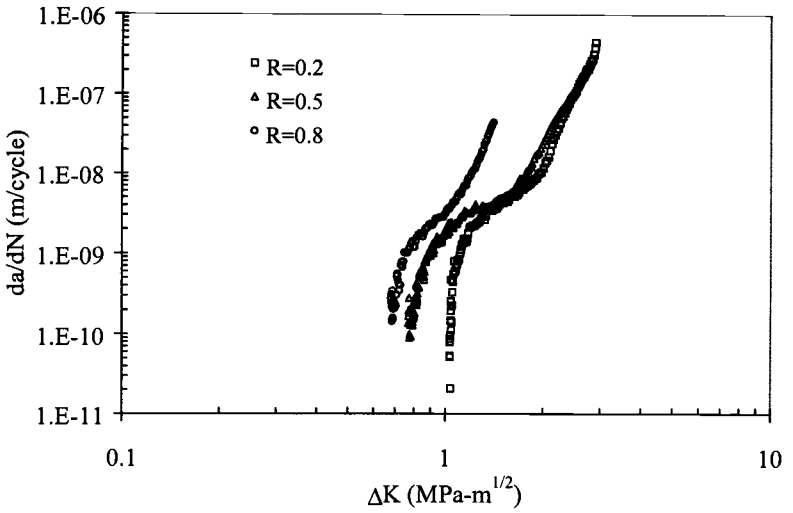


FIG. 2–*Variation of fatigue crack growth rate da/dN with stress intensity range ΔK at stress ratios R = 0.2, 0.5, and 0.8 in laboratory air.*

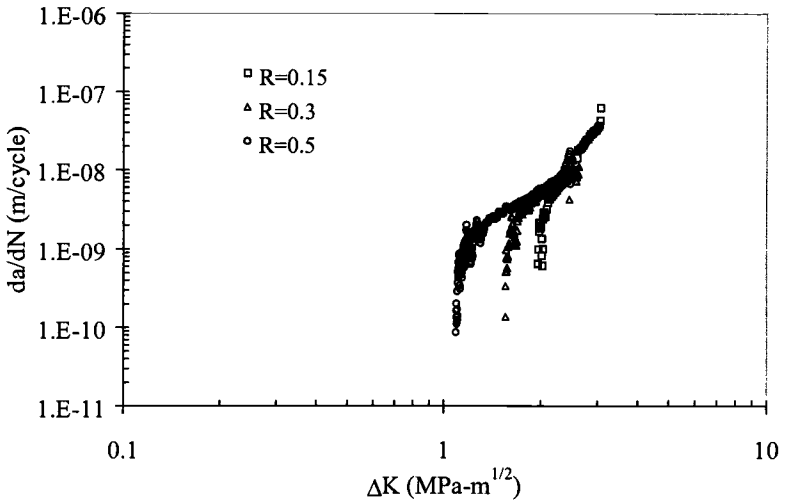


FIG. 3–*Variation of fatigue crack growth rate da/dN with stress intensity range ΔK at stress ratios R = 0.15, 0.3, and 0.5 in an aqueous 3.5% NaCl solution.*

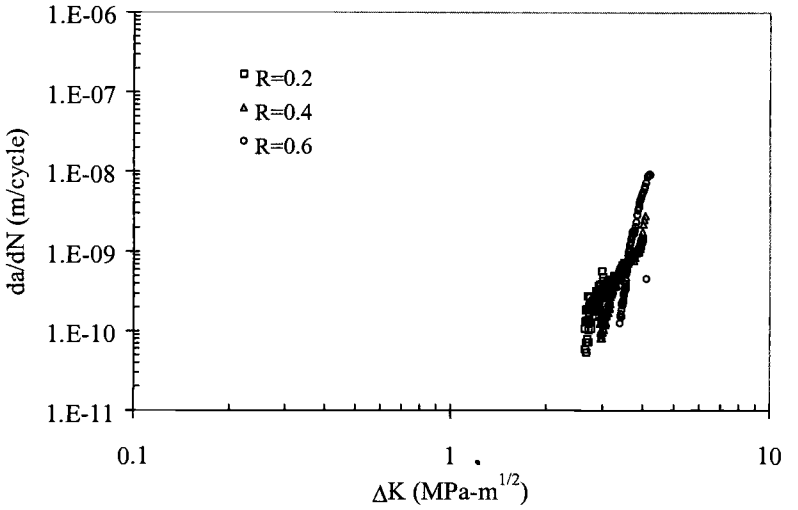


FIG. 4–*Variation of fatigue crack growth rate da/dN with stress intensity range ΔK at stress ratios R = 0.2, 0.4, and 0.6 in vacuum.*

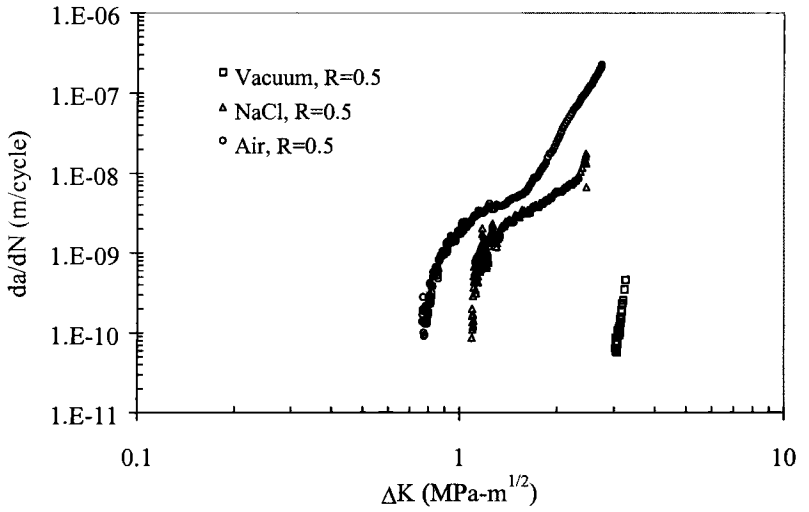


FIG. 5–*Variation of fatigue crack growth rate da/dN with stress intensity range ΔK at a stress ratio R = 0.7 for testing in laboratory air, vacuum, and an aqueous 3.5% NaCl solution.*

Overall, for a given R, ΔK_{th} was greatest in vacuum, intermediate in aqueous 3.5% NaCl solution, lowest in laboratory air. Conversely, da/dN was shown to be greatest in laboratory air, less in 3.5% NaCl solution, and lowest in vacuum over a range of ΔK. Figure 5 depicts this fatigue crack growth behavior for the three aforementioned environments at R = 0.5.

Threshold Stress Intensity Range ΔK_{th} and Maximum Stress Intensity K_{max}

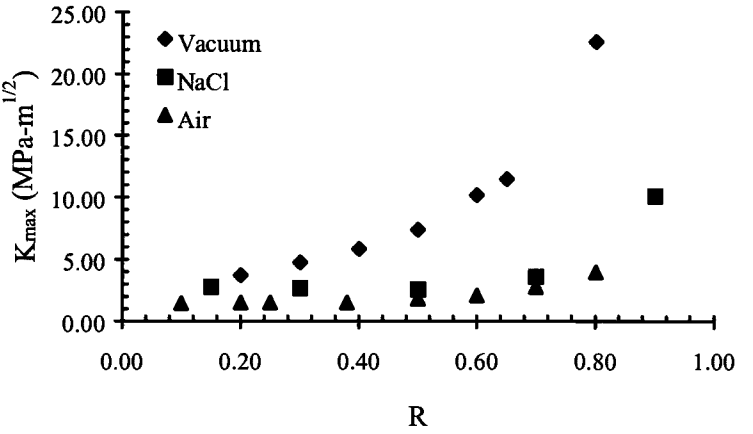
As previously stated, ΔK_{th} varies with R and the environment, as does the corresponding maximum stress intensity K_{max} ($K_{max}=\Delta K_{th}/(1 - R)$). This variation with R is illustrated in Fig. 6.

In both laboratory air and aqueous 3.5% NaCl solution, ΔK_{th} initially decreased with increasing R until a critical stress ratio $R_c = 0.5$ was reached and then leveled off or decreased slightly. Moreover, Figure 6 also shows that these two curves approximately converge at R = 0.9. Extrapolation of the linear portion of the ΔK_{th} vs. R curve for $R < R_c$ intersects the R-axis at $\Delta K_{th} > 0$ for laboratory air and $\Delta K_{th} < 0$ for aqueous 3.5% NaCl solution. The corresponding K_{max} increased slightly for $R < 0.5$ and then rose sharply for $R > 0.5$, confirming $R_c = 0.5$. R_c represents the demarcation in the fatigue regimes below which K_{max} is controlling and above which ΔK is controlling. A similar result has been reported for underaged, peak-aged, and overaged AA 7075 in moist air of 95% relative humidity [*2*].

Mathematically, at R = 1, the cyclic stress amplitude is 0, i.e., $\Delta K = 0$, and $K_{max} = \Delta K/(1\text{-}R)$ becomes indeterminate. Physically, as K_{max} increases with R approaching 1, an alternate damage process should supersede fatigue. This alternate damage process often includes tensile overload fracture characterized by K_{IC} and time-dependent subcritical crack growth processes, such as sustained load crack growth, stress-corrosion crack growth, creep crack growth, etc.

In a vacuum environment, Fig. 6 shows that both ΔK_{th} and K_{max} increase with an increasing R. Furthermore, the increase in K_{max} was greater than in laboratory air or aqueous 3.5% NaCl solution. These particular data suggest that there is a significant difference from the fatigue crack growth behavior in laboratory air and aqueous 3.5% NaCl solution.

Similar observations of greater ΔK_{th} and lower fatigue crack growth rate in a vacuum than in air and corrosive environments have been made for steels and aluminum alloys by a number of investigators [*2, 8, 12, 17-19*]. For example, Cooke et al [*8*] observed that in a vacuum (10^{-5} torr) the fatigue crack growth rate of medium carbon steel had been reduced by a factor of 30 and that there was no significant effect of R on ΔK_{th} by comparison with laboratory air. They accounted for this difference in laboratory air to intergranular fracture as a consequence of reverse crack tip plasticity of a size equivalent to the prior austenite grain size.



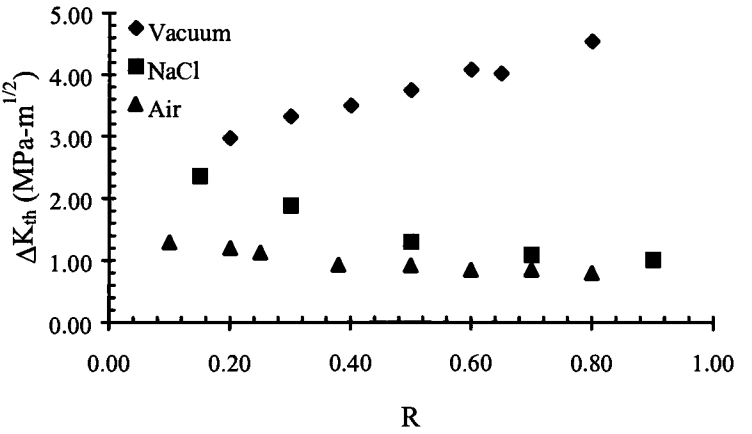


FIG. 6–*Variation of maximum and alternating stress intensities, K_{max} and ΔK_{th}, with stress ratio R in laboratory air, vacuum, and an aqueous solution of 3.5% NaCl solution.*

Lindigkeit et al [*17*] investigated the fatigue crack propagation behavior of age-hardened Al-5.7Zn-2.5Mg-1.5Cu alloy in a vacuum (10^{-7} torr) and 3.5% NaCl solution. Crack propagation occurred along slip bands in vacuum. However, in 3.5% NaCl solution, this occurred along grain boundaries at lower ΔK with reduced ΔK_{th} and then along slip bands at higher ΔK but at an order of magnitude more rapidly than in vacuum. They concluded that the corrosive environment had accelerated crack propagation by the entrapment of hydrogen atoms within the slip bands, which in turn lower the local

fracture stress and the reversibility of dislocation motion.

Stewart [*12*] studied the fatigue crack propagation in low alloy steels, and found a lower fatigue crack growth rate and higher ΔK_{th} in a vacuum (10^{-6} torr) than in humid laboratory air. The linear dependence of ΔK_{th} on R was strong in laboratory air, but greatly reduced, i.e., the value of ΔK_{th} at R = 0.8 is less than the value of ΔK_{th} R = 0.1 in vacuum. He concluded the following: (1) The greater crack propagation rate in humid laboratory air is caused by atomic hydrogen, which is produced by the reaction between the steel and water vapor, that accumulates in regions of highest hydrostatic stress and reduces the cohesive strength/fatigue resistance. (2) This cracking mechanism is absent in a vacuum.

Suresh et al [*2*] investigated fatigue crack propagation in AA 7075 that had been heat-treated to underaged, peak-aged, and overaged conditions over a range of R in 95% relative humidity air and vacuum (10^{-7} torr). Comparison of the near-threshold fatigue behaviors in both humid air and vacuum showed that the presence of moisture leads to a larger reduction in ΔK_{th} and an increase in the crack propagation rate. This is ascribed to an interaction among three mechanisms: the embrittling effect of moisture, the role of microstructure and slip mode in inducing crack deflection, and crack closure arising from a combination of environmental and microstructural contributions. However, in a vacuum, moisture-induced embrittling and crack closure are negligible.

Carter et al [*18*] studied the fatigue crack growth resistance of an AA 7475 in underaged and overaged conditions. The fatigue crack growth resistance was found to be greater in vacuum (10^{-6} torr) than in laboratory air with a relative humidity of 50%. They concluded that this was due to the absence of environmental embrittlement and to the clean metal surface in the crack tip region allowing ease of slip reversibility in vacuum. In another investigation, James and Knott [*19*] observed ΔK_{th} and fatigue crack growth rate to be greater in vacuum (10^{-7} torr) than in air and ΔK_{th} to be virtually independent of R in a vacuum but decreasing with increasing R in air for a Q1N steel. They also rationalized the environmental effect with the greater slip reversibility at the crack tip and the resultant smaller amount of crack extension or lower crack growth rate in vacuum.

The resistance of steels to threshold fatigue crack growth has been reported to be greater in aqueous 3.5% NaCl solution than in laboratory air. This behavior was attributed to crack closure induced by crack-tip corrosion products [9, 11-14]. Therefore, one can expect a similar behavior in other materials fatigue tested in an aqueous 3.5% NaCl solution, as was seen in Fig. 5 for AA 7075-T651. Furthermore, this type of crack closure is more prominent at lower stress ratios [20], which is substantiated by the observed greater crack arrest at lower stress ratios in Fig. 3 for AA 7075-T651.

Figure 7 is a plot of ΔK_{th} against K_{max} for the fatigue tests in the three aforementioned environments. Such a plot, called a fundamental threshold curve [*16*], provides an interrelation between ΔK_{th} and K_{max} that defines regimes where a fatigue crack grows (above the curve) and where it does not (below the curve). In addition, Fig. 7 demonstrates that the resistance to threshold fatigue crack growth is greatest in vacuum, intermediate in an aqueous 3.5% NaCl solution, and least in laboratory air, for a given K_{max}.

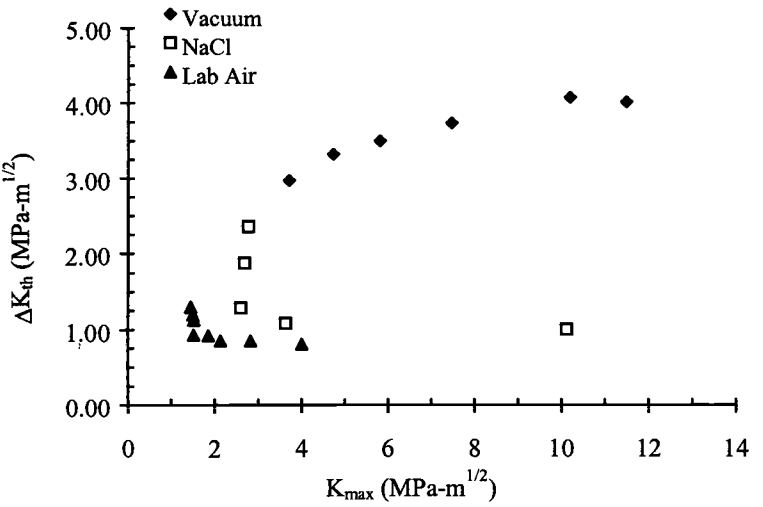


FIG. 7–*Fundamental threshold curves, showing variation of ΔK_{th} with K_{max} in laboratory air, vacuum, and an aqueous 3.5% NaCl solution.*

Crack Path

The crack path can be summarized in the following manner: (1) mostly linear, approximately normal to the loading axis, (2) transgranular, deflecting at grain boundaries and precipitated particles, (3) some branching, and (4) not affected by either R or ΔK. With respect to crack deflection, kinking, forking and zigzagging were seen. Representations of the fatigue crack path morphologies for the three environments are shown in Fig. 8 at R = 0.5.

A fatigue crack can be deviated from its normal Mode I growth plane by crack-tip interaction with microstructural inhomogeneities such as grain boundaries and interfaces, crystallographic separation, or embrittling effect of an aggressive environment [*20*]. Since the effective stress intensity factor for a deflected or branched crack is smaller than that of a straight crack of the same projected length, a crack path change reduces the fatigue crack growth rate. The deflection of a fatigue crack from the nominal Mode I plane induces mixed-mode near-tip conditions even if the far-field loading is Mode I. Therefore, a deflected or branched crack requires a larger driving force than a linear crack to propagate at the same velocity. The crack path morphologies, observed in this study, suggest that the fatigue crack growth rate had been reduced correspondingly by crack deflection and/or branching occurring in the three different environments (vacuum, laboratory air, and 3.5% NaCl solution).

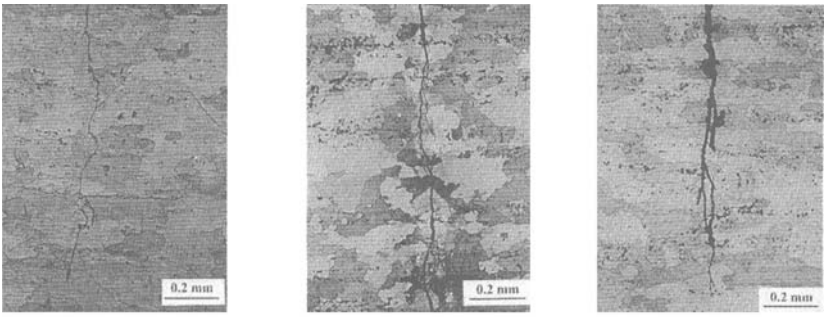


FIG. 8–*Typical crack paths (on a side face) of C(T) specimens that have been fatigue tested in (a) vacuum), (b) laboratory air and (c) an aqueous 3.5% NaCl solution. (Etched in Keller's reagent.)*

Conclusions

1. Raising the stress ratio increases the near-threshold fatigue crack growth with greater da/dN and smaller ΔK_{th} for specimens tested in laboratory air and in an aqueous 3.5% NaCl solution. However, the reverse is true for a vacuum environment.
2. The near-threshold fatigue crack growth is slowest with a smallest da/dN and greatest ΔK_{th} in a vacuum, intermediate with an intermediate da/dN and ΔK_{th} in an aqueous 3.5% NaCl solution, and fastest with the greatest da/dN and smallest ΔK_{th} in laboratory air.
3. In both laboratory air and aqueous 3.5% NaCl solution, ΔK_{th} initially decreases with increasing R until the critical stress ratio $R_c = 0.5$ is reached, and then levels off or decreases slightly. The ΔK_{th} values for these two environments also converge at a higher R-value. Conversely, in a vacuum, ΔK_{th} increases linearly with increasing R.
4. With increasing R, the threshold maximum stress intensity K_{max} slowly increases and subsequently rises sharply for all the three aforementioned environments.
5. The resistance to the threshold fatigue crack growth is greater in aqueous 3.5% NaCl solution than in laboratory air at a lower R. This is presumed to be attributed to crack closure induced by corrosion product accumulating at the crack-tip.

References

[*1*] ASM International Handbook Committee, 1995, *ASM Handbook, Vol. 2, Properties and Selection: Nonferrous Alloys and Special-Purpose Materials*, ASM International, Materials Park, OH, pp. 115-117.

[*2*] Suresh, S., Vasudevan, A. K. and Bretz, P. E., "Mechanism of Slow Fatigue Crack Growth in High Strength Aluminum Alloys: Role of Microstructure and Environment," *Metallurgical Transactions A*, Vol. 15A, 1984, pp. 369-379.

[*3*] Ballon, J. P., ElBoujdaini, M. and Dickson, J. I., "Environmental Effects on ΔK_{th} in

70-30 α-Brass and 2024-T351 Al Alloy," *Fatigue Crack Growth Threshold Concepts*, D. L. Davidson and Suresh, S., ED., The Metallurgical Society of AIME, Philadelphia, PA, 1983, pp. 63-82.

[*4*] Park, D. H. and Fine, M. E., "Origin of Crack Closure in the Near-Threshold Fatigue Crack," *ibid,* pp. 145-161.

[*5*] Bretz, P. E., Petit, J. I. and Vasudevan, A. K., "The Effects of Grain Size and Stress Ratio on Fatigue Crack Growth in 7091 Aluminum Alloy," *ibid.*, pp. 163-183.

[*6*] Blom, A. F., "Near-Threshold Fatigue Crack Growth and Crack Closure in 17-4 PH Steel and 2024-T3 Aluminum Alloy," *ibid.*, pp. 263-279.

[*7*] Cooke, R. J. and Beevers, C. J., "The Effect of Load Ratio on the Threshold Stresses for Fatigue Crack Growth in Medium Carbon Steels," *Engineering Fracture Mechanics*, Vol. 5, 1973, pp. 1061-1071.

[*8*] Cooke, R. J., Irving, P. E., Booth, G. S. and Beevers, C. J., "The Slow Fatigue Crack Growth and Threshold Behavior of a Medium Carbon Alloy Steel in Air and Vacuum," *Engineering Fracture Mechanics*, Vol. 7, 1975, pp. 69-77.

[*9*] Ritchie, R. O., Suresh, S. and Moss, C. M., "Near-Threshold Fatigue Crack Growth in 2 1/4 Cr - 1 Mo Pressure Vessel Steel in Air and Hydrogen," *Journal of Engineering Materials and Technology*, Vol. 102, 1980, pp. 293-299.

[*10*] Nakai, Y., Tanake, K. and Nakanishi, T., "The Effects of Stress Ratio and Grain Size on Near-Threshold Fatigue Crack Propagation in Low-Carbon Steel," *Engineering Fracture Mechanics*, Vol. 15, 1981, pp. 291-302.

[*11*] Suresh, S., Zaminski, G. F. and Ritchie, R. O., "Oxide-Induced Crack Closure: An Explanation for Near-Threshold Corrosion Fatigue Crack Growth Behavior," *Metallurgical Transactions A*, Vol. 12A, 1981, pp. 1435-1443.

[*12*] Stewart, A. T., "The Influence of Environment and Stress Ratio on Fatigue Crack Growth at Near-Threshold Stress Intensities in Low-Alloy Steels," *Engineering Fracture Mechanics*, Vol. 13, 1980, pp. 463-478.

[*13*] Liaw, P. K., Leax, T. R. and Donald, J. K., "Fatigue Crack Growth Behavior of 4340 Steels," *Acta Metallurgica*, Vol. 35,1987, pp. 1415-1432.

[*14*] Matsuoka, S., Takeuchi, E., Kosuge, M., Shimodaira, M., Ohta, A. and Nishijima, S., "A Method for Determining Conservative Fatigue Threshold While Avoiding Crack Closure," *Journal of Testing and Evaluation*, Vol. 14, 1986, pp. 312-317.

[*15*] Lee, Eun U., "Corrosion Fatigue of AerMet 100 Steel," *Report NAWCADPAX-96-209-TR*, Naval Air Warfare Center Aircraft Division, Patuxent River, MD, 9 July 1996.

[*16*] Vasudevan, A. K. and Sadananda, K., "Classification of Fatigue Crack Growth Behavior," *Metallurgical and Material Transactions A,* Vol. 26A, 1995, pp. 1221-1234.

[*17*] Lindigkeit, J., Terlinde, G., Gysler, A. and Lutjering, G., "The Effect of Grain Size on the Fatigue Crack Propagation Behavior of Age-Hardened Alloys in Inert and Corrosive Environment," *Acta Metallurgica*, Vol. 27, 1979, pp. 1717-1726.

[*18*] Carter, R. D., Lee, E. W., Starke, E. A., Jr. and Beevers, C. J., "The Effect of Microstructure and Environment on Fatigue Crack Closure of 7475 Aluminum Alloy," *Metallurgical Transactions A*, Vol. 15A, 1984, pp. 555-563.

[*19*] James, M. N. and Knott, J. F., "Near-Threshold Fatigue Crack Closure and Growth in Air and Vacuum," *Scripta Metallurgica*, Vol. 19, 1985, pp. 189-194.

[*20*] Suresh, S., 1991, *Fatigue of Materials*, Cambridge University Press, Cambridge, Great Britain

Michiel P. H. Brongers,[1] Gerhardus H. Koch,[1] and Arun K. Agrawal[1]

The Use of Atomic Force Microscopy to Detect Nucleation Sites of Stress Corrosion Cracking in Type 304 Stainless Steel

Reference: Brongers, M. P. H., Koch, G. H., and Agrawal, A. K., **"The Use of Atomic Force Microscopy to Detect Nucleation Sites of Stress Corrosion Cracking in Type 304 Stainless Steel,"** *Environmentally Assisted Cracking: Predictive Methods for Risk Assessment and Evaluation of Materials, Equipment, and Structures, ASTM STP 1401,* R. D. Kane, Ed., American Society for Testing and Materials, West Conshohocken, PA, 2000.

Abstract: The nucleation of intergranular stress-corrosion cracking (IGSCC) in Type 304 stainless steel was investigated using atomic force microscopy (AFM). A new test technique with an AFM fluid cell and a miniature specimen bending device was used for the in-situ measurements. It was found that upon plastic deformation of the annealed and sensitized stainless steel slip lines piled up at the grain boundaries. As a result of the increased localized stresses, some of the grain boundaries opened, particularly at grain boundary triple points and grain boundary - twin boundary intersections. These openings were typically 1 to 2 μm wide and about 1 μm deep. After exposure of the specimens to an aqueous 1000 ppm sodium thiosulfate solution small cracks (< 1 grain diameter) formed from the opened sites within a few hours of the exposure. This indicated that the opened triple points act as nucleation sites for the cracks.

Keywords: **Atomic force microscopy, crack nucleation, stress-corrosion cracking, in-situ test technique, IGSCC**

Introduction

Environmental cracking of austenitic stainless steel components in light water reactors has been a major problem, affecting plant reliability and availability. The prevalent forms of environmental cracking include both stress-corrosion cracking and corrosion fatigue, which occur even in high purity water containing ionic contamination at barely detectable levels, ≤ 10 ppb.

Type 304 stainless steel becomes susceptible to intergranular stress-corrosion cracking (IGSCC) because of sensitization during heat treatment or welding. Sensitization refers to precipitation of chromium carbides along the grain boundaries (e.g., in the heat-affected zones of welds), resulting in depletion of chromium in the adjacent regions, making these susceptible to preferential corrosion attack.

[1] Project Engineer, Senior Group Leader, and Senior Scientist, respectively, CC Technologies, 6141 Avery Road, Dublin, OH 43016-8761, U.S.A.

Copyright© 2000 by ASTM International www.astm.org

Until recently, most of the research effort has been directed towards determining the environmental, metallurgical, and mechanical factors responsible for producing cracking, and understanding of the crack growth mechanisms *[1-8]*, and little research effort was focused on crack nucleation mechanisms. To accurately predict the life of a component, one needs to consider both crack nucleation and propagation stages of the crack life.

It has been assumed that similar to pitting, an incubation period is required in which stress-corrosion cracks nucleate. Wilde *[9]* suggested that this incubation time represents a considerable portion, possibly 90 percent, of the stress-corrosion life of any engineered component, and that a relatively small portion of this life is spent during crack propagation. However, Stewart et al. *[10]* reported that in certain environments such as aqueous sodium thiosulfate, the time for crack nucleation is very short, with cracks becoming visible within a few hours after exposure.

If any microscopic changes, which may occur on the alloy surface prior to crack nucleation can be characterized, the crack nucleation process may be better understood, and methods to monitor or even control the nucleation process may be developed. In order to gain a fundamental understanding of the nucleation process of IGSCC in Type 304 stainless steel, the crack nucleation process was examined at its earliest stage. This IGSCC nucleation study *[11-13]* focused on identifying and characterizing crack nucleation sites, i.e., surface changes prior to the development of small cracks, using atomic force microscopy (AFM), supported by optical microscopy and scanning electron microscopy (SEM). A new test technique with an AFM fluid-cell and a miniature specimen bending device was used for the in-situ measurements.

Atomic Force Microscopy

Atomic force microscopy is one of two different scanning probe microscopy (SPM) techniques, namely scanning tunneling microscopy (STM) and atomic force microscopy (AFM). The basic principle of SPM is that images of surfaces of solid materials can be created by moving a probe close to the specimen surface. The high resolution that can be achieved with this technique is determined by factors such as scanning rate, number of data points collected per unit length, and sharpness of the probe tip. The STM technique was developed in 1981 by Binnig, Rohrer, and co-workers *[14]*, and for this development, Binnig and Rohrer were awarded the Nobel Prize in Physics in 1986. STM probes a specimen surface in a vacuum with electrons that tunnel from a conductive specimen to a conductive metal probe tip. A bias voltage is applied between the sharp probe tip and the specimen surface. The tip and the surface are brought within a distance of a few Ångstroms (1Å = 0.1 nm). As a result of the bias voltage and the small distance, a tunneling current flows between the probe tip and the specimen surface due to quantum mechanical electron tunneling. Physical properties such as surface topography and electronic activity at the specimen surface can be investigated by monitoring the tunneling current, while controlling the separation between the tip and the surface. In 1986, Binnig and Rohrer combined a scanning force technique with micro-surface profilometry, which resulted in AFM. AFM is based on a different principle than STM. While STM measures primarily the electronic properties of a surface, AFM measures physical and topographic surface properties. AFM is not restricted to a vacuum, and can be applied in various environments from ambient air to liquid.

Theoretical Background

The AFM operates by measuring the forces between a sharp probe needle and a relatively flat specimen surface in very close proximity of each other. The attractive and repulsive forces include, but are not limited to Van Der Waals forces, ion-ion repulsion forces, electrostatic and magnetic forces, capillary forces, and adhesion and frictional forces. The magnitude of the forces at any location depends on the topography of the specimen surface, the distance between the probe and the specimen, the probe geometry and any contamination on the surface.

While the horizontal specimen displacement is measured from the piezoelectric crystals in the AFM, the vertical probe deflection Δz is measured by following a laser beam directed on the probe cantilever, and reflected onto a detector, see (Figure 1). As the probe experiences a change in force, the deflection of the probe changes and thus the direction of the laser beam changes. The different location of the laser beam on the detector is recorded for every location on the specimen, and related to the probe deflection. The measurement depends on force interactions between probe and specimen, and is independent of their conductivities. Therefore, AFM can be used for both conductive and non-conductive specimens, unlike techniques such as STM and SEM.

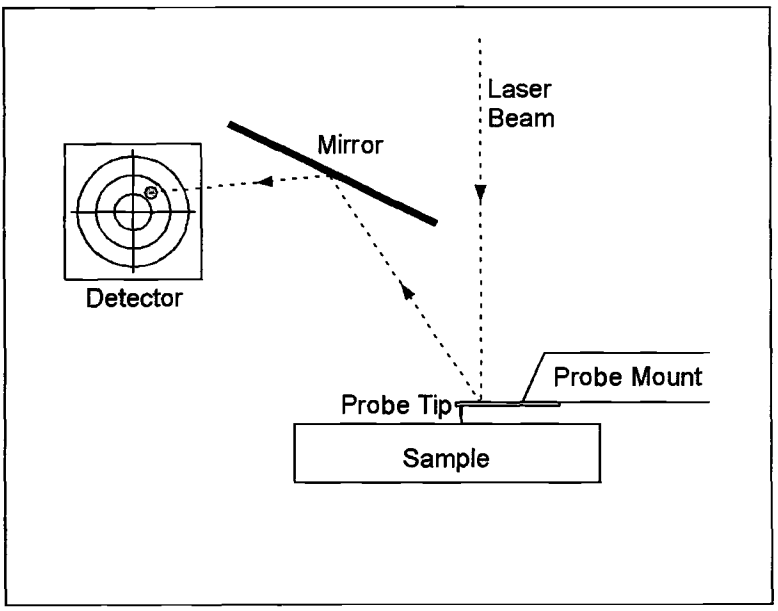
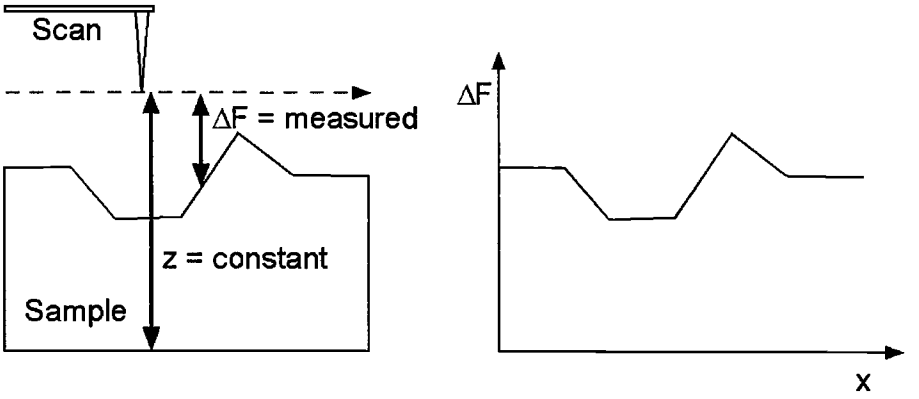


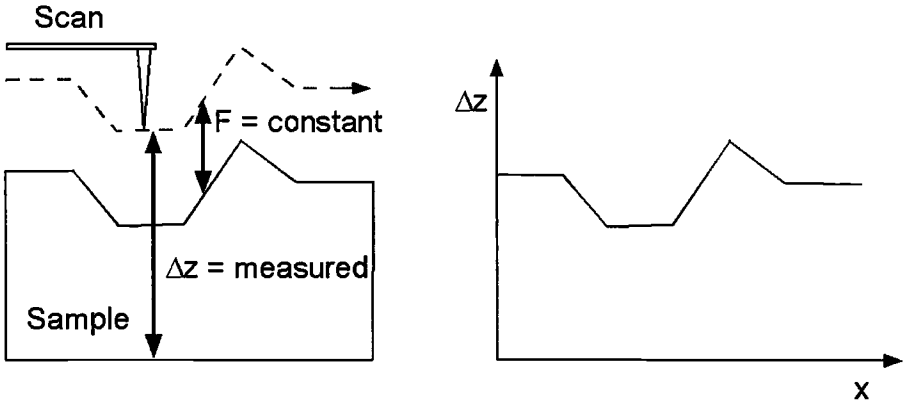
Figure 1 – *Schematic of AFM with dry non-deformed specimen.*

Constant Distance and Constant Force Scans

Two different types of AFM scans are possible. (Figure 2) illustrates the constant distance scanning mode (a) and constant force scanning mode (b). In the constant distance mode, the vertical distance (z) between the probe and the specimen is held constant, as the probe moves horizontally across the specimen surface. The force between the probe tip and the specimen surface is measured at each point. The constant distance mode responds very fast to the surface topography, making it easy to use for an initial scan of an area of 70 × 70 μm to 7 × 7 μm. The constant distance mode is a good



(a) Constant Distance Scanning Mode



(b) Constant Force Scanning Mode

Figure 2 – *Schematic diagram of constant distance (a) and constant force (b) scanning modes.*

option for scanning fast developing (minutes) processes. However, it is relatively difficult to interpret the image. For example, a step on a surface can appear as a dark or a bright band area with two areas of equal brightness on both sides. The actual height of the equal brightness areas can be resolved using the constant force mode.

In the constant force mode, the force between the probe and the surface is held constant, and the constant feedback loop in the AFM hardware responds by adjusting the vertical position of the probe at every point of the scan. The constant force mode provides a scanned image that is easier to interpret. It takes more time to scan the image, and ridges and steps appear less pronounced than in the scanned images of the constant distance mode. For the investigation of crack nucleation sites both scanning modes are used: the initial site for investigation is found with constant distance mode because that is the fastest, whereas the surface changes of the specimen are followed with constant force mode because the interpretation is easier. A topographic map is created by scaling the scanned values of the measured probe deflections to a color (gray) scale; a force map is created from the measured forces. Then, the maps can be displayed as two-dimensional or three-dimensional images.

Factors Affecting Image Quality

The AFM image quality depends on both the shape of the probe tip and the topography of the specimen surface. In addition, the tip geometry, the probe aspect ratio, vibrations, and the probe scanning rate affect the measured AFM image of the surface. The aspect ratio is the length-to-width ratio of a probe. Probes with a larger aspect ratio will have a better horizontal and vertical scanning resolution, but they are more fragile and may deform due to the forces. Vibrations of the AFM equipment must be minimized by placing the microscope on a stable table and an air filled cushion. If vibrations persist, the image will show scanning artifacts like parallel, diagonal oscillation lines at the vibration frequency. The scanning rate affects the responsiveness of the feedback control loop. At higher scanning rates, the probe may skip over features, creating phantom peaks and valleys in the image. Scanning more slowly usually eliminates this problem.

In-Situ AFM Measurements in Liquid

An AFM can perform measurements on polished, dry specimens or it can measure while the probe tip and the specimen are placed under a liquid. A specially designed holder for the specimen is used to contain the liquid while allowing the probe to enter the container and move freely. Surface changes can be followed while they occur, and the same location can be measured before, during, and after exposure.

Experimental Approach

Specimen Preparation

Specimens for this investigation were prepared from a 0.86 mm thick plate stock of Type 304 stainless steel that was supplied in hot-rolled and mill annealed condition.

Electrical discharge machining (EDM) was used to cut 3 to 6 mm wide and 10 to 20 mm long strips from the plates for making miniature test specimens, suitable for use with the AFM. After deburring the edges, the metal strips were sealed under argon in quartz tubes. The strips were then annealed at a temperature of 1093°C (2000°F) for one hour, and water quenched, which resulted in grain sizes between 20 and 65 μm (ASTM #5-8). The annealed specimens were sensitized at 650°C (1202°F) for 4 hours and cooled to room temperature in air. The severity of sensitization in the heat-treated strips was checked in accordance with the ASTM Practice for Detecting Susceptibility to Intergranular Attack in Austenitic Stainless Steel (A262-93a).

AFM specimens require a very fine surface finish for the examination. Therefore, each annealed and sensitized strip was metallographically mounted and one flat surface was wet ground to 1200-grit finish using successively finer silicon carbide polishing papers. The final surface finish was achieved by successively polishing each strip with 3 μm and 1 μm diamond pastes, and 0.05 μm alumina. Following polishing, the strip was carefully removed from the mount without introducing deformation. The annealed and sensitized and polished strips served as the starting coupons for preparing the IGSCC specimens.

The following types of specimens were made to accommodate different stressing or straining techniques used in this work:

(1) Non-deformed,
(2) Flat strip with diamond indentation, and
(3) Bent-beam.

Non-deformed specimens were examined in the as-polished state. The diamond-indented specimens were prepared by indenting the polished surfaces of the flat coupons with a diamond indenter Rockwell-C hardness tester. In such a specimen, the surface stresses decrease with distance away from the diamond indent, and also some relaxation occurs over time. The bent-beam specimens were made by deforming the strip coupons in a miniature bending device of the type shown in (Figure 3). Because of the strength limitation of the loading device, the thickness of strip coupons for the bent-beam specimens was reduced from the normal 0.5 mm to about 0.3 mm, during the metallographic preparation of the strips.

Test Solution

A 1000 ppm sodium thiosulfate solution (1.57 g $Na_2S_2O_3 \cdot 5\ H_2O$ / liter) was used for the investigation. This solution has been used by many investigators, and is known to produce IGSCC in annealed and sensitized Type 304 stainless steel in a few hours to a few days at room temperature. Stewart et al. *[10]* reported that sodium thiosulfate concentrations ranging from 10 ppm to 1000 ppm $Na_2S_2O_3$ are almost equally effective in producing the IGSCC. The test solution was always used at ambient temperature, which ranged between 20°C and 25°C, while exposed to air.

AFM Examination

The surfaces of the various alloy specimens were scanned with a Burleigh[2] ARIS®-3500 Personal Atomic Force Microscope, and an ARIS®-3344 Electronic SPM Controller, with True Image SPM™ software. With this microscope, a maximum area of 70×70 μm with 256×256 data points and a maximum height difference of 4 μm can be measured. Metris®-3352 silicon probes with a reflective coating and high aspect ratio were used, in combination with the ARIS-3350 kit for dry measurements and ARIS-3371 kit for fluid cell measurements.

The annealed and sensitized, polished specimens were examined without deformation and after deformation. The specimens were scanned with the AFM before and after exposure to the sodium thiosulfate solution. In addition, some of the specimens were examined while immersed in the fluid cell.

In this research, a flexible fluid cell with a transparent lid was used to contain the liquid, the specimen, and the probe. Both flat and stressed specimens could be accommodated relatively easily in the fluid cell. (Figure 4) shows a drawing of an AFM fluid cell containing a bending rig with a stressed specimen. Because of the limited size of the fluid cell a very small loading device was needed, and because of the strength limitation of the loading device, the thickness of the strip-shaped specimens was reduced to about 0.3 mm from the normal 0.5 mm, during the metallographic preparation of the strips. During scanning, the probe and the specimen base assembly move in the x- and the y-directions with respect to each other. The fluid was inserted through an opening at the side of the base of the cell. The laser beam can travel unhindered through the transparent liquid, when the cell is completely filled and all air bubbles are eliminated. In the current research, the liquid environment was stagnant. A liquid flow is difficult to achieve in practice without interfering with the measurements. This is because of the delicate balance between surface tension in the cell and introduction or formation of air bubbles with the liquid flow. Air bubbles in the cell make accurate measurements impossible.

(Figure 5) and (Figure 6) show a side view and a top-view of the fluid cell, respectively. The fluid cell consisted of a Type 316 stainless steel base to hold the specimen, inlet and outlet tubes for the test solution, and an elastomeric cup attached to the base. The top of the cup was shaped to form a seal against a clear plastic lid. The AFM probe is mounted to the plastic lid.

[2] Burleigh Instruments, Inc., Burleigh Park, P.O. Box E, Fishers, NY 14453-0755.

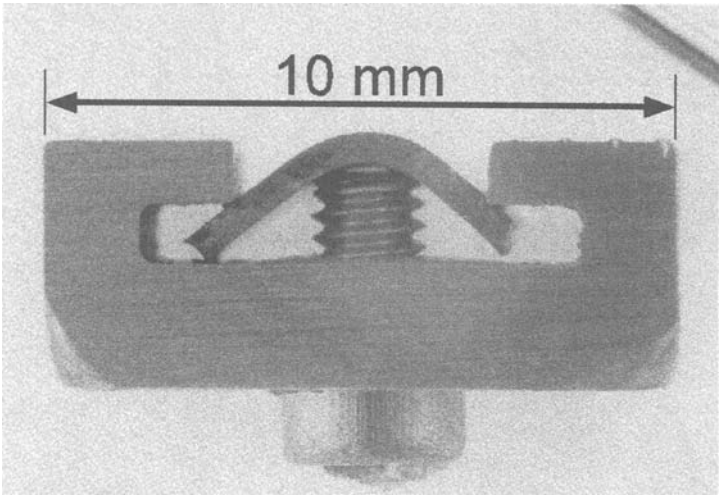


Figure 3 – *Photograph of a stressed specimen in the bending rig. The upper specimen surface was polished before deformation was applied by turning the screw on the unpolished back of the specimen. The 4 points of contact produced essentially 3-point loading conditions, because of the small diameter of the loading screw and the specimen size.*

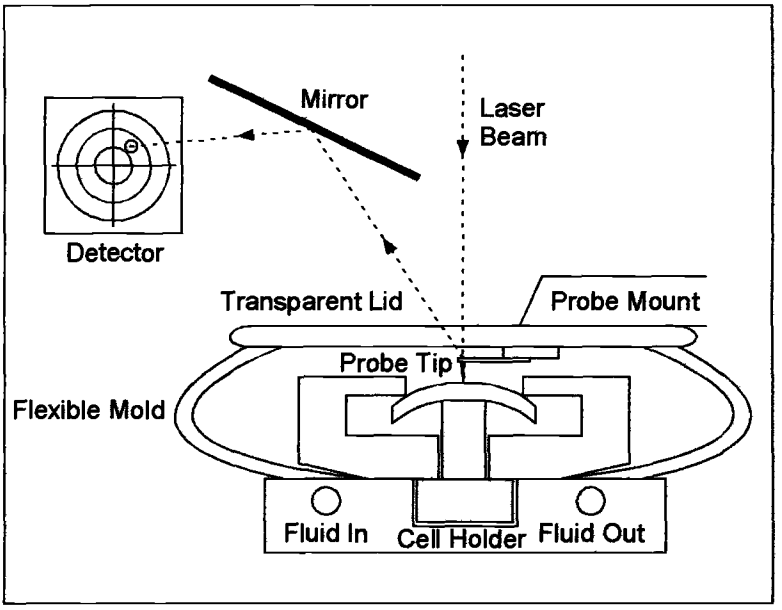


Figure 4 – *Schematic of AFM fluid cell with stressed specimen.*

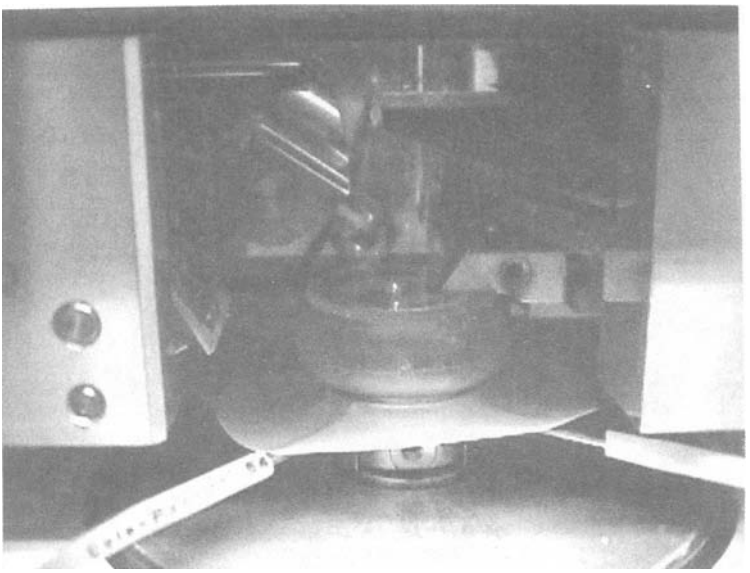


Figure 5 – *Side view of the fluid cell in the AFM.*

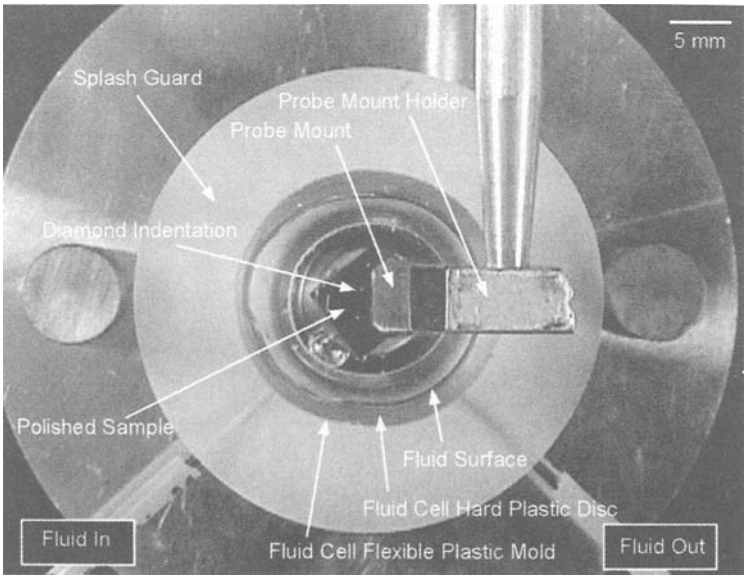


Figure 6 – *Photograph of the fluid cell, showing a Type 316L stainless steel base to hold the specimen, and inlet- and outlet tubes for the test solution. An elastomeric cup is attached to the base with the top of the cup shaped such that it forms a seal against a clear plastic lid to which the probe is attached.*

In a dry cell, a scanning time of at least 15 minutes was required to obtain a quality AFM image without obvious image artifacts such as vibration lines and exaggerated valleys and peaks at steps and particles on the surface. After finding a site of interest, the surface topography was characterized. Typically, detailed characterization of a site of interest took several hours. Then, an additional 15 minutes was needed to introduce the test solution into the fluid cell, to remove any air bubbles, and to realign the laser beam on the AFM probe. A fast, preliminary scan in the constant distance mode was performed to ensure that the same site was retrieved. Finally, slower scans in either the constant force mode or the constant distance mode, ranging from 15 minutes to more than 3 hours each, were taken to document changes on the surface due to exposure to the test solution. In several cases, the solution was introduced immediately after deformation of the specimen and a single fast dry scan. This was done in attempts to detect the earliest surface changes following deformation. The disadvantage of this approach is that little attention could be paid to the exact location where the AFM scan was taken.

Results and Discussion

Non-Deformed Specimens

The polished surfaces of non-deformed Type 304 stainless steel specimens did not reveal features other than the scratches produced by the 0.05 μm alumina. No differences in height or in force response could be detected at the grain boundaries of non-deformed specimens. After electrolytically etching the specimens with oxalic acid, examination with AFM identified the grain boundaries as well as carbides at the grain boundaries. A typical AFM image of an etched specimen is shown in (Figure 7). The oxalic acid etching removed some of the carbides, leaving gaps at the grain boundaries.

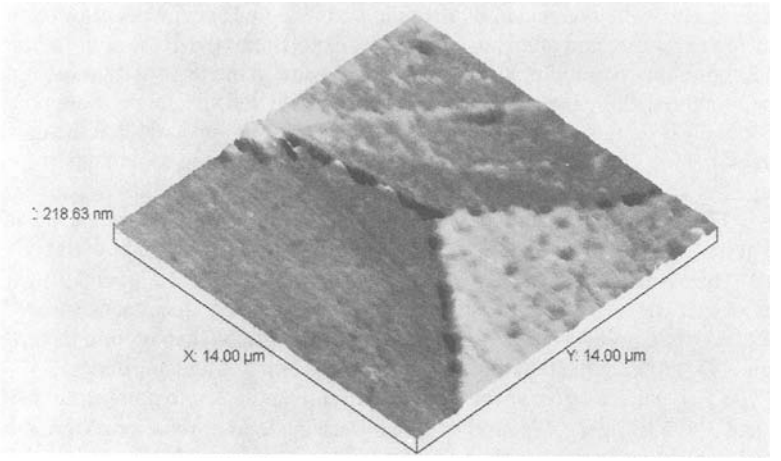


Figure 7 – *Atomic force microscopy constant force scan of oxalic acid etched annealed and sensitized Type 304 stainless steel specimen, showing severe grain boundary ditching.*

Flat Specimens with Diamond Indentation

Diamond indented specimens were investigated to study the effect of sensitization on plastic deformation. Optical microscopy revealed that slip lines originating from the diamond indent traveled about 5 mm towards the edge of the annealed specimen, whereas the slip lines on the annealed and sensitized specimen were confined within about 1 mm radius. (Figure 8a) is an optical photomicrograph showing the slip distribution around the indent of an annealed and sensitized Type 304 stainless steel specimen. The AFM examinations confirmed that the slip lines on the annealed specimen were spread over a large area from the indentation, whereas for the annealed and sensitized specimen the slip lines were confined to several grains around the indentation.

The slip density of a deformed metal surface can be characterized by measuring the distance between slip lines and estimating the amount of cross slip occurring on the surface. For the annealed and sensitized specimens, the slip density adjacent to the grain boundaries was found to be higher than the slip density in the interior of the grains. With AFM, deep gaps and high ridges at grain boundary triple points were found present, examples of which are shown in (Figures 8b and 8c). Such gaps and ridges were not present before deformation of the specimens. The gaps and ridges obviously resulted from high strains due to localized tensile and shear stresses from indentation.

Although stress is a required condition for IGSCC to occur, its role in the nucleation of cracks is not well understood. Fundamental considerations by Hirth and Lothe *[15]* demonstrate that the dislocation density in grain boundary regions increases with increasing misorientation. Although in theory, grain boundaries do not produce long-range stress fields, the stress fields of individual dislocations near grain boundaries can be significant. If the grain boundaries are sensitized, they are decorated with carbides that block dislocation movement through the metal. This was confirmed with the indented annealed and sensitized specimens where slip lines were confined directly around the indent, while the slip lines had run across the entire surface of annealed specimens.

AFM experiments were conducted on the diamond indented specimens prior to exposure, during exposure, and after several days of exposure to the 1000 ppm sodium thiosulfate test solution. Even after seven days of exposure to the test solution, no cracks had developed on the indented specimen surfaces. The indented specimens were not subjected to any other load or strain that could sustain creep. It appeared that the driving forces for crack nucleation and propagation were not present in these specimens.

On the apex of bent-beam specimens, a number of opened triple points were identified by AFM, prior to exposure to the test solution. These features were especially pronounced at the grain boundary triple points and grain boundary - twin boundary intersections. The diameter of these triple-point sites was generally less than 5 μm. The investigation of many locations on the surfaces of several different specimens showed that more opened triple points were present around smaller grains than around larger grains. (Figure 9) shows an example of an opened triple point of an annealed and sensitized Type 304 stainless steel specimen. The fissure at this triple point is almost 1 μm deep, and 1 to 2 μm wide. Several attempts were made to observe crack growth from potential nucleation sites, in-situ, in the test solution. Since only one site can be scanned at one time, and since obtaining high quality AFM images requires time, the chance of capturing a crack nucleating from one of the many potential nucleation sites is

rather small. Consequently, in this research no crack growth was directly captured with the in-situ AFM measurements. During one of the in-situ AFM measurements, a large crack formed in a Type 304 stainless steel specimen after three days exposure to the test solution. (Figure 10) shows the crack as a three-dimensional image.

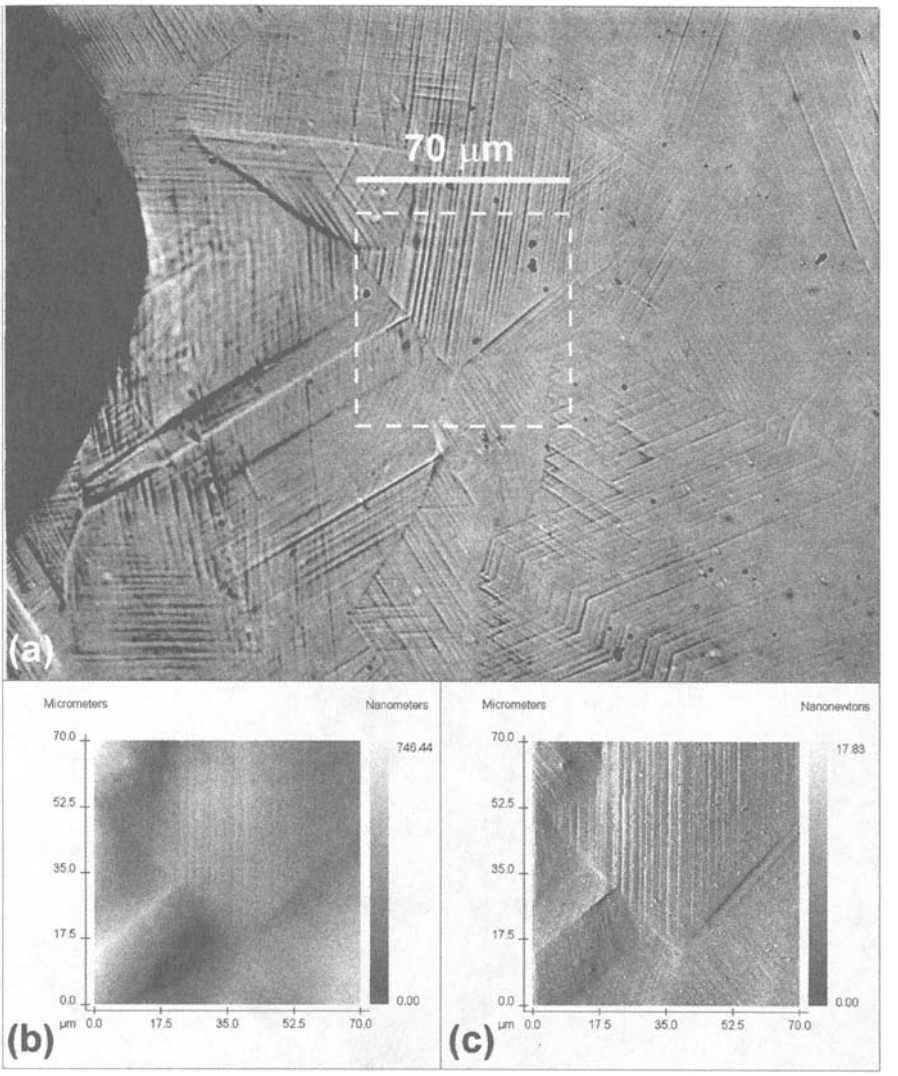


Figure 8 – Optical photomicrograph of annealed and sensitized Type 304 stainless steel specimen after polishing and diamond indenting (black area on the left). The optical photomicrograph (a), the AFM constant force scan (b) and the AFM constant distance scan (c) inserts show the slip distribution around the indentation.

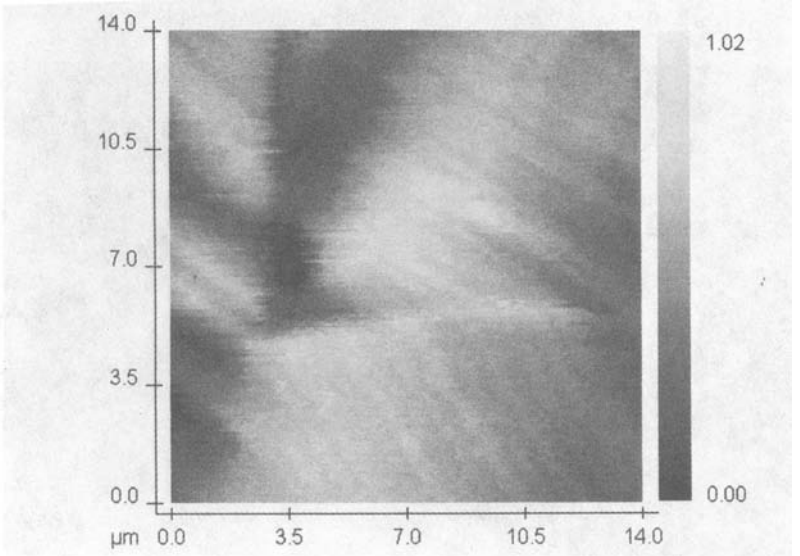


Figure 9 – *Atomic force microscopy constant force scan of annealed and sensitized Type 304 stainless steel specimen, showing a gap at a triple point as a result of plastic deformation.*

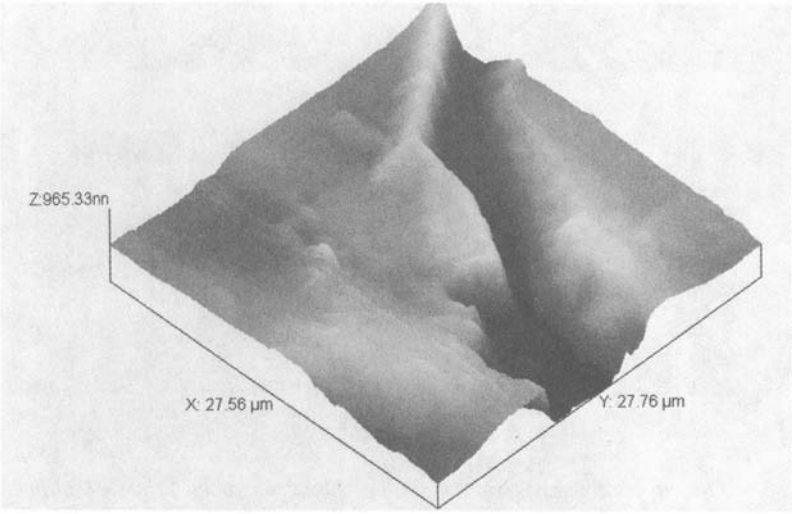


Figure 10 – *Three-dimensional image of atomic force microscopy constant force scan of annealed and sensitized Type 304 stainless steel specimen, showing a crack as a result of exposure to 1000 ppm* $Na_2S_2O_3$ *solution.*

Bent-Beam Specimens

The bent-beam specimens, which were stressed using a constant deflection, showed cracking, indicating that both plastic deformation and elastic strain are required for cracks to grow. This requirement of maintaining the elastic strain for IGSCC propagation has been generally recognized; for example, see Reference *[3]*.

SEM investigations supported the findings of the AFM. Bent-beam specimens of Type 304 stainless steel were examined in the SEM after different periods of exposure to the 1000 ppm $Na_2S_2O_3$ solution. Potential crack nucleation sites in the form of gaps were formed immediately upon deformation, i.e., prior to exposure to any corrosive environment, other than laboratory air. These nucleation sites generally were located at grain boundary triple points and at grain boundary - twin boundary intersections on the specimen surface. After 48 hours of exposure, crack growth from the nucleation sites was easily identified. Examinations at higher magnifications (~5000X) showed that sharp crack tips had formed from some of the nucleation sites during the 48 hour exposure, see (Figure 11). After prolonged exposure, small cracks (~10 μm long) had grown from the nucleation sites. From the earliest stage, the cracks grew by interconnecting several smaller cracks. This demonstrated that in fine grain materials small cracks could grow from a multitude of nucleation sites and coalesce to form large cracks in a relatively short time.

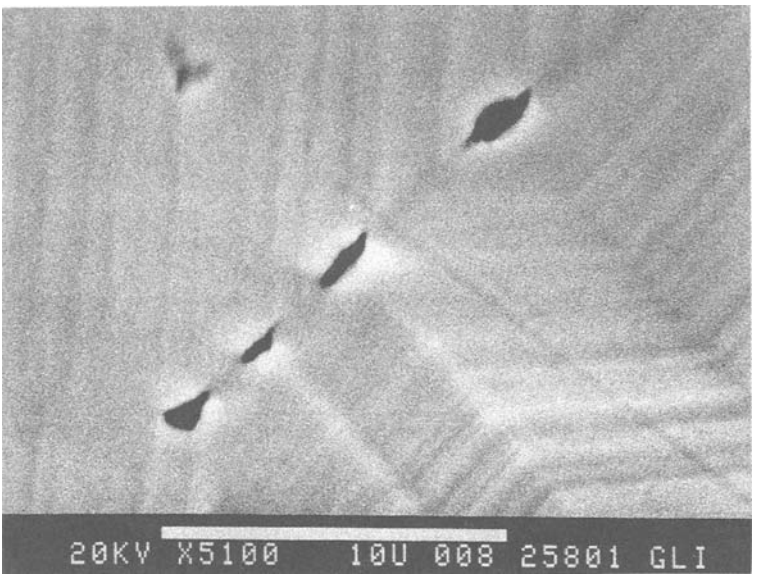


Figure 11 – *SEM photomicrograph showing IGSCC nucleation sites from which small cracks have formed along the grain boundaries of annealed and sensitized Type 304 stainless steel specimen after 48 hours exposure to 1000 ppm $Na_2S_2O_3$ solution.*

Clarke and Gordon *[16]* have conducted detailed SEM studies on annealed and sensitized Type 304 stainless steel specimens after exposure to 288°C (550°F) oxygenated water, and found that intergranular cracks emanated from crevices formed between grain boundary particles (carbides) and the alloy matrix. This is consistent with the present AFM and SEM observations that in annealed and sensitized Type 304 stainless steel separation occurs at the grain boundaries and particularly at the grain boundary triple points, which are subject to high localized stress/strains.

Summary and Conclusions

The atomic force microscopy technique was used to identify the nucleation sites of IGSCC on annealed and sensitized Type 304 stainless steel specimens in the 1000 ppm sodium thiosulfate solution. A new test technique with an AFM fluid-cell and a miniature specimen bending device was used for the in-situ measurements. Stressed specimens showed opened grain boundary triple points and opened grain boundary - twin boundary intersections.

The density of opened grain boundary triple points was greater around smaller grains than around larger grains, and a higher slip density was observed on the surface of smaller grains than on larger grains. The opened grain boundaries could be explained from localized higher strains by using dislocation models applied on materials containing grain boundary sensitization. The opened grain boundary triple points were identified as the nucleation sites for IGSCC by showing that after exposure, small cracks formed from those sites along the grain boundaries. The nucleation sites were generally 1 to 2 μm wide and about 1 μm deep. The small cracks continued to grow and coalesced into larger cracks.

It was further found that the nucleation sites formed upon deformation of the stainless steel and that initial growth occurred within hours of exposing the specimens to the test solution.

The benefits of the AFM technique include the high resolution of the scans, the possibility to create consecutive images of the same surface in two or three dimensions, the fact that non-conductive specimens can be analyzed, and the feature of in-situ measurements in liquid environments. The limitations of the AFM technique are that a minimum of 15 minutes is needed to prepare the instrument before the first measurement of a liquid-exposed specimen can be taken. Applying a liquid flow during an in-situ measurement is difficult, because of the delicate balance between surface tension in the cell and introduction or formation of air bubbles, which interfere with the measurements.

Acknowledgment

The authors acknowledge the support of the Electric Power Research Institute (EPRI), allowing this research to be conducted under work order WO 8041-12. The technical guidance of Dr. B. C. Syrett and Dr. J. L. Nelson of EPRI is greatly appreciated.

References

[1] Swann, P. R., "Dislocation Substructure vs. Transgranular Stress Corrosion Susceptibility of Single Phase Alloys," *Corrosion*, Vol. 19, No. 3, 1963, p. 102.

[2] Hoar, T. P., "Stress-Corrosion Cracking," *Corrosion*, Vol. 19, No. 10, 1963, p. 331.

[3] Jiang, X.-C. and Staehle, R. W., "Effects of Stress and Temperature on Stress Corrosion Cracking of Austenitic Stainless Steels in Concentrated Magnesium Chloride Solutions," *Corrosion*, Vol. 53, No. 6, 1997, p. 448.

[4] Vermilyea, D. A., Journal of the Electrochemical Society, Vol. 119, 1972, p. 46.

[5] Boyd, J. D. and Hoagland, R. G., "Relation Between Surface Slip Topography and Stress Corrosion Cracking in Ti-8wt%Al," *Corrosion*, Vol. 30, No 3, 1974, p. 102.

[6] Parkins, R. N., "Environment Sensitive Fracture – Controlling Parameters," *Proceedings of 3rd International Conference on Mechanical Behavior of Materials*, Cambridge, August 1979, K. J. Miller and R. F. Smith, Eds., Pergamon, New York, Vol. 1, 1980, p. 139.

[7] Ford, F. P., "Stress Corrosion Cracking," *Corrosion Processes*, Ed. R. N. Parkins, Applied Science, 1982.

[8] Ford, F. P., Taylor, D. F., Andresen, P. L., and Balling, R. G., "Corrosion Assisted Cracking of Stainless Steels and Low Alloy Steels in LWR Environments," Report NP-50645, EPRI, Palo Alto, February 1987.

[9] Wilde, B. E., "Technique For Studying The Kinetics Of Intergranular Crack Nucleation on AISI Type 304 Stainless Steel In Oxygenated Water at 289°C," *Corrosion*, Vol. 25, No. 9, 1969, p. 359.

[10] Stewart, J., Wells, B., and Scott, P. M., "The Initiation of Intergranular Stress Corrosion Cracking on Sensitized Stainless Steel in Dilute Thiosulfate Solutions," *Proceedings of Environmentally Induced Cracking of Materials (EICM)*, 1998, p. 517.

[11] Koch, G. H., Agrawal, A. K., Brongers, M. P. H., and Phelps, A. W. "Characterization of the Early Stages of Stress-Corrosion Cracking in Type 304 Stainless Steel," Report TR-112117, EPRI, Palo Alto, CA, December 1998.

[12] Koch, G. H., Agrawal, A. K., Brongers, M. P. H., and Phelps, A. W., "Characterization Of Intergranular Stress-Corrosion Cracking Initiation in Type 304 Stainless Steel Using Scanning Probe Microscopy," *NACE*, Paper 450, Proceedings of CORROSION/99.

[13] Koch, G. H., Agrawal, A. K., Brongers, M. P. H., "Initiation of Intergranular Stress-Corrosion Cracking in Type 304 Stainless Steel and Alloy 600," Report TR-113458, EPRI, Palo Alto, CA, 1999.

[14] Binnig, G., Rohrer, H., Gerber, Ch., and Weibel, E., Appl. Phys. Lett. Vol. 40, 1982, p. 178.

[15] Clarke, W. L. and Gordon, G. M., "Investigation Of Stress Corrosion Cracking Susceptibility Of Fe-Ni-Cr Alloys In Nuclear Reactor Water," *Corrosion*, Vol. 29, No. 1, 1973, p. 1.

[16] Hirth, J. P. and Lothe, J., *Theory of Dislocations*, McGraw-Hill Book Company, New York, 1968.

Raicho Raicheff [1] and Luis Maldonado[1]

An Electrochemical Film-Rupture Model for SCC of Mild Steel in Phosphate Environment

Reference: Raicheff, R. and Maldonado, L., **"An Electrochemical Film-Rupture Model for SCC of Mild Steel in Phosphate Environment,"** *Environmentally Assisted Cracking: Predictive Methods for Risk Assessment and Evaluation of Materials, Equipment, and Structures, ASTM STP 1401,* R. D. Kane, Ed., American Society for Testing and Materials, West Conshohocken, PA, 2000.

Abstract: The stress-corrosion cracking of mild steel (0.17% C) in phosphate media (0.1 – 2.0*M* NaH_2PO_4 at pH = 4 and 20 - 80 °C) is studied using slow strain rate and potential sweep techniques as well as SEM, X-ray diffraction and Mossbauer analysis of the surface films. It is shown that the susceptibility of the steel to SCC depends on the phosphate concentration and it decreases markedly with increase of temperature; the highest SCC susceptibility is observed in the region of active to passive transition of the steel (-0.3 – 0.0 V, SCE). It is established that the films formed at potentials in SCC zone are mixed oxide-phosphates composed by $Fe_3(PO_4)_2.8H_2O$, $Fe_3(PO_4)_2.4H_2O$, $FePO_4.xH_2O$ and Fe_3O_4, while the film formed in the passive region (outside SCC zone) is oxide in nature and consists of γ-Fe_2O_3. It is suggested that SCC may be related to the formation of secondary amorphous iron (III) phosphates in the surface film. An electrochemical model for crack propagation, based on the film rupture concept in SCC and quantitative electrochemical kinetics considerations, and relating the rate of crack propagation with the electrochemical parameters of both metal dissolution and cathodic reactions at the crack tip and outer metal surface is presented. It is shown that the model could be used for calculating the crack propagation rate and defining electrochemical conditions favorable for SCC.

Keywords: Stress-corrosion cracking, electrochemical model, mild steel, phosphate environment, film composition, crack propagation rate, environmental factors

The stress-corrosion cracking (SCC) of mild and low-alloy steels is known today for a large and still increasing number of corrosive environments – hydroxides, nitrates, carbonates, phosphates, etc. Although SCC of mild steels in phosphate environments is rarely observed compared with SCC in hydroxide and nitrate media, the interest in this phenomenon is determined by the widespread use of phosphates (mineral fertilizers in soil, corrosion inhibitors in water systems, metal surface treatment, etc.) and hence – by the potential risk for its observation in the practice.

[1] Professor, Department of Applied Physics, CINVESTAV-Mérida. A. P. 73 Cordemex, C.P. 97310, Mérida, Yuc., México.

Copyright© 2000 by ASTM International www.astm.org

The data in the literature for the environmental conditions that provoke SCC of steels in phosphate media as well as for the mechanisms of SCC, however, are limited [*1-6*]. Schroeder and Partridge [*1*] first observed SCC of mild steel in sodium phosphate (Na_3PO_4) solutions, but later SCC is reported [*2-4*] in environment of various phosphates (Na_2HPO_4, $NH_4H_2PO_4$, $(NH_4)_2HPO_4$ and NaH_2PO_4) with pH in the range 3 to 7. However, there is some discrepancy in the data for the cracking mode. The study of Middleton [*2*] has shown transgranular cracking of mild steel in NaH_2PO_4 solution (pH = 4.8), and also Parkins et al.[*3*] for C-Mn steels in solutions of Na_3PO_4 and Na_2HPO_4 (pH from 3 to about 7). However, Flis [*4*] found, predominantly intergranular cracking for Armco iron and Fe-C alloys (up to 0.1 %C) in NaH_2PO_4 (pH = 4). The influence of the carbon content on the susceptibility of Fe-C alloys to SCC has been associated with its detrimental effect on the protective properties of surface films. It is also established [*3-5*] that the potential range of SCC in phosphate solutions is rather narrow (0.1 – 0.2 V) in comparison to that in hydroxide and especially in nitrate solutions and seems related with the active-passive behavior of the steel.

The main objective of the present paper is to elaborate an electrochemical model of crack propagation in mild steels in phosphate media based on the film-rupture concept in SCC and quantitative electrochemical kinetics considerations. Evaluation of the effect of the main environmental factors as well as surface film composition on the susceptibility of the steels to SCC in phosphate solutions is also an aim of the work.

Experimental Procedures

The SCC studies were carried out using the slow strain rate technique in conjunction with electrochemical polarization measurements, optical microscopy and SEM observations of the fractured surfaces as well X-ray and Mossbauer analysis of the surface films.

Materials and Solutions

The experimental studies were performed with samples of mild steel (produced as hot-rolled bars) of the following composition (%): C – 0.17, Mn – 0.36, Si – 0.016, S – 0.029, P – 0.010, Cr – 0.06, Ni – 0.06, Cu – 0.11 and Fe – the balance. The steel had ferritic-pearlite microstructure (grain size of 30-36 μm) and mechanical parameters: Ultimate Tensile Strength – 430 MPa and Yield Strength – 355 MPa.

Phosphate solutions, prepared from $NaH_2PO_4.H_2O$ and small additions of phosphoric acid (H_3PO_4) or sodium hydroxide (NaOH) for pH adjustment, were used as a corrosive medium. The measurements were made in 0.05 - 2.0*M* concentration range of NaH_2PO_4, temperature range 20 – 80 °C and free access of air to the test solution. The solution pH was always controlled before and after the tests.

Apparatus and Procedures

Electrochemical Polarization Measurements - Cylindrical sample-electrode was used (working area of 1 cm^2) mounted on a Teflon electrode holder. Before every experiment the specimens were finished to 600 grit, degreased with acetone and rinsed

with distilled water. The anodic potentiodynamic polarization curves were automatically recorded in a semilogarithmic scale using a conventional three-compartment cell and a Wenking potentiostat. The potentials were measured vs. reference saturated calomel electrode (SCE). The potentiodynamic method with fast (10 mV/s) and slow (0.1 mV/s) potential sweep rates was applied for preliminary studies of the effect of environmental factors on SCC susceptibility of the steel. The polarization curves obtained with slow potential sweep rate are also used to study the anodic behavior of the steel in various environmental conditions.

Stress-corrosion Cracking Tests - The measurements were made using constant slow strain rate technique (strain rate 2.3×10^{-5} cm^{-1}) at potentiostatic conditions. The quantitative parameters used for assessment of SCC susceptibility of the steel were the relative change of the tensile strength and reduction of the cross–section area of the specimens at fracture in the corrosive medium in comparison to the fracture in air. The mode of stress-corrosion failure was determined through optical microscopy and SEM observation of the fracture surfaces and microcracks. The tensile testing specimens were cylindrically shaped and had the following dimensions: overall length – 180 mm, diameter – 10 mm and reduced gauge diameter – 3 mm. The non-performing part of the specimens was isolated with an inert plastic coating. The electrochemical cell, tensile testing apparatus and experimental procedure were described elsewhere [*6,7*].

X-ray and Mössbauer Analysis of Surface Films - The films for the analysis were formed under potentiostatic conditions on sample-electrodes with a working area of 10 cm^2. The potentials were selected on the basis of the data for the anodic behavior of the steel and the results from SCC tests. The details of the X-ray and Mossbauer analysis were reported in a previous paper [*8*].

Experimental Results

Effect of Some Environmental Factors on SCC

pH *of the Solution* - The polarization study in phosphate solutions with various pH (from 2.8 to 12.0) confirmed the expected strong effect of pH on the anodic behavior of the steel and especially on its susceptibility to passivation and stability of the passive state. pH affects particularly strongly the region of active to passive transition of the steel. A zone of "primary" passivity is observed in the anodic polarization curves of the steel obtained in acidic phosphate solutions (Fig. 1*a*). Such a "primary" passivity zone at potentials preceding the passive region is reported as well for the anodic behavior of iron in phosphate solutions [*9,10*]. Our studies [*11*] have shown that the "primary" passivity is characteristic for the anodic behavior of mild steel in solutions of NaH_2PO_4 with pH from 4 to about 7 and it may be related with the formation of a thick layer of iron phosphates with poor protective properties.

The well-defined and large region of active to passive transition of the steel in NaH_2PO_4 solutions with pH about 4 suggest that the electrochemical conditions could be favorable for SCC in that environment. As it is well known [*12,13*], the potential sweep method gives the potential range in which the low anodic activity in the presence of a surface film is changed to a high anodic activity in the absence of film, i.e., the region where the probability for SCC occurrence is high at conditions of local breakdown of the

film. It is seen from Fig. 1*b* that the dependence of the ratio between the current densities obtained by fast and slow potential sweep (i_f/i_s) on the potential exhibits its largest values for NaH_2PO_4 solution with pH = 4.0, i.e., the environmental conditions for crack

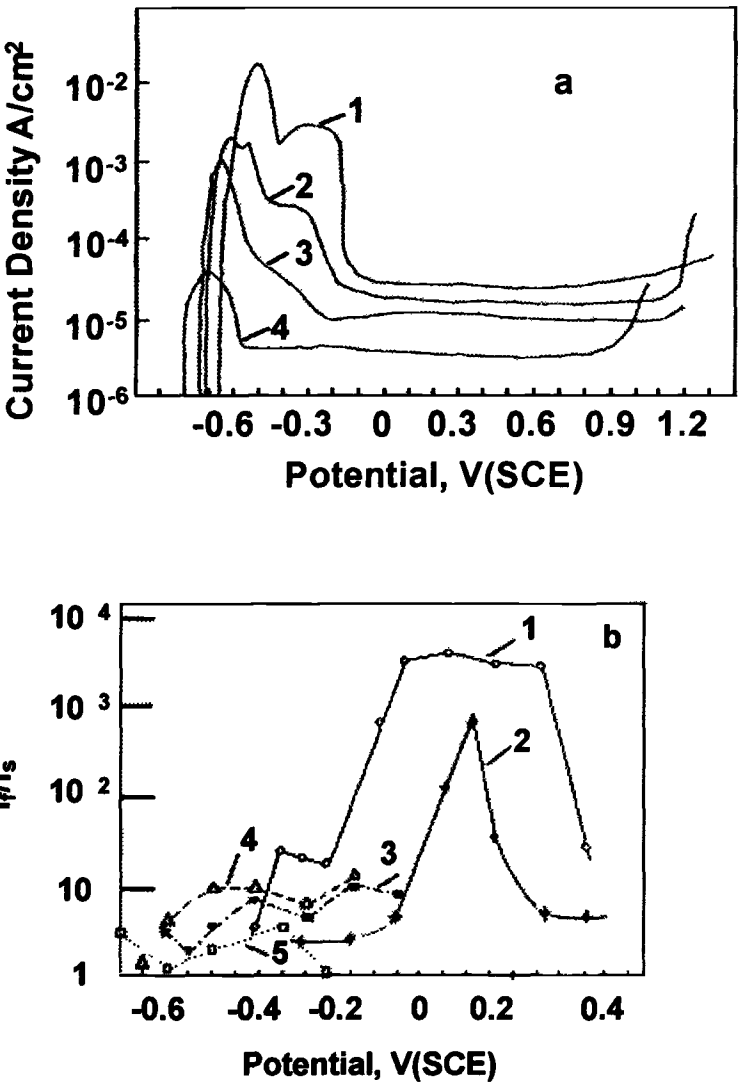


Figure 1 – *Polarization curves (a) and dependence of the ratio i_f/i_s on potential (b) for mild steel in 1M NaH_2PO_4 solutions (20 °C) with pH: 4.0 (1), 5.1 (2), 6.1 (3), 10.0 (4) and 10.9 (5).*

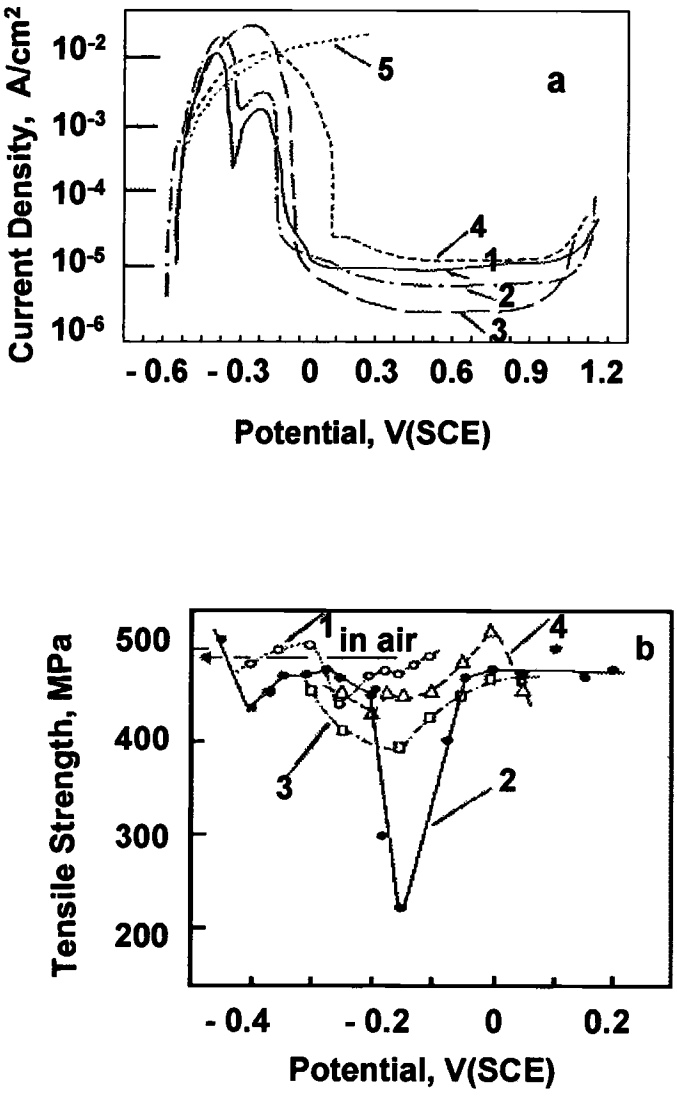


Figure 2 – *Polarization curves (a), and dependence of the tensile strength of mild steel on potential (b) in NaH_2PO_4 solutions (pH = 4.0, 20 °C) with concentration of phosphate: 2.0M (1), 1.0M (2), 0.5M (3), 0.1M (4) and 0.05M (5).*

development seems to be most favorable in that solution. In the subsequent studies, NaH_2PO_4 solutions with pH = 4.0 were used.

Phosphate Concentration - As can be seen from Fig. 2*a* the susceptibility of the steel to passivation changes with the change of phosphate concentration in the range 0.05 – 2.0*M* NaH_2PO_4 (pH = 4.0 for all solutions studied). The strong effect of the solution concentration on the active to passive behavior of the steel (including the zone of "primary" passivity) suggests that this factor may affect the process of SCC as well.

The results of potential sweep measurements indicated that the electrochemical conditions would be most favorable for SCC of the steel in 0.5 – 1.0*M* NaH_2PO_4 solutions and this conclusion was fully confirmed by SCC tests (Fig. 2*b*). The tensile strength of the steel decreases in all solutions studied, however, this decrease is largest in 1*M* NaH_2PO_4, where the tensile strength could reach values about 2.5 times lower compared to that for fracture in air (490 MPa) at the same deformation conditions. The metallographic examinations of the longitudinal section of the specimen gauges as well as SEM observations of the fractured surfaces confirmed the occurrence of SCC in this potential range and showed a mixed mode of SCC (intergranular/transgranular) with predominantly intergranular cracking.

Temperature of the Solution - The polarization measurements have shown that the temperature has a strong effect on the active-passive behavior and susceptibility of the steel to passivation (the region of active to passive transition reduces while the passive region widens and the passivating current density decreases considerably with increase of temperature) and this should affect its susceptibility to SCC as well. Thus, the value of the ratio of the current densities i_f/i_s obtained by potential sweep method decreases with the increase of temperature indicating a lower probability for SCC at higher temperatures.

The results of SCC test show (Fig. 3) that the tensile strength of the steel in corrosive medium (at conditions of most intensive SCC - 1*M* NaH_2PO_4, pH = 4.0 and E = -0.15 V) increases with temperature and at about 60 °C approaches the value for fracture in air, i.e. at higher temperatures SCC obviously does not occur (Fig. 4).

Effect of Potential on SCC

The position of SCC zone is well defined by the dependence of the tensile strength on the potential, which is compared with the anodic polarization curve of the steel obtained at the same environmental conditions (Fig. 5). It is seen that the zone of maximum decrease of the tensile strength (-0.3 – 0.0 V, SCE) is entirely within the region of active to passive transition, i.e., in this region the susceptibility of the steel to SCC is highest. It is obvious that in the region of active to passive transition, the electrochemical conditions are most favorable for SCC, i.e., the properties of the surface film as well as the rate of the film-forming reaction are most appropriate for localization of corrosion attack at the sites of mechanical breakdown of the film.

It should be noted that the zone of SCC obtained by the slow strain rate testing coincides relatively well with the potential region of SCC predicted by the results from potential sweep measurements (cf. Fig. 6). The actual SCC zone, however, is narrower than the "predicted" one and does not correspond so much to the maximum ratio of the current densities i_f/i_s but to the increase rather of this ratio to its maximum value. Thus,

the express potential sweep method could be used in preliminary studies for predicting

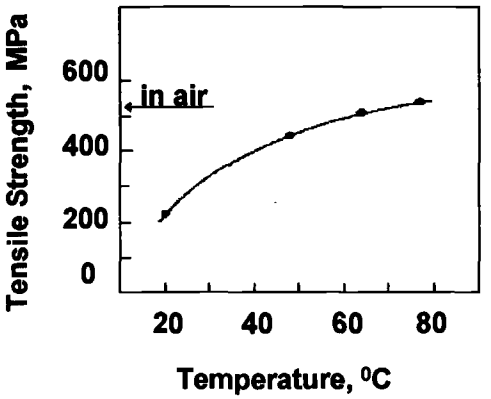


Figure 3 – *Dependence of the tensile strength of mild steel on temperature in 1M NaH_2PO_4 (pH = 4.0).*

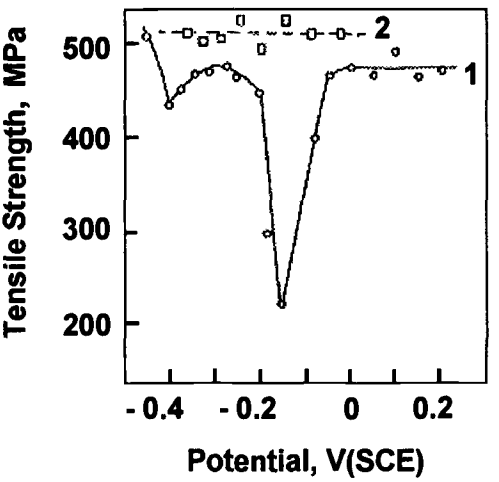


Figure 4 – *Dependence of the tensile strength of mild steel on potential in 1M NaH_2PO_4 (pH = 4.0) at 20 °C (1) and 80 °C (2).*

the possible potential region of SCC of mild steel in phosphate media as well as for a qualitative evaluation of the effect of the environmental factors on SCC susceptibility of the steel in those media. The actual SCC zone, however, could be determined only by slow strain rate tests in conjunction with optical microscopy and/or SEM observations of fractured samples.

Film Composition at SCC Conditions

The films on the steel were formed at constant potentials in 1*M* NaH_2PO_4 (pH = 4.0), at 20 °C and free access of air to the solution (i.e., environmental conditions of most severe SCC). The potentials were selected as typical for the potential ranges: of low susceptibility to SCC, just at the end of SCC zone (-0.35 V); of most intensive SCC (-0.15 V); and outside SCC zone – in the passive region (0.5 V) (cf. Fig. 5).

The results from the Mössbauer analysis show that the films formed in SCC zone consists of iron(II) and iron(III) phosphates (Table 1). In this region the potential affects to some extent only the ratio in the quantity of phosphates. The X-ray analysis data indicated that the films obtained in SCC zone contain also some amount of Fe_3O_4, most probably as a thin film on the metal surface under the much thicker layer of iron phosphates. Fe_3O_4 may be formed as a result of the electrochemical reaction [*3*]

$$6Fe + H_2PO_4^- + HPO_4^{2-} + 4H_2O = Fe_3(PO_4)_2 + Fe_3O_4 + 11H^+ + 14e$$

with a potential of –0.62 to –0.65 V (SCE) at the given environmental conditions. The formation of $Fe_3(PO_4)_2$ is a result of the above reaction and mainly of the secondary reaction [*14*]

$$3Fe^{2+} + 2H_2PO_4^- = Fe_3(PO_4)_2 + 4H^+$$

Table 1 – *Mössbauer analysis of films formed on mild steel in 1M* NaH_2PO_4 *(20 °C).*

Potential, V (SCE)	Composition of the film	wt. %
-0.35	$Fe_3(PO_4)_2.8H_2O$	28
	$Fe_3(PO_4)_2.4H_2O$	11
	$FePO_4.xH_2O$	61
-0 15	$Fe_3(PO_4)_2.8H_2O$	36
	$Fe_3(PO_4)_2.4H_2O$	22
	$FePO_4.xH_2O$	42

At potentials in the passive region of the steel (outside the SCC zone) a thin adherent film is formed. The X-ray analysis indicated that the film is composed by γ-Fe_2O_3, most probably resulting from the following electrochemical reaction [*3*]

$$2\,Fe_3(PO_4)_2 + 9H_2O = 3\gamma\text{-}Fe_2O_3 + 2H_2PO_4^- + 2HPO_4^{2-} + 12H^+ + 6e$$

with a potential of 0.02 to 0.04 V (SCE) at the given environmental conditions.

The present results show that SCC of mild steel in NaH_2PO_4 solutions occurs at conditions of formation of films composed of secondary iron(II) and iron(III) phosphates. The films formed at potentials in SCC zone are mixed oxide-phosphates composed of $Fe_3(PO_4)_2.8H_2O$, $Fe_3(PO_4)_2.4H_2O$, $FePO_4.xH_2O$ and some quantity of Fe_3O_4, while the film in the passive region (outside SCC zone) is of oxide nature and consists of γ-Fe_2O_3.

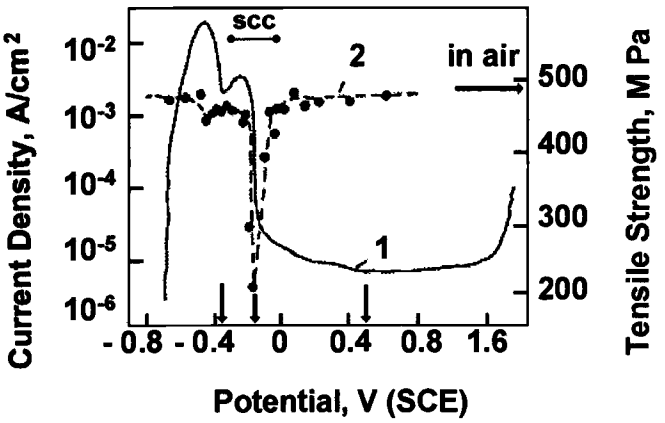


Figure 5 – *Polarization curve (1) and dependence of the tensile strength of mild steel on potential (2) in 1M NaH_2PO_4 (pH = 4.0, 20 °C).*

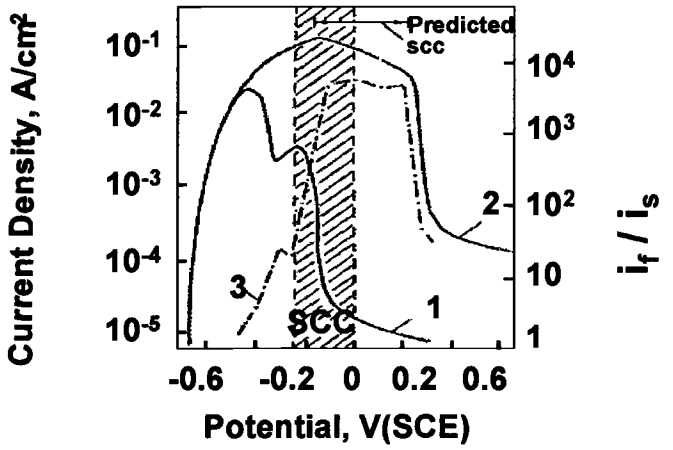


Figure 6 – *Polarization curves obtained with a potential sweep rate of 0.1 mV/s (1) and 10 mV/s (2), and dependence of the ratio i_f/i_s on potential (3) for mild steel in 1M NaH_2PO_4 (pH = 4.0, 20 °C).*

Electrochemical Model for Crack Propagation in Mild Steels in Phosphate Environment

Electrochemical Model for Crack Propagation in Filmed Metals

In previous papers [*15-17*] quantitative electrode kinetics considerations were applied to the problem of SCC of metals, both in the presence and absence of surface films, and general expressions relating the rate of crack propagation to the electrochemical parameters of the SCC metal/solution system were derived.

If the strain-assisted dissolution mechanism of SCC is assumed to be operative, the electrochemical model for crack propagation could be schematically represented as in Fig. 7. The crack growth occurs by dissolution of metal with high rate at the active crack tip, while the rate of dissolution at the outer metal surface as well as at the crack walls is much lower because of the filming. The function of the stress is to cause fractures of the protective film, thus providing active sites for a highly intensive and localized dissolution. Therefore, the effect of the applied stress on the rate of metal dissolution could be expressed by the rate constant, i.e., the exchange current density of the anodic dissolution reaction at the crack tip. The maintenance of crack tip "active" (film-free) depends not only on the electrochemical conditions but also on the strain rate, which is assumed to be constant in the present model.

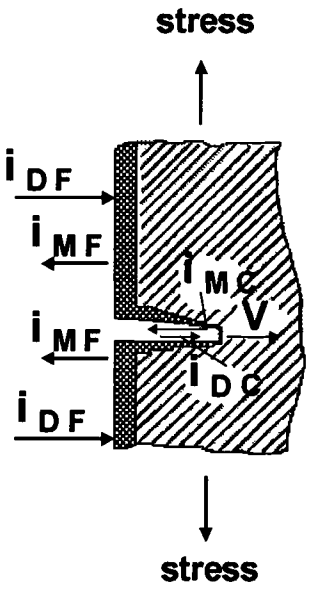


FIG. 7 – *Schematic model of a propagating stress-corrosion crack (V - the rate of crack propagation, i_{MC} and i_{MF} - the metal dissolution current densities at the crack tip and the outer (filmed) metal surface, i_{DC} and i_{DF} - the depolarization current densities at the crack tip and the outer metal surface).*

The rate of crack propagation V could be related to the metal dissolution current densities at the crack tip i_{MC} and outer (filmed) metal surface i_{MF}

$$V = \frac{A}{zF\rho}(i_{MC} - i_{MF}) \tag{1}$$

where

A = the atomic weight of the metal,
z = the number of electrons transferred per atom dissolved,
F = Faraday's constant, and
ρ = the density of the dissolving metal.

This expression assumes a continuous dissolution at the crack tip. In the case of film-forming environment, this means that the strain rate is high enough to maintain bare surface conditions at the crack tip or the time during which the crack tip is relatively inactive is a small proportion of the total time of dissolution. If this is not so, then the frequency of film rupture at the crack tip should be taken into account as suggested by Ford [*18*]. In this case Eq. (1) gives the maximum crack propagation rate at given electrochemical and strain conditions.

Taking into account that for filmed metals $i_{MC} >> i_{MF}$ (i.e., the second term in Eq. (1) can be neglected) and applying basic electrochemical kinetics relationships, the expression for the rate of crack propagation is obtained as [*17*]

$$V \approx \frac{A}{zF\rho} K_1 \left[\frac{(i_o)_{DF}}{(i_o)_{MF}}\right]^{Q_1} (i_o)_{MC} \tag{2}$$

with

$$Q_1 = \frac{\alpha_M}{(a/\delta)\alpha_{MF} + \alpha_{DF}} \tag{3}$$

$$Q_2 = \frac{(a/\delta)\alpha_{MF}}{(a/\delta)\alpha_{MF} + \alpha_{DF}} \tag{4}$$

$$K_1 = \exp\frac{F}{RT}(Q_1\alpha_{DF}E_D + Q_2\alpha_M E_F - \alpha_M E_M) \tag{5}$$

where

E_M = the reversible potential of the metal dissolution reaction,
$(i_o)_{MC}$ = the exchange current density for the metal dissolution reaction at the crack tip,
α_M = the transfer coefficient for that reaction,
E_D = the reversible potential of the depolarization reaction,
$(i_o)_{DF}$ = the exchange current density for depolarization reaction at the outer metal surface
α_{DF} = the transfer coefficient for that reaction,
E_F = the reversible potential of the film-forming reaction,

$(i_o)_{MF}$ = the dissolution current density at that potential,
α_{MF} = coefficient (most often $\alpha_{MF} \sim 0.5$),
δ = the thickness of the passive film, and
a = the width of the energy barrier for ionic diffusion across the film.

It is seen from Eqs. (2) - (5) that the rate of crack propagation depends on electrochemical parameters of the partial electrochemical reactions involved. The rate V is basically determined by the specific rate of metal dissolution at the crack tip. As this rate becomes smaller, the tendency to SCC decreases and may even vanish. The susceptibility to SCC, however, depends also on the ratio between the exchange current densities of depolarization and metal dissolution reactions at the outer surface as well as on the value of K_1 (i.e., the reversible potentials of the metal dissolution, film-forming and cathodic reactions).

Equation (2) indicates that the susceptibility of a given metal to SCC will be higher, the larger the ratio $(i_o)_{DF}/(i_o)_{MF}$. This means that protective films possessing both high electronic and low ionic conductivity as well good electrocatalytic activities for whatever depolarization reaction involved would favor crack development at conditions of local breakdown of the film. Usually the passive films on iron and steel possess relatively good electronic conductivity and low ionic one, so one can expect that the presence of passive films, on the metal surface, would hamper the metal dissolution but it will not affect strongly the rate of cathodic reaction (associated with electron transfer only).

If the crack propagation mechanism result the same under similar conditions in different media, which cause passivity but result in different electrocatalytic activities for the passive films (i.e., different $(i_o)_{DF}$ values), one should expect a faster crack propagation for the environment where the specific rate of the cathodic reaction is higher. This may account for the fact [*3,4,12*] that the rate of crack propagation in mild steels in nitrate solutions ($5.10^{-8} - 6.10^{-7}$ m/s) is 1 – 2 orders of magnitude higher than that for the same steels in phosphate environments ($1.10^{-9} - 6.10^{-9}$ m/s). Thus, the crack propagation rate depends on the specific rate of the cathodic reaction at the outer metal surface.

Application of the Model to Mild Steel/Phosphate SCC System

Since SCC of mild steel in phosphate media occurs at conditions of formation of film, it is possible to apply the electrochemical model for crack propagation in filmed metals to this SCC system.

As it was shown, the film in the SCC zone is oxide-phosphate and the formation of a film of secondary iron phosphates seems to play a key role in SCC process. The layer of iron(II) phosphates is loose, porous and has weak protective properties [*14*]. The presence of oxygen in solution, however, affects strongly the composition and structure of the film because it results in oxidation of iron(II) phosphates and formation of a considerable amount of iron(III) phosphate (cf. Table 1). The resulting $FePO_4.xH_2O$ is amorphous and insoluble, and it can improve the protective properties of the initially formed layer of iron(II) phosphates to some extent by decreasing its porosity. This suggestion finds support in the results of a study [*19*] on oxidation of natural vivianite ($Fe_3(PO_4)_2.8H_2O$), which shows that the diffusion of water and oxygen in the crystal

lattice of vivianite is hampered by the oxidation products (iron(III) compounds) in the surface layer. In this way, by improving the protective properties of the initially formed film of iron(II) phosphates, somewhat better conditions for localization of the corrosion attack at the places of rupture of the film under stress could be created (i.e., conditions for initiation of SCC).

The observed predominantly intergranular SCC of mild steel in phosphate media is likely related to segregation of carbon and other impurities at the grain boundaries of the steel (i.e., with the detrimental effect of carbon on the mechanical and protective properties of the film formed on those places). As shown by Flis [4] the protective properties of the film formed on Fe-C alloys in phosphate solutions and stability of the passive state decrease considerably with increase of the carbon content in the alloys. Thus, the grain boundaries seem to be the most likely places for breakdown of the surface film. The transgranular SCC is a result of rupture of the film at the places of slip steps emerging.

The observed strong effect of some environmental factors (e.g., temperature, pH and phosphate concentration) on the susceptibility of the steel to SCC may be related with their influence on the properties and stability of the iron phosphates in the surface film. Additional study on the effect of those factors on the film composition and structure, however, is necessary in order to make definite conclusions.

The model could be used for calculating the approximate rate of crack propagation of mild steels in phosphate environments. Thus, the values of crack propagation rates in various low-carbon steels in phosphate solutions reported in the literature are in the range 1.10^{-9}- 6.10^{-9} m/s [*3,4,20*]. Using Eq. (2) and the following electrochemical parameters for iron or mild steel [*21-24*]: $\alpha_M = 0.5$, $E_M = -0.44$ V, $E_D = -0.24$ V (hydrogen evolution cathodic reaction), $E_F = 0.36$ V, $(i_o)_{DF} = 10^{-8}$ A/cm^2, $(i_o)_{MF} = 10^{-10}$ A/cm^2 and $(i_o)_{MC} = 10^{-6}$ A/cm^2, a reasonable value of 4.10^{-9} m/s for the crack propagation rate in mild steel in 1*M* NaH_2PO_4 solution (pH = 4.0, 25°C) is obtained.

As it was already pointed out, the susceptibility of a metal to SCC and the resultant crack propagation rate should depend on the ratio between the specific rates of the partial corrosion reactions at the outer metal surface $(i_o)_{DF}/(i_o)_{MF}$ (cf. Eq. 2). Thus, if the activity of the filmed surface for the cathodic reaction increases (e.g., increase of the electronic conductivity of the phosphate film), an increase in the susceptibility of the metal to SCC is also to be expected. Equation (2) indicates also that if the activity of the metal surface for the dissolution process increases as a result of diminishing protective properties of the film, the second term in this expression will also increase (it may not be neglected) and the rate of crack propagation will decrease. If the surface exhibits relatively high activity, the tendency to SCC will decrease and may even vanish. This may account for the effect of Cl^- ions on SCC susceptibility of the steels in phosphate environment. Then, it is established [*25*] that small additions of chlorides to NaH_2PO_4 solutions tend to produce general corrosion and inhibit SCC of mild steels, which is obviously related with the detrimental effect of Cl^- ions on the protective properties of the surface film as well on the rate of its repair after mechanical fracture.

Summary and Conclusions

The SCC behavior of mild steel in phosphate environment has been studied using

slow strain rate technique in conjunction with potentiodynamic polarization measurements, optical metallography and SEM observations of fractured surfaces as well as Mössbauer and X-ray analysis of surface films. The main results are the following.

1. The steel undergoes SCC of "mixed" mode – intergranular/transgranular with predominantly intergranular cracks in NaH_2PO_4 solutions (pH = 4.0) at temperatures up to about 60 °C. The susceptibility of the steel to SCC depends on the phosphate concentration and it decreases markedly with increase of temperature. The highest SCC susceptibility is observed in the region of the active to passive transition of the steel (-0.3 – 0.0 V, SCE).
2. The potentiodynamic method with fast/slow potential sweep rates could be used for predicting the possible potential region of SCC of mild steel in phosphate media as well as for a qualitative evaluation of the effect of some environmental factors on SCC susceptibility.
3. SCC of mild steel in NaH_2PO_4 solutions occurs at conditions of formation of films composed of secondary iron(II) and iron(III) phosphates. The films formed at potentials in SCC zone are mixed oxide-phosphates composed of $Fe_3(PO_4)_2.8H_2O$, $Fe_3(PO_4)_2.4H_2O$, $FePO_4.xH_2O$ and some quantity of Fe_3O_4, while the film in the passive region (outside SCC zone) is of oxide nature and consists of γ-Fe_2O_3.
4. An electrochemical model for crack propagation, based on the film rupture concept in SCC and quantitative electrochemical kinetics considerations, and relating the rate of crack propagation with the electrochemical parameters of metal dissolution and cathodic reactions at the crack tip and outer metal surface has been applied to the mild steel/phosphate SCC system. It is suggested that in this case SCC is related to the formation of secondary amorphous iron(III) phosphates in the surface film. It is shown that the model could be used for calculating the approximate rate of crack propagation and defining electrochemical conditions favorable for SCC.
5. The electrochemical parameters of mild steel/phosphate systems of practical interest, however, are largely missing in order to make a full evaluation of the quantitative aspects of the model presented.

Acknowledgement

The authors are grateful to CINVESTAV-IPN and CONACYT, Mexico, for the support and granting of a Cátedra Patrimonial to one of them (R. Raicheff) under contract 980005.

References

[1] Shroeder, W. C. and Partrige, E. P., *Transactions of ASME*, Vol. 58, 1936, p. 223.
[2] Middleton, W. R., "Stress Corrosion Cracking of Mild Steel in a Phosphate Solution", *British Corrosion Journal*, Vol. 8, 1973, p. 62.
[3] Parkins, R. N., Holroyd, N. J., and Fessler, R. R., "Stress Corrosion Cracking of C-N Steel in Phosphate Solutions," *Corrosion*, Vol. 34, 1978, p. 253.
[4] Flis, J., "The Passivation of Iron-Carbon Alloys in Acidic Phosphate Solutions and its Relation to Stress Corrosion Cracking," *Corrosion Science*, Vol. 25, 1985, p. 317.
[5] Smart, N. R., Scott, P. M., and Procter, R. P. M., "Repassivation Kinetics and Stress

Corrosion Cracking of Mild Steel in Phosphates Solutions," *Corrosion Science*, Vol. 30, 1990, p. 877.

[6] Fachikov, L. and Raicheff, R., "A Cell for Electrochemical and Corrosion Testing of Metals under Stress", *Industrial Laboratory* (Russian), Vol. 55, N 12, 1989, p. 16.

[7] Raicheff, R. and Fachikov, L., "Spannungsrisskorrosion Niedriglegierter Chomstahle in Nitratlosungen," *Zeitschrift für Metallkunde*, Vol. 86, 1995, p.769.

[8] Marcheva, J., Raicheff, R., Nikolov, S., and Haladzova, Tz., "Mossbauer Study of Surface Films on Steels in Phosphate Environments under Stress-corrosion Cracking Conditions," *Journal of Radioanalytical Nuclear Chemistry Letters*, Vol. 212, 1996, p. 383.

[9] Kolotirkin, Y. M., Kononova, M. D., and Florianovich, G. M., "Electrochemical Behaviour of Iron in Neutral Phosphate Solutions," *Protection of Metals* (Russian), Vol. 2, 1966, p. 609.

[10] Zucchi, F. and Trabanelli, G., "Anodic Behaviour of Fe in Phosphate Solutions", *Corrosion Science*, Vol. 11, 1971, p. 141.

[11] Raicheff, R., Marcheva, J., and Fachikov, L., "Effect of pH on Anodic Behaviour of Mild Steel in Phosphate Solutions," *Extended Abstracts, 37-th ISE Meeting*, Vilnus, USSR, Vol. 1, 1986, p. 404.

[12] Parkins, R. N., "Environment Sensitive Fracture and its Prevention," *British Corrosion Journal*, Vol. 14, 1979, p. 5.

[13] Parkins, R. N., "Predictive Approaches to Stress Corrosion Cracking Failure," *Corrosion Science*, Vol. 20, 1980, p.147.

[14] Katrevich, A N., Florianovich, G. M., and Kolotirkin, Y. M., "The Effect of Salt Deposits on the Process of Active Dissolution of Iron in Phosphate Solutions," *Protection of Metals* (Russian), Vol. 10, 1974, p. 69.

[15] Despic, A. R. and Raicheff, R. G., "The Crack-propagation Rate in Terms of the Electrochemical Mechanism of Stress-corrosion Cracking of Metals," *Comptes Rendus de l'Académie Bulgare des Sciences*, Vol. 23, 1970, p. 1091.

[16] Raicheff, R., "An Electrochemical Model for Environmental Cracking of Metals," in *Stability of Materials*, A. Gonis, P. E. A. Turchi and J. Kudronovski Eds., NATO ASI Series, Plenum Press, New York, 1996, p. 669.

[17] Raicheff, R., "Electrochemical Models for Crack Propagation in Stress-corrosion Cracking of Metals," in *Proceedings of the International Symposium "Environmental Effects on High Technology Materials"*, Polish Academy of Sciences, Zakopane, Poland, 1997, p. 191.

[18] Ford, P. F., "Slip Dissolution Model," in *Corrosion sous Contrainte*, D. Desjardin and R. Oltra Eds., Les Editions de Physique, Les Ulis, 1992, p. 308.

[19] Hanzel, D., Meisel, W., Hanzel, Darko and Gutlich, P., *Solid State Communications*, Vol. 76, 1990, p. 307.

[20] Raicheff, R., Marcheva, J., and Fachikov, L., "Effect of Solution Concentration on Stress-corrosion Cracking of Mild Steel in Phosphate Medium," in *Proceedings of the 10th International Congress on Metallic Corrosion*, Vol. 3, Oxford and IBH Publishers, Madras, India, 1987, p. 2133.

[21] Vetter, K. J., *Elektrochemische Kinetik*, Springer, Berlin, 1961.

[22] Tanaka, N. and Tamamushi, R., "Kinetic Parameters of Electrode Reactions," *Electrochimica Acta*, Vol. 9, 1964, p. 963.

[23] Bockris, J. O'M., "Electrode Kinetics," in *Modern Aspects of Electrochemistry*, Vol. 1; J. O'M. Bockris and B. E. Conway Eds., Plenum Press, New York, 1954, p. 180.

[24] Despic, A. R., Raicheff, R. G., and Bockris, J. O'M., "Mechanism of the Acceleration of the Electrodic Dissolution of Metals during Yielding under Stress", *Journal of Chemical Physics*, Vol. 49, 1968, p. 926.

[25] Raicheff, R., "Mechanoelectrochemical Effects and Stress-corrosion Cracking of Metals," D.Sc. dissertation, University of Chemical Technology and Metallurgy, Sofia, Bulgaria, 1998.

Industrial Session—Engineering Applications for New Experimental and Analytical Methods

Sheldon W. Dean,[1] Julio G. Maldonado,[2] and Russell D. Kane[2]

Cyclic Strain Cracking of Stainless Steels in Hot Steam-Hydrocarbon Reformer Condensates: Test Method Development

Reference: Dean, S. W., Maldonado, J. G., and Kane, R. D., **"Cyclic Strain Cracking of Stainless Steels in Hot Steam-Hydrocarbon Reformer Condensates: Test Method Development,"** *Environmentally Assisted Cracking: Predictive Methods for Risk Assessment and Evaluation of Materials, Equipment, and Structures, ASTM STP 1401,* R. D. Kane, Ed., American Society for Testing and Materials, West Conshohocken, PA, 2000.

Abstract: The discovery of a severely cracked mixing tee in the process gas cooling section of a hydrogen plant showed a form of cracking that appeared to have features typical of both fatigue and chloride stress corrosion cracking of 304L stainless steel. However, the conditions were significantly less severe than what would be anticipated for either process alone. It was speculated that a synergism between these processes occurred causing this failure. A laboratory program was undertaken that confirmed that cracking could occur in environments with as little as 1 ppm chloride and 1 ppm NaSCN when both cyclic stressing and anodic polarization were present. Conventional slow strain rate tests on 304L stainless steel in this environment with anodic polarization did not cause environmentally assisted cracking confirming the importance of cyclic stressing. Similar cyclic tests on duplex stainless steel 2205 and nickel alloy 625 did not show cracking regardless of the applied potential up to 600 mV versus Ag/AgCl reference electrode.

Keywords: Environmentally assisted cracking, corrosion fatigue cracking, chloride stress corrosion cracking, slow strain rate testing, cyclic loading, anodic polarization, hydrogen plant, steam hydrocarbon reformer

Introduction

In May 1998, a hydrogen manufacturing facility experienced a leak in a mixing tee where a bypass around a heat exchanger joins the cooler effluent from the exchanger. This plant is a steam-hydrocarbon reformer that converts refinery off gas to syngas at high temperatures and pressures with steam. The leak occurred after the shift converters in a region where heat recovery was being practiced.

[1] Fellow, Corporate Engineering Department, Air Products and Chemicals, Inc., 7201 Hamilton Blvd., Allentown, PA, 18195-1501.

[2] Technical Services Division Manager and President, respectively, *InterCorr* International, Inc., 14503 Bammel N. Houston, Suite #300, Houston, TX, 77014-1149.

Copyright© 2000 by ASTM International www.astm.org

A careful examination of the interior of the tee and piping showed that the cracks occurred only in the bypass reducer, tee, and a short distance downstream. These components were fabricated from welded stainless steel Type 304L (UNS S30403). The cracks were mainly associated with weld heat-affected zones, although there were a few cracks away from welds. A typical weld crack is shown in Figure 1. Many of the cracks were straight transgranular cracks, Figure 2. Some showed multiple branched configurations as seen in Figure 3. When the fracture surfaces were viewed without magnification, features resembling beach marks were seen, Figure 4. High magnification fractography showed quasi cleavage morphology, Figure 5. The fracture surface also showed trace chloride and sulfur peaks in an energy dispersive x-ray analyses. A typical example showing chlorine is shown in Figure 6.



Figure 1--Cracks in toe of weld in reducer.
Photo shows approximately 12 inches of pipe circumference.

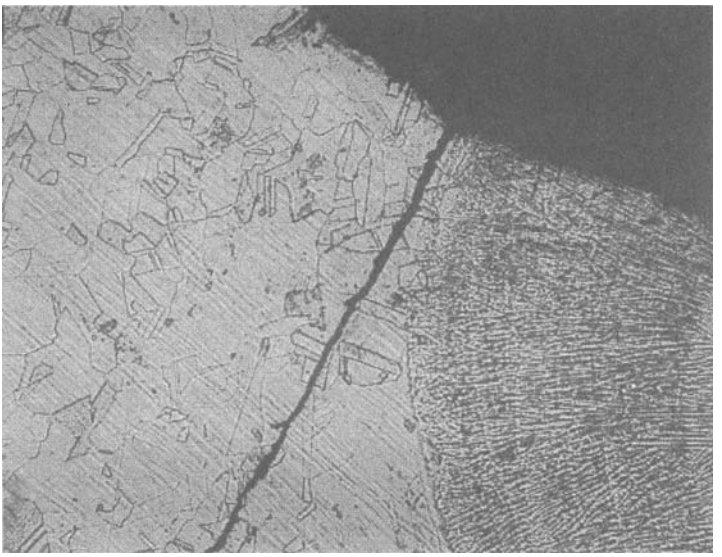


Figure 2--Section through crack showing straight transgranular morphology. 100x - Electrolytic oxalic acid etch

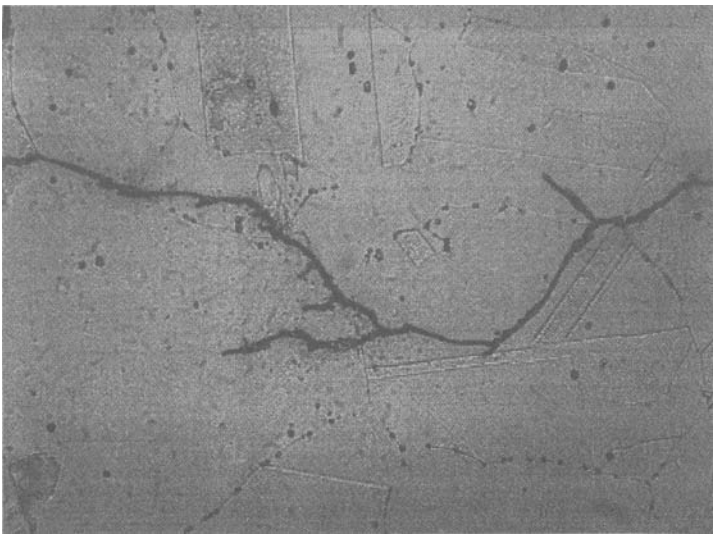


Figure 3--Section through crack showing branched transgranular morphology 500x - Electrolytic oxalic acid etch

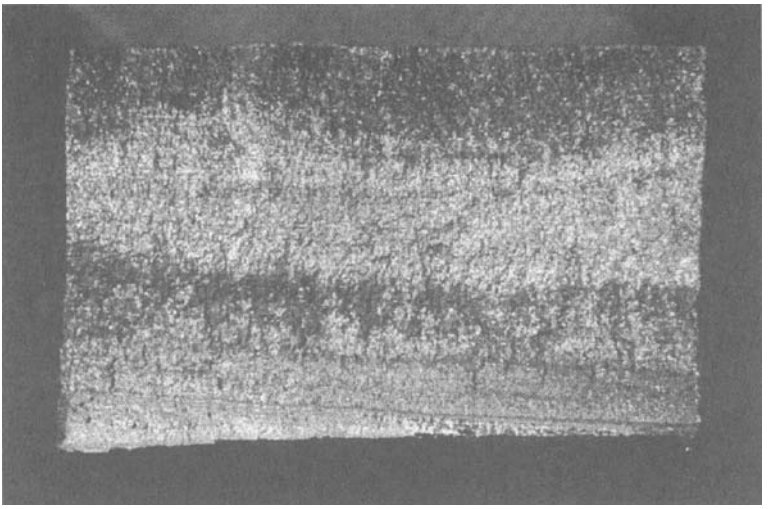


Figure 4--Photograph of fracture surface after breaking cracked piece open - showing beach mark features. Top of picture is wetted surface, about 3X

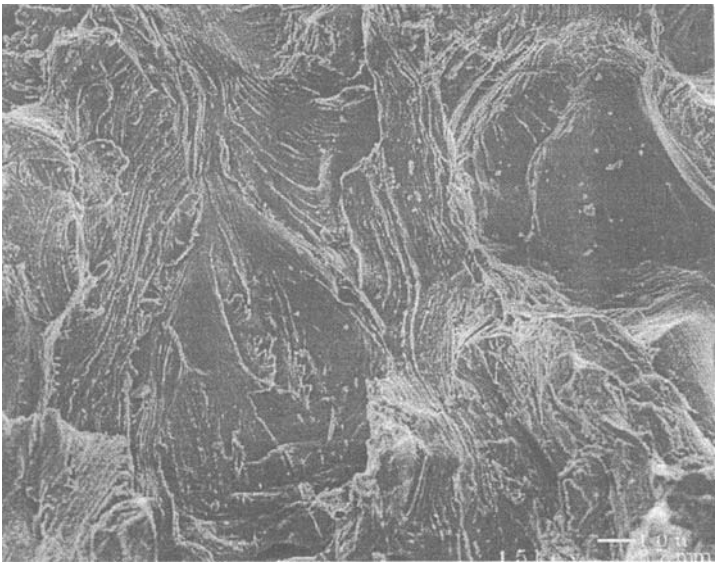


Figure 5--Scanning micrograph of fracture surface showing cleavage features - 600x

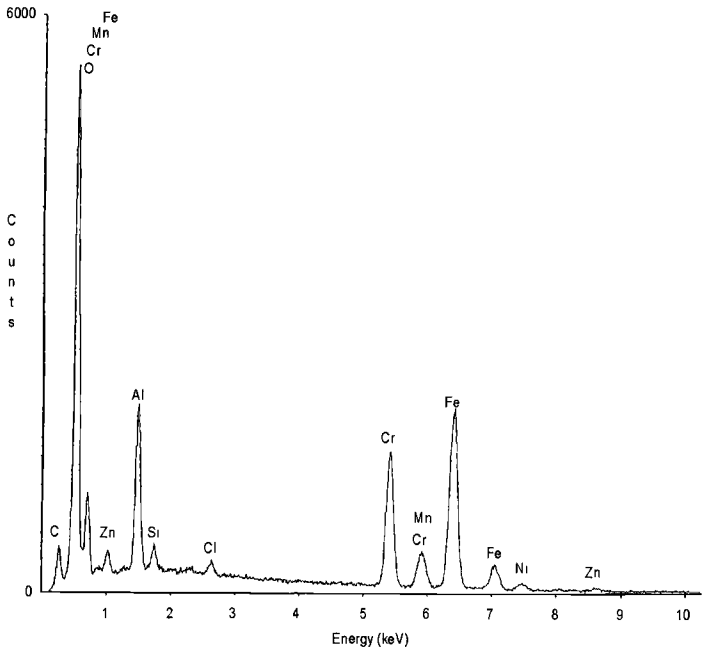


Figure 6--Energy dispersive x-ray spectograph of fracture surface showing chlorine peak. Sulfur was seen in other spectrographs

The interpretation of the metallographic work on this failure was ambiguous. On one hand, the cracks looked like traditional chloride stress corrosion cracks. The presence of chloride together with multiple branched cracks is usually definitive [*1*]. However, the fact that the cracks were limited to a small area on the piping made this conclusion suspect. There were also many characteristics of the cracks that resembled fatigue more than stress corrosion cracks. The condensate from the process was carefully analyzed and chloride levels were never found to be greater than 1.0 ppm and averaged 0.2 ppm during a one-month sampling period. In addition, there is no oxygen nor other components often found in situations where stress corrosion cracking occur. The temperature in the bypass was about 150°C while the cooler stream was close to 100°C. A review of the flow dynamics of the system suggested that slug flow and temperature cycling were probably occurring in the vicinity of the tee and down stream. This is the most likely source of stress cycles that produced fatigue-like features.

Because the chloride content of the environment was so low and the normal aggravating factors of oxygen and pitting were absent, the conclusion of chloride cracking was most troubling. The MTI (Materials Technology Institute) experience survey for chloride stress corrosion cracking [*2*] indicates that the environment was about two orders of magnitude below the chloride concentration where cracking would be anticipated. Furthermore, although stress cycling from the temperature cycling is likely, the magnitude of this cycling was well below the point where fatigue cracking would

have been expected. As a consequence, the failure that was observed appeared to be a synergistic crack propagation mechanism incorporating features of both fatigue and stress corrosion cracking, but occurring at much milder conditions than we would anticipate to be problematic.

In order to confirm this speculation, a laboratory study was undertaken. The purpose of this study was to determine if accelerated cracking could be induced in Type 304L stainless steel using a cyclic straining approach in an environment containing low chloride concentrations. A second objective was to understand better the influence of environmental factors on the cracking process. The third objective was to test other alloys, in particular, duplex 2205 (UNS S31803): Composition %; 0.03 max C, 21.0-23.0 Cr, 2.0 max Mn, 2.5-3.5 Mo, 0.08-0.20 N, 4.5-6.5 Ni, 0.030 max P, 0.020 max S, 1.00 max Si, and Alloy 625 (UNS N06625): Composition %; 0.40 max Al, 0.1 max C, 3.15-4.15 Cl, 20.0-23.0 Cr, 5.0 max Fe, 0.5 Mn, 8.0-10.0 Mo, rem Ni, 0.015 max P, 0.015 max S. 0.50 max Si, 0.40 max Ti, because these alloys were proposed or used to replace the mixing tee and downstream piping.

Experimental

Materials and Environment Description

SSR testing specimens were prepared in accordance with NACE Test Method for Slow Strain Rate Testing for Screening of Corrosion Resistant Alloys (CRAs) for Stress Corrosion Cracking in Sour Oilfield Service (TM0198-98). The specimens had a 1.0 inch (25.4 mm) long gage section with a 0.150 inch (3.8 mm) diameter. The shoulder diameter of the specimen was nominally 0.25 inch (6.4 mm). The specimen gage section had a surface finish of less than 10 μ-inch (0.25 μm).

Table 1 presents the six basic environments that were employed in this study. One or ten (10) ppm chloride levels were in the base solution composition. Carbon disulfide (CS_2) and sodium thiocyanate (NaSCN) were also used at a 1 ppm level in some cases. The gases, hydrogen and/or carbon dioxide, were added to the autoclave head space to give the indicated partial pressure.

Table 1 – Description of testing environments.

Environment No.	Environment Description	Test Temperature (°C)
1	1 ppm Cl^-, 1ppm CS_2 95 psi (0.65 MPa) CO_2	100
2	1 ppm Cl^-, 1ppm CS_2 - 95 psi (0.65 MPa) CO_2/ 350 psi (2.41 MPa) H_2	150
3	10 ppm Cl^-, 1ppm CS_2 - 95 psi (0.65 MPa) CO_2/ 350 psi (2.41 MPa) H_2	150
4	10 ppm Cl^- - 95 psi (0.65 MPa) CO_2/ 350 psi (2.41 MPa) H_2	150
5	1 ppm Cl^- - 95 psi (0.65 MPa) CO_2/ 350 psi (2.41 MPa) H_2	150
6	1 ppm Cl^-, 1 ppm NaSCN - 95 psi (0.65 MPa) CO_2/ 350 psi (2.41 MPa) H_2	150

SSR Testing Procedures

SSR testing was conducted according to procedures given in ASTM Test Method for Slow Strain Rate Testing to Evaluate the Susceptibility of Metallic Materials to Environmentally Assisted Cracking (G 129) and NACE TM0198-98 with some modifications as applicable. Modifications were employed to accommodate the requirements of the testing since cyclic loading of the specimens is not contemplated in either ASTM G 129 or NACE TM0198-98 standards. Cyclic SSR testing procedures employed herein are similar to the procedures employed by Nisbet et al.[3] for the screening of CRA's in sour oilfield service environments. Conventional SSR testing was also conducted at a strain rate of 4×10^{-6} sec^{-1}. A baseline conventional SSR test in air at temperature (150°C) was also conducted.

For cyclic SSR testing, the tensile properties of the material at the temperature of interest were determined beforehand. This information was needed to input stress level limits for cyclic loading. A computer-interfaced SSR testing system (P-CERT™) with an anti-backlash feature to allow for cyclic operation was employed. In most cases, stress limits were set so that the total straining applied was equivalent to 0.001 (0.1%) strain. During the tests, the specimens were first loaded to the desired maximum stress level, which was either 0.2 or 0.3% yield stress, and then cycled between the maximum and minimum stress levels at a pre-determined cycling rate and for a specified number of cycles. Most tests were conducted at a cycling rate of 1 cycle/minute and a total number of 2,000 cycles or until failure.

A potentiostat-galvanostat was used for the application of anodic polarization when required. Specimens were polarized in the +100 to +600 mV range vs. a proprietary Ag/AgCl pressure balanced reference electrode system. After test completion, the

specimens were retrieved from the environment and the surface examined at 10x magnification.

Results

Testing was conducted in several phases, which reflect the sequential adjustments made to increase the severity of the environment to produce cracking. Table 2 presents a summary of the test results for the first four phases corresponding to the testing done on the 304L material.

Phase 1

The first five tests (6171-1, 5, 7, 8 and 10) were conducted to assess, in a preliminary manner, the cycling, cycling rate, pre-stressing and stress level limit parameters. Initially, the test temperature had been defined as 100°C and the cycling rate at 1 complete cycle every two (2) minutes. The temperature was increased to 150°C and the cycling rate to one cycle per minute. All the tests conducted in this initial phase had a 1 ppm Cl^- concentration level. Although the testing conditions were made increasingly more severe, no failures or cracking evidence was observed in any of the specimens.

Phase 2

The second set of tests (6171-12, 13 and 15) corresponds to a series of conventional (i.e., no cyclic loading applied) SSR tests conducted in 10 ppm Cl^- level environments. EAC evidence was only observed in a test specimen (6171-15) that was anodically polarized to +250mV vs. Ag/AgCl reference electrode.

Table 2 –Testing results summary for Phases 1 through 4

Test No.	Material	Env. No.	Scheduled Number of Cycles and Rate	Stress Levels Max-Min ksi (MPa)	Test Results and Observations
6171-1	304L SS	1	1000 1 cycle / 2 min	49-40 (338-276)	Isolated pitting, no EAC evidence
6171-5	304L SS	1	1000 1 cycle / 2 min	57-27 (393-186)	No EAC evidence
6171-7	304L SS	2	1000 1 cycle / min	0.2% Pre-stress[1] 38.5-11.5 (265-79)	No EAC evidence
6171-8	304L SS	2	1000 1 cycle / min	0.3% Pre-stress[1] 40.7-13.7 (281-94)	No EAC evidence
6171-10	304L SS	2	2000 1 cycle / min	0.3% Pre-stress[1] 40.7-13.7 (281-94)	No EAC evidence
6171-12	304L SS	3	N/A Conventional SSR	N/A Strain Rate $4x10^{-6}$	No EAC evidence
6171-13	304L SS	4	N/A Conventional SSR	N/A Strain Rate $4x10^{-6}$	No EAC evidence
6171-15	304L SS	4 +250 mV	N/A Conventional SSR	N/A Strain Rate $4x10^{-6}$	Pitting and EAC evidence observed
6171-16	304L SS	4 +250 mV	2000 1 cycle / min	0.3% Pre-stress[1] 40.7-13.7 (281-94)	Failed after 58 cycles - EAC
6171-17	304L SS	4 +250 mV	2000 1 cycle / min	0.3% Pre-stress[1] 40.7-13.7 (281-94)	Failed after 25 cycles - EAC
6171-18	304L SS	4 +150 mV	2000 1 cycle / min	0.3% Pre-stress[1] 40.7-13.7 (281-94)	Isolated pitting, no EAC evidence
6171-19	304L SS	4 +200 mV	2000 1 cycle / min	0.3% Pre-stress[1] 40.7-13.7 (281-94)	Pitting and EAC evidence observed
6171-24	304L SS	5 +200 mV	2000 1 cycle / min	0.3% Pre-stress[1] 40.7-13.7 (281-94)	No EAC evidence
6171-25	304L SS	5 +300 mV	2000 1 cycle / min	0.3% Pre-stress[1] 40.7-13.7 (281-94)	No EAC evidence
6171-26	304L SS	5 +400 mV	2000 1 cycle / min	0.3% Pre-stress[1] 40.7-13.7 (281-94)	No EAC evidence
6171-27	304L SS	6 +400 mV	2000 1 cycle / min	0.3% Pre-stress[1] 40.7-13.7 (281-94)	Failed after 360 cycles - EAC
6171-28	304L SS	6 +200 mV	2000 1 cycle / min	0.3% Pre-stress[1] 40.7-13.7 (281-94)	Failed after 599 cycles - EAC
6171-29	304L SS	6 +100 mV	2000 1 cycle / min	0.3% Pre-stress[1] 40.7-13.7 (281-94)	No EAC evidence
6171-30	304L SS	6 +200 mV	N/A Conventional SSR	N/A Strain Rate $4x10^{-6}$	No EAC evidence

[1] 0.2 or 0.3% yield stress as determined from tensile testing.

Phase 3

Cyclic SSR tests 6171-16 through 19 were conducted in the environment that produced cracking in Phase 2. All the tests were conducted in the same environment, but with varying degrees of anodic polarization. Both 6171-16 and 17 tests were conducted with an applied potential of +250 mV vs. Ag/AgCl reference electrode and failed rapidly within 58 and 25 cycles, respectively. Figure 7 shows the transgranular cracking evidence observed on 6171-16. The cyclic SSR pre-stress level used in this phase and for the remainder of the 304L SS specimens hereafter presented was 0.3% yield stress. Anodic polarization was then decreased by 100mV, but no cracking susceptibility was observed (6171-18). It was then determined that a minimum of +200mV applied potential was necessary to produce cracking in this particular environment (6171-19).

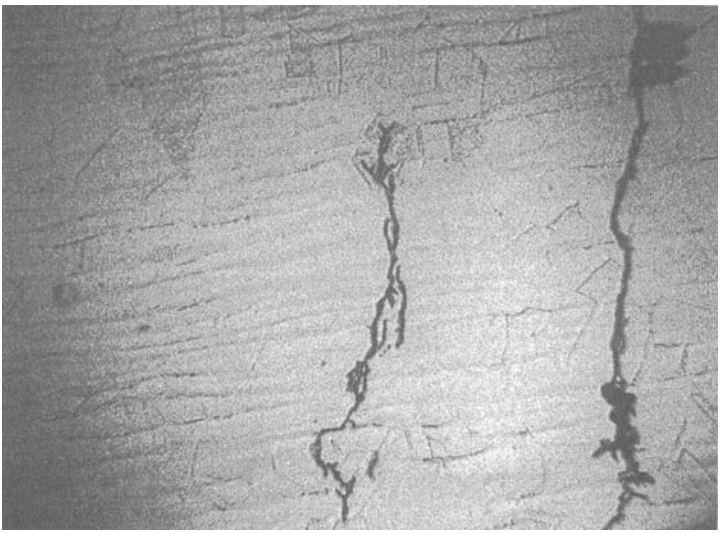


Figure 7--Transgranular cracking in specimen 6171-16, 10 ppm chloride, 250mV vs. Ag/AgCl, 500x oxalic acid etch

Phase 4

Cyclic SSR tests 6171-24 through 26 were conducted in Phase 4. Once cracking susceptibility was clearly established for the 10 ppm Cl^- level environment, the conditions that would lead to EAC at the 1 ppm Cl^- level were sought. Tests 6171-24 through 26 were cyclic SSR tests conducted at increasingly higher levels of anodic polarization (from +200 to +400mV applied potential vs. Ag/AgCl reference electrode), but no cracking evidence or failures were observed. One ppm NaSCN was then added to the environment in an effort to increase its severity. Tests 6171-27 and 28 showed clear evidence of EAC since both specimens failed within 360 and 599 cycles, respectively. Specimen 6171-27 was severely corroded due to the high level of anodic polarization applied (+400 mV vs.

Ag/AgCl reference electrode). Specimen 6171-28 was tested with an applied voltage of +200mV vs. Ag/AgCl reference electrode. A third cyclic SSR test was conducted on 6171-29 at a lower level of anodic polarization (+100mV vs. Ag/AgCl reference electrode), but no cracking was observed.

A conventional SSR test was then conducted in the same environment that produced cracking in the cyclic mode, which was anodically polarized to +200mV vs. Ag/AgCl reference electrode. In this case, the specimen demonstrated a ductile failure mode.

Phase 5

Cyclic SSR tests (6592-2, 6592-2A, 6592-3 and 6591-2 through 4) were conducted in the last phase of testing. This phase was conducted to ascertain the EAC susceptibility of Alloy 625 and Alloy 2205 in the 1 ppm Cl^- environment that produced cracking in 304L SS. Tests 6592-2, 2A and 3 correspond to the Alloy 625 material, which was tested at progressively higher levels of anodic polarization, but no evidence of pitting corrosion or EAC susceptibility was observed even at an applied voltage of +600 mV vs. Ag/AgCl reference electrode. Tests 6591-2 through 4 correspond to the Alloy 2205 material tested under the same conditions as the Alloy 625. Once again, no EAC susceptibility was observed. Only some isolated pitting was noted on the specimen (6591-4) that was anodically polarized to +600mV vs. Ag/AgCl reference electrode. Similarly, Table 3 presents the test results for the alternate materials of construction.

Table 3 –Testing results summary for Phase 5

Test No.	Material	Env. No.	Scheduled Number of Cycles and Rate	Stress Levels Max-Min ksi (MPa)	Test Results and Observations
6592-2	Alloy 625	6 +200 mV	2000 1 cycle / min	0.2% Pre-stress[1] 82.8-53.7 (571-370)	No EAC evidence
6592-2A	Alloy 625	6 +400 mV	2000 1 cycle / min	0.2% Pre-stress[1] 82.8-53.7 (571-370)	No EAC evidence
6592-3	Alloy 625	6 +600 mV	2000 1 cycle / min	0.2% Pre-stress[1] 82.8-53.7 (571-370)	No EAC evidence
6591-2	Alloy 2205	6 +200 mV	2000 1 cycle / min	0.2% Pre-stress[1] 72-46.2 (496-319)	No EAC evidence
6591-3	Alloy 2205	6 +400 mV	2000 1 cycle / min	0.2% Pre-stress[1] 72-46.2 (496-319)	No EAC evidence
6591-4	Alloy 2205	6 +600 mV	2000 1 cycle / min	0.2% Pre-stress[1] 72-46.2 (496-319)	Isolated pitting, No EAC evidence

[1] 0.2% yield stress as determined from tensile testing.

Discussion

The experimental program was set up to simulate the cracking that had occurred in the hydrogen plant. Because we had no understanding of the importance of either the environmental or stressing variables, some preliminary work was necessary to find

conditions that would cause cracking to occur in the specimens. The first five tests conducted were for this purpose and were designated Phase 1. The issues of applied pre-stress, cyclic stress range, number of cycles, and environmental conditions were made progressively more severe in these tests, but no cracking was observed.

It was then decided to run slow strain rate tests according to ASTM G 129 to determine if these conditions would cause stress corrosion cracking. The first two tests did not show any evidence of stress corrosion cracking, even though at 150°C and 10 ppm chloride the 304L material would be expected to show susceptibility according to the MTI publication [2]. The specimens from these tests did not show any sign of corrosion or pitting, and this was significant. It was then decided to apply an electrochemical potential of +250mV versus Ag/AgCl reference electrode to the specimen to cause some corrosive attack during the stressing. The result of this test indicated that pitting and some evidence for environmental cracking did occur in the slow strain rate test, but it was not severe enough to cause measurable change in time to failure or reduction in area.

In the next phase of the program, the cyclic stressing was carried out on specimens while applying anodic polarization in a 10 ppm chloride environment. This procedure caused rapid failures at +250 mV versus Ag/AgCl reference electrode. The potential was then decreased in 50 mV decrements. At +200 mV, there was evidence of environmental cracking, but the specimen did not fail. At +150 mV, no cracking or pitting was noted.

It was then decided to run tests at 1 ppm chloride. The Phase 4 results showed that no cracking occurred in this case even at +400 mV. This was significant because, even at 1 ppm chloride, conditions were higher than any measurement of chloride concentration from plant condensate. However, the fracture surfaces from the plant showed evidence of very small sulfur peaks in some areas, so it was decided to add a sulfur compound to the mixture and see what effect it had. The initial work had included carbon disulfide, but no cracking was noted. It was decided to use a different compound that might have more potency for causing or accelerating localized corrosion of stainless steels. Accordingly, it was noted that the EPR test, ASTM Standard Test Method for Electrochemical Reactivation (EPR) for Detecting Sensitization of Type 304 and 304L Stainless Steels (G 108), uses a thiocyanate compound (KSCN) to accelerate the intergranular corrosion of sensitized 304 stainless steels, so an addition of sodium thiocyanate at 1 ppm was made to the environment and the next series of tests was made. At +400 mV, rapid failure occurred. A test at +200 mV also showed failure but required almost 600 cycles. A section through the specimen tested at 400 mV is shown in Figure 8. There were multiple branched transgranular cracks similar to some seen on the failed pipe. At +100 mV, no evidence of cracking, corrosion, or pitting was observed.

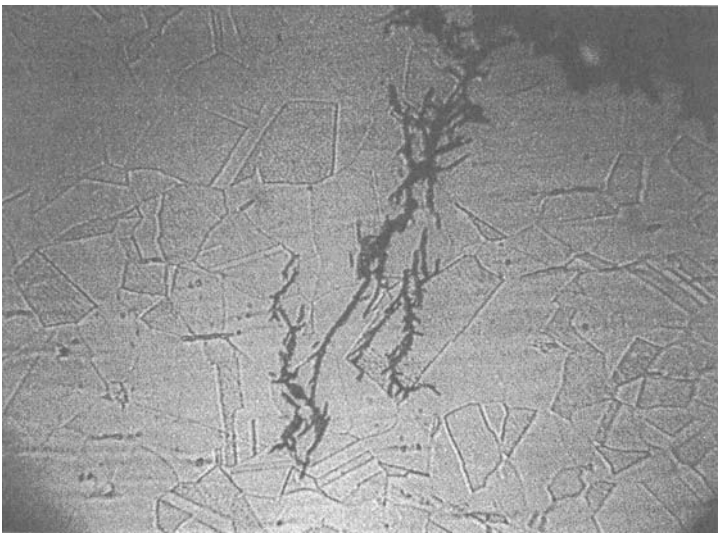


Figure 8--Section through specimen 6171-27. Failed after 360 cycles - 1 ppm chloride, 1 ppm NaSCN, 150°C, 400mV - 500x Electrolytic oxalic acid etch

At this point, it was of interest to run a slow strain rate test, G 129, on the 304L specimen in this environment. No evidence of environmentally assisted cracking was noted at the conclusion of this test. This result demonstrated the aggressive nature of the cyclic stressing as opposed to a continuous stress application.

The final testing was carried out with the duplex 2205 and 625 materials. In each case, three potentials were used, +200 mV, +400 mV, and +600 mV. Neither evidence of environmental cracking nor failures were noted on any of these tests. The duplex 2205 did show some evidence of pitting at +600 mV, but no cracking.

This testing program has demonstrated quite clearly that 304L stainless steel is susceptible to corrosion fatigue cracking in environments where conventional chloride stress corrosion cracking is unlikely. The application of a potential is clearly important in the test program, and this was a cause for concern in understanding the application of these results to field situations. However, it must be noted that field failures required between one and three years of exposure to the environment before failures were observed. The extended time allows some corrosion films to form. It seems apparent that corrosion is a necessary ingredient in the cracking process. The formation of corrosion films leads to variation in corrosion potential with time. This effect will vary with the species present in the system. By the same argument, the effect of the thiocyanate addition predisposes the stainless to corrode and crack. This is probably the explanation of why hydrogen manufacturing facilities based on steam-methane reforming have not experienced this type of failure while a survey of hydrogen plants where refinery off gases are used, revealed cracking in similar situations on a regular basis. The sulfur content of refinery off gases is higher on average and, therefore, the probability of having some sulfur escape the zinc oxide (absorbent used to remove sulfur from feed gas) on

other active surfaces in the system would be higher. It is not known whether thiocyanate is a likely contaminant in reformer condensates, but it is not beyond the realm of possibility that such a compound might be present since nitrogen compounds such as ammonia are also present in refinery off gases.

Conclusions

The combination of electrochemical anodic polarization together with cyclic stressing was able to crack 304L stainless steel in an environment containing 1 ppm chloride and 1 ppm NaSCN at 150°C. This environment also contained 95 psi (0.65 MPa) overpressure of CO_2 and 350 psi (2.41 MPa) overpressure of hydrogen to simulate a reformer syngas environment where similar cracking was observed. The cracks that formed were similar in morphology to those seen in the field - multiple branched transgranular cracks.

Slow strain rate tests run to failure according to G 129 did not produce stress corrosion cracks under similar circumstances even when anodic polarization was applied.

Sulfur in the form of thiocyanate appears to be a potent accelerator of the cracking process in stainless steels.

Alloys, duplex 2205 and nickel-based 625, that show improved resistance to fatigue and chloride stress corrosion cracking did not fail in 1 ppm chloride, 1 ppm thiocyanate cyclic stress tests even at substantially greater anodic potentials.

The constant temperature testing program employing anodic polarization to stimulate corrosion, together with stress cycling in an apparatus similar to the G 129 slow strain rate equipment, was successful in duplicating failures caused by thermal cycling in the field.

Acknowledgment

The authors wish to acknowledge Air Products and Chemicals, Inc. for financial support for this study and *InterCorr* International, Inc. for permission to publish this study. In addition, the authors wish to acknowledge the efforts of W. R. Watkins, and J. J. Hoffman for failure analyses, D. Tenney and K. Sathe for SSR testing, M. D. Wert for metallography, R. J. Haney for surface analysis, and W. E. Wagaman and M. R. Kittek for SEM examination.

References

[1] Dean, S. W. Jr., "Review of Recent Studies on the Mechanics of Stress Corrosion Cracking in Austenitic Stainless Steels," *Stress Corrosion - New Approach ASTM STP 610*, H. L. Craig Jr., Ed., American Society for Testing and Materials, Philadelphia, PA, 1976, pp. 306-337.

[2] McIntyre, D. R., "MTI Publication 27, Experience Survey Stress Corrosion Cracking of Austenitic Stainless Steels in Water," *Materials Technology of the Chemical Process Industries*, St. Louis, MO 1987.

[3] Nesbit, W. J. R., Hartman, R. H. C., and van den Handel, G., "Rippled Strain Rate Test for CRA Sour Service Materials Selection," NACE Corrosion 97, Paper No. 58, NACE International, Houston, TX, 1997.

Jesús Toribio[1] and Elena Ovejero[2]

Environmentally Assisted Cracking of Cold Drawn Eutectoid Steel for Civil Engineering Structures

Reference: Toribio, J. and Ovejero, E., "**Environmentally Assisted Cracking of Cold Drawn Eutectoid Steel for Civil Engineering Structures,**" *Environmentally Assisted Cracking: Predictive Methods for Risk Assessment and Evaluation of Materials, Equipment, and Structures, ASTM STP 1401*, R. D. Kane, Ed., American Society for Testing and Materials, West Conshohocken, PA, 2000.

Abstract: The paper analyzes the environmentally assisted cracking behaviour of eutectoid steels with different degrees of cold drawing subjected to electrochemical conditions promoting localized anodic dissolution. The experimental results showed a progressively anisotropic behaviour as the degree of cold drawing increases, with an evolution in the fracture type from Mode I (isotropic behaviour in slightly drawn steels) to mixed mode propagation (strongly anisotropic behaviour in heavily drawn steels). The fractographic analysis revealed changes in the microscopic topography depending on the fracture propagation mode. The phenomenon of crack tip blunting by selective dissolution in the near-tip area is discussed and the blunting effect increases with the degree of cold drawing. Attention is also paid to the possibility of evolution from smooth blunting to cornered blunting associated with shear at the crack tip vertices, so the markedly oriented pearlitic microstructure favours cornered blunting in the most heavily drawn steels.

Keywords: prestressing steel, cold drawing, pearlitic microstructure, stress corrosion cracking, localized anodic dissolution, anisotropic behaviour

Introduction

In cold drawn eutectoid steels, used as constituents of prestressed concrete structures in civil engineering, manufacturing by cold drawing produces a marked orientation of the pearlitic microstructure at the levels of pearlitic colonies and lamellae, inducing strength anisotropy [*1–6*]. Thus, in spite of the fact that cold drawing enhances the classical mechanical properties of the steel —thereby providing a better material for structural engineering performance— the microstructural changes during manufacture produce strength anisotropy and may affect seriously the fracture behaviour in air [*7–9*] as well as the environmentally assisted cracking (EAC) performance [*10–15*].

In this paper the EAC performance of cold drawn prestressing steels with different degrees of cold drawing is analyzed in the regime of pure environmentally assisted cracking by *localised anodic dissolution*. In addition, since steels with different degrees of cold drawing are studied, the influence of the strain hardening level on the stress corrosion behaviour can be elucidated.

[1] Professor, Department of Materials Science, University of La Coruña, E.T.S.I. Caminos, Campus de Elviña, 15192 La Coruña, Spain.

[2] Technical Staff Member, ITMA, Parque Tecnológico de Asturias, 33428 Coruño-Llanera, Spain.

Copyright© 2000 by ASTM International www.astm.org

Materials and Microstructure

The materials used in this work were high-strength steels taken from a real manufacturing process. Wires with different degrees of cold drawing were obtained by stopping the manufacturing chain and taking samples from the intermediate stages. The different steels were named with digits 0 to 6 which indicate the number of cold drawing steps undergone. Table 1 shows the chemical composition common to all steels, and Table 2 includes the diameter (D_i), the degree of cold drawing (represented by the ratio of the diameter of any steel to the initial diameter before cold drawing D_i/D_0), the yield strength (σ_Y), the ultimate tensile stress (σ_R), and the fracture toughness (K_{IC}).

Table 1 — *Chemical composition (wt %) of the steels.*

C	Mn	Si	P	S	Cr	V	Al
0.80	0.69	0.23	0.012	0.009	0.265	0.060	0.004

Table 2 — *Diameter reduction and mechanical properties of the steels.*

Steel	0	1	2	3	4	5	6
D_i (mm)	12.00	10.80	9.75	8.90	8.15	7.50	7.00
D_i/D_0	1	0.90	0.81	0.74	0.68	0.62	0.58
σ_Y (GPa)	0.686	1.100	1.157	1.212	1.239	1.271	1.506
σ_R (GPa)	1.175	1.294	1.347	1.509	1.521	1.526	1.762
K_{IC} (MPam$^{1/2}$)	60.1	61.2	70.0	74.4	110.1	106.5	107.9

While the fracture behaviour of the slightly drawn steels (0 to 3) is isotropic, i.e., associated with Mode I crack propagation, the most heavily drawn steels (4 to 6) exhibit anisotropic fracture behaviour with crack deflection and mixed mode propagation with an important component in Mode II [9]. Thus the K_{IC}-value given in Table 2 represents only a measure of failure resistance in each steel wire, but it is an actual fracture toughness — i.e., a material property— only in the slightly drawn steels in which cracking develops in Mode I, whereas in the case of the heavily drawn steels it plays the role of an "apparent" toughness that is useful for engineering design but not a material constant, because in this case mixed mode propagation appears, and the K_{IC}-value was evaluated *as if* the crack propagation developed in Mode I. The reason for this increasingly anisotropic fracture behaviour of the steels is the steelmaking process by cold drawing, which produces a microstructural orientation of the two basic microstructural units of the steels: the pearlitic colonies [4] and the pearlitic lamellae [6]. Both units tend to align parallel or quasi-parallel to the wire axis or cold drawing direction in the course of manufacturing. In addition, there is a progressive slenderizing of the pearlitic colonies as the degree of cold drawing increases [3], as well as an increasing packing closeness of the pearlitic microstructure accompanied by reduction of interlamellar spacing with cold drawing [5].

Experimental Program

To analyze the stress corrosion behaviour of the different steels, slow strain rate tests were performed on precracked steel wires. Samples were precracked by axial fatigue in the normal laboratory air environment to produce a transverse precrack, so that the maximum stress intensity factor during the last stage of fatigue precracking was $K_{max} = 0.30K_{IC}$, where K_{IC} is the fracture toughness, and the crack depth was $a = 0.30D$ in all cases, with D as the wire diameter.

After precracking, samples were placed in a corrosion cell containing aqueous solution of 1g/L $Ca(OH)_2$ plus 0.1g/L NaCl (with pH = 12.5) to reproduce the alkaline working conditions of prestressing steel surrounded by concrete. The experimental device consisted of a potentiostat and a three-electrode assembly (metallic sample or working electrode, platinum counter-electrode and saturated calomel electrode (SCE) as the reference one). All tests were conducted under potentiostatic control at –600 mV vs. SCE at which the EAC mechanism is *localised anodic dissolution* [*12*].

The applied displacement rate in axial direction was constant during each test and proportional to each wire diameter so that the smallest rate was 1.7×10^{-3} mm/min for the fully drawn wire (steel 6), and the highest was 3.0×10^{-3} mm/min for the hot rolled bar (steel 0). The load applied on the sample was continuously monitored during the tests and the displacement rate was constant in each experiment.

Experimental Results

Figure 1 gives the time to final fracture in the tests, as well as the susceptibility of the different steels to EAC, evaluated as the ratio of the fracture load in the EAC test F_{EAC} to the fracture load in air F_0. Although the scattering is high, the fracture load in the solution seems to increase with the degree of cold drawing (expressed by the ratio D_i/D_0). With regard to the time to failure the trend is even clearer, which indicates that a significant drawing-induced improvement is detected in the fracture resistance of the steels when the environmental mechanism is anodic dissolution (or pure EAC), so the steel performance is remarkably better in the cold drawn prestressing steel wire than in the hot rolled bar.

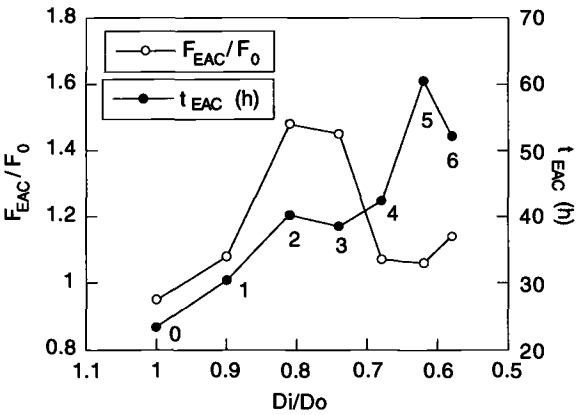


Figure 1 — *Fracture load in EAC conditions (F_{EAC}) divided by the fracture load in air (F_0) and time to fracture in the environment-sensitive cracking tests (t_{EAC}).*

Figure 2 offers the evolution of the fracture profile in EAC as the degree of cold drawing increases. An increasingly anisotropic behaviour with cold drawing is observed, For the slightly drawn steels (0 to 2), the fracture surfaces are macroscopically plane and oriented perpendicularly to the loading axis. Steel 3 shows a certain angle between the plane of the fatigue precrack and the fracture propagation direction. In the most heavily drawn steels (4 to 6) the deviation from the fatigue precrack plane is even higher. It should be emphasised that the steel is able to undergo Mode I subcritical cracking even in the most heavily drawn steels, and this is another reason for the clear improvement of EAC resistance with cold drawing, since crack deflection implies that cracking takes place along a path of minimum resistance to EAC.

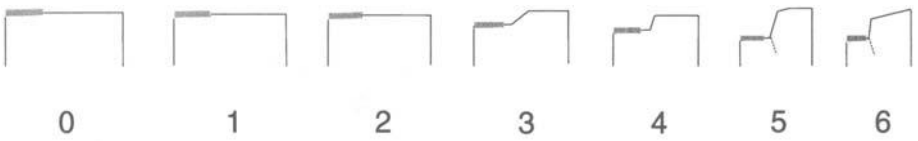


Figure 2 — *Fracture profile of the different steels in the EAC tests.*

Fracture Mechanics Approach

A fracture mechanics approach is presented in this section to evaluate a *characteristic* (or *critical*) stress intensity factor associated with the *transition* from the subcritical regime of EAC to the critical regime of environmentally unassisted fracture by cleavage. This *transition stress intensity factor* is a fundamental issue in engineering design against environmentally assisted fracture. To obtain it, an expression is required of the stress intensity factor K_I for the geometry and loading mode under consideration: a cylinder in tension with an edge crack perpendicular to the tensile loading direction. The following expression [*16*] was used

$$K_I = M(\xi)\,\sigma\sqrt{\pi a} \tag{1}$$

where σ is the remote axial stress (far from the crack), a the crack depth and $M(\xi)$ a dimensionless function given by

$$M(\xi) = (0.473 - 3.286\,\xi + 14.797\,\xi^2)^{1/2}\,(\xi - \xi^2)^{-1/4} \tag{2}$$

where ξ is the ratio a/D of the crack depth to the sample diameter. This function comes from the computation —by the compliance method— of the global energy release rate in the considered geometry and loading mode.

This approach is only valid to establish quantitative relationships in slightly drawn steels in which the fracture process develops in Mode I in the subcritical and critical regimes. On the other hand, the crack deflection that takes place in heavily drawn steels produces a mixed mode stress state (with an important Mode II component) so that the computation of stress intensity factors is an extremely difficult task out of the scope of this paper, since there is not only K_I but also K_{II} during the subcritical crack growth.

However, results expressed in terms of the fracture load in aggressive environment, cf. Figure 1, allow at least a roughly quantitative estimation —although not in the framework of fracture mechanics— of the susceptibility of heavily drawn steels to EAC.

In slightly drawn steel which behave in isotropic manner, the transition stress intensity factor K_{EAC} for EAC may be calculated as follows

$$K_{EAC} = M\,(a_{fat} + x_{EAC})\,\sigma_{EAC}\sqrt{\pi\,(a_{fat} + x_{EAC})} \tag{3}$$

where a_{fat} is the fatigue precrack (that existing at the beginning of the EAC test), x_{EAC} the depth of subcritical crack growth by EAC in Mode I, and σ_{EAC} the remote stress at the critical instant of the EAC tests (maximum values). Since x_{EAC} was measured in direction perpendicular to the crack front, the critical crack depth is $a_{fat} + x_{EAC}$.

In addition, the critical remote stress σ_{EAC} is associated with the maximum load point in the load-displacement curve, i.e., with the instability point reached after the subcritical crack growth and just before cleavage final fracture, which indicates that both the remote stress and the crack depth used to calculate K_{EAC} in Eq. (3) correspond to the same physical situation: the critical instant in the EAC test. The distance x_{EAC} was measured after the test, while the critical remote stress is

$$\sigma_{EAC} = 4F_{EAC}/\pi D^2 \tag{4}$$

where F_{EAC} is given in Fig. 1.

The ratio K_{EAC}/K_{IC} (where K_{IC} is the fracture toughness, cf. Table 2) allows a fracture mechanics evaluation of the EAC susceptibility of each steel. Figure 3 shows the susceptibility K_{EAC}/K_{IC} as a function of the degree of cold drawing D_i/D_0 of slightly drawn steels. A remarkable increase of the EAC resistance of the steels with cold drawing is observed, so that the transition stress intensity factor is as high as $K_{EAC} = 1.61K_{IC}$ in Steel 2, i.e., very clearly higher than the fracture toughness that represents the critical stress intensity factor for failure of the material in air (with no aggressive environment).

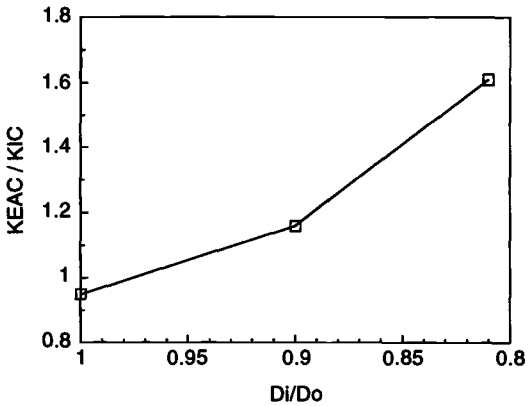


Figure 3 — *Susceptibility of slightly drawn steels to EAC, evaluated as the ratio of the critical stress intensity factor in EAC K_{EAC} to the fracture toughness in air K_{IC}, as a function of the degree of cold drawing D_i/D_0.*

On the Role of Crack Tip Blunting in EAC

The tremendous increase of stress intensity level given in Figure 3 may be attributed to crack blunting in the near-tip area due to the anodic dissolution process itself. The influence of crack tip blunting on the fracture behaviour of high strength steels in air environment has been reported previously [*17*], showing different crack tip shapes ranging from smooth blunting to cornered blunting associated with shear at the crack tip vertices. In addition, the influence of notch root radius on the fracture toughness evaluated by the Charpy V-notch impact test has been demonstrated [*18*], with an increase of toughness with increasing root radius. In the matter of EAC, crack tip blunting may be associated with material dissolution near the tip [*19*], and the crack tip radius has shown to be a key parameter for determining the threshold stress intensity factor for EAC [*20, 21*], so that the threshold is not a really constant material characteristic but depends on the crack tip radius.

With regard to the experimental results analyzed in this paper, the trend in Figure 3 indicates that the blunting effect increases with cold drawing, at least in slightly drawn steels. Subcritical crack growth develops in Mode I by an EAC mechanism of localized anodic dissolution, which is easier in the original direction of the fatigue crack, i.e., in the highly stressed (or strained) material. However, as the level of cold drawing increases, the progressive orientation of the pearlitic microstructure in the steels [*4, 6*] enhances crack tip blunting by selective dissolution in directions which differ from the original propagation direction in Mode I.

Therefore, the crack tip radius ρ is an increasing function of the degree of cold drawing. In mathematical form

$$\rho = \rho\,(D_i/D_0)^{-1} \quad \text{increasing} \tag{5}$$

and considering that an increase of crack tip radius produces an increase of fracture toughness in air [*18*] and a rise of the stress intensity factor threshold for EAC [*21*], the same may be assumed for the critical stress intensity factor K_{EAC} associated with the transition from EAC to unstable fracture by cleavage, that is

$$K_{EAC} = K_{EAC}\,(D_i/D_0)^{-1} \quad \text{increasing} \tag{6}$$

which explains the trend in the plot of Fig. 3.

With regard to heavily drawn steels, the afore-said blunting effect is even more pronounced since it is enhanced by the markedly oriented pearlitic microstructure of the steels [*4, 6*] which favours cornered blunting over smooth blunting (cf. [*17*]) and thus the equivalent crack tip radius is higher than in the case of slightly drawn steels. However, this effect is interrupted by the anisotropic behaviour (cf. Figure 2), which also increases with cold drawing. This could explain why the fracture load F_{EAC} given in Fig. 1 decreases in the final drawing steps. Thus, the beneficial blunting effect is counterbalanced in heavily drawn steels by the mixed mode propagation following directions of minimum resistance to EAC.

Fractographic Analysis

Macroscopic Appearance of the Fracture Surfaces

As shown in the fracture profiles given in Figure 2, the fracture behaviour in conditions of localized anodic dissolution is increasingly anisotropic with cold drawing. Figure 4 gives the definition of parameters that quantify the evolution with cold drawing of the macroscopic crack path. In slightly drawn steels (0 to 2) the subcritical crack

growth distance in Mode I was measured over the scanning electron micrograph, while in heavily drawn steels (3 to 6) the geometric parameters were directly measured on the fracture surface by means of a profile projector.

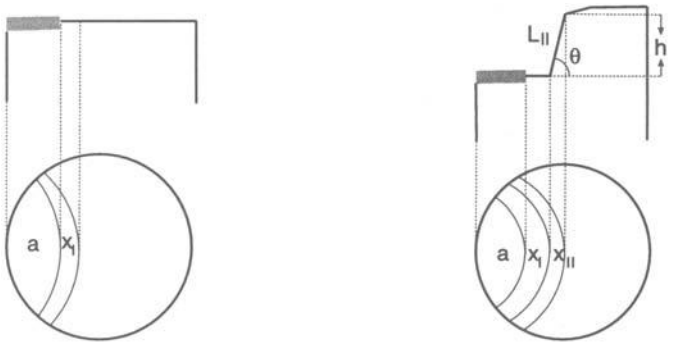


Figure 4 — *Definition of geometric parameters of the macroscopic crack path: (a) subcritical Mode I propagation distance in slightly drawn steels 0 to 2; (b) crack growth distances and deflection angle in heavily drawn steels 3 to 6; a is the fatigue crack depth.*

The evolution with cold drawing of the geometric parameters associated with the macroscopic crack path are given in Figures 5 and 6, which show an increasingly anisotropic trend, i.e., the crack deflection angle θ and the propagation step height h increase with cold drawing, whereas the Mode I propagation distance x_I increases with cold drawing in slightly drawn steels and decreases with it in heavily drawn steels. This changing trend is consistent with the evolution of failure load with cold drawing shown in Figure 1, and the longer the Mode I propagation distance the higher the fracture load in conditions of localized anodic dissolution, so that the ability of each steel to undergo Mode I growth before any crack deflection determines its load bearing capacity.

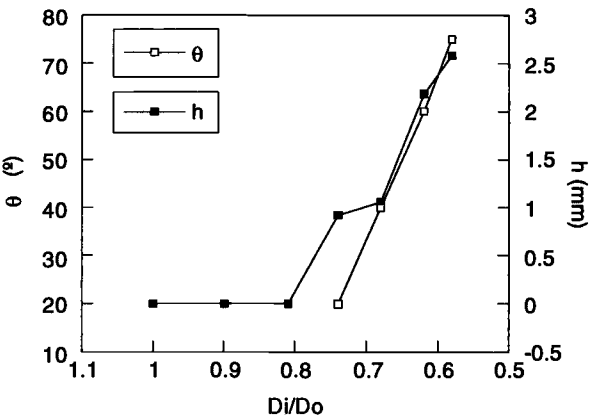


Figure 5 — *Crack deflection angle θ and propagation step height h (cf. Fig. 4).*

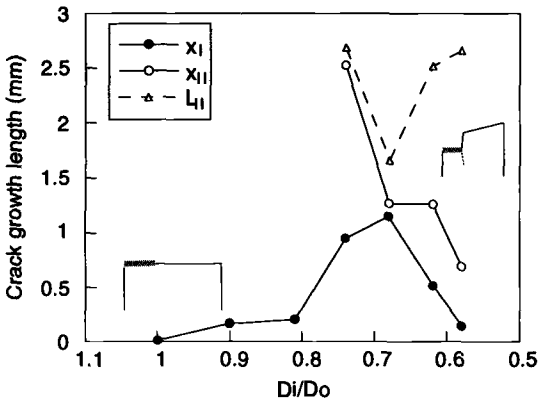


Figure 6 — *Subcritical crack propagation distances (cf. Fig. 4).*

Microscopic Modes of Fracture

A fractographic analysis by scanning electron microscopy (SEM) was carried out on the fracture surfaces to elucidate the microscopic modes of fracture. Figures 7 and 8 offer respectively the microscopic topographies for a slightly drawn steel (number 1, which has undergone only one step of cold drawing) and for a heavily drawn steel (number 5, which has suffered five steps of cold drawing).

In slightly drawn steel 1 (Fig. 7) there is a subcritical crack growth in Mode I by localized anodic dissolution (*LAD I* shown in Fig. 7b) after the fatigue precrack (Fig. 7a) and before the unstable cleavage-like propagation (Fig. 7c), which leads to catastrophic failure of mechanical type. The *LAD I* topography shows no preferential orientation and consists of a mixture of microvoids and quasi-cleavage, with evidence of dissolution and corrosion products associated with the EAC process. Some microcracks at the grain boundaries were also found.

In the heavily drawn steel 5 (Fig. 8) there is also a fatigue precrack (Fig. 8a) followed by subcritical crack growth in Mode I by localized anodic dissolution (*LAD I* shown in Fig. 8b) with no preferential orientation and the same appearance as in the case of steel 1. However, in a heavily drawn steel such as steel 5 there is a smaller number of quasi-cleavage facets than in slightly drawn steels (cf. steel 1). After the Mode I growth (Fig. 8b), crack deflection appears and the crack propagates in mixed mode with a strong Mode II component, exhibiting the microscopic fracture mode shown in Fig. 8c after a discontinuity associated with crack branching that marks the separation between the Mode I and the mixed mode crack paths. The latter is also associated with localized anodic dissolution and is called *LAD II* throughout this paper. It is clearly oriented in the direction of crack growth and consists of a mixture of isolated cleavage facets, microvoid coalescence and tearing. The frequency of appearance of cleavage facets is higher in the vicinity of the discontinuity, i.e., just after crack deflection appears, and decreases as the crack grows up to final fracture which takes place mainly by microvoid coalescence in the case of heavily drawn steels.

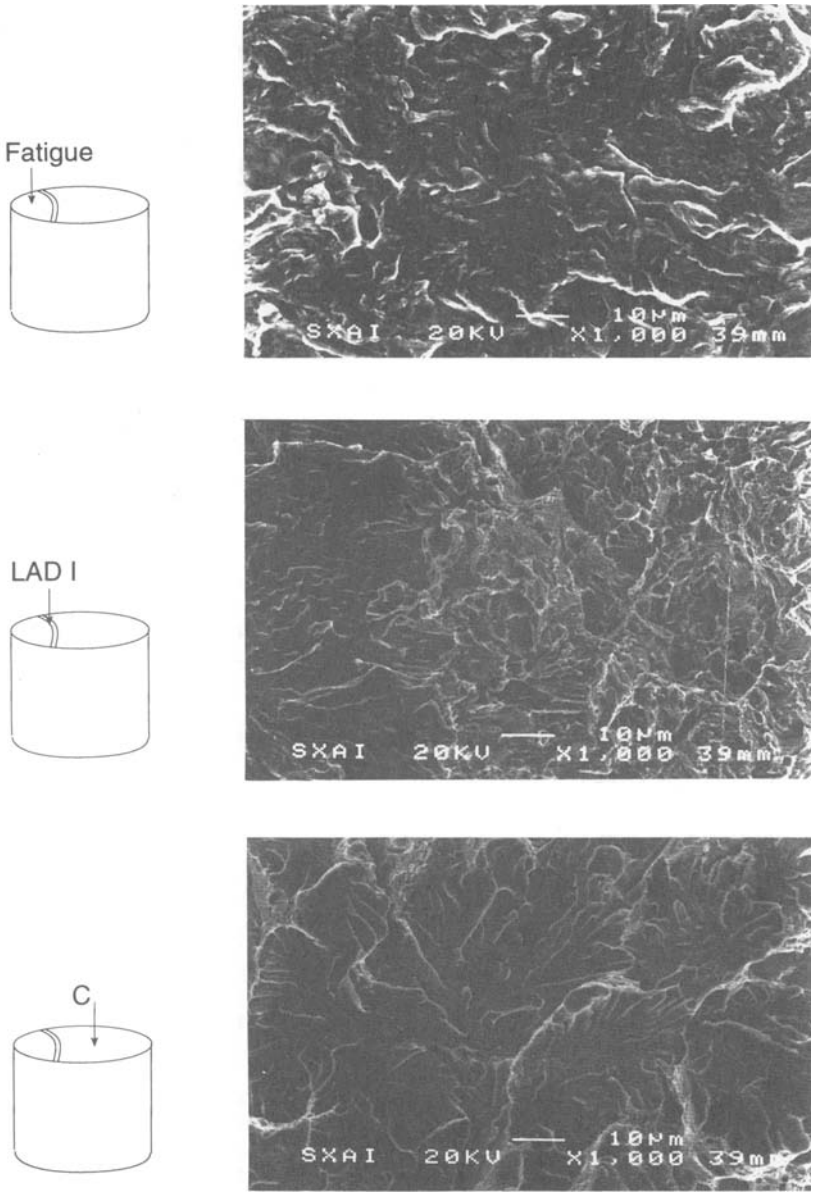


Figure 7 — *Microscopic fracture modes in slightly drawn steel 1: (a) fatigue; (b) localized anodic dissolution in Mode I; (c) cleavage propagation.*

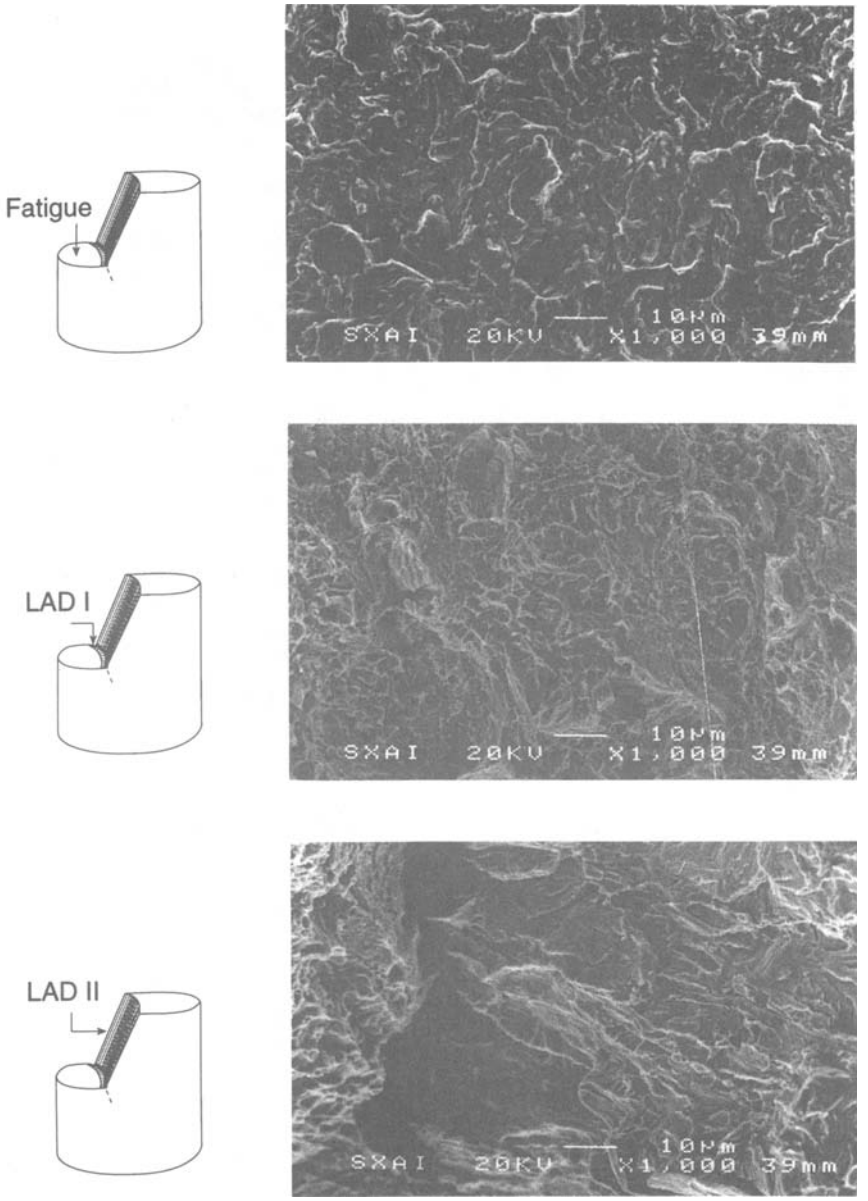


Figure 8 — *Microscopic fracture modes in heavily drawn steel 5: (a) fatigue; (b) localized anodic dissolution in Mode I; (c) localized anodic dissolution in Mode II.*

Materials Science Approach

In this section a material science approach to the phenomenon of localized anodic dissolution in cold drawn eutectoid steel for civil engineering is provided in the form of relationship between the pearlitic microstructure and the macroscopic EAC behaviour in order to provide insight into the micromechanisms of localized anodic dissolution in these high strength cold drawn steels.

Relationship between Microstructure and Macroscopic EAC Behaviour

Figure 9 plots the orientation angles of the two basic microstructural levels, namely the pearlitic colonies [*4*] and the pearlite lamellae [*6*], showing a progressive orientation of both microstructural units with cold drawing, as reflected by the evolution of their respective angles in Fig. 9: angle α between the transverse axis of the wire and the major axis of the pearlite colony modelled as an ellipsoid; angle α' between the transverse axis of the wire and the direction marked by the pearlite lamellae in the longitudinal metallographic section.

Fig. 9 also shows the variation of the macroscopic crack parameters, the deflection angle θ and the step height h, cf. Fig. 4. It is seen that the progressive microstructural orientation (at the two levels of colonies and lamellae) clearly influences the angle and height of the fracture step (increasing with the degree of cold drawing). This change in crack propagation direction can be considered the signal of the anisotropic EAC behaviour of these materials: from a certain degree of cold drawing the cracks find propagation directions with lower fracture resistance, these directions differing from the original Mode I propagation path. This suggests that the macroscopic EAC behaviour of the different steels —progressively anisotropic with cold drawing— is a direct consequence of the microstructural evolution towards an oriented arrangement.

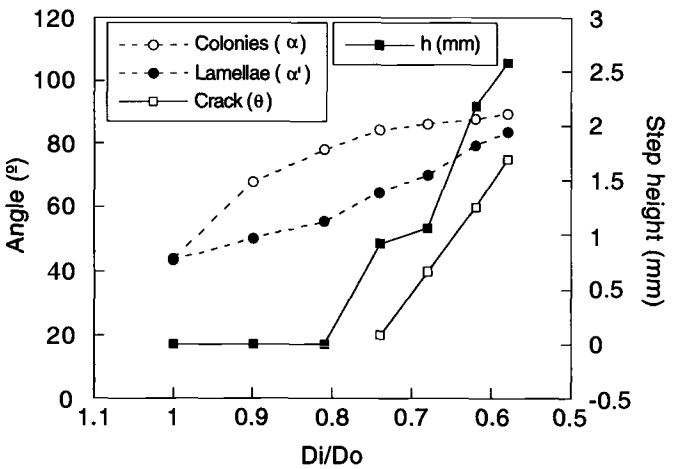


Figure 9 — *Relationship between the microstructural orientation angles α and α' (pearlite colonies and lamellae) and the macroscopic crack parameters (deflection angle θ and step height h) associated with the EAC process by localized anodic dissolution.*

Micromechanics of Localized Anodic Dissolution

In slightly drawn steels, crack advance takes place by localized anodic dissolution of the very highly stressed (and strained) material ahead of the crack tip in contact with the aggressive solution. Since these materials are isotropic or quasi-isotropic, the aforesaid dissolution is more or less homogeneous in the near-tip area, and thus it produces smooth blunting and consequently an increase of the critical stress intensity factor for failure, as discussed previously and plotted in Fig. 3.

In heavily drawn steels the crack also propagates by localized anodic dissolution, but two phases could be suggested to explain the phenomenon, as depicted in Fig. 10. In the initial stage (Fig. 10a), homogeneous dissolution takes place in the whole near-tip area producing smooth blunting which evolves towards a higher crack tip radius and even towards cornered blunting. In the final propagation stage (Fig. 10b), a more preferential dissolution develops in directions differing from the initial one so that cornered blunting is clearly enhanced. The crack is able to grow in Mode I with this very markedly cornered blunted crack tip up to certain instant at which a weaker material unit produces crack deflection as a consequence of the material anisotropy induced by cold drawing.

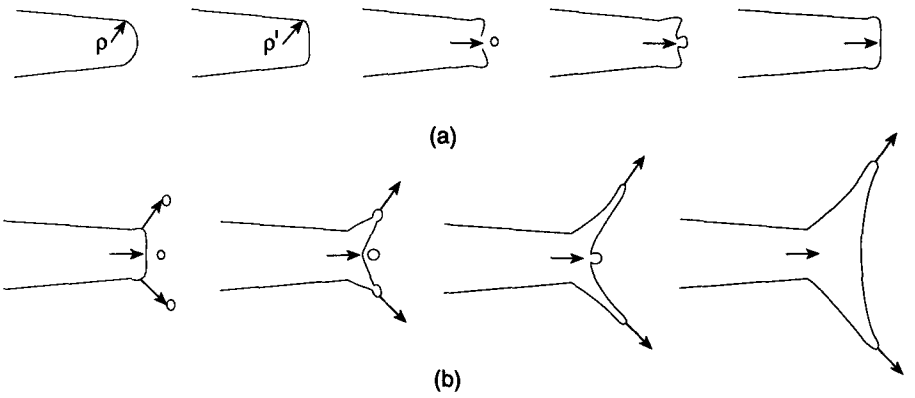


Figure 10 — *Evolution of crack tip profile growing by localized anodic dissolution in heavily drawn steels: (a) initial stage with smooth blunting by dissolution in the near-tip area; (b) propagation stage with cornered blunting enhanced by preferential dissolution in directions which differ from the initial one due to material anisotropy.*

Conclusions

Environmentally assisted cracking of cold drawn eutectoid steel for civil engineering structures was studied in the anodic regime of cracking associated with localized anodic dissolution. The degree of cold drawing was treated as a fundamental variable in the analysis, since progressively drawn steel wires were considered.

The resistance of the steel to environmentally assisted cracking by localized anodic dissolution increases by cold drawing. This drawing-induced improvement is especially important in the matter of time to failure in the corrosive environment, although certain increase of failure load could also be detected.

A fracture mechanics approach to the phenomenon was formulated in terms of critical stress intensity factor K_{IEAC} at the transition from the environmentally assisted cracking subcritical regime to the final mechanical fracture, showing that the factor K_{IEAC} increases with cold drawing.

Crack tip blunting improves the resistance to the steels to environmentally assisted cracking, so that the transition stress intensity factor K_{IEAC} is even higher than the fracture toughness of the material in air, at least in slightly drawn steels, which behave in isotropic manner.

The fractographic analysis demonstrated that the steels exhibit a progressively anisotropic behaviour as the degree of cold drawing increases, with crack deflection and mixed mode propagation in heavily drawn steels as a consequence of the very markedly oriented pearlitic microstructure.

In slightly drawn steels, the microscopic fracture modes resemble localized anodic dissolution in the subcritical fractured area associated with environmentally assisted cracking, the topography consisting of a mixture of microvoids and quasi-cleavage with no preferential orientation.

In heavily drawn steels, the first Mode I propagation is similar to that of slightly drawn steels. After this, crack deflection appears and the microscopic fracture mode becomes clearly oriented in the direction of crack growth and consists of a mixture of isolated cleavage facets, microvoid coalescence and tearing.

There is a material science relationship between microstructure and macroscopic fracture behaviour of the steel in conditions of environmentally assisted cracking, since the progressive microstructural orientation with cold drawing causes the increasingly anisotropic behaviour.

While in slightly drawn steels the localized anodic dissolution is homogeneous producing smooth blunting, in heavily drawn steels there is a preferential dissolution that develops in directions differing from the initial one, favouring cornered blunting over smooth blunting and finally crack deflection.

Acknowledgments

The financial support of this work by the Spanish CICYT (Grant MAT97-0442) and *Xunta de Galicia* (Grant XUGA 11802B97) is gratefully acknowledged. In addition, the authors wish to express their gratitude to EMESA TREFILERIA S.A. (La Coruña, Spain) for providing the steel used in the experimental program.

References

[1] Embury, J. D. and Fisher, R. M., "The Structure and Properties of Drawn Pearlite," *Acta Metallurgica*, Vol. 14, 1966, pp. 147-159.

[2] Langford, G., "A Study of the Deformation of Patented Steel Wire," *Metallurgical Transactions*, Vol. 1, 1970, pp. 465-477.

[3] Toribio, J. and Ovejero, E., "Microstructure Evolution in a Pearlitic Steel Subjected to Progressive Plastic Deformation," *Materials Science and Engineering*, Vol. A234-236, 1997, pp. 579-582.

[4] Toribio, J. and Ovejero, E., "Microstructure Orientation in a Pearlitic Steel Subjected to Progressive Plastic Deformation," *Journal of Materials Science Letters*, Vol. 17, 1998, pp. 1037-1040.

[5] Toribio, J. and Ovejero, E., "Effect of Cumulative Cold Drawing on the Pearlite Interlamellar Spacing in Eutectoid Steel," *Scripta Materialia*, Vol. 39, 1998, pp. 323-328.

[6] Toribio, J. and Ovejero, E., "Effect of Cold Drawing on Microstructure and Corrosion Performance of High-Strength Steel," *Mechanics of Time-Dependent Materials*, Vol. 1, 1998, pp. 307-319.

[7] Astiz, M. A., Valiente, A., Elices M. and Bui, H. D., "Anisotropic Fracture Behaviour of Prestressing Steels," *Life Assessment of Dynamically Loaded Materials and Structures-ECF5* , L. O. Faria, Ed., EMAS, West Midlands, 1984, pp. 385-393.

[8] Toribio, J. and Toledano, M., "Fatigue Crack Propagation in Cold Drawn Wires for Prestressing Concrete,"*Structural Faults and Repair 97: Vol.2* , M.C. Forde, Ed., Engineering Technics Press, Edinburgh, 1997, pp. 493-499.

[9] Toribio, J., Ovejero, E. and Toledano, M., "Microstructural Bases of Anisotropic Fracture Behaviour of Heavily Drawn Steel," *International Journal of Fracture*, Vol. 87, 1997, pp. L83-L88.

[10] Cherry, B. W. and Price, S. M., "Pitting, Crevice and Stress Corrosion Cracking Studies of Cold Drawn Eutectoid Steels," *Corrosion Science*, Vol. 20, 1980, pp. 1163-1184.

[11] Langstaff, D. C., Meyrick, G. and Hirth, J. P, "Hydrogen Induced Delayed Failure of High Strength Alloy Steel Wires," *Corrosion*, Vol. 37, 1981, pp. 429-437.

[12] Parkins, R. N., Elices, M., Sánchez-Gálvez, V. and Caballero, L., "Environment Sensitive Cracking of Pre-stressing Steels," *Corrosion Science*, Vol. 22, 1982, pp. 379-405.

[13] Sarafianos, N., "Environmentally Assisted Stress-Corrosion Cracking of High-Strength Ccarbon Steel Patented Wire," *Journal of Materials Science Letters* , Vol. 8, 1989, pp. 1486-1488.

[14] Price, S. M., Warden, P. G., Chia, T. S., Scarlett, N. V. Y. and Mahoney, J. H., "The Role of Notches in the Hydrogen-Assisted Cracking of Steel Prestressing Tendons," *Materials Forum*, Vol. 16, 1992, pp. 245-251.

[15] Toribio, J. and Lancha, A. M, "Effect of Cold Drawing on Environmentally Assisted Cracking of Cold Drawn Steel," *Journal of Materials Science*, Vol. 31, 1996, pp. 6015-6024.

[16] Valiente, A., *Criterios de Fractura para Alambres*. Ph. D Thesis, Polytechnic University of Madrid, Spain, 1980.

[17] Handerhan, K. J. and Garrison Jr., W. M., "A Study of Crack Tip Blunting and the Influence of Blunting Behavior on the Fracture Toughness of Ultra High Strength Steels," *Acta Metallurgica et Materialia*, Vol. 40, 1992, pp. 1337-1355.

[18] Ritchie, R. O. and Horn, R. M., "Further Considerations on the Inconsistency in Toughness Evaluation of AISI4340 Steel Austenitized at Increasing Temperatures," *Metallurgical Transactions*, Vol. 9A, 1978, pp. 331-341.

[19] Creager, M. and Paris, P. C., "Elastic Field Equations for Blunt Cracks with Reference to Stress Corrosion Cracking," *International Journal of Fracture Mechanics*, Vol. 3, 1967, pp. 247-252.

[20] Chu, W. Y., Hsiao, C. M. and Li, S. Q., "A New Engineering Fracture Toughness Parameter $K_{ISCC}(\rho)$," *Scripta Metallurgica* , Vol. 13, 1979, pp. 1057-1062.

[21] Ray, K. K. and Rao, G. R., "A New Test Principle for Determining Threshold Stress Intensity Factor K_{IEAC} in Environmentally Assisted Cracking," *International Journal of Fracture*, Vol. 61, 1993, pp. R69-R75.

George A. Andersen[1]

Premature Failures of Copper Alloy Valves and Fittings in the New York City Water Supply System

Reference: Andersen, G. A., **"Premature Failures of Copper Alloy Valves and Fittings in the New York City Water Supply System,"** *Environmentally Assisted Cracking: Predictive Methods for Risk Assessment and Evaluation of Materials, Equipment, and Structures, ASTM STP 1401,* R. D. Kane, Ed., American Society for Testing and Materials, West Conshohocken, PA, 2000.

Abstract: Copper alloys are used in various water main components in The New York City Water Supply System. Three copper alloys have been found to fail prematurely. Two manganese bronzes, Copper Development Association (CDA) alloys C86500 and C86300, have previously [*1*] been found to fail in valves and shaft caps as well as nut fasteners in transgranular and intergranular stress corrosion cracking (SCC) modes, respectively.

A valve stem, made of alloy C86500, has just recently been found to fail what appears to be from SCC, but in a combination of transgranular and intergranular modes. Tapping goose necks, and a pressure regular stem made of CDA alloy C83600, have been found to fail prematurely. Failure analyses of the goose necks and the pressure valve stem have been performed; they appear to have failed from SCC with the lead reacting with water. The lead may create an environmental health problem by being absorbed by the potable water and supplied to the buildings they are serving. To corroborate the aforementioned failure analyses, specimens made of alloy C86500 and C83600 were machined from a valve stem and a goose neck respectively and tested in a laboratory with simulated environments. This paper presents the case histories of the two SCC type failures and what action is being taken to remedy these problems.

Keywords : Stress-corrosion cracking, high-strength manganese bronze castings, leaded red brass castings, gate valves, pressure regulated valves, goose necks, scanning electron microscope fractograph

The City of New York supplies 1.5 billion gallons of water per day, gravity fed from three upland surface supplies. Two water tunnels are presently in operation while a third one is under construction. There are 37 distribution shafts throughout the city operated by the

[1]Metallurgical administrative engineer, City of New York, Bureau of Water and Sewer Operations, Department of Environmental Protection, 59-17 Junction Boulevard, Corona, New York 11368.

Copyright© 2000 by ASTM International www.astm.org

Maintenance Division of Field Operations for the Bureau of Water and Sewer Operations.

The Quality Assurance and Metallurgical Engineering Division has performed failure analysis of waterworks equipment for the last 25 years. One (1) 63.5 mm (2½-inch) diameter C86500 copper alloy stem from a 609.6 mm (24-inch) diameter gate valve failed in a spiral circumferential manner after 10 years of service; see (Figure 1). Four (4) C83600 leaded red brass goose-neck taps failed in service; one (1) 19.05 mm (3/4-inch) diameter goose-neck failed after 1½ years of service; see (Figure 2). Two other 19.05 mm (3/4-inch) diameter goose-necks were found to have failed in a similar manner, one after nine (9) months and the other after six(6) weeks. A 38.1 mm (1½-inch) diameter goose neck failed after six(6) months of service; see (Figure 3). One 762 mm (30-inch) diameter pressure regular valve with a 101.6 mm (4-inch) diameter (57.15 mm (2¼-inch) hollow) stem, failed after 10 months of service.

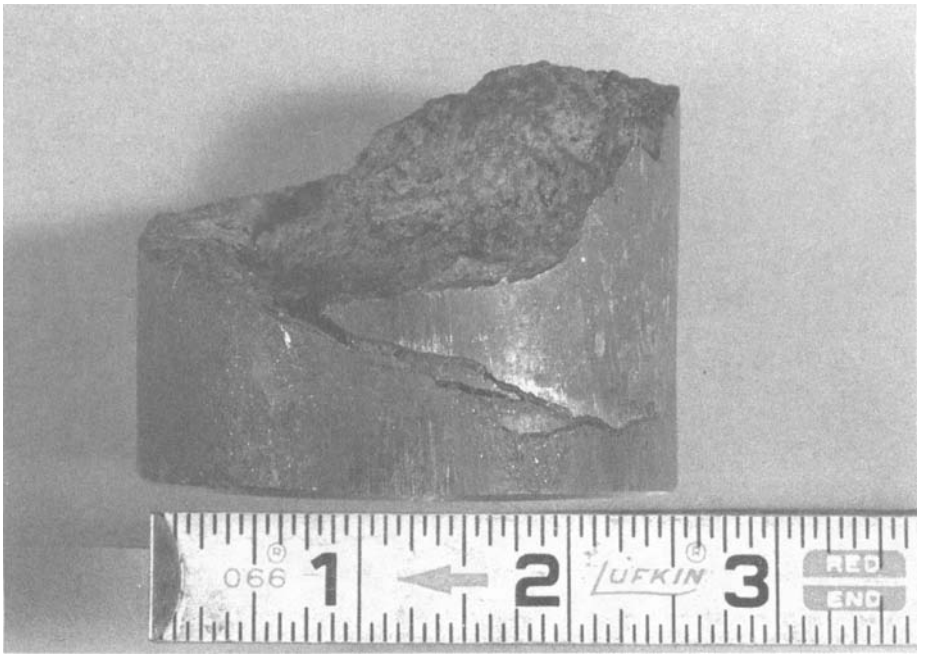


FIG. 1 - *Failed section of a 63.5 mm (2½-inch) diameter valve stem of Alloy C86500.*

Metallographic examination of the valve stem reveals both intergranular and transgranular multiple branched cracking, which is characteristic of SCC in high-zinc copper alloys; see (Figures 4 and 5). The goose-neck taps made of leaded red brass, alloy C83600, failed when a crack resulted in the water perforating the goose-neck. This caused underground reflective sandblasting as shown by the shiny regions in both the goose neck and the connecting nut in (Figures 2 and 3). Metallographic examination of both size goose-necks reveal a hypo-monotectic microstructure with a lead rich secondary phase in a copper rich matrix; the cracking appears to follow the grain boundaries through the voided locations of the lead-rich phase; see (Figures 6 and 7). Additional metallography was performed using an ElectroScan Environmental Scanning Electron Microscope (ESEM). Figures 8 and 9 which show more details on the crack path mode, also show that the secondary phase (predominantly lead) is the sacrificial phase being more anodic under tensile stress.

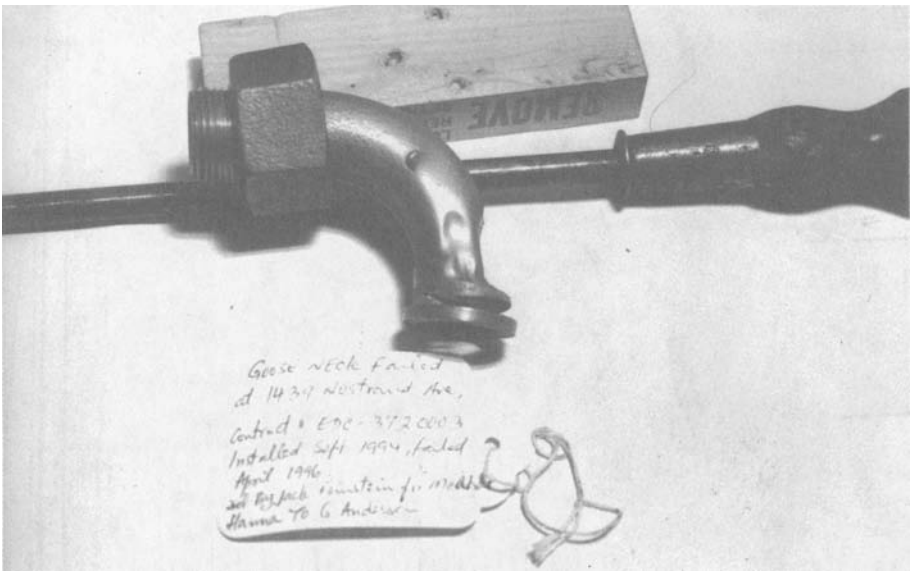


FIG. 2 - *Failed 19.05 mm (3/4-inch) goose neck tap of Alloy C83600.*

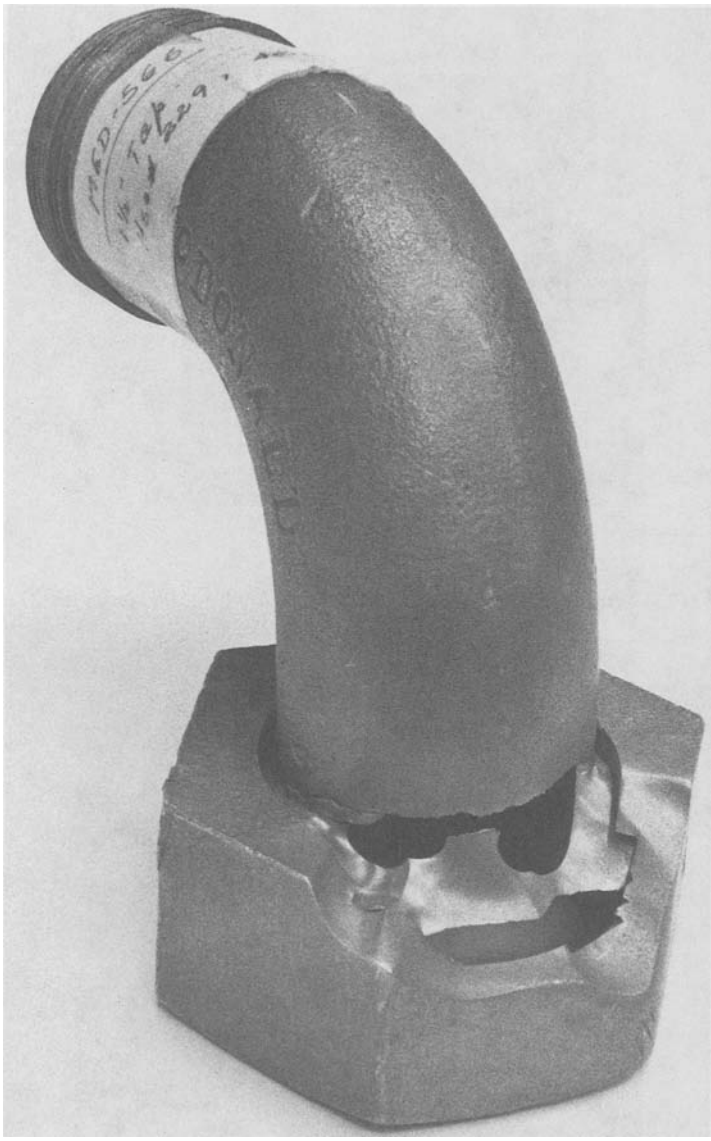


FIG. 3 - *Failed 38.1 mm (1½ -inch) diameter goose neck tap of Alloy C83600.*

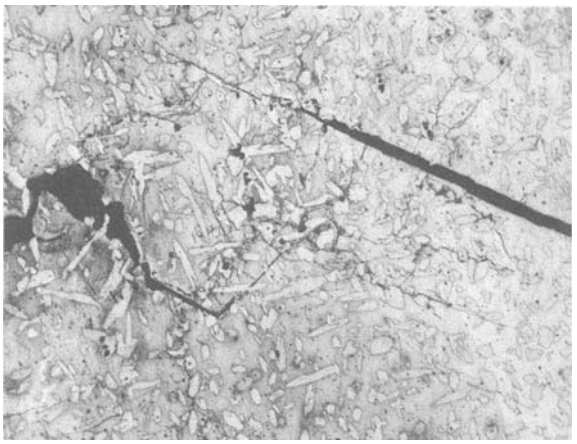


FIG. 4 - *Intergranular cracking at tip of Alloy C86500 stem (100X).*

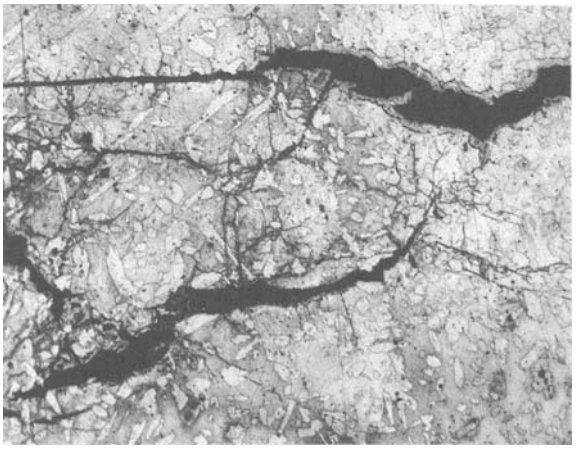


FIG. 5 - *Branched transgranular and intergranular cracking characteristic of SCC failures (100X).*

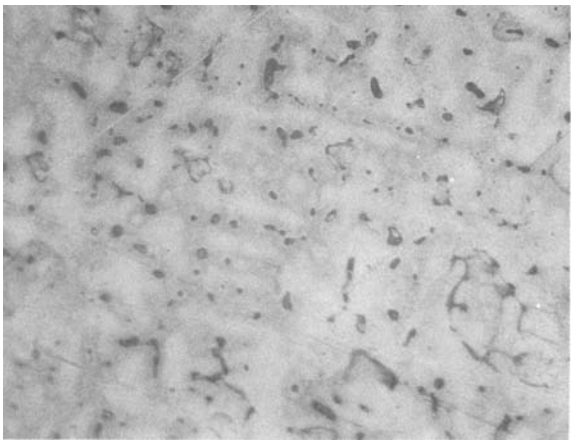


FIG. 6 - *Monotectic microstructure with secondary lead-rich phase in Alloy C83600 (200X).*

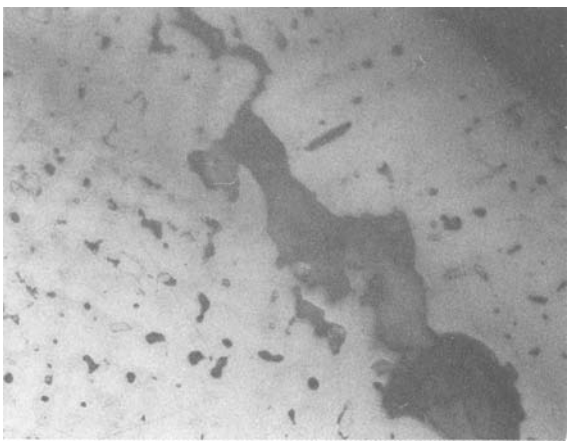


FIG. 7 - *SCC mode of failure through lead-rich phase (200X).*

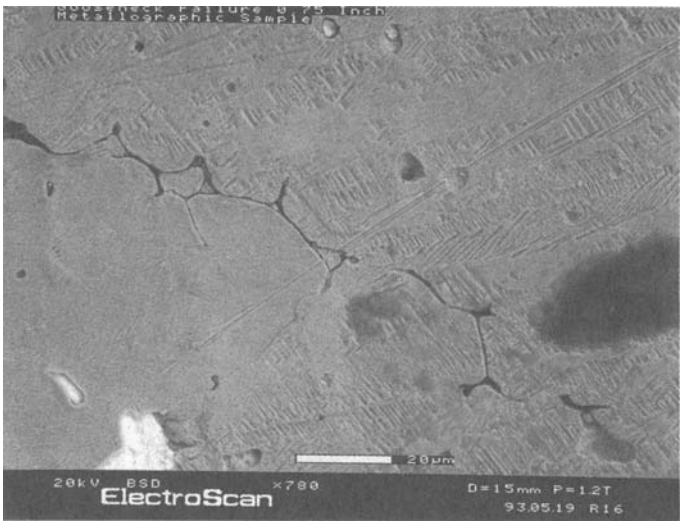


FIG. 8 - *ESEM shows intergranular cracking in Alloy C83600.*

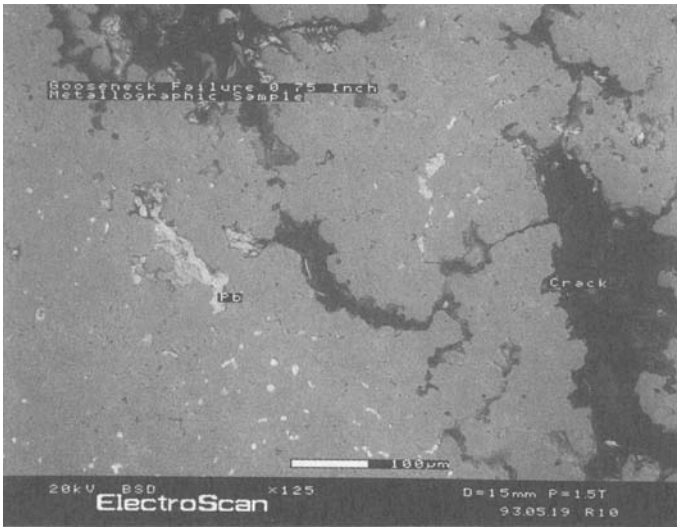


FIG. 9 - *ESEM shows cracking through depleted lead-rich phase.*

ESEM fractography was performed on fracture surfaces of both goose necks, but away from areas which received reflective sandblasting. (Figures 10 through 13) are ESEM fractographs, which indicate that the mode of fracture was dimpled rupture; however, voids were present in the same configurations and sizes as the secondary lead-rich phases. The stress from the connecting nuts put the goose necks into tension right at the origin of failure of all of them. Copper, being more noble than the lead, may have set up a galvanic cell where the service stresses brought about by the torquing of the connecting nuts caused SCC of the goose necks. This type of SCC phenomenon has been known to occur on other alloys where the conditions of a sacrificial secondary phase have been present. The cracking environment is now being shown to be tap water. Please note: this alloy is specified in our N.Y.C. Standards for goose-necks as well as American Water Works Association (AWWA) C-800 Standard for "Underground Service Line Valves and Fittings." The weak sections of the material appear to have been lead depleted. These failures are of a SCC mode with lead reacting with water; the lead does appear to create an environmental health problem by being absorbed by the water and supplied to the connected buildings.

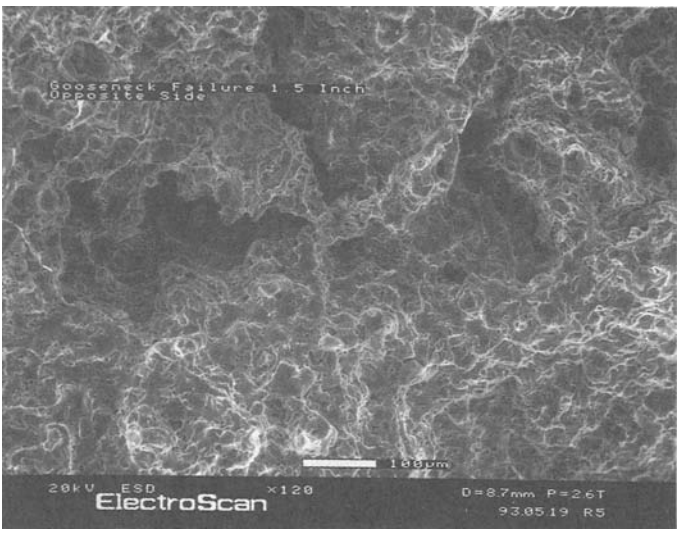


FIG. 10 - *ESEM fractograph reveals dimpled rupture with cracking through lead phase voids of 38.1 mm (1½ -inch) diameter goose neck.*

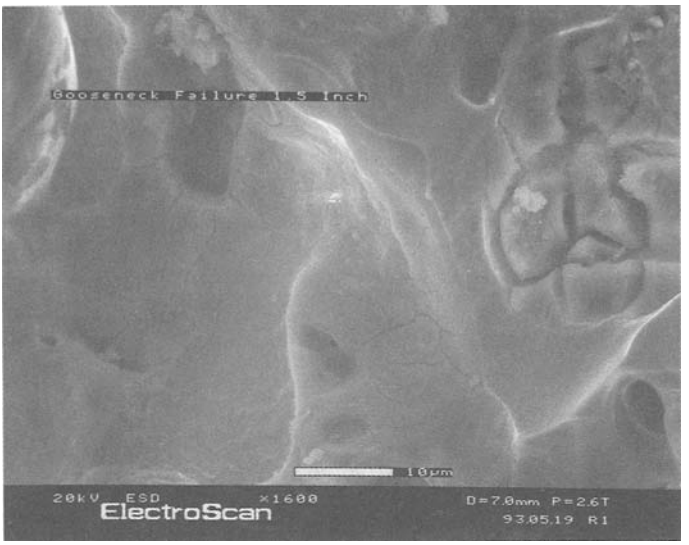


FIG. 11 - *ESEM shows secondary brittle cracking at higher magnification of FIG. 10.*

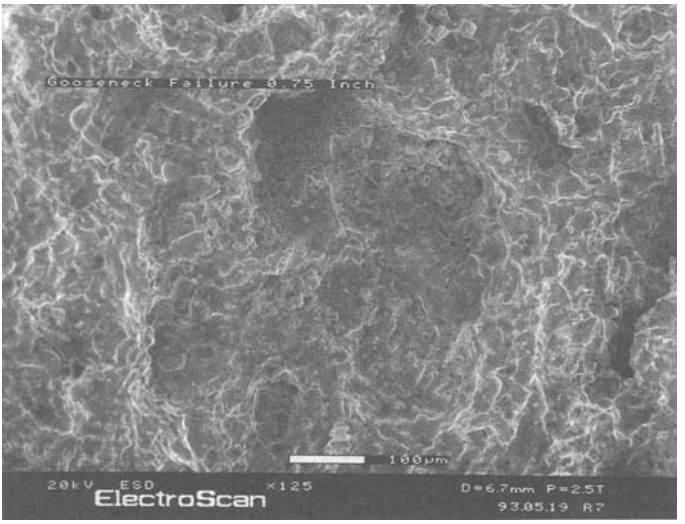


FIG. 12 - *ESEM fractograph of 3/4-inch goose neck also shows dimpled mode with lead void cracking.*

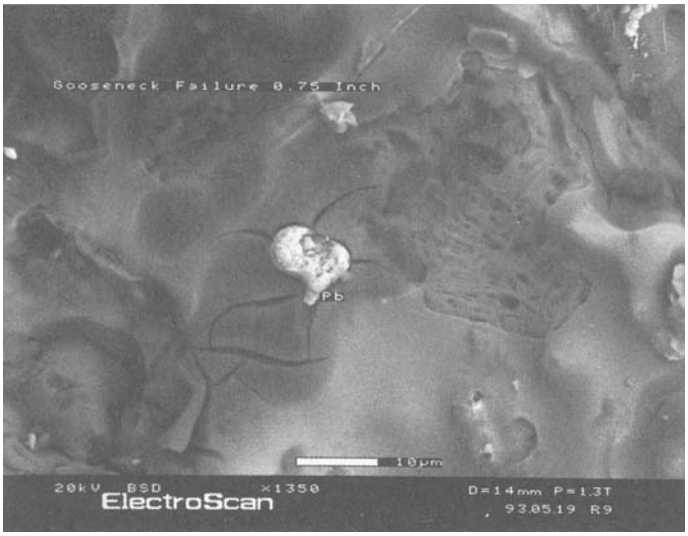


FIG. 13 - *ESEM fractograph shows cracks emanating from lead-rich phase.*

SCC of Specimens in Laboratory Tests

To verify the failure analyses of the stem and the goose-neck taps, specimens of alloys C86500 and C83600 were machined from the subject fittings and tested in a metallurgical laboratory under simulated service environments. Alloy C86500 is a manganese bronze and C86300 is a leaded red brass. All specimens tested were 12.7 mm (½-inch) thick modified compact wedge loaded with a bolt; see (Figure 14). This complies with MC(Wb) of the ASTM Standard Terminology Related to Fracture Testing (E 616). Specimens were not pre-cracked. Strain was introduced by a stainless steel bolt torqued to approximately 1224 N.m (75inch-Pound) and 652.8 N.m (40inch-Pound) on the C86500 and C83600 alloy specimens, respectively. It was determined that this amount of torque brought the specimen wedge tips near its yield strength. Control specimens were loaded and left on an office desk. Some specimens were immersed in jars of stagnant tap water, some in flowing tap water and others suspended in jars above the water to simulate water vapor exposure.

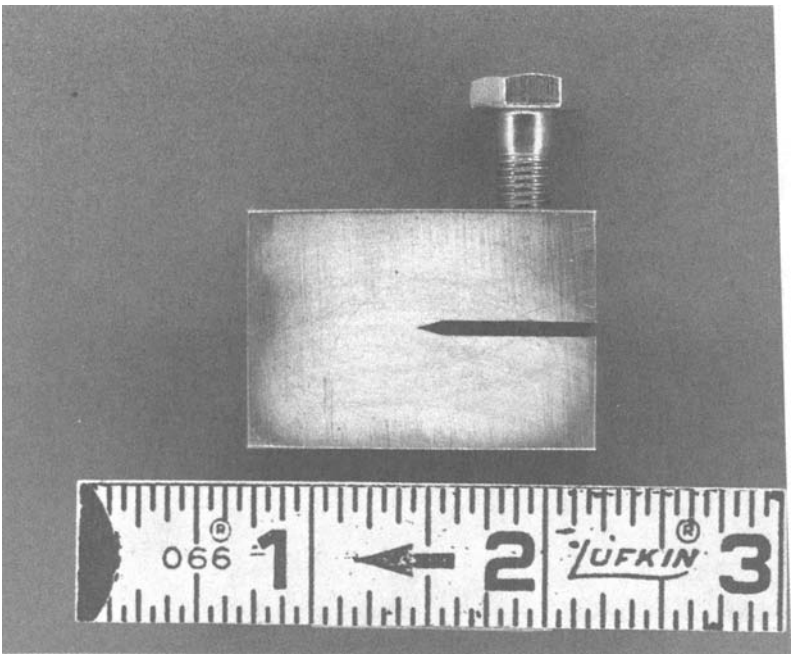


FIG. 14 - *Modified wedge open-loading SCC specimen; 12.7 mm (½-inch) thick.*

Results and Discussion

The chemical analysis of the alloys studied are shown in (Table 1). The results of the laboratory tests are shown in (Table 2). The manganese-bronze specimens, which were torqued to about 90% of their yield strength, failed after two(2) days in fresh flowing tap water and after three(3) days in stagnant water. The manganese bronze alloy specimens failed in fresh water vapor and stagnant water vapor after twelve(12) and nineteen(19) days, respectively. Metallography of a cracked specimen showed the same mode of SCC as the service failure of the stem; see (Figure 15).

Table 2 also shows that alloy C83600 specimens failed in fresh tap water and stagnant water after ten(10) and fifteen(15) days, respectively. These specimens were also torqued to approximately 90% of its alloy's yield strength. Specimens subjected to humid environments have not cracked after one year. Metallography of a cracked specimen showed the same mode of SCC as the service failures of the goose neck taps; see Figure 16. The test in stagnant water were repeated on two separate samples; both were also loaded at 90% yield strength. The chemical analysis of the water, before and after the tests, is shown in (Table 3). The results were cracking after 16 days. Table 3 shows the lead content increasing at five times the rate of copper after cracking (based on the 20:1 volume ratio of copper to lead), which corroborates the metallographic results. Metallography of the failed pressure regulator stem showed that it also cracked in the SCC mode; see (Figure 17).

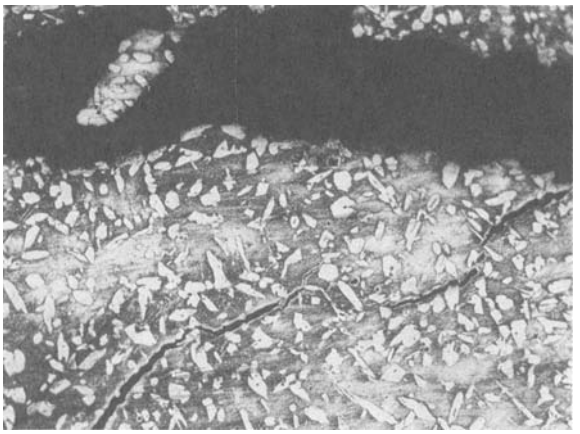


FIG. 15 - *Test sample of Alloy C86500 stem failed from SCC (100X).*

Table 1 - *Chemical composition of service failures*

CDA Alloy	Service Part	Cu	Sn	Zn	Fe	Al	Mn	Pb
C86500	Valve Stem	57.67	0.39	39.11	1.36	1.48	0.12	---
C83600	Goose Neck	84.99	4.83	5.02	---	---	---	5.16

Table 2 - *Results of laboratory SCC tests*

	Time to Cracking in Days	
Alloy/Test Environment	Liquid	Vapor
C86500 / Fresh tap water	2	12
C86500 / Stagnant tap water	3	19
C83600 / Fresh tap water	10	-----
C83600 / Stagnant tap water	15	-----

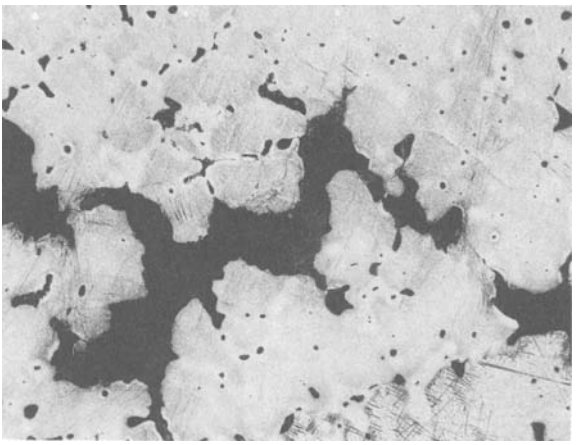


FIG.16-*Tests sample of Alloy C83600 goose neck failed from SCC(100X).*

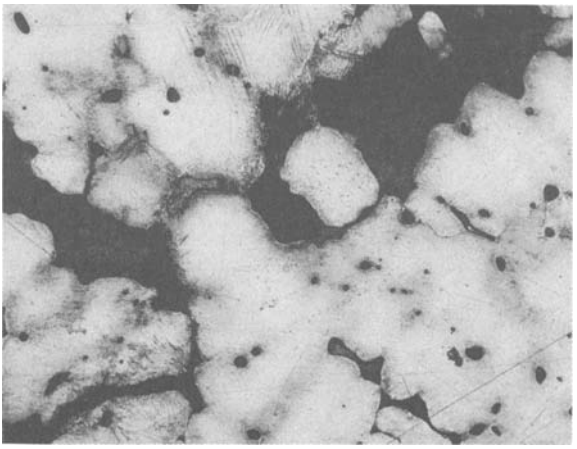


FIG. 17 - *SCC Mode of failure of C83600 Pressure regulator valve stem through leaded depleted phase and along grain boundaries (100X)*

Table 3 - *Water analysis of SCC tests*

Lab ID	Sample Description [1]	Cu mg/L	Zn mg/L	Pb mg/L
1	Tap water blank (contained in glass beaker)	0.031	0.002	<0.001
2	String blank	0.030	<0.002	<0.001
3	# 3 - Alloy C83600 (Figure 14)	0.556	0.093	0.134
4	# 4 - Alloy C83600 (Figure 14)	0.615	0.107	0.109
5	Tap water blank (contained in plastic bottle)	0.027	<0.002	<0.001

[1]All samples were acidified with nitric acid to pH < 2 and held for more than 16 hours before analysis.

Conclusions

Different modes of SCC have been found to be the cause of failures of both a manganese-bronze valve stem and a leaded red brass goose neck taps and pressure regulator valve stem.

To avoid further SCC failures, the manganese bronze stems are being replaced with silicon bronze stems, CDA alloy C87600. Valve bodies and shaft caps, also made of manganese-bronze, have been replaced with valves made of various austenitic stainless steels.

A substitute for leaded red brass goose neck taps is currently being worked on, since the federal government [*2*] has an 8% limit on the lead content of copper alloys used in contact with potable water. The replacement of leaded red brass for goose neck tapping fittings (Corporation Stops) with an alloy low in lead and not prone to SCC will be beneficial both to engineering design and our health environment. The pressure regulator stem failure is presently being evaluated for alloy or wall thickness design change. This is the first time leaded red brass, also known as ounce metal, composition bronze and 85-55-5, has been found to fail from SCC in a tap water environment [*3*].

Acknowledgments

The author wishes to thank T. Sahansra for assisting in the failure analysis. Thanks also go to C. Lercara for supervising the laboratory research test program with assistance from Z. Azam and M. Knight, high school students assigned to this City Agency by The New York Academy of Sciences. Assistance was also provided by Venkatesan Kothandaraman and Monica Buitrago in both metallography and water quality environmental engineering. Thanks are also in order to M.Krysko, Deputy Director., D.Greeley, Deputy Commissioner and J.Miele Sr., Commissioner of the New York City Department of Environmental Protection.

References

[1] Andersen, G.A. and Donnellan, P.B., "Stress-Corrosion Cracking of Mn-Bronze Castings and Test Specimens in New York City Water Distribution Shafts" *Corrosion Testing and Evaluation: Silver Anniversary Volume, ASTM STP 1000*, R. Baboian and S.W. Dean, Eds., American Society for Testing and Materials, Philadelphia, 1990, pp. 138-150.

[2] Pontius, F.W., "New Horizons in Federal Regulation," Journal AWWA March 1998.

[3] Jones, R. H., "Stress Corrosion Cracking," ASM International, Materials Park, Ohio 1992, Vol. I, p212.

W. Zheng,[1] R. Sutherby,[2] R. W. Revie,[1] W. R. Tyson,[1] and G. Shen[1]

Stress Corrosion Cracking of Linepipe Steels in Near-Neutral pH Environment: A Review of the Effects of Stress

Reference: Zheng, W., Sutherby, R., Revie, R. W., Tyson, W. R., and Shen, G., **"Stress Corrosion Cracking of Linepipe Steels in Near-Neutral pH Environment: A Review of the Effects of Stress,"** *Environmentally Assisted Cracking: Predictive Methods for Risk Assessment and Evaluation of Materials, Equipment, and Structures, ASTM STP 1401,* R. D. Kane, Ed., American Society for Testing and Materials, West Conshohocken, PA, 2000.

Abstract: Stress corrosion cracking (SCC), a form of environment-assisted cracking, has caused 24 major pipeline failures in the Canadian oil and gas pipeline system. The role of stress in the SCC of linepipe steels in near-neutral pH environment, as in other SCC systems, is complex. In this paper, the effects of stress on the development of both axial cracking and circumferential cracking are reviewed. The long-term beneficial effect of compressive stress introduced by hydrostatic testing is also discussed.

Keywords: Pipeline SCC, local stress, nominal stress, pressure fluctuation, time rate of J, axial cracking, circumferential cracking, ground movement, low-temperature creep, hydrogen, hydrostatic test, crack retardation, compressive residual stress.

The transgranular stress corrosion cracking in pipelines discovered in the mid-1980s on the Canadian system is known to be associated with a dilute ground water chemistry [*1*], which is very different from the well-known carbonate-bicarbonate solution responsible for the intergranular form of cracking of line pipe steels first reported four decades ago [*2*]. As a result of a nation-wide public hearing held by the National Energy Board (NEB) of Canada [*1*], much attention has been given to the SCC on the Canadian pipeline system. Understanding of this problem has also been facilitated by laboratory research, carried out in Canada and elsewhere, in the past several years. However, a great deal remains unknown or uncertain in terms of the cracking mechanism(s) and the roles played by the key factors such as stress and steel metallurgy.

The available evidence from laboratory work [*3-9*] suggests that stress fluctuation,

[1]Research scientists, CANMET/Materials Technology Laboratory, 568 Booth St. Ottawa, Ontario, Canada, K1A 0G1.

[2]Senior integrity specialist, TransCanada Transmission, 801 - Seventh Avenue S, Calgary, Alberta, Canada, T2P 3P7.

©Minister of Natural Resources Canada, 2000.

Copyright© 2000 by ASTM International www.astm.org

even minor, is necessary for crack initiation and growth. The source of stress can be both operational, resulting from the internal pipeline pressure, and secondary resulting, for example, from localized bending or axial tension in the pipe, as in the case of circumferential SCC. In fact, the level of secondary stress can be dominant and result in cracks at high angle to the axis of the pipe.

This paper is a review of recent results related to the effects of stress and stress fluctuation on the development of axial and circumferential SCC as well as the beneficial effects of residual stress produced by high-pressure hydrostatic testing.

The Effects of Stress on the Severity of Axial SCC

The great majority of SCC failures in the Canadian system occurred as axial cracking, driven by the hoop stress caused by the operating pressure of oil or gas pipelines. In the NEB Report on Pipeline SCC [*1*], it is shown, in Figure 1, that SCC colonies could form on pipe sections where the operating stress was as low as 64% of the specified minimum yield stress (SMYS). It should be pointed out that the operating pressure for this particular pipeline is generally quite stable, with most of the pressure fluctuation events being associated with R-values of 0.9 or greater (R=minimum pressure / maximum pressure) and only infrequent excursions to lower R-values. For such loading conditions (i.e., maximum stress 64% SMYS and R=0.9), it has been difficult to initiate stress corrosion cracks under laboratory test conditions. In fact, it was reported that even for a lower R-value of 0.85, cracks could only be grown in the laboratory at a stress level of 72% SMYS or higher [*10*].

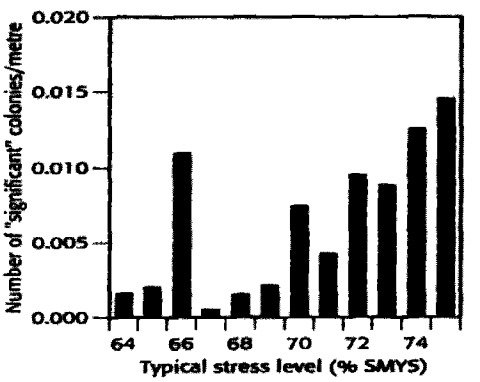


Figure 1 Variation of SCC severity as a function of operating stress for one gas pipeline [*1*].

One can list a number of reasons for this discrepancy. The principal ones related to stress would include the stress concentration effect of pipe surface features such as welds and corrosion pits and the presence of residual stress. Either of these effects raises the net

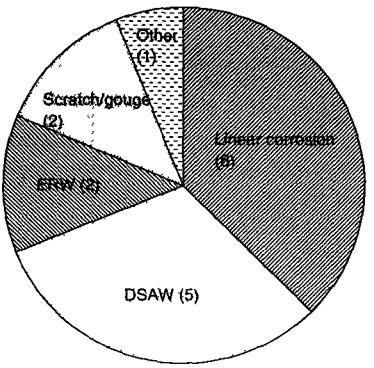


Figure 2 Distribution of axial SCC ruptures as a function of pipe surface features.

section stresses at crack sites higher than the nominal operational stress. Figure 2 shows the distribution of the major axial SCC failures among various pipe surface features. Eleven of the sixteen axial SCC failures are associated with stress raisers such as corrosion grooves (so called 'linear corrosion') and the toe of double-submerged arc welds (DSAW).

In the case of DSAW, finite element calculations revealed that the stress level in the vicinity of the weld toe can be significantly higher than that in the pipe body. Figure 3 shows the stress profile for a typical seam weld geometry. Only half of the pipe wall thickness is indicated in the figure, as the weld was assumed to be symmetrical across the mid-wall line. Under an applied stress of 340 MPa (77% of SMYS for the pipe in question), there is a zone a few mm width in which the actual local stress is close to the

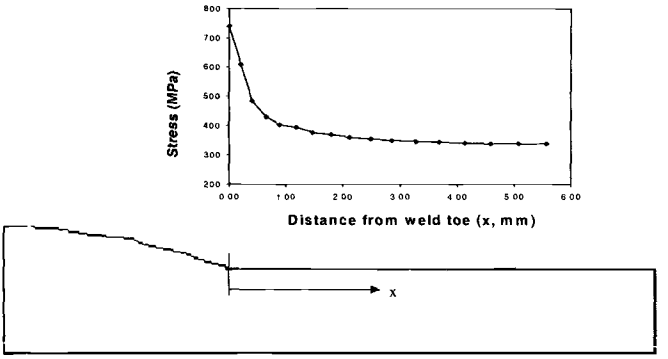


Figure 3 Results of finite element calculation of stress levels in the vicinity of a weld.

SMYS of the base steel. At the very toe, the stress is above the actual yield point of the material.

However, many SCC colonies were found on smooth pipe surfaces, away from weld and corrosion defects. For these sites, the presence of surface residual stress could cause the net local stress to be greater than the nominal value. In one series of measurements of residual stress in pipes retrieved from service, tensile residual stresses in the range of 20% SMYS were often found to exist in the pipe wall up to a depth of about 1 mm [*11*], and the level of residual stress varied as a function of distance from the pipe surface. Thus if the nominal operating stress is at 72% of SMYS, the total net stress could be at 92% SMYS in the metal at this depth under the surface; such a stress level is conceivably high enough for crack initiation for many SCC systems.

When assessing the potential SCC susceptibility of a pipeline, therefore, it would be useful to take into consideration the likely secondary stresses acting on the pipe. In the vicinity of 'stress raisers' on the pipe surface, the maximum local stress can be considerably higher than the bulk stress in the pipe body.

Effects of Stress Fluctuation

As in the case of pipeline SCC in carbonate-bicarbonate environment, the severity of transgranular SCC is not only affected by stress level *per se*, but also the degree of stress fluctuation. In a CANMET study on crack initiation [*6*], detectable cracks could be produced when stress was applied in a cyclic wave with a maximum of 90% SMYS and R=0.6. More severe cracking could be produced when the R-value was reduced to 0.4, under the same environmental conditions, maximum stress, load frequency and wave form. While these R-values are not reflective of many gas transmission pipelines, the results do show a trend of increasing cracking severity with decreasing R-values.

Laboratory results on the growth of deep SCC cracks demonstrate dramatic effects of pressure fluctuation. Figure 4 shows typical growth behaviour of cracks in a full-scale test. In such tests, sections of full-size pipes containing sharp fatigue pre-cracks were

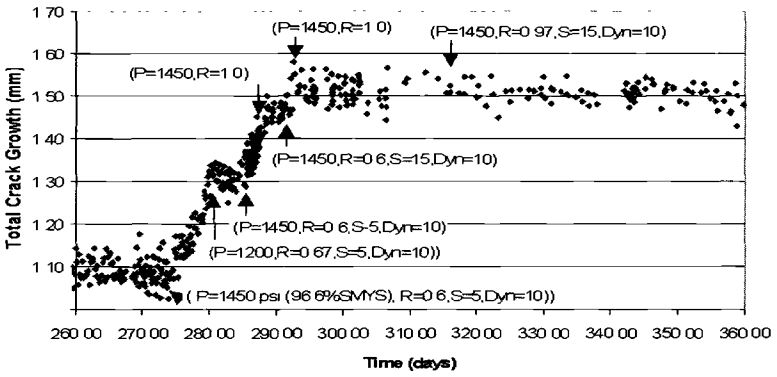


Figure 4 Typical growth behaviour of cracks during full-scale tests showing the effect of pressure fluctuation. ("P"- pressure in psi, "S" - static hold period (min.) and "Dyn" - Dynamic load period (min.))

buried in soil, some in clay [3] and the others in a gravel-type soil [4], and then loaded hydraulically under a cyclic saw-tooth loading spectrum comprised of realistic R-values, frequency and in some cases realistic maximum stresses. The load spectrum was designed to include the fluctuating loading conditions in real pipelines, although with some acceleration in terms of a somewhat accelerated load cycle and higher than design maximum stress. A direct current potential drop (DCPD) technique with a detection resolution of about 30 μm was used to monitor the crack depth [3].

At a pressure equivalent to 96.6% of the SMYS of the X-60 pipe used (1450 psi), the crack grew when R=0.6. However, growth could not be detected when the loading changed to static (R=1.0) or quasi-static (R=0.97). Results for the X-52 pipes are similar with respect to the effects of pressure fluctuation. Significant crack growth was measured for stress levels up to 80% of actual yield with R in the range of 0.6 to 0.9 [4].

When stress corrosion cracks are found on a particular pipeline, it is likely that cracks of various lengths and depths exist on the system, with the maximum crack depth being determined by the age of the pipeline and the yearly crack growth rate. The effects of a particular pressure fluctuation event on SCC would vary with crack size. One approach that allows a systematic evaluation is to examine the dependence of the crack growth rate on the mechanical crack driving force, and then the effect of a pressure variation can be assessed on the basis of the change in the driving force associated with this variation, and the rate at which this change occurs.

In the CANMET studies on crack growth behaviour, the crack growth rate data such as those included in Figure 4 are analyzed and plotted as a function of the time rate of J. A typical result of this transformation is shown in Figure 5.

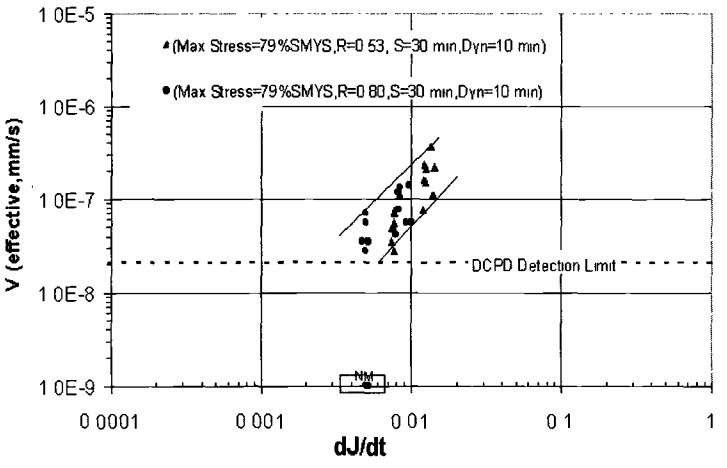


Figure 5 Variation of crack growth rate as a function of the time rate of J. ("S" - static hold period (min.) and "Dyn" - Dynamic load period (min.))

It is shown that the growth rate varies almost linearly with the time rate of J on the log-log plot. It implies that when the severity of pressure fluctuation is reduced, by reducing the magnitude of the excursion in the pressure, the growth rates of existing cracks would decrease. Assuming a continued linearity, under the extreme circumstance of a static load, cracks should tend to become effectively dormant.

The Effects of Stress on the Growth of Circumferential SCC

In the case of circumferential cracking, the driving force is in the axial direction of the pipe, which is largely due to such secondary stresses as bending stress or axial tension caused by ground movement. The characteristics of circumferential cracking are described in a review by Sutherby [*12*], which includes a rupture on a SNAM pipeline located in southern Italy [*13*], and in a recent CANMET investigation report on the St. Norbert (Manitoba, Canada) failure [*14*], which occurred at a river-crossing.

The failure in southern Italy [*13*] and near St. Norbert [*14*] both involved axial stress in excess of the SMYS level of the respective linepipe. In the seven failures that occurred in Alberta, it was believed that the axial stress at the failure sites was also close to or greater than the SMYS of the steel. Indeed, over half of the cases were associated with denting or buckling of the pipe in the cracked region [*12*].

One common feature of these circumferential cracks, as shown in the pertinent fractographs of the fracture surfaces, is that the overall crack growth was distinctly discontinuous. That is, the cracks seemed to grow for some distance, became dormant for a considerable length of time, and then grew again. Such "cycles" of growth and arrest were clearly observed in the St. Norbert case.

Figure 6 is a close-up view of the transition point between the end of the previous growth cycle and the most recent growth. While the fracture surface of the recent growth (at "B") is characterized by a clean quasi-cleavage topography, the zone of prior growth

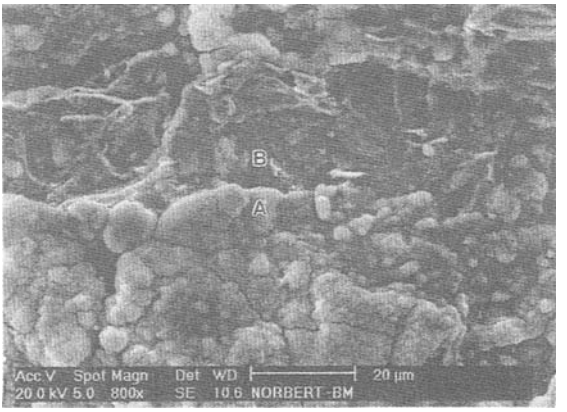


Figure 6 Close-up view of the transition point between previous crack growth (A) and recent crack growth (B).

(at "A") was covered with a thick layer of corrosion product or deposit. This means that the crack was dormant for some time before it was active again, which, during the most recent growth, resulted in the crack reaching the critical depth for unstable propagation. On the macroscopic level, the overall crack depth consisted, apparently, of six cycles of growth events, with well-defined arrest markings between them, as seen in Figure 7.

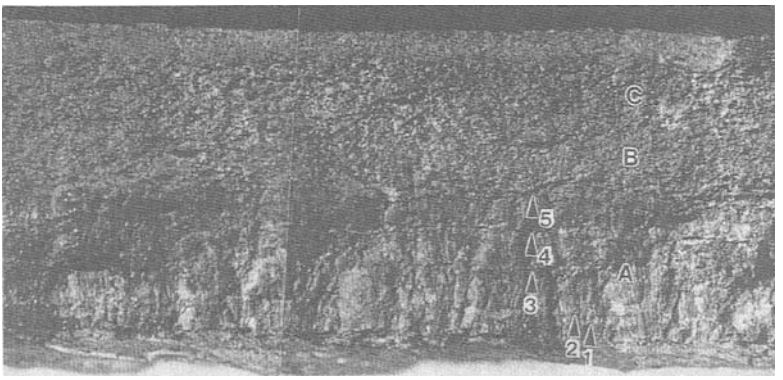


Figure 7 A macro-fractograph taken from the St. Norbert failure showing the various growth periods separated by crack arrest markings.

For the St. Norbert case there is sufficient geotechnical data to suggest that the sliding of the clay soil on the river bank occurred in bursts when the water level in the river rose above a certain threshold. In the past several years, this threshold was surpassed in late spring when the run-off from the melting snow poured into the river. Similarly, in the case of the SNAM line in Italy, the pipe was found, from the readings of the strain gauges instrumented on the pipe, to undergo a period of elongation at relatively high strain rate during the yearly rainy season [*13*].

Since the sliding movement of the soil does not reverse, the overall pattern of axial loading in pipelines associated with the land slide would, under ideal conditions without slippage between the pipe and the soil, be analogous to a monotonic tensile loading with a superimposed low-frequency wave component. When the total load exceeds the yield point of the steel and is sustained for some time, straining due to low-temperature creep could generate sufficient plastic deformation at the crack tip for the growth to resume. For a line pipe steel, room-temperature creep can produce a strain rate in the order of 10^{-6} s^{-1} at a load close to the yield point of the steel [*15*]. Low-temperature creep-induced plasticity is a transient occurrence, and the strain rate in steels like linepipe at pipeline operating temperature decays to an insignificant level within 20 or 30 minutes of the initial loading. In one study [*16*], creep in an X-52 linepipe steel at 70 °F stopped within about 1000 seconds (~17 minutes) of loading to stress levels up to about 65 ksi. However, when the applied stress was held continuously at 95% UTS, creep continued to failure.

For linepipe steels exposed to a near-neutral pH environment, hydrogen-assisted

plasticity can also occur, which may delay the exhaustion of the primary creep. In a recent review on pipeline SCC [*17*], Parkins pointed out, in his discussion of cyclic micro-plasticicty, the relevance of the work on hydrogen-assisted creep by Oriani and Josephic [*18*]. In their creep measurement using a spheroidized mild steel, the rate of room-temperature creep of a prestressed wire, with a pre-strain of 5.5%, was found to increase dramatically when hydrogen gas fugacity was increased to 40 MPa. In fact, strain rates as high as 10^{-6} s^{-1} were reported after an increase in the hydrogen fugacity. However, it is unclear what level of cathodic charging is required to produce such a hydrogen fugacity in linepipe steels. For a 4340-steel polarized in a 0.1N NaOH solution at a potential of -1100 mV (SCE), the surface hydrogen fugacity is only about 0.1 MPa [*19*].

It is believed that some hydrogen is produced in the course of crack propagation in the near-neutral pH environment, as a result of the cathodic reaction occurring on the crack flank as well as at the crack tip. It is possible that this hydrogen could be sufficient to influence the low-temperature creep of linepipe steels. Relevant data in the existing open literature is limited on this subject.

Effects of Compressive Residual Stress Introduced by Hydrostatic Testing

Hydrostatic testing is the primary operational measure for eliminating major axial defects in pipelines. Since hydrostatic tests can be performed at pressure levels of 125% to 140% of the maximum operating pressure, the critical defect size at hydrotest pressure is smaller than that associated with normal service conditions. Because of this difference, hydrostatic testing provides a safety margin against subsequent service failure.

In order to evaluate quantitatively the effects of hydrotesting on SCC growth behaviour, two independent test programs were carried out, one using pre-cracked CT-type specimens [*7*] and the other using an X-52 full-scale pipe [*20*]. In both cases, SCC growth was started by applying cyclic loading and a high load excursion was applied to simulate a field hydrotest event. Following the excursion, the SCC growth rate was measured again for some time until reliable, consistent growth rate data could be obtained.

Figure 8 [*20*] shows a comparison of the crack growth rates for fifteen cracks before and after a hydrotest performed on a full-scale pipe. The highest pressure reached during the hydrotest equaled 108% of the yield stress of the line pipe. All cracks showed detectable reduction in growth rate after the hydrotest. Before the first hydrotest, three cracks showed growth rates in the order of $2.0*10^{-3}$ mm/day or about 0.73 mm per year. The highest growth rates of all 15 cracks, of depths generally between 35 to 50% of the wall thickness of the pipe, was about $0.8*10^{-3}$ mm per day after the test. In fact, two cracks became practically dormant, and their growth rates were not measurable by the crack detection [DCPD] system.

It has been argued that hydrotesting could significantly increase the crack tip radius, thus reducing the effective mechanical driving force for subsequent SCC growth. However, in the full-scale study, metallographic examination suggested this is not the case. Most of the nine cracks examined metallographically following the test program had a crack tip opening of a few microns, usually less than 5 microns. Therefore, the crack was essentially a sharp one for

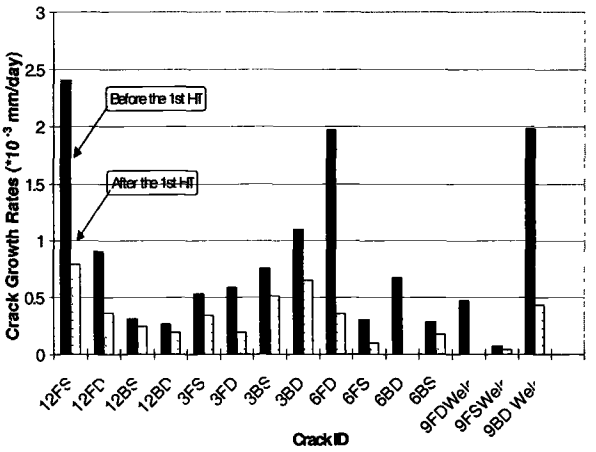


Figure 8 Effects of Hydrostatic Testing on SCC Growth Rates [20].

practical purposes. Again, the effect of hydrogen or the corrosion environment on the behaviour of a crack during and after the overload remains unclear. In one recently reported study using A537 steel (yield strength 380 MPa) [*21*], the behaviours of a fatigue crack during and after a single overload in air, in a 3.5% NaCl solution at the free corrosion potential, and in the same solution but under cathodic polarization were all different. Whereas the instantaneous crack extension upon the overload was significantly greater when the steel was under cathodic polarization, the overall overload retardation zone was much smaller when the steel was tested in the salt solution than in air. The embrittling effect of hydrogen was surmised by the authors to be the reason for this observation.

In the case of linepipe steel in near-neutral pH environment, the retarding effects of hydrotesting on SCC growth may be a result of the creation of compressive residual stress in front of the crack tip. It is well-known that a compressive region is generated at a crack tip by overloading; the compressive stress can be as large as the yield stress [*22*].

Conclusions

The following conclusions can be drawn from the preceding discussions:

1) Depending on the surface geometry of the pipe, the net total stress available for the initiation and growth of stress corrosion cracks may be greater than the nominal operating stress as the presence of residual stress and stress raisers contribute to the local stress.

2) In the laboratory tests carried out using cyclic loading with the maximum load below the yield stress of the steels, stress fluctuation is required for crack initiation and

growth. The crack growth rates seem to increase with the time rate of J on a log-log plot. Thus if the degree of pressure fluctuation is small, as in the case of many gas pipelines, the crack growth rates predicted would be low.

3) When a linepipe steel is stressed close to its yield point in a susceptible environment, cracks may develop with very minor pressure fluctuation. In these cases, low-temperature creep can be a factor in generating the necessary plastic straining and the presence of hydrogen in the steel may facilitate this creep process.

4) Hydrostatic testing retards subsequent crack growth. It is probable that compressive residual stress plays a key role in the retardation. Hydrogen effects may also be involved.

References

[1] National Energy Board, Calgary, Alberta, Canada, *"Stress Corrosion Cracking on Canadian Oil and Gas Pipelines,"* Report # MH-2-95, Nov. 1996.

[2] Fessler, R.R., "Stress Corrosion Cracking," *4th Symposium on Line Pipe Research*, American Gas Association, Arlington, VA, 1969, pp. F1-F18.

[3] Zheng, W., MacLeod, F. A., Revie, R.W., Tyson, W. R., Shen, G., Shehata, M., Roy, G., Kiff, D., and McKinnon, J.,"Growth of Stress Corrosion Cracks in Pipelines in Near-Neutral pH Environment: *The CANMET Full-Scale Tests - Final Report to the CANMET/Industry Consortium*," CANMET/MTL, Ottawa, MTL 97-48(CF), 1997.

[4] Zheng, W., Revie, R. W., Dinardo, O., Macleod, F. A., Tyson, W. R., and Kiff, D., "Pipeline SCC in Near-Neutral pH Environment: Effects of Environmental and Metallurgical Variables," *9th Symposium on Pipeline Research*, AGA, Arlington, VA, 1996, pp. 1471-1478.

[5] Zheng, W., Revie, R. W., Tyson, W. R., Shen, G., and Macleod, F. A., "Effects of Pressure Fluctuation on the Growth of Stress Corrosion Cracks in an X-52 Linepipe Steel," *8th International Conf. On Pressure Vessel Technology*, ICPVT-8, ASME, New York, 1996, pp.321-326.

[6] Wang, Y.-Z., Revie, R. W., Shehata, M. T., Parkins, R. N., and Krist, K., "Initiation of Environment Induced Cracking in Pipeline Steel: Microstructural Correlation," *International Pipeline Conference*, Calgary, Vol. 1, ASME, New York, 1998, pp. 529-542.

[7] Beavers, J.A. and Hagerdorn, E.L., "Near-Neutral pH SCC: Mechanical Effects on Crack Propagation," *9th Symposium On Line Pipe Research*, PRCI, Arlington, VA,1996.

[8] Plumtree, A,, Lambert, S. B. and Sutherby, R., "Stress Corrosion Crack Growth of Pipeline Steels in Simulated Ground Water", in *Corrosion-Deformation Interaction CDI'96*, Nice, France, 1996, Inst. Of Materials, London, 1977,pp.262-269.

[9] Plumtree, A,, Lambert, S. B., and Sutherby, R., "Crack Growth in Stressed Pipeline Steel in NS4 Solution," Paper No. 6.2, *NACE Northern Area Eastern Conference*, Oct. 24-27, 1999, Ottawa, Ontario, Canada.

[10] Parkins, R. N., in "*CEPA Submission to the National Energy Board*", *Proceedings of Public Inquiry Concerning SCC on Canadian Oil and Gas Pipelines, MH-2-95, Vol. 2, Appendix* D, Tab 6. National Energy Board, Calgary, 1996.

[11] Roy, G., Kiff, D., Revie, R. W., Cousineau, E. J.-C., Williams, G., and Sinigaglia, E., "*Residual Stresses in Linepipe Specimens*", MTL Report 94-17(TR), 1994.

[12] Sutherby, R. L., "The CEPA Report on Circumferential Stress Corrosion Cracking," *International Pipeline Conference*, Vol. 1, ASME, New York, 1998, pp. 493-503.

[13] Arrigoni, B., and Sinigaglia, E., "Transverse Stress Corrosion Cracking in a Landslide Area," *Proceedings of the 11th Biennial PRCI-EPRG Joint Technical Meeting*, Arlington, VA, April 7-11, 1997, p. 10-1.

[14] Zheng, W., Shen, G., Gianetto, J. A., Bouchard, R., Brown, J. R., Macleod, F. A., and Tyson, W. R., "Analysis of St. Norbert Failure - Final Report," MTL 96-44 (CF), September, 1996.

[15] Festen, M. M., Erlings, J.G., and Fransz, R.A., "Low-temperature Creep of Austenitic-ferritic and Fully Austenitic Stainless Steels and a Ferritic Pipeline Steel," *Environment-Induced Cracking of Metals*, NACE-10, NACE, 1990, pp.229-232.

[16] Leis, B. N., Walsh, W. J., and Brust, F., W., "Mechanical Behaviour of Selected Line-Pipe Steels," *NG-18 Report No. 192*, Sept. 1990.

[17] Parkins, R. N., "Intergranular and Transgranular Stress Corrosion Cracking of High Pressure Gas Pipelines - Similarities and Differences", in *Proceedings of NACE Northern Area Eastern Conference*, Oct. 24-27, 1999, Ottawa, Ontario, Canada, pp. 1-22.

[18] Oriani, R. A. and Josephic, P. H., "The Effect of Hydrogen on the Room Temperature Creep of Spheroidized 1040-Steel," *Acta Metallurgica*, Vol. 29, 1981, p.669.

[19] Oriani, R. A. and Josephic, P. H., in *Proceedings of the Symposium on Environment-Sensitive Fracture of Engineering Materials*, Foroulis, Z. A., Ed., The Metallurgical Society of the AIME, 1979, pp. 440-450.

[20] Zheng, W., Tyson, W. R., Revie, R. W., Shen, G., and Braid, J.E.M., "Effects of Hydrostatic Testing on the Growth of Stress Corrosion Cracks," *International Pipeline Conference*, Vol. 1, ASME, New York, 1998, pp. 459-472.

[21] Wei, Xuejun, Li Jin and Ke Wei, "Crack Growth Retardation of Single Overload for A537 Steel in a 3.5% NaCl Solution under Cathodic Potential and Free Corrosion Condition," *International Journal of Fatigue*, Vol. 20, no. 3,1998, pp. 225-231.

[22] Broek, D., "*The Practical Use of Fracture Mechanics*," Kluwer Academic Publishers, the Netherlands, 1989, p.139.

Author Index

A

Agarwala, V. V., 382
Agrawal, A. K., 394
Anderko, A., 241
Andersen, G. A., 458

B

Bakker, A., 303
Bayle, B., 343
Brongers, M. P. H., 394

C

Cameron, J., 363
Chou, P. H., 352
Cragnolino, G. A., 273

D

Dean, S. W., 429
De Curiere, I., 343
Devine, T. M., 352
Deydier, D., 210
Dietzel, W., 317
Dunn, D. S., 241, 273

E

Ellis, P. F., II, 363
Engelhardt, G. R., 166
Etien, R., 352

F

Fujimoto, K., 224

G

Gangloff, R. P., 104
George, K., 382

I

Iwamura, T., 224

J

Jones, R. H., 259

K

Kaji, Y., 191
Kane, R. D., 429
Kharin, V., 329
Koch, G. H., 394
Koers, R. W. J., 303
Krom, A. H. M., 303

L

Lee, E. U., 382

M

Macdonald, D. D., 166
Magnin, T., 343
Maldonado, J. G., 429
Maldonado, L., 411
Meunier, M.-C., 210
Miwa, Y., 191
Munson, R. E., 363

N

Nakajima, H., 191
Nishida, S., 224

O

Ovejero, E., 444

P

Pan, Y.-M., 273

R

Raicheff, R., 411
Rebak, R. B., 289
Revie, R. W., 473
Richey, E., III, 104

Copyright© 2000 by ASTM International www.astm.org

S

Sanders, H. C., 382
Scott, P. M., 210
Scully, J. R., 40
Shen, G., 473
Silvestre, S., 210
Sofronis, P., 70
Sridhar, N., 241
Staehle, R. W., 131
Sutherby, R., 473

T

Taha, A., 70
Toribio, J., 329, 444
Trenty, A., 210
Tsuji, H., 191
Tsukada, T., 191
Turnbull, A., 23
Tyson, W. R., 473

W

Wei, R. P., 3

Y

Yonezawa, T., 224

Z

Zheng, W., 473

Subject Index

A

Accelerated testing, 131
Acidic solutions, effect on
  stainless steels, 352
Adsorption, chloride ion, 352
Aging, 224
  material, 3
Aircraft, 3
Alloy 825, 273
Aluminum, 3, 191, 382
Annealing, solution, 224
Anodic dissolution, 444
Anodic polarization, 429
Anodic processes, 363
API 5L grade X56 line pipe
  steel, 303
ASTM Committee G01 on
  Corrosion of Metals, 317
ASTM standards, 317
  A 193, 224
Atomic force microscopy, 394
Axial cracking, 473

B

Baffle/former bolts, 210, 224
Blunting effect, 444
Boiling water reactors, 166, 210
Bolt cracking, 210
Bond percolation, 40
Brass castings, 458

C

Cantilever beam, double, 303
Cathodic hydrogen
  embrittlement, 363
Cathodic processes, 363
Cathodic protection, 241
Cathodic reactions, 411
Caustic cracking, 363
Chemical process industry, 289
Chloride cracking, 289
  stress corrosion, 273, 363, 429
Chloride ion adsorption, 352
Chloride solution, 104, 273
Chromium
  iron-nickel-chromium-
    molybdenum
    alloys, 273
Circumferential cracking, 473
Coating, disbonded, 241
Cobalt alloys, 289
Component design, 259
Component performance, 259
Compressive residual stress, 473
Coolant circuits, power plant, 166
Copper, 343
  valves and fittings, 458
Copper Development
  Association, 458
Crack growth kinetics, 23
Creep, 191
  low temperature, 473
Crevice corrosion, 166
Crystallographic grain
  misorientation, 40
Cyclic loading, 429
Cyclic pre-loading, 329
Cyclic pre-straining, 343
Cyclic strain cracking, 429

D

Damage accumulation, 166
Damage delay, 343
Deformation
  near-tip, 329
  plastic, 394
Design approach, 259
  corrosion based, 131
Diffusion, stress-assisted, 329
Dislocation structure, 343
Displacement
  rising load/rising displacement
    testing, 317
Double cantilever beam, 303
Ductile fracture, 104

E

Electrochemical conditions, 444

Electrochemical film-rupture model, 411
Electrochemical noise analysis, 343
Embrittlement, hydrogen, 23, 40, 70, 104, 303, 363
Environmental definition, 131
Erosion-corrosion, 166
European Structural Integrity Society, 317
Eutectoid steel, 444
Evolution prediction, crack, 23

F

Failure definition, 131
Fatigue
  corrosion, 166, 363
  crack growth, 3, 191, 382
  cracking, corrosion, 429
  dislocation structure, 343
Field performance, 259
Film rupture, 411
Fluid cell, atomic force microscopy, 394
Fracture evolution, 444
Fracture mechanics
  linear elastic, 317
  testing, 273
Fracture toughness, 303

G

Gas industry, 303
Gas lines, 241, 473
Gate valves, 458
Grain boundary, 394
Ground movement, 473

H

Hydrocarbon reformer, steam, 429
Hydrochloric acid, 352
Hydrofluoric acid cracking, wet, 289
Hydrogen, 473
Hydrogen assisted cracking, 329
Hydrogen diffusion, 329
Hydrogen embrittlement, 23, 40, 70, 104, 303, 363
Hydrogen environments, 303
Hydrogen plant, 429
Hydrogen transport, 70
Hydrogen trapping, 40, 70
Hydrostatic test, 473

I

IASCC susceptibility, 191
Initiation strain, crack, 343
Inspection, risk-based, 23
Intergranular cracking, 40, 224, 241, 458
International Organization for Standardization
  ISO TC 156, 317
Iron alloys, 289
  iron-nickel-chromium-molybdenum alloys, 273
Irradiation assisted stress corrosion cracking, 191, 210, 224

J

Japan Atomic Energy Research Institute
  Material Performance Database, 191
JPMD, 191

L

Life cycle management, 3
Life prediction, 3
Light water reactors, 191, 224
Load/displacement testing, 317
Loading
  cyclic, 429
  monotonic, 329
  pre-loading, cyclic, 329
  rate, 104
  rate, effects, 303
Locations for analysis matrix, 131

M

Manganese bronze castings, high strength, 458
Magnesium chloride, 343
Material definition, 131

Material performance, 273
Material Performance Database, JAERI, 191
Materials Technology Institute of the Chemical Process Industries, 289
Mechanistically based probability model, 3
Micromechanical model, 70
Microscopy, 444
  atomic force, 394
  scanning electron, 411
Microstructure, pearlitic, 444
Mode definition, 131
Modeling, 259
  crack growth kinetics, 23
  electrochemical, 411
  intergranular cracking, 40
  mechanistically based probability, 3
  micromechanical, 70
  numerical, 303
  quantitative, hydrogen diffusion, 329
  reactive-transport, 241
  thermodynamic, 241
Molybdenum
  iron-nickel-chromium-molybdenum alloys, 273
Mossbauer analysis, 411

N

Near threshold fatigue crack growth, 382
New York City water supply system, 458
Neutron fluence, 191
Nickel, 224
  alloys, 289, 429
  iron-nickel-chromium-molybdenum alloys, 273
Nitrite, 343
Noise analysis, electrochemical, 343
Nomenclature, environmentally induced cracking, aqueous systems, 363
Nuclear reactors, 166, 191, 210, 224
Nucleation, crack, 394
Numerical model, pipeline steel fracture toughness, 303

O

Oil pipeline, 473
Oxygen, dissolved, 191

P

Path connectivity, crack, 40
Phosphate environment, 411
Pipeline
  API 5L grade X56 line pipe steel, 303
  gas transmission, 241
  stress corrosion cracking, 473
Pitting, 3, 23, 166, 273
Plasticity, 40, 70
  corrosion/plasticity interactions, 343
Power plant coolant circuits, 166
Pre-cracked specimens, 329
Pressure fluctuation, 473
Pressure regulated valves, 458
Pressurized water reactors, 210, 224
Propagation rates, crack, 411

Q

Quantitative model, hydrogen diffusion, 329

R

Radiation-induced segregation, 224
Radioactive waste containers, high level, 273
Raman spectroscopy, surface enhanced, 352
Reactive-transport model, 241
Reactors, 166, 191, 210, 224
Reliability assessment, 3
Repassivation, 273
Rising load/rising displacement tests, 317

S

Scanning electron microscopy, 411, 458
Segregation, radiation-induced, 224
Silicon, 224
Silver, 429
Sodium chloride solution, 382
Sodium thiosulfate, 394
Solute depletion, 40
Solute segregation, 40
Solution annealing, 224
Specimen bending device, 394
Standards (See also ASTM standards), 259, 317
Statistical definition, 131
Steam and hydrocarbon reformer condensates, 429
Steels, 273
  A 193, 224
  austenitic, 191, 210, 352
  chromium, 224
  eutectoid, 444
  high strength, 329
  linepipe, 303, 473
  low alloy, 166, 191
  mild, 411
  stainless, 166, 289
    Type 304, 352, 394
    Type 304L, 429
    Type 316L, 210, 224, 273, 352
Strain rate, crack tip, 104
Strain rate testing, slow, 191, 273, 317
  high strength steel, 329
  mild steel, 411
  stainless steel, 224, 429
  tensile, 343
Stress-assisted diffusion, 329
Stress, compressive residual, 473
Stress corrosion cracking, 166, 259, 289, 429
  chloride, 273, 363
  eutectoid steel, 444
  gas transmission lines, 241
  intergranular, 241, 394, 458
  irradiation assisted, 191, 210, 224
  mechanical aspects, 70
  mild steel, 411
  nomenclature, 363
  nucleation sites, 394
  pipeline steels, 473
  prediction, 131
  rising load/rising displacement, 317
  stainless steel, 343, 352
  titanium alloys, 104
  transgranular, 241, 458
  valves and fittings, 458
  waste container materials, 273
Stress distributions, residual, 329
Stress intensity, 382
  factors, 104
  factors, threshold, 317
Stress, local, 473
Stress, nominal, 473
Stress ratio, 382
Stress strain field, 329
Surface films, 352
Sweep techniques, 411

T

Taxonomy, environmentally induced cracking, 363
Tensile data, 191
Tensile stress, 40
  stainless steels, 352
Thermodynamic model, 241
Threshold fatigue crack growth, near, 382
Threshold stress intensity factor, 317
Titanium alloy, 104
Transgranular stress corrosion cracking, 241, 458
Trapping, hydrogen, 40, 70
Turbine disks, steam, 166

U

U-bend specimens, 289
Ultrasonic nondestructive examination, 210

V

Vacuum, 382
Valves and fittings, water, 458

W

Waste containers, high level radioactive, 273
Water supply system, valves and fittings, 458
Water, trapped, 241
Wedge-loaded specimens, 289

X

X-ray diffraction, 411